NOTE TO USERS

This reproduction is the best copy available.

UMI®

University of Alberta

Microstructure and Property Examination of the Weld HAZ in Grade 100 Microalloyed Steel

by

Kioumars Poorhaydari-Anaraki ©

A thesis submitted to the Faculty of Graduate Studies and Research in partial fulfillment of the requirements for the degree of Doctor of Philosophy

in

Materials Engineering

Department of Chemical and Materials Engineering

Edmonton, Alberta

Fall 2005

Library and
Archives Canada

Published Heritage
Branch

395 Wellington Street
Ottawa ON K1A 0N4
Canada

Bibliothèque et
Archives Canada

Direction du
Patrimoine de l'édition

395, rue Wellington
Ottawa ON K1A 0N4
Canada

0-494-08718-8

Your file Votre référence
ISBN:
Our file Notre reference
ISBN:

NOTICE:
The author has granted a non-exclusive license allowing Library and Archives Canada to reproduce, publish, archive, preserve, conserve, communicate to the public by telecommunication or on the Internet, loan, distribute and sell theses worldwide, for commercial or non-commercial purposes, in microform, paper, electronic and/or any other formats.

The author retains copyright ownership and moral rights in this thesis. Neither the thesis nor substantial extracts from it may be printed or otherwise reproduced without the author's permission.

AVIS:
L'auteur a accordé une licence non exclusive permettant à la Bibliothèque et Archives Canada de reproduire, publier, archiver, sauvegarder, conserver, transmettre au public par télécommunication ou par l'Internet, prêter, distribuer et vendre des thèses partout dans le monde, à des fins commerciales ou autres, sur support microforme, papier, électronique et/ou autres formats.

L'auteur conserve la propriété du droit d'auteur et des droits moraux qui protège cette thèse. Ni la thèse ni des extraits substantiels de celle-ci ne doivent être imprimés ou autrement reproduits sans son autorisation.

In compliance with the Canadian Privacy Act some supporting forms may have been removed from this thesis.

While these forms may be included in the document page count, their removal does not represent any loss of content from the thesis.

Conformément à la loi canadienne sur la protection de la vie privée, quelques formulaires secondaires ont été enlevés de cette thèse.

Bien que ces formulaires aient inclus dans la pagination, il n'y aura aucun contenu manquant.

Canada

I dedicate this thesis to my beloved parents,

Fereshteh and Kaykhosro.

If it were not for their love and support,

I would not be able to achieve this.

Abstract

The microstructure and mechanical property variations across different regions of the heat-affected zone (HAZ) of a Grade 100 microalloyed steel were examined for a range of heat inputs from 0.5 to 2.5 kJ/mm. Autogenous gas tungsten arc welding was performed on plates of Grade 100 steel to create the HAZ. The weld thermal cycles were recorded by embedding thermocouples at different locations in the plates. Examination of precipitate alterations (dissolution, coarsening and reprecipitation) was carried out theoretically and/or experimentally using transmission electron microscopy (TEM). Iron matrix phase transformations and grain size changes were examined with optical microscopy as well as TEM (both thin foils and carbon replicas). Hardness measurements (macro-, micro- and nano-hardness) were mainly used for examination of mechanical properties across the HAZ.

Hardness measurements across the HAZ showed hardening in 0.5 kJ/mm weld samples and softening in the 1.5 and 2.5 kJ/mm weld samples. This was mainly due to the difference in cooling rates, since fast cooling results in microstructures with finer structures (especially grain size) and higher levels of solutes and sub-structure in the matrix. The coarse-grained HAZ (CGHAZ) had a higher hardness relative to the fine-grained HAZ (FGHAZ), regardless of the heat input, due to the formation of bainitic and martensitic fine structures (laths/plates) inside large prior austenite grains. The CGHAZ-0.5 kJ/mm consisted of packets of untempered lath martensite and coarse regions of autotempered martensite or aged massive ferrite. Increasing the heat input to 1.5 and 2.5 kJ/mm resulted in mainly bainitic microstructures (e.g., granular bainite) with some acicular ferrite and grain-boundary ferrite in the CGHAZ. The FGHAZ was mainly made up of polygonal ferrite, with considerable amounts of bainitic ferrite in the case of the 0.5 kJ/mm weld sample. Nb-rich carbides mostly survived the thermal cycles experienced in FGHAZ, but were dissolved in the CGHAZ due to exposure to higher temperatures. Ti-rich nitrides mostly survived even in the CGHAZ, but they had limited contribution to grain growth control due to their coarse distribution in the base metal. Transformation twins were observed in some regions across the HAZ. Their formation is believed to relieve high thermal, solidification-induced and transformation-induced stresses, at places where deformation by slipping was not achievable.

Acknowledgements

The author wishes to thank Professor D.G. Ivey as the main supervisor, Professor B.M. Patchett as the co-supervisor (prior to his retirement) and Professor Emeritus M.L. Wayman as the member of supervisory committee (prior to his retirement) for this research project. Their contributions to the development of this thesis through guidance and discussions over the past few years are greatly appreciated. The author also wishes to thank Professor T.H. Etsell and Dr. W. Chen, as the replaced members of the supervisory committee, for their kind acceptance of reviewing and recommending the thesis for defence. Thanks also goes out to the members of the IPSCO research group, in particular Professor H. Henein, for their comments during our monthly meetings. The author wishes to thank the National Sciences and Engineering Research Council (NSERC) of Canada and IPSCO Inc. for their financial support of this project.

The success of the experimental portion of this research is partly owed to the assistance and support of the technicians in the department of Chemical and Materials Engineering, University of Alberta, in particular Clark Bicknell for welding, Les Dean for writing the LabVIEW 5.0 code, Walter Boddez for discussions on thermocouple selection and purchasing and Bob Konzuk and Shiraz Merali for advice in heat treatment and furnace set up. Assistance of Dr. X. Wang, for carrying out nano-hardness measurements, is also appreciated.

Table of Contents

Chapter 1: Introduction 1
- 1-1. Overview 1
- 1-2. Objectives and methodology 1
- 1-3. Thesis format and layout 2

Chapter 2: Grade 100 steel 3
- 2-1. Introduction 3
- 2-2. Microalloyed steels 3
  - 2-2-1. Classifications 3
  - 2-2-2. Applications 3
- 2-3. Production aspects of Grade 100 4
  - 2-3-1. Chemical composition and effect of alloying elements 4
  - 2-3-2. Thermo-mechanical controlled processing (TMCP) 8
  - 2-3-3. Microstructural developments 10
    - 2-3-3-1. Precipitation 10
    - 2-3-3-2. Iron matrix phase transformation 10
- 2-4. Properties of Grade 100 12
  - 2-4-1. Mechanical Properties 12
    - 2-4-1-1. Strength 12
    - 2-4-1-2. Toughness 13
  - 2-4-2. Weldability 13
  - 2-4-3. Susceptibility to HAC and HIC 13
  - 2-4-4. Reaction to heat treatments 14
    - 2-4-4-1. Full annealing 14
    - 2-4-4-2. Quenching 14
    - 2-4-4-3. Sub-critical aging 15
- 2-5. Summary 16

Chapter 3: Welding and HAZ 19
- 3-1. Introduction 19
- 3-2. Welding processes 19
- 3-3. Weld structure 20
  - 3-3-1. HAZ of single-pass welds 21
    - 3-3-1-1. Partially melted zone 22
    - 3-3-1-2. Coarse-grained HAZ 22
    - 3-3-1-3. Fine-grained HAZ 22
    - 3-3-1-4. Inter-critical HAZ 23
    - 3-3-1-5. Sub-critical HAZ 23
  - 3-3-2. HAZ of multi-pass welds 23
- 3-4. Welding considerations 24
  - 3-4-1. Preheating 24
  - 3-4-2. Post-weld heat treatment 25
- 3-5. HAZ sample making 25
- 3-6. Summary 26

Chapter 4: Thermal analysis of welding in the HAZ 29
- 4-1. Introduction 29
- 4-2. Historical background 29
- 4-3. Theoretical approach 30

4-3-1. Heat source energy 30
4-3-2. Heat input 30
4-3-3. Thermal efficiency 31
4-3-4. Rosenthal's equations for 2D and 3D conditions 32
4-3-5. Method of weighting for intermediate-size plates 33
4-3-6. General form of cooling time equation 35
4-4. Experimental procedure 36
4-5. Results and discussion 38
4-5-1. Weighting factors 38
4-5-2. Cooling time / cooling rate 41
4-5-3. Increase in plate temperature or heat accumulation effects 41
4-5-4. Instantaneous cooling rate 42
4-5-5. Solidification cooling time 43
4-5-6. Transformation heat release 43
4-5-7. Effect of radial position 43
4-5-8. Effect of heat input 43
4-5-9. Effect of plate thickness 43
4-5-10. Peak temperature profiles 45
4-5-11. Estimation of T-t curves 48
4-5-12. Heating rate 55
4-5-13. Thermal stresses 55
4-6. Summary 55

Chapter 5: Precipitate analysis in the HAZ 58
5-1. Introduction 58
5-2. Microalloy precipitates 58
5-2-1. Chemical composition and crystal structure 58
5-2-1-1. Niobium compounds 58
5-2-1-2. Titanium compounds 58
5-2-1-3. Vanadium compounds 59
5-2-2. Size, morphology and interface with iron matrix 59
5-2-3. Precipitate stability and solubility products 60
5-2-4. Microalloy precipitates and TMCP 62
5-2-4-1. As-cast precipitation 63
5-2-4-2. Reheating precipitation 63
5-2-4-3. Strain-induced precipitation 63
5-2-4-4. Interphase precipitation 63
5-2-4-5. General precipitation 64
5-2-5. Microalloy precipitates and HAZ 64
5-2-5-1. Titanium carbonitrides 65
5-2-5-2. Niobium carbonitrides 65
5-2-5-3. Titanium-Niobium carbonitrides 65
5-2-5-4. Vanadium carbonitrides 66
5-3. Precipitation in Grade 100 66
5-3-1. Thermodynamic calculations 66
5-3-2. Other considerations (kinetic effects) 68
5-4. Precipitate alterations in the HAZ 70
5-4-1. Particle dissolution 71
5-4-1-1. Non-equilibrium solubility curves 71
5-4-1-2. Effective temperature and time for a weld thermal cycle 72
5-4-2. Particle coarsening 75
5-4-3. Particle reprecipitation 79
5-5. Precipitate quantification 79
5-5-1. Quantification problems 79
5-5-2. Other analytical methods than TEM replicas 81

5-5-3. Modification of the existing theories 82
    5-5-3-1. Matrix with one type/size-range of particles 82
    5-5-3-2. Matrix with more than one type/size-range of particles 83
5-6. Experimental procedure 84
5-7. Results and discussions 85
5-7-1. Qualitative analysis of precipitates in different sub-zones 85
    5-7-1-1. BM 86
    5-7-1-2. ICHAZ 90
    5-7-1-3. FGHAZ 97
    5-7-1-4. CGHAZ 102
5-7-2. Quantitative results in the BM and the FGHAZ 111
    5-7-2-1. Size distributions 111
    5-7-2-2. Volume fractions 114
5-8. Summary 114

Chapter 6: Phase transformations and grain growth in the HAZ 118
6-1. Introduction 118
6-2. Phase transformation 118
6-2-1. Reaustenitization 118
6-2-2. Retransformation 119
    6-2-2-1. Ferrite 119
    6-2-2-2. Pearlite 122
    6-2-2-3. Bainite 123
    6-2-2-4. Martensite 125
6-2-3. Twinning 128
    6-2-3-1. Introduction to twinning 128
    6-2-3-2. Different types of twinning 130
    6-2-3-3. Twinning in the HAZ 132
    6-2-3-4. Effect of twinning on mechanical properties 133
6-2-4. Microstructural examination of the HAZ in low-C microalloyed steels 133
6-3. Grain growth 135
6-3-1. Grain growth kinetics 135
6-3-2. Grain growth inhibition 136
6-3-3. Grain growth in the HAZ 137
6-3-4. Grain coarsening temperature 138
6-3-5. Effect of heat input on grain growth 138
6-4. Experimental procedure 139
6-5. Results and discussions 140
6-5-1. BM phase microstructure 140
6-5-2. Phase microstructure across the HAZ 141
    6-5-2-1. ICHAZ 143
    6-5-2-2. FGHAZ 145
    6-5-2-3. CGHAZ 154
6-5-3. Twinned regions 169
    6-5-3-1. Across the HAZ 169
    6-5-3-2. Simulated samples 169
    6-5-3-3. Final comments regarding twinning 176
6-5-4. Bainitic transformation 180
6-5-5. Grain-size variations across the HAZ 180
6-5-6. Effect of peak temperature on matrix phase structure 183
6-5-7. Effect of heat input on matrix phase structure 183
6-5-8. Advantages of Low-Mag TEM using replicas 184
6-6. Summary 184

Chapter 7: Mechanical analysis 188
7-1. Introduction 188
7-2. Mechanical properties 188
7-2-1. HAZ toughness 188
7-2-2. HAZ toughness improvement 188
7-2-2-1. Refinement of effective grain size 188
7-2-2-2. Decrease of M-A constituents 189
7-2-2-3. Reduction of impurities 189
7-2-2-4. Control of heat input 190
7-3. Mechanical tests 191
7-3-1. Charpy test 191
7-3-2. CTOD test 191
7-3-3. Tensile test 192
7-3-3-1. Sub-size tensile specimens 192
7-3-3-2. Simulated HAZ samples 192
7-3-3-3. Miniature tensile samples 192
7-3-4. Shear-punch test 192
7-3-5. Hardness test 192
7-3-6. Conversion of hardness to other mechanical properties 193
7-4. Experimental procedure 193
7-5. Results and discussions 194
7-5-1. Macrohardness measurements: hardness averages 194
7-5-2. Microhardness measurements: hardness profiles across the HAZ 194
7-5-3. Hardening and softening in the HAZ 195
7-5-4. Nanohardness measurements: hardness contours 195
7-5-5. Maximum hardness in the HAZ 196
7-5-6. Conversion of hardness to tensile parameters 200
7-6. Summary 202

Chapter 8: Correlation between mechanical properties and microstructure 206
8-1. Introduction 206
8-2. Strengthening mechanisms 206
8-2-1. Grain refinement 206
8-2-2. Solid solution strengthening 207
8-2-3. Precipitation hardening 207
8-2-4. Dislocation hardening 208
8-2-5. Other mechanisms 208
8-2-6. Combined strengthening effects 209
8-3. Correlation between yield strength and microstructure of BM 209
8-3-1. Grain-size strengthening 209
8-3-2. Solid solution strengthening 209
8-3-3. Precipitation hardening 209
8-3-4. Texture hardening 209
8-3-5. Combined strengthening effects in Grade 100 210
8-4. Correlation between hardness and microstructure in the HAZ 210
8-4-1. ICHAZ 211
8-4-2. FGHAZ 211
8-4-3. CGHAZ 214
8-5. Martensite strength 215
8-6. Summary 216

Chapter 9: Concluding remarks 218
9-1. Introduction 218

9-2. General discussion and conclusions 218
    9-2-1. Overview 218
    9-2-2. General discussion 218
    9-2-3. Property assessment of the HAZ and the effect of heat input 219
    9-2-4. Composition effects 219
9-3. Novel methods and achievements 220
9-4. Future work 221

List of Tables

Table 2-1. Chemical composition (wt%) of Grade 100 microalloyed steel produced by IPSCO......4
Table 2-2. Tensile properties of Grade 100 12
Table 2-3. Tensile properties of heat-treated samples of Grade 100.. 15

Table 4-1. Typical values of nominal heat input for different processes.................................. 31
Table 4-2. Definition, units, and values of parameters used in Equations 4-3 to 4-13................. 33
Table 4-3. Values of n, m and F_t in Equation 4-31.. 36
Table 4-4. HAZ widths and weighting factors for three weld samples...................................... 40
Table 4-5. Heating rate, cooling time and cooling rate for three weld samples.......................... 41
Table 4-6. Austenite transformation temperature during cooling in the CGHAZ......................... 43
Table 4-7. Values of 5 points representing the dwell part of the modelled thermal cycle.............. 50
Table 4-8. Time above 900°C for several thermal cycles... 50

Table 5-1. Values of solubility product constants used in this study for several compounds......... 60
Table 5-2. Amount of precipitation (wt%) of TiN and matrix composition upon cooling............. 66
Table 5-3. Fraction of different elements precipitated as revealed by chemical dissolution methods.69
Table 5-4. Volume fraction (f_V) estimation for different precipitates...................................... 70
Table 5-5. Volume fraction estimation for fine precipitates... 70
Table 5-6. Approximate values of activation energy for diffusion of various metal atoms............ 71
Table 5-7. Estimation of coarsening of TiN particles based on the initial particle size................. 79
Table 5-8. Volume fraction of different types of precipitates in Grade 100 steel.........................80
Table 5-9. Fine-precipitate size measurements in BM (different condition) and FGHAZ (several heat inputs)..113
Table 5-10. Comparison of volume fraction values for NbC (<5 nm) obtained with different assumptions, ...114

Table 6-1. Twin planes and twin directions for different crystal structures.............................. 129
Table 6-2. Mean linear intercepts, i, measured at different magnifications for the BM and FGHAZ of Grade 100 steel.. 183

Table 7-1. Average macrohardness numbers obtained at the mid-plane of each sub-region........... 194
Table 7-2. Average nanohardness numbers obtained from the center of each sub-region for a weld section with a heat input of 0.5 kJ/mm...196
Table 7-3. Hardness variation in CGHAZ for low values of heat input...................................... 198
Table 7-4. Mechanical properties estimated based on hardness measurements and Equations 7-1 to 7-4 200
Table 7-5. Mechanical properties obtained experimentally from tensile tests.......................... 201

Table 8-1. Solid solution strengthening coefficients in α-iron.. 207
Table 8-2. Solid solution strengthening contribution of each element in Grade 100.................... 209
Table 8-3. Estimated values for the strengthening contribution of different mechanisms............. 210

List of Figures

FIG. 2-1. Schematic showing the effect of (a) heat input, and (b) microalloying elements and prior austenite grain size on the CCT curve........ 5
FIG. 2-2. Effect of N level on HAZ toughness in 0.1%V steel........ 8
FIG. 2-3. Schematic illustration of thermomechanical processing for Grade 100........ 9
FIG. 2-4. CCT diagram of Grade 100 steel obtained based on cooling from the controlled rolling temperature of 850°C........ 11
FIG. 2-5. Hardness variation of different phases obtained from the CCT diagram of Fig. 2-4........ 11
FIG. 2-6. Stress-strain curve obtained from the tensile test of Grade 100........ 12
FIG. 2-7. Effect of quenching and annealing on the flow curves for Grade 100........ 15
FIG. 2-8. Sub-critical aging of Grade 100; aging time 1 hr........ 16

FIG. 3-1. Classification of the most common welding processes........ 19
FIG. 3-2. Schematics of two arc welding processes: a) Gas tungsten arc welding; b) submerged arc welding........ 20
FIG. 3-3. The two types of pipe making: a) UOE/ERW; b) spiral........ 21
FIG. 3-4. Schematic illustration of the main three zones in the weld........ 21
FIG. 3-5. Schematic diagram of different weldment zones and their corresponding positions on the Fe-Fe_3C equilibrium diagram for a given carbon concentration of 0.15%........ 22
FIG. 3-6. Schematic illustration of the effect of multi-pass welding on HAZ microstructure........ 24
FIG. 3-7. Vector diagram of factors affecting toughness in C-Mn-Nb weld metal........ 25
FIG. 3-8. a) Schematic of a weld section in transverse and longitudinal directions. b) Macrostructure of 0.5 kJ/mm longitudinal weld section; hardness mapping indentations are also visible........ 26

FIG. 4-1. a) Thermocouple/plate attachment on the bottom of the plate (the picture is taken after the welding); b) The GTA welding setup........ 37
FIG. 4-2. The electrical configuration for data acquisition during welding........ 37
FIG. 4-3. Plunging test for a bare thermocouple junction........ 38
FIG. 4-4. Transverse section of a 0.5 kJ/mm weld sample showing the location of a thermocouple tip in the HAZ. The red background area is Bakelite used for metallographic mounting. The other regions are base metal (BM) and weld metal (WM)........ 38
FIG. 4-5. Actual thermal cycles at four locations along the weld run with various depths for three nominal heat input weld samples: a) 0.5 kJ/mm; b) 1.5 kJ/mm; c) 2.5 kJ/mm........ 39
FIG. 4-6. Variation of HAZ width with heat input. The experimental values lie between the upper- and lower-bound lines (thin- and thick-plate solutions) predicted from the Rosenthal's theory........ 40
FIG. 4-7. As-welded plates for two values of heat input: 0.5 kJ/mm (left) and 2.5 kJ/mm (right). Note the increase in the HAZ width in the higher heat input weld as the welding process proceeded........ 42
FIG. 4-8. Effect of heat input on cooling time (d = 8 mm; η = 0.75)........ 44
FIG. 4-9. Effect of plate thickness on cooling time (q/v = 0.5 kJ/mm; η = 0.75)........ 44
FIG. 4-10. Calibrated peak temperature profiles for a nominal heat input of 0.5 kJ/mm. The weighted profile is plotted along with the thick- and thin-plate solutions........ 45
FIG. 4-11. Peak temperature profiles for three different weld samples: a) 0.5 kJ/mm; b) 1.5 kJ/mm; c) 2.5 kJ/mm........ 47
FIG. 4-12. Thermal cycles for two locations, one reading a peak temperature expected from the thermocouple location (TC4) and one reading a peak temperature ~250°C lower than the temperature expected (TC3)........ 47
FIG. 4-13. Peak temperature profiles weighted and fitted for three different weld samples (heat input values of 0.5, 1.5 and 2.5 kJ/mm)........ 48
FIG. 4-14. Thermal cycles at selected peak temperatures as predicted by thick- and thin-plate solutions and as obtained experimentally: a) 0.5 kJ/mm; b) 1.5 kJ/mm; c) 2.5 kJ/mm........ 50

FIG. 4-15. Thin-plate solution predictions with weighted values of cooling time....................... 51
FIG. 4-16. A selected thermal cycle for modelling: some points are chosen from the actual high-resolution curve to form a simplified curve.. 51
FIG. 4-17. The thermal cycle divided into three parts: heating, dwell time around peak temperature, and cooling.. 52
FIG. 4-18. The modelled and estimated thermal cycles at several locations (T_P) across the HAZ for three heat inputs.. 53
FIG. 4-19. The thermal cycles for the same peak temperature for different values of heat input: a) the actual cycles experimentally obtained for a $T_P \approx 1435$°C; b) the modelled and estimated thermal cycles for a $T_P = 1100$°C.. 54
FIG. 4-20. The weld strips cut out of the plates after the welding for two values of heat input: 0.5 kJ/mm (above) and 2.5 kJ/mm (below). Note the considerable deflection for the case of the low heat input.. 56

FIG. 5-1. Solubility products for carbides and nitrides as a function of temperature: a) in ferrite (25-695°C); b) in austenite (840-1410°C)... 61
FIG. 5-2. Solubility diagram showing the stoichiometric ratio between V and N..................... 62
FIG. 5-3. Aluminium extraction replicas showing: a) the dendritic shape of as-cast Nb-Ti carbonitrides; b) the cubic shape of the substitute precipitates in (a) after reheating at 1300°C for 1 h.... 63
FIG. 5-4. TEM samples showing fine precipitation through different mechanisms: a) a carbon extraction replica showing strain-induced NbC after a prestrain of 0.3 at 950°C followed by holding for 32 s and quenching; b) TEM-BF image showing interphase NbCN precipitates; c) TEM-DF image showing general NbCN precipitates in ferrite.. 64
FIG. 5-5. Dissolution of complex Ti-Nb(C,N).. 65
FIG. 5-6. Precipitation as a function of temperature for Grade 100 steel based on thermodynamic calculations.. 67
FIG. 5-7. Variation of the content of Ti, Nb, V, Mo, C and N in the matrix as a function of temperature for Grade 100 steel, based on thermodynamic calculations...................................... 67
FIG. 5-8. Non-equilibrium solubility curves for several precipitates in Grade 100 steel.............. 72
FIG. 5-9. Non-equilibrium solubility curves for several fractions of precipitate dissolution for NbC in Grade 100 steel.. 72
FIG. 5-10. Effective peak temperature and time for dissolution of NbC at a Tp = 1468°C........... 73
FIG. 5-11. Effective peak temperature and effective time available for dissolution of NbC at several locations (or several T_P) and for various fractions of dissolution.......................... 74
FIG. 5-12. Superposition of the effective temperature-effective time curves on the non-equilibrium solubility curves for heat inputs 0.5 kJ/mm in Grade 100 steel.............................. 74
FIG. 5-13. The linear relationship between T_P and $T_{P\text{-}Eff}$.. 75
FIG. 5-14. Precipitate dissolution maps for Grade 100 steel shown in two forms...................... 76
FIG. 5-15. Precipitate dissolution profiles across the HAZ in Grade 100 steel for heat inputs of: a) 0.5 kJ/mm; b) 2.5 kJ/mm.. 77
FIG. 5-16. Maximum solute level in the matrix across the HAZ of Grade 100 steel for heat inputs of: a) 0.5 kJ/mm; b) 2.5 kJ/mm.. 78
FIG. 5-17. The solubility of cementite (Fe_3C) in ferrite compared with the solubilities of microalloy carbides.. 80
FIG. 5-18. Schematic suggesting a correction factor of ½ in calculation of N_V (modified from the work of Ashby and Ebeling).. 82
FIG. 5-19. Schematic demonstration of the sampling depth in replica preparation in case of a matrix with one type/size-range of particles.. 83
FIG. 5-20. Schematic demonstration of the sampling depth in replica preparation for the case of a matrix with several types/size-ranges of particles.. 84
FIG. 5-21. Schematic of carbon extraction replica procedure: a) polished surface; b) etched surface; c) carbon coated surface; d) extracted replica with precipitates.................................. 85
FIG. 5-22. Optical image from the BM showing a large TiN particle (~8 μm).......................... 85
FIG. 5-23. Mosaic of TEM micrographs at low magnification from the BM of the Grade 100 steel..86

FIG. 5-24. TEM bright-field (BF) images and EDX spectra from the BM of the Grade 100 steel: a) a BF image of the region indicated in Fig. 5-23 showing some intermediate-size precipitates; b) EDX spectrum from the Ti-rich carbonitride in the inset of (a); c) EDX spectrum from one of the Nb-rich carbonitrides in the inset of (a); d) a BF image showing the dispersion of fine precipitates.......... 87
FIG. 5-25. A BF image from fine particles (a), and the corresponding EDX spectrum (b), obtained by chemical dissolution method.......... 88
FIG. 5-26. Mosaic of TEM micrographs at low magnification from the BM of the Grade 100 steel..88
FIG. 5-27. TEM–BF images and EDX spectrum from the BM of the Grade 100 steel: a) a BF image of the region indicated in Fig. 5-27 showing several cementite precipitates; b) EDX spectrum from the sliver-like precipitates in (a); c) BF image showing a Ti-Nb carbonitride and some very small iron carbides (denoted by arrows); d) a BF image showing dispersion of fine precipitates.89
FIG. 5-28. Mosaics of TEM micrographs from the ICHAZ: a) 0.5 kJ/mm; b) 1.5 kJ/mm; c) 2.5 kJ/mm.......... 91
FIG. 5-29. TEM-replica examination of precipitates in the ICHAZ–0.5 kJ/mm: a), b) and c) BF images showing the intermediate-size precipitates; d) The EDX spectrum from the particle in (c); e) regions of fine irregular precipitates at grain boundaries; f) The EDX spectrum from the particle circled in (e); g) The EDX spectrum from the bare replica; h) The sliver-like Nb-rich particles.......... 93
FIG. 5-30. Fine precipitates in the ICHAZ–0.5 kJ/mm sample: a) BF image; b) SAD pattern from the precipitates in (a); c) DF image from the part of the ring circled in (b); d) EDX spectrum from precipitates in (a); e) DF image under the same condition as (c) but from another region.94
FIG. 5-31. TEM examination of precipitates in ICHAZ-1.5 kJ/mm: a) BF image from an intermediate-size Ti-rich CN; b) SAD pattern; c) EDX spectrum from the particle in (a); d) BF image from an intermediate-size Nb-rich CN; e) and f) BF images of fine precipitates.......... 95
FIG. 5-32. TEM examination of precipitates in the ICHAZ-2.5 kJ/mm: a) and b) BF images showing some intermediate-size Ti-rich precipitates; c–e) BF images from fine precipitates; f) EDX spectrum from the fine particles in (e).......... 97
FIG. 5-33. Mosaics of TEM micrographs from the FGHAZ: a) 0.5 kJ/mm; b) 1.5 kJ/mm; c) 2.5 kJ/mm.......... 99
FIG. 5-34. TEM images of precipitates from the FGHAZ-0.5 kJ/mm: a) and b) BF images, at different magnifications, showing some intermediate-size precipitates; c) partially dissolved precipitate in (b) at higher magnification; d) corresponding DF image of the particle in (c); e) fine precipitates within the grains; f) DF image showing some fine precipitates in (e).......... 100
FIG. 5-35. GIF images of two intermediate-size particle groups: a) TEM-BF image of a partially dissolved Ti-Nb carbonitride; b) TEM-BF image of a Ti-rich cubic particle and two Nb-rich caps attached to it. Note the bright regions in the accompanying GIF images indicate the distribution of the element tagged on the image.......... 101
FIG. 5-36. TEM examination of precipitates in FGHAZ-1.5 kJ/mm: a) BF image showing an intermediate-size Nb-rich carbonitride at a grain boundary; b) BF image showing several intermediate-size Ti-rich carbonitrides; c) and d) fine precipitates at two magnifications.......... 102
FIG. 5-37. TEM-BF images of precipitates in the FGHAZ-2.5 kJ/mm: a) three groups of intermediate-size carbonitrides at grain boundaries; b) magnified region in (a), showing regions of mixed precipitates; c) a grain free of intermediate-size precipitates; d) fine precipitates in the region marked in (c).......... 103
FIG. 5-38. Mosaics of TEM micrographs from the CGHAZ: a) 0.5 kJ/mm; b) and c)1.5 kJ/mm; d) 2.5 kJ/mm.......... 105
FIG. 5-39. TEM replica images of precipitates in the CGHAZ-0.5 kJ/mm: a) partially dissolved intermediate-size precipitates; b) magnified region in (a), showing two Nb-rich carbonitrides and a region of partial dissolution and reprecipitation; c) EDX spectrum from the region marked in (b); d) SAD pattern from the region marked in (b); e) DF image from the part of the rings marked in (d); f) Ti-rich cuboidal particle and a spherical Nb-rich particle; g) matrix of lath martensite devoid of fine precipitates.......... 107
FIG. 5-40. TEM replica images of precipitates in the CGHAZ-1.5 kJ/mm: a) region of mixed precipitation of Fe-rich and microalloy precipitates; b) region with several intermediate-size cubioidal Ti-rich particles; c) region with some intermediate-size Nb-rich particles; d) magnified region marked

in (c) showing spherical Nb-rich carbides; e) matrix with a small amount of fine precipitates; f) matrix with a considerable amount of fine precipitates.. 108
FIG. 5-41. TEM replica images of sliver-like Fe-rich particles in the CGHAZ-1.5 kJ/mm: a) a region with many intragranular precipitates; b) morphology of particles in (a); c) EDX spectrum from the region indicated in (b); d) SAD pattern from the region indicated in (b), showing the particles are cementite.. 109
FIG. 5-42. TEM replica images of precipitates in the CGHAZ–2.5 kJ/mm: a) large TiN particles 1–2 μm in size, some on a prior austenite grain boundary; b) intermediate-size cubioidal Ti-rich particles; c) intermediate-size spherical Nb-rich particles; d) cementite particles; e) matrix with coarsened fine precipitates, especially on lath boundaries; f) matrix with very little fine precipitates.110
FIG. 5-43. Fine-precipitate size distribution in the BM of Grade 100 steel................................ 111
FIG. 5-44. Comparison of size distribution curves expressed in two ways: a) in absolute numbers; b) in relative numbers. The curves represent fine precipitates in the FGHAZ–1.5 kJ/mm..... 112
FIG. 5-45. Effect of aging on the size distribution of fine precipitates in the BM of Grade 100 steel.113
FIG. 5-46. Effect of heat input on the size distribution of fine precipitates in the FGHAZ of Grade 100 steel, as compared with the BM.. 113

FIG. 6-1. A schematic CCT diagram for microalloyed linepipe steels.................................... 118
FIG. 6-2. Polygonal ferrite (PF) in a 0.18%C-1.86%Mn-1%Si-0.73%Mo steel......................... 120
FIG. 6-3. Grain boundary ferrite (GF) in the coarse-grained HAZ of a V-Ti microalloyed steel..... 120
FIG. 6-4. Massive ferrite (MF) in a plain C-Mn steel (0.18 %C and 1.86 %Mn)........................ 120
FIG. 6-5. Widmanstatten ferrite (WF): a) a thin-foil TEM image showing WF and pearlite; b) Schematic illustration of WF formation... 121
FIG. 6-6. Acicular ferrite showing: a) the "basket weave" structure; b) nucleation on an inclusion using thin foil TEM.. 122
FIG. 6-7. ferrite with aligned second phase (AC).. 122
FIG. 6-8. Granular bainite in a low-C HSLA steel: a) OM; b) TEM showing bainite laths (B) coexisting with massive ferrite (MF)... 124
FIG. 6-9. TEM images showing: a) upper bainite; b) lower bainite.. 124
FIG. 6-10. TEM- BF images of a 0.2%C-3.6%Ni steel isothermally transformed at 400°C for 1000s, showing two ferrite morphologies: a) lath-like; b) plate-like.............................. 125
FIG. 6-11. Martensite start temperature (M_s) as a function of carbon content in steels............... 126
FIG. 6-12. Lath martensite (LM) in a low-carbon steel (0.03%C, 2%Mn) : a) OM (100x); b) thin-foil TEM (26000x).. 127
FIG. 6-13. Plate martensite (PM) in a medium-carbon steel (0.57%C): a) OM showing PM, marked *P*, (1000x); b) Thin-foil TEM image showing twinned substructure in a region marked in (a) at a higher magnification (26000x).. 127
FIG. 6-14. Autotempered martensite in the coarse-grained HAZ of a low-carbon, low-alloy steel weldment.. 128
FIG. 6-15. Schematic diagram showing both starting and finishing temperature of twinning (t_s^T and t_f^T) and starting and finishing temperatures for conventional martensite transformation (M_s and M_f) as a function of carbon content... 128
FIG. 6-16. Crystallographic demonstration of twining... 129
FIG. 6-17. Two kinds of twin boundaries and their corresponding energies.............................. 130
FIG. 6-18. The different shapes of transformation twins in high-purity irons and low-carbon steels..131
FIG. 6-19. Dark-field electron micrograph showing mechanical and transformation twins in a low-carbon steel microalloyed with vanadium.. 132
FIG. 6-20. Twinned martensite in the coarse-grained HAZ of a low-carbon HSLA steel weldment (left) and precipitated along ferrite boundaries (right) - dark field TEM images.................... 132
FIG. 6-21. HAZ properties of a low-carbon (0.09%) microalloyed steel, after Thaulow *et al.*: a) The weld CCT diagram; b) simulated CGHAZ microstructure as function of cooling time; c) Variation of notch toughness and hardness in the CGHAZ (T_P= 1350°C) as a function of cooling time; d) variation of transformation temperature and microstructure across the HAZ for a cooling time of 8–9s.. 134

FIG. 6-22. Effect of austenitizing temperature and steel chemistry on austenite grain growth. Heat treatments last for 1 h.......... 136
FIG. 6-23. Effect of heating rate on the grain-coarsening temperature (T_{GC}) for a V-Ti microalloyed steel.
FIG. 6-24. The various steps in making TEM lift-out samples by FIB technique.......... 138
FIG. 6-25. The furnace setup for heat treatment and simulation of the CGHAZ.......... 139
FIG. 6-26. The mill-out location on the sample chosen for preparation of the TEM-FIB sample: a) macrograph; b) micrograph - the location of the mill-out was exactly specified by the cross on the micrograph and by the hardness indentations in a triangular pattern.......... 140
FIG. 6-27. OM from the BM (longitudinal section) at two magnifications.......... 141
FIG. 6-28. Mosaic of TEM replicas from the BM: a) longitudinal section; b) transverse section.... 143
FIG. 6-29. Grain structure of the BM revealed by TEM–replicas: a) longitudinal section; b) transverse section.......... 144
FIG. 6-30. TEM-BF images from FIB samples from BM.......... 144
FIG. 6-31. Optical micrographs from ICHAZ as compared with BM: a) BM; b) ICHAZ–0.5kJ/mm; c) ICHAZ–1.5kJ/mm; d) ICHAZ–2.5kJ/mm.......... 145
FIG. 6-32. Grain structure in the ICHAZ revealed using TEM–replicas: a) 0.5 kJ/mm; b) 1.5 kJ/mm; c) 2.5 kJ/mm. (a) and (b) transverse to rolling; (c) longitudinal to rolling.......... 148
Fig. 6-33. Mosaics of TEM micrographs from the ICHAZ showing retransformed polygonal ferrite at grain boundaries of untransformed bainitic ferrite: a) 0.5 kJ/mm; b) 2.5 kJ/mm.......... 149
FIG. 6-34. TEM-BF images of FIB samples from ICHAZ-0.5 kJ/mm.......... 149
FIG. 6-35. Optical micrographs from the FGHAZ as compared with BM: a) BM; b) FGHAZ–0.5kJ/mm; c) FGHAZ–1.5kJ/mm; d) FGHAZ–2.5kJ/mm.......... 150
FIG. 6-36. Grain structure in the FGHAZ revealed using TEM–replicas: a) 0.5 kJ/mm; b) 1.5 kJ/mm; c) 2.5 kJ/mm.......... 152
FIG. 6-37. TEM-replicas from the FGHAZ comparing the grain structure for two heat inputs: a) 0.5 kJ/mm; b) 1.5 kJ/mm.......... 153
FIG. 6-38. TEM-BF images from FIB samples showing grain and sub-grain structures in the FGHAZ: a–b) 0.5 kJ/mm; c–d) 1.5 kJ/mm; e) 2.5 kJ/mm (a mosaic).......... 155
FIG. 6-39. Optical micrographs from the CGHAZ as compared with the BM: a) BM; b) CGHAZ–0.5kJ/mm; c) CGHAZ–1.5kJ/mm; d) CGHAZ–2.5kJ/mm. Prior austenite grains are visible in the CGHAZ.......... 156
FIG. 6-40. Optical micrographs from the CGHAZ as compared with the BM: a) BM; b) CGHAZ–0.5kJ/mm; c) CGHAZ–1.5kJ/mm; d) CGHAZ–2.5kJ/mm. The lamellar structures within the prior austenite grains are better resolved here.......... 156
FIG. 6-41. Grain structure in the CGHAZ–0.5 kJ/mm revealed using TEM–replicas: a) the grid locations with respect to the fusion line (FL); b–d) Grids R_1–R_3.......... 159
FIG. 6-42. Selected images from the CGHAZ–0.5 kJ/mm revealing different microstructures: a) selected from grid R_2; b) selected from grid R_1; d) selected from grid R_2; e) and f) selected from grid R_3.......... 161
FIG. 6-43. Thin-foil TEM (FIB) showing fine lath martensite in CGHAZ-0.5 kJ/mm.......... 162
FIG. 6-44. Grain structure in the CGHAZ–1.5 kJ/mm revealed using TEM–replicas: a) the grid locations with respect to the fusion line (FL); b–f) Grids R_1–R_5.......... 163
FIG. 6-45. Selected images from the CGHAZ–1.5 kJ/mm, grid R_4 in Fig. 6-40. GF: grain-boundary ferrite; MF: massive ferrite; M: martensite; (L)B: (Lower) bainite; A: retained austenite.......... 164
FIG. 6-46. A FIB-TEM image from the CGHAZ–1.5 kJ/mm showing some cementite particles.... 165
FIG. 6-47. Grain structure in the CGHAZ–2.5 kJ/mm revealed using TEM–replicas: a) a whole grid in the mid width; b–d) selected images from regions 1–3 in (a); e–f) selected images from other grids.......... 168
FIG. 6-48. A FIB-TEM images from CGHAZ–2.5 kJ/mm showing wide plates of bainitic ferrite... 168
FIG. 6-49. FIB-TEM images from the FGHAZ-1.5 kJ/mm: a) two regions of striations; b) SAD from region 2; c) DF image from the spot circled in (b).......... 170
FIG. 6-50. FIB-TEM images from another region in FGHAZ-1.5 kJ/mm: a) before tilting to a [012] zone axis; b) after tilting to a [012] zone axis; c) SAD from the dark region in (b); d) DF image from the spot circled in (c). The arrow in (d) indicates the normal direction to the twin plane..171
FIG. 6-51. A mosaic of FIB-TEM images from a region in FGHAZ-2.5 kJ/mm, which shows twinning.......... 172

FIG. 6-52. FIB-TEM images from the middle of CGHAZ–0.5 kJ/mm: a) A mosaic of TEM-BF images showing several striated regions– The inset shows one of the regions at a higher magnification; b) TEM-BF image from showing striation in low contrast with the matrix; c) TEM BF image after tilting showing striations in high contrast with the matrix.............................. 173
FIG. 6-53. TEM images from another FIB sample from the middle of CGHAZ–0.5 kJ/mm: a) TEM-BF image tilted suitably for SAD; b) SAD pattern from (a); c) DF image from the 200 twin spot shown with an arrow in (b); d) Interpretation and indexing of the spots in (b) as matrix, twin and double-diffraction spots.............................. 174
FIG. 6-54. Optical micrographs from the simulated samples: a) short-time anneal (1150 °C, 4 min); b) long-time anneal (~1225°C, 30 min).............................. 174
FIG. 6-55. BF-TEM micrographs from the first simulated sample (1150°C and 4 min): a) A mosaic showing the grain structure of lath martensite (LM) and massive ferrite (MF); b) several twinned regions; c) A twinned region with SAD pattern in the inset.............................. 175
FIG. 6-56. A mosaic of TEM images showing the microstructure of the FIB sample prepared from the second simulated sample (~1225°C and 30 min). The alternating regions of massive ferrite (MF) and packets of fine lath martensite (LM) are outlined on the schematic inset............ 177
FIG. 6-57. FIB-TEM images from the second simulated sample (~1225°C; 30 min): a) A mosaic of TEM-BF images showing the locations where twins were found; b) a twin region selected for SAD analysis; c) SAD pattern from (b) after proper tilting; c) DF image from the 121 twin spot circled in (c); d) the corresponding BF image of (d).............................. 179
FIG. 6-58. A transition microstructure between pearlite and upper bainite.............................. 180
FIG. 6-59. Grain size variation across the HAZ for two heat inputs of 0.5 and 2.5 kJ/mm............ 181
FIG. 6-60. TEM bright field (BF) low magnification images of replicas prepared from different regions: a) BM-transverse; b) BM-longitudinal; c) FGHAZ-0.5 kJ/mm; d) FGHAZ-1.5 kJ/mm; e) FGHAZ-2.5 kJ/mm; f) the pattern for lines superimposed on the micrographs for grain size measurements.............................. 182

FIG. 7-1. Effect of carbon equivalent on HAZ Charpy toughness of HSLA steels.............................. 189
FIG. 7-2. Effect of cooling time on the CGHAZ Charpy toughness at –40°C for low-carbon microalloyed steels.............................. 190
FIG. 7-3. Microhardness profiles across the HAZ for a range of heat inputs.............................. 194
FIG. 7-4. Hardness mapping indentations– 0.5 kJ/mm.............................. 195
FIG. 7-5. Hardness mapping result for the sample with a heat input of 0.5 kJ/mm.............................. 196
FIG. 7-6. Nanohardness contours for different sub-regions of the weld section with a heat input of 0.5 kJ/mm: a) BM; b) FGHAZ; c) CGHAZ.............................. 197
FIG. 7-7. Variation of martensite hardness with carbon content.............................. 198
FIG. 7-8. Microhardness profiles across the CGHAZ on samples with very low heat input values... 198
FIG. 7-9. Maximum microhardness in the CGHAZ as a function of heat input.............................. 199
FIG. 7-10. Macrohardness variation across the HAZ sub-regions for a wide range of heat input..... 199
FIG. 7-11. The log P-log d curve, resulting in the Meyer parameter, m, from the Meyer equation $P=k.d^m$.............................. 200
FIG. 7-12. The stress-strain curves.............................. 201
FIG. 7-13. Correlation between uniform strain and work-hardening exponent.............................. 202
FIG. 7-14. Stress-strain curves obtained from hardness-based Meyer conversions along with corresponding experimental curves.............................. 202

FIG. 8-1. HAZ profiles showing variations of grain size, hardness, peak temperature and precipitate dissolution (NbC and TiN) across the HAZ of Grade 100 for two heat inputs: a) 0.5 kJ/mm and b) 2.5 kJ/mm.............................. 212
FIG. 8-2. Relationship between Vickers hardness and apparent grain size (mean linear intercept) for the BM of several grades of steel and for the FGHAZ of Grade 100 steel at several heat inputs.............................. 213

List of Symbols and Abbreviations

α	bcc iron
A	Atomic weight; also solubility product constant
A_1	Lower critical temperature (Fe-Fe3C phase diagram)
A_3	Upper critical temperature (Fe-Fe3C phase diagram)
A_C	Coarsening constant
A_{c1}	A_1 temperature upon heating
A_{c3}	A_3 temperature upon heating
AF	Acicular ferrite
AP	Atom probe
A_{r1}	A_1 temperature upon cooling
A_{r3}	A_3 temperature upon cooling
B	Solubility product constant
b	Burgers vector
bcc	Body-centred cubic
bct	Body-centred tetragonal
BM	Base metal
c	Heat capacity
C.E.	Carbon equivalent
CCT	Continuous cooling transformation
CGHAZ	Coarse-grained HAZ
CR	Controlled rolling
CTOA	Crack tip opening angle
CTOD	Crack tip opening displacement
CVN	Charpy V-notch
d	Plate thickness
Δt	Cooling time
Δt_{8-5}	Cooling time from 800 to 500C
E	Voltage
EDX	Energy dispersive X-ray (spectroscopy)
f	Fraction
F	A general function specified by its subscript
f_A	Area fraction
fcc	Face-centred cubic
FGHAZ	Fine-grained HAZ
FIB	Focused ion beam
FIM	Field ion microscopy
f_V	Volume fraction
γ	fcc iron
G	Elastic shear modulus
GF	Grain-boundary ferrite
GIF	Gaton image filter
GMAW	Gas metal arc welding
GTAW	Gas tungsten arc welding
η	Arc/thermal efficiency

HAC	Hydrogen assisted cracking
HAZ	Heat-affected zone
hcp	Hexagonal close-packed
HIC	Hydrogen induced cracking
HSLA	High-strength low alloy
HSMA	High-strength microalloyed
i	Intercept length
I	Current
ICHAZ	Inter-critical HAZ
ICP	Inductively coupled plasma
IRCGHAZ	Intercritically reheated CGHAZ
k_S	Solubility product
λ	Thermal conductivity
L	Interparticle spacing
LBZ	Local brittle zone
LM	Lath martensite
M	Martensite
M	Metal element in precipitate compounds
M-A	Martensite/retained austenite
M_S	Martensite-start temperature
MX	Binary precipitate compound
N_S	Number per unit area
N_V	Number per unit volume
OM	Optical microscopy
OR	Orientation relationship
PAGS	Prior austenite grain size
P_{cm}	Carbon equivalent for low-carbon microalloyed steels
PF	Polygonal ferrite
PM	Plate martensite
θ	A temperature function
q	Welding power
Q	Activation energy
q/v	Heat input
ρ	Density
r	Radial distance from the centreline of the heat source; also particle radius
R	Gas constant
r_0	Initial particle radius
σ	Stress
SANS	Small angle neutron scattering
SAW	Submerged arc welding
SMAW	Shielded metal arc welding
SCC	Stress corrosion cracking
SCHAZ	Sub-critical HAZ
SEM	Scanning electron microscopy
SMYS	Specified minimum yield strength
t	Time

T	Temperature
T_0	Initial temperature
TEM	Transmission electron microscopy
T_{fine}	Temperature below which the fine carbides precipitate
T_m	Melting point
TMCP	Thermo-mechanical controlled processing
T_P	Peak temperature
T_S	Solidus temperature; also dissolution temperature
v	Welding travel speed
W	HAZ width
WF	Widmanstatten ferrite
WM	Weld metal
X	C/N element in precipitate compounds; also particle size
x	Particle size

Chapter 1

Introduction

1-1. Overview

Despite many achievements over the past decades in the development of novel processing methods for production of metallic materials with improved mechanical properties, there has been little development in welding processes to control the microstructural evolution in the weld metal (WM) and the heat-affected zone (HAZ). One significant example of the former from the steel industry was the development of thermo-mechanical controlled processing (TMCP) to control the microstructural evolution in steels. This has resulted in fine-grained microstructures formed by controlled rolling, microalloying and subcooling below the equilibrium temperature for the transformation of austenite to ferrite [1]. Fine-grained microstructures show an excellent combination of mechanical properties, such as strength and toughness. The strength of polycrystalline materials is a function of the grain size, following the well-known Hall-Petch relationship. Fracture toughness and impact transition temperature are also related to grain size [2].

The developments of semi-automated pipeline welding, power beam processes (laser or electron), multi-torch systems, cored wires, etc., have been advances related to speed for economics of construction, while still trying to maintain or improve the integrity of the welds and weld properties [3]. Most of the improvements in weldability, however, have come from modifications in the base metal (BM) and filler metal chemical compositions. Reduction of carbon content in the BM of high-strength low-alloy (HSLA) and microalloyed steels has resulted in increased weldability, by reducing the tendency to formation of untempered or twinned martensite during welding. Microalloying to form carbides and nitrides has contributed to grain refinement through solute drag effects and grain boundary pinning [4]. Introducing oxide-based or nitride-based nucleants into the steel (in the BM and/or the filler metal) has been another method for microstructural control through the formation of acicular ferrite and refinement of the microstructure [5]. It should be added that it is the responsibility of both the steel and welding industries to work together, as the progress of one without the other would not be useful. This becomes important as the high-strength structural steels are increasingly used for welded construction [6].

The WM and HAZ microstructure alterations are mainly a product of thermal processes. The weld zone is very similar to a casting. Metallurgists realized a long time ago that the coarse and inhomogeneous microstructures in the castings are responsible for their poor mechanical properties. The HAZ evolution is due to a rapid and intense thermal cycle [7]. Wrought materials on the other hand, produced by mechanical forming of the cast material, had superior properties due to a higher degree of homogeneity and a finer structure. These essentially set the difference between microstructure and properties in the WM/HAZ and BM. HAZ alterations are of more concern, as no chemical control can be applied there. Austenite grain growth is the major cause of mechanical property deterioration in the HAZ [8]. Therefore in general, there is still a great demand for studies that find ways for improvements in the HAZ properties. This becomes more significant when a new grade of steel (often with higher strength) is produced. These studies should start with characterization of microstructures and properties.

Grade 100 microalloyed steel used in this study is a new grade of high-strength, low-carbon microalloyed steel produced by IPSCO, Inc. The weldability of this steel was studied previously by Hoskins [9]. Although Grade 100 showed a good overall weldability (in particular in terms of strength matching with BM), it demonstrated higher susceptibility to hydrogen cracking when compared with a Grade 80 steel (with lower C and Mn levels) in welded conditions. This was one of the reasons for further microstructural examination of the HAZ of Grade 100 steel. One of the recommendations of the earlier study was investigation of the role of precipitates in conjunction with the iron matrix microstructural alterations during the welding with various heat inputs (0.5–2.5 kJ/mm).

1-2. Objectives and methodology

It was the objective of this project to characterize the microstructural and property changes in the HAZ of Grade 100 microalloyed steel. Of particular interest was understanding precipitate alterations during the weld thermal cycle, as well as their effects on iron matrix microstructure and mechanical properties. Three different analyses were designed:

1) Thermal analysis (experimental and theoretical), to obtain temperature-time characteristics of the weld thermal cycles for various heat inputs and different locations across the HAZ. This was required for analysis of precipitate alterations and interpretation of other microstructural changes.

2) Microstructural examination, in terms of precipitate alterations, iron matrix phase transformation and grain growth. These were carried out by optical microscopy (OM) and transmission electron microscopy (TEM).

3) Mechanical analysis. Mechanical properties were mainly assessed through hardness measurements across the HAZ. For the BM, tensile tests were also performed in addition to the hardness measurements.

Finally, correlation between the microstructure and mechanical properties was to be carried out in the BM and across the HAZ for several heat inputs (0.5–2.5 kJ/mm).

1-3. Thesis format and layout

In this thesis, a paper-based format is adopted and different aspects of characterization of the HAZ are handled in separate chapters. Each chapter starts with an introduction and is followed by background information collected from the literature. If applicable, theoretical calculations, experimental procedure, tests and results, and discussion of the analyses and results are addressed next. These are followed by a short summary and the list of references used in that chapter. Chapter 2 (Grade 100 microalloyed steel) and Chapter 3 (welding and HAZ) introduce the material and how the HAZ is formed, and therefore serve as background information for the analyses of the next chapters. The main analyses in this study include thermal analysis (Chapter 4), precipitate analysis (Chapter 5), iron matrix phase transformation and grain growth (Chapter 6) and mechanical analysis (Chapter 7) in the HAZ of the Grade 100 steel. Chapter 8 aims at connecting the main results of these analyses by correlating mechanical property values (strength and/or hardness) and the microstructure both in the BM and the HAZ. This thesis is wrapped up with the concluding remarks (Chapter 9).

Note, that IPSCO's Grade 100 microalloyed steel used in this study is referred to as Grade 100 steel throughout the thesis and the properties and characteristics of this particular material will be discussed (unless otherwise stated specifically). It is realized that other Grade 100 microalloyed steels produced by other suppliers might have other properties or characteristics. Also note that the compositions will be stated in weight percent (wt%), unless specified otherwise.

This study can be considered as the start of the characterization of the HAZ in Grade 100 microalloyed steel, and by no means is complete. Further study needs to be pursued. Nevertheless, it is hoped that the results of this study will bring a better understanding of the alterations in the microstructure and properties of the HAZ, highlight the points where more study is needed and indicate areas that show promise for development and control of HAZ properties.

References

[1] Gladman, T., 1997, The Physical Metallurgy of Microalloyed Steels, The Institute of Materials, London.

[2] Petch, N. J., 1953, "The Cleavage Strength of Polycrystals," Journal of the Iron and Steel Institute, **174**, pp. 25-28.

[3] Dolby, R. E., 2000, "Joining Issues for New Constructional Steels," Science and Technology of Welding and Joining, **5** (6), pp. 341-346.

[4] Kanazawa, S., Nakashima, A., Okamoto, K., and Kanaya, K., 1976, "Improvement of Weld Fusion Zone Toughness by Fine TiN," Trans. Iron Steel Inst. Jpn., **16** (9), pp. 486-495.

[5] Terada, Y., Chijiiwa, R., Tamehiro, H., Kikuma, T., and Funato, K., 1990, "Titanium-Oxide Bearing Steels for Offshore Structures," 1992, *Proc., HSLA Steels: Processing, Properties and Applications*, The Minerals, Metals & Materials Society, Warrendale, PA, pp. 519-524.

[6] Hulka, K., and Heisterkamp, F., 1998, "Development Trends in HSLA Steels for Welded Constructions," *Proc., Microalloying in Steels*, Materials Science Forum, **284-286**, pp. 343-350.

[7] Easterling, K. E., 1992, Introduction to the Physical Metallurgy of Welding, Butterworth-Heinemann Ltd, Oxford.

[8] Hrivnak, I., 1995, "Weldability of Modern Steel Materials," ISIJ International, **35** (10), pp. 1148-1156.

[9] Hoskins, S. J., 2002, Weldability of Grade 80 and Grade 100 Microalloyed Steels, M.Sc. dissertation, University of Alberta, Edmonton.

Chapter 2

Grade 100 Steel

2-1. Introduction

The material used in this study is a Grade 100 microalloyed steel produced in the as-rolled condition by IPSCO, Inc. Grade 100 steel is a high-strength low-carbon low-alloy structural steel. The designation 100 refers to the specified minimum yield strength (SMYS) in 'ksi' (approximately 690 MPa). The strength, gained through thermomechanical controlled processing (TMCP), is a result of the combination of two microstructural characteristics: small grains of oriented bainitic ferrite and a distribution of fine microalloy carbides and carbonitrides [1].

In this chapter, initially the microalloyed steels are introduced, and then different aspects of steel making applied to Grade 100 are reviewed. Finally, different properties of this steel are discussed. This will form the background information on the material to be used in the analysis of the next chapters.

2-2. Microalloyed steels

Microalloyed steels are a group of high-strength, low-alloy carbon steels, produced in the as-rolled condition [2]. The term '*microalloyed steel*' was first used to address a class of low-carbon high-strength steels, containing a small amount of niobium and/or vanadium [3]. Now, this class definitely includes more elements like aluminium, vanadium and titanium, in amounts of less than 0.1% of each element. So the term 'microalloyed steel' refers to those steels whose strength is increased drastically by addition of a small amount of such elements (like titanium, niobium, and vanadium), through grain refinement and/or precipitation hardening mechanisms [3]. They may also benefit from addition of small amounts of other elements, such as boron and aluminium.

The beneficial properties of microalloyed steels do not mainly originate from their chemistries per se, but from the thermomechanical treatments they undergo throughout processing. Thermomechanical controlled processing (TMCP), which consists of controlled rolling (CR) and interrupted accelerated cooling (IAC or simply AC), has provided "on-line control" of the microstructure and mechanical properties [4-6]. This is perhaps why IAC is also referred to as on-line accelerated cooling (OLAC).

Now microalloy additions have been extended to medium and high carbon steels; the carbon level in microalloyed steels normally varies from a few hundredths of a percent to the eutectoid composition [7]. However, the microalloyed steels used for linepipes are normally characterized by a low carbon content (<0.14%) and total alloy content in the range of 2-3 % [8].

2-2-1. Classifications

As carbon has traditionally been the element by which different grades of steel have been defined, the same classification is still valid in microalloyed steels. So there are three classes of microalloyed steels, i.e., low carbon (<0.2%), medium carbon (0.2-0.5%) and high carbon (0.5-0.8%).

Another classification is according to the main microalloying element(s). Some examples are niobium-bearing microalloyed steel, titanium-bearing microalloyed steel, or titanium-niobium-bearing microalloyed steel.

The other way to address these steels is according to their main/matrix phase, e.g., ferritic-pearlitic microalloyed steel, ferritic-bainitic microalloyed steel, and multiphase microalloyed steel.

A very common designation used in North America, however, is that of the American Petroleum Institute (API), where a number designates the specified minimum yield strength (SMYS) in 'ksi', e.g., X70 or X100 pipeline steels. The designation suggested by Canadian Standards Association (CSA) [9], however, uses "Grade" instead of "X" and the accompanying number designates the SMYS in megapascal. Therefore, CSA Grade 690 would be strength-wise equivalent to API X100 or the Grade 100 designation used in this thesis.

2-2-2. Applications

Modern microalloyed steels have proven to be "the most cost-effective, multipurpose materials" [12]. Examples of microalloyed/HSLA steels application areas are the automotive industry, gas pipelines, mining, naval vessels and offshore platforms [13].

The development of microalloyed steels used for linepipes was based on the need for higher strength, good impact toughness, weldability, resistance to hydrogen assisted cracking and, above all, economy. The increase in the use of oil and gas brought the need for transporting larger volumes over longer distances. Larger diameter pipes, which could tolerate higher transmission pressures, would save a lot of money. A significant weight saving also occurs in applications of high-strength structural steels, used in bridges and vehicle fabrication (typically in truck frames and bodies), which leads to greater payloads and improved fuel economy. Reduction in the fuel consumption has important worldwide environmental as well as political (peace related) benefits too. The increase in strength reduces the tonnage required, which means energy savings in iron extraction and steel refinement. This, as Gladman explains [3], translates into reduced environmental contamination and material conservation.

2-3. Production aspects of Grade 100 steel

2-3-1. Chemical composition and effect of alloying elements

Grade 100 steel is a low-carbon steel microalloyed with Ti, Nb and V. The chemical composition of the Grade 100 steel used in this work is shown in Table 2-1. It contains 0.08% C, 0.01% N and approximately a total of 0.2% Ti, Nb and V as primary microalloying elements.

Table 2-1. Chemical composition (wt%) of Grade 100 microalloyed steel produced by IPSCO [1, 14]

C	Mn	Si	S	P	Ti	Nb	V	Mo	Cr	Ni	Cu	Al	Ca	N
0.08	1.80	0.24	0.001	0.013	0.06	0.09	0.05	0.30	0.2	0.26	0.42	0.05	0.005	0.01

It is obvious now that lowering the carbon content of the base metal has a beneficial effect on the HAZ toughness of microalloyed steels. This can be attributed to a decrease in M-A constituent and an increase in autotempered martensite by an increase in the martensite start (M_S) temperature. However, any reduction in carbon content must be balanced by addition of microalloying elements to achieve the desired microstructure; otherwise sideplate microstructures may develop [13].

It seems that the effect of microalloying elements on microstructure, and consequently the HAZ toughness, can be studied from two angles. One is their effect on the transformation kinetics, and the other is their precipitation effect on the microstructure. In the latter, precipitates may act as precipitation hardening particles, or they may slow austenite grain growth by pinning the austenite grain boundaries.

The effect of alloying elements on the γ/α transformation can be readily seen in Fig. 2-1, where the shift of the continuous cooling transformation (CCT) diagram by each element is shown schematically. The most important elements used in microalloyed or HSLA steels are manganese, copper, boron, nitrogen, vanadium, titanium, niobium, molybdenum and nickel.

Carbon

Carbon, which is normally present in iron for increasing its hardness and/or hardenability, has a primary use for the formation of carbides in microalloyed steels. As mentioned earlier, carbon levels should be kept low for improvement of hydrogen assisted cracking (HAC) resistance and weldability. Carbon content in pipeline applications is recommended to be <0.10%, or even more conservatively between 0.01 and 0.05% [15]. Extremely low carbon content (<0.01%), however, was reported to embrittle the grain boundaries in the HAZ, resulting in intergranular fractures and subsequently deteriorating hydrogen-induced cracking (HIC) and Charpy impact properties, especially in Nb-bearing steels [15]. This, although not clearly explained, was attributed to the effect of Nb and C on the grain boundary strength. It was observed that the fraction of intergranular fracture increased with an increase in Nb content or decrease in C content. This was even found to be more pronounced at high sub-critical reheating temperatures (i.e., 550–700 °C; simulating inter-critically reheated coarse-grained HAZ). Some researchers consider a threshold value of 0.09%C, to avoid the peritectic reaction during solidification, which is believed to be responsible for microsegregation and therefore deterioration of the HAZ toughness [16].

Manganese

Manganese, along with nickel and copper, are austenite formers and therefore suppress the γ/α transformation temperature and slow the rate of transformation [13]. They stabilize the austenite by reducing the nucleation rate for ferrite formation [8]. The lower the transformation temperature, the finer the ferrite grain size and the better the HAZ toughness. These elements, if added in sufficient quantities (especially Mn of 1.5-2.0%), will cause formation of lower transformation temperature products, such as acicular ferrite and bainite. This is why acicular-ferritic steels often contain 1.4-2.0% Mn [8].

To avoid inhomogeneity and anisotropy in mechanical properties of the rolled sheets and the HAZ microstructure, which originate from solidification segregation and banded microstructure in rolling, manganese additions should be limited [13]. Manganese also reduces weldability [17].

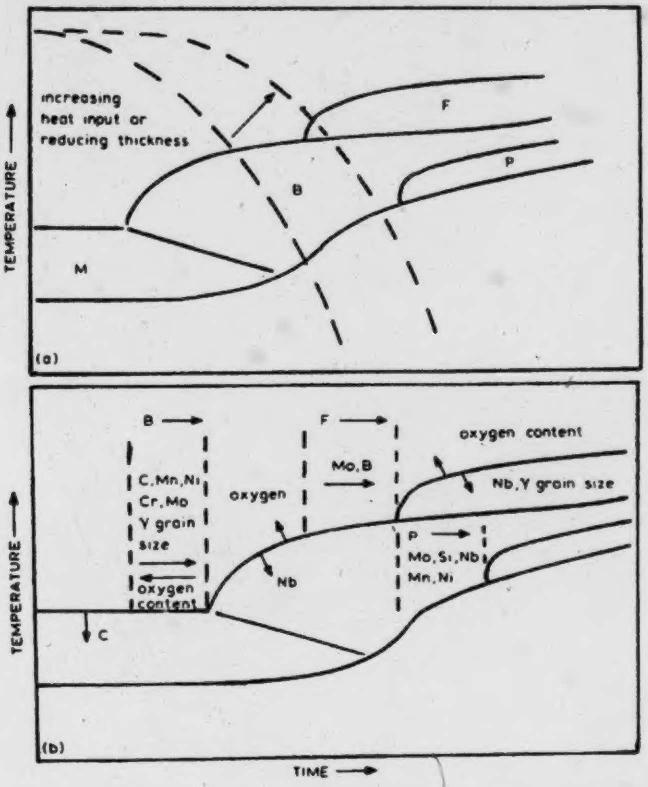

FIG. 2-1. Schematic showing the effect of (a) heat input, and (b) microalloying elements and prior austenite grain size on the CCT curve [13].

Silicon

Silicon is often used in steel making as a deoxidant. Si has a solid solution strengthening effect and in low carbon steels compensates to some degree for the decrease of strengthening due to reduction of carbon [11]. It also increases notch toughness and hardenability. Si increases the carbon equivalent and hence reduces weldability [17].

Nickel

Nickel (0-0.4%) can also enhance low-temperature fracture toughness, though it is not as effective as manganese [8, 13]. Additions of nickel in amounts of about half the copper content are effective in maintaining the surface quality during hot working, which is endangered by the presence of copper (usually >0.5%) which may cause hot shortness [17]. Ni reduces weldability [17].

Copper

Copper in amounts up to ~0.35% is very effective in improving the resistance of carbon and microalloyed steels to atmospheric corrosion [17]. Higher amounts of ~0.5–1.5% are added to microalloyed and HSLA steels because of copper's considerable contribution to strength through precipitation hardening [13, 18]. Copper does not seem to affect the transformation kinetics [8].

Molybdenum

Molybdenum strongly affects the transformation kinetics in the range of 600-700°C. It shifts the ferrite and pearlite curves of the CCT diagram to the right (longer times) and therefore promotes the formation of lower-temperature products like acicular ferrite, bainite, and martensite [13]. Acicular-ferritic steels often contain 0.25-0.35% Mo [8]. Mo improves weldability [17]. It also forms mutually soluble carbides with Nb.

Chromium

Chromium (0-0.3%) seems to promote the formation of low-temperature products by stabilizing austenite and retarding the γ-α transformation [8]. It also improves resistance to abrasion as well as to atmospheric corrosion, but reduces the weldability [17].

Boron

Boron is one of those elements that have received a lot of attention since the 1970's, especially after the introduction of low-carbon bainitic steels. Boron promotes the formation of bainite and martensite by preventing ferrite nucleation at austenite grain boundaries, and, therefore, suppressing the γ/α transformation. To achieve this, boron should not form compounds with N, and therefore addition of Ti and/or Al are necessary in boron-bearing steels, to absorb all N in solution. Boron is known to have a synergistic effect with Mo and Nb on the retardation of ferrite formation [8, 13]. Addition of 10 ppm of boron is enough to suppress ferrite formation in the coarse-grained HAZ.

Addition of a small amount of boron is favourable as it can replace large additions of elements like Mn, Mo and Ni, to obtain fully bainitic steels. This also eliminates the considerable reduction in weldability of the steel because of the presence of Mn, Mo and Ni in those quantities [8].

Titanium

Titanium is frequently used in microalloyed steels because of the high thermal stability of TiN even at peak temperatures above 1300°C. This precipitate effectively restricts austenite grain growth. Furthermore, it has been claimed that sufficient addition of Ti to V-N steels also promotes the formation of fine polygonal ferrite, which makes the "effective grain diameter" smaller, and reduces the amount and size of M-A constituent in the coarse-grained HAZ [19]. These improvements in microstructure increase the impact toughness.

Depending on the level of Ti and N in the steel, TiN may form in the liquid. These particles are usually too large to have any significant grain-boundary pinning effect in austenite. It has been confirmed that the particle size for optimum grain-boundary pinning in austenite is less than 50 nm, and the optimum level of Ti is ~0.015% [20]. Ti content in excess of that required to combine stoichiometrically with N will tie up C at lower temperatures of the austenite region. Ti and Nb carbides are mutually soluble and usually appear as Ti/Nb carbides. These carbides can act as austenite grain refiners. Another compound of interest, used in some Ti-bearing steels for achievement of properties, is TiO_2 that has extremely low solubility even at 1450°C [21].

Niobium

Niobium was the first microalloying element added to steels that made the development of the new group of high-strength low-alloy steels possible. The trials and studies on the effect of Nb additions go back to the 1950's, after the discovery of extensive ore bodies in Canada and Brazil, which dramatically decreased the price of niobium [3]. Small additions of Nb (0.03%) have beneficial effects in steel fabrication when thermomechanical controlled processing (TMCP) is applied, as it dramatically reduces the rate of recrystallization of austenite during hot rolling. Inclusion of Nb is a requirement by steel fabricators in Japan. Some of the benefits, beyond the usual applications of Nb, are control of HAZ softening caused by reduction of the carbon equivalent, effective increase of the steel strength by promoting bainite formation and increase in hot rolling efficiency by extending the non-recrystallization-region temperature range [22]. All this occurs without lowering the HAZ toughness, as the addition is small.

Niobium has considerable effects on microstructure (recrystallization and transformation), both when in solution and when in carbonitride precipitate form. Nb has the most pronounced effect on increasing the no-recrystallization temperature [23]. Both experimental observations and theoretical analyses show that this effect is relatively small when Nb is in solution, compared to the retarding effect of strain induced precipitation of Nb(C, N) [24]. Nb in solution lowers the A_{C3} temperature (8°C per 100 ppm Nb) and reduces the ferrite nucleation rate [8, 13]. By shifting the CCT diagram to longer times and lower temperatures, Nb promotes the formation of Widmanstatten ferrite and bainite in the coarse-grained HAZ [13]. Nb(C,N) on the other hand, may accelerate the γ/α transformation [13]. To benefit from the precipitation effect of Nb, small additions of this element (<0.1%) are sufficient [8].

The promotion of upper bainite formation by the solute Nb is found to be detrimental to toughness, as it increases the "effective grain diameter" in the coarse-grained HAZ [19]. Niobium addition to microalloyed steels may increase the impact transition temperature (reduce toughness) significantly. Only a very small addition of Nb (<0.05%), and only when the carbon content level is very low (e.g., 0.03%), can have no detrimental effect on the HAZ toughness for high heat input welding. For low heat inputs, the detrimental effect of Nb is smaller [21].

Vanadium

Vanadium has greater solubility in austenite than Nb and is more likely to stay in solution before the γ-α transformation [8]. It has two effects on the transformation: one on the primary products and the other on the secondary products. Vanadium promotes the formation of polygonal ferrite and shifts the ferrite nose to higher temperatures and shorter times. On the other hand, it suppresses the bainite and pearlite transformation and therefore promotes the formation of M-A [8, 13]. This property of vanadium has led to the production of a low-carbon Mn-0.45%V steel with a martensite/polygonal-ferrite structure, suitable as an X-70 linepipe steel [8].

VC is the most effective precipitate for precipitation hardening. This is due to the inter-particle spacing of these precipitates, which results from the relatively low precipitation temperature of VC in ferrite. It is found that the precipitation strengthening in V-microalloyed steels (~0.10 %V) greatly increases with the carbon content of the steel; an increase of ~5.5 MPa in strength per 0.01 %C [25].

Nitrogen

N is considered an essential element in microalloyed steels, because of its several beneficial effects as a result of interaction with other alloying elements like V, Ti and Nb. Nitride particles are effective in raising the γ grain growth temperature during reheating and welding, preventing grain growth during rolling, delaying recrystallization, increasing the γ-α transformation ratio and of course in precipitation hardening [26].

However, there is much controversy as to whether or not nitrogen has a detrimental effect on HAZ toughness. It has been reported that free nitrogen and coarse nitride precipitates reduce the HAZ hardness and toughness and, therefore, high nitrogen contents should be avoided. Yet, there are other results that do not completely agree with this, and demonstrate that free nitrogen is not directly responsible for the HAZ properties in Ti-V steels. Careful addition of microalloying elements and control of the welding parameters (selection of the correct heat input to control the cooling rate and the correct number of passes) can result in enhanced toughness even with a high level of N (Fig. 2-2). This is mostly attributed to a fine distribution of TiN precipitates [26]. It is usually recommended that the N content should be above the stoichiometric level for TiN, in order to suppress the grain coarsening in the HAZ and improve the HAZ toughness [25].

Aluminium

Aluminium is commonly added to steel as a deoxidant. There is usually some residual aluminium content (~0.02–0.05%) in the steel. AlN has a very low solubility product in steel. The only common microalloy nitride that has a lower solubility product than AlN is TiN. AlN, with a distinctive hexagonal crystal structure, forms as a separate nitride from any other fcc (face-centred cubic) microalloy carbides and nitrides. It should be noted that aluminium carbide is not stable in steel [3].

Other elements

Calcium is essentially added for desulphurisation and to make the steel cleaner. Phosphorous improves the corrosion resistance but reduces toughness and weldability. Sulfur is not completely removed during the steelmaking process. It causes hot shortness during rolling and hot cracking in welding. Manganese counteracts these effects by forming manganese sulfide (MnS). Nevertheless, the S level should be kept below 0.05% [17].

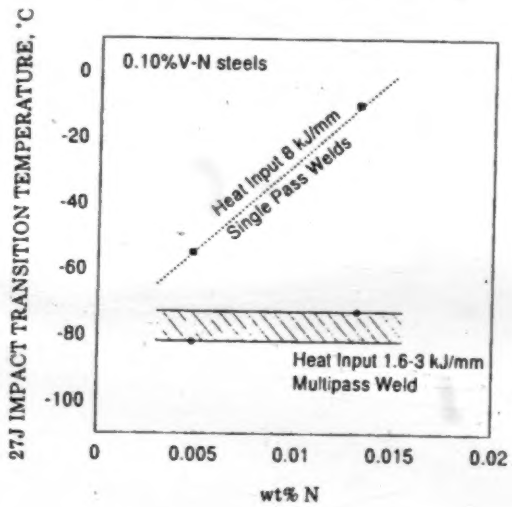

FIG. 2-2. Effect of N level on HAZ toughness in 0.1%V steel [26].

2-3-2. Thermo-mechanical controlled processing (TMCP)

Studies on rolling practices and in particular controlled rolling (CR) were carried out extensively in the mid-1960s. Commercialization of continuous casting technology in that decade brought about a great deal of economic benefits, compared to ingot casting practiced before. The cast product in continuous casting is already in slab form. The first stage in TMCP is reheating to a soaking temperature (1150-1350°C) for homogenization of austenite. This is followed by CR at different stages, and finally cooling down to room temperature either naturally (in air) or by accelerated cooling (e.g., by water jets). CR, which is applicable to plain carbon steels as well as to microalloyed steels, can be carried out through some or all of the following three stages [3]:

1- At temperatures above ~1000°C, where sequential rolling at recrystallization temperatures will break down the coarse "as-soaked" austenite grain structure.
2- Between A_3 and ~1000°C, where further grain refinement takes place by deforming the austenite in the no-recrystallization zone, in the case of microalloyed steels.
3- Below A_3 (normally limited to the inter-critical zone), where deformation causes work-hardening in the ferrite.

Relatively low temperature reheating and heavy reduction below the recrystallization temperature were found to be necessary for improvement of toughness in low-carbon high-strength steels [15]. According to Williams *et al.* [24], lowering the finish rolling temperature below A_3 to increase the strength of the final product was found to be an "inappropriate approach" especially in the case of C-Mn-Nb-V steels (such as Grade 100). The addition of Mo was found to be a better approach to compensate for strengthening through the effects on transformation kinetics (Section 2-3-1).

Microalloying additions have three major effects on the microstructural evolution during hot rolling [3]:

1- Undissolved carbonitrides at the soaking temperature (in particular TiN) can control to some degree the austenite grain growth and, therefore, influence the starting grain size at the commencement of CR.

2- Small amounts of dissolved Ti, V, and especially Nb, may retard dynamic or static recrystallization during CR, by segregation to the grain and sub-grain boundaries. This is referred to as the "solute drag" effect.

3- Strain-induced precipitation of microalloy carbonitrides (especially NbCN) can pin the sub-grain boundaries and inhibit recrystallization.

In microalloyed steels, the no-recrystallization temperature is much higher than that in plain carbon-manganese steels. Recrystallization inhibition is done by particles of relatively small diameter (<300 nm) and short inter-particle spacing (<1 μm) [23]. These particles can exert pinning forces on the austenite grain and sub-grain boundaries. Deformation at temperatures below the no-recrystallization temperature will result in *pancaked* austenite grains, which transform into much finer ferrite grains. Pancaking and recrystallization prohibition will affect all properties of the resultant grains, such as size, sub-grain size (dislocation density) and even texture. The pancaked austenite grains will no longer have the preferred so-called *cube* crystallographic orientation; the main crystallographic orientations will be those called *brass* and *copper*. This will dictate specific textures for the resultant ferrite grains, which in turn will affect anisotropy of the mechanical properties [27].

Refinement of prior austenite grain size and the retention of strain energy in the deformed austenite grains are important for the refinement of the ferrite grains. These factors increase nucleation rate by increasing the austenite grain boundary area, formation of deformation bands and corrugation of the grain boundaries, all of which provide favoured locations for ferrite nucleation [3].

In the processes that employ OLAC after CR, a finished-rolled plate is immediately sent to the cooling zone for water-cooling in specified temperature ranges. It will be subsequently air-cooled to room temperature. OLAC can increase strength without sacrificing the toughness [15].

The thermo-mechanical cycle for Grade 100 steel is shown schematically in Fig. 2-3. The slab is reheated at about 1250°C, rough-rolled above 1000°C, finish-rolled in the no-recrystallization region (800–850°C), followed by accelerated cooling at moderate cooling rates (~15–20 °C/s) to a stop cooling temperature of ~400–600°C, where it is slightly deformed (<10% strain) by levelling or rolling. This last stage of deformation not only enhances the dimensional accuracy of the product (removing bends and ripples and/or produce the exact plate thickness), but also is believed to accelerate precipitation by a further increase in the dislocation density in ferrite [1, 28].

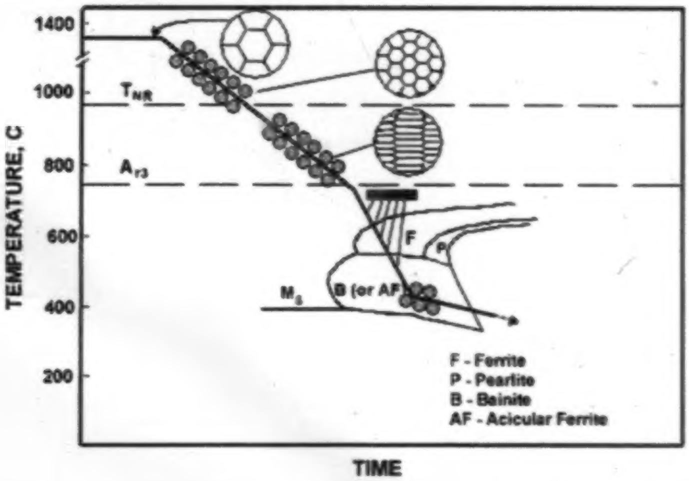

FIG. 2-3. Schematic illustration of thermomechanical processing for Grade 100 (redrawn based on an schematic in [28]).

2-3-3. Microstructural developments

2-3-3-1. Precipitation

In order to have a strong steel, two sets of microalloying particles (carbides and nitrides) are desirable [3]:

1- Those that remain undissolved in the austenite temperature range. These help maintain a fine austenite grain size (which will result to finer α grains after transformation), by pinning the austenite grain boundaries.
2- Those that precipitate during austenite/ferrite transformation (interphase precipitates) or after that in ferrite. These, in particular the latter, strengthen the matrix by dispersion hardening and are usually 3-5 nm in size.

The presence of C, N and the microalloying elements guarantees formation of a series of nitrides, carbonitrides and carbides during cooling in the thermomechanical processing of Grade 100 steel steel, as listed below, after Akhlaghi and Ivey [29]:

1- Large Ti nitrides (2-8 μm) that form in the liquid steel or during solidification.
2- Intermediate size Ti-rich carbonitrides (100-500 nm).
3- Intermediate size Nb-rich carbonitrides (30-150 nm). Types 2 and 3 form on cooling through the austenite range during processing.
4- Interphase fine precipitates (10-20 nm), primarily Nb-rich carbides, that form during the austenite-ferrite transformation (transformation induced).
5- Very fine (<5 nm) Nb-rich carbides that precipitate out in the ferrite in the 400-600°C range. These fine precipitates, with small particle spacing, contribute to the strength of the steel through precipitation hardening.

Precipitation of these carbonitrides will be discussed in detail in Section 5-3, from a thermodynamic point of view, and the amount of precipitation of different compounds will be estimated at several temperature intervals as a result of cooling during TMCP.

Whether or not Cu precipitates in Grade 100 steel is not clear. There have been no reports on such precipitation [29]. The fact that Cu precipitates are dissolved in acid make them unsuitable for collection by TEM carbon replicas, and their small sizes make them difficult to be discerned in the iron matrix of TEM thin-foil samples. Nevertheless, as the copper level is low in Grade 100 steel (~0.4%), there is not much expectation for precipitation. On the other hand, it is suggested that the solubility limit of copper in iron and steel is approximately 0.1 at% (almost the same in wt% for Cu in steel), using atom probe field ion microscopy (APFIM). The critical size for these precipitates is believed to be in the range of 2.3 to 3 nm (in radius). The precipitation of copper, which is usually observed in the temperature range 400 to 650°C, consists of several transformations as the precipitates grow [30].

2-3-3-2. Iron matrix phase transformation

The objective of all TMCP is the development of a fine microstructure. Ferrite nucleates in austenite and grows as the temperature drops below A_3. The ferrite type, grain size and properties depend greatly on the effective austenite grain size, the austenite retained strain (as sub-grain boundaries and deformation bands) and the cooling rate, as these factors influence the nucleation sites and rate. Intergranular nucleation can occur at grain corners and edges, or even at grain faces if, for instance, cooling rate increases. Intragranular nucleation can occur on deformation bands in austenite grains with retained strain, or on non-metallic inclusions [3]. Basically, the effect of increased cooling rate is the supercooling of austenite and a decrease in transformation start temperature. This, being in favour of increased nucleation sites but less growth, results in finer transformed ferrite. However, there is a limit. At cooling rates above that limit, polygonal ferrite can be replaced by acicular ferrite, bainite or martensite. Fig. 2-4 shows the continuous cooling transformation (CCT) diagram for Grade 100. The transformation originates from controlled-rolled, pancaked austenite grains at ~850°C. Fig. 2-4 shows the effect of cooling rate on the transformation product. Also on the diagram, the corresponding hardness values of the transformed material for each cooling rate are shown. Fig. 2-5 shows these effects better. The amount of each phase constituent is estimated from the transformation curves on the CCT diagram. A cooling rate of ~20°C/s results in a 100% bainitic microstructure with an accompanying hardness number of ~250 HV10. Other microstructural changes that take place in the processing of the Grade 100 steel, after stop cooling (i.e., levelling/slight rolling), can result in slight work hardening and some precipitation hardening.

Militzer *et al.* (cited by Gladman [3])‌ have found that the effect of austenite grain size on the transformed ferrite grain size is complicated. They show that decreasing the austenite grain size has little effect on the ferrite grain size at a given cooling rate, while reducing the austenite grain size at a given degree of undercooling (same transformation temperature) dramatically refines the ferrite grain size.

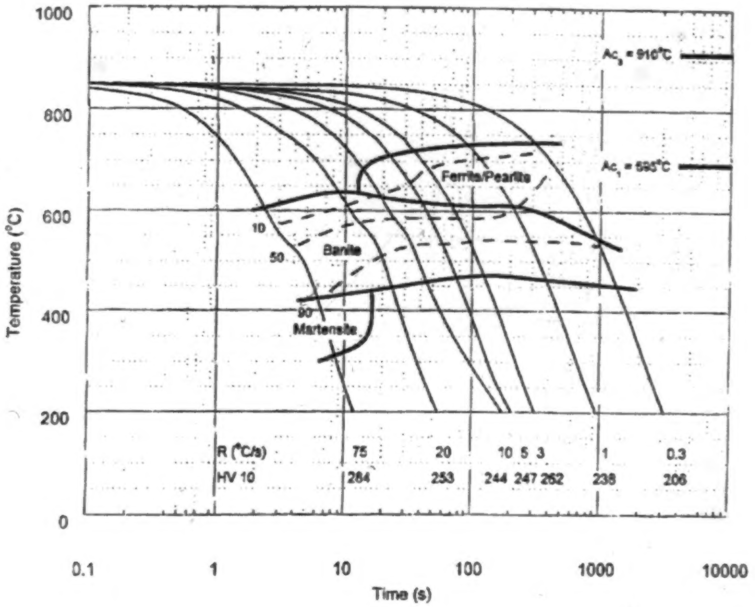

FIG. 2-4. CCT diagram of Grade 100 steel obtained based on cooling from the finish-rolling temperature of 850°C [31].

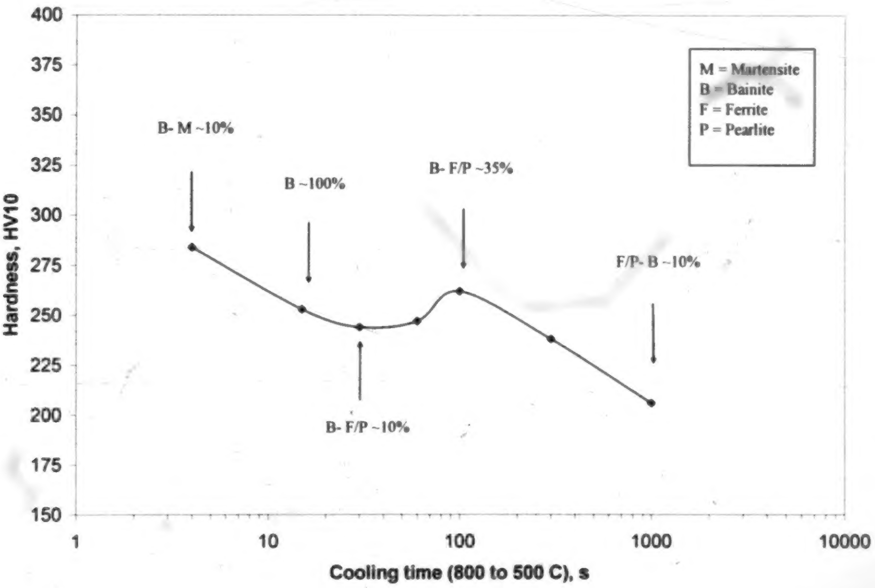

FIG. 2-5. Hardness variation of different phases obtained from the CCT diagram of Fig. 2-4.

2-4. Properties of Grade 100

There are several aspects and properties of microalloyed steels, which have made this group of steel distinctive. The main properties of industrial interest, which are still under development, are the mechanical properties (such as strength and toughness), weldability, formability, and resistance to environmental situations (such as hydrogen-induced cracking and stress-corrosion cracking). Some of these properties are briefly reviewed below, with emphasis on the properties of Grade 100 steel.

2-4-1. Mechanical properties

2-4-1-1. Strength

It is known that a microalloying addition of less than one part in a thousand can increase the strength of a plain carbon steel 2-3 times [3]. Pipeline and structural steels with SMYS of 60 to 100 ksi (400–700 MPa) are the result of microalloyed steel developments. This improvement will result in a higher strength/weight ratio for the steel, which in turn leads to economic benefits.

Fig. 2-6 shows an engineering stress-strain curve obtained from a tensile test on the as-received Grade 100 steel material. Round dog-bone tensile samples were machined to a reduced section diameter of 4 mm, reduced section length of 20 mm and a total length of 87 mm, according to ASTM A370 standard [32]. Three samples were prepared from each direction longitudinal and transverse to the rolling direction (RD). The flow curves were analysed to obtain the mechanical parameters (Table 2-2). As can be seen, there is only a little difference in the results from the two directions. This suggests little anisotropy and texture effect. The curves showed continuous yielding and the yield strengths were well above 690 MPa.

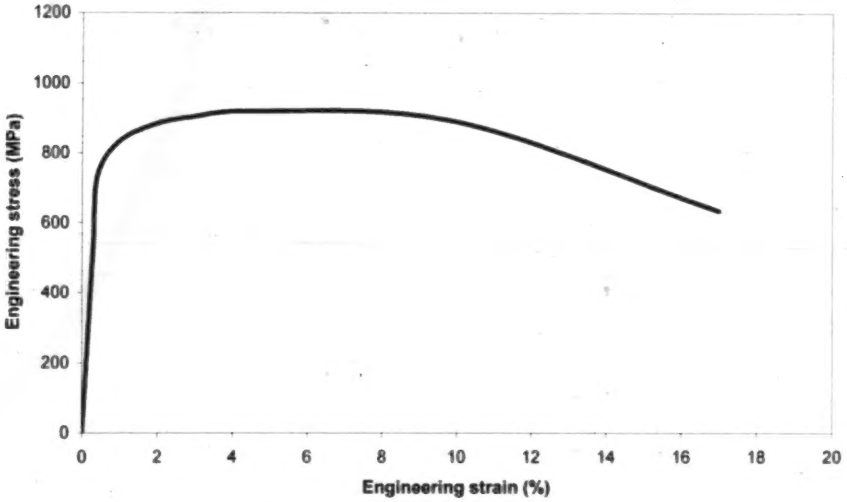

FIG. 2-6. Stress-strain curve obtained from the tensile test of Grade 100

Table 2-2. Tensile properties of Grade 100

w.r.t. RD	E (GPa)	Y.S. (MPa)	UTS (MPa)	Elongation (%)
Longitudinal	214.6±22.0	788.0±33.4	920.8±5.7	17.1±2.4
Transverse		800.1±13.4	935.8±1.9	16.3±2.4

2-4-1-2. Toughness

The increased strength of microalloyed steels should be accompanied with good ductility. In other words, good toughness is what is expected from structural and pipeline steels. Experimental determination of impact toughness was deemed beyond the scope of this study.

2-4-2. Weldability

There have been several problems associated with welding of plain carbon, C-Mn and low-alloy steels. Some of these problems take place during welding or post-weld heat treatment (PWHT), such as hydrogen assisted-cracking (HAC) in the HAZ or WM, reheat cracking in the HAZ or weld metal (WM), HAZ liquation cracking, lamellar tearing and solidification cracking in the WM. Some other problems are encountered during service, such as stress-corrosion cracking (SCC), fatigue/corrosion fatigue, creep and failure in hydrogen environments [20].

The word weldability has been used in the literature over the past decades with different connotations. Weldability literally means the ability to weld a material. This, however, finds limited application nowadays. Most of the industrial materials can be welded with varying degrees of ease or care, and no weld is completely free of defects and discontinuities. So weldability of a material is related to how susceptible a weld is to cracking during or after welding [20]. With the developments in welding metallurgy and practices, especially for steels, the term weldability is used as a criterion for the quality of the weld and even the service behavior of weldments [33]. The weldability of a material depends not only on the material properties (such as chemical composition), but also on the welding parameters. Therefore, *weldability tests* can be mechanical tests to see if the mechanical properties of the weld metal or HAZ (as a criterion for quality and susceptibility to a specific failure) are satisfactory or not [18, 34, 35].

The traditional way to increase the tensile strength was based on increasing the carbon and/or manganese level in steel, but this would result in reduced weldability [3]. According to Easterling [36], the weldability of steels is usually expressed in terms of a carbon equivalent (*C.E.*) limit – generally considered to be 0.4– that shows composition allowances to avoid cold cracking or hydrogen cracking. The current formulation of *C.E.* according to IIW for carbon steels with carbon levels >0.15% is given by Equation 2-1 [37]. Fortunately, microalloyed steels had the advantage of employing very low carbon levels and reduced manganese levels, meaning low carbon equivalents, which assure increased weldability, while demonstrating high strength [38]. These steels also have greater freedom in welding processing with little or no preheat, which reduces the cost [39]. For low carbon (<0.15%) microalloyed steels, the Ito-Besseyo formula (Equation 2-2) is a more accurate way to determine *C.E.* than the older equations [37]. For Grade 100 the value of *C.E.* is found to be 0.58 according to the IIW equation and a value of P_{cm} (C.E. for low carbon microalloyed steels) of 0.24 is obtained according to the Ito-Bessyo equation.

$$C.E. = \%C + \frac{\%Mn+\%Si}{6} + \frac{\%Cr+\%Mo+\%V}{5} + \frac{\%Cu+\%Ni}{15} \qquad (2\text{-}1)$$

$$P_{cm} = \%C + \frac{\%Mn+\%Cr+\%Cu}{20} + \frac{\%Si}{30} + \frac{\%Mo}{15} + \frac{\%V}{10} + \frac{\%Ni}{60} + 5\%B \qquad (2\text{-}2)$$

Mechanical tests by Hoskins [40] showed that Grade 100 steel has good overall weldability. The susceptibility of welded Grade 100 to hydrogen cracking was found to be of some concern (when compared with a Grade 80 microalloyed steel), unless very low levels of diffusible hydrogen were available in the system. The susceptibility depended on the welding process and the heat input.

2-4-3. Susceptibility to HAC and HIC

Hydrogen-assisted cracking (HAC) and hydrogen-induced cracking (HIC) are sometimes interchangeably used in the literature. However, it seems appropriate and less confusing to distinguish between the two by referring to the failure during or after welding related to hydrogen as HAC and the failure during service in hydrogen environments as HIC.

HAC, sometimes referred to as *cold cracking* in welding, is a serious problem, in particular when the strength is high. "HAC occurs by a mechanism that involves the concentration of hydrogen in the biaxial stress field at the tip of a crack by diffusion" [13]. In fusion welding, hydrogen is generated in the arc from moisture and gets dissolved in the weld metal. It diffuses to the HAZ after solidification, and therefore cracking can happen either in the WM or HAZ after decomposition of austenite [41]. Although the fine-grained ferrite microstructure, achieved by addition of the microalloyed elements and use of thermomechanical processing, is expected to have improved resistance to HAC, stress-corrosion cracking, and brittle fracture initiation in the HAZ [42], reduction in the number of sulfides in microalloyed steels, due to the reduction in the sulfur levels, is believed to make the steel more susceptible to hydrogen cracking. MnS inclusions provide a sink for hydrogen and so reduce the risk of HAC. They also help nucleation of acicular ferrite, and therefore, their absence causes the formation of lower temperature transformation products and results in higher hardness values in the HAZ [20]. The susceptibility of steel to HAC increases with strength and the presence of hard microstructural constituents, and also depends on the microstructure in general even at a certain overall hardness [13, 43]. The most susceptible phases (in order of decreasing susceptibility) are twinned martensite, bainite (upper or lower), granular bainite and lath martensite (the least susceptible) [41, 44]. Despite the controversy about the effect of retained austenite, recent studies have shown that it is beneficial in preventing HAC [13]. For these reasons, lower electrode hydrogen contents are now a requirement for low-sulfur, clean steels [3]. Careful storage and electrode baking procedures, or wire cleanliness and control of flux type, coupled with a reduction in carbon and carbon equivalent and preheat (needed for steels of 700 MPa yield strength and higher) are the only means to reduce the risk of hydrogen cracking [45].

Taira *et al.* [15] believe that the susceptibility to HIC in as-rolled pipeline steels (X44 to X70) is due to the segregation of Mn to the centerline, which promotes the formation of a "hard band" (i.e., low-temperature transformation products) in this zone. They have observed that the HIC susceptibility is high in the steels containing 0.05-0.15%C, when the manganese level is above 1%.

2-4-4. Reaction to heat treatments

It is of interest to know the reaction of any new grade of steel to the conventional heat treatments and tests. Among these are aging, annealing and quenching. Strain aging can also reveal some properties and characteristics of the material. For instance, it can show if there are sufficient interstitials in the steel to increase the strength through dislocation locking by the Cottrell atmosphere of the interstitials. Some of these tests have been carried out along with the main study on the HAZ and, therefore, are reported here.

2-4-4-1. Full annealing

Small samples (15x10x5 mm^3) were cut from a Grade 100 plate. They were solution treated at 970°C for ~10 min and then furnace cooled. The average hardness on the polished sample was 183.7 ± 5.9 HV_{500}, compared with the hardness of ~285 HV_{500} of the as-received sample.

Also, three tensile samples were machined similar to the samples from the BM (Section 2-4-1-1) from the annealed strips (950°C; 8 min; furnace cooled). The flow curves and the tensile properties are shown in Fig. 2-7 and Table 2-3, respectively. These tensile samples had higher hardness values (~208 HV) than the small samples discussed above. Nevertheless, all these results show that Grade 100 can have a very low as-annealed hardness of ~180 HV and yield strength of ~350 MPa.

2-4-4-2. Quenching

Penny-shaped samples (15x10x1.5 mm^3) were cut from a Grade 100 plate. They were solution treated at 1150°C for 4 min and then quenched in iced-brine. The average hardness on the polished sample was 364.2 ± 3.6 HV_{500} This level of hardness corresponds to the hardness of martensite for this level of carbon [46].

Also, three tensile samples were machined similar to the samples from the BM (Section 2-4-1-1) from the annealed-and-quenched strips (1150°C; 8 min; quenched in iced-brine). The flow curves and the tensile properties are also shown in Fig. 2-7 and Table 2-3, respectively, and these are compared with those of the annealed sample. These samples had a slightly lower hardness (~353 HV) at the surface than those penny-shaped samples explained above. The hardness in the core of the sample was probably even lower, as the cooling rate decreases with increasing distance from the surface. This can explain why the tensile samples showed higher ductility than expected from a fully martensitic sample. Nevertheless, all these results show that Grade 100 can have a very high as-quenched hardness of ~360 HV and yield strength of ~900 MPa.

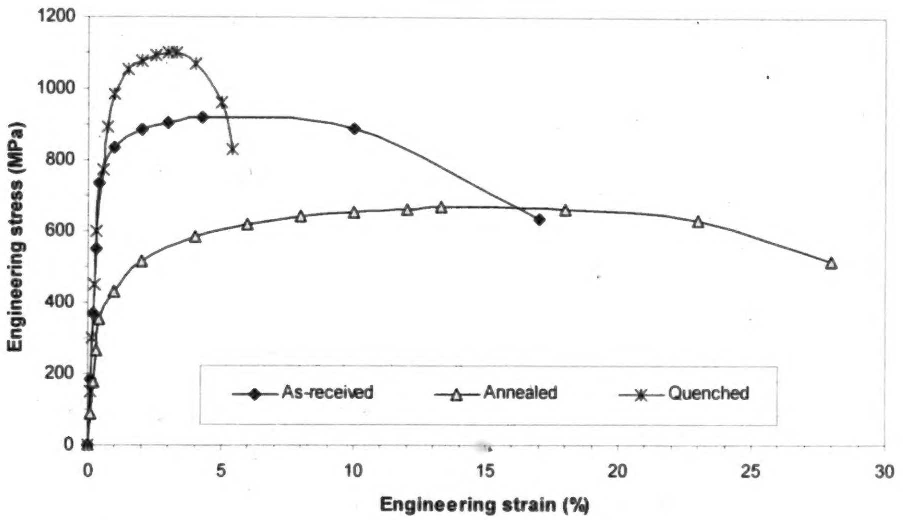

FIG. 2-7. Effect of quenching and annealing on the flow curves for Grade 100.

Table 2-3. Tensile properties of heat-treated samples of Grade 100

Condition	YS (MPa)	UTS (MPa)	Elongation (%)
Annealed	349.8±1.2	667.9±4.7	28.1±0.3
Quenched	877.6±1.4	1126.5±29.0	6.4±1.4

2-4-4-3. Sub-critical aging

To see the effect of aging on Grade 100 some tests were initiated. These were not completed as the time required for the heat treatment tests and further microstructural and mechanical tests made them difficult to carry out in parallel to the main study of the HAZ. These tests, which can show effect of precipitate hardening on the strength of Grade 100, are therefore recommended for future work.

Small cubic samples (10x10x8 mm^3) were cut from Grade 100 plates. These were annealed at various temperatures from 200 to 700°C for 1 hour and then either quenched in water or furnace cooled. Fig. 2-8 shows the variation in the hardness as a result of aging. The initial increase from ~285 to ~305, achieved at aging temperatures of 200–300°C, is likely due to strain aging. The plates of Grade 100 were cold worked slightly during leveling. This increases the dislocation density and frees the dislocations from the Cottrell atmospheres of the interstitial solutes. Aging will facilitate diffusion of the interstitials to the dislocation ends, hence locking them again, which will result in an increase in strength and hardness [47].

The drop in hardness at higher temperatures (400–700°C) is likely due to recovery (dislocation rearrangement) and/or precipitate coarsening. The chance for coarsening may found to be minimal, when some of the published work on the precipitation hardening of Nb carbonitrides is consulted (e.g., Bucher and Grozier, 1966, as cited in [3]). For instance, it was found that holding at 650°C for 5–45 min will result in softening. About 1 hour at this temperature was needed to cause precipitation and to reach a maximum hardness. Coarsening of the precipitates, that would result in a drop of hardness, would only occur at this temperature for long periods of holding, e.g., 110–230 min. However, it can be argued that the fine precipitates in the Grade 100 have considerable amounts of V, Mo and Ti, which may add to the average mobility of the microalloying solutes, hence, making coarsening happen at shorter times. Evidence of coarsening of fine carbides was actually found for the sample aged at 600°C for 1 hour (see Fig. 5-45). As mentioned earlier, these tests are incomplete and more tests, such as holding for longer times, careful precipitate analysis and tensile tests, are required.

2-5. Summary

Grade 100 microalloyed steel is a high-strength low-carbon low-alloy structural steel produced in the as-rolled condition. The strength is gained through thermo-mechanical controlled processing (TMCP). Grade 100 contains 0.08% C, 0.01% N and approximately a total of 0.2% Ti, Nb and V as primary microalloying elements. Carbides and carbonitrides of Nb and Ti pin the austenite grain and sub-grain boundaries and hence retard recrystallization during rolling between ~1000°C and A_3. Accelerated cooling from above A_3 to temperatures well below A_1 cause formation of fine-grained bainitic ferrite. It also suppresses interphase precipitation and, therefore, results in a finer precipitate distribution coming out in ferrite at the levelling stage. The fine precipitates with small interparticle spacing (3–5 nm) contribute to the strength of the steel through precipitation hardening. Grade 100 shows good strength and ductility. The susceptibility of the HAZ to HAC/HIC, however, can be of concern, as the susceptibility to HAC/HIC increases with strength, the presence of martensite, reduction of sulfides and increase in Mn content.

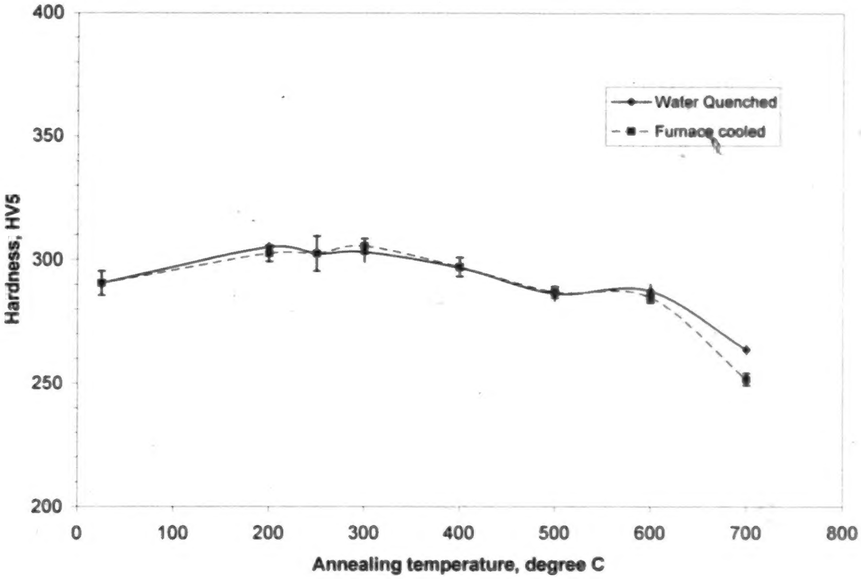

FIG. 2-8. Sub-critical aging of Grade 100; aging time 1 hr.

References

[1] Akhlaghi, S., Ivey, D. G., and Collins, L., 2000, "Microstructural Study of Grade 100 Steel," *Proc., 42nd Mechanical Working and Steel Processing Conference*, Iron and Steel Society/AIME, Warrendale, P.A., USA, **38**, pp. 419-428.

[2] 1993, *High-Strength Structural and High-Strength Low-Alloy Steels*, in ASM Handbooks Online, Vol.1: Properties and Selection: Irons, Steels, and High-Performance Alloys, ASM International, Materials Park, Ohio.

[3] Gladman, T., 1997, The Physical Metallurgy of Microalloyed Steels, The Institute of Materials, London.

[4] DeArdo, A. J., 1995, "Modern Thermomechanical Processing of Microalloyed Steel: A Physical Metallurgy Perspective," *Proc., ISS, Proceedings of the International Conference "Microalloying '95"*, pp. 15-33.

[5] Tanaka, T., 1995, "Science and Technology of Hot Rolling Process of Steel," *Proc., ISS, Proceedings of the International Conference "Microalloying '95"*, pp. pp. 165-181.

[6] Pereloma, E. V., Bayley, C., and Boyd, J. D., 1996, "Microstructural Evolution During Simulated OLAC Processing of a Low-Carbon Microalloyed Steel," Materials Science and Engineering A (Switzerland), **210** (1-2), pp. 16-24.

[7] Korchynsky, M., 1995, "Twenty Years since Microalloying '75," *Proc., ISS, Proceedings of the International Conference "Microalloying '95"*, pp. 3-13.

[8] Collins, L. E., Godden, M. J., and Boyd, J. D., 1983, "Microstructures of Linepipe Steels," Can. Metall. Q., **22** (2), pp. 169-179.

[9] 2002, CSA Standard Z245.1-02, Steel Pipe, Canadian Standards Association.

[10] Sharma, U., and Ivey, D. G., 2000, "Microstructure of Microalloyed Linepipe Steel," IPC00-0153, *Proc., International Pipeline Conference (IPC 2000)*, ASME, **1**, pp. 193-201.

[11] Williams, J. G., Killmore, C. R., Barbaro, F. J., Meta, A., and Fletcher, L., 1995, "Modern Technology for ERW Linepipe Steel Production (X60 to X80 Beyond)," *Proc., ISS, Proceedings of the International Conference "Microalloying '95"*, pp. 117-139.

[12] Hulka, K., 1992, "Modern Processing Facilities Favour the Application of Microalloyed Steels," *Proc., Clean Steel 4*, The Institute of Materials (UK), 1992, pp. 82-100.

[13] Losz, J. M. B., and Challenger, K. D., 1990, "HAZ Microstructures in HSLA Steel Weldments," *Proc., First United States--Japan Symposium on Advances in Welding Metallurgy*, American Welding Society, Miami, pp. 323-357.

[14] *Chemical Analysis of a Steel Plate Sample*. 2002, Canspec: Edmonton.

[15] Taira, T., Matsumoto, K., Kobayashi, Y., Takeshige, K., and Kozasu, I., 1983, "Development of Super-Tough Acicular Ferrite Steel for Line Pipe--Optimization of Carbon and Niobium Content in Low-Carbon Steel," *Proc., HSLA Steels, Technology and Applications*, American Society for Metals, 1984, pp. 723-731.

[16] Hulka, K., and Heisterkamp, F., 1998, "Development Trends in HSLA Steels for Welded Constructions," *Proc., Microalloying in Steels*, Materials Science Forum (Switzerland), **284-286**, pp. 343-350.

[17] Brockenbrough, R. L., 1999, *Properties of Structural Steels and Effects of Steelmaking and Fabrication*, in Structural Steel Designer's Handbook, R.L. Brockenbrough, and F.S. Merritt, eds., McGraw Hill, pp. 1.33-1.35.

[18] Smith, N. J., Mcgrath, J. T., Gianetto, J. A., and Orr, R. F., 1989, "Microstructure/Mechanical Property Relationships of Submerged Arc Welds in HSLA 80 Steel," Welding Journal, **68** (3), pp. 112-s to 120-s.

[19] Yan, T., Yunfeng, L., and Yunhui, W., 1990, "Precipitation Behaviour of Nb, V, Ti in Low Alloy Steels and Their Influence on Toughness," *Proc., HSLA Steels*, The Minerals, Metals and Materials Society (USA), pp. 501-505.

[20] Dolby, R. E., 1983, "Advances in Welding Metallurgy of Steel," Metals Technology, **10** (9), pp. 349-362.

[21] Mitchell, P. S., Hart, P. H. M., and Morrison, W. B., 1995, "The Effect of Microalloying on HAZ Toughness," 1995, *Proc., Microalloying '95*, Iron and Steel Society Inc, Warrendale, pp. 149-162.

[22] Shiga, C., and Saito, Y., 1990, "Toughness Improvement in HAZ of HSLA Steels by TMCP in Japan," American Welding Society), pp. 177-205.

[23] Palmiere, E. J., 1995, "Precipitation Phenomena in Microalloyed Steels," *Proc., ISS, Proceedings of the International Conference "Microalloying '95"*, pp. 307-320.

[24] Dutta, B., and Sellars, C. M., 1987, "Effect of Composition and Process Variables on Nb(C,N) Precipitation in Niobium Microalloyed Austenite," Materials Science and Technology, **3** (3), pp. 197-206.

[25] Lagneborg, R., Siwecki, T., Zajac, S., and Hutchinson, B., 1999, "The Role of Vanadium in Microalloyed Steels," Scandinavian Journal of Metallurgy (Denmark), **28** (5), pp. 186-241.

[26] Zajac, S., Langerborg, R., and Siwecki, T., 1995, "The Role of Nitrogen in Microalloyed Steel," *Proc., ISS, Proceedings of the International Conference "Microalloying '95"*, pp. 321-338.

[27] Butron Guillen, M. P., and Jonas, J. J., 1993, "Effect of Austenite Recrystallization on Ferrite Transformation Textures," Materials Science Forum, **113-115**, pp. 691-696.

[28] Bai, D. Q., Cook, M. A., Asante, J., and Dorricott, J.: *Process for Making High Strength Micro-Alloy Steel*. 2004, IPSCO Enterprises Inc.: US 6,682,613 B2.

[29] Akhlaghi, S., and Ivey, D. G., 2002, "Precipitation Behaviour of a Grade 100 Structural Steel," Canadian Metallurgical Quarterly, **41** (1), pp. 111-119.

[30] Deschamps, A., Militzer, M., and Poole, W. J., 2001, "Precipitation Kinetics and Strengthening of a Fe-0.8 Wt% Cu Alloy," ISIJ International, **41** (2), pp. 196-205.

[31] "CCT Diagram for Grade 100 Microalloyed Steel," Private communication between D.G. Ivey (University of Alberta) and L. Collins (IPSCO, Inc).

[32] 2000, *Standard Test Methods for Tension Test; A370*, in Annual Book of ASTM Standards, American Society for Testing and Materials, Philadelphia, pp. 145.

[33] Gourd, L. M., 1995, Principles of Welding Technology, Edward Arnold.

[34] Egner, D., and Cochrane, R., 1998, "Process History, Microstructure and Weldability Interactions in Microalloyed Steels," Materials Science Forum (Switzerland), **284-286**, pp. 279-286.

[35] Collins, L. E., and Liu, W. J., 1995, "Effects of Niobium on the Transformation Behaviour of HSLA Steels," *Proc., Phase Transformations During the Thermal/Mechanical Processing of Steel*, Canadian Institute of Mining, Metallurgy and Petroleum, Montreal, PQ, Canada, pp. 419-427.

[36] Easterling, K. E., 1992, Introduction to the Physical Metallurgy of Welding, Butterworth-Heinemann Ltd, Oxford.

[37] Patchett, B. M., 1998, *Welding Metallurgy*, in The Metals Blue Book, CASTI Publishing Inc. and AWS, Edmonton, AB, Canada.

[38] Scoonover, T. M., Lukens, W. E., and Pande, C. S., 1984-1985, "Correlation of Heat Affected Zone Microstructure with Peak Heating Temperature in HSLA-80 Steel Weldments," 1986, *Proc., Unusual Techniques and New Applications of Metallography. Volume II*, American Society for Metals, pp. 91-104.

[39] Spanos, G., Fonda, R. W., Vandermeer, R. A., and Matuszeski, A., 1995, "Microstructural Changes in HSLA-100 Steel Thermally Cycled to Simulate the Heat-Affected Zone During Welding," Metall. Mater. Trans. A (USA), **26A** (12), pp. 3277-3293.

[40] Hoskins, S. J., 2002, Weldability of Grade 80 and Grade 100 Microalloyed Steels, University of Alberta, Edmonton.

[41] Boniszewski, T., and Watkinson, F., 1973, "Effect of Weld Microstructures on Hydrogen Induced Cracking in Transformable Steels: Part 1," Metals and Materials, 7 (2), pp. 90-96.

[42] Handeland, T., Erkkila, E., and Gjonnes, J., 1986, "A Combined Electron Microscope and Optical Metallographic Study of Microstructures in High-Strength, Low-Alloy (HSLA) Steels after Welding," J. Microsc., **144** (3), pp. 251-259.

[43] Bhole, S. D., and Fox, A. G., 1996, "Influence of GTA Welding Thermal Cycles on HSLA-100," Canadian Metallurgical Quarterly, **35** (2), pp. 151-158.

[44] Deb, P., Challenger, K. D., and Clark, D. R., 1986, "Transmission Electron Microscopy Characterizations of Preheated and Non-Preheated Shielded Metal Arc Weldments of Hy-80 Steel," Materials Science and Engineering, **77**, pp. 155-167.

[45] Dolby, R. E., 2000, "Joining Issues for New Constructional Steels," Science and Technology of Welding and Joining, **5** (6), pp. 341-346.

[46] Krause, G. E., 1990, Properties and Selection: Irons, Steels and High Performance Alloys, ASM International, Metals Park, Ohio, pp. 127.

[47] Leslie, W. C., 1981, The Physical Metallurgy of Steels, Hemisphere Publishing Corp, McGraw-Hill Book Co, New York.

Chapter 3

Welding and HAZ

3-1. Introduction

Welding is a process of joining two pieces of material permanently by making part of them fuse together by forging or melting. As a result of welding, the microstructure and properties of the regions around the weld will change. Before any examination of the thermal, microstructural or mechanical aspects of these regions, welding processes and the resulting zones and sub-regions should be addressed. In this chapter, some of the arc welding processes used in the welding of microalloyed steels are briefly introduced first. The weld structure, in particular the HAZ, is defined and its different sub-regions are discussed next. This is followed by some of the heat treatments associated with welding. Finally, the experimental procedure used to make HAZ samples in this study is described.

3-2. Welding processes

Welding processes have been grouped under two main branches: fusion welding and pressure welding [1]. Fig. 3-1 shows the classification of the most common welding methods. In fusion welding the binding between two pieces is made by melting part of both pieces. Gas tungsten arc welding (GTAW) is an example of fusion welding. In pressure welding, bulk fusion does not occur. The binding between two surfaces occurs through friction, sparking (that causes very localized melting), diffusion, etc. Cold roll-welding of aluminum sheets is an example of pressure welding.

The welding processes used in pipe making are generally under the fusion welding category and more precisely a sort of arc welding. In *arc welding*, metals at the welded joint are melted by a heat source provided by an electric arc. Some of the most important processes of this kind are shielded metal arc welding (SMAW; a.k.a. manual metal arc welding- MMAW), gas metal arc welding (GMAW; a.k.a. MIG/MAG), gas tungsten arc welding (GTAW; a.k.a. TIG), and submerged arc welding (SAW). SAW and SMAW are the most common welding processes used for structural steels [2].

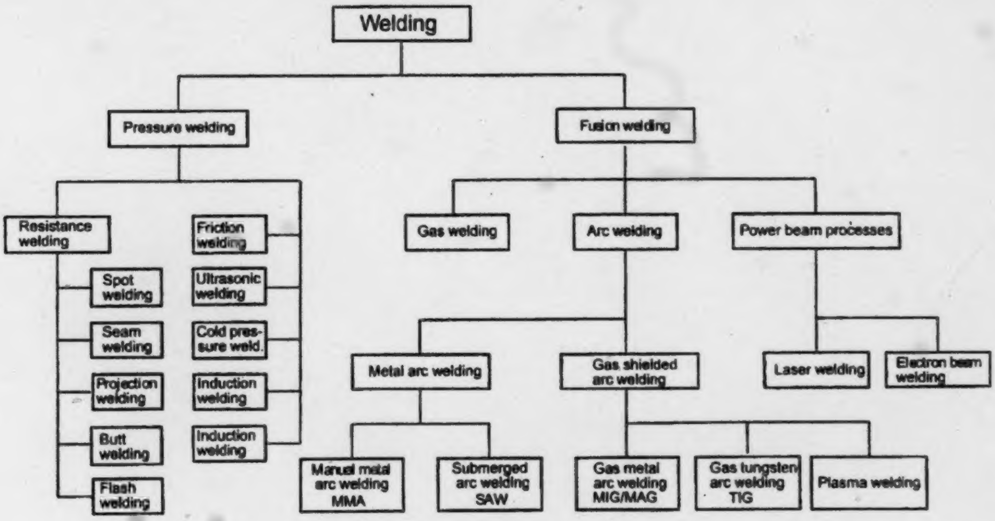
Welding
Pressure welding
Fusion welding
Resistance welding
Friction welding
Spot welding
Ultrasonic welding
Seam welding
Cold pressure weld.
Projection welding
Induction welding
Butt welding
Induction welding
Flash welding
Gas welding
Arc welding
Power beam processes
Metal arc welding
Gas shielded arc welding
Laser welding
Electron beam welding
Manual metal arc welding MMA
Submerged arc welding SAW
Gas metal arc welding MIG/MAG
Gas tungsten arc welding TIG
Plasma welding

FIG. 3-1. Classification of the most common welding processes [1].

GTAW, which is used in this study to produce the weld HAZ, is the most widely used process where excellent weld quality is most important. The welds are free of porosity and slag inclusions, since slag is never produced. High welding speeds can be used in all positions, and post-weld grinding can be eliminated. It is used for joining of a wide range of metals, even those considered hard-to-weld, such as aluminium. During GTAW, the pieces being welded are protected from the atmosphere by a continuous stream of a shielding inert gas, usually argon or helium (Fig. 3-2a). The electrode material is normally tungsten, which is non-consumable. Filler metal may or may not be used [3]. When no filler metal is used, the process is called *autogenous*.

SAW is an automatic or semiautomatic welding process, which employs higher heats and faster welding speeds. It is one of the most common, economical and practical techniques used for the welding of large-diameter steel pipes. In SAW the electrode rod (wire) and the coating flux are added to the weld area separately (Fig. 3-2b). The arc and melting take place under the flux (submerged). The arc streams run between the wire and the plate to be welded [3].

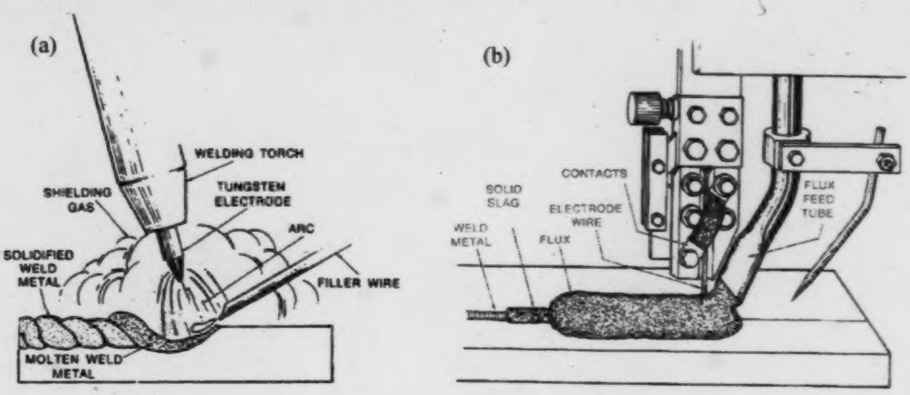

FIG. 3-2. Schematics of two arc welding processes: a) Gas tungsten arc welding; b) submerged arc welding [3].

Pipe making out of flat plates is carried out by either spiral or UOE (first forming a 'U', then changing to an 'O' and finally 'Expanding' it) techniques for larger pipes, and direct forming to circular shapes and welding by ERW (electric resistance welding) technique for smaller pipes, as shown in Fig. 3-3 [4]. UOE and spiral welding are done by SAW, while ERW is a seam welding technique carried out by pressuring the heated edges together. In fusion arc welding, whether single-pass or multi-pass welding is required and whether one side or two sides of the plate should be welded depend on the toughness requirement for a certain application. For example, one-side, one-pass SAW can be applied to structures with service temperatures of -10°C, one-side, two-pass SAW for -30°C, and multi-pass SAW for -50°C [5]. This is because heat input in multi-pass welding is smaller and, therefore, exposure time to high peak temperatures becomes shorter and HAZ width will be smaller. Also, subsequent passes temper the hard constituents in the CGHAZ.

ERW is a very fast process (~8 times faster than spiral) and therefore has economic advantage over arc welding. The disadvantages include a not-so-round profile and lower toughness than arc welding. One of the reasons for the inferior quality is the "fiber up-turn" by weld upsetting, exposing centerline segregation to the weld fusion line and also hoop stresses [6].

3-3. Weld structure

In every fusion welding practice, the metal around the welding line can be divided into three main regions, i.e. weld metal (WM), heat-affected zone (HAZ) and unaffected base metal (BM) (Fig. 3-4). Each region has its own microstructure and properties as they undergo totally different thermal cycles. The weld metal is the weld pool region after solidification, and therefore experiences melting and probably a change in chemical composition due to dilution. The study of the weld metal, although important, is beyond the scope of this research. Some selected references on weld metal microstructure and properties of HSLA and microalloyed steels can be consulted if needed [7-16]. On the other end of this spectrum, there is the rest of base metal that is not affected metallurgically by the thermal cycle of welding, as it is far enough from the fusion line.

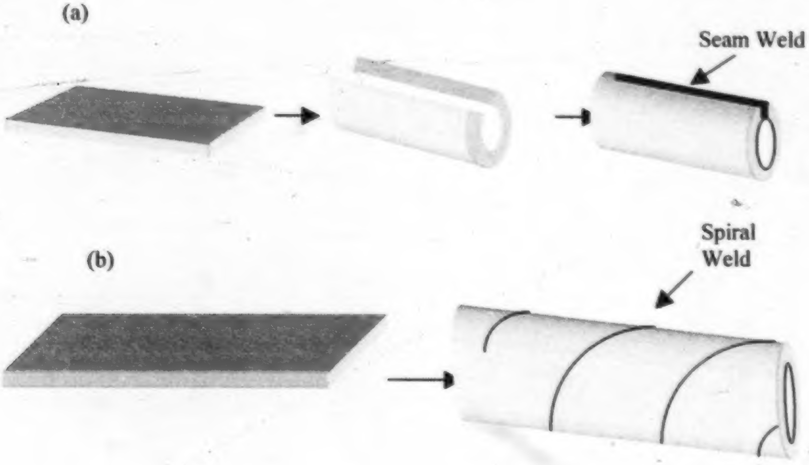

FIG. 3-3. The two types of pipe making: a) UOE/ERW; b) spiral [4].

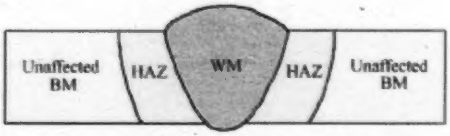

FIG. 3-4. Schematic illustration of the main three zones in the weld.

The main region of interest in this research lies in between the above-mentioned regions, namely the HAZ metal. The HAZ has received a lot of attention from experts in the welding and pipeline industries, because of its inferior mechanical properties, especially at a sub-zone adjacent to the weld metal. The HAZ is defined as a region of base metal, adjacent to the weld metal, which has undergone a *metallurgical change* because of the welding thermal cycle [17].

It is not easy to detect all metallurgical changes, and the extent to which they can be detected depends on the microstructure examination technique applied and the precision of that technique. For this reason, in some practical engineering applications, the term *visible HAZ* is used which can be defined as the part of base metal that undergoes metallurgical change(s) detectable by optical microscopy. This outer boundary of visible HAZ corresponds to A_{C1} for transformable steels. To examine different sub-regions of the weld HAZ, one should distinguish between the HAZ in single-pass welds and multi-pass welds. In multi-pass welds, as will be demonstrated, some zones undergo further thermal cycles.

3-3-1. HAZ of Single-pass Welds

The HAZ of single-pass welds may be divided into five zones, according to the peak temperature they undergo (Fig. 3-5). Some zones, such as the inter-critical and sub-critical HAZs, have further been divided into "the inner" and "the outer parts" by some researchers [18], due to a change in Vickers hardness and microstructure across these zones. In general, moving across the HAZ away from the fusion line, the peak temperature, the austenite grain size and the hardenability decrease.

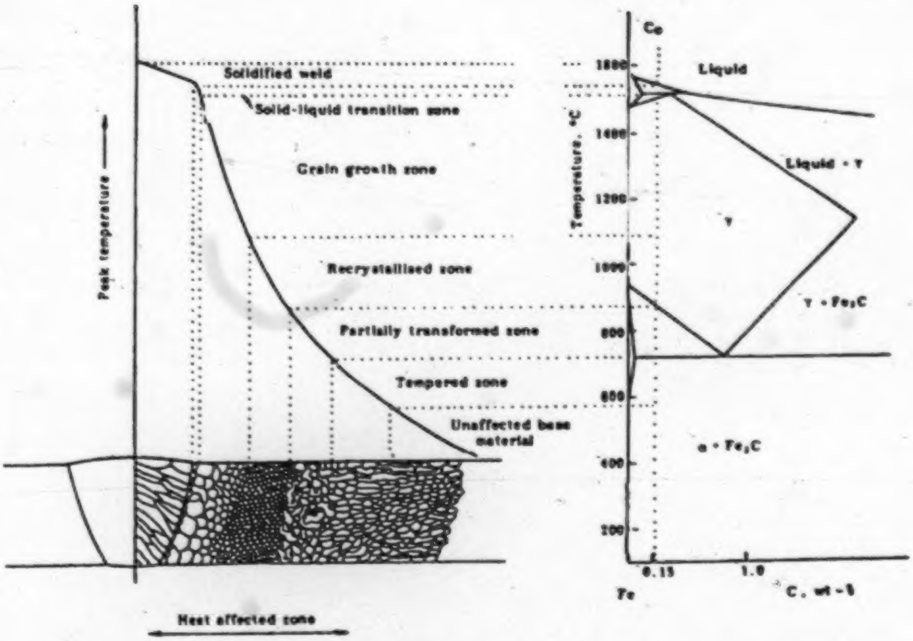
Solidified weld
Solid-liquid transition zone
Grain growth zone
Recrystallised zone
Partially transformed zone
Tempered zone
Unaffected base material
Peak temperature
Heat affected zone
Ce
Liquid
Liquid + γ
γ
γ + Fe₃C
α + Fe₃C
Temperature, °C
1600
1400
1200
1000
800
600
400
200
0.15
1.0
Fe
C, wt-%

FIG. 3-5. Schematic diagram of different weldment zones and their corresponding positions on the Fe-Fe_3C equilibrium diagram for a given carbon concentration of 0.15% [19].

3-3-1-1. Partially melted zone (PMZ)

This very narrow zone (shown in Fig. 3-5 as a solid-liquid transition zone) has a peak temperature between the solidus and liquidus lines on the phase diagram, and the metal experiences partial melting [20]. The effect of dilution by the weld metal is mainly restricted to this region. Note, that many researchers regard this zone just as the fusion line/zone, as it is in fact the interface between the weld metal and the main HAZ. They divide the HAZ, therefore, into four regions, i.e., the zones described below [18, 21].

3-3-1-2. Coarse-grained HAZ (CGHAZ)

The CGHAZ, also known as grain growth zone (as labeled in Fig. 3-5), usually has the poorest mechanical properties [5]. Here the peak temperature is in the range of about 1100-1450°C, and therefore austenite grains grow greatly, to around 100 μm in a typical submerged arc welding process. In addition, the high temperature dissolves almost all precipitates. These two factors result in increased hardenability and low-temperature transformation products like bainite, and probably localized martensite in some regions- depending on carbon level in the base metal [20, 21]. The microstructure, in low-carbon microalloyed steels, consists of coarse packets of bainite in each grain, and the packets consist of dislocated parallel laths. The majority of carbon-rich particles are found at packet boundaries, while some may form at the lath boundaries too [20].

3-3-1-3. Fine-grained HAZ (FGHAZ)

The fine-grained HAZ (a.k.a. the recrystallised zone as labeled in Fig. 3-5) is usually a wide sub-region in microalloyed steels, consisting of fine ferrite grains. The peak temperature is higher than A_{C3}, but lower than the grain coarsening temperature (around 1100°C). As the temperature is not too high, sufficient amounts of precipitates prevail to prevent austenite grain growth, and hence the large area of grain boundaries promotes ferrite formation, transformed from austenite during cooling. Depending on the carbon level of the base metal, the remaining austenite after transformation may transform to pearlite or ferrite-carbide aggregates [20]. The thermal cycle experienced in this region is equivalent to a normalizing heat treatment [22].

3-3-1-4. Inter-critical HAZ (ICHAZ)

The inter-critical HAZ, or partially transformed zone (as labeled in Fig. 3-5), experiences peak temperatures between A_{C1} and A_{C3}. Although the ferrite matrix is not completely transformed to austenite (temperature does not exceed A_{C3}), the carbon-rich constituents transform to austenite on heating above the A_{C1} temperature. On the cooling part of the thermal cycle, depending on the cooling rate, the austenite may transform to pearlite, upper bainite, or martensite, resulting in a multiphase microstructure in this zone. Dislocation density reduction and precipitate coarsening are the other possible changes in the ferrite matrix [20, 21].

The ICHAZ has been reported to have low fracture toughness for HSLA steels with ferrite–pearlite microstructures, especially with the presence of relatively high amounts of Si and V in solid solution, which increases the hardenability [23]. The eutectoid constituents transform to high carbon austenite upon heating. Not all the ferrite transforms to austenite, and therefore the carbon in those carbon-rich austenite grains cannot be shared by other grains. These grains can transform to local brittle zones (LBZ) of martensite–austenite (M-A) or bainite constituents, depending on the cooling rate and the hardenability. This is not a concern in low-carbon steels microalloyed with Nb. Firstly, the eutectoid transformation does not usually take place in the TMCP of the BM, due to both process characteristics (accelerated cooling and sub-cooling) and chemistry (presence of microalloy carbides in the austenite). Secondly, even if there is little pearlite in the BM, chances are the hardenability of the carbon-rich austenite in the ICHAZ is not high due to the presence of more stable carbides of Nb than V, and therefore upon cooling these regions transform to bainite more than they transform to M-A. These effects of Nb and accelerated cooling were observed by Fairchild *et al.* [23]. It should be noted that multi-pass welding will temper any martensite regions during subsequent thermal cycles, and therefore the ICHAZ of ferrite–pearlite steels will not have LBZ [18].

3-3-1-5. Sub-critical HAZ (SCHAZ)

As the peak temperature is below A_{C1}, no considerable microstructural changes are observed, especially by optical microscopy, and this region is identical to the base metal. The only change, detectable by electron microscopy, is tempering, i.e. dislocation rearrangement and reduction. This is why this zone is also known as the tempered zone. Even strain aging, reported in the SCHAZ of other steels, is not expected to happen in microalloyed steels due to the low concentration of free N and C in these steels [20].

3-3-2. HAZ of Multi-pass Welds

When several weld passes are necessary to complete the welding process, the HAZ formed at each pass undergoes another thermal cycle by the subsequent pass. This will change the HAZ microstructure locally, depending on the relative location of each region with regard to the fusion line of the subsequent passes [19, 20, 23]. Several combinations of overlapping HAZ zones will lead to a complicated microstructure. Fig. 3-6 shows schematically the multi-pass effect on the HAZ in a three-pass welding process [5].

The tempering effect of multi-pass welding is of significance for low heat input welds, where low-temperature transformation products are formed. The CGHAZ has been reported to be eliminated in thick sections by a "narrow-gap welding technique", which uses multiple passes to normalize this region [21].

However, when examining the HAZ more carefully, one notices there are regions that are deteriorated because of being subjected to the subsequent passes. Case *C* in Fig. 3-6, inter-critically reheated CGHAZ (IRCGHAZ), is one of these regions. Reheating in $\gamma+\alpha$ two-phase region will lead to M-A formation in prior austenite grain and lath boundaries, which deteriorates the microstructure greatly. The M-A constituents become LBZ, very sensitive in the crack tip opening displacement (CTOD) tests [5]. The IRCGHAZ has been considered the most crucial LBZ in a multi-pass weld HAZ of modern TMCP steels [24, 25].

Multi-pass welding was reported to improve the HAZ toughness in high nitrogen, V-microalloyed steel (without Ti). It was found that VN precipitates, which dissolve during the first pass, reprecipitate in the following pass and inhibit the austenite grain growth in the subsequent passes [26].

It should be noted that even in multi-pass welding, the last pass creates a microstructure identical to the one by single-pass welding, as there is no subsequent welding pass, and the weakest region in the whole

HAZ can be the one that controls the toughness. The only difference, however, is the inter-pass temperature that acts as a preheat for the last pass and decreases the cooling rate (Section 3-4-1).

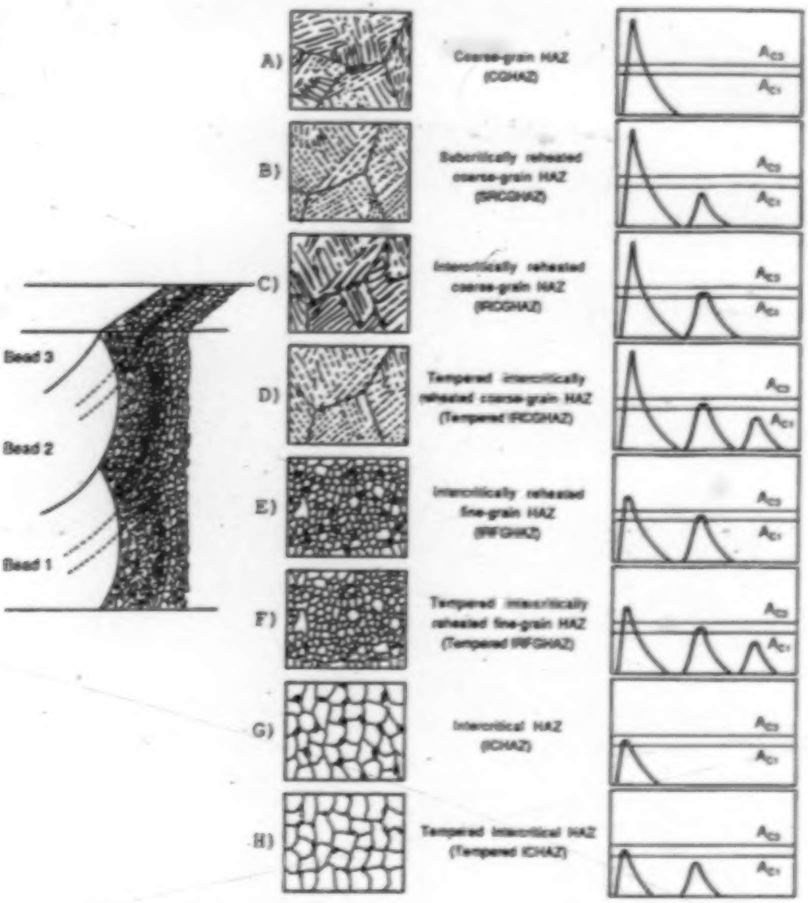
Bead 3
Bead 2
Bead 1
A)
Coarse-grain HAZ
(CGHAZ)
B)
Subcritically reheated coarse-grain HAZ
(SRCGHAZ)
C)
Intercritically reheated coarse-grain HAZ
(IRCGHAZ)
D)
Tempered intercritically reheated coarse-grain HAZ
(Tempered IRCGHAZ)
E)
Intercritically reheated fine-grain HAZ
(IRFGHAZ)
F)
Tempered intercritically reheated fine-grain HAZ
(Tempered IRFGHAZ)
G)
Intercritical HAZ
(ICHAZ)
H)
Tempered intercritical HAZ
(Tempered ICHAZ)
A_{c3}
A_{c1}

FIG. 3-6. Schematic illustration of the effect of multi-pass welding on HAZ microstructure [5].

3-4. Welding considerations

3-4-1. Preheating

Preheating is heating the parent metal before welding. Preheating to temperatures in the range 150–200°C may be applied to ferritic steels for two reasons [27]:

a) Decreasing the cooling rate, especially when the heat input is low, the ambient temperature is low, or the plate thickness is large.

b) Removing hydrogen from the weld area.

Preheating may not be as necessary in normal welding of microalloyed steels (due to the low carbon equivalent) as in welding of other steels. However, as the strength of modern steels increases, especially above 700 MPa, a preheat of around 100°C may become necessary, as the risk of cold cracking increases with strength [28]. In multi-pass welding, preheating is only considered for the first pass, as the inter-pass temperature will be high enough.

3-4-2. Post-weld heat treatment (PWHT)

PWHT is a heat treatment applied to weldments after welding. It may be applied to ferritic steels in the temperature range, e.g., 500–650°C, for different purposes [27, 29]:

a) Tempering the CGHAZ. The CGHAZ may have a martensitic structure with high hardness value, which is susceptible to HAC as the weld cools, and also to reheat or stress relief cracking. PWHT should be applied immediately after welding to temper this microstructure.
b) Reduction of residual stress.
c) Removing hydrogen from the WM and HAZ, hence reducing the chance of fabrication and in-service cracking.

However, there are some other microstructural changes that may happen during PWHT, such as:

a) Carbide spheroidization.
b) Carbide precipitation from enriched zones in ferrite.
c) Dislocation recovery.

These may have some opposing effects on mechanical properties. The overall effect of these opposing factors can be presented in vector diagrams, like the one in Fig. 3-7. This diagram compares qualitatively, rather than quantitatively, the several factors that affect the toughness in a C-Mn weld metal [14]. The actual vector size depends on the material composition and microstructure.

Therefore, PWHT is somewhat tricky. In general, it can restore the HAZ toughness and relieve the local brittle zones, and thereby reduce the susceptibility to hydrogen assisted cracking, by tempering the coarse high carbon martensite particles along the prior austenite grain boundaries. However, it is not recommended for some microalloyed steels, as some intergranular precipitation can take place, which results in reduction of the HAZ toughness, promoting stress relief cracking [20].

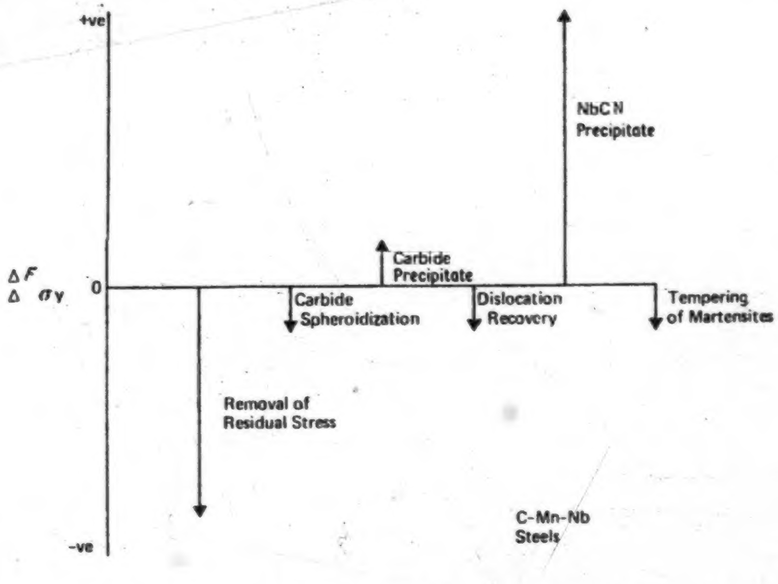

FIG. 3-7. Vector diagram of factors affecting toughness in C-Mn-Nb weld metal [14].

3-5. HAZ sample preparation

The HAZ samples used in microstructural and mechanical analyses in this study were obtained from weld samples prepared previously for another study [30] on the same material, i.e., Grade 100 microalloyed steel. A plate of Grade 100 steel, 8 mm in thickness, was used for welding. The oxide scales were removed from both surfaces by milling to allow for good arc conductivity and stability, as well as to remove small bumps on the surface and make the surfaces very flat. Welding was performed by DCEN (direct current electrode negative polarity; a.k.a., straight polarity) autogenous GTAW (gas tungsten arc welding with no filler metal) shielded with argon gas. This provided bead-on-plate welds (as opposed to full penetration butt welds used mostly in industry) to be used for the HAZ examination (Fig. 3-8). Nominal heat inputs of 0.5 to 2.5 kJ/mm were applied by selecting an arc voltage of 12.5 V, an arc current of 150 A, and travel speeds of 0.7 to 4.0 mm/s. The tungsten electrode rod had a diameter of 1/8" (~3.18 mm) ending in a pointed cone shape with an angle of 45°. The distance between the electrode tip and the plate was ~1.75 mm in all cases.

For this study, the HAZ samples were cut out of the welded plates and then mounted, ground, polished (standard metallographic procedures) and etched (2% Nital in most cases) in order to perform microstructural and mechanical analyses (Chapters 5 to 7). Transverse and longitudinal sections were made from the welded plates (Fig. 3-8a). Fig. 3-8b shows the macrostructure of the longitudinal weld section (0.5 kJ/mm) revealed by etching with 2% Nital for ~20 s. The various regions, i.e., BM, WM and HAZ, as well as the HAZ sub-regions, are visible. These sub-regions consist of the CGHAZ, FGHAZ and ICHAZ. The SCHAZ, which is located between the ICHAZ and the unaffected BM, is not a visible sub-region.

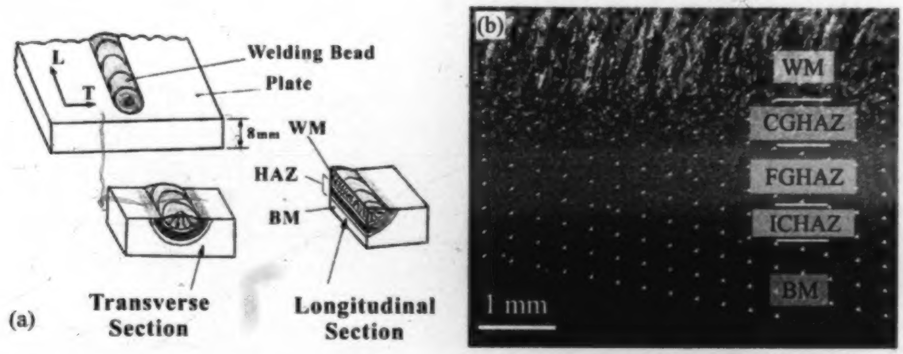

FIG. 3-8. a) Schematic of a weld section in transverse and longitudinal directions. b) Macrostructure of 0.5 kJ/mm longitudinal weld section; hardness mapping indentations are also visible.

3-6. Summary

The HAZ is defined as a region of base metal, adjacent to the weld metal, which has undergone a *metallurgical change* because of the welding thermal cycle. The main sub-regions of the HAZ in single-pass welds are the coarse-grained HAZ, fine-grained HAZ and inter-critical HAZ. In low carbon microalloyed steel, the CGHAZ receives the most attention as it experiences very high peak temperatures and as a result has the largest austenite grain size and the highest degree of hardenability. As mentioned in the previous chapter, hydrogen assisted/induced cracking may be of concern in a high-strength, low sulphur steel such as Grade 100. For this reason, preheat or PWHT may be needed for reduction of hardness in the HAZ and removal of hydrogen from the weld area.

References

[1] Weman, K., 2003, Welding Processes Handbook, Woodhead Publishing ltd., Abington.

[2] Gladman, T., 1997, The Physical Metallurgy of Microalloyed Steels, The Institute of Materials, London.

[3] Kennedy, G. A., 1982, Welding Technology, Bobbs-Merrill Educational Publishing, Indianapolis.

[4] Sharma, U., and Ivey, D. G., 2000, "Microstructure of Microalloyed Linepipe Steel," IPC00-0153, *Proc., International Pipeline Conference (IPC 2000)*, ASME, **1**, pp. 193-201.

[5] Shiga, C., and Saito, Y., 1990, "Toughness Improvement in HAZ of HSLA Steels by TMCP in Japan," American Welding Society), pp. 177-205.

[6] Williams, J. G., Killmore, C. R., Barbaro, F. J., Meta, A., and Fletcher, L., 1995, "Modern Technology for ERW Linepipe Steel Production (X60 to X80 Beyond)," *Proc., ISS, Proceedings of the International Conference "Microalloying '95"*, pp. 117-139.

[7] Mangonon, P. L., 1985, "Transmission Electron Microscopy of Welded Cb-Microalloyed Steel," Welding Journal, **64** (1), pp. 13-s to 17-s.

[8] Grong, O., and Matlock, D. K., 1986, "Microstructural Development in Mild and Low-Alloy Steel Weld," Int. Met. Rev., **31** (1), pp. 27-48.

[9] Evans, C., 1995, "Microstructure and Properties of Ferritic Steel Welds Containing Aluminum and Titanium," Welding Journal, **74** (no. 8), pp. 249-s to 261-s.

[10] Evans, G. M., 1993, "The Effect of Titanium in Manganese-Containing SMA Weld Deposits," Welding Journal, **72** (3), pp. 123-s to 133-s.

[11] Moon, D. W., Fonda, R. W., and Spanos, G., 2000, "Microhardness Variations in HSLA-100 Welds Fabricated with New Ultra-Low-Carbon Weld Consumables," Welding Journal, **79** (10), pp. 278-s to 285-s.

[12] Brownlee, J. K., Matlock, D. K., and Edwards, G. R., 1986, "Effects of Aluminum and Titanium on the Microstructure and Properties of Microalloyed Steel Weld Metal," *Proc., Advances in Welding Science and Technology*, ASM International (USA), pp. 245-250.

[13] Signes, E. G., and Baker, J. C., 1979, "Effect of Niobium and Vanadium on the Weldability of HSLA Steels," Welding Journal, **58** (6), pp. 179-s to 187-s.

[14] Farrar, R. A., and Ferrante, M., 1982, "Properties and Microstructure of Stress-Relieved Submerged-Arc Weld Metal Containing Niobium," J. Mater. Sci., **17** (8), pp. 2405-2412.

[15] Wang, W., 2002, "Alloying and Microstructural Management in Developing SMAW Electrodes for HSLA-100 Steel," Welding Journal, **81** (7), pp. 132-s to 145-s.

[16] Nemade, J. B., and Bhole, S. D., 2003, "Characterization and Comparison of Spirally Welded HSLA Steel Line-Pipe Submerged Arc Production Weld and a Laboratory Weld," *Proc., Conference of Metallurgists 2003, The international symposium on transformation and deformation mechanisms in advanced high-strength steels*, M. Militzer, and W.J. Poole, eds., Metallurgical Society of the Canadian Institute of Mining, Metallurgy and Petroleum, pp. 261-275.

[17] Gourd, L. M., 1995, Principles of Welding Technology, Edward Arnold.

[18] Scoonover, T. M., Lukens, W. E., and Pande, C. S., 1984-1985, "Correlation of Heat Affected Zone Microstructure with Peak Heating Temperature in HSLA-80 Steel Weldments," 1986, *Proc., Unusual Techniques and New Applications of Metallography. Volume II*, American Society for Metals, pp. 91-104.

[19] Easterling, K. E., 1992, Introduction to the Physical Metallurgy of Welding, Butterworth-Heinemann Ltd, Oxford.

[20] Losz, J. M. B., and Challenger, K. D., 1990, "HAZ Microstructures in HSLA Steel Weldments," *Proc., First United States--Japan Symposium on Advances in Welding Metallurgy*, American Welding Society, Miami, pp. 323-357.

[21] Collins, L. E., Godden, M. J., and Boyd, J. D., 1983, "Microstructures of Linepipe Steels," Can. Metall. Q., **22** (2), pp. 169-179.

[22] Godden, M. J., and Boyd, J. D., 1981, "Characterization of Microstructures in Weld Heat-Affected Zones by Electron Microscopy," *Proc., Microstructural Science, Vol. 9. 13th Annual Technical Meeting of the International Metallographic Society*, Elsevier North-Holland Inc., New York, pp. 343-354.

[23] Fairchild, D. P., Bangaru, N. V., Koo, J. Y., Harrison, P. L., and Ozekcin, A., 1991, "A Study Concerning Intercritical HAZ Microstructure and Toughness in HSLA Steels," Welding Journal, **70** (12), pp. 321-s to 329-s.

[24] Aihara, S., and Okamoto, K., 1990, "Influence of Local Brittle Zone on HAZ Toughness of TMCP Steels," *Proc., The Metallurgy, Welding, and Qualification of Microalloyed (HSLA) Steel Weldments*, American Welding Society (USA), pp. 402-426.

[25] Davis, C. L., and King, J. E., 1996, "Cleavage Initiation in the Intercritically Reheated Coarse-Grained Heat Affected Zone. Ii. Failure Criteria and Statistical Effects," Metallurgical and Materials Transactions A, **27A** (10), pp. 3019-3029.

[26] Zajac, S., Langerborg, R., and Siwecki, T., 1995, "The Role of Nitrogen in Microalloyed Steel," *Proc., ISS, Proceedings of the International Conference "Microalloying '95"*, pp. 321-338.

[27] Lant, T., Robinson, D. L., Spafford, B., and Storesund, J., 2001, "Review of Weld Repair Procedures for Low Alloy Steels Designed to Minimise the Risk of Future Cracking," International Journal of Pressure Vessels and Piping, **78** (11-12, Special Issue), pp. 813-818.

[28] Dolby, R. E., 2000, "Joining Issues for New Constructional Steels," Science and Technology of Welding and Joining, **5** (6), pp. 341-346.

[29] Shiga, C., Gotoh, A., Kojima, T., Horii, Y., Fukada, Y., Ikeuti, K., and Matuda, F., 1996, "State of the Art Review on the Effect of PWHT [Post Weld Heat Treatment] on Properties of Steel Weld Metal," Welding in the World/Soudage dans le Monde, **37** (4), pp. 163-176.

[30] Hoskins, S. J., 2002, Weldability of Grade 80 and Grade 100 Microalloyed Steels, M.Sc. dissertation, University of Alberta, Edmonton.

Chapter 4

Thermal Analysis of Welding in the HAZ

4-1. Introduction

During the weld thermal cycle, a series of microstructural changes take place in the HAZ. In microalloyed steels, such as Grade 100, these changes consist of phase transformations (reaustenitization and retransformation), grain growth and precipitate alteration (dissolution, coarsening and reprecipitation). All these changes depend on the actual thermal cycle experienced at a particular location. To be able to examine these changes, interpret them appropriately or predict them correctly, a series of thermal history information is required:

1- The thermal cycle (T-t curves) at any location in the HAZ; this defines the extent of any phase change or precipitate alteration by specifying the time spent above a certain temperature.
2- The peak temperature distribution across the HAZ.
3- The heating and cooling rates; the latter affects the γ-α transformation and carbonitride reprecipitation.

This information is necessary, if microstructure is to be correlated with the properties. This becomes more significant if the effect of heat input on the microstructural changes in the HAZ is to be examined for a given material, as the heat input is only a rough, simplified parameter specific to a welding process and particularly used in the welding industry, and has little scientific value when it comes to the study of microstructures and/or properties. Since the values of the above-mentioned parameters at all locations and/or times are difficult, if not impossible, to obtain experimentally, some mathematical models are required.

4-2. Historical Background

Perhaps, the most-widely used and the best-known analytical solutions to predict weld thermal history are those of Daniel Rosenthal. Rosenthal was not necessarily a pioneer in this area as, for instance, "some of the results obtained independently by Rosenthal had been obtained earlier by Roberts, in 1923, who was interested in some diffusion problems and Wilson, in 1904, who considered some cases of convection" [1]. Rosenthal's attempts on the mathematical theory of heat distribution in welding were first published in 1935. He and Schmerber [2] verified the validity of the theoretical assumptions and equations later in 1938 by performing experiments only for the plane state, i.e., 2D heat distribution. However, the main works of Rosenthal that most researchers refer to are those from 1941 [3] and 1946 [4], in which he analysed the heat distribution in welding and cutting for various conditions (1D, 2D and 3D) under a "quasi-stationary" state. His approach was based on the following simplifying assumptions:

1- The thermal properties of the material do not change with temperature.
2- The heat source is considered as a point on the plate surface directly below the arc.
3- Heat losses through the surfaces are neglected.
4- The plate is wide enough and long enough to be considered infinitely wide.
5- Heat created by the Joule effect in the plate is neglected.
6- The physical state of the plate does not change (no melting); this makes the analysis applicable only to the regions outside the fusion zone, i.e., the HAZ and BM.

Since the original papers were published, there have been many other rigorous approaches with more realistic assumptions to add to or modify Rosenthal's work. Among these are the works of Tanaka [5] with the assumption of surface heat transfer, or that of Kasuya and Yurioka [6] with the assumption of an extended heat source beneath the plate surface (necessary for the case of high heat input welding) in addition to taking into account surface heat transfer. Grosh and Trabant [1] added a function to the heat equation to account for the dependence of thermal properties on temperature. Christensen *et al.* [7], without changing the assumptions of Rosenthal, worked on generalisation of his equations of temperature variations in a semi-infinite body (thick plates) in order to construct a "temperature chart" with *dimensionless* parameters, that can be used for estimation of zone widths and depths, cooling rate and time of residence between two temperatures for a wide range of materials and variable heat input energies.

Some other examples of refinement to Rosenthal's equations with respect to the heat source are the works of Nunes [8], Dikshit and Atteridge [9], Eagar and Tsai [10], Ashby and Easterling [11], and Shah *et* *al.* [12]. Nunes replaced the point source by a multi-pole distribution. Dikshit and Atteridge split the heat source into different numbers of equal parts at fixed locations on the workpiece and then calculated an effective heat input by summing the heat input of each part, which was a function of location. Eagar and Tsai assumed a Gaussian heat distribution. Ashby and Easterling considered a disk of finite radius for the heat source. Shah *et al.* replaced the real source by an *apparent* diffuse Gaussian source above the surface. These refinements allow for having finite temperatures at the surface and, therefore, more accurate temperatures at the fusion line and the weld pool.

In addition to the above mentioned analyses which are based on instantaneous temperature distribution around a heat source, some researchers have tried to directly calculate parameters, such as peak temperature and cooling rate, by deriving a relationship between geometric parameters and the thermal/welding parameters. For instance, Adams analyzed a geometric characteristic of peak temperature isotherm locus [13]. Rykaline and Beketov [14] calculated the thermal cycles in high temperature regions of the HAZ by equating the calculated and experimentally determined outlines of the molten pool (i.e., solidus isotherm) and introducing certain auxiliary heat sources/sinks into the calculation, which allow for evolution and absorption of latent heat of melting at the solid-liquid boundary.

In addition to all these analytical solutions, numerical approaches have also been adopted in order to replace the rather simplified assumptions with more realistic ones. For instance, Kuo [15] used a finite difference method to predict temperature distributions in thin plates, which resulted in more accurate estimations in regions of very high temperature, such as the weld pool and liquid-solid boundary. Goldak *et al.* [16] used a non-linear transient finite element method to compute temperature distribution from a non-axisymmetric 3D heat source. Unfortunately, all these modifications or replacements are rather complicated and in most cases not necessary for most applications concerning the temperature distribution and variation in the HAZ. It is worthy to mention that one of the findings of most of these investigations (e.g., [6]) was that cooling rate (or cooling time) in the HAZ did not depend on the location of the point heat source and, therefore, could be found from Rosenthal's solution.

Ashby and Easterling [17] simplified the two limiting solutions derived by Rosenthal to obtain temperature/time profiles in the HAZ. One set of solutions was derived for thick plates (assuming 3D heat flow) and the other for thin plates (assuming 2D heat flow). There was also an equation to determine a critical thickness for a given heat input (or a critical heat input for a given plate thickness, if used in reverse) at which the 2D condition changes to 3D [18]. However, this criterion may be too simplistic. Real welds are more likely to lie between the two limiting solutions; a situation classified by some researchers as 2.5D [19], for which there is no simple solution [3]. The question then is where a particular case lies with respect to the 2D and 3D conditions.

4-3. Theoretical approach

4-3-1. Heat source energy

The energy of the heat source in most fusion welding processes comes from the arc that forms between the tip of an electrode and the workpiece (plate). In most early analyses, the heat source was assumed to be extremely small (having no volume) and infinitely intense. In reality, however, the source has a finite dimension and therefore a finite intensity. There are not many investigations based on the intensity of the heat source, while this is the most important factor that, if sufficient, causes melting and is different from process to process and when the welding parameters vary [20]. The power density distribution is often approximated to be Gausian:

$$Q' = \frac{3q}{\pi a^2} \exp\left(\frac{-3r^2}{a^2}\right) \qquad (4\text{-}1)$$

Q' is the power density, q is the power transferred to the workpiece, a is the effective radius of the heat source and r is the radial distance from the centreline of the heat source. The advantages of increasing the power density of the heat source are: deeper penetration, higher welding speeds, and better weld quality with less damage to the workpiece [20].

4-3-2. Heat input

Heat input, q/v, is defined in electric arc processes as:

$$q/v = \frac{E.I.\eta}{v} \qquad (4\text{-}2)$$

E is the arc voltage, I is the arc current, η is the thermal efficiency and v is the travel speed of the electrode over the workpiece. Thermal efficiency, which is in fact the ratio between the actual heat input to the work piece and the energy output of the welding machine, is lower than 1, because some part of the arc energy is dissipated to the surroundings by radiation, convection or conduction and is therefore lost. In this thesis, the term actual heat input (a.k.a. *effective* heat input or *net* heat input) refers to q/v with $\eta < 1$, and the term nominal heat input refers to q/v with $\eta = 1$.

Hess *et al.* [21] introduced an "input factor" to account for derivation from a point heat source. They noticed that the presence of the molten metal pool constitutes a delayed heat input after the passing of the electrode, and has an effect of increasing the actual heat input. This is an interesting point that may cancel out some of the other factors that act to reduce the actual heat input. These include the voltage drop due to losses in the components of the welding configuration, making the actual arc voltage less than the power source voltage [22], or latent heat effects that temporarily cause some of the heat to be removed and stored in the weld pool. Different forms of correction of the heat input, to account for the effect of latent heat, have been proposed by Ashby and Easterling [11] and Shah *et al.* [12]. However, as shown in Section 4-5-2, the time for solidification is very short and so it does not seem necessary to account for the latent heat in the calculation of effective heat input, as the heat should be returned to the sample upon solidification, before the thermal cycle wave reaches the HAZ. Therefore this should not by any means affect calculation of peak temperature profiles and cooling time from 800 to 500°C.

In processes with higher heat densities, lower heat inputs to the workpiece are required. For instance, heat inputs required in high-energy beam welding are usually very low. The typical values of heat input for different processes are shown in Table 4-1. Reducing the heat input is of potential interest to many industries such as the aerospace and electronics industries [23], where microwelding applications are widespread, or structural and pipeline industries [24], where productivity and mechanical properties are important. The advantages of application of low heat input are: a) reduction in melting volume and HAZ volume, which in turn will result in reduction in the distortion and the volume of degraded mechanical properties; and b) increase in welding speed, which will result in an increase in productivity. However, the drawback is an increase in the risk of producing martensite and local brittle zones. This, however, can be controlled by a suitable weld-bead overlap technique [25].

Heat input as defined by Equation 4-2, and used widely in industry, expresses the amount of thermal energy per unit length of the weld run deposited on the workpiece. As seen in Section 4-3, plate thickness has a significant effect on the thermal cycle characteristics too; something that should be remembered when considering "typical values of heat input" (Table 4-1). Therefore, it may be necessary to define another parameter that includes both heat input and the plate thickness. One example is a parameter that defines the "heat input per unit length of the weld per unit thickness of the workpiece", expressed in kJ/mm/mm" [20]. To reach the best definition, some experiments on the effect of plate thickness on parameters such as cooling rate are required, which are beyond the scope of this study.

Table 4-1. Typical values of nominal heat input for different processes [18]

Welding Process	Approximate heat-input range (kJ/mm or MJ/m)
Electroslag	5-50
Submerged arc	1-10
Gas-metal arc	0.5-3.0
Manual metal arc	0.5-3.0
Gas-tungsten arc	0.3-1.5
Electron beam	0.1-0.6
Laser beam	0.1-0.6

4-3-3. Thermal efficiency

Thermal efficiency, a.k.a. arc efficiency, depends on many factors such as the weld process, welding equipment and setup, travel speed, the material to be welded (anode work function), arc voltage and current. Voltage and anode material have the greatest effect after polarity [26]. Thermal efficiency, very much like thermal parameters of materials (such as thermal conductivity), is not easy to determine, not well understood and has been subjected to manipulation to obtain the best correlation between the mathematical formulations and experimental data. The most accurate way to determine thermal efficiency is through calorimetric tests [20]. In GTAW, thermal efficiency is highest for DCEN and increases as the travel speed increases. Fuerschbach and Knorovsky [23] reported arc efficiencies of around 0.7-0.8 for GTAW–DCEN after conducting calorimetric tests on two types of steels and a Ni-based alloy. Arc efficiency reached a plateau of 0.8 as the travel speed increased. Values within the same range were also confirmed by Kou [20] and used by others (e.g., [12]). Although much lower values for the thermal efficiency in GTAW were reported in the literature elsewhere (e.g., [7], [3] and [18]), a value of $\eta = 0.75$ obtained through more recent calorimetric experiments, is deemed more reasonable for the setup and welding characteristics used here, which is in agreement with the value reported in the ASM Handbook [26].

There is also another way to determine the efficiency, and that is through an equation, derived by Rosenthal (Equation 4-36 in Section 4-5-3), that estimates the saturation or equilibrium temperature after the welding on a plate of finite width. As one of the assumptions in deriving Equation 4-36 was the absence of heat loss to the atmosphere, the test should be carried out in vacuum and the workpiece should be thermally isolated from all fixtures [27]. However, there are some other assumptions in deriving the equation (see Rosenthal's assumptions in Section 4-2) that are not very realistic. Unless a correction is applied to the equation, the values of the thermal efficiency estimated may be somewhat (similar to the estimation of the cooling time and peak temperature) questionable.

4-3-4. Rosenthal's equations for 2D and 3D conditions

The differential equation for heat flow in welding can be expresses as follows:

$$\frac{\partial^2 T}{\partial x^2}+\frac{\partial^2 T}{\partial y^2}+\frac{\partial^2 T}{\partial z^2}=\frac{\rho c}{k}.\frac{\partial T}{\partial t} \qquad (4\text{-}3)$$

The two limiting solutions to the Rosenthal equations of a moving point heat source for regions outside the fusion zone are laid out below. The solutions give the temperature variation during cooling as a function of time for a given location, the peak temperature, T_P, as a function of distance from the heat source, and the weld time constant, $\Delta t_{8\text{-}5}$ (cooling time from 800 to 500°C), which is a criterion for cooling rate.

Thick plates (3D):

$$T-T_0=\frac{q/v}{2\pi\lambda t}\exp(-\frac{r^2}{4at}) \qquad (4\text{-}4)$$

$$T_P-T_0=\left(\frac{2}{\pi e}\right)\frac{q/v}{\rho c r^2} \qquad (4\text{-}5)$$

$$\Delta t_{8\text{-}5}=\frac{q/v}{2\pi\lambda\theta_1} \qquad (4\text{-}6)$$

$$\frac{1}{\theta_1}=\left(\frac{1}{500-T_0}-\frac{1}{800-T_0}\right) \qquad (4\text{-}7)$$

Combining Equations 4-4 to 4-7 together, gives the temperature variation as a function of cooling time, peak temperature and initial temperature:

$$T-T_0=\frac{\theta_1\Delta t}{t}\exp[\frac{-\theta_1\Delta t}{et(T_P-T_0)}] \qquad (4\text{-}8)$$

Thin plates (2D):

$$T-T_0=\frac{q/v}{d(4\pi\lambda\rho c t)^{1/2}}\exp(-\frac{r^2}{4at}) \qquad (4\text{-}9)$$

$$T_P-T_0=\left(\frac{2}{\pi e}\right)^{1/2}\frac{q/v}{d\rho c 2r} \qquad (4\text{-}10)$$

$$\Delta t_{8-5} = \frac{(q/v)^2}{4\pi\lambda\rho c d^2\theta_2} \tag{4-11}$$

$$\frac{1}{\theta_2} = \left(\frac{1}{(500-T_0)^2} - \frac{1}{(800-T_0)^2}\right) \tag{4-12}$$

Combining Equations 4-9 to 4-12 together gives:

$$T - T_0 = (\frac{\theta_2 \Delta \mathrm{t}}{\mathrm{t}})^{1/2} \exp[\frac{-\theta_2 \Delta \mathrm{t}}{2et(T_P - T_0)^2}] \tag{4-13}$$

The parameters in the above equations are defined and their values are reported in Table 4-2. The thermal property values do not differ among most of the low alloy steels (e.g., [21]), making it possible to apply this information to all ordinary plain carbon and low alloy steels. Note that the unique characteristic of the cooling rate is that it is independent of the distance from the heat source in the HAZ. This characteristic has also been confirmed by numerical analysis (e.g., [28]) as well as experiments. Hess *et al.* [21] reported only a slight increase in the cooling rate in the HAZ at points closer to the fusion line and confirmed the validity of the assumption that cooling rate is only dependent on heat input, plate geometry/thickness, and plate initial temperature (i.e., preheating). This assumption is widely accepted now (e.g., [12, 18, 29]).

Table 4-2. Definition, units, and values (for carbon steel) of parameters used in Equations 4-3 to 4-13 [17]

Symbol	Definition and unit	Value
T	Temperature (°C)	-
T_P	Peak temperature (°C)	-
t	Time (s)	-
Δt_{8-5}	Cooling time from 800° to 500°C (s)	-
r	Radial/lateral distance from heat source (m)	-
T_0	Initial Temperature (°C)	25
λ	Thermal conductivity (J/sm°C)	41
a	Thermal diffusivity (m^2/s)	9.1×10^{-6}
ρc	Specific heat per unit volume (J/m^3°C)	4.5×10^{6}
d	Plate thickness (m)	8×10^{-3}
q	Arc power (J/s)	-
v	Travel speed (m/s)	-
q/v	Heat input (J/m)	-

4-3-5. Method of weighting for intermediate-size plates[§]

When using the Rosenthal equations, the question of whether to use thin- or thick-plate solutions arises. Equation 4-14 calculates a critical plate thickness, d_C, over which the crossover between the 2D and 3D conditions of heat flow takes place [18].

$$d_C = \left[\frac{q/v}{2\rho c}.\left(\frac{1}{500-T_0} + \frac{1}{800-T_0}\right)\right]^{1/2} \tag{4-14}$$

This equation can be used in reverse to find a critical heat input for a fixed plate thickness. Assuming a critical value for heat input, such that 3D conditions hold for values of heat input below the critical one and 2D conditions for values above, is too simplistic. The real situation is expected to fall somewhere between the two for a plate of finite thickness. Another criterion, presented by Adams [13], which states the equations that predict the highest peak temperature or the lowest cooling rate are more close to the real situation, is not reasonable either. Moreover, the criterion stated by Myers *et al.* [19], that the larger the dimensionless parameter $G = \rho cvd/2\lambda$ the closer the condition is to 3D, would not help in deciding which equation to use or which solution would be valid for situations between the extremes. The same problem exists with the criterion of "relative plate thickness", which suggests that the thick-plate condition prevails if a dimensionless parameter, τ, is greater than 0.75, and a thin-plate condition applies if it is less than 0.75 [30]. The parameter τ is calculated with the following equation.

[§] A version of this section has been accepted for publication. K. Poorhaydari, B.M. Patchett and D.G. Ivey. 2005. Welding Journal (October issue), American Welding Society.

$$\tau = d\sqrt{\frac{\rho c\ (T_C - T_0)}{q / v}} \qquad (4\text{-}15)$$

T_C is a critical temperature, usually assumed to be 550°C for most steels.

A more reasonable, yet simple, method to answer this question is presented here. The actual values of parameters (as opposed to the lower-bound or upper-bound values), such as cooling rate and peak temperature profile, are estimated for a given weld section. This can be very useful as experimental measurement of weld thermal cycles, for example by embedding thermocouples in the HAZ, is not trivial, and in some cases is impractical or unsatisfactory considering the small size of the HAZ. In addition the weld process and configurations sometimes do not allow implementing the instrumentation for recording the thermal cycle. The approach, explained in this section, is based on deriving a parameter (i.e., HAZ width) that can be measured post-mortem on a sample, and used to calculate a weighting factor to apply to the thick- and thin-plate values of the parameters of interest. Although this approach is developed for transformable steels in this chapter, it can be expanded to other materials, so long as the HAZ has visible boundaries in the etched macro section and the peak temperatures for the boundaries are known.

It is well known that the visible HAZ boundaries in transformable steels correspond to the T_S (solidus temperature or peritectic temperature) on the side adjacent to the weld zone and to the Ac_1 (the lower critical temperature upon heating), or simply A_1 [18], on the side adjacent to the unaffected base metal. Therefore, the HAZ width, W, can be simply formulated as:

$$W = r_{A1} - r_{Ts} \qquad (4\text{-}16)$$

r_{A1} and r_{Ts} are the distances of the HAZ/BM and HAZ/WM boundaries, respectively, from the heat source. Finding the corresponding values of r_{A1} and r_{Ts} from Equations 4-5 and 4-10 and substituting them into Equation 4-16 will yield the HAZ width for thick- and thin-plate assumptions, respectively:

$$W_{Thick\text{-}plate} = C_1.(q / v)^{\frac{1}{2}} \qquad (4\text{-}17)$$

$$C_1 = \left[\frac{2}{\pi e \rho c}\right]^{\frac{1}{2}} \cdot \left[\frac{1}{(A_1 - T_0)^{\frac{1}{2}}} - \frac{1}{(T_S - T_0)^{\frac{1}{2}}}\right] \qquad (4\text{-}18)$$

$$W_{Thin\text{-}plate} = C_2.(q / v) \qquad (4\text{-}19)$$

$$C_2 = \left[\frac{2}{\pi e}\right]^{\frac{1}{2}} \cdot \left[\frac{(T_S - A_1)}{2d\rho c(T_S - T_0)(A_1 - T_0)}\right] \qquad (4\text{-}20)$$

Based on the assumption that the actual situation lies between the two limiting solutions, the actual HAZ width can be related to the above values (Equations 3-17 and 3-19) as:

$$W_{Actual} = W_{Thick\text{-}plate} + F_W\ .\ (W_{Thin\text{-}plate} - W_{Thick\text{-}plate}) \qquad (4\text{-}21)$$

F_W, varying between 0 and 1, is the weighting factor that determines the deviation from the thick-plate solution with respect to the thin-plate solution. It can be shown that Equation 4-21 can be easily derived, if the same kind of relationship for estimation of r_{A1} and r_{Ts} was considered initially (i.e., the following equations), and then substituted into Equation 4-16.

$$r_{A1-Actual} = r_{A1-Thick\text{-}plate} + F\ .\ (r_{A1-Thin\text{-}plate} - r_{A1-Thick\text{-}plate}) \qquad (4\text{-}22)$$

$$r_{Ts-Actual} = r_{Ts-Thick\text{-}plate} + F\ .\ (r_{Ts-Thin\text{-}plate} - r_{Ts-Thick\text{-}plate}) \qquad (4\text{-}23)$$

Rearranging Equation 4-21 gives the value of F_W for any given weld sample:

$$F_W = (W_{Actual} - W_{Thick\text{-}plate})\ /\ (W_{Thin\text{-}plate} - W_{Thick\text{-}plate}) \qquad (4\text{-}24)$$

It is proposed that the thermal parameters of importance can be estimated by weighting the thick- and thin-plate solutions, using the weighting factor F_W:

$$\Delta t_{Actual} = \Delta t_{Thick\text{-}plate} + F_W\ .\ (\Delta t_{Thin\text{-}plate} - \Delta t_{Thick\text{-}plate}) \qquad (4\text{-}25)$$

$$T_{P,Actual} = T_{P,Thick\text{-}plate} + F_W \,.\, (T_{P,Thin\text{-}plate} - T_{P,Thick\text{-}plate}) \tag{4-26}$$

Equation 4-25 is similar to one proposed by Hess *et al.* [21]. They proposed that a "correction factor", which would represent "the degree of infiniteness", should be calculated by determining the instantaneous cooling rate at a particular time from an experimentally obtained thermal cycle. This value would then be compared with the corresponding values obtained from Rosenthal's equations for thick- and thin-plate conditions through Equation 4-25. This correction factor would then be used to obtain corrected values of the cooling rate at other times (or temperatures). The approach adopted here, and shown to be reliable in the next section, demonstrates that this factor can be obtained from the measurement of the HAZ width independently and, therefore, the instrumented welding test can be eliminated. The need to apply a correction factor to the cooling time equations was also addressed, rather poorly, by Shah *et al.* [12], who added a correction factor coefficient, called "notch factor", to Equation 4-11 (thin-plate solution), to account for the effects of joint geometry, not considered by the Rosenthal equations. However, there was no attempt to find a way to systematically determine the factor.

Another point is that, as mentioned earlier, the location of the heat source does not affect the cooling rate, but shifts the peak temperature profile relative to the plate geometry. In reality, the heat source may not coincide to the top surface of the plate. Going back to the fundamental assumption that the location and peak temperatures of the HAZ boundaries are known, the exact peak temperature profile can be plotted with respect to the distance from the top surface of the plate, which is a tangible reference point. A calculated profile (either based on thick-plate/thin-plate assumptions or weighted as proposed by Equation 4-26) will be shifted and fitted into the known locations designated by the T_S temperature and the A_1 temperature. Equation 4-27 formulates this mathematically.

$$r^{*}_{Tp} = r_{Tp} - (r_{Ts} - r^{*}_{Ts}) - S_{Tp} \tag{4-27}$$

$$S_{Tp} = (W_C - W_M) \,.\, \frac{(T_S - T_P)}{(T_S - A_1)} \tag{4-28}$$

The symbol * on r values in Equation 4-27 designates the distance of a given point in the plate (specified by a peak temperature) from the top surface. Otherwise, r designates the distance with reference to the heat source. Therefore, r_{Tp} values are a series of points for which T_P is calculated from Equation 4-26, r_{Ts} is one of these points where $T_P = T_S$, and r^{*}_{Ts} is measured from the weld section. W_C and W_M are the calculated and measured values of the HAZ width, respectively. The first terms in Equation 4-27 shift the entire profile so that the T_S temperature fits on the location of the fusion line. The term S_{Tp} in Equation 4-27 (and calculated from Equation 4-28) represents an additional adjustment needed to fit the other points on the profile. This adjustment is proportional to the temperature difference in T_P from the reference point used here for the initial shifting (i.e., T_S). Note that this adjustment is also proportional to the difference between the calculated and measured values of the HAZ width, which is considerable when the calculations are based on thick- or thin-plate assumptions. For the case where calculation of peak temperature is based on weighted values (i.e., Equation 4-26), the adjustment is minimal (even null theoretically as the calculated width should represent the actual width in the first place, but minimal due to accumulated errors from rounding throughout the calculations).

Note the following equations can be used to find the critical temperatures A_1 and T_m (melting point; an upper-bound value for T_s), in case this information is not readily available. The alloying additions are in wt% and the temperatures are calculated in K [31].

$$A_1 = 996 - 30\,Ni - 25\,Mn - 5\,Co + 25\,Si + 30\,Al + 25\,Mo + 50\,V \tag{4-29}$$

$$T_m = 1810 - 90\,C \tag{4-30}$$

4-3-6. General form of cooling time equation

As mentioned earlier, there is no solution in simple form for the case of a plate with finite thickness (i.e., 2.5D condition). However, looking at the solution form for 2D and 3D equations, a general form might be derived for cooling time:

Approach 1:

$$\Delta t_{8-5} = \frac{(q/v)^n}{d^m} \,.\, F_t \tag{4-31}$$

The values of n, m, and F_t (ρ, c, λ, T_0) are shown for 2D and 3D conditions in Table 4-3. It can be concluded that for an actual welding process, $1<n<2$ and $0<m<2$. The challenge is to derive a general form for F_t that converges to the value for 2D, when d is small relative to q/v, and to the value for 3D, when d is infinitely large relative to q/v.

Approach 2:

$$\Delta t_{8\text{-}5} = \Delta t_{8\text{-}5,\,Thick} \cdot F_D \tag{4-32}$$

F_D is the dimensionality factor, equal to unity for the 3D condition and a function of $(q/v, \rho, c, \lambda, d, T_0)$ for the 2D condition.

$$F_D = \frac{q/v}{2\rho c d^2 \theta_3} \tag{4-33}$$

$$\theta_3 = \frac{1}{(500-T_0)} + \frac{1}{(800-T_0)} \tag{4-34}$$

Apparently, Easterling used $F_D = 1$ as the criterion for transition from 3D to 2D conditions, which yields Equation 4-14. However, as will be shown later, a sudden transition from 3D to 2D does not happen in real welds. Therefore, there is a need to find a general form for F_D that converges to unity, when d is very small relative to q/v, and to the value of Equation 4-33, when d is infinitely large relative to q/v. The other task would be defining a parameter, such as $q/v/d^2$, to determine the dimensionality condition and limits for cases of 2D and 3D.

Table 4-3. Values of n, m and F_t in Equation 4-31

Condition	n	m	F_t
Thick-plate	1	0	$\frac{1}{2\pi\lambda\theta_1}$
Thin-plate	2	2	$\frac{1}{4\pi\lambda\rho c\theta_2}$

4-4. Experimental procedure

A plate of Grade 100 microalloyed steel, 8 mm in thickness, was cut into pieces with approximate dimensions of 285 mm by 165 mm, to be used for instrumented welding. The oxide scales were removed from both surfaces by milling to allow for good arc conductivity and stability, as well as to remove small bumps on the surface and make them very flat. Holes were drilled about 2 inches (50.8 mm) apart on the bottom side of the plates along the central line with variable depths. Four thermocouples (three of type K and one of type S) were used for each experiment. The type S thermocouple was used for the hole close to the fusion line that experienced the highest temperatures. Thermocouple wires, 0.010" (0.254 mm) in diameter were passed through a ceramic insulator (1/8" or 1/16" OD) and spot-welded at one end to make the junction. The thermocouples were secured to the plate with springs as shown in Fig. 4-1, which provided gentle pressure on the back of the ceramic insulator to maintain contact between the thermocouple junction and the plate throughout welding. The remaining lengths of the wires were covered with duct tape for insulation. At the other end, the wires were connected to a terminal board through appropriate extension wires. An 8-channel data acquisition card and a program written in LabView 5.0 (with maximum sampling rate of 40 points per second) were used to collect the data. Fig. 4-2 shows the electrical configuration used for welding. The electrical continuity from plate to the thermocouples was tested before and after the welding with a voltmeter to ensure proper contact.

To check the performance of the computer program under high heating rates and the response time of the thermocouple, a thermocouple similar to those used in the welding process was plunged in liquid brass (brass rods melted in a steel crucible) and then quenched in water. Fig. 4-3 shows the response of the thermocouple. It shows high heating rates of ~4000°C/s (temperature range 100–900 °C), a $T_P \approx 1060$°C (expected from the liquid brass), and a cooling rate of ~2000°C/s (temperature range 900–100°C).

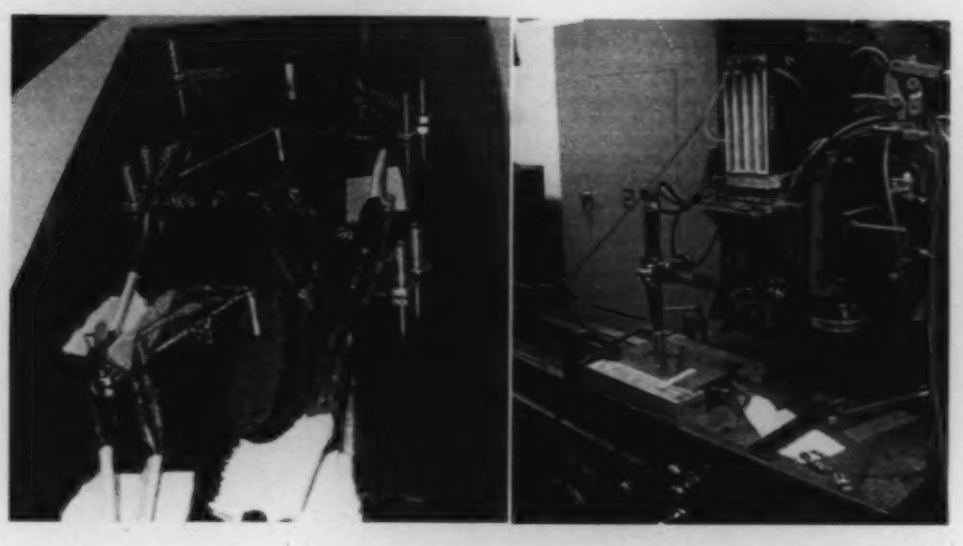

FIG. 4-1. a) Thermocouple/plate attachment on the bottom of the plate (the picture is taken after the welding); b) The GTA welding setup.

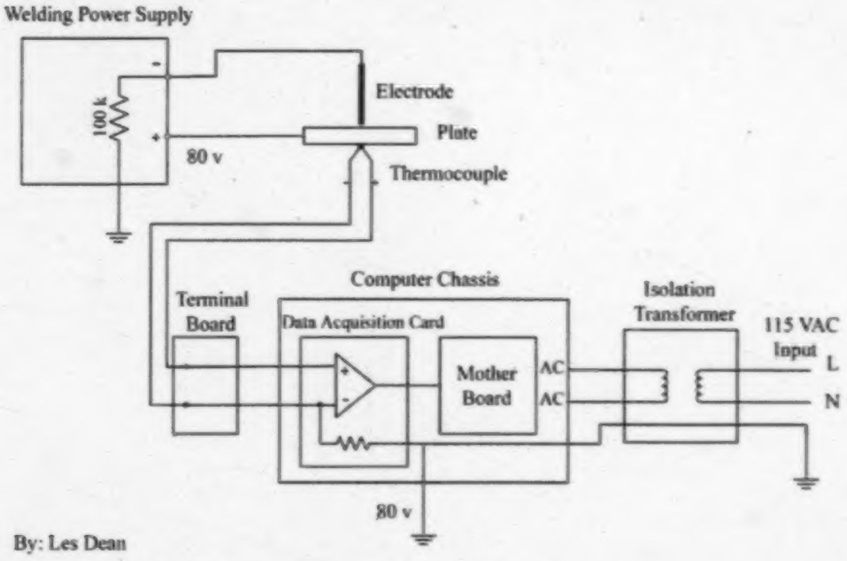
Welding Power Supply
-
100 k
+
80 v
Electrode
Plate
Thermocouple
Computer Chassis
Terminal Board
Data Acquisition Card
+
-
Mother Board
AC
AC
Isolation Transformer
115 VAC Input
L
N
80 v

By: Les Dean

FIG. 4-2. The electrical configuration for data acquisition during welding.

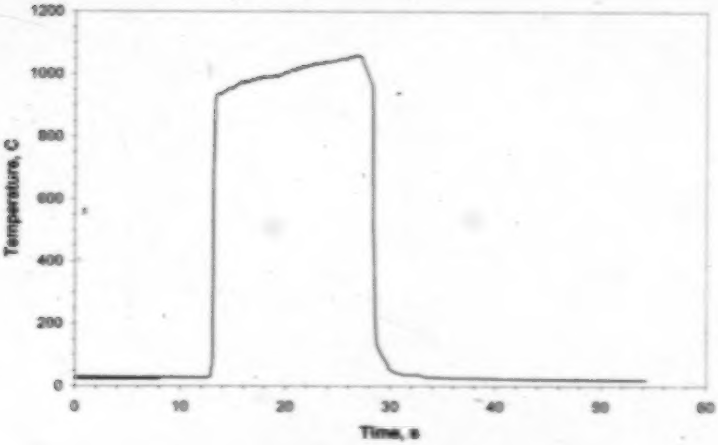

FIG. 4-3. Plunging test for a bare thermocouple junction.

Welding was performed according to the procedure explained in Section 3.5. After welding, the plates were precision-cut transversely from the centre of the thermocouple holes and then mounted, ground, polished and etched, in order to determine the location of the hot junction with respect to the fusion line and the HAZ width to the best of practical accuracy. Steep gradients in the peak temperature and the finite size of the junctions can produce considerable error in determining the location of the junction. Fig. 4-4 shows a cross-section for one of the samples.

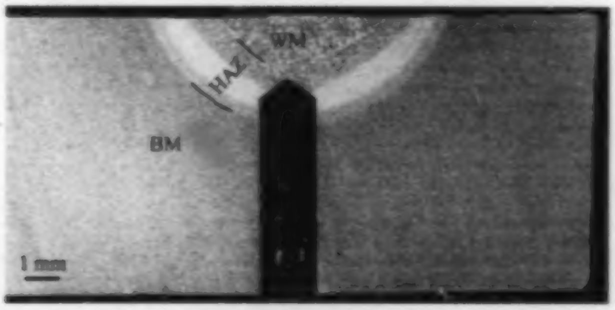

FIG. 4-4. Transverse section of a 0.5 kJ/mm weld sample showing the location of a thermocouple tip in the HAZ. The red background area is Bakelite used for metallographic mounting. The other regions are base metal (BM) and weld metal (WM).

4-5. Results and discussion

Actual thermal cycles, obtained experimentally, are shown in Fig. 4-5 for three nominal heat inputs of 0.5, 1.5 and 2.5 kJ/mm. The curves were analysed to obtain cooling times and peak temperature profiles, as described below. The thermal cycle peaks at some locations were lower than expected. This will be discussed later.

4-5-1. Weighting factors

Fig. 4-6 compares the values of the HAZ widths measured from several weld samples (nominal heat inputs 0.5-2.5 kJ/mm) with the theoretical thick- and thin-plate solutions found from Equations 4-17 and 4-19. The calculated weighting factors for the three main weld samples, for which instrumented welding was performed, are reported in Table 4-4.

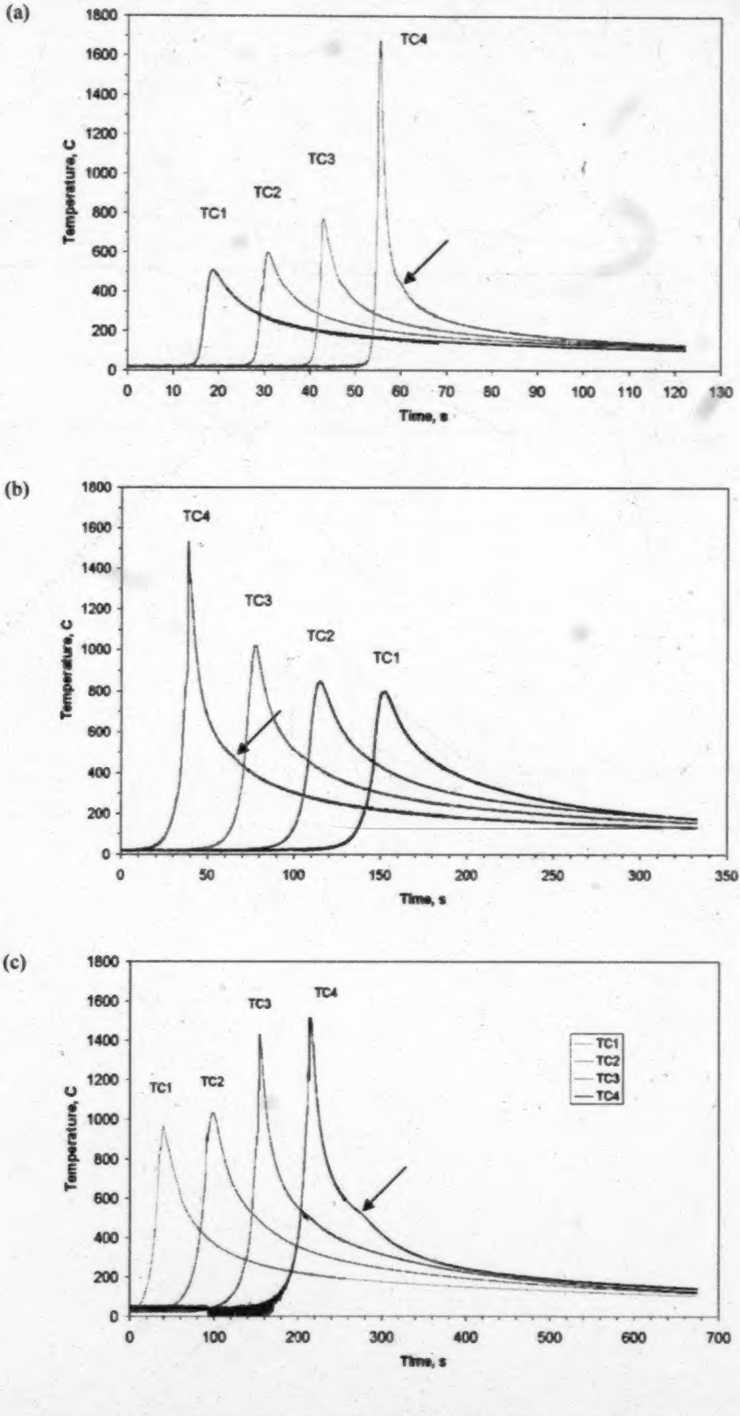

FIG. 4-5. Actual thermal cycles at four locations along the weld run with various depths for three nominal heat input weld samples: a) 0.5 kJ/mm; b) 1.5 kJ/mm; c) 2.5 kJ/mm.

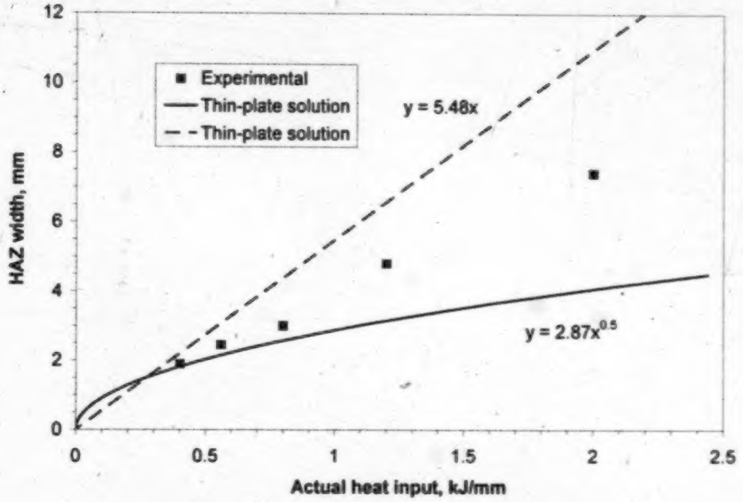

FIG. 4-6. Variation of HAZ width with heat input. The experimental values lie between the upper- and lower-bound lines (thin- and thick-plate solutions) predicted from the Rosenthal's theory.

Table 4-4- HAZ widths and weighting factors for three weld samples

Nominal heat input, kJ/mm	HAZ width, mm			Weighting factor, F_W (Eq. 4-24)
	Thick-plate (Eq. 4-17)	Thin-plate (Eq. 4-19)	Measured	
0.5	1.76	2.05	1.86	0.34
1.5	3.05	6.16	4.80	0.56
2.5	3.93	10.27	7.40 [a]	0.55

a) An estimated value based on the extension of the HAZ boundary curves, as the HAZ/BM boundary intersects the bottom of the plate for the heat input of 2.5 kJ/mm.

A value of Ae_1 = 695°C was used here, which was obtained from the CCT diagram for the specific Grade 100 microalloyed steel [32]. This value is somewhat higher than the equilibrium value of A_1 = 684°C obtained from Equation 4-29. As Equation 4-30 calculates T_m rather than the solidus temperature, a value of T_S = 1500°C was used here, which is slightly lower than the T_m = 1530°C obtained from Equation 4-30. This value also lies between the peritectic temperatures for the Fe-C and Fe-Mn binary systems (i.e., 1493 and 1504°C, respectively [33]). A value of $\eta = 0.75$ was used in Equation 4-2 to obtain the actual values of heat input.

The finding that the experimental values for lower heat-input samples are closer to the thick-plate solution in Fig. 4-6 is reasonable as the HAZ sizes for these samples are relatively small with respect to the thickness of the plate. Using Equation 4-14 in reverse gives a critical heat input of 0.17 kJ/mm, corresponding to a nominal heat input of 0.23 kJ/mm assuming $\eta = 0.75$, for a fixed plate thickness of 8 mm. However, as can be seen, assuming heat transfer behaviour is 2D above the critical value is not reasonable, as none of the actual data lie on the thin-plate solution line. For 2D situation to prevail, the weld metal zone should span over the whole width of a thin plate, so that the heat transfer occurs only within the plane of the plate, which is not the case even for the highest heat input used here.

4-5-2. Cooling time / cooling rate

The most common parameter for evaluation of cooling rate is the time of cooling from 800 to 500°C, which relates to the transformation of austenite to ferrite and also covers the temperature range where the nose of CCT diagrams is located for most types of steels. Nevertheless, other temperature ranges were also suggested for certain applications. For instance, cooling time from 400 to 150°C was considered to be a controlling factor in diffusion of hydrogen in steel, when cold cracking of the welds was of concern [16]. The cooling time between 1200 and 800°C is considered important in welding of duplex stainless steels, as it influences the ferrite/austenite phase balance and the possibility of formation of σ phase in the HAZ [22]. As transformation of austenite upon cooling is the most important matter in this study, the cooling time from 800 to 500°C was chosen as the controlling factor, which was also found to be used in most of the literature. Table 4-5 compares the values of cooling time and cooling rate predicted, for nominal heat inputs of 0.5, 1.5 and 2.5 kJ/mm, with those experimentally obtained. Note, that mean cooling rate for the temperature range 800 to 500°C is calculated in °C/s from a simple equation:

$$T'_{8\text{-}5} = \frac{300}{\Delta t_{8-5}} \tag{4-35}$$

Table 4-5. Heating rate, cooling time and cooling rate for three weld samples

Nominal heat input, kJ/mm	Heating rate, °C/s	Cooling time ($\Delta t_{8\text{-}5}$), s				Mean cooling rate, °C/s (Eq. 4-35)	
		Thick-plate (Eq. 4-6)	Thin-plate (Eq. 4-11)	Estimated (Eq. 4-25)	Measured	Estimated	Measured
0.5	1537 ± 857	1.2	2.6	1.7	1.8 ± 0.1	178.8	171.0 ± 6.2
1.5	248 ± 151	3.6	23.6	14.8	17.2 ± 1.5	20.2	16.8 ± 1.2
2.5	70 ± 20	5.9	65.6	38.6	37.7 ± 10.1	7.8	8.0 ± 2.9

The experimental values reported in Table 4-5 are the averages among the thermocouple readings, as long as the peak temperature is above 800°C. The theoretical range of cooling time for a 0.5 kJ/mm weld sample was found to be between 1.2 and 2.6 s. This translates to mean cooling rates approximately between 110 and 250°C/s. The range of mean cooling rates for the other weld samples was found to be approximately 13–85°C/s for a heat input of 1.5 kJ/mm and 5–50°C/s for a heat input of 2.5 kJ/mm. The wide range of cooling values suggests a great deal of uncertainty. Having more specific numbers, using the technique proposed here and confirmed by experiments, is essential for correlating microstructural changes or for any simulations. The method introduced in this chapter can be applied to weld sections with complicated geometries, as it basically assesses the actual behaviour of the section without speculation. Even some uncertainty about the material thermal properties and/or welding parameters may become less important for the proposed method. The proposed method compares theoretical solutions with and fits them to the actual behaviour of the welded section, whose behaviour is based on *effective* values of the parameters, probably unknown to the investigator.

4-5-3. Increase in plate temperature or heat accumulation effects

The standard deviation of measured cooling time values increased relative to the average value as the heat input increased due to heat accumulation in the plate during welding. Heat accumulation increased the effective initial temperature in the plate as welding continued, and this caused an increase in the cooling time and an increase in the weld HAZ width (Fig. 4-7). For instance, the first thermocouple for the 2.5 kJ/mm weld recorded a cooling time of 23.5 s, while the next three thermocouples recorded cooling times of 38.0, 42.6, and 46.8 s in sequence. The rise in temperature in a plate of finite width can be calculated from the equation below [3]:

$$T_f - T_0 = \frac{q/v}{wd\rho c} \tag{4-36}$$

w is the width of the plate (perpendicular to the welding path) and T_f is the uniform equilibrium temperature of the plate after welding is stopped. Substituting the corresponding values for a nominal weld heat input of 2.5 kJ/mm for a plate with w=165 mm in Equation 4-36 gives a temperature rise of ~337 °C. This will result in ~6–16 times increase in the cooling time as calculated by Equations 4-6 and 4-11, if one assumes that the entire temperature rise occurs prior to the drop of temperature from 800 to 500°C. However, this is not the case and only a fraction of the temperature rise calculated above will occur immediately at the time of temperature recording. In addition, the model does not consider any heat loss (radiation, convection, or conduction), which is also not correct. These two factors can explain why an increase of only two times in the measured values of cooling time was observed. By calculating the initial temperature needed for such an increase, and averaging the values obtained from thick- and thin-plate solutions, a temperature rise of 130–160°C can be estimated to occur at the time temperature measurements for thermocouples 2, 3 and 4. This is more reasonable when considering that the uniform temperature, reached by the plate at the locations of the four thermocouples after welding was finished, was only around 200°C (Fig. 4-5c).

The heating-up phenomenon would not be a major factor for the lower heat inputs (Fig. 4-7), as the travel speed would be high enough to prevent too much of a temperature rise during welding. Using a larger plate would also result in a smaller standard deviation. Nevertheless, the range between the experimental readings is still much smaller than the range between the thick- and thin-plate values.

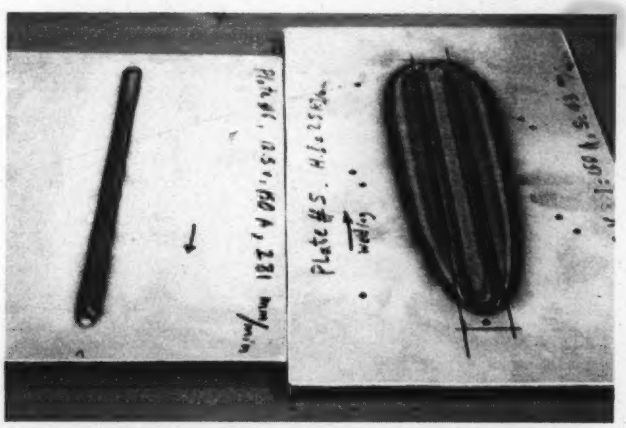

FIG. 4-7. As-welded plates for two values of heat input: 0.5 kJ/mm (left) and 2.5 kJ/mm (right). Note the increase in the HAZ width in the higher heat input weld as the welding process proceeded.

4-5-4. Instantaneous cooling rate

Instantaneous cooling rate at a certain temperature during the cooling cycle can be calculated by differentiating Equations 4-4 and 4-9. The corresponding values for thick [3] and thin plates [13] are, respectively:

$$\frac{\partial T}{\partial t} = -\frac{2\pi\lambda}{q/v}(T - T_0)^2 \qquad (4\text{-}37)$$

$$\frac{\partial T}{\partial t} = -2\pi\lambda\rho c\left(\frac{d}{q/v}\right)^2 (T - T_0)^3 \qquad (4\text{-}38)$$

The theoretical values for thick and thin plates, as well as the measured values of cooling rate at a critical temperature of 550°C are calculated and shown in Table 4-6. These values can be compared with cooling rates on the CCT diagram for Grade 100 steel, to evaluate the effect of prior austenite grain size (PAGS) and dissolution of carbonitrides on the hardenability, which distinguishes CGHAZ from FGHAZ.

4-5-5. Solidification cooling time

The cooling time for solidification can be assessed by Equation 4-39 that calculates the solidification time in seconds [30]:

$$S_t = \frac{Lq/v}{2\pi\lambda\rho c(T_m - T_0)^2} \tag{4-39}$$

L is the heat of fusion (2 J/mm^3 for carbon steels). This equation estimates cooling times of 0.3, 0.9 and 1.5 s for nominal heat input values of 0.5, 1.5 and 2.5 kJ/mm, respectively.

4-5-6. Transformation heat release

The cooling rate drop, as the temperature drops, shows an additional decrease at the temperature of transformation of austenite. This, usually observed as a small bump in the cooling portion of the thermal cycle, is shown in Fig. 4-5 with arrows. This drop is due to release of heat of transformation [21]. Examination of the thermal cycles obtained in the CGHAZ (some of which are not shown here) reveals the variation in the temperature of transformation during cooling in different samples (Table 4-6). The fact that this temperature is much below A_1 is due to presence of large prior austenite grains that increase the hardenability and suppress the transformation temperature. Increase in the transformation temperature with an increase of heat input is due to a decrease in cooling rate, which as shown in the next chapters will result in formation of different transformation products such as martensite, bainite and Widmastatten ferrite, or a mixture of them.

Table 4-6. Austenite transformation temperature during cooling in the CGHAZ

Nominal heat input (kJ/mm)	HAZ width (mm)	Transformation temperature (°C)	Cooling rate at 550°C, °C/s		
			Thick plate	Thin plate	Measured
0.5	1.9	400-430	189.3	76.3	111.7±7.2
1.5	4.7	470-480	63.1	8.5	10.9±1.2
2.5	7.4	500-510	37.9	3.1	6.1±2.2

4-5-7. Effect of radial position

One important practical point in examining the weld HAZ, or in selecting the welding parameters to reach a certain cooling rate in the joint, is that cooling rate is not the same in all radial directions on a transverse section. It has been observed experimentally in very early measurements [21], that on plates of intermediate thickness (2.5 D heat flow condition) the cooling rate is higher at the top of the plate adjacent to the either side of the bead than at the bottom (directly under the deposited metal) and the HAZ width is smaller. This is due to the difference in the availability of quenching material in different radial directions. It is interesting to add, that the proposed method of correction based on HAZ width presented in Section 4-3-4, is capable of determining the actual cooling rate along the direction of interest, by measuring the HAZ width along that direction.

4-5-8. Effect of heat input

The effect of heat input on the cooling time is better demonstrated in Fig. 4-8, where the values predicted by thick- and thin-plate solutions are compared. The estimated values for five samples with nominal heat input values 0.5-2.5 kJ/mm, as well as the measured values for three of these samples, are included too. Equation 4-31 shows that Δt is a function of $(q/v)^n$, where $1<n<2$.

4-5-9. Effect of plate thickness

As was expected from Equation 4-11, the increase in the heat input resulted in an increase in the cooling time (Fig. 4-9). The effect of plate thickness was not studied here, but it can be expected that an increase in the thickness would act in almost the same way as a decrease in the heat input. This is due to availability of more quenching material as the thickness increases. It should be noted that all these analyses are applicable only to normal welding practices in calm air, where cooling by convection can be neglected in the presence of cooling by conduction. In cases such as underwater welding, where the effect of quenching by the flow of water cannot be neglected, an increase in plate thickness may have quite an opposite effect on the cooling rate. Lindstrom and Ulfvarson [34] modified the Rosenthal equation to account for the cooling by a forced flow and showed that cooling rate increases as the plate thickness decreases.

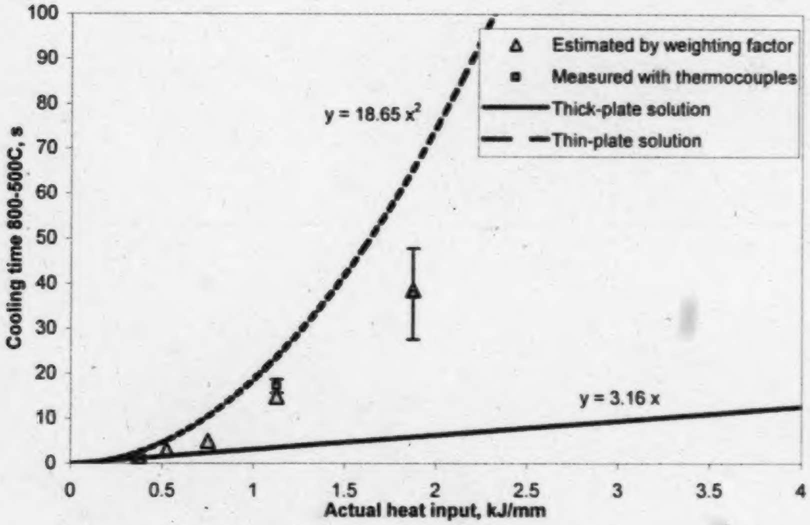

FIG. 4-8. Effect of heat input on cooling time ($d = 8$ mm; $\eta = 0.75$).

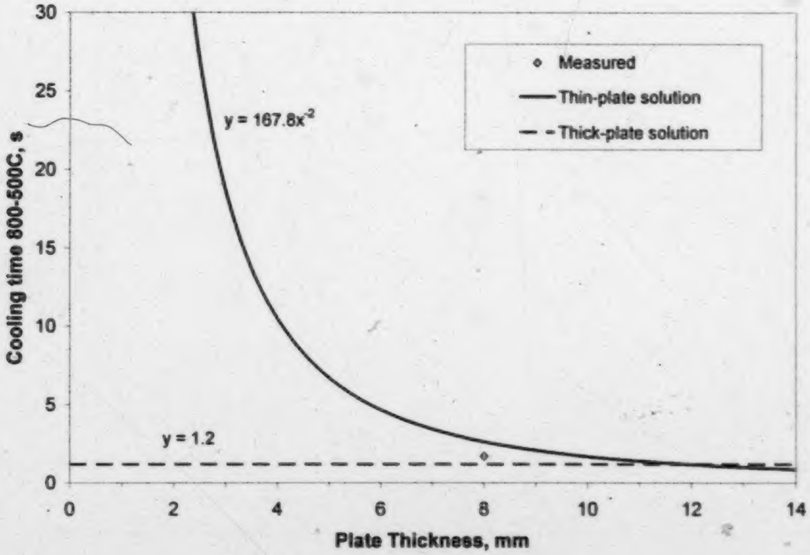

FIG. 4-9. Effect of plate thickness on cooling time ($q/v = 0.5$ kJ/mm; $\eta = 0.75$).

4-5-10. Peak temperature profiles

A weighted peak temperature profile obtained from Equation 4-26 is shown in Fig. 4-10 (solid line) for a weld sample with a nominal heat input of 0.5 kJ/mm. The theoretical results with thin- and thick-plate assumptions are also plotted (dashed and solid lines). All profiles are calibrated with respect to the actual plate geometry and location of the HAZ boundaries according to Equation 4-27, to show the differences in the shapes (curvatures) only. As can be seen, the different assumptions do not markedly change the shape of the peak temperature profiles. For this heat input, the corresponding weighting factor (Table 4-5) predicts a profile with a shape close to that predicted by the thick-plate solution.

The peak temperature profiles obtained from Equation 4-26 and scaled to the actual plate geometry according to Equation 4-27 are shown in Fig. 4-11 for different weld samples. The results of thermocouple readings are plotted too. As can be seen, the peak temperatures are below expected values if the T_P is below roughly 1300°C. Above that, the results match very well with the expected values. This discrepancy likely comes from the contact type between the thermocouple tip and the plate that limits the heat transfer. The actual microscopic contact area between the thermocouple junction and the plate might be small. This area increases at very high temperatures when material gets softened and results in a better contact with the junction, which means better heat transfer from the plate to the thermocouple junction.

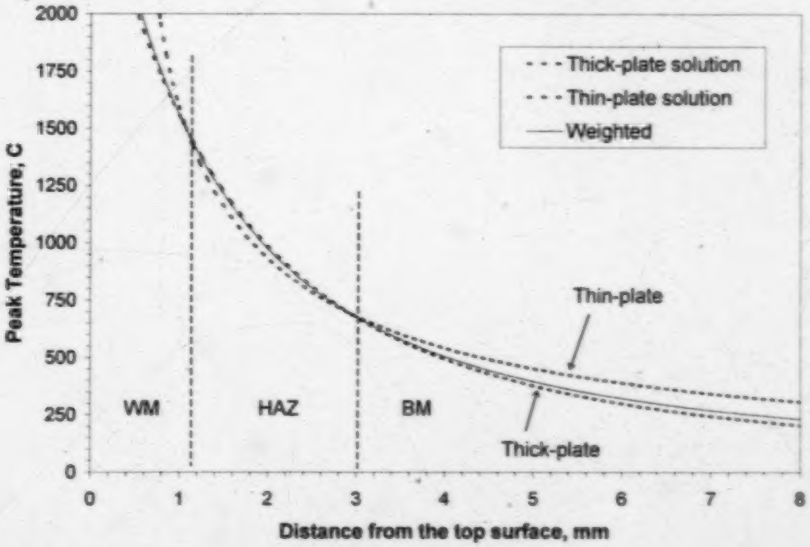

FIG. 4-10. Calibrated peak temperature profiles for a nominal heat input of 0.5 kJ/mm. The weighted profile is plotted along with the thick- and thin-plate solutions.

There is some evidence for the above explanation; this phenomenon can be seen in some of the thermal cycles when enlarged. Fig. 4-12 shows the thermal cycles for two of the thermocouples in the 1.5 kJ/mm weld sample. For TC4 the temperature rises relatively slowly initially due to the poor contact, until ~900°C, whereupon it rises much more rapidly. Therefore, a reading of 900°C probably corresponds to an actual temperature in excess of 1300°C. This phenomenon was more or less observed for all the thermocouples located close to the fusion line. Thermocouple locations that have peak temperatures below ~1300°C start to cool off before the peak temperature can be recorded. It was also observed that the lower the heat input, the larger the discrepancy, since the thermal cycle is faster. Another explanation could be that as the plate expands with increasing temperature, the contact between the junction and the bottom of the hole loosens for a short while, until the insulator is pushed by the pressure from the backing spring (Fig. 4-1) after the friction between the insulator and the wall of the hole is overcome. This is less likely to happen as there was no sticking or side pressure between the insulators and the wall of the hole. No matter which mechanism is responsible, the discrepancy observed in some cases is believed to be due to the type of contact. It would be ideal for heat transfer if the thermocouple junction could be spot/flash welded to the plate (as reported by Hess *et al.* [21] or Ion *et al.* [31]) or soldered to the plate with a small mass of a high remelt temperature silver solder (Grosh *et al.* [1]), as the best response time is expected from small bead volumes but with maximized surface contact. Spot welding at the bottom of drilled holes was deemed initially too difficult and unnecessary for the present setup that consisted of small diameter holes and small thermocouple junction size.

a) 0.5 kJ/mm

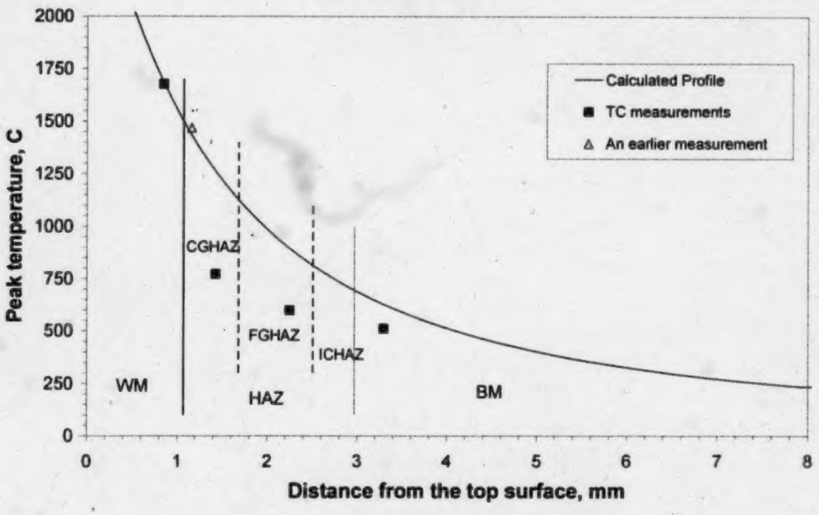

b) 1.5 kJ/mm

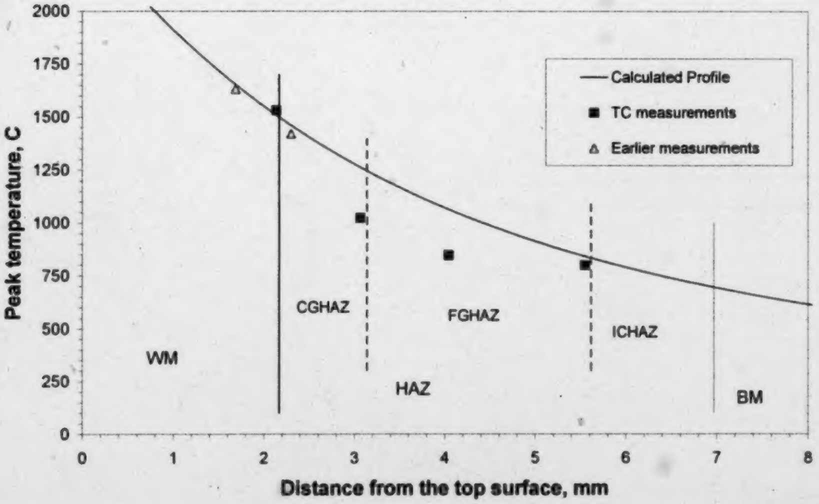

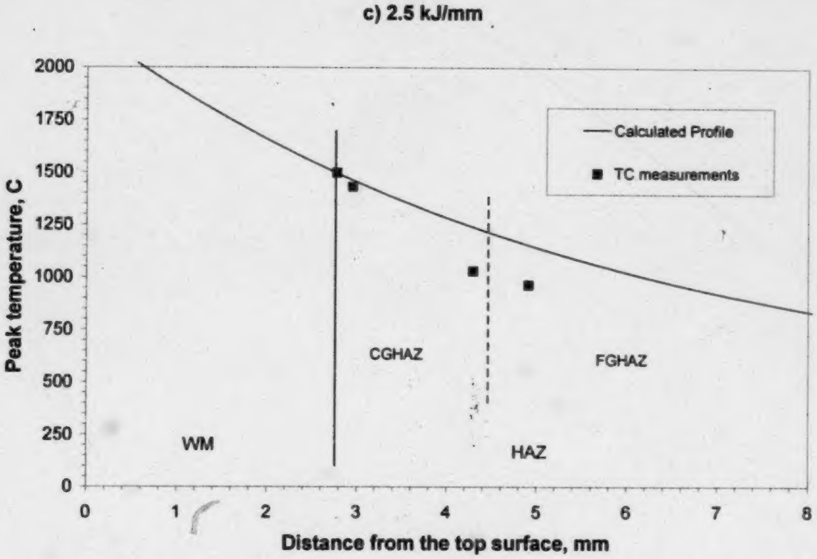

FIG. 4-11. Peak temperature profiles for three different weld samples: a) 0.5 kJ/mm; b) 1.5 kJ/mm; c) 2.5 kJ/mm.

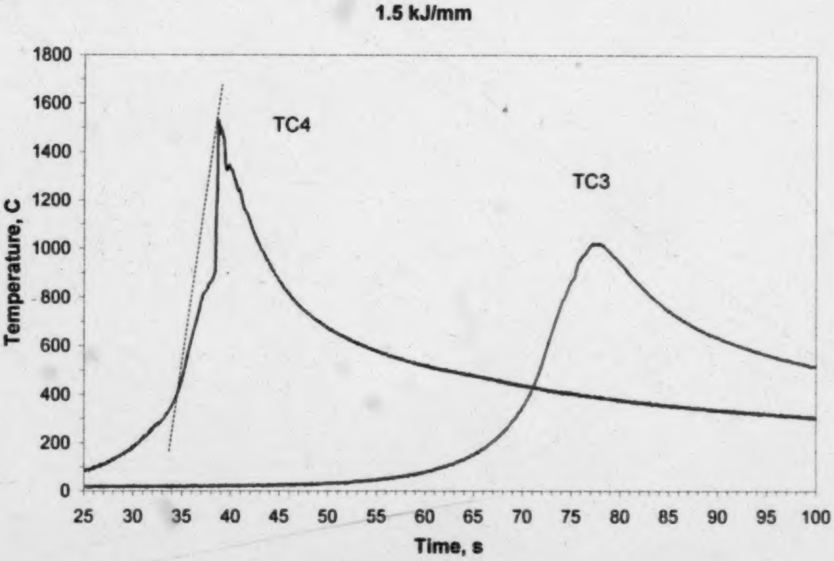

FIG. 4-12. Thermal cycles for two locations, one reading a peak temperature expected from the thermocouple location (TC4) and one reading a peak temperature ~250°C lower than the temperature expected (TC3).

Fig. 4-13 shows all peak temperature profiles on the same graph with the actual experimental readings from the thermocouples that kept good contact throughout the welding process. The beauty of having a mathematical solution is, as pointed out by Hess *et al.* [21], that "the mathematical solutions are able to intelligently average and evaluate the reliability of experimentally measured values and to greatly extend the coverage of the experimental data".

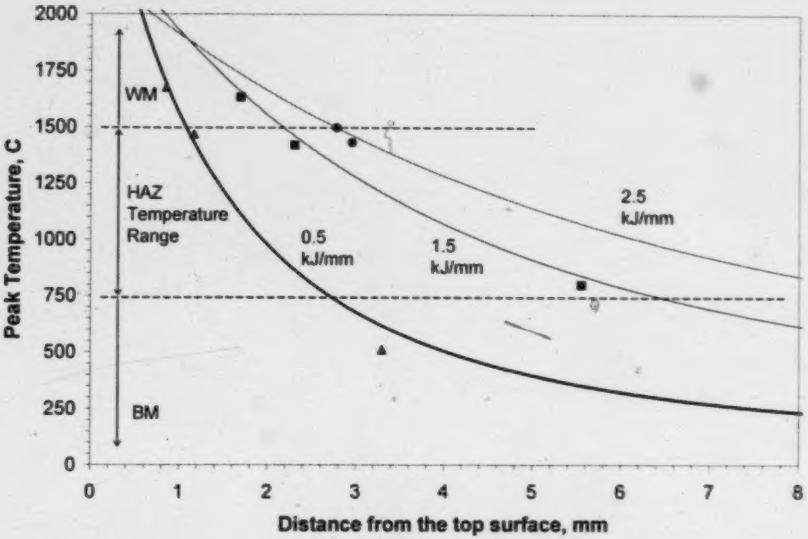

FIG. 4-13. Peak temperature profiles weighted and fitted for three different weld samples (heat input values of 0.5, 1.5 and 2.5 kJ/mm).

4-5-11. Estimation of T-t curves

Again, the problem with using the Ashby-Easterling solutions to the Rosenthal equations is that they predict the extreme cases of 2D and 3D conditions. Fig. 4-14 compares the thermal cycles predicted by Equations 4-8 and 4-13 with the selected ones obtained experimentally for each heat input. The actual thermal cycle falls between the two predictions. For the low heat input of 0.5 kJ/mm, the heat condition is very close to the 3D condition and, therefore, the thick-plate solution has a very close prediction. By applying the weighted values of cooling time (close to the measured values; see Section 4-5-1) to Equation 4-13 for higher heat inputs of 1.5 and 2.5 kJ/mm, thermal cycles closer to the experimental values are obtained (Fig. 4-15). This, however, may not apply to heat inputs in between (e.g., 0.7-1.5 kJ/mm), as neither the thick- nor thin-plate conditions are close to the actual situation.

Alternatively, one can model and estimate the T-t curve for any point in the HAZ for that given heat input by analyzing a selected T-t curve from a thermocouple reading that maintained good contact at the highest temperature locations in the HAZ. This is possible because it is known that the heating and cooling rates are independent of the position in the HAZ. The procedure is described as follows.

As the number of readings was too high for all the thermal measurements (40 points/s), first the curves needed to be simplified by choosing fewer points for numerical analysis. Fig. 4-16 shows this for one of the thermocouples in the case of the 0.5 kJ/mm welding process. The re-established curve from the chosen data was then divided into three parts, namely, heating, dwell time around the peak temperature and cooling. The transition points were where the curvature of the plot changed, which were found to be ~0.99 *Tp* on the heating side and ~0.98 *Tp* on the cooling side. Basically, the heating part from around 400°C to the dwell part is linear, the dwell part around the peak temperature has a negative curvature, and the cooling part has a positive curvature. The heating and cooling parts were easy to determine and model as it was assumed that they were the same across the HAZ, and only the point where they are connected to the dwell part depends on the peak temperature. The most challenging part was the dwell part, as it was observed that the dwell time, τ, would increase as the peak temperature decreased. Ion *et al.* [31] defined a time constant around the peak temperature which is similar to the parameter presented here as the dwell time, and they defined it to be a function of $1/(T_P-T_0)^n$, where $n = 1$ for thick-plate conditions and $n = 2$ for thin-plate conditions. The same relationship was used here. Fig. 4-17 shows the simplified thermal cycle of Fig. 4-16, on which the three parts are separately indicated. A linear fitting is applied to the heating part, from which the heating equation and the heating rate can be obtained.

Therefore, to model a thermal cycle at a location designated by T_P and for a given heat input (0.5 kJ/mm in the current examples), the heating part is determined first from the equation obtained by fitting, for a temperature range from 400°C up to 0.986 T_P. Five points will form the dwell part, with the time-temperature dependence shown in Table 4-7.

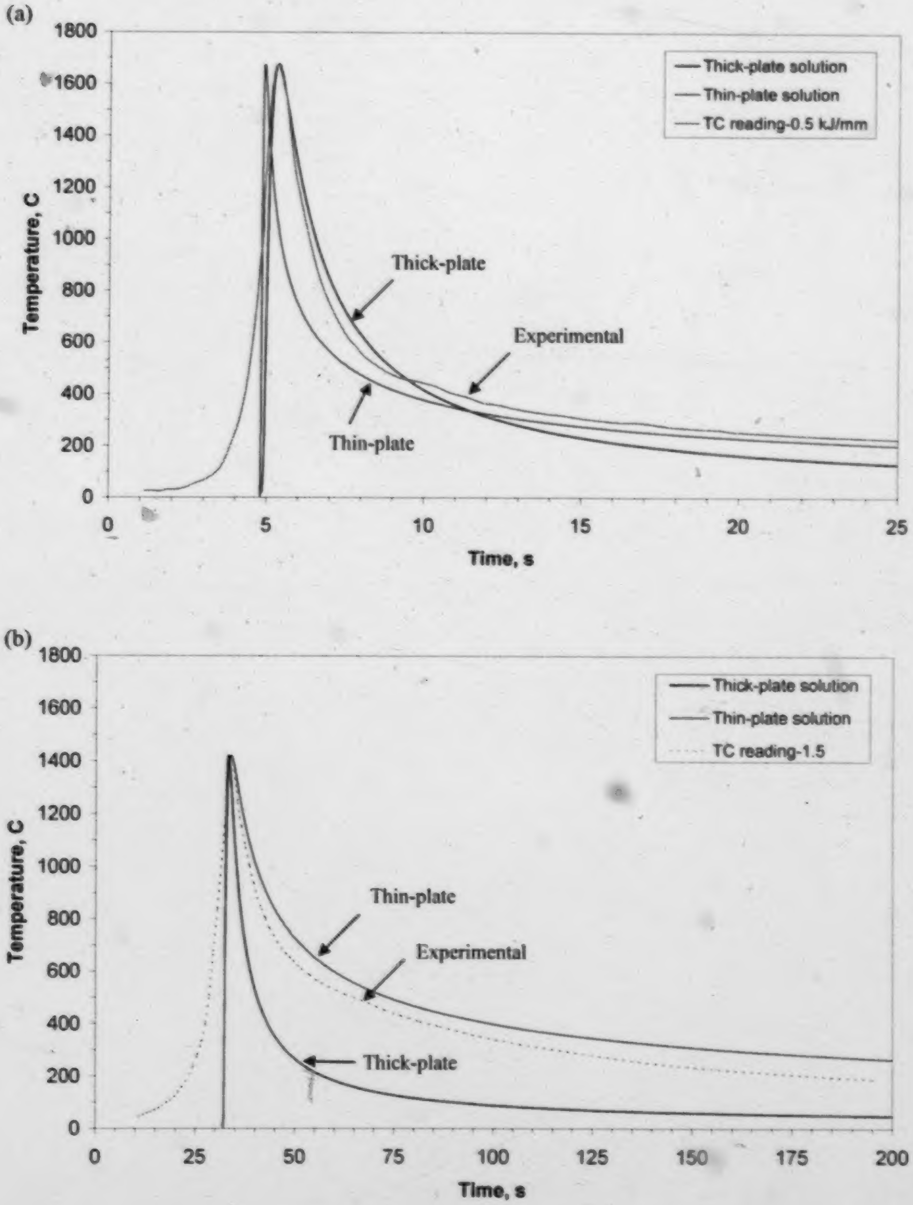

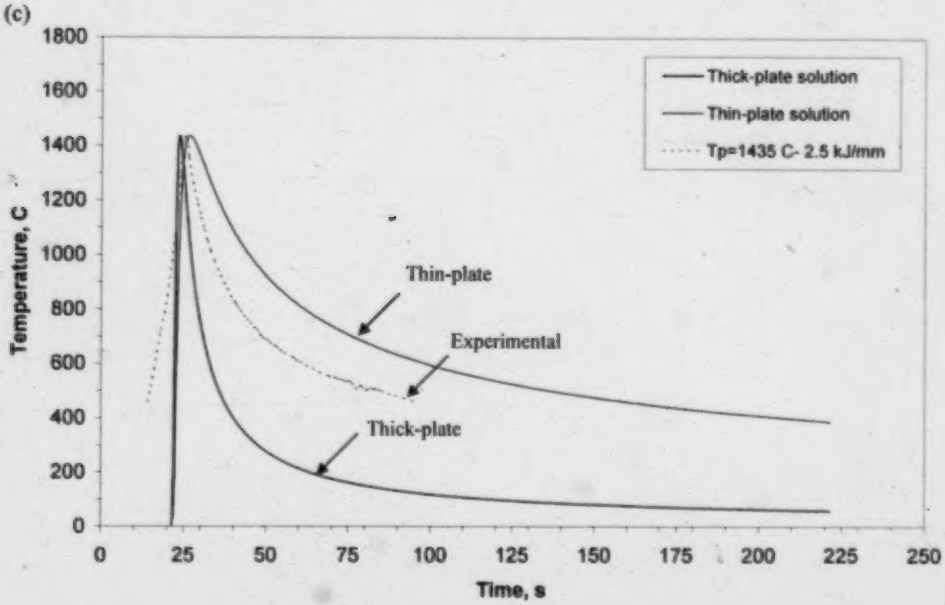

FIG. 4-14. Thermal cycles at selected peak temperatures as predicted by thick- and thin-plate solutions and as obtained experimentally: a) 0.5 kJ/mm; b) 1.5 kJ/mm; c) 2.5 kJ/mm.

The value t_l is determined from the heating equation when T=0.986 T_P, and the dwell time, τ, is determined from the following equation:

$$\tau = \tau^* \left[(T^*_P - T_0)/(T_P - T_0) \right]^n \qquad (4\text{-}40)$$

The values of the τ^* and T^*_P are obtained from the selected thermal cycle for each heat input. A value of $n = 1$ was used for a low heat input of 0.5 and $n = 1.5$ for heat inputs of 1.5 and 2.5 kJ/mm. The coefficients for T_P in Table 4-7 were obtained after analyzing the selected thermal cycles from all three heat inputs. They represented well the dwell parts in all thermal cycles experimentally obtained. The cooling part was basically the cooling leg of the selected thermal cycle, cut from T = 0.975 T_P and then shifted and attached to the dwell part at $t = t_l + \tau$. The modelled thermal cycle was used to plot the estimated thermal cycles at several peak temperatures for each heat input, as shown in Fig. 4-18. These thermal cycles can be used for analysis of precipitate alterations and grain growth. The equilibrium dissolution temperatures for a few dissolution fractions are also indicated on each graph for TiN and NbC.

Table 4-7. Values of five points representing the dwell part of the modelled thermal cycle

Point #	t	T
1	t_l	$0.986\ T_P$
2	$t_l + 0.25\ \tau$	$0.993\ T_P$
3	$t_l + 0.5\ \tau$	T_P
4	$t_l + 0.7\ \tau$	$0.990\ T_P$
5	$t_l + \tau$	$0.975\ T_P$

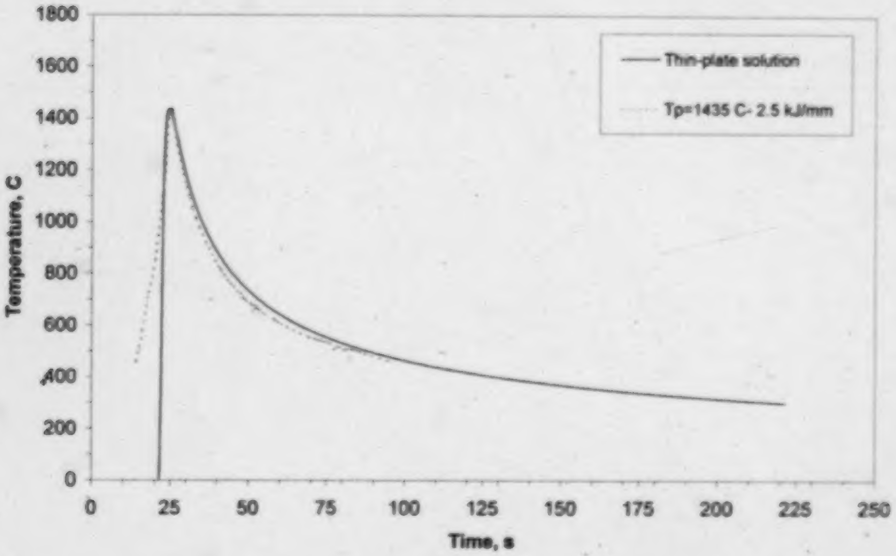

FIG. 4-15. Thin-plate solution predictions with weighted values of cooling time.

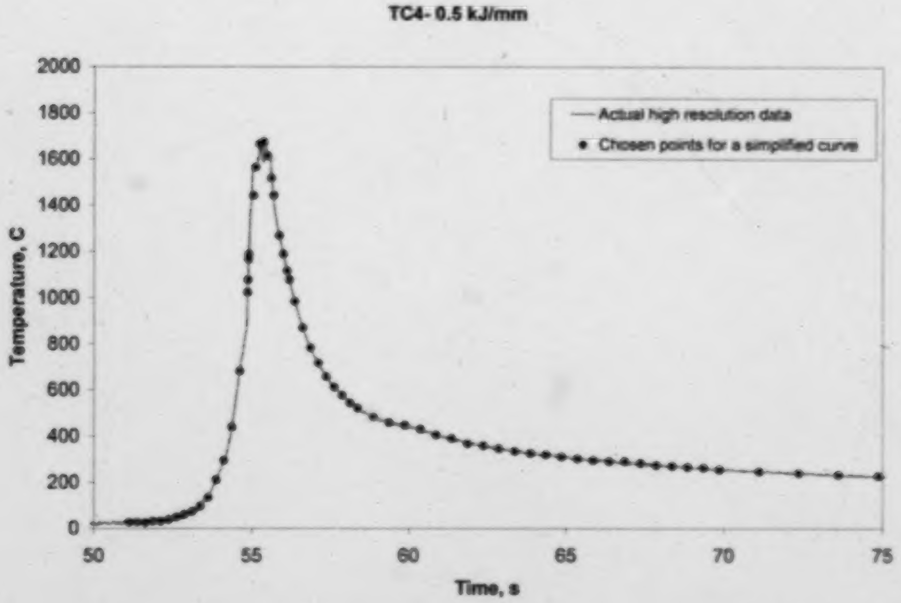

FIG. 4-16. A selected thermal cycle for modelling: some points are chosen from the actual high-resolution curve to form a simplified curve.

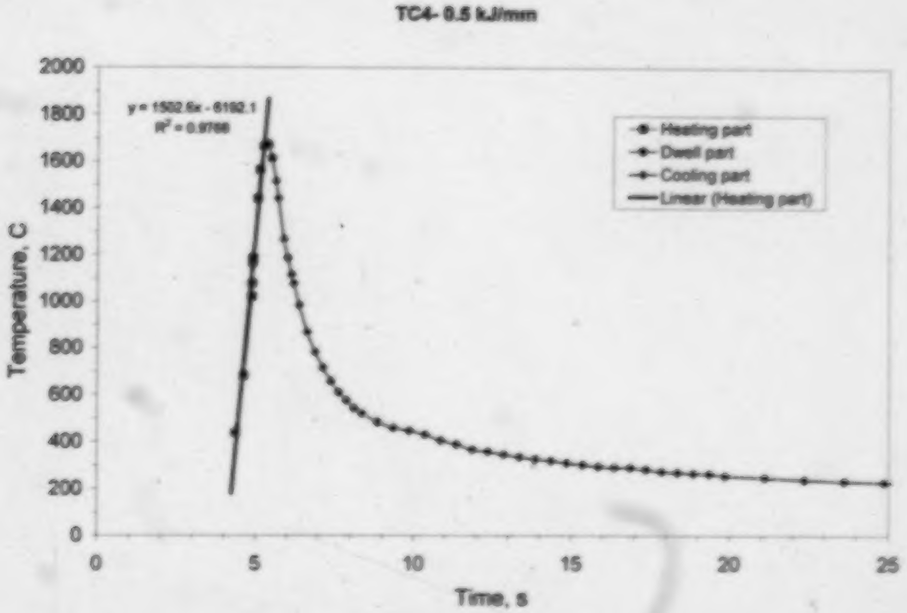

FIG. 4-17. The thermal cycle divided into three parts: heating, dwell time around peak temperature, and cooling.

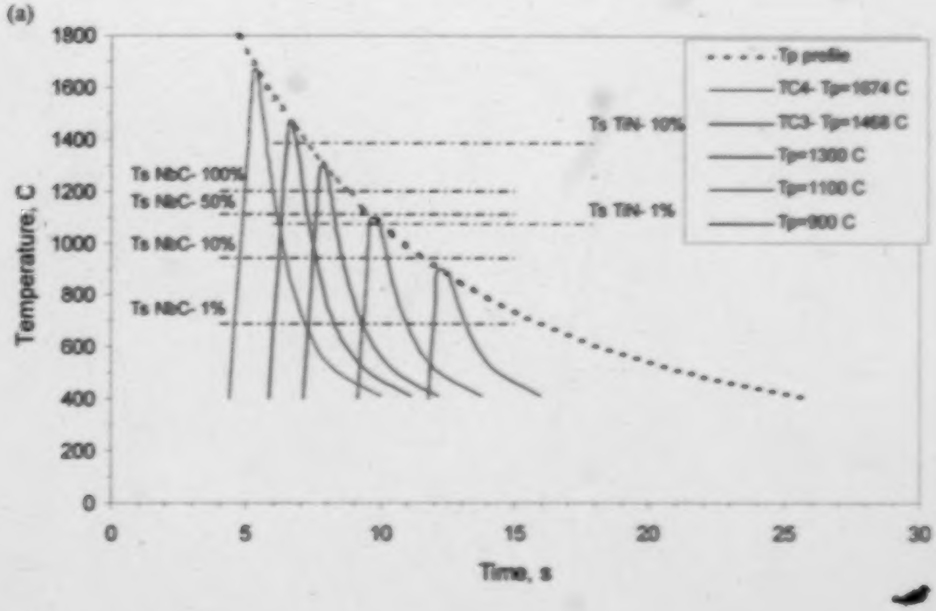

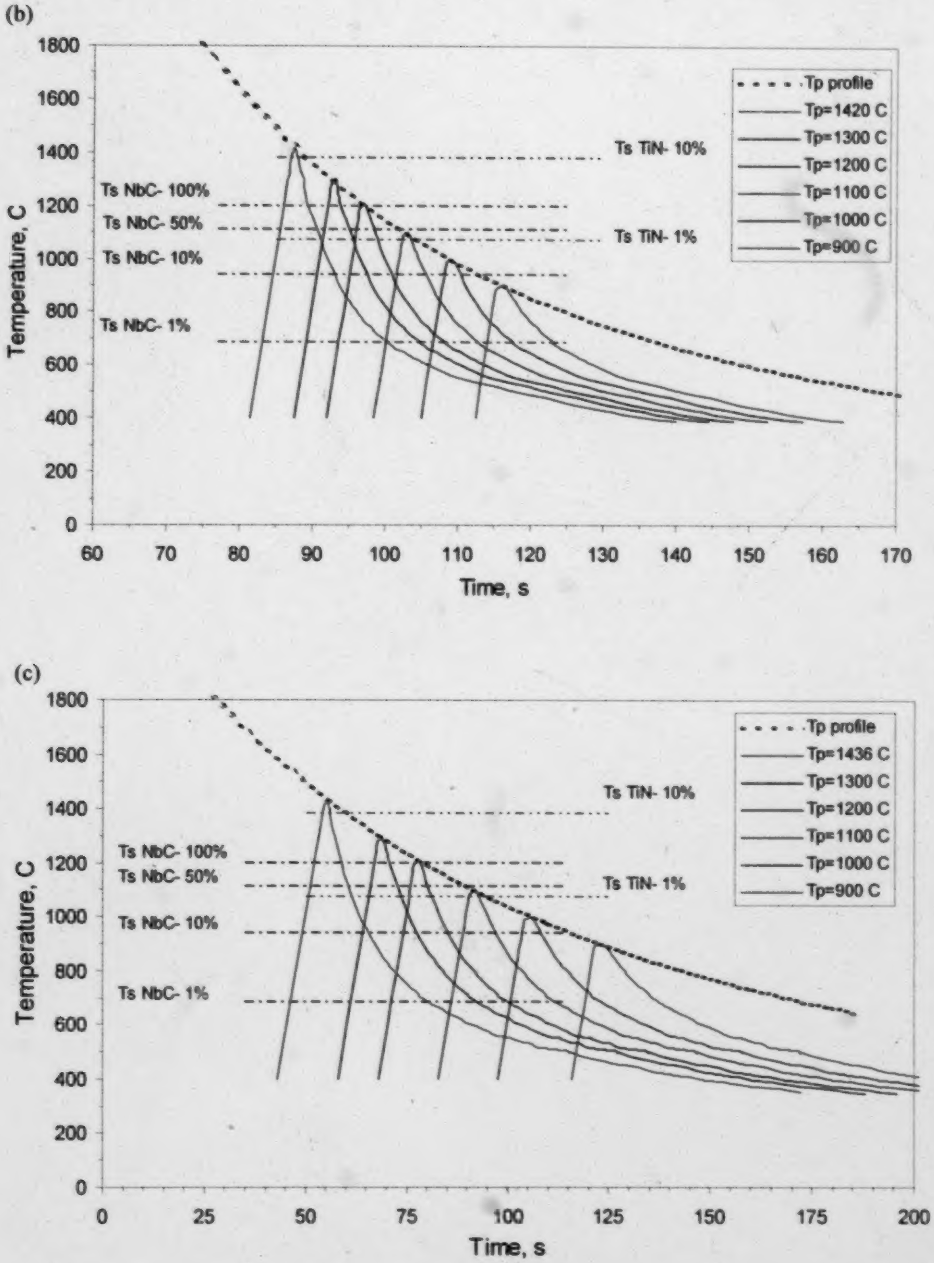

FIG. 4-18. The modelled and estimated thermal cycles at several locations (T_P) across the HAZ for three heat inputs: a) 0.5 kJ/mm; b) 1.5 kJ/mm; c) 2.5 kJ/mm.

It is noteworthy to add that some variation in the assumptions used in modelling the thermal cycles would not produce considerable difference when the thermal cycles for different heat inputs are compared. Fig. 4-19 compares the thermal cycles experimentally obtained for three heat inputs at a high $T_P \approx 1435°C$ (i.e., in the CGHAZ close to the fusion line), and those modelled and estimated for a T_P = 1100°C (i.e., close to the boundary between the FGHAZ and CGHAZ). As can be seen, the rates of the thermal cycles are so different that a slight variation in the shape and size of the dwell part around the peak temperature would not affect the cycle and the thermal energy associated with it. Also interesting to note is that the time above a certain temperature is much higher for the heat inputs of 1.5 and 2.5 kJ/mm than for 0.5 kJ/mm, as shown in Table 4-8.

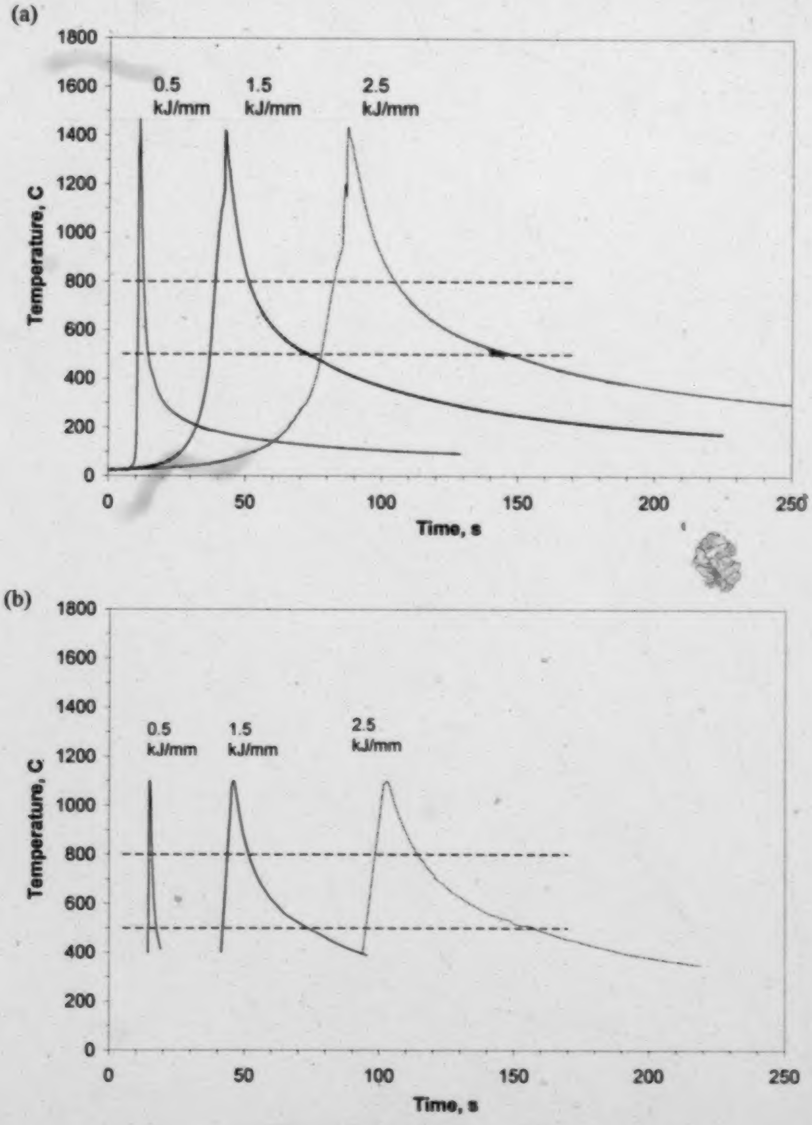

FIG. 4-19. The thermal cycles for the same peak temperature for different values of heat input: a) the actual cycles experimentally obtained for a $T_P \approx 1435°C$; b) the modelled and estimated thermal cycles for a $T_P = 1100°C$.

Table 4-8. Time above 900°C for several thermal cycles

Heat input, kJ/mm	$T_p = 1435$°C	$T_p = 1100$°C
0.5	1.7	0.9
1.5	9.4	5.0
2.5	15.6	10.0

4-5-12. Heating rate

The heating rate values reported in Table 4-5 were calculated by fitting linear trend lines to the heating part of each thermal cycle (the limits of which are explained in Section 4-4-4) obtained experimentally. The relatively large standard deviations associated with these measurements are due to plate heating and the initial temperature rise along the weld run. In the analysis of Section 4-4-4, however, it was assumed that this temperature rise will not take place and, therefore, the heating rate was assumed to be constant.

The heating rate of the thermal cycle can affect such parameters as the amount of superheating in the $\alpha \rightarrow \gamma$ transformation (in transformable steels), grain growth, the rate of coarsening of carbides and nitrides, and the dissolution temperature of carbides and nitrides. These will be discussed in the next chapters.

4-5-13. Thermal stresses

The temperature gradient in the HAZ will cause a differential thermal expansion in this region. This is usually sufficient to produce a state of stress that causes plastic deformation during heating. Upon subsequent cooling, again another state of stress will be formed [21]. This is in addition to the strain induced by transformation.

The thermal stresses can cause distortion in the welded joints. An example of distortion is shown in Fig. 4-20, where the weld strips are cut out of the plates. Deflection in the case of low heat input showed itself immediately upon cutting and release from the confinement by the rest of the plate. The reason the deflection is high at low heat input is the location of a small weld zone and HAZ at the top of the upper half of the plate which produces a greater bending moment, compared with the situation in the higher heat input which causes a wider stressed region over both halves of the plate thickness.

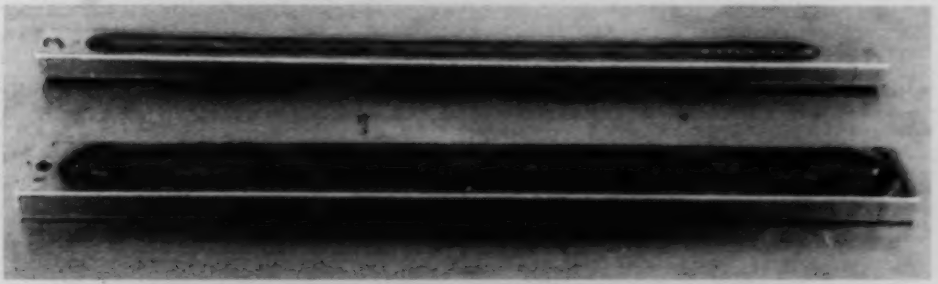

FIG. 4-20. The weld strips cut out of the plates after the welding for two values of heat input: 0.5 kJ/mm (above) and 2.5 kJ/mm (below). Note the considerable deflection for the case of the low heat input.

4-6. Summary

Along with examining the theoretical approach of Rosenthal for calculation of the thermal parameters of a weld thermal cycle, a method for quick estimation of cooling rate in a welded section was developed. The method was based on applying a weighting factor to the Rosenthal analytical solutions for thick and thin plates. The factor is determined from the HAZ width, obtained from etched sections, which reflects the actual response of the plate to the heat flow conditions. While the lower- and upper-bound solutions to Rosenthal's equation, derived by assuming thick- and thin-plate conditions, provide a wide range of values for cooling rate during the weld thermal cycle, the method and formulations presented here yielded specific numbers very close to those obtained experimentally. The advantage of this method is the simplicity of the calculations and the experimental procedure; only a macro-etched weld section is needed. Instrumented welding tests (by embedding thermocouples), which are difficult and sometimes not reliable, can be eliminated. The method was also used to calibrate the shape and size of the HAZ peak temperature profiles.

The method was applied only to horizontal flat plates, where the Rosenthal equations directly apply. More work is needed for application of this method (or the general idea) to plates with other geometries/positions and examination of a wider range of welding variables. Nevertheless, the limited experimental work has demonstrated the promise of this simple method, as an initial step in the extraction of useful information from a weld HAZ section that contains thermal history information. This information can be applied to correlation studies involving microstructure, simulation and modelling.

Some other specific conclusions follow:

1) All thermal parameters of interest, namely, heating rates, peak temperature profiles, cooling rates and the time spent above a certain temperature of interest, were determined for three weld samples.
2) The selected thermal cycles for each heat input were also analyzed to obtain a model that could estimate the thermal cycle for any location of interest, designated by a specific peak temperature. The estimated thermal cycle was composed of three separate parts put together, namely, heating, dwell time around the peak temperature, and cooling. The estimated thermal cycles at several locations can be used for evaluation of precipitate dissolution/coarsening as well as prior austenite grain growth.
3) Rosenthal's solutions and most of his simplifying assumptions produced satisfactory results for determining lower- and upper-bound values for each thermal parameter.
4) There is a need to define a parameter that expresses the heat input relative to the plate thickness.
5) A thermal efficiency value of 0.75 for GTAW yielded reasonable results when the common values of thermal parameters (independent of temperature) were used in Rosenthal's equations.
6) The equations and criteria for distinguishing between 2D and 3D heat flow conditions are too simplistic and inaccurate. A spectrum of heat flow conditions between two and three dimensions exists in actual welding.

References

[1] Grosh, R. J., and Trabanat, E. A., 1956, "Arc-Welding Temperatures," Welding Journal, **35** (8), pp. 396-s to 400-s.

[2] Rosenthal, D., and Schmerber, H., 1938, "Thermal Study of Arc Welding - Experimental Verification of Theoretical Formulas," Welding Journal, **17** (4), pp. 2-s to 8-s.

[3] Rosenthal, D., 1941, "Mathematical Theory of Heat Distribution During Welding and Cutting," Welding Journal, **20** (5), pp. 220-s to 234-s.

[4] Rosenthal, D., 1946, "The Theory of Moving Sources of Heat and Its Application to Metal Treatments," Trans. ASME, **48**, pp. 848-866.

[5] Tanaka, S., 1943, "A Study on Heat Conduction of a Moving Heat Source," Journal Japan Welding Society, **13** (9), pp. 347-359.

[6] Kasuya, T., and Yurioka, N., 1993, "Prediction of Welding Thermal History by a Comprehensive Solution," Welding Journal, **72** (3), pp. 107-s to 115-s.

[7] Christensen, B. N., Davies, V. D. L., and Gjermundsen, K., 1965, "Distribution of Temperatures in Arc Welding," British Welding Journal, (February), pp. 54-75.

[8] Nunes, A. C., Jr., 1983, "An Extended Rosenthal Weld Model," Welding Journal, **62** (6), pp. 165-s to 170-s.

[9] Dikshit, V. A., and Atteridge, D. G., 1993, "Electroslag Strip Surfacing Thermal History Predictions Using Simple Analytical Approach," *Proc., Modelling and Control of Joining Processes, International Conference*, American Welding Society, Miami, FL, pp. 53-60.

[10] Eagar, T. W., and Tsai, N.-S., 1983, "Temperature Fields Produced by Traveling Distributed Heat Sources," Welding Journal, **62** (12), pp. 346-s to 355-s.

[11] Ashby, M. F., and Easterling, K. E., 1984, "The Transformation Hardening of Steel Surfaces by Laser Beam. Part 1: Hypo-Eutectoid Steels," Acta Metallurgica, **32** (11), pp. 1935-1948.

[12] Shah, A. K., Kulkarni, S. D., Gopinathan, V., and Krishnan, R., 1995, "Weld Heat Affected Zone in Ti-6al-4v Alloy, Part 1: Computer Simulation of the Effect of Weld Variables on the Thermal Cycles in the HAZ," Welding Journal, **74** (9), pp. 297-s to 304-s.

[13] Adams, C. M., Jr., 1958, "Cooling Rates and Peak Temperatures in Fusion Welding," Welding Journal, **37** (5), pp. 210-s to 215-s.

[14] Rykalin, N. N., and Beketov, A. I., 1967, "Calculating the Thermal Cycle in the Heat-Affected Zone from the Two-Dimensional Outline of the Molten Pool," Welding Production, **14** (9), pp. 42-47.

[15] Kou, S., 1981, "Simulation of Heat Flow During the Welding of Thin Plates," Metallurgical Transactions A., **12A** (12), pp. 2025-2030.

[16] Goldak, J., Chakravarti, A., and Bibby, M., 1984, "A New Finite Element Model for Welding Heat Sources," Metall. Trans. B, **15B** (2), pp. 299-305.

[17] Ashby, M. F., and Easterling, K. E., 1982, "A First Report on Diagrams for Grain Growth in Welds," Acta Metall., **30** (11), pp. 1969-1978.

[18] Easterling, K. E., 1992, Introduction to the Physical Metallurgy of Welding, Butterworth-Heinemann Ltd, Oxford.

[19] Myers, P. S., Uyehara, O. A., and Borman, G. L., 1967, "Fundamentals of Heat Flow in Welding," Weld. Res. Council Bull., **123**, pp. 1-46.

[20] Kou, S., 2003, *Heat Flow in Welding*, in Welding Metallurgy, Wiley-Interscience, Hoboken, N.J., pp. 37-43.

[21] Hess, W. F., Merill, L. L., E F Nippes, J., and Bunk, A. P., 1943, "The Measurement of Cooling Rates Associated with Arc Welding and Their Application to the Selection of Optimum Welding Conditions," Welding Journal, **22** (9), pp. 377-s to 422-s.

[22] Baxter, C. F. G., and Warburton, G. R., 1994, "The Development of a Thermal Model as a Basis for Welding Zeron 100," 1995, *Proc., Duplex Stainless Steels '94*, T.G. Gooch, eds., Abington Publishing for Woodhead Publishing Ltd (UK), Cambridge, **2**.

[23] Fuerschbach, P. W., and Knorovsky, G. A., 1991, "A Study of Melting Efficiency in Plasma Arc and Gas Tungsten Arc Welding," Welding Journal, **70** (11), pp. 287s-297s.

[24] Dorling, D. V.: *Weld Procedure Ps-18-124-Gmaw-Ml File #2680*. 1999, TransCanada Pipelines Ltd.

[25] Alberry, P. J., Chew, B., and Jones, W. K. C., 1977, "Prior Austenite Grain Growth in Heat-Affected-Zone of a 0.5cr-Mo-V Steel," Metals Technology, **4** (6), pp. 317-325.

[26] Key, J. F., 1993, *Arc Physics of Gas-Tungsten Arc Welding*, in ASM Handbooks Online, Vol.6: Welding, Brazing, and Soldering, ASM International, Materials Park, Ohio.

[27] Stone, H. J., Roberts, S. M., and Reed, R. C., 2000, "A Process Model for the Distortion Induced by the Electron-Beam Welding of a Nickel-Based Superalloy," Metallurgical and Materials Transactions A (USA), **31A** (9), pp. 2261-2273A.

[28] Zhang, W., Elmer, J. W., and Debroy, T., 2002, "Modeling and Real Time Mapping of Phases During GTA Welding of 1005 Steel," Materials Science and Engineering A (Switzerland), **333** (1-2), pp. 320-335.

[29] Collins, L. E., Godden, M. J., and Boyd, J. D., 1983, "Microstructures of Linepipe Steels," Can. Metall. Q., **22** (2), pp. 169-179.

[30] Tsai, C. L., and Tso, C. M., 1993, *Heat Flow in Fusion Welding*, in ASM Handbook, Vol 6: Welding, Brazing and Soldering, ASM International, Materials Park, OH, pp. 7-18.

[31] Ion, J. C., Easterling, K. E., and Ashby, M. F., 1984, "A Second Report on Diagrams of Microstructure and Hardness for Heat-Affected Zones in Welds," Acta metall., **32** (11), pp. 1949-1962.

[32] "CCT Diagram for Grade 100 Microalloyed Steel," Private communication between D.G. Ivey and L. Collins, IPSCO, Inc.

[33] Hansen, M., 1958, Constitution of Binary Alloys, McGraw-Hill, New York.

[34] Lindstrom, R. M., and Ulfvarson, A., 2002, "Weld Repair of Shell Plates During Seagoing Operations," Paper OMAE2002/28583, *Proc., Offshore Mechanics and Arctic Engineering (OMAE 2002), 21st International Conference*, American Society of Mechanical Engineers, New York.

Chapter 5

Precipitate Analysis in the HAZ

5-1. Introduction

The weld thermal cycle causes alterations in the precipitate composition, size distribution and volume fraction through dissolution, coarsening and reprecipitation. These alterations affect the mechanical properties of the heat-affected zone (HAZ) directly, through a precipitate hardening mechanism and stress concentration at the location of precipitates (which affects the fracture toughness), or indirectly, by affecting the austenite grain growth and effective composition of the austenite (changed by dissolution of precipitates). It is, therefore, necessary to understand the properties and functions of these precipitates and the changes at different sub-regions of the HAZ and under different heat inputs.

As most of the precipitates that change during the weld thermal cycle are sub-micron in size, high-resolution techniques such as transmission electron microscopy (TEM) are essential to resolve them. However, even TEM has a detectability limit. In practice, it is very difficult to resolve particles smaller than 3-5 nm in diameter, or to characterize such fine particles in terms of structure and composition with conventional analytical TEM. In addition, evaluation of precipitate volume fraction has always been a challenge, even for not-so-fine particles, due to difficulties originating from errors involved in estimation of film thickness (in the case of TEM thin-foil samples) or depth of matrix dissolution (in the case of TEM replicas) [1, 2]. These facts make quantitative analysis of precipitates challenging.

Before examining precipitate alteration in the HAZ, some information on the precipitate characteristics as well as the state of precipitation in the BM is required. Therefore, this chapter starts with a short review on different aspects of microalloy precipitates, as background knowledge on their characteristics and functions. Then precipitation in the Grade 100 steel is analyzed, mainly through thermodynamic calculations with some discussion on the kinetic effects, followed by kinetic analysis of precipitate alteration in the HAZ. Challenges in the quantification of these precipitates are discussed next and some modifications to the existing theories for calculation of the volume fraction are presented. The experimental procedure is then described, followed by the test results, in particular with carbon replica TEM samples, accompanied by discussion of the results, both qualitatively and quantitatively.

5-2. Microalloy precipitates

5-2-1. Chemical composition and crystal structure

The precipitate compositions range from almost pure binary compounds to complex phases. The main precipitates that form in microalloyed steels are carbides, nitrides and carbonitrides of Nb, Ti, and V. Titanium oxide has also been used in these steels as it is very stable at the highest temperatures for austenite.

5-2-1-1. Niobium compounds

DeArdo [3] has reviewed all aspects of niobium application and technology in modern steels. Nb has a strong tendency to form carbonitrides, but little tendency to form oxides or sulphides. NbC has several forms and combinations. Three of these forms are NbC-α, NbC-β and NbC-γ. These are single phases of the Nb-NbC system. NbC-α has little solid solubility for C with a bcc (body-centered cubic) crystal structure. NbC-β has a composition of Nb_2C with a hcp (hexagonal close packed) crystal structure. The phase of most interest in steels is the NbC-γ phase with the composition NbC_x ($x \leq 1$; at 1100°C $0.72<x<1$). It has a NaCl-type fcc (face-centered cubic) crystal structure. The lattice parameter of NbC_x is strongly dependent on x. Pure, stoichiometric NbC has a lattice parameter of 0.4470 nm. The lattice of NbC-γ has three main constituents: Nb atoms, C atoms and vacancies (of Nb atoms or C atoms). The vacancies may allow substitution of other elements, such as Mo, Ti, V and N. NbN is very similar to NbC, and in fact the two have complete solid solubility. The composition of Nb carbonitride is usually shown as NbC_xN_y.

5-2-1-2. Titanium compounds

Titanium precipitates may appear, in Ti-bearing steels, as single binary compounds, i.e. ,TiN and TiC, or complex compounds of Ti(C,N), or even mixed precipitates with a TiN-rich core and TiC-rich skin [4]. Titanium, unlike Nb and V, has a very strong tendency to form nitrides, sulfides and oxides. TiC will not form until all O, N, and S have been consumed by Ti or other elements at higher temperatures [3]. TiN and TiC have NaCl-type fcc crystal structures.

5-2-1-3. Vanadium compounds

Vanadium has a large solubility in both austenite and ferrite. As a precipitate, it has a tendency to form carbonitrides, but has very little tendency to form oxides or sulphides [3]. Lagneborg *et al.* [5] have reviewed all aspects of vanadium application and technology in modern steels. In the Fe-V-C ternary system, three carbides of V, namely VC, V_2C and V_3C_2 can be found. The one that usually forms in microalloyed steels is VC, which has a NaCl-type fcc crystal structure. The Fe-V-N ternary system shows two nitrides of V, namely VN (fcc) and V_2N (hcp). VN, which is found in most V-bearing microalloyed steels, may not be seen in modern steels with considerable amounts of Ti and Nb.

5-2-2. Size, morphology and interface with iron matrix

The size of the precipitates is largely a function of temperature of precipitation (thermodynamics), and the amount of supercooling (kinetics). In general, precipitates that form at higher temperature tend to grow larger. Supercooling favours nucleation but does not allow much growth, resulting in a fine dispersion of particles. Deformation and cold work also enhance nucleation by providing suitable locations (dislocations) for heterogeneous precipitation, resulting in a finer distribution. This is especially the case for strain-induced precipitation in austenite during controlled rolling (CR) and in ferrite during levelling (Section 5-2-4).

The shape of the precipitates depends on their composition, crystal structure, mismatch with the matrix, and thermal history. Thermodynamic studies of precipitation suggest that the equilibrium shape of a precipitate is an "oblate spheroid" (a ball flattened at top and bottom, like the Earth) with a c/a value that balances the opposing effects of interfacial energy (due to the formation of the new interface) and elastic strain energy (due to existing volume mismatch between the precipitate and the matrix) [6]. However, the actual shapes observed in the steel during TMCP may be different. For instance, according to DeArdo [3], at normal Nb levels in microalloyed steels (<0.04%) the carbonitrides of Nb have cubic shapes. Higher levels of Nb (>0.10%) and N (>0.012%) give rise to formation of non-cubic compounds. These compounds can have other compositions and crystal structures than NbC-γ. Non-cubic shapes of NbC-γ (e.g., spherical) has been also observed in Grade 100 steel [7]. The evolution of precipitates during TMCP is further explained in Section 5-2-4.

The crystallographic relationship between the precipitates and the matrix has two important aspects: orientation relationship (OR) and lattice mismatch [3]. The OR between carbonitrides of Ti, Nb, and V and austenite (both having a fcc crystal structure) was found to be of the "parallel" type, i.e.,

$$(100)_{M(CN)} \parallel (100)_{\gamma} \tag{5-1}$$

$$[010]_{M(CN)} \parallel [010]_{\gamma} \tag{5-2}$$

The OR of precipitation in ferrite, however, is different. NbCN precipitates in ferrite with the so-called Baker–Nutting OR, i.e.,

$$(100)_{Nb(CN)} \parallel (100)_{\alpha} \tag{5-3}$$

$$[011]_{Nb(CN)} \parallel [010]_{\alpha} \tag{5-4}$$

OR examination can help distinguish between the precipitates that nucleated in austenite and those nucleated in ferrite. For instance, NbC that nucleated in ferrite will have the Baker–Nutting OR with the ferrite at room temperature. However, NbC that nucleated in austenite will have Kurdjumov–Sachs OR with the ferrite at room temperature. This is because ferrite has a Kurdjumov–Sachs OR with the parent austenite, i.e.,

$$(111)_{\gamma} \parallel (110)_{\alpha} \tag{5-6}$$

$$[110]_{\gamma} \parallel [111]_{\alpha} \tag{5-7}$$

Calculations of lattice mismatch are based on finding the linear strain in the matrix lattice that would bring the two lattices of the matrix and precipitate into coincidence at the interface. Initially, precipitates usually have a coherent interface with the matrix, due to the balance between a low interfacial energy and a high strain energy [6]. Apparently, as precipitates with high elastic matrix strain grow, coherency is lost since the strains cannot be accommodated by a few interfacial dislocations. It has been shown that for the orientation relationship between the carbonitrides and austenite, there is ~23% mismatch in lattice spacings and hence the carbonitrides are expected to be incoherent or at most semicoherent with the austenite matrix [8]. Therefore, these precipitates are bound to form on grain boundaries, sub-grain boundaries or dislocation arrays. Experimental examination shows that this is the case for NbC [3].

5-2-3. Precipitate stability and solubility products

To calculate the amount of precipitation, the amount of elements consumed in precipitation and the amount of elements left in the matrix at different temperatures, the following notations, used by Gladman [9], will be used here:

M_T = wt% M (metal atom) in the alloy
$[M]$ = wt% M dissolved in the matrix
M_{MX} = wt% M present as MX (a compound between a metal atom and C or N)
X_T = wt% X (C or N) in the alloy
$[X]$ = wt% X dissolved in the matrix
X_{MX} = wt% X present as MX
(MX) = wt% MX precipitated out from the matrix

In a reaction

$$[M] + [X] \leftrightarrow (MX) \tag{5-8}$$

the equilibrium constant, referred to as the solubility product, is written as:

$$k_S = a_{[M]} \cdot a_{[X]} \; / \; a_{(MX)} \tag{5-9}$$

a is the activity. With further assumptions that the activity of a pure compound is equal to 1 and the activities of the dilute solutes can be replaced by their concentrations (in wt%), k_S is simplified to:

$$k_S = [M].[X] \tag{5-10}$$

The temperature dependence of k_S has an Arrhenius type of relationship (i.e. $k_S = A.e^{-Q/RT}$) and is expressed in the form:

$$Log\, k_S = A - B/T . \tag{5-11}$$

Temperature is in Kelvin. The values of A and B, which are in fact related to changes in entropy (ΔS) and enthalpy (ΔH) respectively [8], have been determined by isothermal experiments for a number of precipitates. The results of different experiments are not exactly the same, and that has led to a number of values from which to choose A and B for a given compound. In this study, the values that most frequently appeared in the literature were used (Table 5-1). The solubility of different types of precipitates can be better compared by plotting $logk_S$ vs. $1/T$. Fig. 5-1 shows k_S for different precipitates in both ferrite and austenite. Note, that this information does not determine which compound precipitates first or last for a given steel, as the order also depends on the compositions. Fig. 5-1 does show that for similar amounts of microalloy elements, TiN is the most stable and VC and Mo_2C are the least stable precipitates.

Table 5-1. Values of solubility product constants used in this study for several compounds

Compound	Matrix	A	B (K)	Reference
VC	Ferrite	8.05	12265	[10]
	Austenite	5.36	8000	[11]
NbC	Ferrite	5.43	10960	[9]
	Austenite	2.96	7510	[9, 11]
NbN	Ferrite	4.96	12230	[9]
	Austenite	4.04	10230	[9, 11]
Nb(CN)	Austenite	2.26	6770	[11]
TiC	Ferrite	4.40	9575	[10]
	Austenite	2.75	7000	[10, 11]
TiN	Austenite	0.32	8000	[9, 11]
	Liquid iron	5.90	16586	[9]

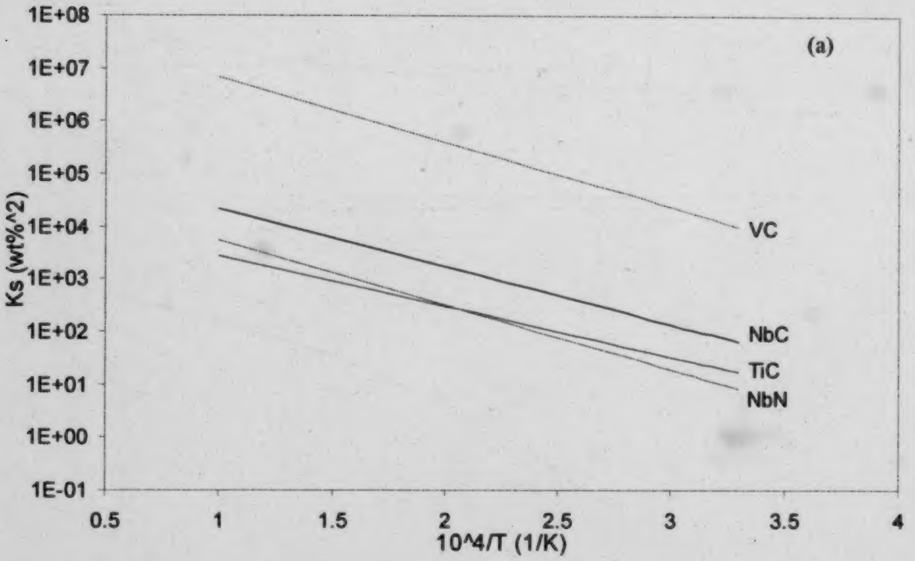

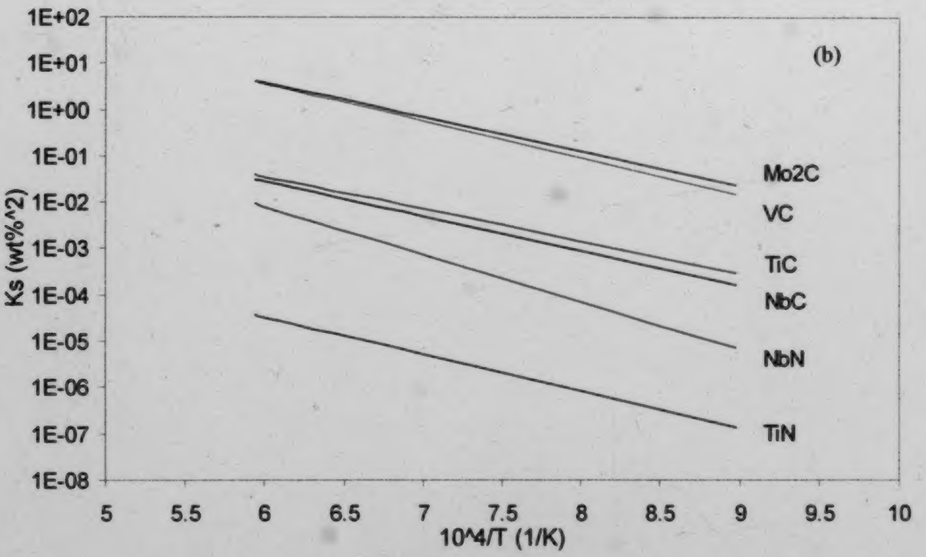

FIG. 5-1. Solubility products for carbides and nitrides as a function of temperature: a) in ferrite (25-695°C); b) in austenite (840-1410°C).

To form a compound, the components react together in the appropriate ratio of their atomic masses, known as the *stoichiometric ratio*. This fact, along with the k_S information, determines the matrix composition at any temperature, if the equilibrium state is attained. This is shown schematically Fig. 5-2. The intersection between the stoichiometric line (in fact the line passing through point P, designating the total amount of solutes M and X in the alloy, at an stoichiometric tangent) and the solubility limit curve determines the amount of solutes M (denoted by letter D) and X (denoted by letter E) that can remain in solution at the specific temperature. The amount of solutes consumed by precipitation can then be found by subtracting the amount remaining in solution from the total amount of the solutes in the alloy (designated by C for element M and F for element X, in Fig. 5-2). This translates to the following formulation [9]:

$$\frac{(C-D)}{(F-E)} = \frac{A_M}{A_X} \tag{5-12}$$

where A_M and A_X are the atomic weights (a.k.a. relative atomic mass) of elements *M* and *X*, respectively.

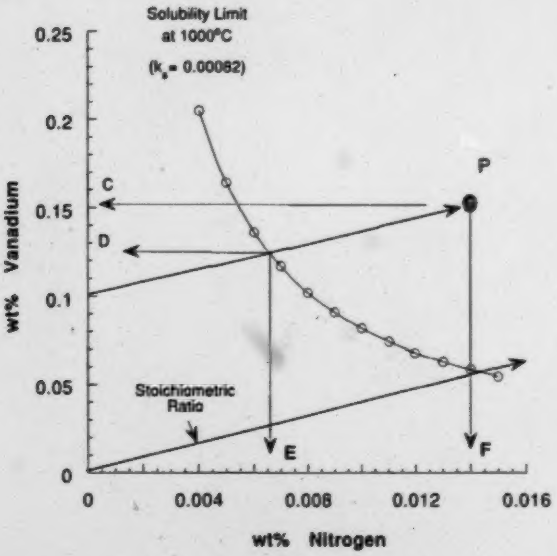

FIG. 5-2- Solubility diagram showing the stoichiometric ratio between V and N [9].

From a number of simple relationships, a quadratic equation for M_{MX} can be derived [9]:

$$M_{MX} = A_M\left[\left(X_T + M_T.A_X / A_M\right) - \left(\left(X_T + M_T.A_X / A_M\right)^2 - 4A_X\left(M_T.X_T - k_S\right)/A_M\right)^{1/2}\right]/2A_X \tag{5-13}$$

Then, the other parameters can be obtained from the following simple equations:

$$X_{MX} = M_{MX}.A_X / A_M \tag{5-14}$$

$$(MX) = M_{MX}.(A_X + A_M)/A_M \tag{5-15}$$

$$[M] = M_T - M_{MX} \tag{5-16}$$

$$[X] = X_T - X_{MX} \tag{5-17}$$

Note that these equations only apply to precipitates of the form *MX*. The solutions for compounds of the general form M_aX_b do not have a simple form, and should be approached individually.

5-2-4. Microalloy precipitates and TMCP

Here, precipitation is classified according to the particular stage during TMCP, as the thermomechanical processing will affect morphology, composition, size, and OR with the austenite or ferrite matrix.

5-2-4-1. As-cast precipitation

It has been shown by Hong *et al.* [12] that the precipitates of Ti-NbCN in the as-cast condition have a dendritic morphology (Fig. 5-3a). The HSLA steel they examined had 0.06%C, 0.018%Ti, 0.039%Nb, 0.03%V and 0.004%N, i.e., similar to the chemistry of Grade 100 used in this study, but with leaner compositions. The dendritic shape, which is a typical morphology of solidification, is a result of non-equilibrium cooling and precipitation in liquid iron. This was also reported by Jun *et al.* [13], who observed three kinds of morphologies (dendritic, semi-dendritic and rod-like) of complex Ti-Nb CN in a similar steel to that examined by Hong *et al.* but with a higher level of Nb and N (0.056% and 0.006%, respectively).

5-2-4-2. Reheating precipitation

Hong *et al.* [12] also showed that reheating the slab at temperatures between 1100–1400°C for 1 h will cause a change in precipitate morphology. The Nb-rich, Ti/Nb CN disappeared and new cubic Ti-rich Ti/Nb CN replaced them (Fig. 5-3b). This was because at the reheating temperatures the dendritic Nb-rich precipitates were not stable, while the cubic Ti-rich precipitates were stable. Dissolution of the dendritic precipitates close to the austenite grain boundaries was accompanied by diffusion of the solutes to the grain boundaries and reprecipitation as N-rich cubic precipitates at these preferred locations. Those within the matrix were also dissolved and replaced by smaller cubic precipitates rich in C.

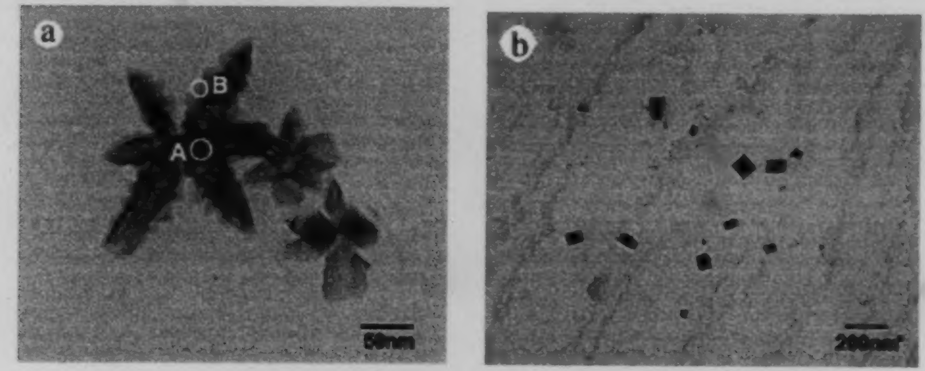

FIG. 5-3. Aluminium extraction replicas showing: a) the dendritic shape of as-cast Nb-Ti carbonitrides; b) the cubic shape of the reformed precipitates in (a) after reheating at 1300°C for 1 h [12].

5-2-4-3. Strain-induced precipitation

It is well established that mechanical work during hot rolling enhances precipitation of NbC in austenite, especially below the no-recrystallization temperatures. Hong *et al.* [14] studied the strain-induced precipitation of NbC in low-carbon microalloyed steels. The steel they used had 0.084%C, 0.043%Nb, 0.016%Ti and 0.005%N, i.e., leaner in Nb and N, and especially Ti than the Grade 100 steel used in this study. They used a hot deformation simulator for compression of rough-rolled plates at temperatures from 850 to 975°C. A pre-strain of 0.3 was followed by holding at the same temperature for various periods of time, and then water-quenched to preserve the state of precipitation. Fig. 5-4a shows some strain-induced NbC after holding for 32 s, believed to form at dislocations and sub-grain boundaries. Note, how small these precipitates are (<10 nm).

5-2-4-4. Interphase precipitation

NbCN precipitate distribution in ferrite depends on the kinetics of the austenite-to-ferrite transformation. If the transformation occurs at relatively high temperatures, the ferrite will have a polygonal morphology and the precipitates will have an "interphase" distribution, i.e., the microstructure will consist of numerous arrays of precipitates that were left behind as the austenite-ferrite interface swept through the grains [3]. Fig. 5-4b shows a TEM-BF image of some interphase precipitates in a microalloyed steel with 0.1%C and 0.04%Nb. The precipitates are roughly 2–8 nm in size. The interaction of a dislocation with the array of precipitates is visible as well [9].

As DeArdo [3] points out, "the chances of encountering interphase NbC in a commercial strip product seem highly remote, given that the strip would be water-spray cooled at 30-80°C s^{-1} to around 650-600°C and then very slowly cooled to room temperature". He also believes that even accelerated cooling at moderate rates of ~10°Cs^{-1} to around 600°C and below, followed by air cooling, would largely suppress interphase precipitation, and interphase precipitation might occur only at slow rates of ~1°Cs^{-1}. The same arguments also apply to interphase precipitation of VC [5]. This suggests that the type 4 precipitates in Grade 100, i.e., Nb-rich carbides 10-20 nm (Section 2-3-3-1), which were categorized initially as interphase precipitates [7], are more likely either strain-induced precipitates that formed in austenite, or general precipitates that formed in ferrite (Section 5-2-4-4) similar to type 5.

5-2-4-5. General precipitation

If the transformation product has an acicular or bainitic morphology (i.e., cooling rates higher than ~10°Cs^{-1}), interphase precipitation will be suppressed and precipitation will have a "general" distribution in ferrite at temperatures lower than A_1 [3]. Fig. 5-4c shows some general precipitates of NbCN in ferrite. The image is a TEM-DF obtained from the (111) NbC reflection. General precipitates are usually <5 nm in size.

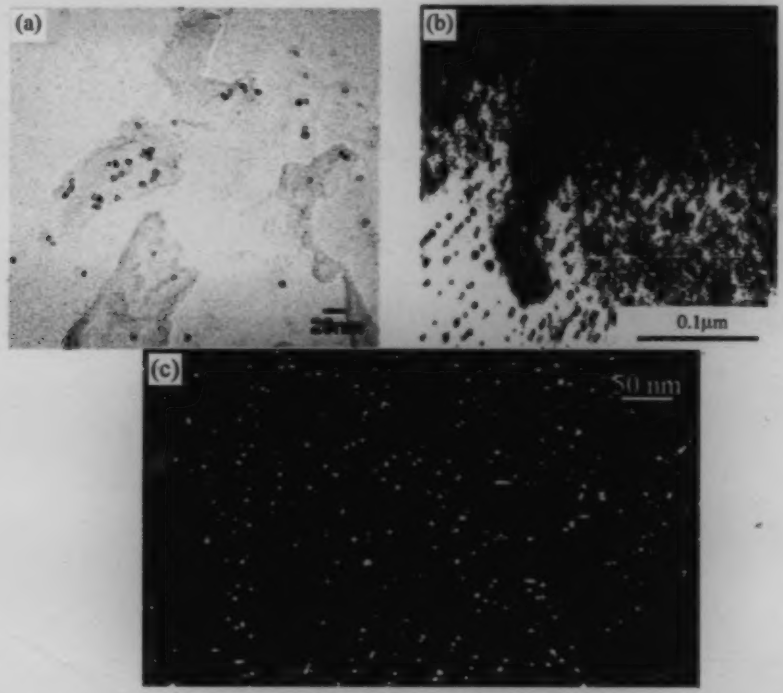

FIG. 5-4. TEM samples showing fine precipitation through different mechanisms: a) a carbon extraction replica showing strain-induced NbC after a prestrain of 0.3 at 950°C followed by holding for 32 s and quenching [14]; b) TEM-BF image showing interphase NbCN precipitates [9]; c) TEM-DF image showing general NbCN precipitates in ferrite [3].

5-2-5. Microalloy precipitates and HAZ

In this section, some practical aspects of different precipitate compounds with respect to HAZ thermal cycle are discussed.

5-2-5-1. Titanium carbonitrides

In the case of a sufficient amount of Ti, say around 0.06%, austenite grain growth in the HAZ is suppressed by the sluggish dissolution of Ti(C,N) particles and the presence of solute Ti atoms [4]. However, some researchers [15] believe that the Ti content should be kept lower than 0.02%, as excessive Ti can raise the precipitation temperature to above the liquidus, and lead to formation of large TiN precipitates, which decrease the potential for dispersion of fine TiN precipitates. They believe that large TiN particles may be a source for brittle fracture in the CGHAZ. The large precipitates do not act as effective austenite grain-growth inhibitors either. A fine distribution of small precipitates is what is desirable. The optimum Ti:N wt% ratio for HAZ toughness was found to be around two [16].

5-2-5-2. Niobium carbonitrides

Nb(C,N) get dissolved and reprecipitation does not usually occur in the CGHAZ during SAW, unless high heat inputs are applied or thick plates are to be welded. In this case, Nb(C,N) precipitation will reduce the CGHAZ toughness considerably [17, 18].

In the fine-grained HAZ however, sufficient Nb(C,N) is present due to the lower peak temperature, and also some precipitation can occur during or shortly after the transformation because of higher transformation temperatures [18]. Liu *et al.* [19], using an analytical TEM, found that the C/N ratio in Nb(C,N) is sensitive to the precipitation temperature (which could vary from 1050 to 1150°C) as well as Si concentration.

5-2-5-3. Titanium-niobium carbonitrides

It is possible to have complex particles containing Ti, Nb, N and C. The "coring" of these precipitates happens because of the difference in their temperature of formation. At high temperature the precipitate is rich in Ti and N, while at low temperatures the compound is rich in Nb and C [7, 20, 21]. Although the diagram in Fig. 5-5 shows the equilibrium situation, it still provides a good guide for welding conditions.

This complex precipitate is found in Ti-Nb bearing steels, where the precipitate sizes are much smaller than in the Ti-bearing steels and, therefore, contribute more to grain growth control. In these steels, Nb-rich particles dissolve during the heating cycle, freeing up Ti and N present in them to reprecipitate as cuboidal TiN-rich particles, which prevent austenite grain growth at the peak temperatures [4].

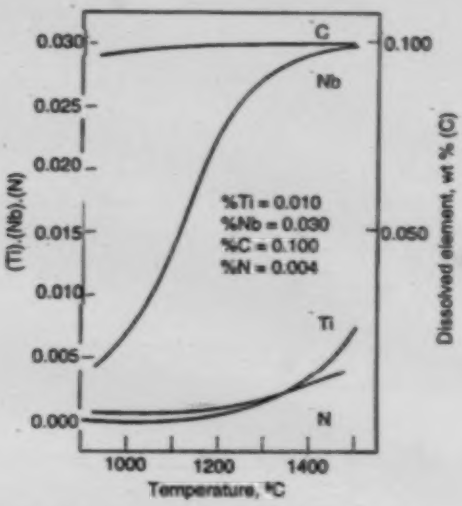

FIG. 5-5. Dissolution of complex Ti-Nb(C,N) [21].

5-2-5-4. Vanadium carbonitrides

V(C,N) is not as effective as other precipitates, discussed above, for controlling austenite grain growth. The solubility of V(C,N) is much higher than for Ti and Ni carbonitrides. Like Ti, but unlike Nb, the solubility of VN is about two orders of magnitude smaller than for VC [5].

5-3. Precipitation in Grade 100

For any precipitation or precipitation alteration there are two main conditions that should be satisfied: a thermodynamic driving force should exist and atomic mobility should be provided. In this section, precipitation in Grade 100 is first discussed and analysed from a thermodynamic viewpoint, followed by a discussion on the kinetic effects.

5-3-1. Thermodynamic calculations

Simple thermodynamic calculations based on the information available in the literature on the solubility products of these precipitates (Table 5-1) can give an approximation on how much precipitate will form at a given temperature during the TMCP. A typical thermo-mechanical cycle for Grade 100 steel was shown in Fig. 2-1. As an example of the calculation procedure, Table 5-2 shows the result of calculations for TiN. The table contains the amount of Ti and N precipitated as TiN and amount of Ti and N left in the matrix for a number of temperatures. These calculations were also carried out for NbN, NbC, VC, TiC and Mo_2C as well. Fig. 5-6 shows the amount of each precipitate as a function of temperature. The amount of each element left in the matrix as a function of temperature is shown in Fig. 5-7.

The calculations show that TiN first precipitates in the liquid at ~1551°C. By the time the temperature drops to the melting point (~1500°C), 0.164% TiN has formed in the liquid. As the solubility limit of the microalloying elements in austenite is much lower than in the liquid, the amount of TiN jumps to ~0.457% upon solidification (and after passing through the δ-ferrite region). At this temperature, only 0.025% Ti and 0.0015% N (about 44% and 13% of the initial values, respectively) are left dissolved in the matrix. TiN precipitation continues in austenite as the temperature drops. Simple calculations show that ~31% of all TiN precipitates in the liquid, ~56% during solidification, and only ~13% in austenite. At about 1200°C, a slight amount of N is left dissolved in the matrix (~4 ppm). Therefore, almost all N is tied up with Ti at high austenite temperatures and all precipitation below 1200°C is in the form of carbides. The rest of the Ti after consumption of N, which is ~0.20 wt%, will precipitate as TiC below 1200°C until Ti is totally consumed before the temperature drops to ~500°C.

Table 5-2. Amount of precipitation (wt%) of TiN and matrix composition upon cooling

	T (°C)	log k_S	k_S	wt% present as TiN		wt% TiN	wt% left in matrix	
				Ti_{TiN}	N_{TiN}	(TiN)	[Ti]	[N]
Liquid	1600	-2.96	0.001108	0.000	0.000	0.000	0.058	0.0110
	1500	-3.45	0.000351	0.012	0.003	0.015	0.046	0.0076
Austenite	1490	-4.22	0.000061	0.030	0.009	0.039	0.028	0.0022
	1410	-4.43	0.000037	0.033	0.010	0.042	0.025	0.0015
	1400	-4.46	0.000035	0.033	0.010	0.043	0.025	0.0014
	1300	-4.77	0.000017	0.035	0.010	0.045	0.023	0.0007
	1200	-5.11	0.000008	0.036	0.011	0.047	0.022	0.0004
	1100	-5.51	0.000003	0.037	0.011	0.048	0.021	0.0001
	1000	-5.96	0.000001	0.037	0.011	0.048	0.021	0.0001
	900	-6.50	0.000000	0.038	0.011	0.049	0.020	0.0000
	840	-6.87	0.000000	0.038	0.011	0.049	0.020	0.0000

Calculations for NbN show that even if all the N was available for the precipitation of NbN (which is absolutely not the case in this steel), NbN would not form above 1183°C. From TiN calculations, it is clear that almost no N is left in the matrix at that temperature. Therefore, it would be a reasonable assumption that Nb precipitates as carbides in the austenite. Other evidence to support this conclusion is the absence of any AlN in this steel. As mentioned in Section 2-3-1, AlN has a lower solubility than NbN. If there was any N left in the steel, AlN would form at high temperatures in the austenite. AlN, which has a distinctive crystal structure (i.e., hcp) was not observed in the Grade 100 steel in this work. The counter-argument, however, is that these analyses are based on thermodynamics only, and the kinetics of precipitation of AlN in austenite may be slower than that for NbN, for instance.

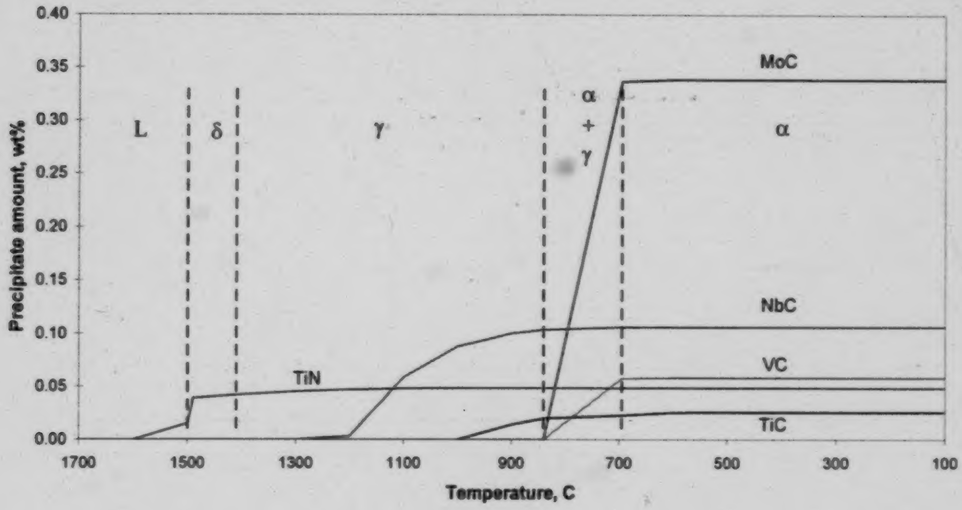

FIG. 5-6. Precipitation as a function of temperature for Grade 100 steel based on thermodynamic calculations.

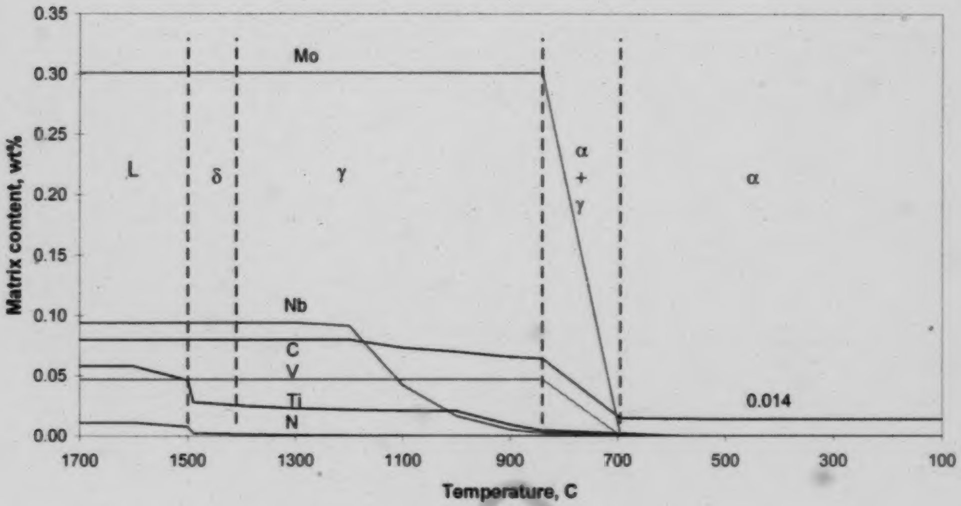

FIG. 5-7. Variation of the content of Ti, Nb, V, Mo, C and N in the matrix as a function of temperature for Grade 100 steel, based on thermodynamic calculations.

Calculations for NbC show that the precipitates form first at ~1204°C in austenite. NbC is the initial precipitate to form at that temperature, as TiC and VC have higher solubilities in austenite than NbC. The Nb content in the matrix drops rapidly as the temperature drops (Fig. 5-7), so that there is only ~0.002 wt%Nb left in the matrix at 840°C (~A_3). This amount will precipitate upon transformation of austenite to ferrite (i.e., interphase precipitation), and little precipitation is predicted to take place in ferrite. This does not happen in practice, as Ti and Nb are mutually soluble. In fact, most of the Ti calculated to be left in the matrix at the end of the austenite region could be tied up with Nb and C to form TiNbC, hence, leaving more Nb dissolved in the matrix just before austenite tranforms to ferrite. It is worth mentioning that the stoichiometry conditions require that Nb precipitation to NbC only consumes 0.012 wt%C. The total carbide formation in austenite due to the formation of TiC and NbC was found to be ~0.033 wt%, which will leave a significant amount (~0.064 wt%C) of C in the matrix at A_3. As shown later, further precipitation takes place during the austenite-to-ferrite transformation as well as in ferrite in the form of Ti/Nb/Mo/V carbides.

For the calculation of carbides for Nb, Ti, V and Mo, a step-by-step procedure was adopted, where the total amount of C available for precipitation of a compound of lower stability was assumed to be the carbon content in the matrix after precipitation of a compound of higher stability at a given temperature. This was done at several temperatures as shown in Fig. 5-6. VC and Mo_2C are expected to form mostly during the austenite-to-ferrite transformation, while NbC and TiC form mostly in the austenite. In fact, TiNbC is what forms in austenite in the Grade 100 steel. General precipitation in ferrite is also in the form of complex precipitates having various amounts of Ti, Nb, Mo and V (see Section 5-7).

Stoichiometric relations show that if Mo does not precipitate, but all the Ti, Nb and V precipitate, a significant amount of 0.052 wt%C (~65% of the total value) would still remain dissolved in the matrix. However, as will be shown in Section 5-7, Mo is present in the fine carbides that have a considerable volume fraction. Assuming all the Mo would precipitate out, there is still a considerable amount of carbon, i.e., ~0.014%, present in the ferrite matrix of the Grade 100 steel. The maximum solubility of carbon in ferrite is 0.008% at room temperature [22]. Bainitic ferrite, the dominant microstructure in Grade 100, may be able to dissolve more C in the matrix than ferrite. The excess C, if any, should either precipitate as cementite, or remain in solid solution in M/A islands. At any rate, these calculations show that not all C is tied up with the microalloying elements, and therefore Grade 100 steel is not an interstitial-free (IF) steel. This should be examined further by some experiments, for instance, strain aging.

5-3-2. Other considerations (kinetic effects)

Calculations from Section 5-3-1 were based on the solubility products of Table 5-1. The effects of mutual solubilities, reheating, non-equilibrium cooling and mechanical processing were not considered there. It is understood that the presence of other elements can affect the solubility of a given compound by altering the activity coefficients of each element in that compound. For example, the solubility limit of NbC in unalloyed austenite at 1150°C is approximately $5x10^{-3}$. The addition of 1.5%Mn and 0.4%Si was reported to reduce the solubility to $4x10^{-3}$ (i.e., ~20% reduction) [6].

It was also assumed in the previous section that the steel was cooled continuously from the liquid state to room temperature. It has been shown that reheating causes dissolution of as-cast dendritic Nb-rich Ti-NbCN, and subsequent cooling causes reprecipitation of different kinds of precipitates, mostly rich in Ti [12].

Moreover, equilibrium (assumption for thermodynamic calculations) will not be reached at all temperatures in practice, unless the holding time is long enough, and therefore some supersaturation of solutes occurs. This may have several implications. One effect is retardation of precipitation (e.g., interphase precipitation), meaning that the amount of precipitate calculated at each temperature in the previous section (Table 5-2) may be an upper bound. Nevertheless, holding at the coiling temperature and levelling [23] is expected to bring out some of the delayed precipitation eventually, resulting in different precipitate size distributions of course. The other effect is coring of the complex carbonitrides. There is substantial evidence of heavily cored particles, with a TiN-rich core and a NbC-rich shell. If formation or growth of TiN is somewhat suppressed, there is a possibility that Nb, Ti, C and N will precipitate together, especially at temperature ranges between those of precipitation of TiN and NbC. This will also depend on the composition of the steel and the relative abundance of the microalloying elements at a given location [9]. Coring occurs because homogenization of metal atoms (Nb and Ti in this case) in a mixed carbonitride does not occur, due to fast cooling. Depending on the composition of the steel, and at lower temperatures in austenite where NbC is a dominant precipitate, precipitation of NbC can take place after formation and growth of TiN. In this case, if the temperature is high enough, or cooling is slow enough, to allow for diffusion, NbC caps will form epitaxially on TiN cuboidal precipitates. However, if the temperature is low or the cooling rate is fast, nucleation can become relatively easy and diffusion can become relatively difficult, resulting in the formation of NbC particles in the matrix totally separate from TiN (instead of a NbC shell or cap). This kinetic effect contributes to precipitates of different chemistries and in different size ranges, a feature that is often observed in steels microalloyed with several elements [9].

Mechanical deformation, on the other hand, accelerates the precipitation when the solid solution is supersaturated [9]. Deformation increases dislocation density and the amount of sub-grain boundaries, which can act as nucleation sites for easy precipitation. This can have the opposite effect of the high cooling rates practiced at some stages during TMCP. Particle size also has an influence on the solubility product. It has been found that smaller particles (particularly when <10 nm) tend to be less thermodynamically stable [6].

One way to measure the actual amount of precipitation and the retained solute level in the matrix is the method of chemical dissolution and ICP-MS (inductively coupled plasma – mass spectroscopy). Lu *et al.* [24] applied this method to Grade 100 microalloyed steel. They determined the amount of solutes in solid solution with the matrix by ICP. Comparing the amount in solid solution with the total in the steel they estimated the amount precipitated (Table 5-3). The results show that most of the Nb and Ti precipitate in the BM, but only 50% of the total V and 18% of the total Mo precipitate, while the remaining Mo and V are in solid solution with the matrix. This seems reasonable as most of the Ti and Nb precipitates form in austenite, while all the Mo and V precipitate in ferrite, where the accelerated cooling will suppress the precipitation. Holding at a relatively low temperature of stop cooling (accompanied by levelling) may not be sufficient for all precipitation to happen.

Table 5-3. Fraction of different elements precipitated as revealed by chemical dissolution methods [24].

Element	Ti	Nb	Mo	V
Total amount in steel (wt%)	0.060	0.094	0.301	0.047
Amount in solid solution (wt%)	0.014	0.008	0.246	0.024
Amount precipitated (wt%)	0.046	0.086	0.055	0.024
Fraction precipitated	0.77	0.91	0.18	0.50

The volume fraction, f_V, of a particular type of precipitate can be estimated according to Equation 5-18, when the proportion of the precipitate is small [9].

$$f_V = \frac{(MX)}{100} \times \frac{\rho_{Fe}}{\rho_{MX}} \tag{5-18}$$

MX is the amount of precipitate (in wt%) and ρ is the density. Now the results of the thermodynamic calculations can be converted to volume fractions, and then adjusted based on the experimental results in Table 5-3. Table 5-4 shows these calculations. The density values for the different precipitates in column 2 were found from the literature [9]. The composition of the Mo carbide was considered as MoC in the precipitate calculations of Section 5-3-1, as Mo precipitates with Nb, and Nb carbide has a composition of NbC. It should be noted that if Mo would precipitate as pure binary carbide the composition would be Mo_2C, for which a density of 9.440 g cm^{-3} can be obtained from the literature [25], based on an fcc crystal structure with a lattice parameter of 0.4155 nm. Two density values for hexagonal MoC were found: 9.382 and 8.779 g cm^{-3} [25]. As an approximation a mean value of 9.0 g cm^{-3} was used here. A density of 7.917 g cm^{-3} (approximated to 7.9 g cm^{-3}) was experimentally found for the Grade 100 steel. The maximum amount reported in the third column is the result of the thermodynamic calculations of Section 5-3-1. The forth column reports the corresponding volume fraction calculated with Equation 5-18. The amount of metal atom consumed (M) can be calculated from Equation 5-19 (column 5).

$$M_{MX} = (MX).A_M / (A_X + A_M) \tag{5-19}$$

The amount calculated from Equation 5-19 is the maximum amount under equilibrium conditions. The actual amount of metal tied up in the formation of precipitates (column 6) is obtained from Table 5-3. Note, it was assumed that all the calculated TiN would precipitate out, as the reheating would provide a condition close to equilibrium for this precipitate, and the rest of the Ti (Table 5-3) would precipitate as

TiC. Comparison of the values in columns 5 and 6 gives the precipitation efficiency. This factor could be applied to the amount of precipitation (column 3) and volume fraction (column 4) to obtain the corresponding *estimated* values (columns 8 and 9). The other interesting result, from the adjustment of the thermodynamic calculations, is the estimation of the interstitial level retained in the matrix in a form other than microalloying precipitates. This value can be estimated from the precipitation efficiency and Equation 5-14. The total N left in the matrix was found to be zero, while a total of 0.05%C can be estimated to remain in the matrix. Assuming that a total of only 0.008%C can remain in solid solution in ferrite at room temperature, the rest (~0.042%C) would remain in the M-A particles or as iron carbides (mainly cementite).

Table 5-4. Volume fraction (f_V) estimation for different precipitates

Precipitate type	ρ (g/cm3) [9, 25]	Max amount (wt%)	Max f_V	Max M precipitated (wt%)	Measured M precipitated (wt%)	Precipitation efficiency	Estimated amount (wt%)	Estimated f_V
TiN	5.43	0.0486	7.07E-04	0.038	0.038	1.00	0.0486	7.07E-04
NbC	7.85	0.1062	1.07E-03	0.094	0.086	0.91	0.0971	9.77E-04
TiC	4.96	0.0255	4.07E-04	0.020	0.008	0.41	0.0105	1.68E-04
VC	5.85	0.0581	7.84E-04	0.047	0.024	0.51	0.0297	4.01E-04
MoC	9.00	0.3387	2.97E-03	0.301	0.055	0.18	0.0619	5.43E-04

It is also of interest to make an estimation of the amount of fine precipitates. Fine precipitates in Grade 100 steel consists of strain-induced Nb-Ti carbides formed in austenite and general Nb-Mo-Ti-V carbides formed in ferrite. It was assumed, therefore, that the total amount of fine precipitation could be obtained by adding the amount of all different types of precipitates that form below a certain temperature in austenite (T_{Fine}). Four values of T_{Fine} have been considered and the corresponding values of estimated volume fractions were calculated (Table 5-5), based on the procedure explained above. As can be seen, the total f_V was estimated to be ~ 10^{-3} for the highest T_{Fine} of 1000–1100°C. These precipitates generally have sizes <15 nm. This estimated value can be used for the estimation of the strengthening contribution through dispersion hardening (Chapter 8).

Table 5-5. Volume fraction estimation for fine precipitates

Precipitate type	T_{Fine}, °C			
	<A3	<900	<1000	<1100
TiN	0.00E+00	5.67E-07	2.97E-06	9.15E-06
NbC	2.49E-05	5.48E-05	1.71E-04	4.39E-04
TiC	3.69E-05	7.54E-05	1.68E-04	1.68E-04
VC	4.01E-04	4.01E-04	4.01E-04	4.01E-04
MoC	1.64E-04	1.64E-04	1.64E-04	1.64E-04
Total	6.26E-04	6.95E-04	9.06E-04	1.18E-03

5-4. Precipitate alterations in the HAZ

The precipitate reactions, such as coarsening and dissolution, are diffusion-controlled, in which time and temperature are both important parameters. Since the carbide and nitride formers in steels (e.g. Ti, Nb, and V) are substitutional elements, their diffusivities appear to be rate controlling in the precipitate reactions. Data exists for equilibrium solubility products of carbides and nitrides (e.g., Table 4.1), from which the temperature for complete dissolution of the particles, for instance, can be obtained. One question that arises is how the dissolution temperatures are affected by a rapid heating cycle. In most cases in welding, equilibrium is not reached and superheating takes place. The lower the heat input the higher the amount of superheating [11].

5-4-1. Particle dissolution

As the temperature rises due to the weld thermal cycle, the precipitates may start to dissolve to some degree, since the solubility of the microalloy elements increases with increasing temperature. The dissolution rate of precipitates in the HAZ depends on temperature, holding time, particle size and composition, and C and N levels in the base metal [4].

Two sets of information are needed to find out how much certain precipitates are dissolved due to a thermal cycle at a certain location in the weld HAZ and a given heat input: first, non-equilibrium solubility information for that precipitate, and second, the thermal cycle characteristics (effective T_P and dwell time) at that location and for that weld sample.

5-4-1-1. Non-equilibrium solubility curves

The theory of particle dissolution, as a result of superheating above the equilibrium temperature of particle dissolution and applied to the rapid thermal cycle of welding, has been developed by Ashby and Easterling [26, 27]. The particles were assumed to be spherical. The two resulting equations from their analysis that relates the time of dissolution, t, to the temperature of super heating, T, are as follows:

$$f = \frac{1}{1 + \left[\frac{t^*}{t} \exp - \frac{Q_V}{R} \left(\frac{1}{T^*} - \frac{1}{T} \right) \right]^{3/2}} \qquad (5\text{-}20)$$

$$T_S = \frac{B}{A - \log \left[\frac{C_M^a C_C^b}{f^{a+b}} \right]} \qquad (5\text{-}21)$$

f is the volume fraction to be dissolved, Q_V is the activation energy for diffusion of the metal atom , t^* is the time at which dissolution is complete at a temperature T^* and C is the concentration of elements M or C in the reaction "$aM + bC \leftrightarrow M_aC_b$". A pair of values for t^* and T^* were used from a set of experiments by Ikawa *et al.* (as cited by Easterling [11]), where the time for dissolution of NbC at the equilibrium temperature of dissolution was estimated to be about 20 s. Combining the above two equations will give Equation 5-22. With this equation, the non-equilibrium solubility curves for a number of carbides and nitrides can be plotted as a function of holding time and temperature, similar to that of Easterling [11]. This is shown in Fig. 5-8 for Grade 100 steel, assuming the solubility of each precipitate is not affected by presence of other microalloy elements. Values for Q_v were the approximated values used by Easterling (Table 5-6).

$$t = \frac{t^* \exp \left[\frac{-Q_V}{R} \left(\frac{1}{T^*} - \frac{1}{T_S} \right) \right]}{\left[\left(\frac{\exp 2.3 [A - B / T_S]}{k_S} \right)^{1/(a+b)} - 1 \right]^{2/3}} \qquad (5\text{-}22)$$

Table 5-6. Approximate values of activation energy for diffusion of various metal atoms [11].

Metal element	Ti	Nb	V	Mo
Q_V/RT_m	14.4	23.1	16.1	20.1

To find the non-equilibrium solubility curves for different fractions of precipitate dissolution, k_S in Equation 5-22 was replaced with the value of Equation 5-23 for a given fraction of precipitate solution, f. This modification is believed to make the estimations more accurate than the method used by Ashby and Easterling [26], as it also takes into account the amount of solutes already in the matrix. The amount already in the matrix is the sum of the residual levels in solid solution in the BM and the solutes added to the matrix due to the dissolution of precipitates with higher solubility, which were estimated through the analysis of Section 5-3-1. The non-equilibrium solubility curves for several fractions of dissolution of NbC in Grade 100 steel are shown in Fig. 5-9.

$$k_s = (f.M_{MX} + [M]).(f.X_{MX} + [X]) \qquad (5\text{-}23)$$

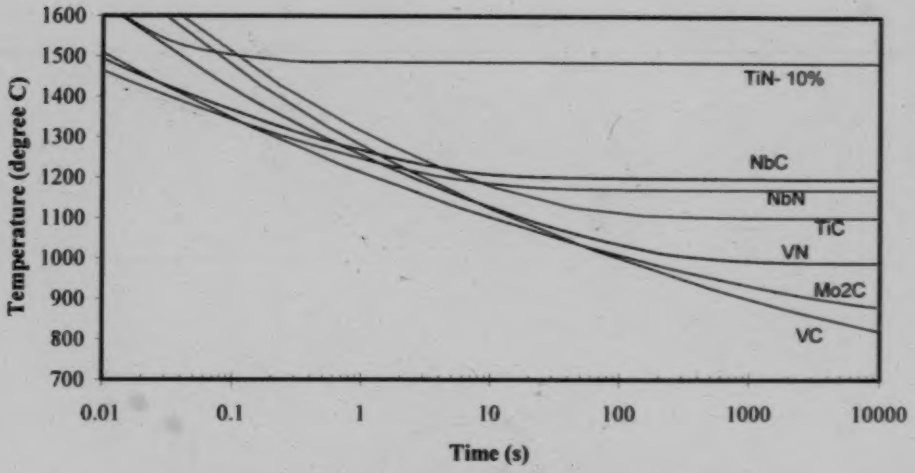

FIG. 5-8. Non-equilibrium solubility curves for several precipitates in Grade 100 steel.

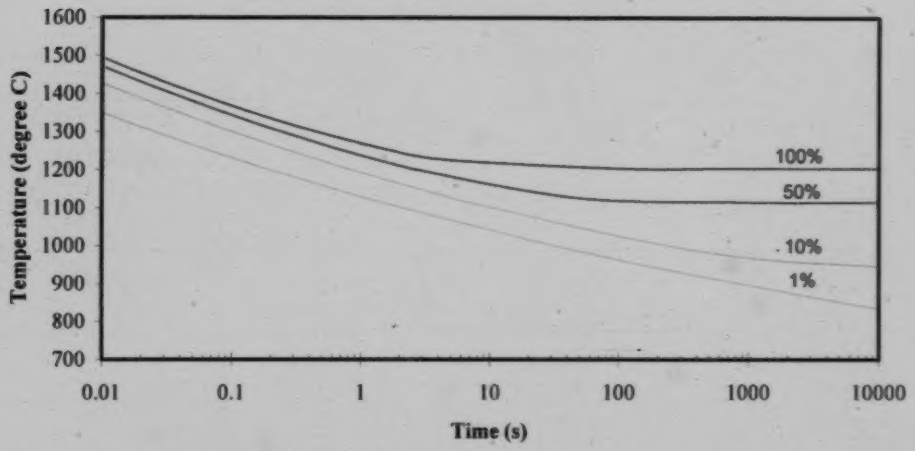

FIG. 5-9. Non-equilibrium solubility curves for several fractions of precipitate dissolution for NbC in Grade 100 steel.

5-4-1-2. Effective temperature and time for a weld thermal cycle

As mentioned earlier, the non-equilibrium solubility curves were constructed based on isothermal heating above the equilibrium temperature. Apparently, the only conclusion Easterling made on the non-equilibrium solubility curves (such as those shown in Fig. 5-8), was that "the shorter the weld thermal cycle, the greater the superheating of the carbonitrides" [11]. Here, it will be shown that by estimating a set of effective temperatures and effective times for a given thermal cycle, some interesting quantitative results can be obtained.

It is assumed that the portion of the weld thermal cycle with its temperature above the equilibrium dissolution temperature of a precipitate is responsible for dissolution (Fig. 5-10). The larger this portion, the more efficient will be the diffusion which controls the rate of dissolution. An effective peak temperature, $T_{P\text{-}Eff}$, can be calculated over a specified time, t_{Eff}, so that the diffusion criterion under the isothermal heating would be equal to that of the actual thermal cycle. The diffusion criterion used here is defined as the product $D.t$, which is a function of diffusion distance:

$$D.t = D_0.t.\exp\left(\frac{-Q}{RT}\right) \tag{5-24}$$

So,

$$\exp\left[\frac{-Q}{RT_{P\text{-}Eff}}\right].t_{Eff} = \int_{t_S}^{t_S+t_{Eff}} \exp\left[\frac{-Q}{RT(t)}\right].dt = I \tag{5-25}$$

D_0 is the frequency factor, D is the diffusion constant, t and T are time and temperature during the weld thermal cycle, Q is the activation energy for diffusion of the metal atom M in iron, R the gas constant and t_S is the moment during the weld thermal cycle when the temperature goes above the equilibrium temperature for dissolution of the precipitate, T_S. Equation 5-25 can be rewritten as the following equation that was used to calculate the effective peak temperature:

$$T_{P\text{-}Eff} = \frac{-Q}{R.\ln(I/t_{Eff})} \tag{5-26}$$

The effective time, t_{Eff}, is in fact the period of time spent above T_S (Fig. 5-10) and I is the integral of the curve $\dfrac{-Q}{R.T(t)}$ vs. t over the time t_{Eff}. These curves were obtained by appropriate conversion of the estimated temperature-time (T-t) curves for each weld sample and for several dissolution temperatures representing different fractions of dissolution, as obtained in Section 4-5-11. As seen in Fig. 5-10, the effective peak temperature ($T_{P\text{-}Eff}$) is considerably higher than the average temperature between the T_P and T_S (as denoted by $T_{P\text{-}Average}$). This is because diffusion is exponentially faster at high temperatures. From each set of calculations, a pair of $T_{P\text{-}Eff}$ and t_{Eff} can be obtained. From the calculations for various values of T_P (thermal cycles) and various fractions of dissolution, a graph like the one shown in Fig. 5-11 is obtained. The graph shows how much time (t_{Eff}) is available at an isothermal effective peak temperature ($T_{P\text{-}Eff}$, which defines a particular location across the HAZ) for dissolution of a given fraction of a particular precipitate. This, however, does not indicate, yet, if the given fraction of precipitate will be dissolved at the location of interest.

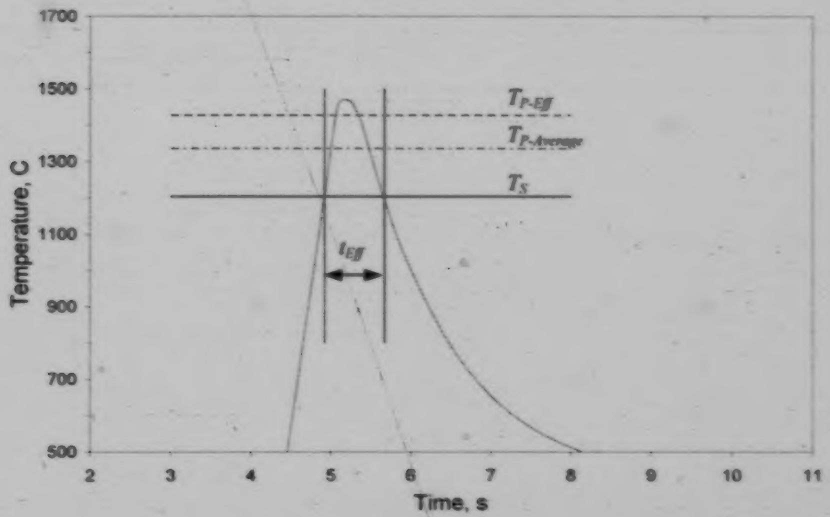

FIG. 5-10. Effective peak temperature and time for complete dissolution of NbC at a T_P = 1468°C.

Superimposing the available $T_{P\text{-}Eff}$ and t_{Eff} data on the non-equilibrium solubility curves will show if the portion of the thermal cycle above the dissolution temperature is large enough to cause dissolution (Fig. 5-12). Moreover, the intersection between the effective T-t curves (obtained from charts similar to the one in Fig. 5-11) and the non-equilibrium solubility curves will determine a *critical* pair of $T_{P\text{-}Eff}$ and t_{Eff} that is necessary for dissolution of a fraction f of a precipitate. This is marked with circles in Fig. 5-12. Then, finding that there is a linear relation between the T_P and $T_{P\text{-}Eff}$ (Fig. 5-13), the corresponding critical T_P for the critical $T_{P\text{-}Eff}$ can be interpolated or extrapolated. This critical T_P can be related to a distance from the fusion line through the T_P profiles (Section 3-5-3). The same procedure was applied for 1, 5 and 10% dissolution of TiN.

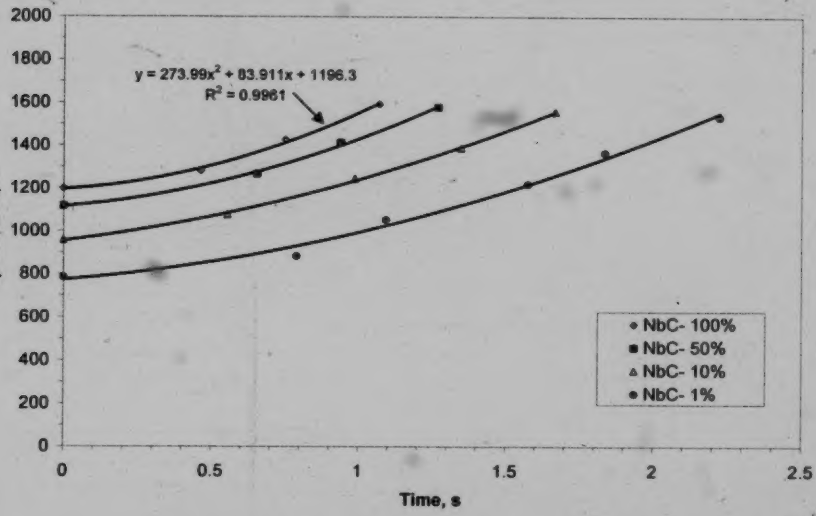

FIG. 5-11. Effective peak temperature and effective time available for dissolution of NbC at several locations (or several T_P) and for various fractions of dissolution.

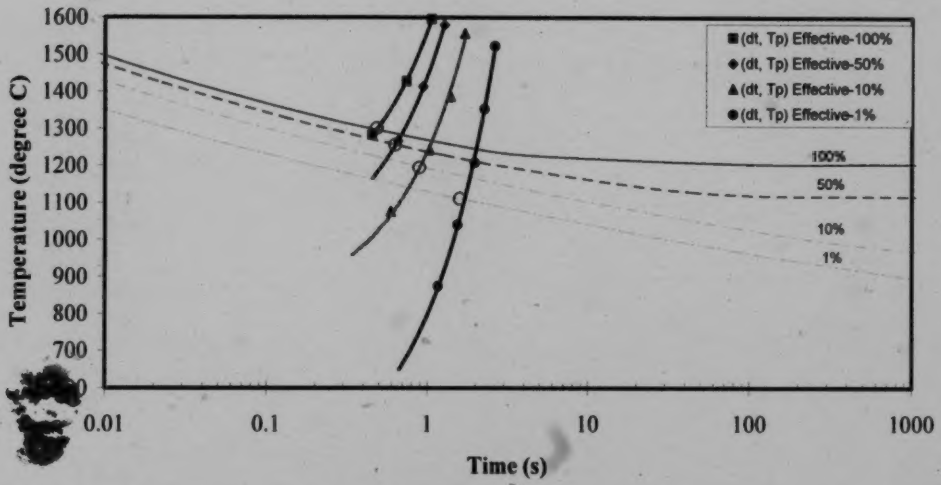

FIG. 5-12. Superposition of the effective temperature-effective time curves on the non-equilibrium solubility curves for heat inputs 0.5 kJ/mm in Grade 100 steel.

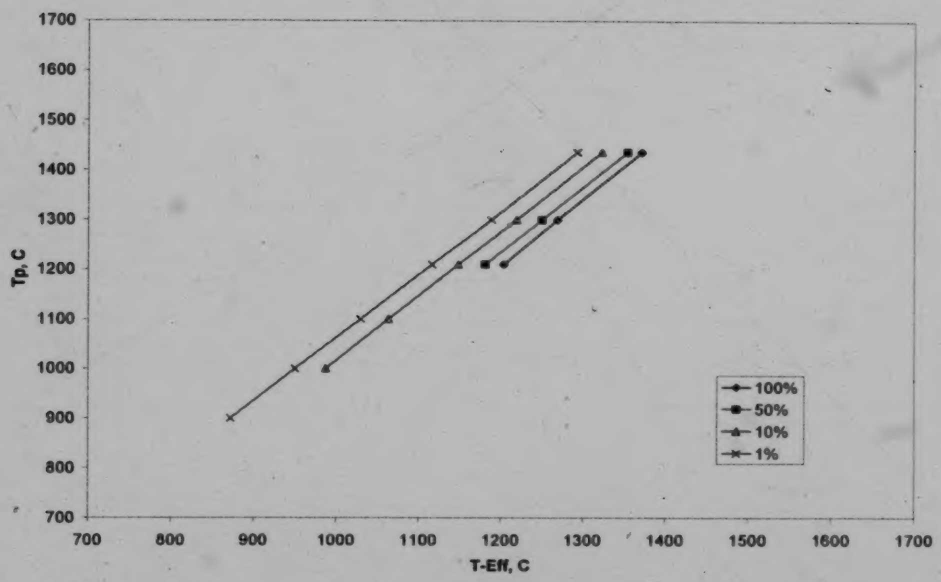

FIG. 5-13. The linear relationship between T_P and $T_{P\text{-}Eff}$.

The findings are summarized in Fig. 5-14, as *precipitate dissolution maps*, where the variation of precipitate dissolution is shown vs. the weld heat input. Also, the boundaries of different HAZ sub-regions obtained from the macrostructures are superimposed on the graphs, to demonstrate how much of a given type of precipitate is dissolved during the weld thermal cycle of a given heat input at a certain position (sub-region) in the HAZ. The graph shows that dissolution of NbC does not occur in the ICHAZ or in most of the FGHAZ. Dissolution of NbC starts close to the boundary between the FGHAZ and CGHAZ and is completed (100% dissolution) somewhere in the CGHAZ, the exact locations depending on the heat input. TiN dissolution starts in the CGHAZ but barely exceeds 10% before the fusion line. Another way to show the results is through *precipitate dissolution profiles*, which show the fraction of precipitate dissolution vs. distance from the fusion line for a given heat input. Fig. 5-15 shows the dissolution profiles across the HAZ for two values of heat input (0.5 and 2.5 kJ/mm). By means of interpolation or extrapolation, the location for dissolution of any fraction of NbC or TiN can be found in the HAZ using these profiles. For instance, a maximum amount of about 9% of the total TiN precipitated in the Grade 100 steel is dissolved in the HAZ, due to a weld thermal cycle with a nominal heat input of 0.5 kJ/mm. Increasing the heat input to 2.5 kJ/mm, will increase the amount of dissolution of the TiN to 15%.

In addition, the maximum solute level in the matrix as a result of the dissolution of precipitates can be calculated. Fig. 5-16 shows this across the HAZ for the two values of heat input in Grade 100 steel. Obviously, the solute level will change during cooling (i.e., reprecipitation), but it can be used for estimation of the maximum austenite composition, which affects the hardenability. In the CGHAZ of the 0.5 kJ/mm weld sample, where martensite is the dominant microstructure, solutes will be supersaturated at room temperature.

5-4-2. Particle coarsening

It seems that the term coarsening has been used with different meanings. It may be considered as precipitation of particles on particles that already exist. It may also result from the growth of large particles at the expense of smaller particles (*Ostwald ripening*) [28]. The latter meaning is more widely accepted, as it occurs with the average precipitate size increasing with increasing time, while maintaining an almost constant volume fraction. The driving force for precipitate coarsening is the reduction of the interfacial area [29].

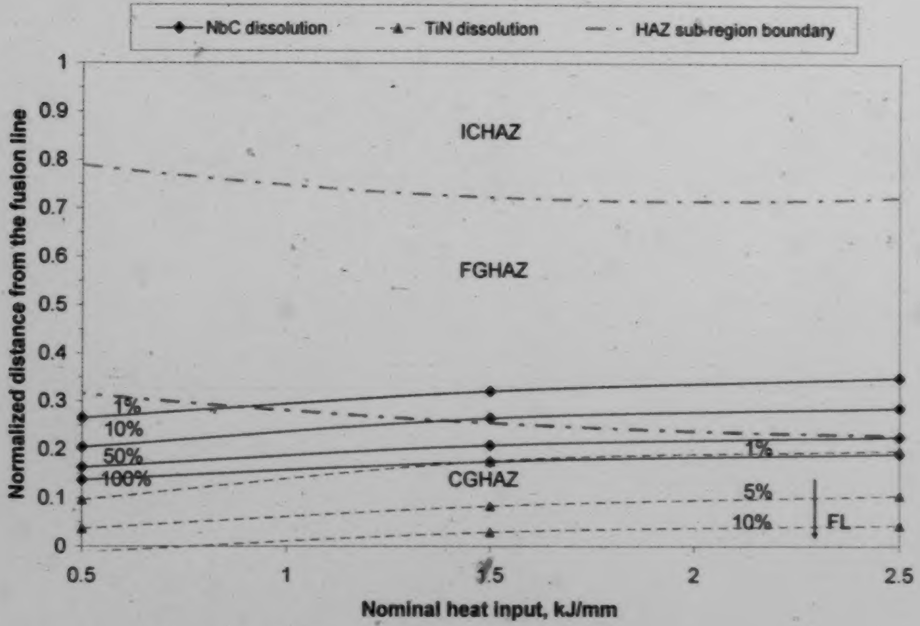

FIG. 5-14. Precipitate dissolution maps for Grade 100 steel shown in two forms.

Coarsening can be quantitatively examined by comparing the precipitate size distribution of a certain particle before and after the weld thermal cycle, in terms of average particle sizes. Equation 5-27 shows a relationship based on the Lifshitz-Wagner theory for Ostwald ripening, that approximates the change in the particle size, given the thermal cycle variation, *T(t)*, and the activation energy for diffusion of metal atoms between particles, Q_v.[11].

$$r^3 - r_0^3 = \int_0^\infty \frac{A_C}{T(t)} \exp - \left(\frac{Q_V}{RT(t)}\right) dt = I \tag{5-27}$$

r and r_0 are the new and original particle radii, respectively and A_C is a constant depending on the matrix composition. It should be pointed out that this approach is only an approximation and neglects, for example, changes in solid solubility with temperature variation. To estimate A_C, the amount of coarsening of a precipitates for a known thermal cycle should be measured. Knowing A_C, the amount of coarsening for any thermal cycle can be estimated. Unfortunately, there are no measured values for the coarsening of precipitates in Grade 100 to provide values of r^* and $T^*(t)$ (* designates a known pair of variables that can be used to determine the constant A_C in the equation), but with some approximations the experimental values of Easterling [11] for coarsening of very small TiN particles can be used. The values used by Easterling were $2r_0 = 8.2$ nm, $2r^* = 14.1$ nm, $\Delta t^* = 40$ s, $T_P{}^* = 1291°C$ and $Q_V/RT_m = 14.5$. The thermal cycle $T^*(t)$ can be established from Equations 3-8 or 3-13. Solving Equation 5-27 for A_C will yield values of 7.20×10^{-16} and 2.00×10^{-15} °K.s^{-1}.m^3, for thick- and thin-plate conditions.

Table 5-7 shows the amount of coarsening for various sizes of TiN particles after applying the values of A_C to a thermal cycle at a location close to the fusion line ($T_P = 1435°C$) and a high heat input ($\Delta t = 43.2$ s), where the coarsening of TiN particles is expected to be the most pronounced. As can be seen, coarsening is considerable only when the initial particle size is small. For TiN particles in Grade 100 steel, namely intermediate-size precipitates (~200 nm on average) and large precipitates (~4 μm on average), coarsening can be neglected. The reason that coarsening of larger particles does not occur over the typical weld thermal cycles, is that diffusion distance between particles is too large.

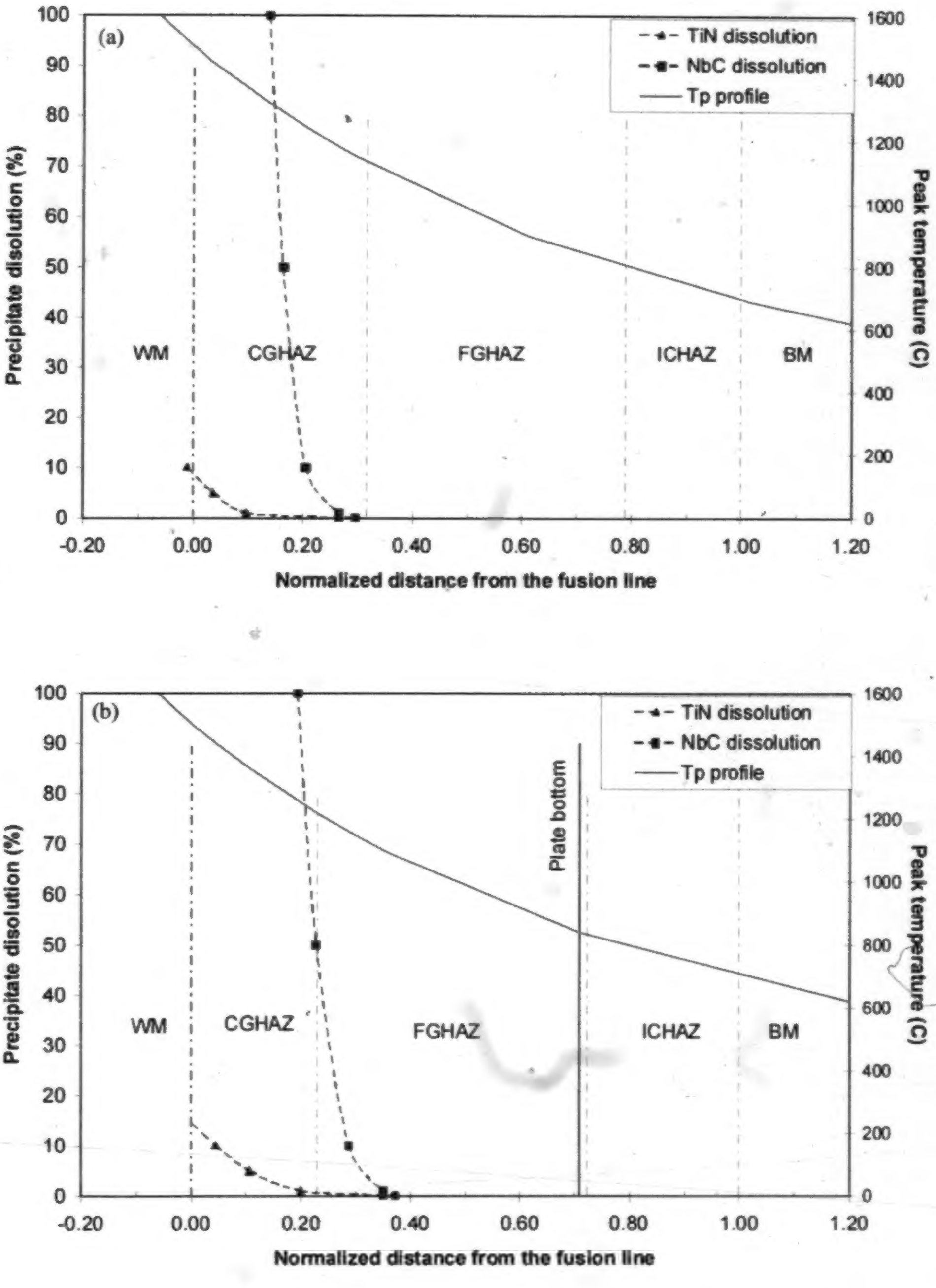

FIG. 5-15. Precipitate dissolution profiles across the HAZ in Grade 100 steel for heat inputs of: a) 0.5 kJ/mm; b) 2.5 kJ/mm.

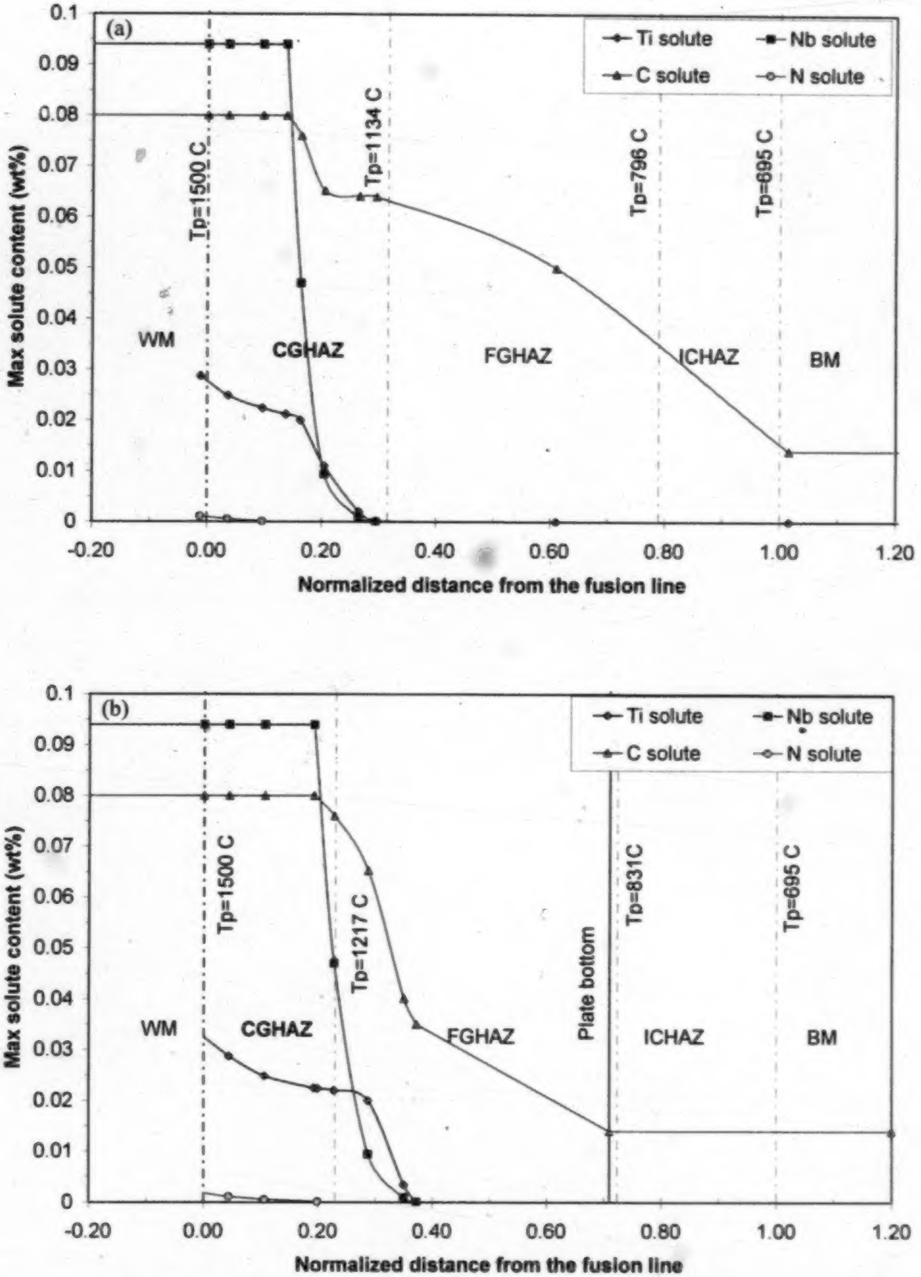

FIG. 5-16. Maximum solute level in the matrix across the HAZ of Grade 100 steel for heat inputs of: a) 0.5 kJ/mm; b) 2.5 kJ/mm.

Table 5-7. Estimation of coarsening of TiN particles based on the initial particle size

r_0, nm		4	40	100	2000
r, nm	Thick plate	7.4	40.1	100.0	2000
	Thin plate	10.1	40.2	100.0	2000
$(r-r_0)/r_0$	Thick plate	8.59E-01	1.81E-03	1.16E-04	1.45E-08
	Thin plate	1.52E+00	4.99E-03	3.21E-04	4.01E-08

At higher heat inputs coarsening may occur, especially for particles with higher solubilities than TiN. Coarsening of Ti(C,N) has been observed at a heat input of 20 kJ/mm, which was attributed to reprecipitation of Ti and C that had gone into solution during the heating leg of the thermal cycle [4]. The fine NbC precipitates (<20 nm), may have a chance of coarsening at locations where dissolution does not occur, i.e., the FGHAZ, ICHAZ and SCHAZ. Determination of the likelihood of coarsening, however, requires a knowledge of the constant A_C, or a set of experimental values of coarsening to determine A_C.

5-4-3. Particle reprecipitation

As the weld sample cools down below the equilibrium dissolution temperature of a precipitate during the cooling leg of a weld thermal cycle, the solubility limit for the microalloying elements, enriching the matrix due to dissolution during heating and part of the cooling cycle, drops. The result is a tendency for reprecipitation, provided that the cooling rate is low enough to allow diffusion of microalloying atoms. In most cases, however, cooling rates during welding are too high, leaving the matrix relatively supersaturated with microalloying elements.

There seems to be no kinetic analysis on reprecipitation of the particles during welding in the literature and the cooling rates are too high to make thermodynamic calculations useful. However, some of the results of isothermal precipitation experiments can give insight. It was reported that the precipitation of Nb-rich carbonitrides at 900°C, even after 67% reduction (which is a very high amount of deformation), can take up to a minute. With smaller amounts of deformation, practiced in commercial rolling passes, the precipitation time could take several minutes or even several tens of minutes [9]. Remembering that in a weld thermal cycle holding at temperatures suitable for precipitation does not happen and there is no deformation to accelerate precipitation, it seems reasonable to accept that reprecipitation can be largely suppressed. If it happens, therefore, it should be restricted to reprecipitation in the form of small-sized particles with short inter-particle spacing in the matrix or accumulation on the grain/sub-grain boundaries. This will result in some solid solution supersaturation in the HAZ, which not only increases the hardenability, but also increases the matrix strength.

Cementite precipitation may happen, however, as carbon supersaturation occurs, and the mobility of microalloying substitutional solutes becomes extremely low at sub-critical temperatures. This is another kinetic effect, which could not be predicted based on thermodynamic calculations, as the solubility of cementite is much higher than that of the microalloy carbides (Fig. 5-17).

5-5. Precipitate quantification

To have a systematic and scientific analysis of precipitate alteration, quantitative analysis is required. As Kelly [30] states, "It is only by expressing results in numerical form that will change electron microscopy from an art into a science." However, quantitative experimental analysis of the precipitates is not trivial, especially with replicas. The objective of this section is to demonstrate the difficulties in the quantification of the precipitates by carbon extraction replicas. Some theoretical discussions are also presented.

5-5-1. Quantification problems

Ashby and Ebeling in 1966 [1] stated that the extraction replica method is not suitable for determination of particle volume fraction, because the number of precipitates captured by the replicas vary from replica to replica and the apparent number may not be the actual number. They indicated that volume fraction estimates could be in error by a factor of two or more because of this fact, and concluded that electron microscopy is not a good method for measuring volume fraction, and indirect methods (such as electrical resistance, chemical analysis, density, or magnetic methods) should be used. This, however, did not stop researchers from using replicas for volume fraction estimations of precipitates (e.g., [31]).

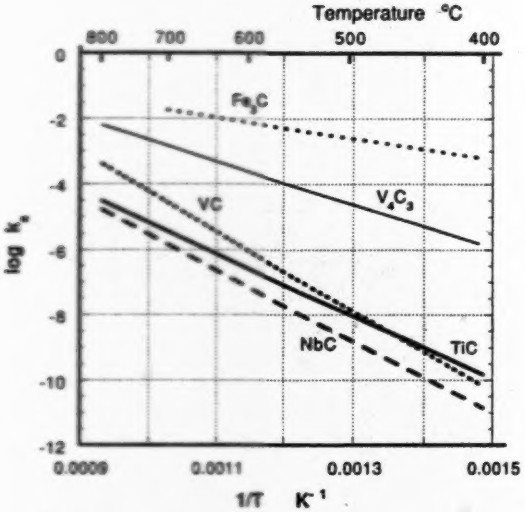

FIG. 5-17. The solubility of cementite (Fe_3C) in ferrite compared with the solubilities of microalloy carbides [9].

Dissatisfaction with the values of precipitate volume fraction in Grade 100 microalloyed steel determined by replicas has been reported by Heglund *et al.* [32]. Table 5-8 summarizes these results for various size ranges/types of precipitate. The weight percent of the metal consumed was also calculated according to the Equations 5-15 and 5-18, in reverse.

Table 5-8- Volume fraction of different types of precipitates in Grade 100 steel, after Heglund *et al.* [32]

Particle type	Size range, nm	Composition assumption	Area fraction	Volume fraction	Wt% of M consumed
I	>1000	TiN	7.92E-04	2.23E-05	1.187E-03 Ti
II	100-300	TiNbCN	1.70E-03	1.13E-03	0.531E-03 Nb 0.274E-03 Ti
III	25-100	TiNbCN	1.06E-04	7.06E-05	3.317E-03 Nb 1.712E-03 Ti
IV	5-20	NbC	8.25E-04	5.50E-04	0.484 Nb
V	<5	NbC	1.26E-02	8.41E-03	0.740 Nb

For the calculation in Table 5-8, the type of precipitates in each size range was simplified. For the complex precipitates of TiNbCN, it was assumed that there were equal fractions of each element (as if they are half TiCN and half NbCN). With this simple assumption, the densities of TiCN, NbCN and TiNbCN were calculated based on the rule of mixtures, and found to be 5.195, 8.135, and 6.665 g cm^{-3}, respectively. The density of binary carbides or nitrides of Ti and Nb were found in the literature [9]. A density of 7.9 g cm^{-3} was assumed for the iron matrix.

The problem is that the volume fraction for the very fine particles (<5 nm) was overestimated. The amount of Nb consumed (total of 1.228%), based on the volume fractions determined from replicas, was much higher than that available in Grade 100 steel (0.094% Nb). Such a problem does not occur for Ti, where the total amount consumed in precipitate formation was estimated to be 0.003%, while there is 0.060% Ti in the alloy. Note, that the fine precipitates were assumed to be pure NbC, which can lead to overestimation of the amount of NbC and the amount of Nb consumed. It is known that they contain comparable amounts of Mo and considerable amounts of Ti and V. This, however, can only account for a fraction of the overestimation. The main factors that caused such an overestimation were likely incorrect estimation of the sampling depth (depth of matrix dissolved during replication) and not having enough resolution to estimate true sizes (TEM could not resolve the precipitate shape and size below 3–4 nm even at the highest magnifications [33], while it appears that Heglund *et al.* used a low magnification of x50,000). Wagner *et al.* [33] believe that the main source for error in determination of the volume fraction arises from the size measurement of each particle (± 5 to 10%), and errors involved with the instrumental magnification (± 10%). This can result in an uncertainty in f_V values of up to 50%, as the first error enters the calculations with a factor of three, and the second error with a factor of two. Another reason could be overpopulation of fine precipitates in a small, non-representative region (e.g., centreline of the plate). Instances of dissatisfaction and disagreement among the many different methods for precipitate quantification were reported in many other papers as well [2, 33-39]. As Wagner *et al.* [33] stated, the uncertainty for determination of volume fraction is an "inherent characteristic" of all methods.

5-5-2. Analytical methods other than TEM replicas

Many other methods have been used for volume fraction estimation and some methods have shown more reliability than others. Kallqvist and Andren [40] used backscattered SEM for quantitative examination of coarse microalloy precipitates (1–10 μm), and energy filtered TEM (EFTEM using thin foils) for fine microalloy precipitates (~30 nm). EFTEM was also used by Hattestrand and Andern [41] for measuring the volume fraction of VC. The basis of EFTEM, also known as electron spectroscopic imaging (ESI), is spatially resolved electron energy loss spectroscopy (EELS) [37]. Hattestrand and Andern [42] had to apply EFTEM, as it was not possible to distinguish between different types of precipitates present in a chromium steel using a conventional TEM. There were different precipitates with overlapping sizes and similar shapes. EFTEM visualizes chemically different phases separately, by forming so-called "jump-ratio images" of the major metal elements. Hofer *et al.* [43] were able to detect some VN particles by EFTEM that were not detected by conventional TEM, as this technique provided a higher resolution (~2 nm). Because of these advantages, fewer particles in each population need measuring for EFTEM than for TEM, for statistical reliability.

Haasen [44] has studied precipitate alteration for a number of selected alloy systems by atom probe field ion microscopy (APFIM). He states that the best method of resolving small precipitates is field ion microscopy (FIM), for size and morphology analysis, combined with an atom probe (AP) for analytical analysis. The size of precipitates along an <hkl> direction is determined by counting the number of (hkl) planes that have to be evaporated between the appearance and disappearance of the particle. The chemical analysis of the precipitate is conducted by measuring the time-of-flight of the emitted ion, and then evaluating its mass-to-charge ratio.

Degischer *et al.* [34] used small angle neutron scattering (SANS) combined with APFIM to determine the various quantitative parameters, including volume fraction, of γ' (Ni_3Al), carbides and carbonitrides in a Nimonic Alloy (Ni-base superalloy). The ratio of magnetic to nuclear scattering intensity from non-magnetic precipitates in a ferromagnetic matrix provides information about the composition of the precipitates. Knowing the magnetic scattering length of the matrix, the volume fraction of precipitates can be obtained from the magnetic cross-section [37]. In comparison with TEM, SANS can provide quantitative information averaged over bulk samples (~1 cm^3), such as the average size and shape of particles (or other defects), their volume fraction and their size distribution function. The drawback is the limitation for studying complex materials where different kinds of microstructural defects can be present simultaneously. In that case, it is difficult to separate the contribution of each defect in the SANS spectrum. Nevertheless, SANS is considered an attractive technique for physical metallurgy studies of complex steels, provided that some complementary microscopic information (e.g., from TEM) is available [45]. Deschamps *et al.* [46] used small angle x-ray scattering (SAXS) for evaluation of size and volume fraction of copper precipitates, in an interstitial-free HSLA steel with a relatively low level of copper (0.8 wt%). Preuss *et al.* [47] used high-resolution synchrotron x-ray diffraction profile measurements to obtain the volume fraction of γ' (Ni_3Al) across the welded region in a nickel-base superalloy.

One method that has recently been used by many investigators for volume fraction quantification is chemical dissolution and filtration. For instance, Jun *et al.* [13] extracted precipitates by electrochemically dissolving the matrix of a low carbon microalloyed steel with a tetramethyl ammonium chloride solution, and then filtered them with a polycarbonate membrane filter. The filtered precipitates were dissolved in a buffer solution and mixed with 10% HCl to perform ICP analysis. Alternatively, quantification of the precipitates in the dissolved matrix could be performed by centrifuging the solution, drying and weighing the particles [34].

The uncertainties in the absolute values of the volume fraction (or other quantitative parameters) of precipitates lead to expression of the parameters in relative forms, e.g., the ratio of the volume fractions in the condition/location of interest to the corresponding value in the as-received BM, for the same type or size range of the precipitates [48]. This is, however, only valid when the precipitate distributions in the original or as-received state are measured over a representatively large area. Variation in precipitate distribution over different areas/sections can produce unacceptable errors. Also note, the problems associated with measurement of volume fraction do not extend as much to precipitate size distribution analyses [2].

5-5-3. Modification of the existing theories §

From the discussion above, it seems that the problems associated with determining volume fraction can depend on the precipitate size or size distribution. The problem with precipitates of one size range can be different from the problem of those with several size ranges, such as those in Grade 100 steel. In both cases, however, underestimation of the sampling depth of the iron matrix appears to be the major problem.

5-5-3-1. Matrix with one type/ size-range of particles

Ashby and Ebeling [1] used a factor of $\overline{x}$ (average particle diameter) in conversion of "number per unit area", N_S, to "number per unit volume", N_V, i.e.:

$$N_V = N_S / \overline{x} \tag{5-28}$$

The volume fraction, f_V, was approximated as:

$$f_V = \frac{\pi}{6} N_V \overline{x}^3 \tag{5-29}$$

It seems that, at least as a lower bound, a factor of $2\overline{x}$ could be used in Equation 5-28, since the particles that can be attached to the replica come from a depth of matrix measuring $2\overline{x}$, as shown schematically in Fig. 5-18. This would result in a calculated value for volume fraction which is half of that estimated by Equation 5-29.

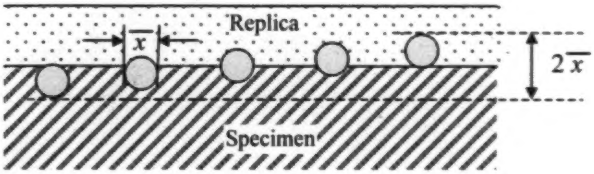

FIG. 5-18. Schematic suggesting a correction factor of ½ in calculation of N_V (modified from the work of Ashby and Ebeling [1]).

This approach can also be applied to the large particles in Grade 100 microalloyed steel. The large TiN cuboidal particles (2–8 μm) can be observed by OM. The particles stand out of the polished and etched matrix, as they are harder than the matrix and inert to the etching. Fig. 5-19a schematically shows the depth they correspond to. An average size is again assumed.

$$d_M = a \, . \, \overline{x} \tag{5-30}$$

---

§ A version of this section has been published. K. Poorhaydari, B.M. Patchett and D.G. Ivey, 2005. Proc., Conference of Metallurgists 2005 – the international symposium on pipelines for the 21st century, pp. 231-247.

a is the depth factor (in reality $1<a<2$) and d_M is the sampling depth to be measured. There are two extreme cases, i.e., $a=1$ and $a=2$, which provide upper bound and lower bound conditions, respectively, for calculation of the volume fraction.

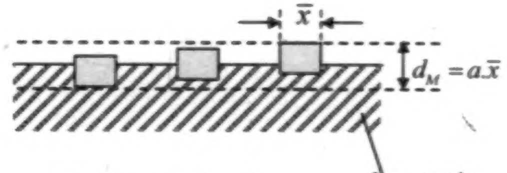

a) Real situation: 1<a<2

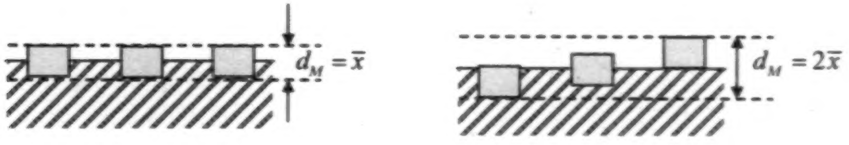

b) Upper-bound situation: a=1

c) Lower-bound situation: a=2

FIG. 5-19. Schematic demonstration of the sampling depth in replica preparation in case of a matrix with one type/size-range of particles.

Area fraction, f_A, and volume fraction, f_V, for cubic particles can be calculated as follows:

$$f_A = \frac{\Sigma x_i^2}{S} \approx \frac{n.\bar{x}^2}{S} \tag{5-31}$$

$$f_V = \frac{\Sigma x_i^3}{S.a.x} \approx \frac{n.\bar{x}^2}{a.S} = \frac{f_A}{a} \tag{5-32}$$

where x_i is the individual particle size, $\bar{x}$ is the average size, S is the area of the sample over which the particles are counted, n is the total number of particles counted and a is the depth factor described above. Note that the conversion equation for f_A to f_V for spherical precipitates will have an inherent factor of 2/3 (arising from the conversion of area of a circle to the volume of a sphere [30]) in addition to a introduced here, i.e.:

$$f_V = \frac{2f_A}{3a} \tag{5-33}$$

5-5-3-2. Matrix with more than one type/size-range of particles

In a matrix with several types/size ranges of particles (as in most HSMA steels), it seems that replicas do not detach from the sample until the largest group of precipitates captured by them is free from the matrix (Fig. 5-20). Since some of the largest precipitates may already be exposed on the surface (after light etching), the depth of the matrix needed to be dissolved away, d_M, can be formulated as:

$$d_M = \eta \, . \, d_P \tag{5-34}$$

d_P is the particle size of the largest precipitates captured by the replica and η is the depth fraction of these particles still in the matrix. For simplicity, this factor can be assumed to be 1 as a first approximation. According to this approach, the volume fraction of each group of precipitates can be corrected by a factor of $\bar{x}_i / d_M$, where $\bar{x}_i$ is the average size of particles in the i^{th} group. This gives a volume fraction of spherical particles and cuboidal particles according to Equations 5-35 and 5-36, respectively.

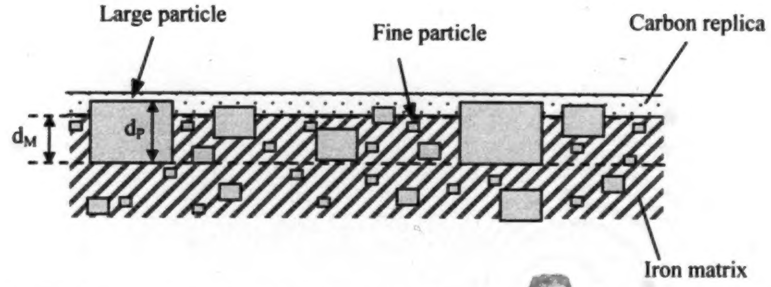

FIG. 5-20. Schematic demonstration of the sampling depth in replica preparation for the case of a matrix with several types/size-ranges of particles.

$$f_V = \frac{\pi}{6} N_V \frac{\overline{x}_i^4}{d_M} \tag{5-35}$$

$$f_V = N_V \frac{\overline{x}_i^4}{d_M} \tag{5-36}$$

Note that N_V should still be calculated according to Equation 5-28. This correction will be very large for very small particles, when for instance $\overline{x} = 4$ nm and $d_M = 400$ nm. The assumption is that all the precipitates, released during dissolution of the surface, stick to the replica by Van der Waals forces. Since all fine precipitates are not likely captured by the replica, this approach can calculate a lower bound.

It should be noted that the general idea behind this model is not new and can be found in earlier works [2, 49, 50]. The application to a matrix with several size-groups of precipitates and the explanations can be considered as supplementary. Note that Equation 5-35 still differs from a similar equation proposed by McCall and Boyd [49] by a factor of two. Also, it can be added that the estimation of the sampling depth, d_M, based on the size of the largest particle on the replica may still be an underestimation. There are particles in HSMA steels that are a few microns in size (e.g., large TiN particles in Grade 100 steel). Particles larger than 1 μm are not usually captured on the replicas, as they are too large to be supported by replicas [51]. Nevertheless, they can still anchor the replicas during the final etching process. The replicas finally float off leaving a large hole in them (outline of the large particle) or get torn from the location of some of these large particles.

5-6. Experimental procedure

Metallographic samples were prepared according to the procedure explained in Section 3-5. A conventional carbon extraction replica method was used to make TEM samples from four distinct regions, namely the BM, ICHAZ, FGHAZ and CGHAZ. Fig. 5-21 shows schematically the procedure for making carbon extraction replicas. The metallographically prepared and polished surface was etched with 2% Nital. This solution makes some precipitates protrude from the surface. The sample is then coated with carbon, and then placed in 5% Nital until the replica is separated from the substrate and floats away. The replica is then picked up with a carbon grid, which also acts as a support for the replica in the TEM. Extraction carbon replicas make very good TEM samples for examination of precipitate type, morphology, and size distribution, without having to deal with the iron matrix. The iron matrix in thin-foil TEM samples diffract most of the electrons and make it difficult to clearly view the precipitates, in either bright-field (BF) or dark-field (DF) modes, and to analyze their chemical composition by energy dispersive x-ray (EDX) spectroscopy. It is worth mentioning that although carbon replicas are most widely used for extraction of precipitates, aluminium replicas have also been used for this purpose [12].

Relatively site-specific carbon replicas were prepared by masking off regions of interest on the metallographically prepared samples from the longitudinal weld sections, wherever possible. Longitudinal sections provide larger parallel-sided sub-regions, which are easier for replica formation compared with transverse sections. The sample from the ICHAZ of the 2.5 kJ/mm weld section was prepared from the transverse section, as this sub-region does not appear on the longitudinal section. All samples were examined in a JEOL 2010 TEM operated at 200 kV and equipped with an ultra thin window EDX system.

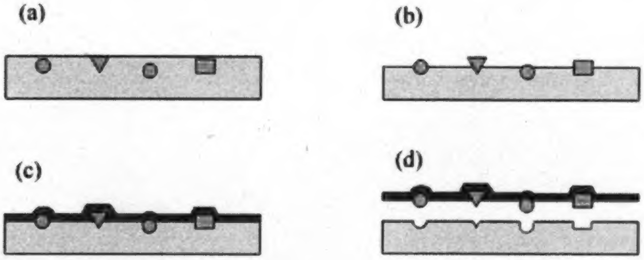

FIG. 5-21. Schematic of carbon extraction replica procedure: a) polished surface; b) etched surface; c) carbon coated surface; d) extracted replica with precipitates.

5-7. Results and discussion

5-7-1. Qualitative analysis of precipitates in different sub-zones

Results of TEM precipitate analysis in the different sub-regions of the HAZ, namely the ICHAZ, FGHAZ and CGHAZ, are reported below. The effects of variation in the heat input are also provided and discussed for each sub-region. Some of the analysis on the BM is also presented here, as a baseline for comparison of the alterations in the HAZ. Different types of precipitates in the BM were discussed in Chapter 1. Large TiN precipitates (type 1; Section 12-3-3-1) were not studied here as they do not contribute to the strength or austenite grain-growth control due to their size, and do not change much during the typical weld thermal cycles in the HAZ due to their stability. These are cuboidal TiN particles, 2-8 μm in size, sometimes attached to inclusions (Fig. 5-22). They are the only particles in Grade 100 that are visible in an optical microscope. They occupy an area fraction of 7.92×10^{-4} and a volume fraction of 2.23×10^{-5} in Grade 100 steel, as estimated by Heglund *et al.* [32]. The estimated total volume fraction of TiN from the precipitate analysis of Section 5-3-2 was 7.07×10^{-4} (Table 5-4). It seems that the measured value is an underestimation, likely due to examination of a region with a non-representative distribution. The BM is very inhomogeneous with respect to TiN distribution, as it forms during solidification and reheating. For the same reason, many TiN precipitates may form near the centreline and therefore the rest of the plate can be low in TiN.

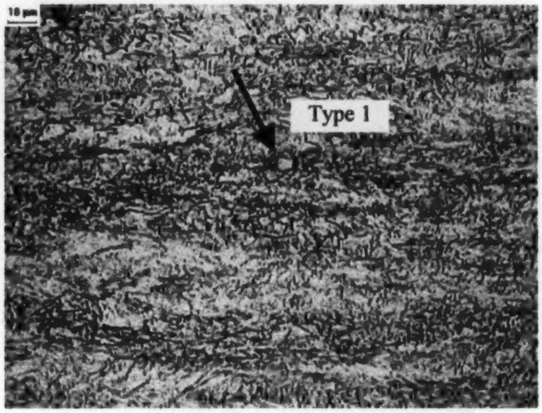

FIG. 5-22. Optical image from the BM showing a large TiN particle (~8 μm).

5-7-1-1. BM

Fig. 5-23 shows a mosaic of relatively low-magnification micrographs obtained from the BM of the Grade 100 steel. A relatively uniform distribution of precipitates of different sizes is apparent. The precipitates are better resolved at higher magnifications. The area indicated in Fig. 5-23 is magnified in Fig. 5-24a. Two types of intermediate-size precipitates, types 2 and 3 (Section 2-3-3-1), are visible. One of the Ti-rich particles in Fig. 5-24a (indicated by the arrow) is further magnified in the accompanying inset. The particle actually consists of multiple particles, i.e., several Nb-Ti carbonitrides (denoted by the arrows) growing epitaxially on the cuboidal Ti-rich particle. The epitaxial growth is favourable as the decrease in interfacial free energy between the Nb-rich "cap" and TiN "core" is much larger than the increase in strain energy from the small lattice misfit (~2%) [14]. EDX spectra (Fig. 5-24b and c) show roughly the composition of each (there are always signals from the areas around the target point). Most of the C detected is likely from the C support film. The Cu peaks are from the copper grid, which supports the carbon film.

Although the elemental analysis here (EDX) could not show the composition of intermediate-size and fine precipitates with respect to C and N, the analysis of Section 5-3-1 showed that these particles are carbides rather than nitrides, as most of the N would be tied up with Ti at the higher processing temperatures (precipitate type 1).

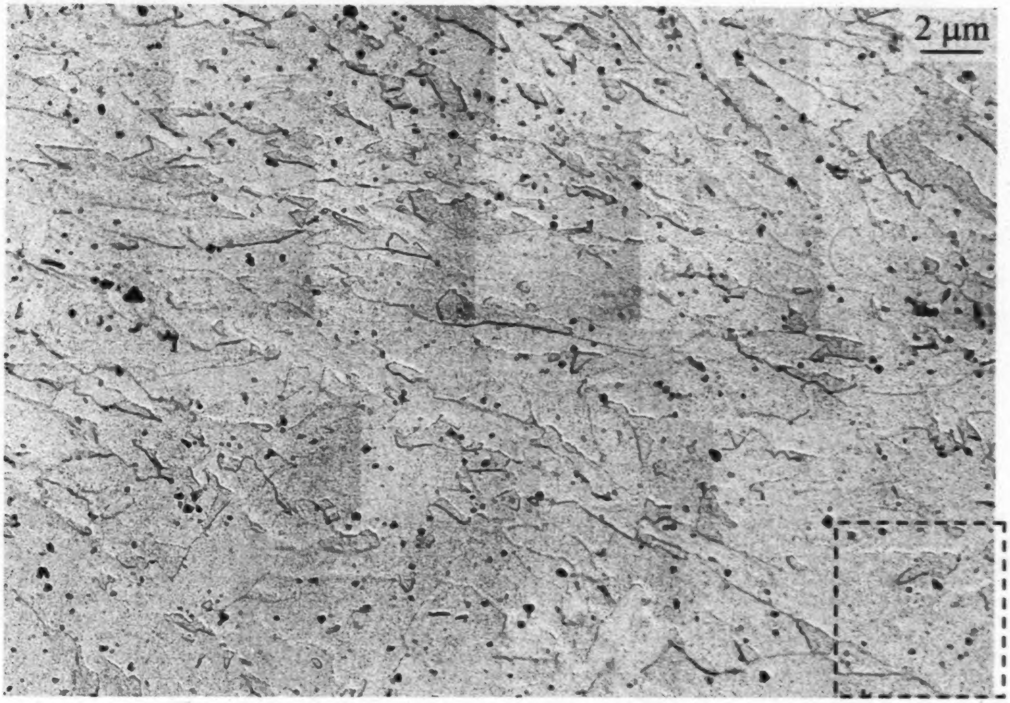

FIG. 5-23. Mosaic of TEM micrographs at low magnification from the BM of the Grade 100 steel.

Fine precipitates, primarily Nb-rich carbides and responsible for most of the precipitation hardening in these steels, were uniformly distributed throughout the steel (Fig. 5-24d). Two size ranges were distinguishable; type 4, 10-20 nm size range, and type 5, less than 5 nm in size. Type 4 is likely strain-induced precipitates that form in austenite and type 5 are general precipitates that form in ferrite. These particles are too small to generate a good EDX spectrum from an individual particle. However, EDX spectra from the fine precipitates extracted by chemical dissolution of the matrix showed that they were essentially Nb-Mo carbides with some Ti and V. Fig. 5-25a shows these particles placed on a carbon replica after extraction by Lu *et al.* [24].. The EDX spectrum from the region indicated in Fig. 5-25a is shown in Fig. 5-25b. The microalloying elements and iron come from the carbide precipitates, Si comes from SiO_2 particles likely formed during dissolution of the matrix or after, Ca comes from the water and Cu comes from the copper grid.

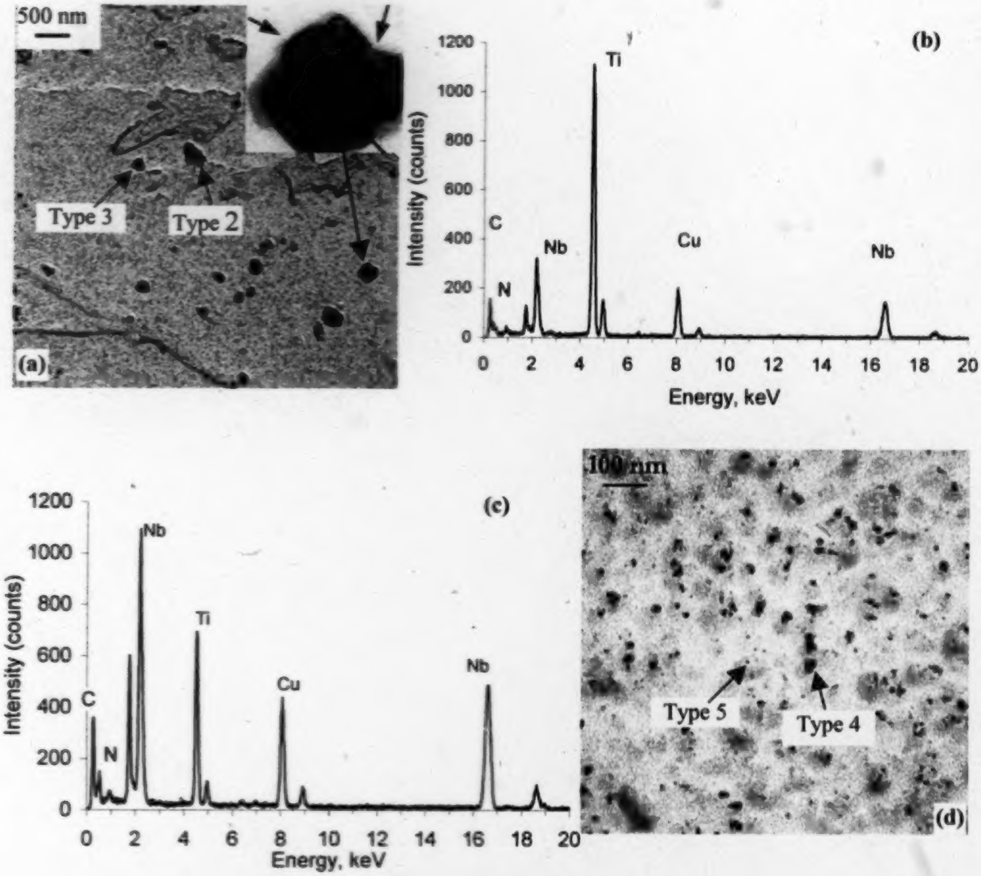

FIG. 5-24. TEM bright-field (BF) images and EDX spectra from the BM of the Grade 100 steel: a) a BF image of the region indicated in Fig. 5-23 showing some intermediate-size precipitates; b) EDX spectrum from the Ti-rich carbonitride in the inset of (a); c) EDX spectrum from one of the Nb-rich carbonitrides in the inset of (a); d) a BF image showing the dispersion of fine precipitates.

An important point is that the amount of intermediate-size precipitates was found to vary greatly from section to section. Fig. 5-26 shows a mosaic of TEM micrographs from another section in the BM. As can be readily seen, the number of intermediate-size particles is much lower than for the section in Fig. 5-23. The other difference is the presence of many Fe-rich particles (Fig. 5-27a and b) relative to Ti-Nb carbides (Fig. 5-27c). SAD analysis (not shown here) showed that the Fe-rich particles are cementite. This makes the amount of Ti-Nb carbides for the section shown in Fig. 5-26 even lower than what would be apparent initially. The precipitate distribution has had a considerable effect on the grain size and shape too. The fine particles were still in abundance in the matrix (Fig. 5-27d).

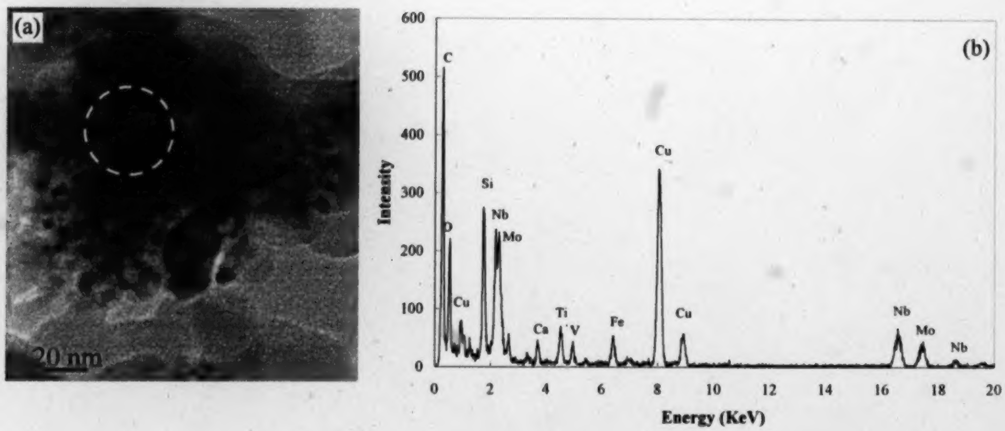

FIG. 5-25. A BF image from fine particles (a), and the corresponding EDX spectrum (b), obtained by chemical dissolution method [24].

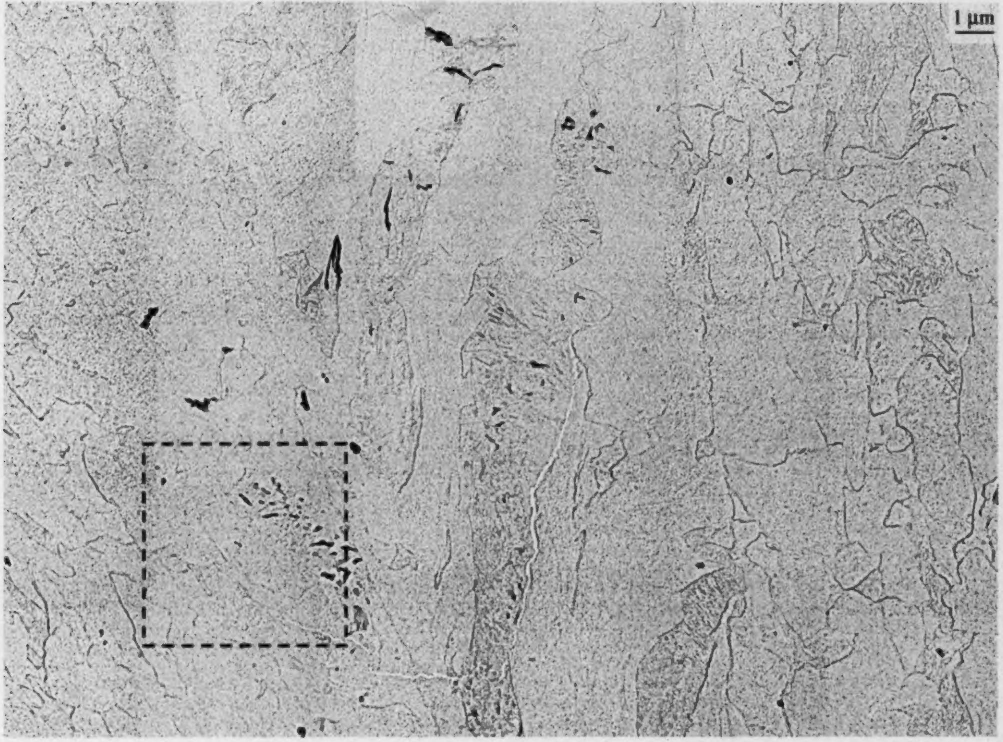

FIG. 5-26. Mosaic of TEM micrographs at low magnification from the BM of the Grade 100 steel.

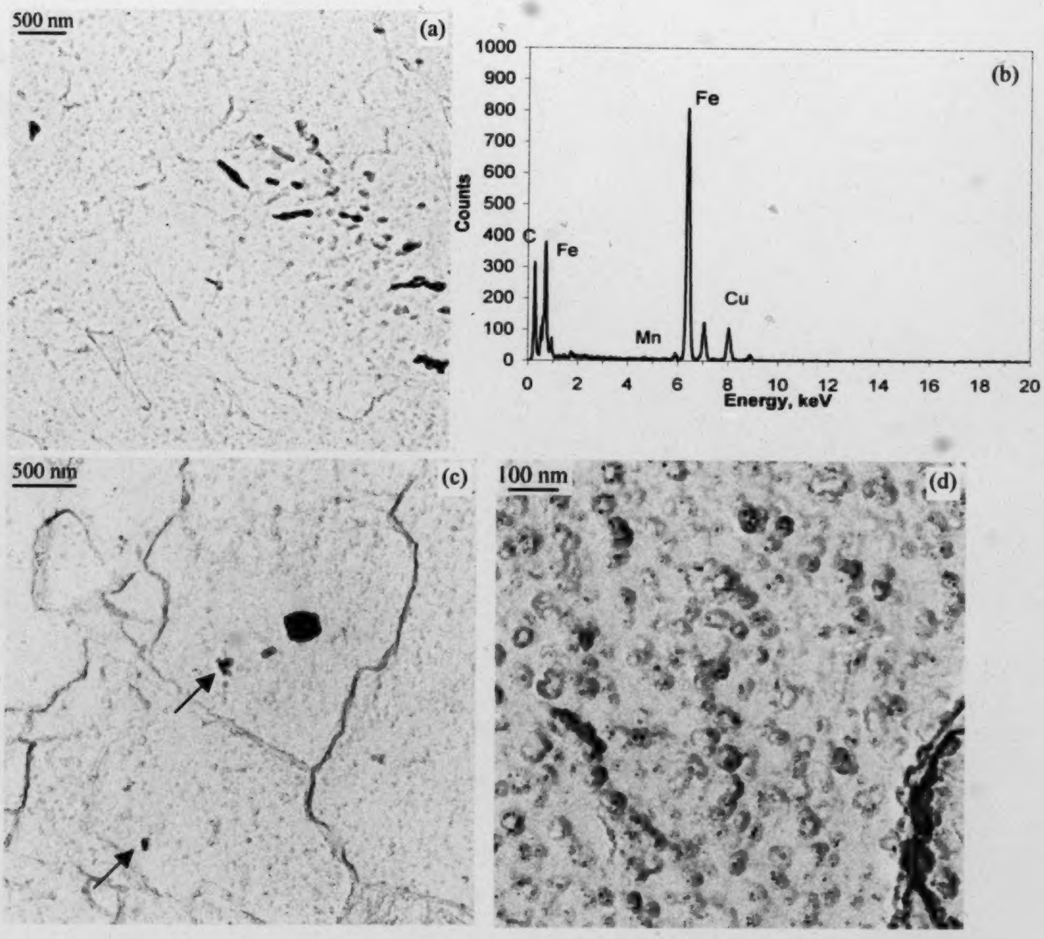

FIG. 5-27. TEM–BF images and EDX spectrum from the BM of the Grade 100 steel: a) a BF image of the region indicated in Fig. 5-27 showing several cementite precipitates; b) EDX spectrum from the sliver-like precipitates in (a); c) BF image showing a Ti-Nb carbonitride and some very small iron carbides (denoted by arrows); d) a BF image showing dispersion of fine precipitates.

Differences in precipitate distribution are probably due to segregation during solidification and lack of homogenization in the subsequent processing stages with respect to the microalloying elements in the plate. The semi-equilibrium hold at the reheating temperature depletes the matrix of excess Nb and Ti, and gives a precipitate distribution according to the level of these microalloying elements in those sections. The amount left in the matrix would not depend much on the initial local amount of solutes and, therefore, the general precipitation that happens later is more or less the same in most regions. Low levels of microalloying elements in the section shown in Fig. 5-26, however, paves the way for formation of cementite upon cooling. A too high volume fraction obtained from the mosaic of Fig. 5-23, which did not match with the mass balance (Section 5-5), supports the possibility that the microstructure examined in that section was not a representative one and locally had a high density of precipitates.

5-7-1-2. ICHAZ

Fig. 5-28 shows mosaics of TEM micrographs from the ICHAZ for different heat input values. The apparent distributions of intermediate-size precipitates are closer to that of the BM section shown in Fig. 5-26. These precipitates are not expected to have changed in this sub-region. The kinetic analysis of Section 5-4-1 showed that a combination of a relatively low peak temperature and a fast thermal cycle does not cause any dissolution of Nb carbides (applicable to intermediate-size Nb-rich carbides). Again, it should be emphasized that quantitative comparison of these particles may lead to erroneous conclusions, as they vary drastically from section to section, in particular at regions with peak temperatures lower than NbC dissolution temperature, i.e., the FGHAZ, ICHAZ and BM.

ICHAZ–0.5 kJ/mm

The replicas for the heat input of 0.5 kJ/mm still show many precipitate sites at higher magnifications. Fig. 5-29a and b show some of the intermediate-size Ti-rich and Nb-rich precipitates. Some are on the grain boundaries and some are within the grains. A group of two intermediate-size precipitates attached together is shown at a higher magnification in Fig. 5-29c with the corresponding EDX spectrum in Fig. 5-29d. The high Ti peak comes from the Ti-rich particle and the high Nb peak comes from the Nb-rich particle. There were also some regions of irregular particles close to the grain or sub-grain boundaries, as shown in Fig. 5-29e, where the compositions are labeled for several particles. Some are rich in Nb with different amounts of Ti, V and Mo. Fig. 5-29f shows an example of an EDX spectrum from a very small particle (~20 nm) circled in Fig. 5-29e. Some other particles are rich in Fe. The Fe peak likely arises from iron carbides, in particular cementite. Cementite could have been originally in the microstructure, as it has been detected in the BM.

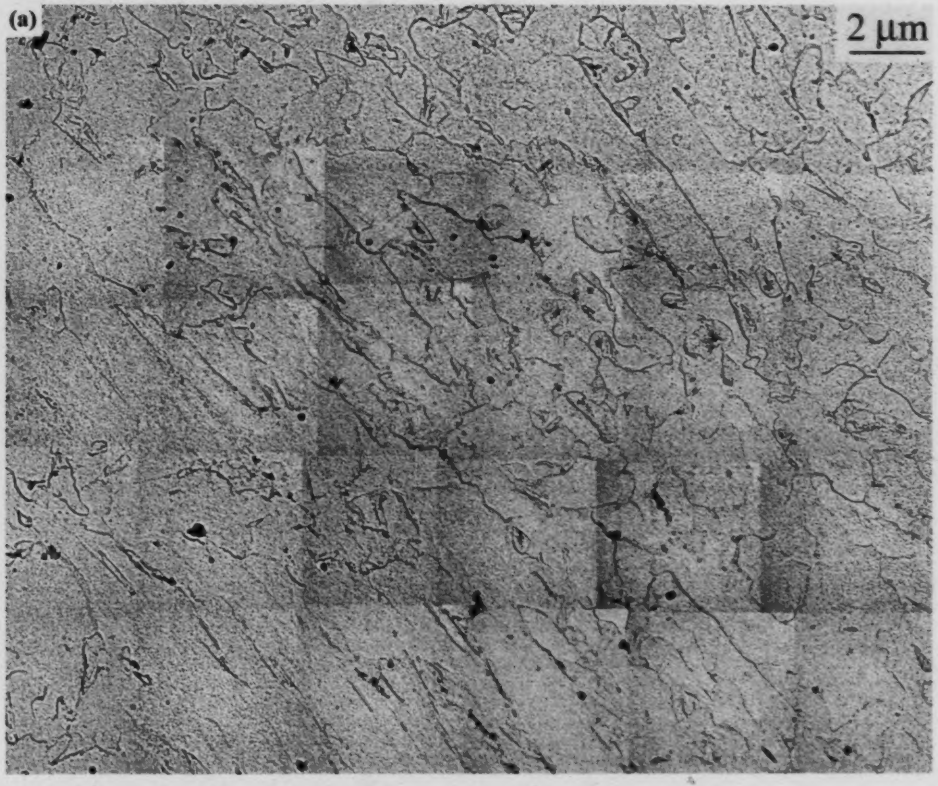

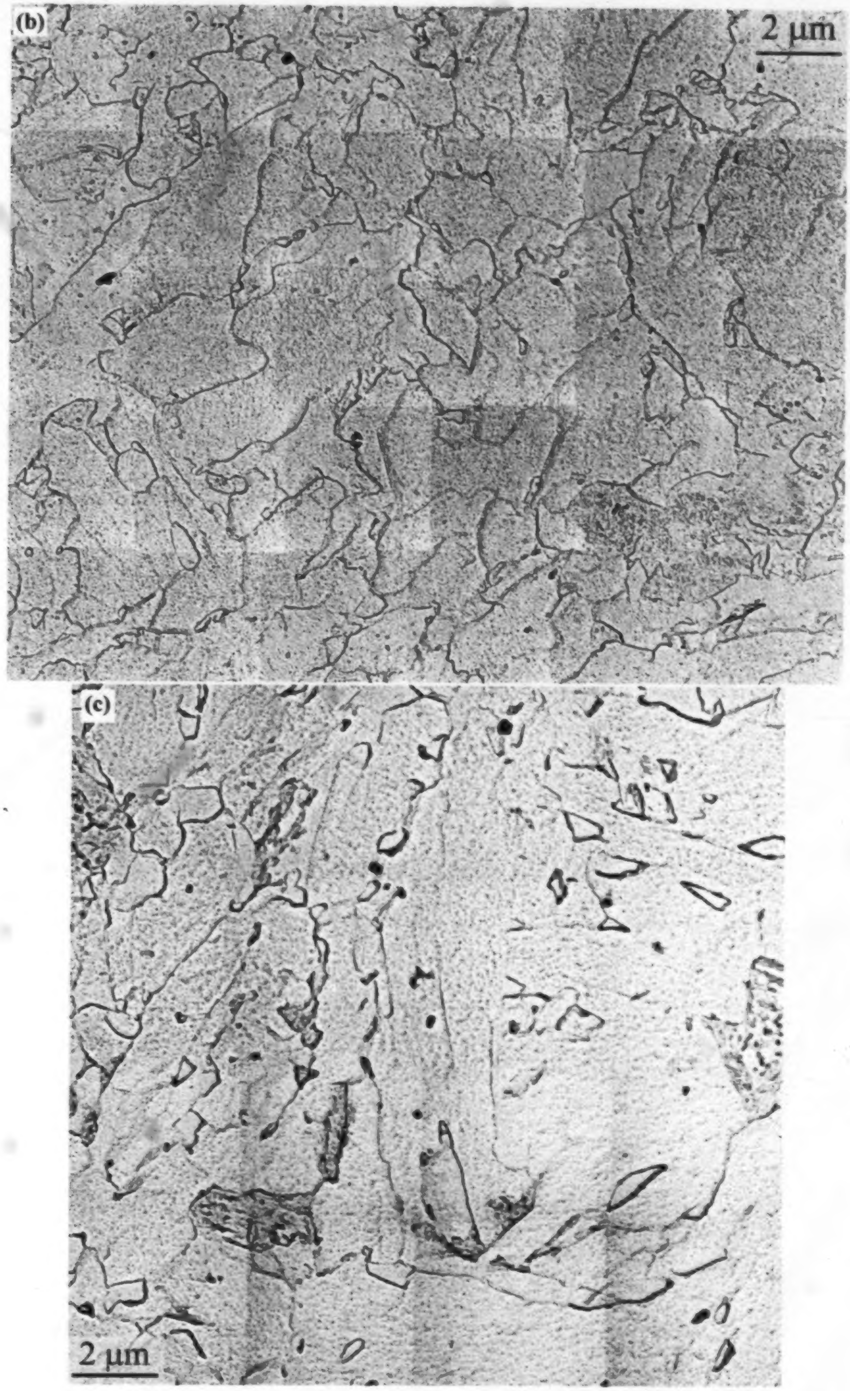

FIG. 5-28. Mosaics of TEM micrographs from the ICHAZ: a) 0.5 kJ/mm; b) 1.5 kJ/mm; c) 2.5 kJ/mm.

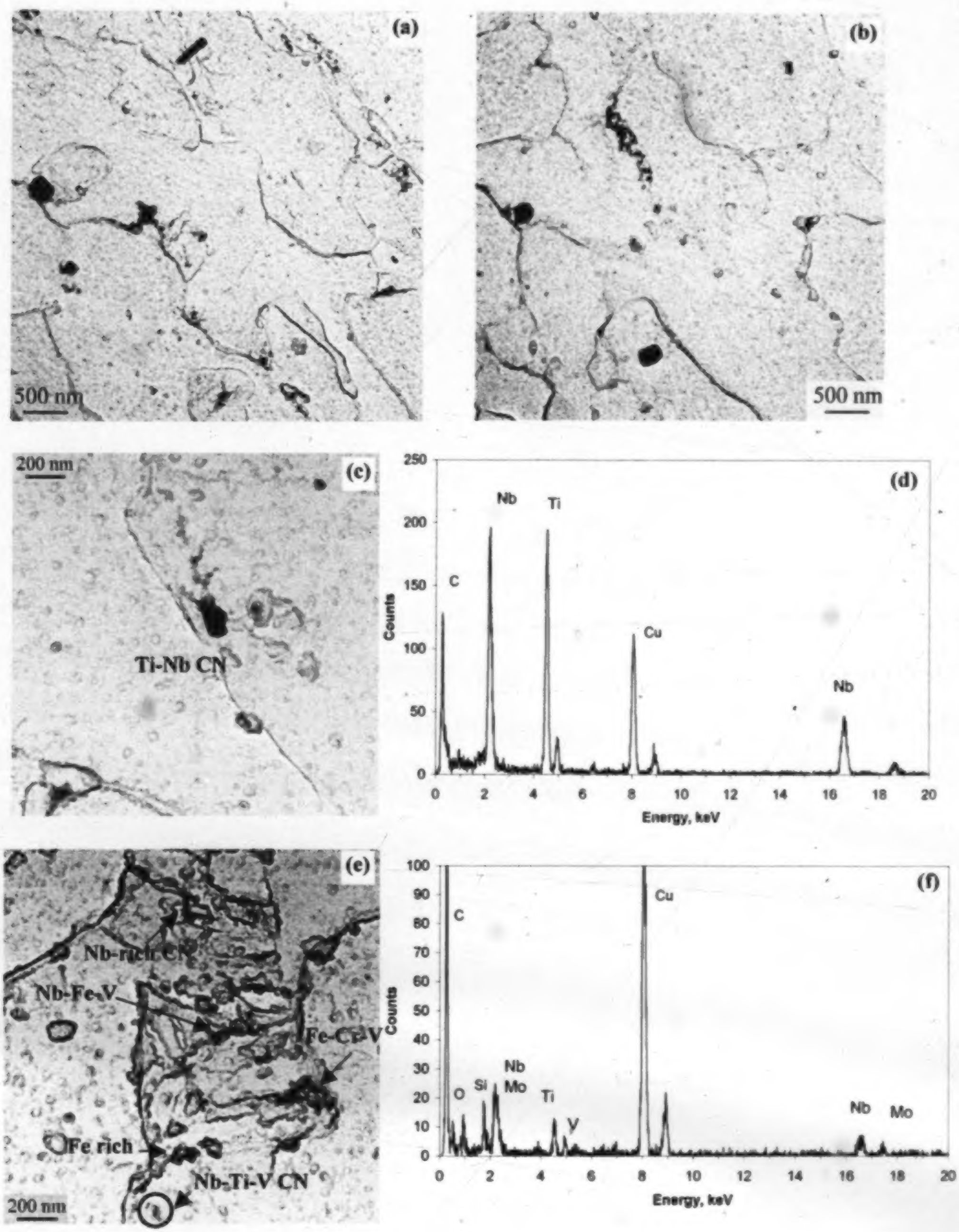
(a)
500 nm
(b)
500 nm
200 nm
(c)
Ti-Nb CN
(d)
Counts
Energy, keV
0
50
100
150
200
250
0
2
4
6
8
10
12
14
16
18
20
C
Nb
Ti
Cu
Nb
(e)
Nb-rich CN
Nb-Fe-V
Fe-Cr-V
Fe rich
Nb-Ti-V CN
200 nm
(f)
Counts
Energy, keV
0
10
20
30
40
50
60
70
80
90
100
0
2
4
6
8
10
12
14
16
18
20
C
O
Si
Nb
Mo
Ti
V
Cu
Nb
Mo

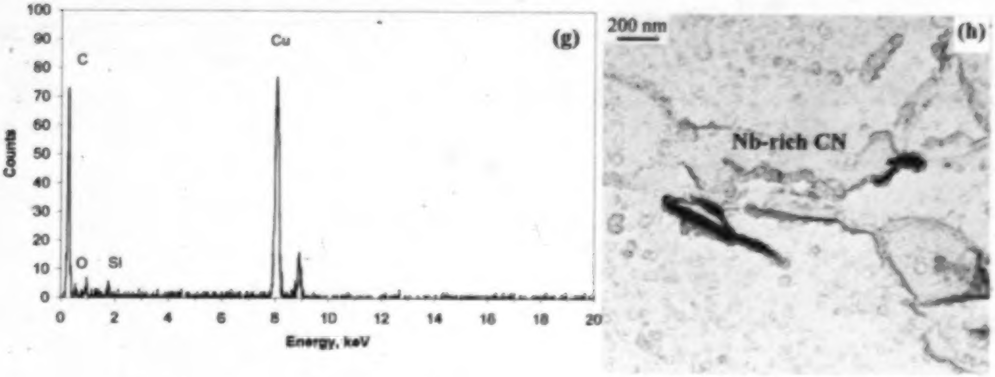

FIG. 5-29. TEM-replica of precipitates in the ICHAZ–0.5 kJ/mm: a), b) and c) BF images showing the intermediate-size precipitates; d) EDX spectrum from the particle in (c); e) regions of fine irregular precipitates at grain boundaries; f) EDX spectrum from the particle circled in (e); g) EDX spectrum from the bare replica; h) Sliver-like Nb-rich particles.

The Si peak, present in almost all the spectra from the replicas, likely comes from the carbon rod or dust in the carbon evaporator system. The other possibility is that the Si from dissolving the matrix during replica preparation forms an oxide, producing a thin amorphous layer on the replica. An EDX spectrum from a bare region on the replica (where there are no particles) shows some amount of Si (Fig. 5-29g). TEM examination in BM and HAZ showed that intermediate-size Nb-rich particles could have several kinds of irregular shapes. Fig. 5-29h shows some sliver-like Nb-rich particles.

It was shown that the fine particles in the BM had considerable amounts of Mo, Ti and V, which increases the solubility of these particles relative to that of NbC. Moreover, it is known that fine precipitates are thermodynamically less stable than larger ones. Therefore, it is possible that the very fine particles in this sub-region are dissolved during the heating leg and reprecipitated back during the cooling leg of the thermal cycle (especially in the grains that have transformed to austenite and re-transformed back to ferrite). Fig. 5-30 shows two types of fine-precipitate distributions. An example of local colonies of fine Nb-rich particles is shown in Fig. 5-30a. This type of distribution could be either a result of dissolution of intermediate Nb-rich particles during the heating leg of the thermal cycle or an artifact.

In the case of dissolution, the solutes enrich the matrix locally and do not diffuse very far due to the short time of the thermal cycle. Upon cooling the solutes could reprecipitate in the form of very fine particles in close proximity. The complete dissolution of intermediate-size Nb-rich particles was not expected in this sub-region, however. An alternative explanation for the observed distribution is the coalescence of particles during replica preparation. It is known that the sampling volume during the etching of the matrix is several times larger than the size of fine precipitates. Therefore, fine particles may move in the solvent, stick together and stick to the replica by Van der Waals forces. Overestimation of the volume fraction for these particles (Section 5-5) supports this theory.

The corresponding SAD pattern, DF image from part of the ring in the SAD pattern and the EDX spectrum of the precipitates in Fig. 5-30a are shown in Figs. 5-30 b–d. The ring pattern in the SAD pattern is a result of various orientations among the particles. Either this is due to the fast cooling rates that do not allow precipitation with a preferred orientation relationship with the matrix, or the particles have randomly agglomerated during the replica preparation. The presence of comparable amounts of elements, such as Mo, Ti and V, in the EDX spectrum of Fig. 5-30d is similar to that of the BM.

The other type of fine particle distribution is uniform dispersion within the matrix. Fig. 5-30e shows a DF image, taken under the same condition as shown in Fig. 5-30b, from within the grains. The morphology may be the result of dissolution of the original fine precipitates (types 4 and 5) and reprecipitation around the same locations, in the grains transformed to austenite, or the original fine precipitates, especially in the grains not experiencing re-transformation.

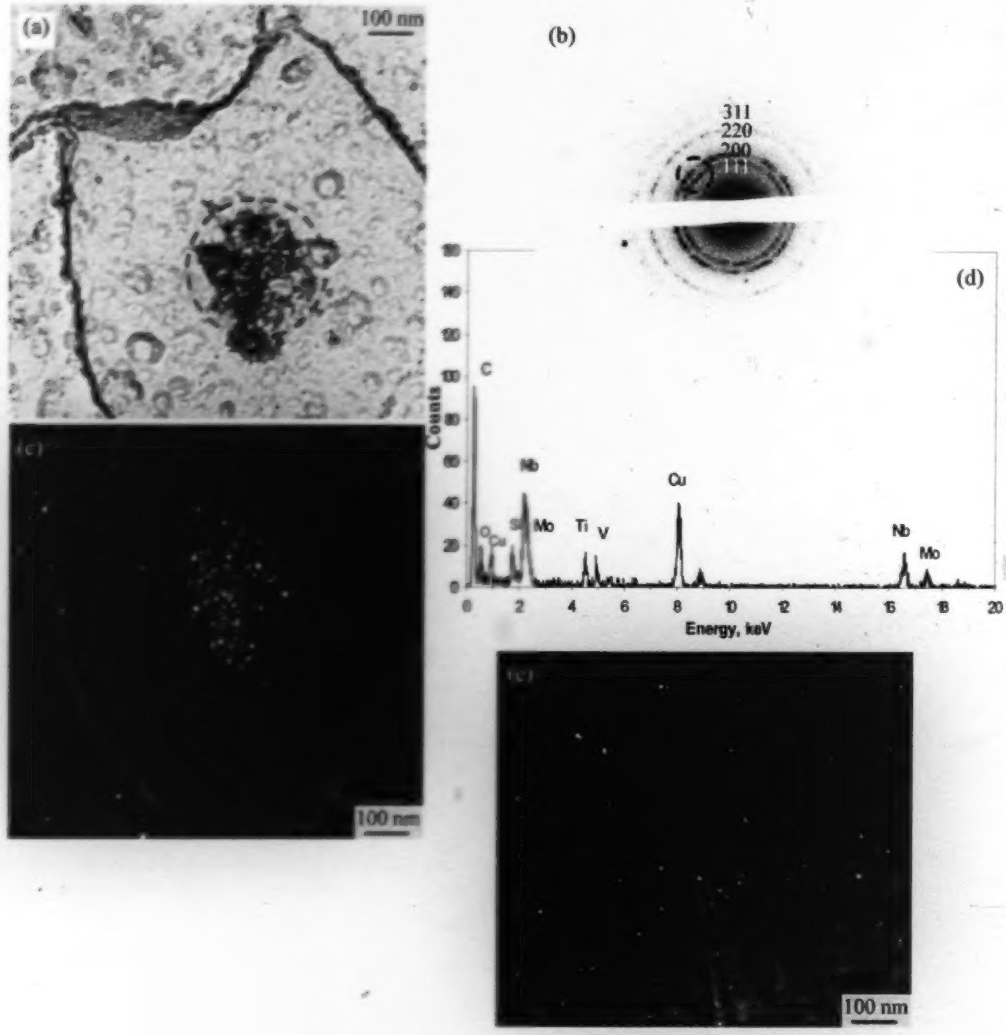
(a)
100 nm
(b)
311
220
200
111
(c)
100 nm
(d)
Counts
Energy, keV
C
O
Cu
Si
Nb
Mo
Ti
V
Cu
Nb
Mo
0
20
40
60
80
100
120
140
160
0
2
4
6
8
10
12
14
16
18
20
(e)
100 nm

FIG. 5-30. Fine precipitates in the ICHAZ–0.5 kJ/mm sample: a) BF image; b) SAD pattern from the precipitates in (a); c) DF image from the part of the ring circled in (b); d) EDX spectrum from precipitates in (a); e) DF image under the same condition as (c) but from another region.

ICHAZ–1.5 kJ/mm

Fig. 5-31 shows some of the intermediate-size precipitates in the ICHAZ of the 1.5 kJ/mm weld sample. The cuboidal Ti-rich particle in Fig. 5-31a, about 300 nm in size, has pinned a grain boundary. The corresponding SAD pattern and EDX spectrum from the particle show that it is indeed a Ti carbonitride with a face-centered cubic structure (Fig. 5-31b and c). Most of the intermediate-size particles have pinned the grain-boundaries.

Fine precipitates (<10 nm) were dispersed throughout the grains (Fig. 5-31d). No segregation to the grain boundaries was observed. It seems, however, the fine precipitates have different densities in some neighboring grains (e.g., Fig. 5-31e). The reason for this is not clear. Colonies of fine precipitates, similar to those seen with low heat input (Fig. 5-31a), were not seen in this sample. If this was due to dissolution of intermediate-size Nb-rich particles, it is likely that the slower thermal cycle at this heat input allowed more diffusion and less concentration of solutes.

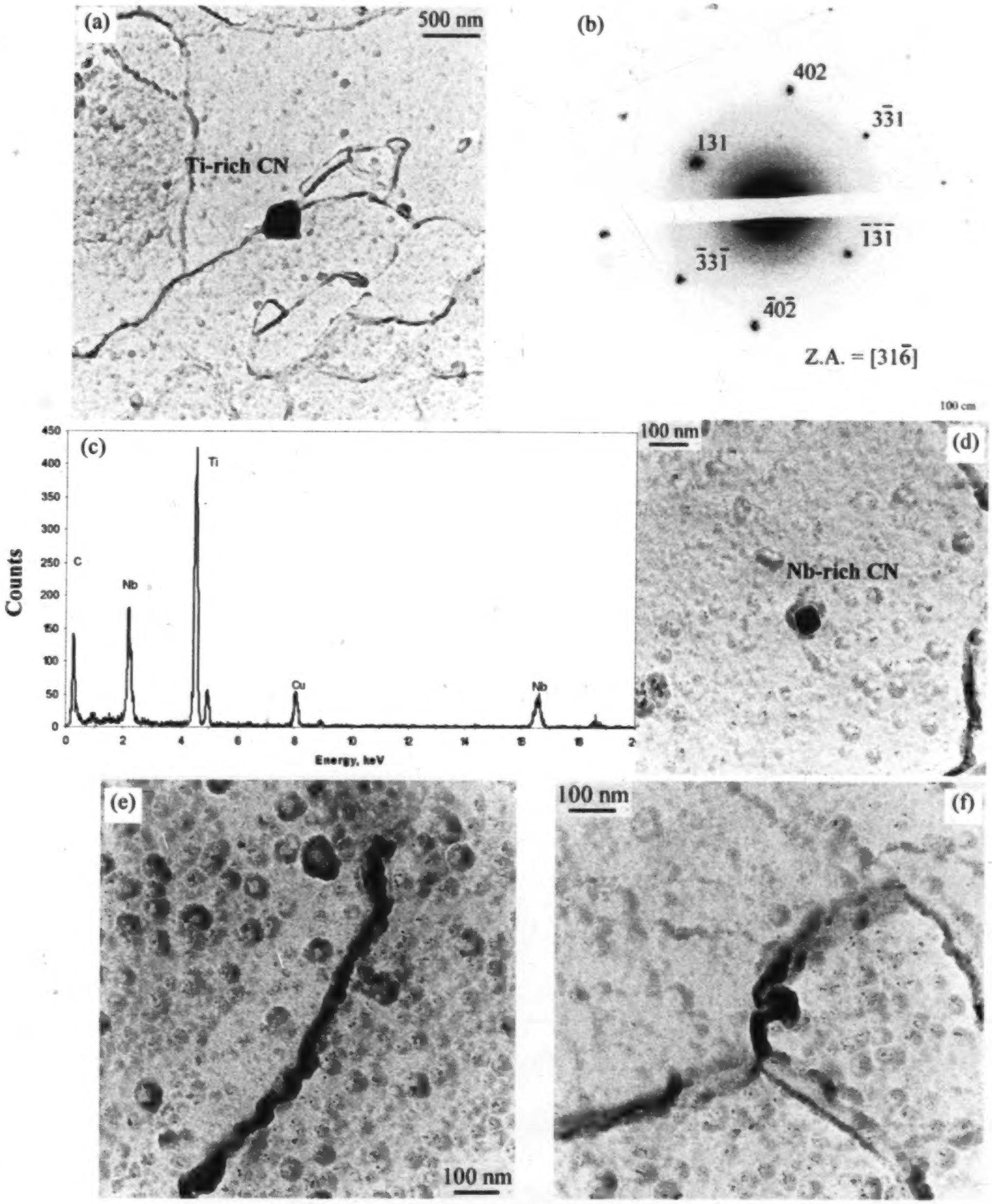
(a)
500 nm
Ti-rich CN
(b)
402
$3\bar{3}1$
131
$\bar{1}\bar{3}\bar{1}$
$\bar{3}3\bar{1}$
$\bar{4}0\bar{2}$
Z.A. = $[31\bar{6}]$
100 nm
(c)
Counts
450
400
350
300
250
200
150
100
50
0
C
Nb
Ti
Cu
Nb
0
2
4
6
8
10
12
14
16
18
20
Energy, keV
100 nm
(d)
Nb-rich CN
(e)
100 nm
100 nm
(f)

FIG. 5-31. TEM examination of precipitates in ICHAZ-1.5 kJ/mm: a) BF image from an intermediate-size Ti-rich CN; b) SAD pattern; c) EDX spectrum from the particle in (a); d) BF image from an intermediate-size Nb-rich CN; e) and f) BF images of fine precipitates.

ICHAZ–2.5 kJ/mm

TEM examination of the precipitates in the 2.5 kJ/mm weld samples showed similar distributions to those seen in the 1.5 kJ/mm sample. Two regions with several intermediate-size precipitates (not representative of most regions) are shown in Fig. 5-32a and b. Again, most of the particles pinned the grain boundaries. EDX analysis showed a higher number of Ti-rich particles than Nb-rich particles. This, if representative of the sub-region, can be due to dissolution of the Nb-rich caps (in the case of several particles attached together) or shells (in the case of particles with coring), as a result of the lengthier thermal cycle relative to the other heat inputs, especially 0.5 kJ/mm.

The fine precipitates were re-distributed similar to those with a heat input of 1.5 kJ/mm. Again, it was observed that some neighboring grains had different precipitate densities (Fig. 5-32c). There was, however, some packing along the grain boundaries (Fig. 5-32d). The region indicated in Fig. 5-32d is further magnified in Fig. 5-32e, where some fine particles roughly 5 ± 3 nm in diameter are shown on a grain boundary. Fig. 5-32f shows the corresponding EDX, revealing the particles were Nb carbides with some amount of Mo, Ti, V and Fe. There have been reports that iron was found in the small Nb/V carbides. The percent of iron increased as the size of particles decreased [2]. This confirms the well-known observation that the precipitates may have non-equilibrium compositions. The addition of iron to the NaCl lattice of transition metal carbonitrides results in formation of an (Fe, M)$_x$C$_y$N$_z$ compound with significantly larger particle volume fraction than that calculated based on the stoichiometry ratio. However, the addition of Mn would result in a decrease in the Fe level in the particles [52].

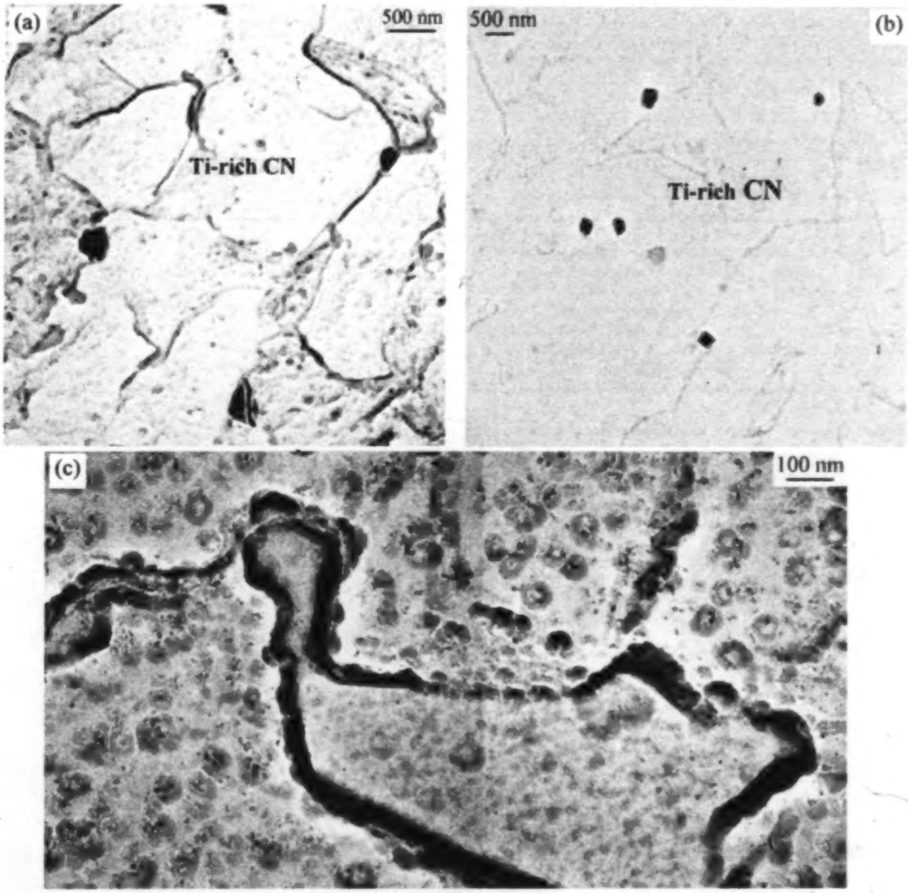

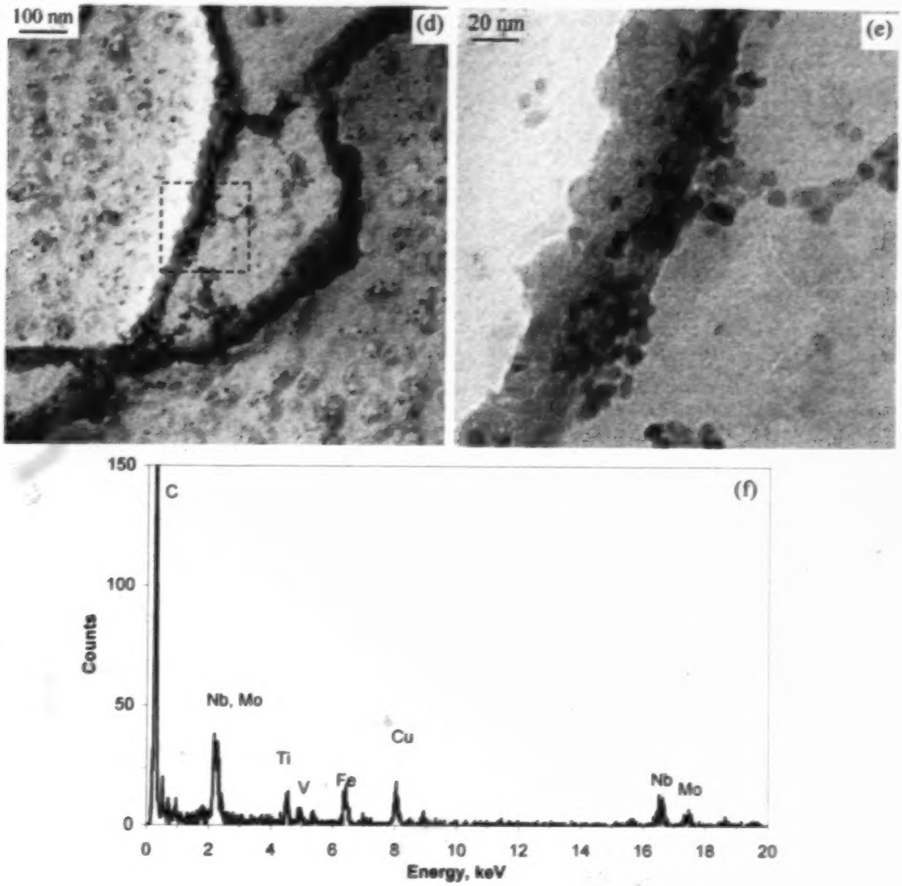

FIG. 5-32. TEM examination of precipitates in the ICHAZ-2.5 kJ/mm: a) and b) BF images showing some intermediate-size Ti-rich precipitates; c–e) BF images from fine precipitates; f) EDX spectrum from the fine particles in (e).

5-7-1-3. FGHAZ

Fig. 5-33 shows mosaics of TEM micrographs from the FGHAZ for different heat input values. Although some of the intermediate-size precipitates show partial dissolution, most of them are not changed in this sub-region. The fine precipitates rich in Nb and Mo must have dissolved and reprecipitated due to their higher effective solubilities. The precipitates in this sub-region will be examined for each weld sample in the following sections.

FGHAZ–0.5 kJ/mm

The region indicated in Fig. 5-33a is shown in Fig. 5-34a, and further magnified in Fig. 5-34b, where some of the intermediate-size precipitates are better resolved. A Ti-rich, a Nb-rich and a region of partially dissolved precipitates are visible in Fig. 5-34b. The region of partial dissolution is further magnified in Fig. 5-34c. EDX spectra (not shown) obtained from the partially dissolved particle showed peaks of Ti and Nb. This region consists of remains of a Ti/Nb carbonitride, on which fine particles of NbC have reprecipitated. This is better discerned in the accompanying DF image obtained from part of the (111)-NbC and (200)-NbC rings. Reprecipitation on the remains of partially dissolved particles is again a result of the fast thermal cycle for this heat input, where the solutes remain around the partially dissolved particle.

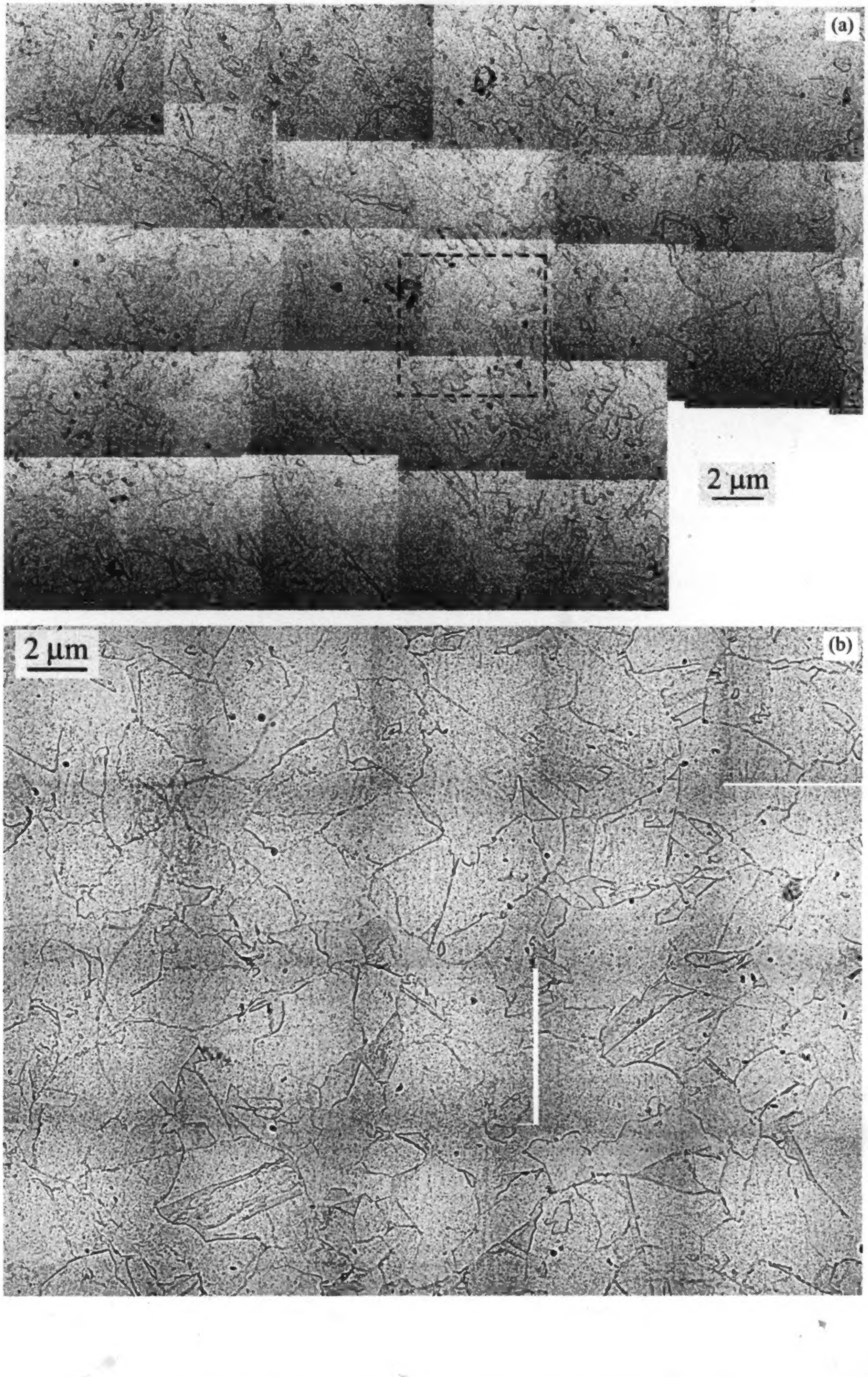
(a)
2 µm
2 µm
(b)

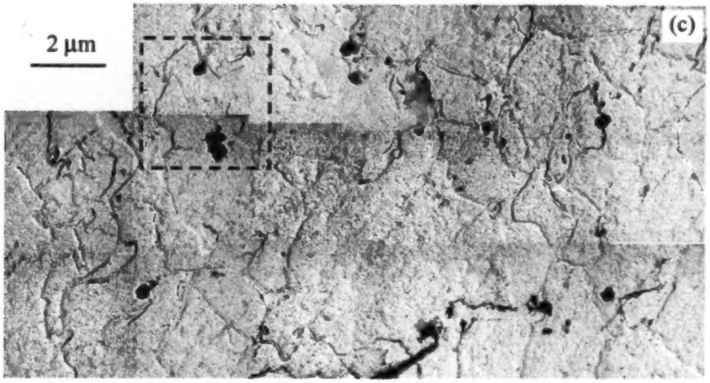

FIG. 5-33. Mosaics of TEM micrographs from the FGHAZ: a) 0.5 kJ/mm; b) 1.5 kJ/mm; c) 2.5 kJ/mm.

Examination of the matrix region indicates that there is a fine distribution of sub-10 nm particles (Fig. 5-34e). The two smallest size precipitates originally in the BM (10–20 nm and <5 nm particles; Fig. 5-24d) must have dissolved during heating and reprecipitated during cooling. Some of these fine particles appear in the accompanying DF image (Fig. 5-34f) obtained from the same condition as in Fig. 5-34d. DF images have better contrast, but they may tend to show the sizes as being slightly larger. These precipitates are essentially complex carbides of Nb, Mo, Ti and V and, therefore, have higher solubilities than pure NbC. Their instability is increased by their small sizes.

Electron energy filtered images, using a Gatan image filtering (GIF) system, of two types of intermediate-size particles are shown in Fig. 5-35. Fig. 5-35a shows a partially dissolved particle. The remaining particle is richer in Ti, meaning most of Nb has dissolved. Nevertheless, Ti and Nb elements are mixed within the region. Fig. 5-35b shows a group of particles, seemingly unaffected by the thermal cycle, consisting of TiN in the middle and two NbC caps attached to it. The GIF images show that Ti is present only in the cubic part in the middle; it must have formed at higher temperature. These two cases confirm the results of the analysis of Section 5-3-1, that Ti precipitates first as TiN (Fig. 5-35b) and the remaining Ti forms as TiC within the temperature range of NbC precipitation and, therefore, can form mixed carbides with Nb (Fig. 5-35a).

FGHAZ–1.5 kJ/mm

Fig. 5-36 shows precipitates in the FGHAZ of a 1.5 kJ/mm weld sample. The distribution of Nb-rich intermediate-size particles (Fig. 5-36a) and Ti-rich intermediate-size particles (Fig. 5-36b) did not seem to change considerably in this sub-region. Fine precipitates, however, seemed slightly larger than those in the FGHAZ of the 0.5 kJ/mm weld sample. Nevertheless, the fine precipitates were still uniformly dispersed in all grains.

FGHAZ–2.5 kJ/mm

The intermediate-size precipitate distribution in the FGHAZ for the 2.5 kJ/mm weld sample was similar to that in the lower heat inputs. Almost all these precipitates were at the grain boundaries. These precipitates pin the prior austenite grain boundaries. Nucleation of ferrite grains at the grain boundaries will leave these particles at the grain-boundaries of the final microstructure. Fig. 5-37a shows several groups of precipitates. Each group consists of two or more Ti-rich and Nb-rich precipitates attached together. The region marked in Fig. 5-37a is shown in Fig. 5-37b at a higher magnification. EDX analysis (not shown here) showed that some regions (indicated by circles) are rich in Nb and some rich in Ti. This is likely a location where several intermediate-size particles existed in the BM. Some of these particles, or part of them, were dissolved during the weld thermal cycle and reprecipitated as smaller particles around the region. This, however, was seen only in few places. Overall, the intermediate-size precipitate distribution in the FGHAZ (all heat input values) was not changed much.

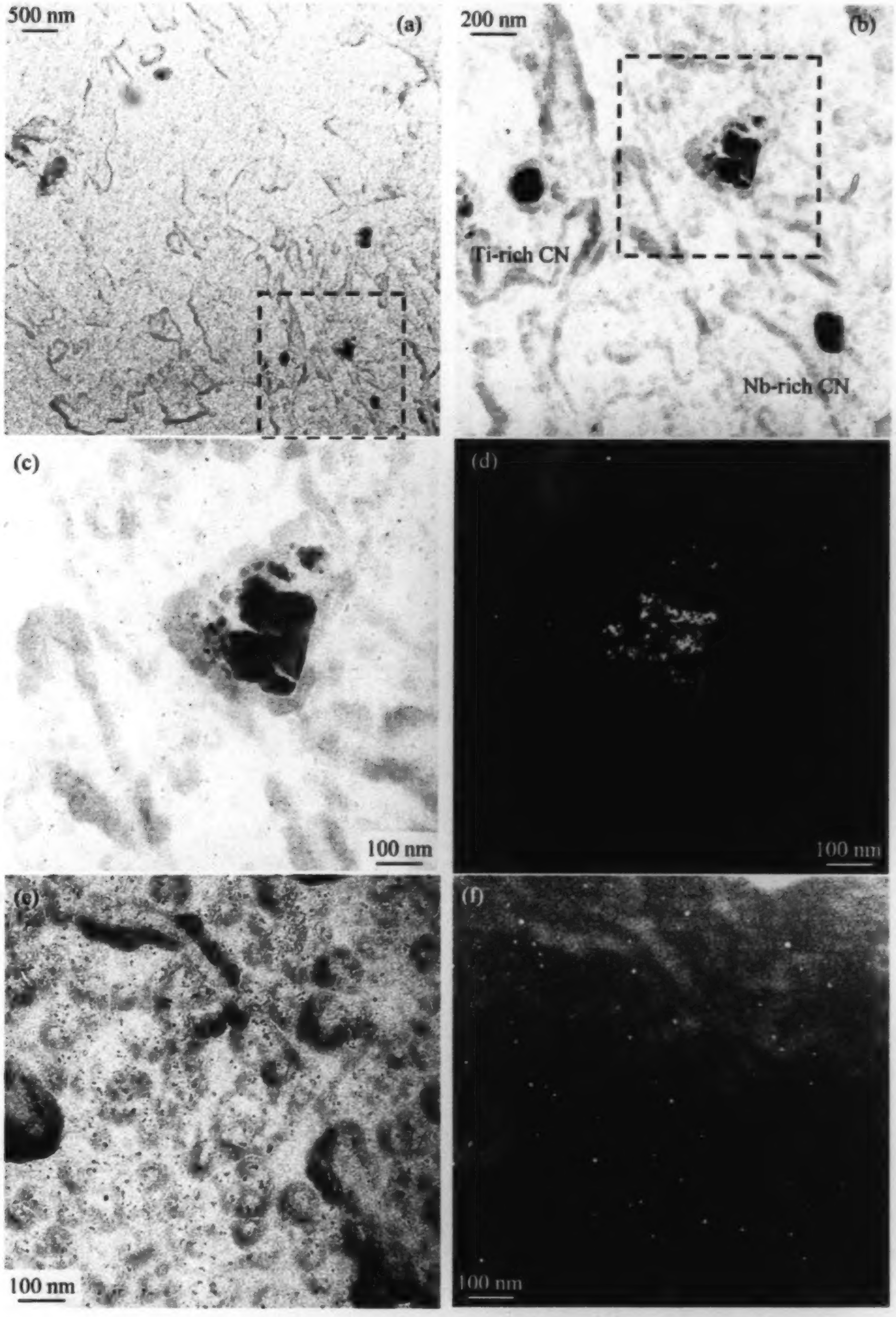
500 nm
(a)
200 nm
(b)
Ti-rich CN
Nb-rich CN
(c)
100 nm
(d)
100 nm
(e)
100 nm
(f)
100 nm

FIG. 5-34. TEM images of precipitates from the FGHAZ-0.5 kJ/mm: a) and b) BF images, at different magnifications, showing some intermediate-size precipitates; c) partially dissolved precipitate in (b) at higher magnification; d) corresponding DF image of the particle in (c); e) fine precipitates within the grains; f) DF image showing some fine precipitates in (e).

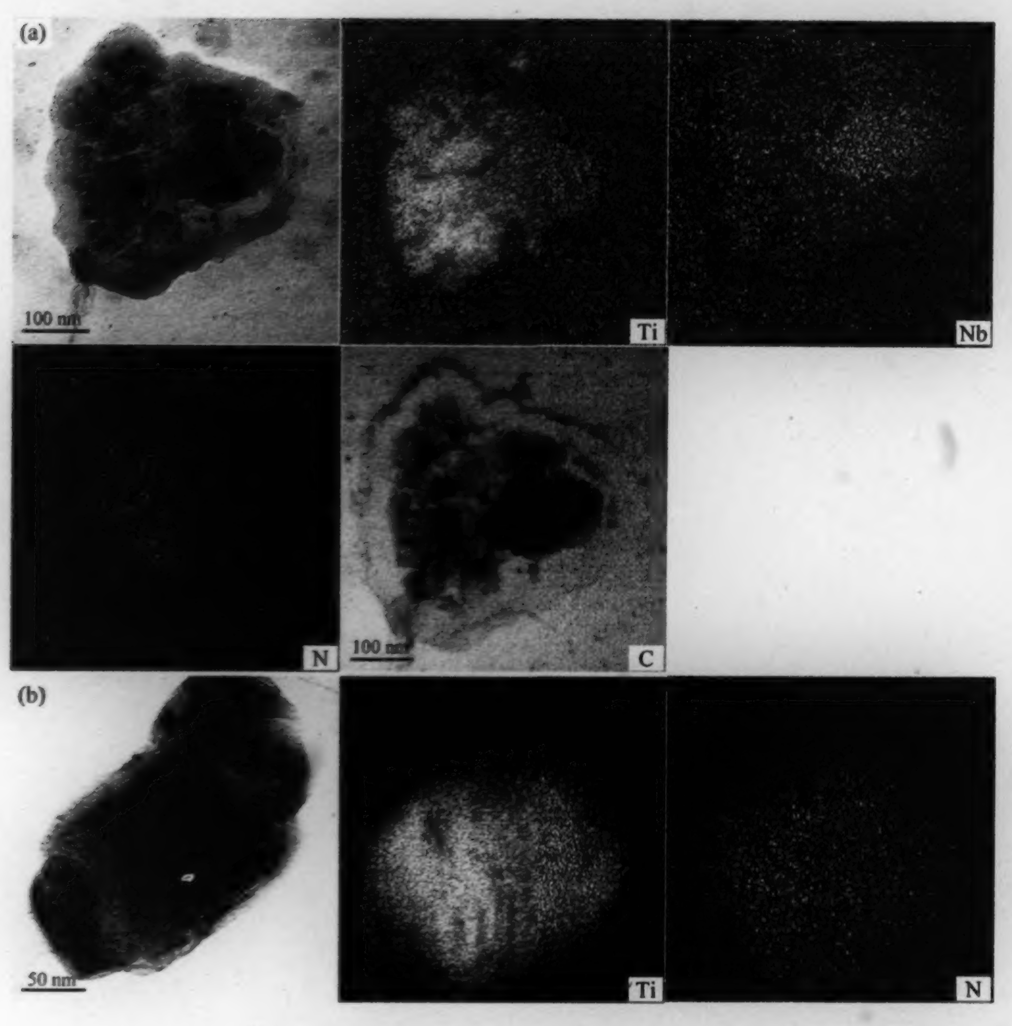

FIG. 5-35. GIF images of two intermediate-size particle groups: a) TEM-BF image of a partially dissolved Ti-Nb carbonitride; b) TEM-BF image of a Ti-rich cubic particle and two Nb-rich caps attached to it. Note the bright regions in the accompanying GIF images indicate the distribution of the element tagged on the image.

Fig. 5-37c shows a ferrite grain with no intermediate-size particles, but covered with fine precipitates. The size distribution of these fine precipitates is not very different from those in the previous samples (i.e., heat inputs 0.5 and 1.5 kJ/mm). It appears that some are aligned along a direction indicated by the arrow. This could be a result of interphase precipitation, where the fine carbides have a sheet distribution perpendicular to the austenite-ferrite interface movement direction during the transformation. This can happen at this heat input, as the cooling rate was relatively low (a mean cooling rate of ~8°Cs^{-1} – Table 3-4). This was discussed in Section 5-2-4. Nevertheless, interphase precipitation does not seem to be a major mechanism of precipitation even in this sample. Overall, the fine precipitate distribution seemed to be more or less the same in the FGHAZ for all heat inputs. This means there should not be considerable change in the portion of strength coming from dispersion strengthening. This point will be discussed further in Chapter 8.

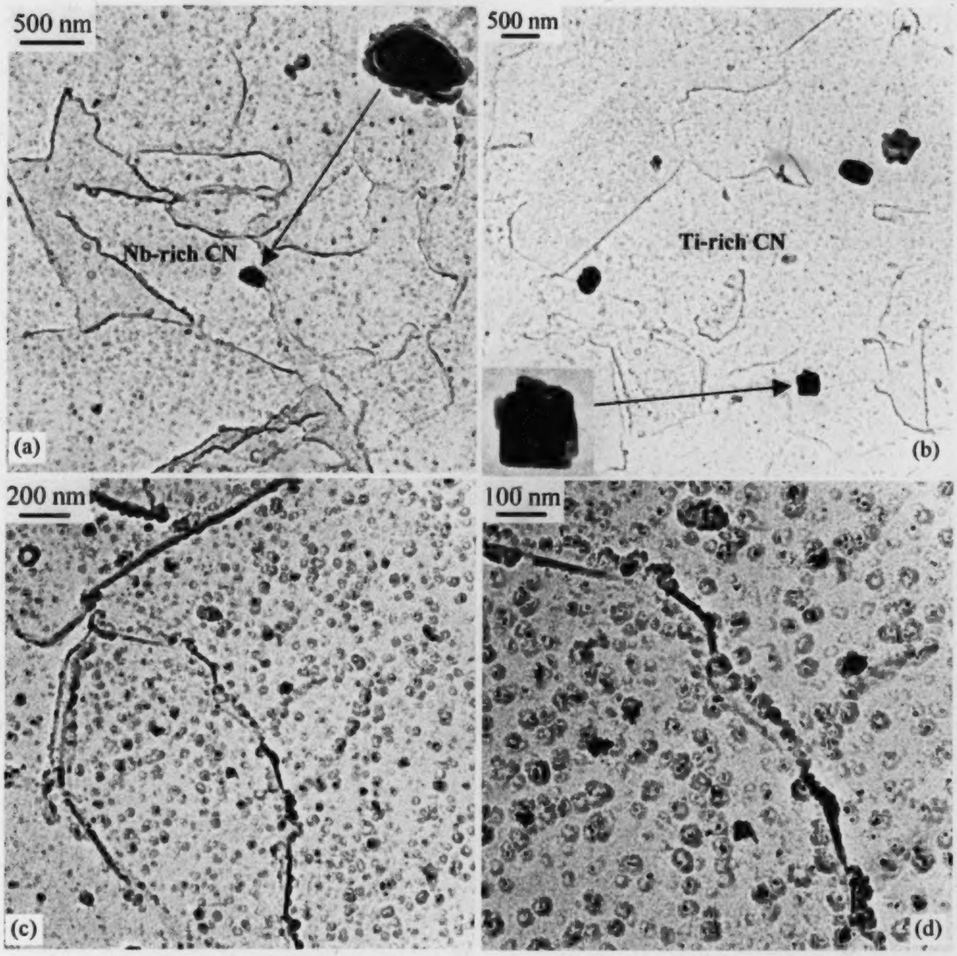

FIG. 5-36. TEM examination of precipitates in FGHAZ-1.5 kJ/mm: a) BF image showing an intermediate-size Nb-rich carbonitride at a grain boundary; b) BF image showing several intermediate-size Ti-rich carbonitrides; c) and d) fine precipitates at two magnifications.

5-7-1-4. CGHAZ

Fig. 5-38 shows mosaics of TEM micrographs from the CGHAZ for different heat input values. There is a considerable change, both in the intermediate-size precipitates (especially at higher heat inputs) and the fine precipitates, as will be shown here. There are two mosaics for the heat input of 1.5 kJ/mm. These two represent different precipitate characteristics. One has a considerable amount of sliver-like sub-micron iron-rich particles, in addition to the intermediate-size microalloy carbonitrides. Several sections were examined. Some did not have these particles but many did. The precipitates in this sub-region will be examined for each weld sample in the following paragraphs.

CGHAZ–0.5 kJ/mm

Fig. 5-39a shows the region indicated in the mosaic of Fig. 5-38a at higher magnification. This region, which consists of some small Nb-rich particles and a region of partial dissolution and reprecipitation, is further magnified in Fig. 5-39b. The EDX spectrum (Fig. 5-39c) from the region of partial dissolution indicated in Fig. 5-39b shows a large peak of Ti and a smaller peak of Nb. The SAD pattern from the same region shows a quasi-ring pattern. This indicates that there are several precipitates (with different orientations) in that region. The pattern belongs to the fcc crystal structure of Nb-Ti carbonitrides. The DF image (Fig. 5-39e) from part of the 111- and 200-rings shows that the formation of the quasi-ring pattern is the result of diffraction from the fine precipitates on the remains of the larger particle (rich in Ti). All these analyses indicate that the intermediate-size precipitate was likely a complex Ti-NbCN. As a result of the thermal cycle, the Nb-rich shell of the complex particle has dissolved. The fast thermal cycle does not allow Nb to diffuse very far out from the particle, and the region remains locally high in the solute. Fine NbC particles reprecipitate out on the remaining Ti-rich precipitate, probably in the austenite. There were also some regions with little or no apparent alteration. Fig. 5-39f shows a cuboidal Ti-rich particle and a spherical Nb-rich particle, similar to those observed in the BM and the other sub-regions of the HAZ. It should be remembered that the reduction in the number of intermediate-size precipitates depends on the distance from the fusion line, even within the CGHAZ. This was well illustrated through the precipitate analysis of Section 5-4-1.

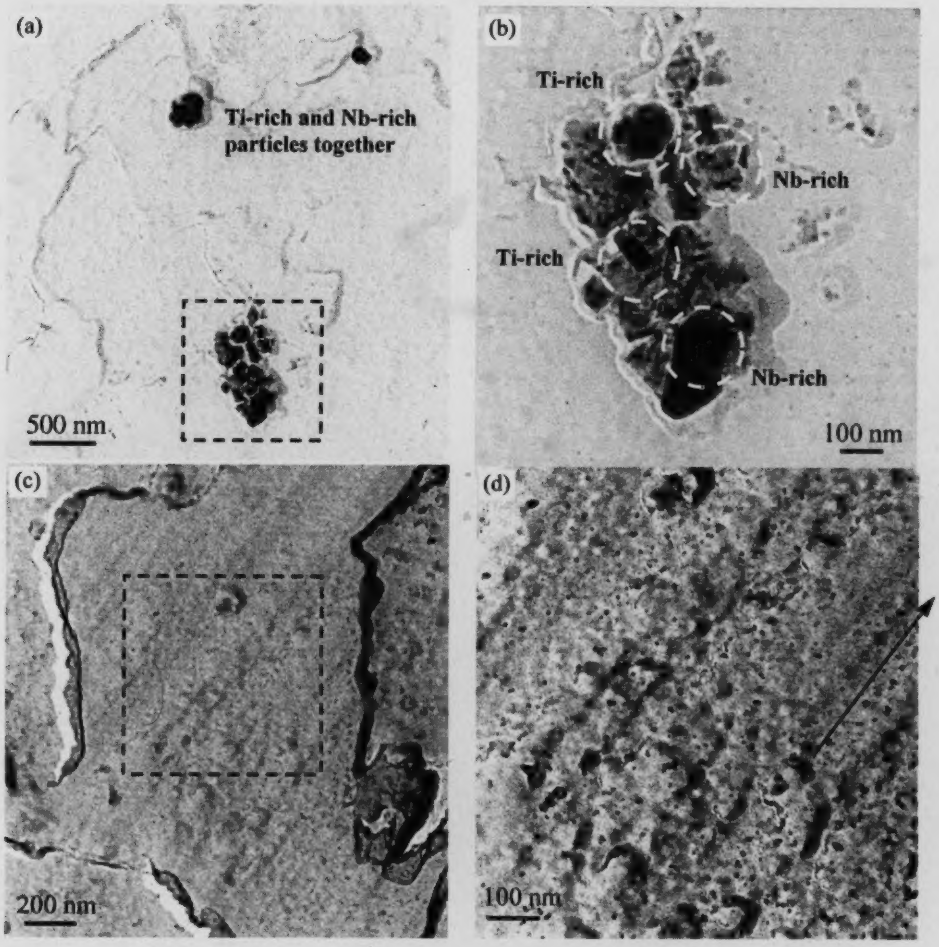

FIG. 5-37. TEM-BF images of precipitates in the FGHAZ-2.5 kJ/mm: a) three groups of intermediate-size carbonitrides at grain boundaries; b) magnified region in (a), showing regions of mixed precipitates; c) a grain free of intermediate-size precipitates; d) fine precipitates in the region marked in (c).

(a)

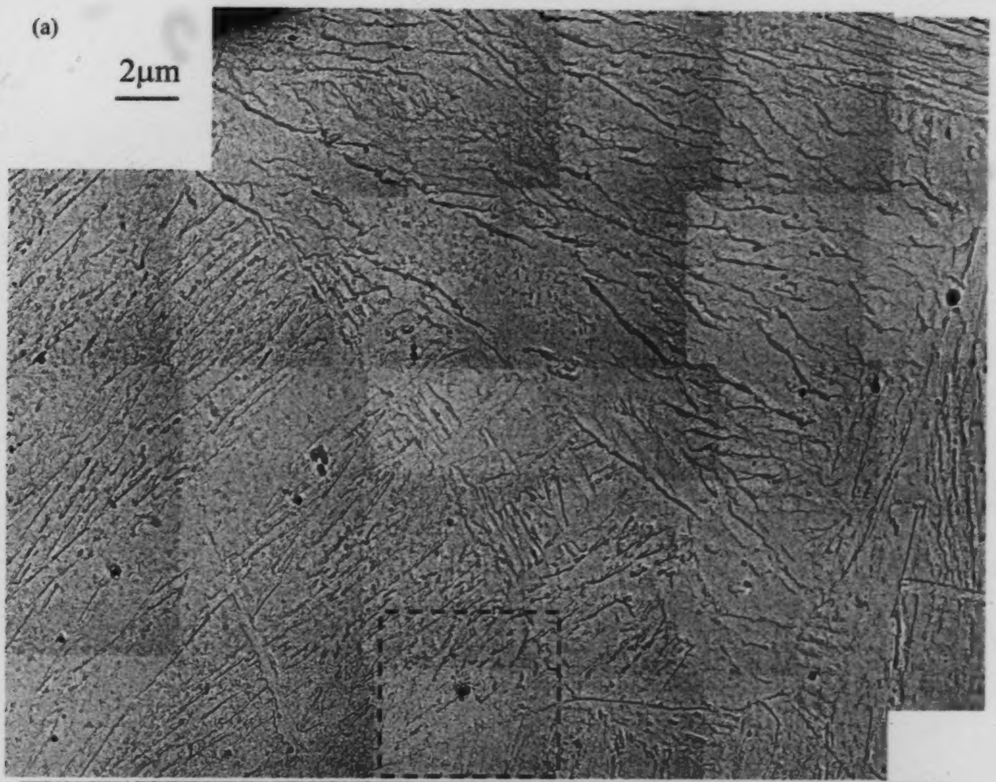

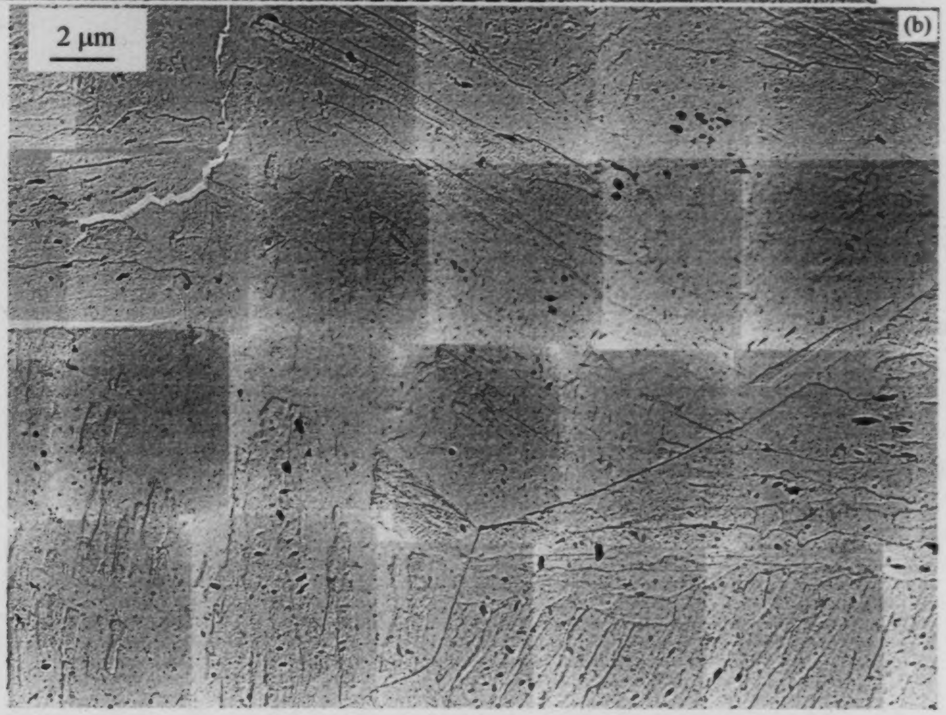

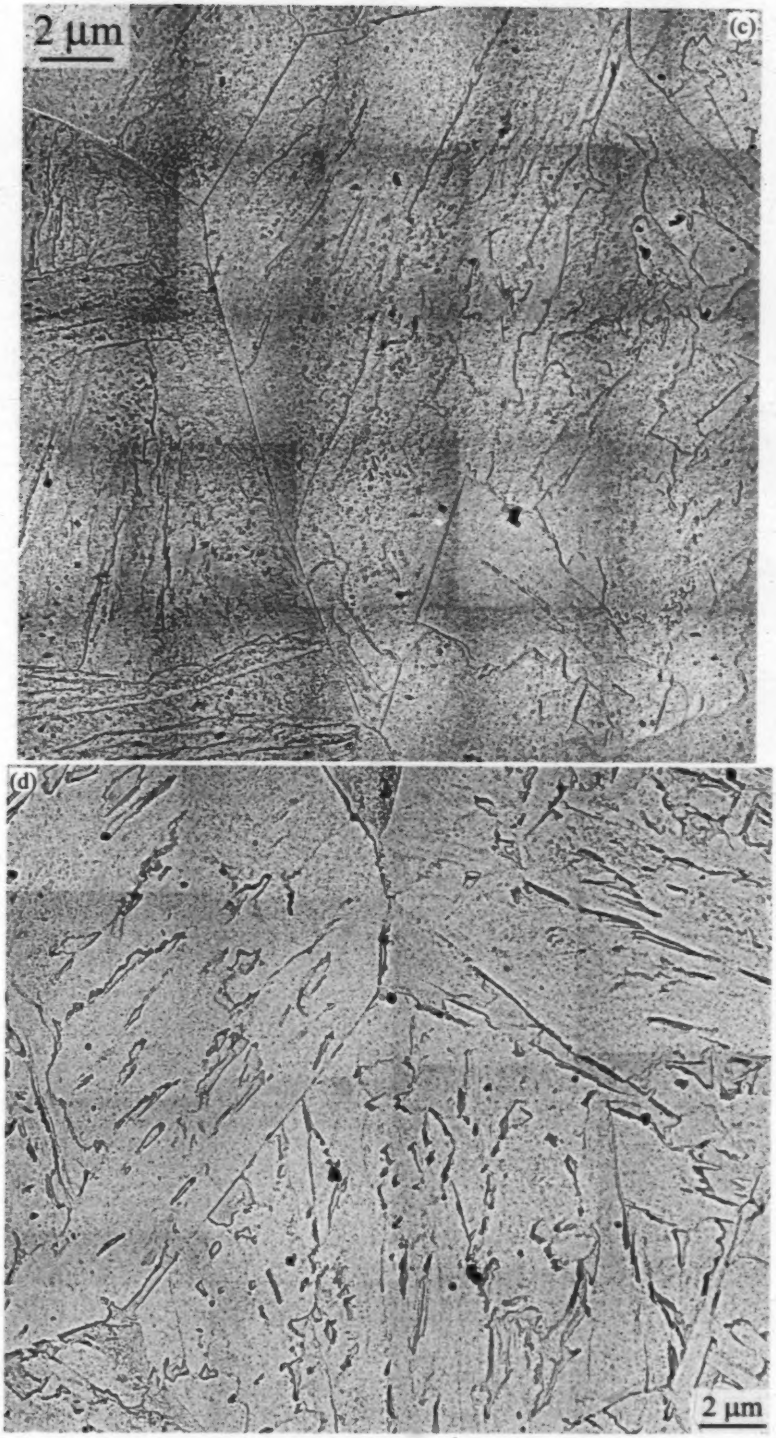

FIG. 5-38. Mosaics of TEM micrographs from the CGHAZ: a) 0.5 kJ/mm; b) and c)1.5 kJ/mm; d) 2.5 kJ/mm.

The most important feature of the precipitate evolution in this sub-region and for this heat input, is the suppression of the reprecipitation of Nb-Mo carbides in the matrix. Fig. 5-39g shows the lath martensite region devoid of fine precipitates. The fine Nb-Mo carbides that were present in the BM dissolve during the heating portion of the welding process and do not reprecipitate during the cooling portion, since the rapid cooling and transformation to martensite retain all the solutes in the matrix.

CGHAZ–1.5 kJ/mm

As mentioned earlier, the CGHAZ of the 1.5 kJ/mm weld sample had a particular precipitation characteristic, i.e., the presence of sliver-like Fe-rich particles in most regions within the matrix and in some regions at the lath boundaries. Most of the intermediate-size particles were either cuboidal Ti-rich particles or sliver-like Fe-rich particles. Fig. 5-40a shows a region with some Fe-rich and some Ti-rich precipitates. A region with several cuboidal Ti-rich carbonitrides is shown in Fig. 5-40. Nb-rich particles were also observed, but they had very small sizes (Fig. 4.40c and d), some with spherical shapes (as opposed to irregular shape in the BM) showing various amount of dissolution (in agreement with the precipitate analysis predictions). There was not much evidence of regions of partial dissolution and reprecipitation, as observed in the FGHAZ and CGHAZ of the 0.5 kJ/mm weld sample. This was likely due to the slower thermal cycle that allowed for more uniform dissolution as well as diffusion of dissolved atoms to other regions. Reprecipitation of dissolved fine particles was observed with different distributions on different replicas. Some replicas/regions showed very little reprecipitation (Fig. 5-40e), while some replicas/regions showed considerable reprecipitation (Fig. 5-40f). This shows a transition state between suppression (as in the 0.5 kJ/mm weld sample) and reprecipitation (as in 2.5 kJ/mm weld sample – next section) for this thermal cycle. Note, where there are significant numbers of fine precipitates, they are slightly larger in average and more dispersed than those in the BM, ICHAZ and FGHAZ. This suggests higher degree of solid solution strengthening and lower degree of dispersion strengthening (Chapter 8).

Fig. 5-41a shows a region with a considerable amount of intragranular Fe-rich particles. The sliver-like morphology of these particles is better discerned at higher magnification (Fig. 5-41b). EDX analysis showed they are rich in Fe with a small amount of Mn (dissolved in the particle, partially replacing Fe). SAD patterns tilted close to zone axes were indexed to cementite (Fe_3C). This could not be mistaken for any microalloyed precipitates, retained austenite/martensite or the ferrite-matrix (either plucked out as an artefact of replication or from twinned regions – Chapter 5), as the lattice parameters of cementite (with an orthorhombic crystal structure) are almost double those of the above-mentioned structures (with cubic crystal structures). The formation of cementite can be a result of a moderate cooling rate during this weld thermal cycle (1.5 kJ/mm), being too fast for more stable microalloyed carbides. The availability of Fe atoms for the formation of cementite compensates for its higher solubility compared to microalloyed carbides. The regions with intragranular cementite have the microstructural characteristics of lower bainite or auto-tempered martensite.

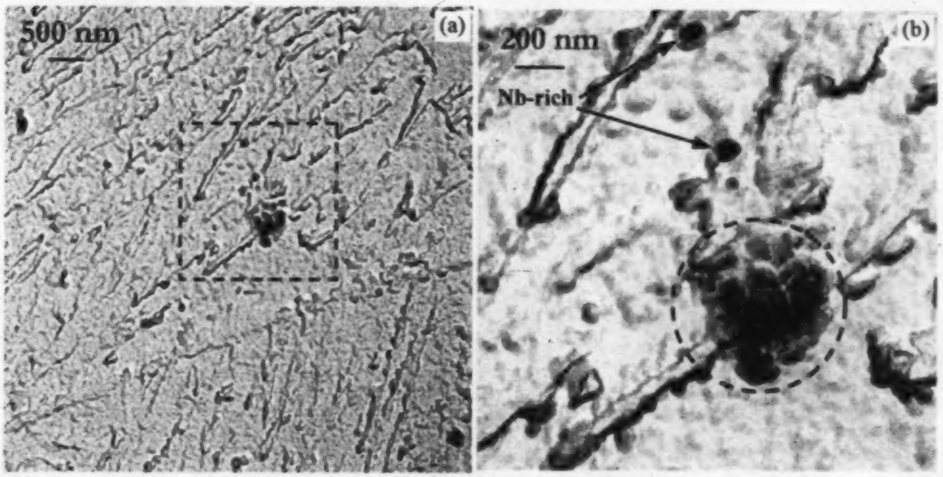

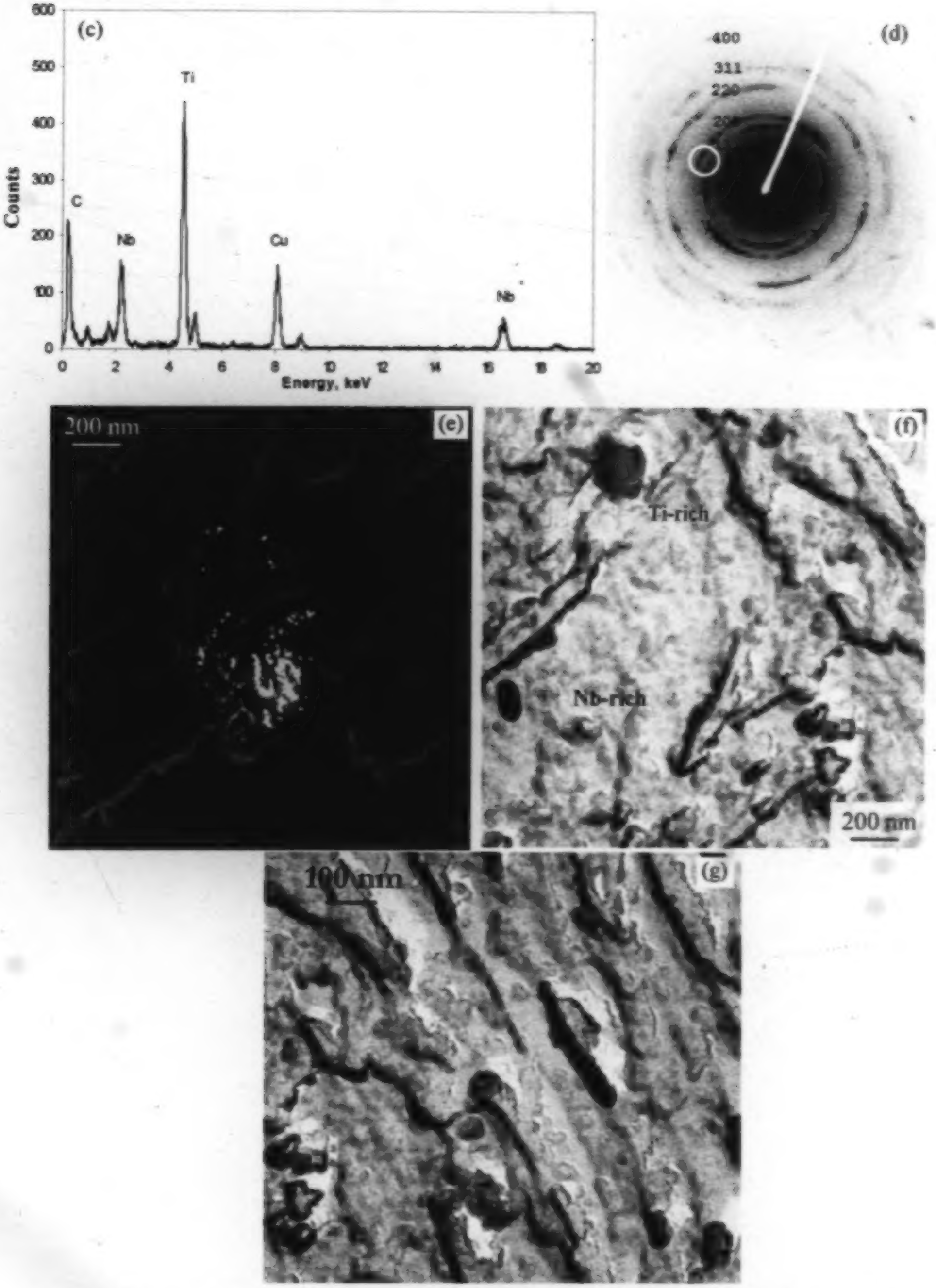
(c)
Ti
C
Nb
Cu
Nb
Counts
0
100
200
300
400
500
600
0
2
4
6
8
10
12
14
16
18
20
Energy, keV
400
311
220
(d)
200 nm
(e)
(f)
Ti-rich
Nb-rich
200 nm
100 nm
(g)

FIG. 5-39. TEM replica images of precipitates in the CGHAZ-0.5 kJ/mm: a) partially dissolved intermediate-size precipitates; b) magnified region in (a), showing two Nb-rich carbonitrides and a region of partial dissolution and reprecipitation; c) EDX spectrum from the region marked in (b); d) SAD pattern from the region marked in (b); e) DF image from the part of the rings marked in (d); f) Ti-rich cuboidal particle and a spherical Nb-rich particle; g) matrix of lath martensite devoid of fine precipitates.

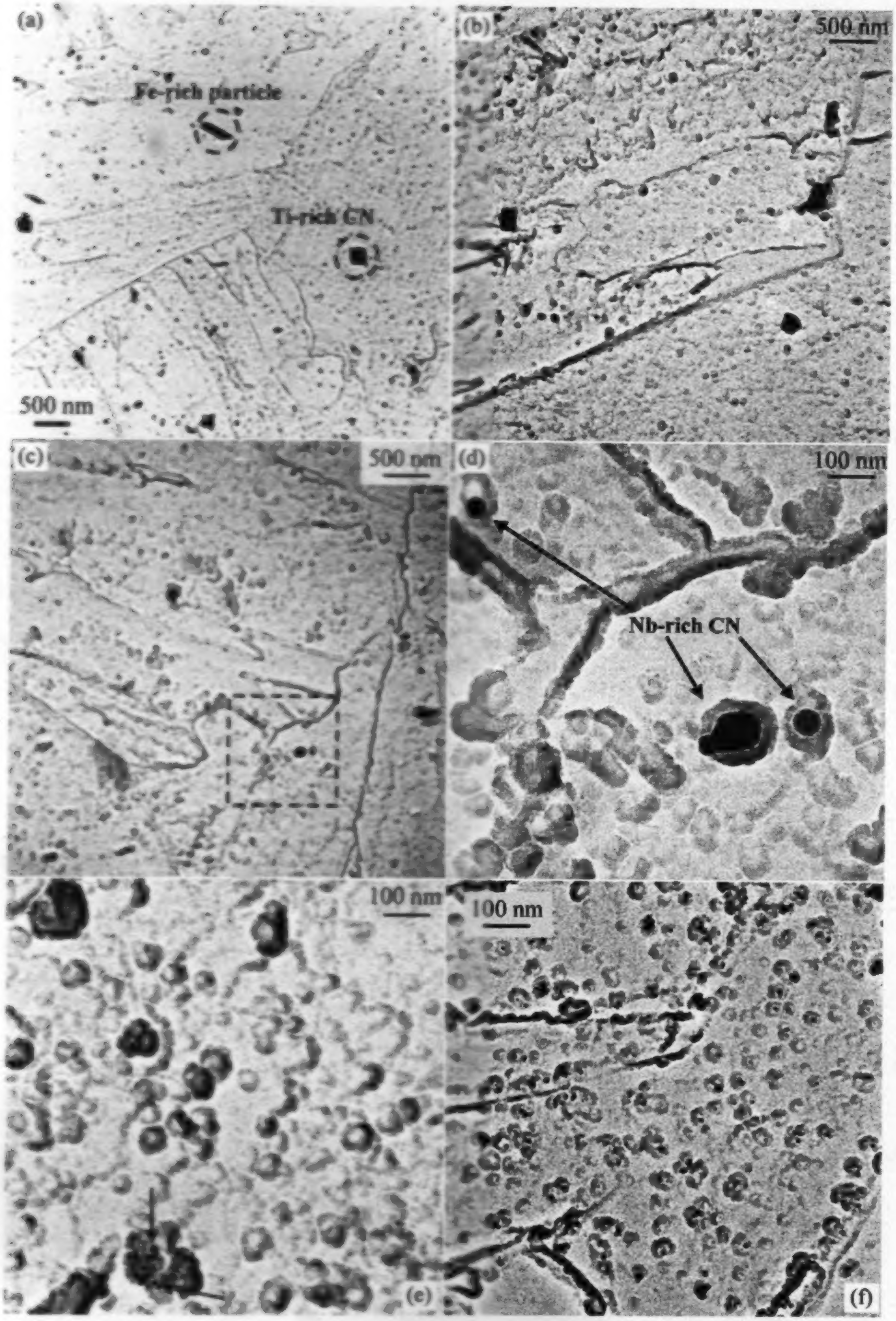
(a)
Fe-rich particle
Ti-rich CN
500 nm
(b)
500 nm
(c)
500 nm
(d)
100 nm
Nb-rich CN
100 nm
(e)
100 nm
(f)

FIG. 5-40. TEM replica images of precipitates in the CGHAZ-1.5 kJ/mm: a) region of mixed precipitation of Fe-rich and microalloy precipitates; b) region with several intermediate-size cubioidal Ti-rich particles; c) region with some intermediate-size Nb-rich particles; d) magnified region marked in (c) showing spherical Nb-rich carbides; e) matrix with a small amount of fine precipitates; f) matrix with a considerable amount of fine precipitates.

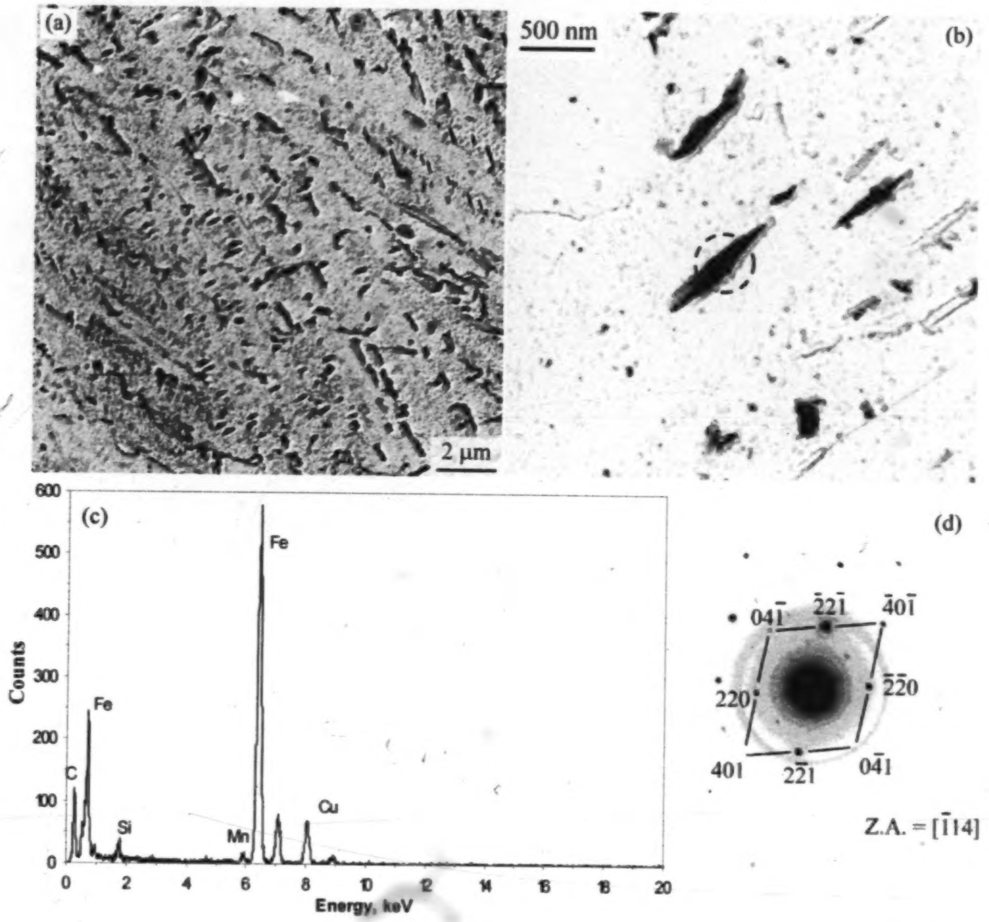

FIG. 5-41. TEM replica images of sliver-like Fe-rich particles in the CGHAZ-1.5 kJ/mm: a) a region with many intragranular precipitates; b) morphology of particles in (a); c) EDX spectrum from the region indicated in (b); d) SAD pattern from the region indicated in (b), showing the particles are cementite.

CGHAZ–2.5 kJ/mm

Fig. 5-42a shows some large cuboidal TiN particles, 1–2 μm in size. These particles are normally too large to be captured by the replicas. Some of them have pinned a prior austenite grain boundary. Intermediate-size Ti-rich carbonitrides are shown in Fig. 5-42b. Note, that even a rather small Ti-rich particle (indicated by an arrow in the picture) has a cuboidal form. Ti-rich particles of this size (~50 nm) were not detected in the BM. These are likely Nb-Ti carbonitrides that have lost most of the Nb. The Ti-rich core, which is stable in the CGHAZ, has aged, and as a result formed a cuboidal shape. The Nb-rich particles were almost completely dissolved. There were very few of them, with spherical shapes (Fig. 5-42c). They are likely the remains of partially dissolved particles. The spherical shape of these particles is likely a result of a relatively slow dissolution rate during the relatively slow thermal cycle at this heat input. There were also very few iron carbides (cementite) observed in the several sections examined (Fig. 5-42d). Reprecipitation was in the form of coarsened carbides, located primarily at the grain and sub-grain boundaries (Fig. 5-42e). These were ~10–20 nm in diameter. Similar to the case of the 1.5 kJ/mm weld samples, some replicas from the CGHAZ showed very little reprecipitation in the matrix (Fig. 5-42f). Particles that precipitate on grain or sub-grain boundaries are more prone to coarsening by Ostwald ripening than those that precipitate in the matrix. This is because accelerated diffusion can occur along the boundaries for particles on a common grain/sub-grain boundary [9].

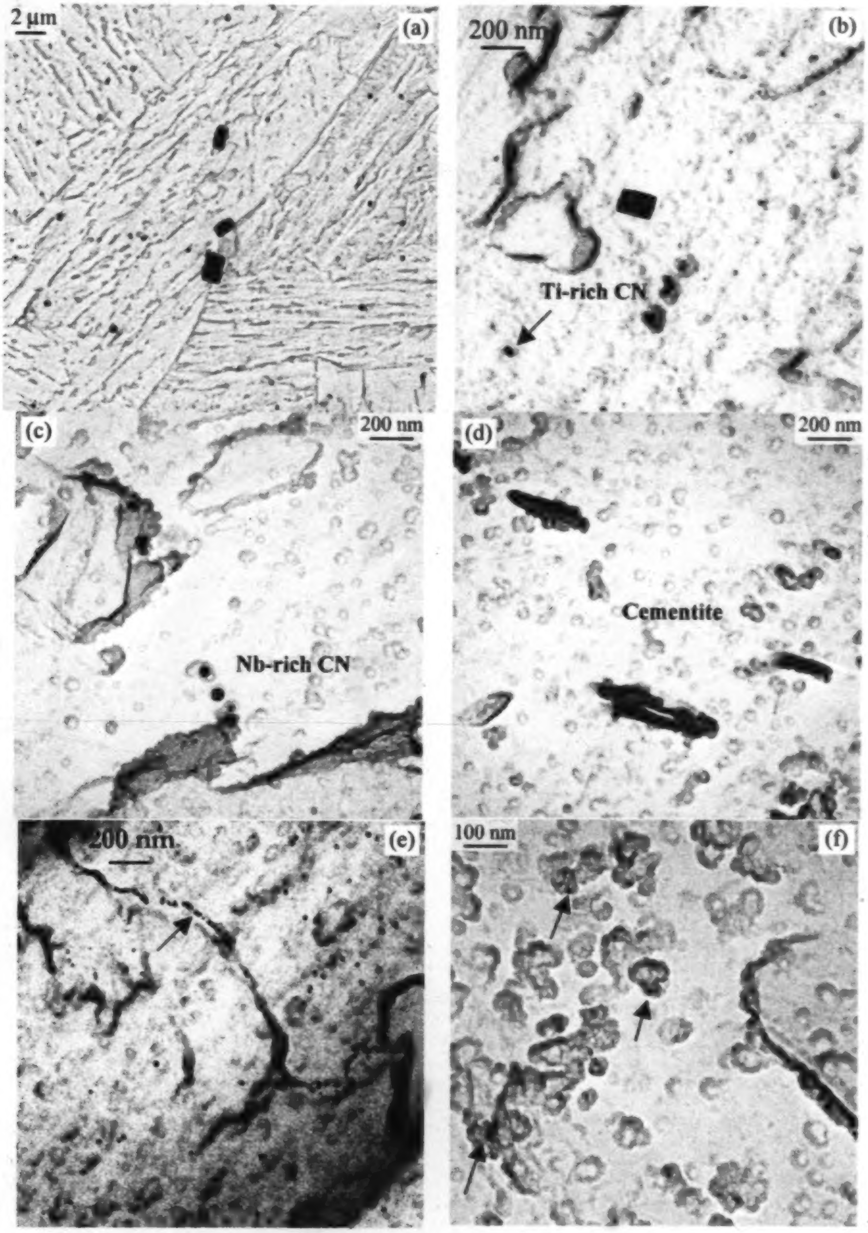
2 µm
(a)
200 nm
(b)
Ti-rich CN
(c)
200 nm
Nb-rich CN
(d)
200 nm
Cementite
200 nm
(e)
100 nm
(f)

FIG. 5-42. TEM replica images of precipitates in the CGHAZ–2.5 kJ/mm: a) large TiN particles 1–2 µm in size, some on a prior austenite grain boundary; b) intermediate-size cubioidal Ti-rich particles; c) intermediate-size spherical Nb-rich particles; d) cementite particles; e) matrix with coarsened fine precipitates, especially on lath boundaries; f) matrix with very little fine precipitates.

5-7-2. Quantitative results in the BM and the FGHAZ of Grade 100 steel

As mentioned earlier, the intermediate-size precipitates in Grade 100 steel appear to have a large variation in distribution density at different locations and sections (compare Fig. 5-23 and 5-26). This discrepancy is in addition to the problems associated with quantification by replicas discussed in Section 5-5-1. To overcome these problems, many sections should be examined in a systematic way, which is recommended for future work. The same problem applies to most of the sub-regions in the HAZ. These quantification issues make the estimation of the dissolution and coarsening based on the replica results virtually impossible for the intermediate-size particles.

Assuming that the reheating stage approaches an equilibrium condition, all the microalloying solutes in excess of the equilibrium solubilities will precipitate out as intermediate-size carbonitrides. This will leave the matrix relatively homogenous in composition with respect to the solutes dissolved in the austenite. If the amount of cold work below the no recrystallization temperature and the cooling rate during accelerated cooling were the same for all sections (which is not the case in practice), the fine precipitation in austenite and ferrite would be almost uniform. Then, one could compare the amount (volume fraction) of fine precipitates in the BM and across the HAZ, and relate that to amount of dispersion hardening.

5-7-2-1. Size distributions

In order to obtain the size distribution of the precipitates, several TEM-BF images at magnification of 100,000x were examined individually. The precipitates in each micrograph were measured point-to-point using available image analysis software. Fig. 5-43 shows the size distribution of fine precipitates in the BM. About 500 precipitates were counted over an area of ~1.69 μm^2. The average size was found to be 4.6 ± 2.4 nm. Note that the vertical axis reads "relative frequency", which is defined as the ratio of the number of particles, *n*, within a given size range, to the total number of particles counted in that region, *N*. This is important as it eliminates the main errors of quantification, originating from: a) inhomogeneous particle distribution in different regions, b) reproducibility issues related to the ability of replicas to extract precipitates representative of the true volume fraction and c) counting errors. This is well illustrated in Fig. 5-44, where the size distributions of fine precipitates in the FGHAZ–0.5 kJ/mm measured over three regions/images are shown in two ways. In Fig. 5-44a, the vertical axis shows the absolute number, *n*, while in Fig. 5-44b the relative frequency, *n/N*, is shown. Differences between the two approaches arise because one of the regions/images showed a large number of precipitates, while the other two showed moderate numbers. However, the size distributions and the average sizes obtained from these distributions were very close for all regions/images. This shows again that the replicas are not good for measuring the absolute number of precipitates (and volume fraction), while they are suitable for examining the size distribution (and average size).

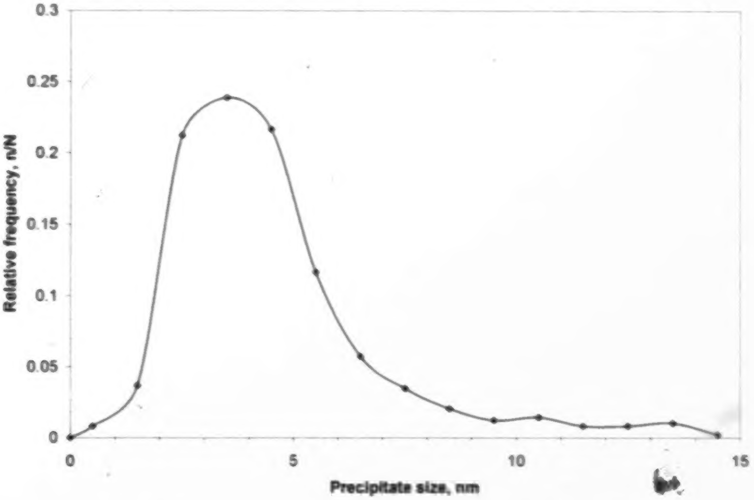

FIG. 5-43. Fine-precipitate size distribution in the BM of Grade 100 steel.

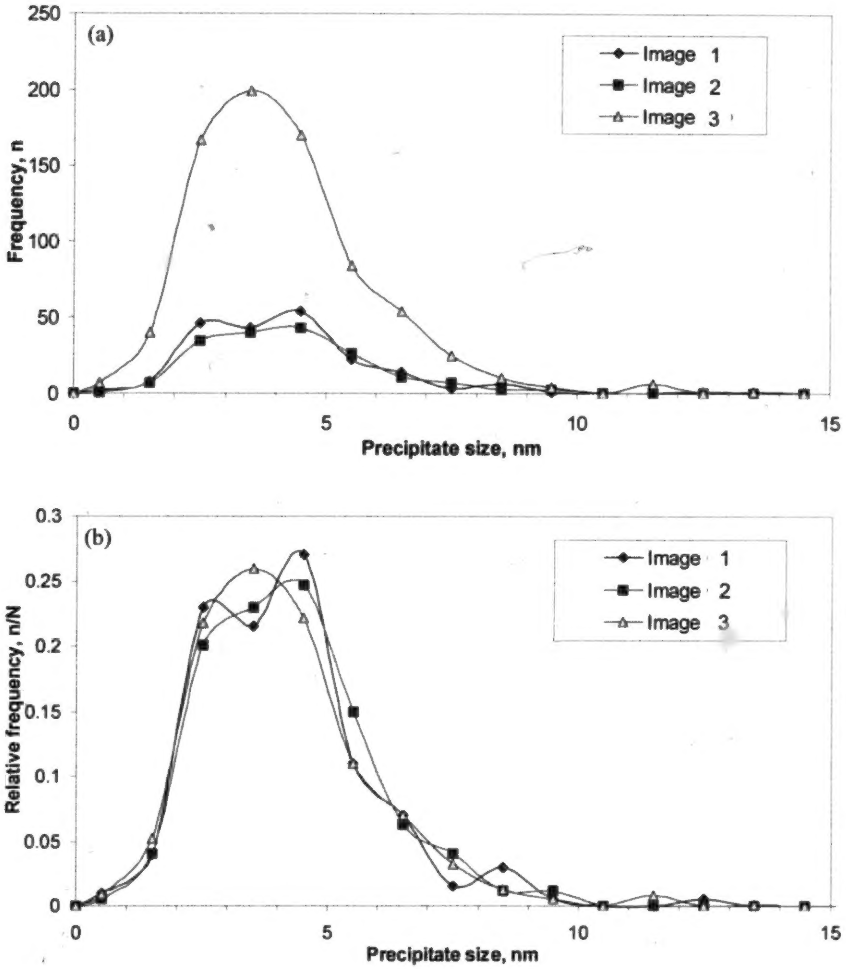

FIG. 5-44. Comparison of size distribution curves expressed in two ways: a) in absolute numbers; b) in relative numbers. The curves represent fine precipitates in the FGHAZ–1.5 kJ/mm.

The size distribution in the BM was compared with two series of samples; first of all, with those obtained from aging of the BM at different sub-critical temperatures (Section 2-4-4-3) and secondly with those from the FGHAZ (0.5–2.5 kJ/mm). The results of precipitate size measurements are summarized in Table 5-9. Fig. 5-45 shows the ageing effect on the fine-precipitate size distribution. Aging for 1 hr at 300°C does not result in any change in the distribution and the average particle size, while ageing at 600°C results in a considerable amount of coarsening. It would be interesting to use these results to find the constant *A* in Equation 5-27, and then determine whether coarsening would happen to these precipitates during the thermal cycles experienced during welding in the SCHAZ or ICHAZ (where the peak temperature is not high enough to cause dissolution). This is recommended for future work.

Fig. 5-46 shows the effect of heat input on the size distribution of fine precipitates in the FGHAZ, as compared with that of the BM. It can be readily seen that the size distributions and average sizes are similar. This result suggests that the strengthening contributions from the fine precipitates are virtually the same for this range of heat inputs in the FGHAZ samples.

Table 5-9. Fine-precipitate size measurements in BM (different condition) and FGHAZ (several heat inputs)

Region	n	Min (nm)	Max (nm)	Average (nm)	S.D. (nm)	95% confidence	Area covered (μm^2)
BM-AR	490	0.9	16.4	4.6	2.4	0.2	2.54
BM-300AC	731	0.9	13.8	4.3	1.9	0.1	1.69
BM-600WQ	669	0.9	12.2	5.5	1.9	0.1	1.69
FG-05	1141	0.9	13.6	4.2	1.7	0.1	2.54
FG-15	644	0.9	13.6	4.2	1.7	0.1	1.69
FG-25	850	0.9	20.4	4.5	2.4	0.2	2.54

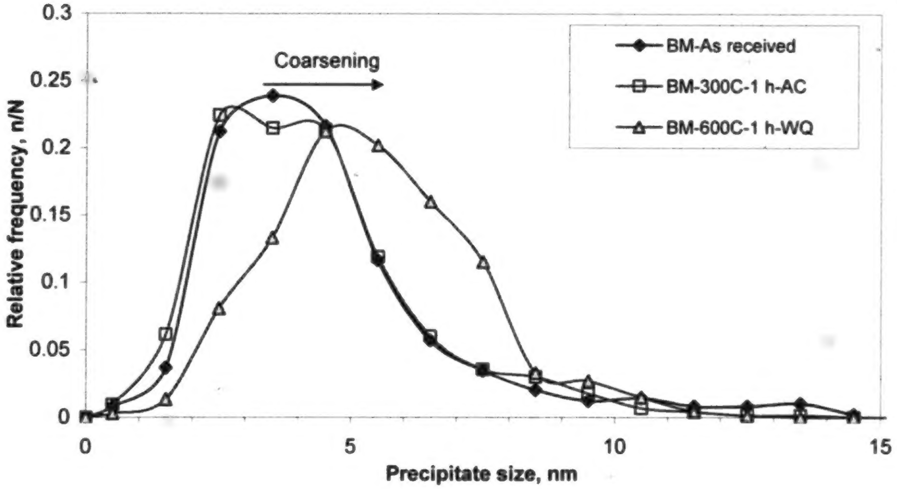

FIG. 5-45. Effect of aging on the size distribution of fine precipitates in the BM of Grade 100 steel.

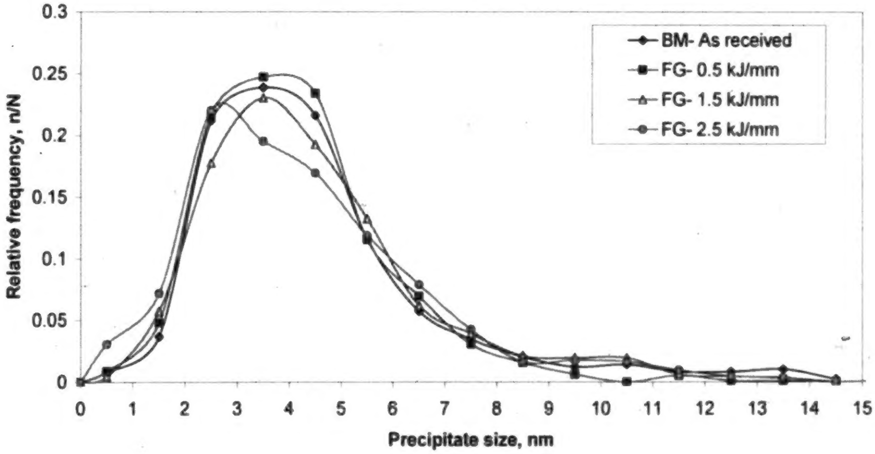

FIG. 5-46. Effect of heat input on the size distribution of fine precipitates in the FGHAZ of Grade 100 steel, as compared with the BM.

5-7-2-2. Volume fractions

As shown in Fig. 5-44, the quantification results from the replicas are not reliable for measurement of absolute precipitate numbers and volume fractions. It was also pointed out in Section 5-5-3-2 that the sampling depth for fine precipitates can be orders of magnitude larger than their sizes (Fig. 5-20), and this will lead to an overestimation of the volume fractions by orders of magnitude. Table 5-10 shows that if the correction factor suggested in Section 5-5-3-2 is applied to the volume fraction measurement of Heglund *et al.* [32], a lower-bound value for the volume fraction of fine precipitates can be found. The values in Table 5-10 were obtained by assuming values of d_P=500 nm, η=1, and x=5 nm in Equations 5-33 and 5-34. Also, note that the estimated volume fractions of fine precipitates, e.g., those that form below A_3 (Table 5-5), lie between the upper- and lower-bound values in Table 5-10.

Table 5-10. Comparison of volume fraction values for NbC (<5 nm) obtained with different assumptions

Criterion	**f_V**	**Description/Note**
Replica	8.410×10^{-3}	Heglund's [32] – overestimated
Upper bound	5.231×10^{-3}	Absolute maximum: Total carbides of Nb, Mo, Ti and V (Table 5-4)
Lower bound	0.084×10^{-3}	Proposed theory of largest particle on replica; correction factor of 5nm/500nm applied to the replica measurement
Estimated	0.626×10^{-3}	Thermodynamic results adjusted through experimental findings (Table 5-5)

5-8. Summary

In this chapter, the precipitate characteristics in the BM as well as precipitate alterations in the HAZ were determined through both calculations and experimentation. The following points can be summarized for the state of precipitation in the BM:

1) The cuboidal shape of the large TiN particles (2–8 µm) appears to be the result of ageing during reheating after casting. The precipitates that form during solidification are dendritic Ti-NbCN. Reheating causes dissolution of Nb and C and coarsening of TiN.
2) Intermediate-size Ti-rich and Nb-rich carbonitrides (50–300 nm) likely form during cooling of the austenite. Some precipitates may have formed during solidification and reheating as well. The area fraction of these precipitates was found to vary greatly from section to section, likely due to segregation during solidification and lack of homogenization in the subsequent processing stages.
3) Some fine Nb-rich carbides (<20 nm) form during rolling of the austenite below no-recrystallization temperature (strain-induced precipitation).
4) Interphase precipitation is not likely during accelerated cooling from austenite to ferrite in Grade 100 steel. Rapid cooling leaves the transformed ferrite supersaturated in solutes during transformation.
5) Fine Nb-Mo carbides (<20 nm; mostly ~5 nm), with considerable amounts of Ti and V, form at the stop cooling temperature after accelerated cooling of the ferrite. Levelling or rolling may enhance precipitation.
6) The total volume fraction of fine Nb/Mo/Ti/V carbides that form below 1000–1100°C was estimated to be $\sim 10^{-3}$, based on thermodynamic calculations adjusted by chemical dissolution results. Fine precipitates were measured to have a diameter of 5 ± 2 nm.
7) Stoichiometric relations (either with thermodynamic calculations or chemical dissolution tests) showed that the carbon level in Grade 100 steel is hyper-stoichiometric with respect to the microalloying elements. This means that the bainitic ferrite matrix will have a carbon level at the maximum possible and the excess carbon will be trapped in M-A regions or form isolated iron carbides (e.g., cementite).

The following results summarize the precipitation alterations in the HAZ as a result of the weld thermal cycle for a range of heat inputs between 0.5 and 2.5 kJ/mm:

1) Large TiN and intermediate-size Ti-rich carbonitrides do not change in most regions of the HAZ. Dissolution of these precipitates may occur only in regions of the CGHAZ very close to the fusion line. TiN may have a maximum dissolution of about 15% at the fusion line for a heat input of 2.5 kJ/mm.
2) The kinetic calculations show that the dissolution of pure NbC can start close to the FGHAZ/CGHAZ boundary; the exact location depends on the heat input. This means that the intermediate-size Ti-Nb precipitates may dissolve very little in FGHAZ. They are believed to have a limited role in austenite grain growth control. The intermediate-size precipitates, however, dissolve to a large extent in the CGHAZ, especially for higher heat inputs of 1.5 and 2.5 kJ/mm. The reprecipitation of intermediate-size microalloyed particles is suppressed in most regions as the cooling rates are high. There is some reprecipitation (in the form of fine precipitates) on the remains of the partially dissolved particles, where the solute levels are locally high especially at lower heat inputs. This leaves the austenite with higher solute levels, which in turn increases the hardenability. The difficulty in reprecipitation of microalloy carbides leads to the formation of intermediate-size iron carbides (cementite) in the CGHAZ of 1.5 kJ/mm weld sample, where the cooling rate is between that of 0.5 kJ/mm weld sample (suppression of any reprecipitation) and 2.5 kJ/mm weld sample (reprecipitation on grain boundaries).
3) The size distributions of fine carbides (<20 nm) in the FGHAZ of various weld samples (0.5–2.5 kJ/mm) showed little change from the distribution in the BM. These fine precipitates have complex compositions varying from NbC to NbTiC or NbMoTiVFeC, and likely varying solubility products. It is likely that they do not get dissolved in FGHAZ, except for a heat input of 2.5 kJ/mm at a location close to the CGHAZ or when the particles have considerable amounts of Mo and V. Those that dissolve will likely reprecipitate in the ICHAZ and FGHAZ, due to the relatively high transformation temperature for austenite to ferrite during cooling. In the CGHAZ, all fine precipitates dissolve completely, but the reprecipitation is limited within the matrix, mainly due to the relatively low transformation temperatures of austenite to ferrite. Reprecipitation is mainly at the grain boundaries for a heat input of 2.5 kJ/mm and almost totally suppressed at a heat input of 0.5 kJ/mm.
4) Coarsening of TiN does not occur in the HAZ of the Grade 100 steel, mainly due to the large size of these particles. Coarsening of the Nb carbides at temperatures lower than their dissolution temperatures (for example, in the SCHAZ, ICHAZ and FGHAZ, particularly for higher heat inputs) needs investigation.

References

[1] Ashby, M. F., and Ebeling, R., 1966, "On the Determination of the Number, Size, Spacing, and Volume Fraction of Spherical Second-Phase Particles from Extraction Replicas," AIME Met Soc Trans, **236** (10), pp. 1396-1404.

[2] Baker, T. N., 1982, "Determination of the Friction Stress from Microstructural Measurements," *Proc., Yield, Flow and Fracture of Polycrystals*, Applied Science Publishers, 1983, pp. 235-273.

[3] DeArdo, A. J., 2003, "Niobium in Modern Steels," International Materials Reviews, **48** (6), pp. 371-402.

[4] Suzuki, S., and Weatherly, G. C., 1985, "Characterization of Precipitates and Grain Growth in Simulated HAZ Thermal Cycles of Ti--Nb Bearing Steel Weldments," *Proc., HSLA Steels: Metallurgy and Applications*, J.M. Gray, *et al.*, eds., ASM International, Metals Park, pp. 675-682.

[5] Lagneborg, R., Siwecki, T., Zajac, S., and Hutchinson, B., 1999, "The Role of Vanadium in Microalloyed Steels," Scandinavian Journal of Metallurgy (Denmark), **28** (5), pp. 186-241.

[6] Palmiere, E. J., 1995, "Precipitation Phenomena in Microalloyed Steels," *Proc., ISS, Proceedings of the International Conference "Microalloying '95"*, pp. 307-320.

[7] Akhlaghi, S., and Ivey, D. G., 2002, "Precipitation Behaviour of a Grade 100 Structural Steel," Canadian Metallurgical Quarterly, **41** (1), pp. 111-119.

[8] Dutta, B., and Sellars, C. M., 1987, "Effect of Composition and Process Variables on Nb(C,N) Precipitation in Niobium Microalloyed Austenite," Materials Science and Technology, **3** (3), pp. 197-206.

[9] Gladman, T., 1997, The Physical Metallurgy of Microalloyed Steels, The Institute of Materials, London.

[10] Taylor, K. A., 1995, "Solubility Products for Titanium-, Vanadium-, and Niobium-Carbide in Ferrite," Scr. Metall. Mater., **32** (1), pp. 7-12.

[11] Easterling, K. E., 1992, Introduction to the Physical Metallurgy of Welding, Butterworth-Heinemann Ltd, Oxford.

[12] Hong, S. G., Jun, H. J., Kang, K. B., and Park, C. G., 2003, "Evolution of Precipitates in the Nb–Ti–V Microalloyed HSLA Steels During Reheating," Scripta Materialia, **48** (8), pp. 1201-1206.

[13] Jun, H. J., Kang, K. B., and Park, C. G., 2003, "Effects of Cooling Rate and Isothermal Holding on the Precipitation Behavior During Continuous Casting of Nb-Ti Bearing HSLA Steels," Scripta Materialia, **49** (11), pp. 1081-1086.

[14] Hong, S. G., Kang, K. B., and Park, C. G., 2002, "Strain-Induced Precipitation of NbC in Nb and Nb–Ti Microalloyed HSLA Steels," Scripta Materialia, **46** (2), pp. 163-168.

[15] Yan, T., Yunfeng, L., and Yunhui, W., 1990, "Precipitation Behaviour of Nb, V, Ti in Low Alloy Steels and Their Influence on Toughness," *Proc., HSLA Steels*, The Minerals, Metals and Materials Society (USA), pp. 501-505.

[16] Shiga, C., and Saito, Y., 1990, "Toughness Improvement in HAZ of HSLA Steels by TMCP in Japan," American Welding Society), pp. 177-205.

[17] Losz, J. M. B., and Challenger, K. D., 1990, "HAZ Microstructures in HSLA Steel Weldments," *Proc., First United States--Japan Symposium on Advances in Welding Metallurgy*, American Welding Society, Miami, pp. 323-357.

[18] Collins, L. E., Godden, M. J., and Boyd, J. D., 1983, "Microstructures of Linepipe Steels," Can. Metall. Q., **22** (2), pp. 169-179.

[19] Liu, W. J., Botton, G. A., Carpenter, G. J. C., Es-Sadiqi, E., and Charest, M., 1998, "A Study of the Precipitation of Nb(Cn) in Microalloyed Steels Using TEM," *Proc., Thirty First Annual Technical Meeting of the International Metallographic Society*, ASM International, Analysis of In-Service Failures and Advances in Microstructural Characterization. Vol. 26 (USA), pp. 221-224.

[20] Huang, H., Lehtinen, P., and Tiainen, T., 1997, "A TEM Thin Foil Study on Precipitate Stability in the Heat Affected Zone of a Ti and Nb Microalloyed Steel Weld," *Proc., ASM International European Conference on Welding and Joining Science and Technology*, ASM International Europe, Belgium, pp. 641-646.

[21] Mitchell, P. S., Hart, P. H. M., and Morrison, W. B., 1995, "The Effect of Microalloying on HAZ Toughness," 1995, *Proc., Microalloying '95*, Iron and Steel Society Inc, Warrendale, pp. 149-162.

[22] Avner, S. H., 1974, Introduction to Physical Metallurgy, McGraw-Hill Book Company.

[23] Bai, D. Q., and Asante, J., 2003, "Precipitation Strengthening in Low Carbon Microalloyed Steels," *Proc., Conference of Metallurgists 2003, The international symposium on transformation and deformation mechanisms in advanced high-strength steels*, M. Militzer, and W.J. Poole, eds., Metallurgical Society of the Canadian Institute of Mining, Metallurgy and Petroleum, pp. 235-244.

[24] Lu, J., Henein, H., and Ivey, D. G., 2005, "Quantification of Precipitates in Microalloyed Steels," *Unpublished Results*, Department of Chemical and Materials Engineering, University of Alberta.

[25] *JADE*. 1994, Materials Data, Inc.

[26] Ashby, M. F., and Easterling, K. E., 1982, "A First Report on Diagrams for Grain Growth in Welds," Acta Metall., **30** (11), pp. 1969-1978.

[27] Ion, J. C., Easterling, K. E., and Ashby, M. F., 1984, "A Second Report on Diagrams of Microstructure and Hardness for Heat-Affected Zones in Welds," Acta Metall., **32** (11), pp. 1949-1962.

[28] Handeland, T., Erkkila, E., and Gjonnes, J., 1986, "A Combined Electron Microscope and Optical Metallographic Study of Microstructures in High-Strength, Low-Alloy (HSLA) Steels after Welding," J. Microsc., **144** (3), pp. 251-259.

[29] Ardell, A. J., 1987, "Precipitate Coarsening in Solids: Modern Theories, Chronic Disagreement with Experiment," *Proc., Phase Transformations '87*, The Institute of Metals, 1988, pp. 485-494.

[30] Kelly, P. M., 1982, "Quantitative Electron Microscopy," Met. Forum, **5** (1), pp. 13-23.

[31] Palmiere, E. J., Garcia, C. I., and DeArdo, A. J., 1996, "The Influence of Niobium Supersaturation in Austenite on the Static Recrystallization Behavior of Low Carbon Microalloyed Steels," Metallurgical and Materials Transactions A (USA), **27A** (4), pp. 951-960.

[32] Heglund, K., He, A., and Ivey, D. G.: *Quantitative Metallography of Microalloyed Steels*. 2001, Department of Chemical and Materials Engineering, University of Alberta: Edmonton.

[33] Wagner, W., Piller, J., Degischer, H.-P., and Wollenberger, H., 1985, "Comparative FIM, SANS and TEM Study of the Cu--2 At.% Co Decomposition," Z. Metallkd., **76** (10), pp. 693-700.

[34] Degischer, H. P., Hein, W., Strecker, H., Wagner, W., and Wahi, R. P., 1987, "Quantitative Analysis of Precipitation in Nimonic Alloy Pe16," Z. Metallkd., **78** (4), pp. 237-249.

[35] Georget, D., and Peyroutou, C., 1990, "Characterization of the Gamma ' Phase in Am1 Superalloy by Image Analysis," *Proc., High Temperature Materials for Power Engineering 1990. II*, Kluwer Academic Publishers, pp. 1377-1386.

[36] Galbraith, J. M., and Howell, P. R., 1990, "Quantitative Microscopy of an Al--4.6Cu--1.1Li--0.12Zr Alloy," *Proc., Advanced Aluminium and Magnesium Alloys*, ASM International, pp. 57-64.

[37] Staron, P., Jamnig, B., Leitner, H., Ebner, R., and Clemens, H., 2003, "Small-Angle Neutron Scattering Analysis of the Precipitation Behaviour in a Maraging Steel," Journal of Applied Crystallography (UK), **36** (Part 3, Number 1), pp. 415-419.

[38] Bourhettar, A., Hazotte, A., and Troyon, M., 1995, "Atomic Force Microscopy Imaging to Measure Precipitate Volume Fraction in Nickel-Based Superalloys," Mater. Charact. (UK), **34** (4), pp. 265-270.

[39] Madden, P. K., and Callen, V. M., 1983, "The Variation of Gamma Prime Particle Size and Volume Fraction in Nimonic PE16 Aged at 700 Deg C," J. Mater. Sci., **18** (11), pp. 3363-3376.

[40] Kallqvist, J., and Andren, H. O., 2000, "Development of Precipitate Size and Volume Fraction of Niobium Carbonitrides in Stabilised Stainless Steel," Materials Science and Technology (UK), **16** (10), pp. 1181-1185.

[41] Hattestrand, M., and Andren, H.-O., 1999, "Quantitative Evaluation of Particle Size Distributions of Different Phases in Steel P92 Exposed at 600 Deg C and 650 Deg C Using EFTEM," *Proc., 5th International Conference on the Microstructure of High Temperature Materials*, Institute of Materials, Quantitative Microscopy of High Temperature Materials (UK), 2001, pp. 331-344.

[42] Hattestrand, M., and Andren, H.-O., 2001, "Influence of Strain on Precipitation Reactions During Creep of an Advanced 9% Chromium Steel," Acta Materialia (USA), **49** (12), pp. 2123-2128.

[43] Hofer, P., Miller, M. K., David, S. A., and Cerjak, H., 2000, "Atom Probe Field Ion Microscopy Investigation of Boron Containing Martensitic 9% Chromium Steel," Metallurgical and Materials Transactions A (USA), **31A** (3A), pp. 975-984A.

[44] Haasen, P., 1985, "The Early Stages of the Decomposition of Alloys," Metall. Trans. A, **16A** (7), pp. 1173-1184.

[45] Abis, S., Caciuffo, R., and Coppola, R., 1987, "Small Angle Neutron Scattering Investigation of Mg Sub 2 Si Precipitates in a Single Crystal of an Al--Mg--Si Alloy," Mater. Sci. Forum, **13-14**, pp. 295-299.

[46] Deschamps, A., Militzer, M., and Poole, W. J., 2001, "Precipitation Kinetics and Strengthening of a Fe-0.8 Wt% Cu Alloy," ISIJ International, **41** (2), pp. 196-205.

[47] Preuss, M., Pang, J. W. L., Withers, P. J., and Baxter, G. J., 2002, "Inertia Welding Nickel-Based Superalloy: Part I. Metallurgical Characterization," Metallurgical and Materials Transactions A (USA), **33A** (10), pp. 3215-3225A.

[48] Grosdidier, T., Hazotte, A., and Simon, A., 1998, "Precipitation and Dissolution Processes in Gamma / Gamma ' Single Crystal Nickel-Based Superalloys," Materials Science and Engineering A (Switzerland), **256** (1-2), pp. 183-196.

[49] McCall, J. L., and Boyd, J. E., 1968, "Quantitative Metallography of Dispersion-Strengthened Alloys from Extraction Replicas-- Volume Fraction and Interpartical Spacing," *Proc., the Annual Technical Meeting of the International Metallographic Society*, pp. 153-155.

[50] Seher, R. J., James, H. M., and Maniar, G. N., 1971, "Quantitative Metallography of the Age Hardening Precipitate in Superalloys by Replica Electron Microscopy," *Proc., stereology and quantitative metallography*, ASTM, Philadelphia, pp. 119-137.

[51] Ruhle, M., 1995, *Transmission Electron Microscopy*, in ASM Handbook. Vol. 9. Metallography and Microstructures, ASM International, Materials Park, OH, pp. 103-122.

[52] Baker, T. N., and Duckworth, S. P., 1981, "Transition Metal Carbides in Low-Alloy Steels," *Proc., Quantitative Microanalysis With High Spatial Resolution*, The Metals Society, 1982, pp. 73-79.

Chapter 6

Phase Transformations and Grain Growth in the HAZ

6-1. Introduction

The iron matrix microstructural changes in the HAZ can be studied in terms of two aspects: phase transformations and grain size alteration. These two aspects have the most important effects on mechanical properties. Identification of the various phases, which are present at any location in the HAZ and vary across the HAZ, and measurements of the grain size across the HAZ will help understand some property changes (such has hardness and strength) and permit prediction of some others (such as fracture properties). TEM, both with thin foils and replicas, is an essential tool for this purpose.

The objective of this chapter is examination of the iron matrix microstructure (phase identification and grain size measurement) in the BM and the various regions of the HAZ (heat inputs of 0.5–2.5 kJ/mm). Twin formation in the HAZ is one of the specific subjects that will be examined. First, various aspects of the phase transformations (especially transformation products of austenite decomposition during cooling) and fundamentals of grain growth in the HAZ, collected from the literature, will be reviewed.

6-2. Phase transformations

Phase transformations during the weld thermal cycle consist of two separate parts: a) reaustenitization during the heating leg of the thermal cycle and b) retransformation from austenite to other products such as ferrite, bainite and martensite during the cooling leg of the thermal cycle. The HAZ microstructural changes during welding are not the same as those during hot rolling or heat treatment of steels, as non-equilibrium conditions and steep temperature gradients, induced by very rapid local heating during welding, cause very different conditions from those occurring in steel production [1]. The large prior austenite grain size (PAGS) developed during heating in the CGHAZ will increase hardenability so much that the CCT diagrams developed in steelmaking (e.g. Fig. 6-1), by austenitization at temperatures ~800–900°C, cannot be used [2]. Weld CCT diagrams are based on very high austenitizing temperatures, e.g., 1350–1400°C, which correspond to the CGHAZ [3]. For all these reasons, the microstructural changes and the phases developed across the HAZ can be very diverse, and variable from location to location.

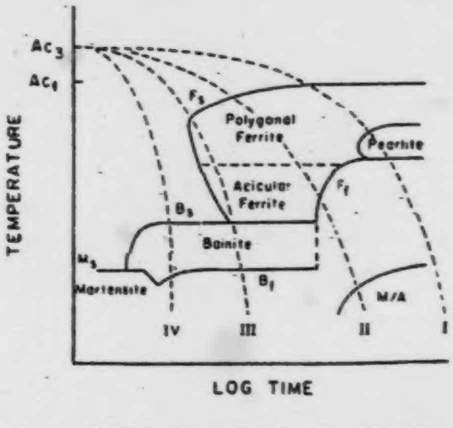

FIG. 6-1. A schematic CCT diagram for microalloyed linepipe steels [4].

6-2-1. Reaustenitization

As the temperature increases, both the driving force for austenite nucleation and the diffusion rates increase simultaneously, hence increasing the rate of transformation progressively [5]. This is in contrast to the case of transformation during cooling where the driving force and diffusion rates change in opposite directions, and as a result transformation curves have a C-shape.

The implication of a high heating rate is that the $\alpha \rightarrow \gamma$ transformation occurs at temperatures higher than the equilibrium temperature (A_1), predicted by the Fe-Fe_3C phase diagram. This means that ferrite can be substantially superheated before the transformation. Moreover, the dissolution of cementite (if present in the BM) will occur at higher temperatures, and austenite homogenization, with respect to carbon concentration, will require very high temperatures or relatively long periods of time [3].

The effect of heating rate on austenitization will be discussed in Section 6-3-5, from a *diffusional* nucleation and growth point of view. It should be added here that there also exists another theory for reaustenitization during the fast heating of welding. It was suggested [6] that rapid heating ($200–300°Cs^{-1}$ or more) may lead to a "reverse martensitic transformation" of $\alpha \rightarrow \gamma$ in some cases, and the resulting transformation induced deformation may accelerate grain growth. In this case, the precipitates cannot have any major effect on the growth rate. Rasanen and Tenkula [6] suggested that heating rates in the 800–1100°C range should be reduced, so that the $\alpha \rightarrow \gamma$ transformation could occur by a normal diffusional process.

Regardless of how the austenite forms, there are two factors about it that affect the final structure: first its grain size and second its effective composition. It is well known that large prior austenite grains provide fewer nucleation sites for ferrite, which will result in fewer ferrite grains and a coarse final matrix grain size. The "effective austenite composition" changes across the HAZ as well [4]. This is due to the non-uniform dissolution of carbides and nitrides, which was analysed in detail in Section 5-4-1. Both the PAGS and the effective composition of austenite have a great influence on hardenability, i.e., the tendency to form hard phases like bainite and martensite [7].

6-2-2. Retransformation

The HAZ microstructure is determined by many factors, such as the chemical composition of the steel, the austenite grain size, the cooling rate in the thermal cycle and the localized inclusion content [1]. The HAZ microstructure normally consists of a mixture of some constituents. Those constituents which result from austenite transformation, also known as primary transformation products (like different types of ferrite), as well as those related to the carbon-rich regions, known as secondary transformation products (like bainite and martensite-austenite), are discussed here, in order of decreasing transformation temperature. It should be noted that steel structures are very diverse and their classifications are controversial. Although the advent of low carbon HSLA steels has introduced low-carbon structures, not exactly falling under the classic categories, the controversies regarding the names of the products as well as the concepts and nature of the transformation are not anything new. It was about 80 years ago that martensite was thought to be the first and incomplete stage of transformation of austenite to pearlite, and that quenching would interrupt this transformation [8]. Although many of the basic concepts are now clarified, there still exists a great deal of confusion, in particular around the structures between those of martensite and polygonal ferrite (i.e., massive ferrite, acicular ferrite, Widmanstatten ferrite, bainitic ferrite, upper bainite, lower bainite, etc.).

6-2-2-1. Ferrite

Ferrite (bcc iron) is the most stable phase resulting from austenite transformation during cooling. Depending on the cooling rate, PAGS and chemical composition, various types of ferrite can be formed that vary in transformation temperature, location and type of nucleation, growth mechanism, shape, internal structure and carbon content.

1) Polygonal ferrite

Polygonal ferrite (PF) is an equiaxed structure developed normally at low rates of cooling (Fig. 6-2). This structure has a low density of dislocations, as few dislocations are introduced during the transformation to PF and many will be removed by rearrangement and annihilation at high temperature [4]. A morphological characteristic of PF is that each grain has a distinct grain boundary. Also the prior austenite grain boundary may not be discernable anymore in the final structure.

2) Grain-boundary ferrite

Grain-boundary ferrite (GF), also referred to as allotriomorphic ferrite or proeutectoid ferrite, nucleates at the corners of austenite grain boundaries, as the temperature falls below A_{C3}. The ferrite grains further grow into the austenite "behind a planar incoherent front" [1]. This is how grain boundary allotriomorphs are formed. They appear elongated or granular along the prior austenite grain boundaries

(Fig. 6-3) [1]. Decreasing the cooling rate will result in a gradual change from elongated to polygonal form. Some researchers [9] distinguish between these two forms by referring to the former as grain-boundary allotriomorphic ferrite and the latter as grain-boundary polygonal ferrite. Grain-boundary ferrite is usually discerned when the PAGS is large, in which case the microstructure inside the austenite grain is different.

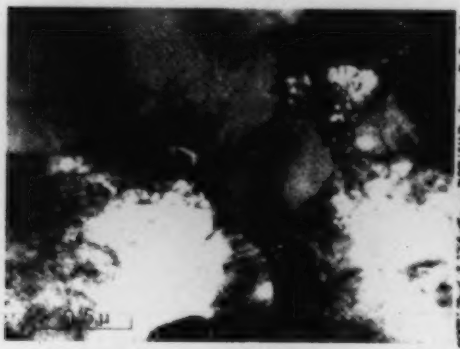

FIG. 6-2. Polygonal ferrite (PF) in a 0.18%C-1.86%Mn-1%Si-0.73%Mo steel [10].

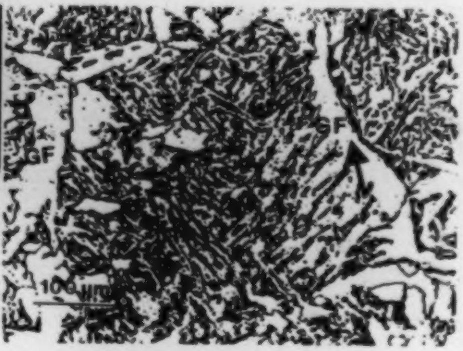

FIG. 6-3. Grain boundary ferrite (GF) in the coarse-grained HAZ of a V-Ti microalloyed steel [1].

3) Massive Ferrite

Massive ferrite (MF) is a structure that forms by short-range diffusion. It is free from carbides and has a dislocation density between that of PF and martensite. The grain boundaries of MF are not very distinct (Fig. 6-4) and the prior austenite grain boundaries can be noted, as MF presumably nucleates within the grains [10].

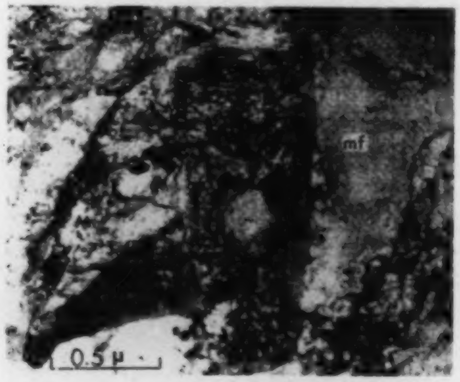

FIG. 6-4. Massive ferrite (MF) in a plain C-Mn steel (0.18 %C and 1.86 %Mn) [10].

MF may be present in the microstructure of quenched low-carbon steels, if the cooling rate is not very high (e.g., 10^4 °Cs^{-1} or less) or the carbon content is low (e.g., <0.013%). Speich and Warlimont [11] showed that carbide can precipitate in MF after aging at room temperature. MF has the same carbon concentration as quenched austenite, while the dislocation density that could accommodate the higher than equilibrium carbon level is not that high. Lath martensite and internally twinned martensite replace MF with increasing cooling rate, increasing carbon content, some alloying elements and increasing prior austenite grain size.

4) Widmanstatten Ferrite

At intermediate cooling rates or undercooling, ferrite is prone to grow bilaterally as plates or laths from the prior austenite grain boundary or within the austenite grain (Fig. 6-5a). These plates/laths, known as Widmanstatten sideplates, have a Kurdjumov-Sachs (K-S) orientation relationship with austenite (Equations 5-6 and 5-7). As the sideplates grow thicker, rejected carbon increases the carbon concentration in the space between the sideplates, and this will lead to formation of pearlite or carbide aggregates at temperatures below A_{C1} [1, 12]. Widmanstatten ferrite (WF) formation occurs as a mixed displacive and diffusional mechanism, as shown schematically in Fig. 6-5b. The schematic shows the stages of the formation of WF sideplates from an austenite grain boundary. Nucleation is via a diffusional manner with a K-S orientation relationship (OR). The side-plates then grow in an edgewise direction by a displacive mechanism. The thickening of the laths, however, takes place by "the coalescence of the sub-laths and the diffusional migration of ferrite/austenite interfaces" [13].

WF can be similar to bainite or bainitic ferrite in terms of formation mechanisms, morphology and crystallography. The main distinction between WF and bainite is the transformation temperature, which is higher for the former. In addition, WF laths are usually terminated at a GF allotriomorph, while the bainitic ferrite (or bainite) laths nucleate directly at an austenite grain boundary [13].

Surface relief studies [13] have shown that in order to produce a WF lath, several sub-laths in a common growth direction form side-by-side. These sub-laths have opposite shape strain directions, reducing the total elastic strain that should be accommodated both in the austenite and the ferrite.

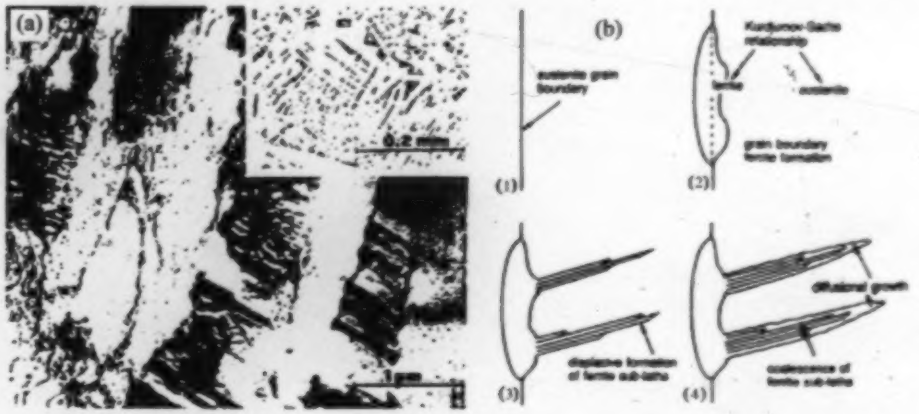
(a)
0.2 mm
1μm
(b)
austenite grain boundary
(1)
Kurdjumov-Sachs relationship
ferrite
austenite
grain boundary ferrite formation
(2)
displacive formation of ferrite sub-laths
(3)
diffusional growth
coalescence of ferrite sub-laths
(4)

FIG. 6-5. Widmanstatten ferrite (WF): a) a thin-foil TEM image showing WF and pearlite [1]; b) Schematic illustration of WF formation [13].

4) Acicular ferrite

Acicular ferrite (AF) is a highly substructured, fine irregular ferrite transformed from austenite at low temperature just above the bainite start temperature (Fig. 6-6a). This non-polygonal ferrite is formed by a combination of diffusion and shear modes, at cooling rates higher than those of other types of ferrite [1, 4].

After grain boundaries are filled with proeutectoid allotriomorphic ferrite, AF forms in two stages. First, large primary plates of ferrite nucleate within grains at inclusions, and then small side arms nucleate and grow from the primary plates [1].

Since AF with this morphology needs inclusions for nucleation (Fig. 6-6b), some researchers [1] believe that it is not expected to be observed in the HAZ of HSLA or microalloyed steels, as there is normally a low density of inclusions present. They believe there must be other explanations or mechanisms involved in formation of AF in the HAZ of microalloyed steels. Japanese researchers have shown that addition of titanium oxides during steelmaking will help AF form on the complex inclusions containing

Ti_2O_3, which are very stable even at very high temperatures [1]. In fact, some believe that AF is WF intragranularly nucleated on oxide inclusions or nitride particles [14]. This actually sounds reasonable.

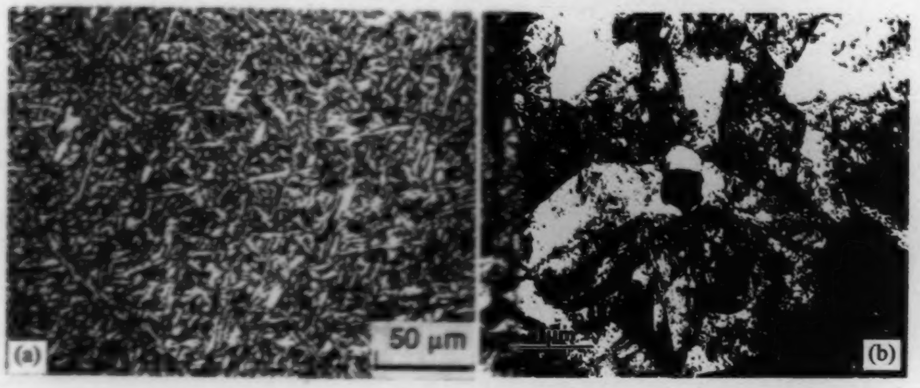

FIG. 6-6. Acicular ferrite showing: a) the "basket weave" structure [5]; b) nucleation on an inclusion using thin foil TEM [1].

5) Ferrite with aligned second phase/M-A-C

Ferrite with aligned second phase (martensite/austenite/carbide) is a lamellar structure [14] similar to what some researchers refer to as bainitic ferrite or upper bainite, on the basis of optical micrographs [6, 15]. Fig. 6-7 shows this microstructure in a ferritic steel [14]. Apparently, those who find exact identification and classification of different bainitic structures (bainitic ferrite, granular bainite, acicular ferrite/bainite, upper bainite and lower bainite) difficult and confusing or prefer to avoid it due to various terminologies, use a general term "ferrite with aligned second phase" [9].

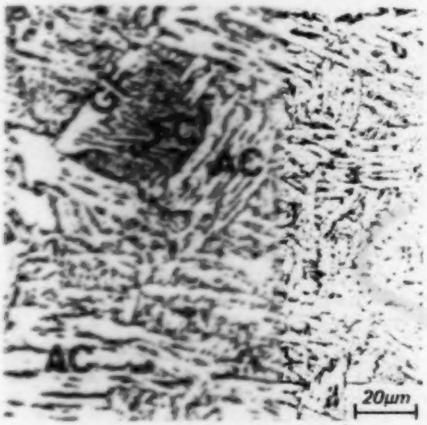

FIG. 6-7- ferrite with aligned second phase (AC) [14].

6-2-2-2. Pearlite

The normal pearlite, which is a lamellar mixture of ferrite and cementite, is formed on very slow cooling, which is not often found in welding. Therefore, this phase is not usually expected in the HAZ microstructure, though under some conditions, this phase also may be present. Moreover, low carbon levels and the presence of carbide formers in most microalloyed steels reduce the chance of formation of pearlite.

Nevertheless, "degenerate pearlite", also known as ferrite-cementite aggregate (a mixture of ferrite and cementite without a definite morphology or order), may be found in the HAZ microstructure [16].

6-2-2-3. Bainite

The pioneering work that shed light on the formation of bainite is that of Davenport and Bain in the late 1920's [17]. As Bhadeshia [18] tells the story, Davenport and Bain discovered a new microstructure that consisted of an "acicular, dark etching aggregate", dissimilar to either pearlite or martensite. They called it "martensite-troostite". This microstructure was named "Bainite" in 1934 by the staff of the United States Steel Corporation, in honour of their colleague E.C. Bain, who inspired the studies. Bainite can be considered as "a non-laminar aggregate of ferrite and cementite" that forms during austenite decomposition at temperatures below that of pearlite [19]. Nevertheless, many researchers find it very difficult and controversial to define bainite, and to identify it when it is part of a mixed microstructure [1].

A distinguishing feature between bainite and acicular ferrite structures, apart from the location of nucleation, is the prior austenite grain boundaries that are retained in the former but not distinguishable in the latter microstructures. This is also why the properties of the bainitic steels can be related to the prior austenite grain size [4]. This method is, of course, for distinguishing between fully bainitic and fully acicular ferrite microstructures. In a bainitic structure with some acicular ferrite, the prior austenite grains are still distinguishable and the properties are likely something between the two.

The factors contributing to the strength of bainite include a small grain size (lath size), carbide distribution (depending on size and location), a relatively high dislocation density and carbon supersaturation. The lath thickness (~0.5–2.0 μm) causes significant strengthening when considered in the context of the Hall-Petch equation. The packet size, found to be smaller than the PAGS but directly proportional to it, constitutes the unit cleavage length [5].

Although some researchers still deem it sufficient to use "Mehl's original classification of bainite to upper bainite and lower bainite" [20], in general, others believe that decomposition of austenite in the temperature range of bainite leads to the formation of three types of bainite in HSLA steels [21, 22]. These will be reviewed briefly below.

1) Granular bainite

In welded joints, as well as in continuously cooled microstructures in modern high-strength steels, a special type of bainite can be observed that was referred to in the late 1960's by Habraken and Ekonomopoulos (as cited in [22]) as granular bainite (GB). GB deteriorates the toughness of the welded joint. GB is essentially massive ferrite (MF) coexisting with "granules" or islands of M-A constituents (i.e., high-carbon twinned martensite and/or retained austenite) [10]. Although early researchers described MF to be free of carbides, other works [23] showed the presence of discrete, fine cementite particles both in MF and the granules. This is probably due to natural aging and precipitation of cementite in MF [11]. Samuel [21] reported a kind of GB, consisting of MF and granules of bainite laths (Fig. 6-8), on normalizing an HSLA steel with 0.11 %C, 1.5 %Mn, 1 %Cr, 0.25 %Mo and 0.003 %B. They found a high dislocation density and discrete, fine cementite particles in both constituents. Hrivnak [22] examined the structure of M/A granules and found that the martensite part can be either dislocated lath martensite or internally-twinned plate martensite, and that cementite can form from both the retained austenite constituent and the autotempered martensite constituent. Reduction of carbon in modern HSLA steels and application of high heat inputs (which reduce the cooling rate) favour the formation of this type of bainite [22].

2) Upper bainite

Upper bainite is the product of a relatively high transformation temperature (in comparison with lower bainite). In upper bainite, carbides are formed between the ferrite laths. As ferrite laths grow during the transformation, carbon is driven into austenite ahead of γ/α interface. Finally, the carbon-rich austenite may be transformed to cementite along the lath boundaries, transformed to martensite, or even retained in the final structure [1]. The cementite particles have an OR with the ferrite named after Bagaryaskii [19].

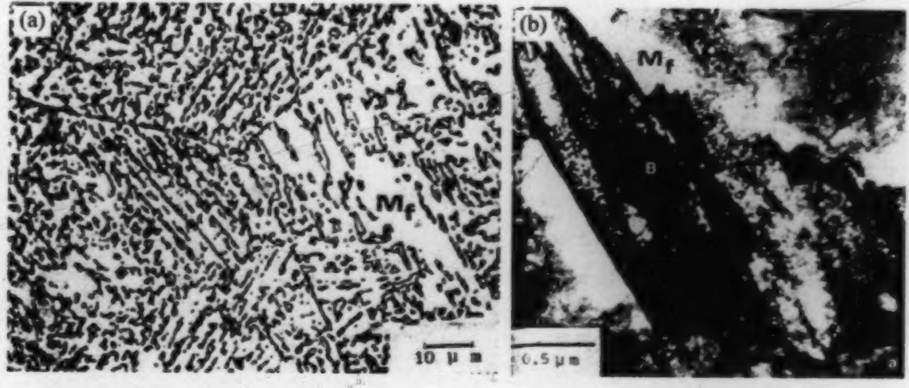

FIG. 6-8- Granular bainite in a low-C HSLA steel [21]: a) OM; b) TEM showing bainite laths (B) coexisting with massive ferrite (MF).

3) Lower bainite

Lower bainite forms at lower transformation temperatures and the carbides are enclosed entirely within the ferrite laths/plates [1]. The carbides have sharp angles to the boundaries. Fig. 6-9 shows upper and lower bainite in HSLA steels.

4) Other morphologies and terminologies

Bainite is usually described in terms of two features: (1) ferrite lath/plate size and shape and (2) carbide size, location and distribution. The latter is the basis of distinction between upper and lower bainite in classical definitions [1]. However, Ohmori *et al.* [13] believe that bainite should be instead classified by ferrite morphology, i.e., whether it is lath-like or plate-like. Fig. 6-10 shows both lath-like and plate-like morphologies of ferrite formed by isothermal holding of a 0.2%C-3.6%Ni steel at 400°C for 1000s, with cementite within the matrix, after Joarder and Sarma [19]. Both microstructures could be considered lower bainite according to the classic definitions. According to Ohmori *et al.* [13], the morphological transition between lath-like and plate-like ferrite takes place at ~350°C in Fe-C binary alloys. This temperature, coinciding with the martensite-start temperature, corresponds to the change from lath-like to plate-like morphology with increasing carbon content and is believed to have a metallurgical significance. However, it is not clear from the literature (e.g., the paper of Ohmori *et al.* [13]) what distinguishes laths from plates in the first place.

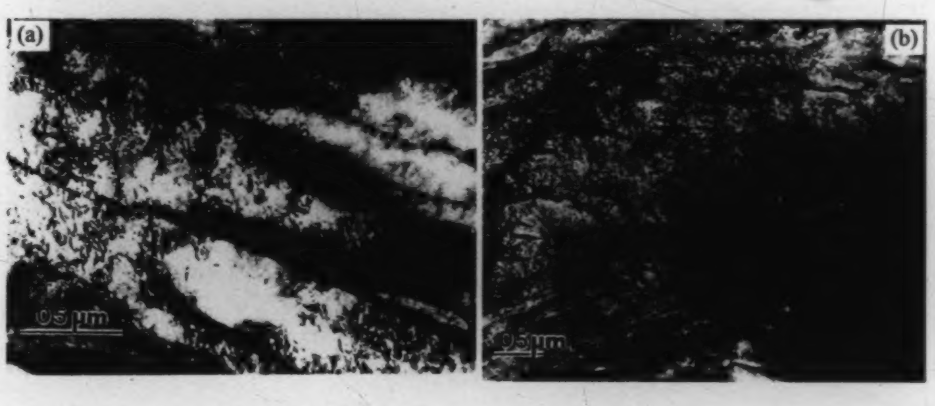

FIG. 6-9. TEM images showing: a) upper bainite; b) lower bainite [1].

In addition to the three distinct types of bainite mentioned above, there are some other morphological forms, such as "nodular bainite" and "inverse bainite", that were reported in high-carbon steels [19]. In fact, there has been a great deal of study on bainite and it has been further classified to several kinds with specific designations (e.g., BI to BIV [24]), which is beyond the scope of this survey. It should be added that the term "bainitic ferrite" is used to refer to the bainite structure in very low carbon steels, where the cementite particles may be too small and sparse to be observed or even non-existent [1, 4]. According to some definitions bainitic ferrite is a "carbide-free" bainite [20]. Bainitic ferrite is formed at relatively high temperatures in the range between B_s and M_s (the range of formation of bainite) [13].

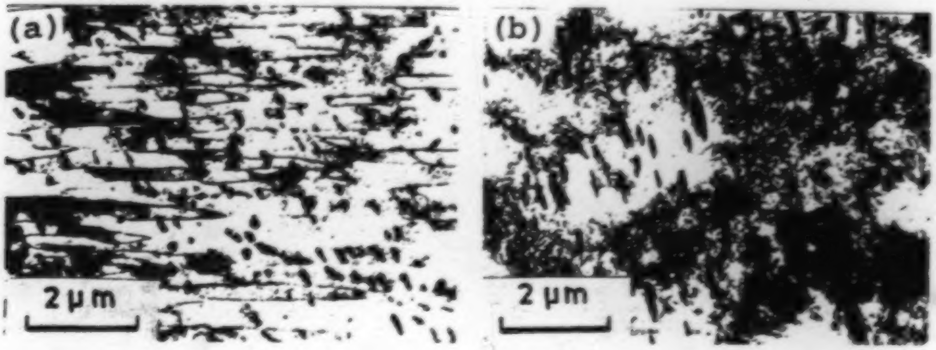

FIG. 6-10. TEM- BF images of a 0.2%C-3.6%Ni steel isothermally transformed at 400°C for 1000s, showing two ferrite morphologies: a) lath-like; b) plate-like [19].

6-2-2-4. Martensite

Martensite (M) is formed from carbon-enriched austenite by shear mechanisms during very fast cooling. The shear mechanism can be further divided into "primary shear + gliding (slip)" in low-carbon M or "primary shear + twinning" in high-carbon M [6]. Martensite has a *bct* (body-centred tetragonal) structure, which will approach *bcc* (body-centred cubic) in low carbon steels. The martensitic transformation from austenite starts from a plane, called a "mid-rib". The planes above and below the mid-rib shear and displace, but the mid-rib remains in its original location with respect to the parent austenite. The mid-rib may have a distinctive fine structure. The plane crystallographically coincides to a plane of the austenite called the "habit plane" [25]. The OR between M and the parent austenite is such that the close-packed rows and close-packed planes of the *bct* (or *bcc*) martensite and *fcc* austenite are parallel. Propagation in the perpendicular-to-plate direction ceases when the cross-section reaches a certain length-to-width ratio, because of strain-energy effects or cessation of interface mobility [25].

An important characteristic of martensite is its start temperature (M_S). It reflects how much driving force is needed to initiate the shearing in the $\gamma \rightarrow \alpha$ transformation. The higher the carbon (and other alloying elements) in solid solution with γ, the higher the strength or shear resistance of the matrix, and therefore the greater the driving force (i.e., undercooling) that will be required (Fig. 6-11). The martensite finish temperature, M_f, is approximately 120°C below M_S [25]. From the graph, M_S should be roughly around 500–520°C for Fe-0.08%C (e.g., Grade 100 steel). This makes M_f approximately 380–400°C. Note that somewhat lower temperatures can be found in other reports.

Martensite is sometimes accompanied with retained austenite in some locations in the microstructure of HSLA steels. This is sometimes referred to as one constituent, called martensite-retained austenite (M-A), as it is also difficult and/or unnecessary to separate them. The occurrence of M-A depends on composition (Mn, Mo and to a lesser extent Nb) and cooling rate [16]. M-A is known to reduce the toughness [16, 26].

The two main types of M in ferrous materials are lath martensite and plate martensite, which will be briefly reviewed in the following sections. There is also a third type, called sheet martensite (consisting of thin-sheet units), observed in certain high alloy steels [25].

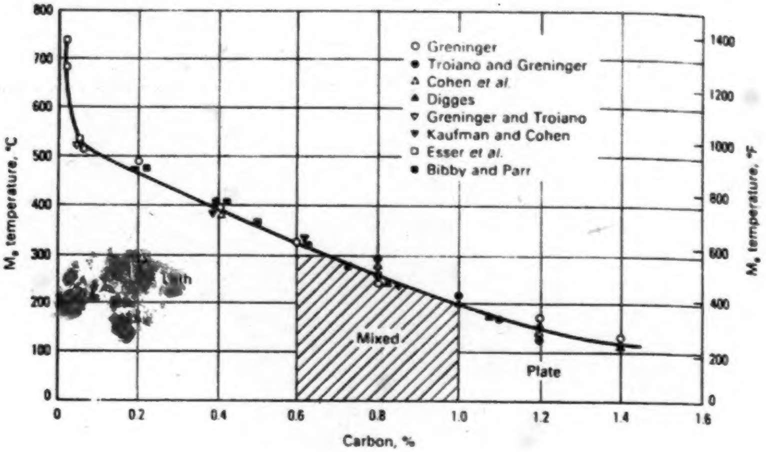

FIG. 6-11. Martensite start temperature (M_s) as a function of carbon content in steels [25].

1) Lath martensite

Lath martensite (LM), also known as "massive martensite" or "packet martensite", consists of lath-shape units grouped in sheaves or packets. It has a morphology that is acicular or "needle-like" in 2D and lath or plate shape in 3D [25]. Fig. 6-12 shows optical and TEM micrographs of lath morphology in a 0.03%C-2%Mn steel. Note that the laths have a high dislocation density. Some investigators [27] consider three basic morphologies for lath martensite, i.e., convergent, parallel and large laths. Mean lath widths can be around 0.2–0.4 µm.

Kelly [28] has reviewed the crystallography of LM in steels. He used a theory based on double lattice invariant shear to explain/predict all known crystallographic features of lath martensite, i.e., the habit planes, the OR's, the shape strain, the internal substructures and the interface dislocations. Briefly it can be said that LM forms in low-carbon, low-alloy steels. It has a small size compared with plate martensite, normally shows no sign of internal twinning, and has a substructure consisting of a dense tangle of dislocations, with $a/2[11\bar{1}]$ screw dislocations dominant. Packets or bundles consist of parallel laths. Adjacent laths are mostly misoriented (2-3°) and sometimes twin-related, relative to each other, in a packet. LM has a characteristic long direction parallel to $\langle 111\rangle_M$ (i.e., $\langle 110\rangle_A$). The OR of lath martensite with parent austenite in low-carbon steels is close to K-S (Equations 5-6 and 5-7), with habit planes close to $(557)_A$ or $(223)_A$ (i.e., 9-12° from $(111)_A$). The theory also predicts that almost twin-related laths can form within a packet and this provides mutual accommodation of the shape strain that is of magnitude of 0.3 or greater [28].

Due to similarities of lath martensite and upper bainite in appearance, it was suggested that lath martensite should be considered as "incomplete transformed upper bainite" [1]. In some regions of the HAZ with a high local concentration of carbon, M-A constituents had a twinned substructure. The presence of twinned regions is assumed to be indicative of carbon levels >0.5% and these regions are considered to be quite brittle [29]. LM can even be produced in high-purity iron by extremely rapid quenching or shock loading [25].

2) Plate martensite

Plate martensite (PM) consists of "individual, lenticular, plate-shape units" [25]. It forms in medium and high-carbon steels, Fe-Ni and Fe-Bi-C alloys, and has a *bct* crystal structure. Fig. 6-13a shows a region of mixed lath and plate martensite in a medium-carbon (0.57%C) steel. The plates are marked with *P*. Fig. 6-13b shows a thin-foil TEM micrograph of one of the regions of PM marked in Fig. 6-13a. The microstructure consists of plates with fine internal twins (6–10 nm spacing). The twins do not extend to the sides of the plate. They degenerate into "complex dislocation arrays". They have habit planes of $(225)_A$ or $(259)_A$ [25]. The presence of twinned martensite is usually associated with low toughness properties [30].

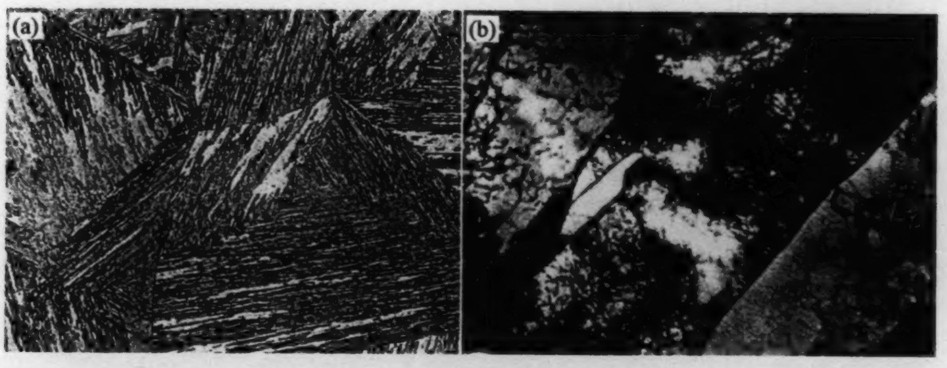

FIG. 6-12. Lath martensite (LM) in a low-carbon steel (0.03%C, 2%Mn) : a) OM (100x); b) thin-foil TEM (26000x) [25].

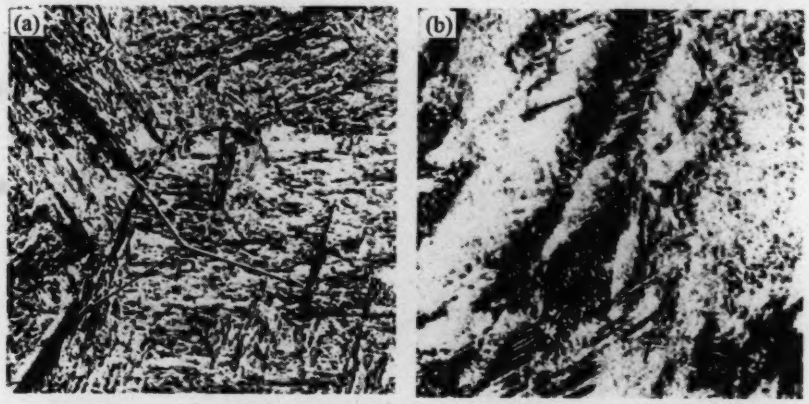

FIG. 6-13. Plate martensite (PM) in a medium-carbon steel (0.57%C): a) OM showing PM, marked *P*, (1000x); b) Thin-foil TEM image showing twinned substructure in a region marked in (a) at a higher magnification (26000x) [25].

3) Autotempered martensite

Autotempered martensite is a special martensite, which can be found in low carbon steels with high martensite-start (M_S) temperatures. In this structure, iron carbide precipitates within the laths (autotempering), and therefore this phase is more ductile than upper bainite. However, this only occurs when carbide precipitation can take place, otherwise the structure becomes fully martensitic [1].

The only minute difference between autotempered martensite and lower bainite is that cementite particles show more than one crystallographic variant in the former (Fig. 6-14). Except for this, the two microstructures are difficult to tell apart even with TEM [1].

3) Other classifications

Martensite is sometimes categorized according to the mode of deformation, in which case it is referred to as “slipped martensite” vs. “twinned martensite” [31]. It seems to be “illogical” to some researchers [31] to mix two criteria and compare, e.g., lath martensite (morphological classification) with twinned martensite (mode-of-deformation classification).

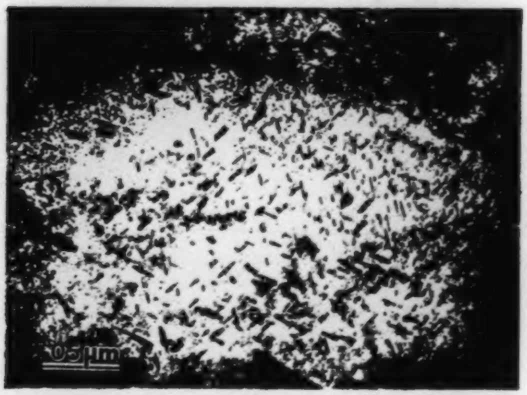

FIG. 6-14. Autotempered martensite in the coarse-grained HAZ of a low-carbon, low-alloy steel weldment [1].

Note that although LM and slipped (dislocated) martensite are observed often for low levels of carbon while PM and twinned martensite are observed for high levels of carbon, the morphological and deformational classifications do not coincide exactly. Many researchers have reported an overlap of these, e.g., internally twinned lath martensite [27, 32] or untwinned plate martensite [31, 33]. Considering this, Yu *et al.* [34] have classified martensite in plain carbon steels into four groups, based on transformation temperatures and the effect of carbon level (Fig. 6-15):

I. Fully dislocated M (e.g., dislocated LM)
II. Half-dislocated M (e.g., twinned LM)
III. Half-twinned M (including twinned PM, butterfly M, lenticular M, etc.)
IV. Fully twinned M (e.g., thin PM and fully twinned PM)

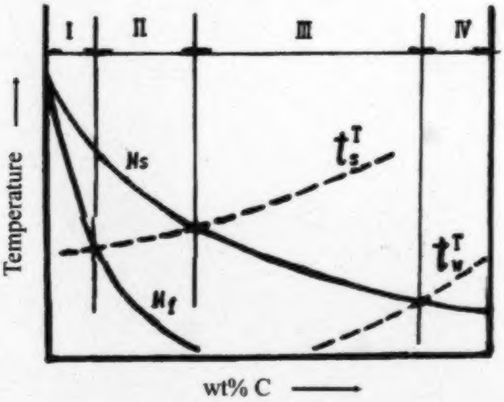

FIG. 6-15. Schematic diagram showing both starting and finishing temperature of twinning (t_s^T and t_f^T) and starting and finishing temperatures for conventional martensite transformation (M_s and M_f) as a function of carbon content [34].

6-2-3. Twinning

6-2-3-1. Introduction to twinning

Twinning is considered as the second important mechanism (after slip) by which metals deform [35]. In twinning, a portion of the crystal takes an orientation that is related to the orientation of the original matrix in a mirror symmetrical manner (Fig. 6-16). A shearing force accomplishes twinning. The plane of symmetry between the twinned and untwinned regions is called the *twinning plane*. Twinning occurs on a specific twin plane and in a specific twin direction for each crystal structure (Table 6-1). The atoms in the twinned region move in a manner that the twinned region becomes a mirror image of the untwinned region. Twinning is accompanied by surface relief on a polished surface. Note that even if this surface is polished (to section AA shown in Fig. 6-16b) the elevation is removed, but the twinned region can still be discerned after etching due to the difference in the orientations of the twinned and untwinned regions [36]. They also diffract in a symmetrical manner during electron microscopy. These are the basis of observation of twinning in OM and TEM. In fact, the surface relief on a polished surface as a result of twinning in a single crystal can be used for determination of twinning elements (plane, direction and shear strain) in a given alloy [37].

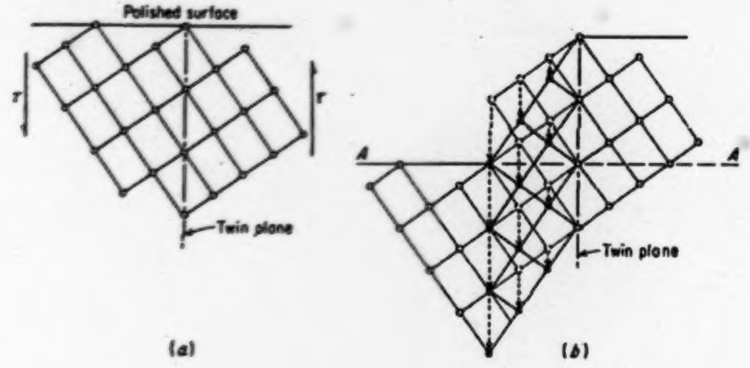

FIG. 6-16. Crystallographic demonstration of twining [36].

Table 6-1. Twin planes and twin directions for different crystal structures [36]

Crystal structure	Typical examples	Twin plane	Twin direction
bcc	α-Fe, Ta	(112)	[111]
hcp	Zn, Cd, Mg, Ti	$(10\bar{1}2)$	$[\bar{1}011]$
fcc	Ag, Au, Cu	(111)	[112]

Twinning occurs when the slip systems are restricted or when the critical resolved shear stress is increased for some reason so that the stress required for twinning is less than the stress required for slip. Also note that the time required for twinning is much shorter than the time required for slip (microseconds in the former compared to milliseconds for the latter) [36].

The energy of a twin boundary depends on the orientation of the boundary plane [38]. Fig. 6-17 shows the two kinds of twin boundaries and their corresponding energies. When the twin boundary is parallel to the twin plane a coherent twin boundary forms (Fig. 6-17a). This is a case of an undistorted, but high-angle boundary, and therefore the boundary energy is extremely low (an order of magnitude smaller than the grain boundary energy). When the twin boundary does not lie parallel to the twinning plane, an incoherent twin boundary forms (Fig. 6-17b), and the energy of this random high-angle boundary is high (almost comparable to the grain boundary energy). Fig. 6-17c shows schematically the energy of a twin boundary as a function of the deviation angle (Φ) of the twin boundary from the twinning plane [38].

Generally, twinning is believed to have three main origins: mechanical deformation, annealing and transformation [39]. There is also a fourth type (relaxation twinning) that is not discussed very much. These mechanisms are briefly reviewed in the following sections, followed by a literature review on twinning in the HAZ of steels and the effects of twinning on mechanical properties.

6-2-3-2. Different types of twinning

1) Mechanical twinning

Mechanical twinning, also known as deformation twinning or Neumann bands [40], is produced in *bcc* and *hcp* metals under conditions of high strain rate (shock loading) and low temperature. There are fewer cases of mechanical twinning in *fcc* metals. All aspects of mechanical twinning (such as crystallography, nucleation, propagation, effects on plasticity and effects on fracture) are reviewed in great detail by Mahajan and Williams [35].

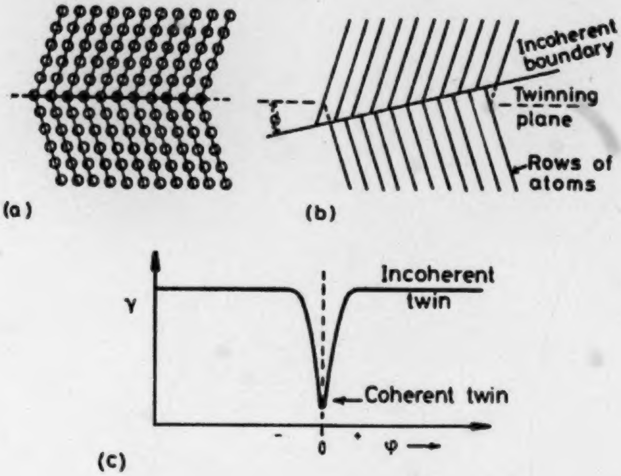

FIG. 6-17. Two kinds of twin boundaries and their corresponding energies [38].

The important role of twinning in plastic deformation is not the amount of strain accommodated (which is small in the case of twinning), but is the change in orientations that may place new slip systems in a favourable orientation with respect to the stress axis, so that additional slip can take place [36]. It seems that occurrence of mechanical twinning in ferrous materials depend on the alloying elements. Igata *et al.* [41] observed twin deformation under high strain rate ($10s^{-1}$) in pure iron, but no mechanical twinning happened under high strain rate in a mild steel with 0.16%C. Alloying with Si, however, increases the occurrence of mechanical twinning in iron [42].

2) Annealing twinning

Annealing twinning occurs mostly in *fcc* metals, especially in those with low stacking fault energy (e.g., brass). Twins form after prior mechanical deformation. For this reason, it is likely that they grow from twin nuclei produced during deformation. Annealing twins are usually broader and with straighter sides than mechanical twins [36]. According to Avner [43], annealing twins are formed because of a change in the normal growth mechanism.

Inagaki [44] examined the formation and behaviour of annealing twins in austenite (*fcc* iron) during the hot rolling of a low-carbon microalloyed steel. These twins are very similar in appearance to deformation bands. They deform during rolling and affect austenite recrystallization, since their coherent boundary lies on a specific crystallographic plane. Roytburd and Khachaturjan [45] theoretically predicted that the $\{011\}\langle 011\rangle$ twins in martensite could form as a result of $\{111\}\langle 112\rangle$ twinning in austenite followed by the transformation of the austenite twins to martensite twins upon quenching. This was experimentally confirmed by Danil'chenko [46] in high-carbon steels with high stacking fault energy (manganese steels).

3) Transformation twinning

Transformation twins are the twins that form during phase transformations in metals and alloys. Transformation twins are not exclusive to iron alloys. They can also happen in some other metals such as Ti. Although classically twinned martensite was assumed to form in medium and high carbon steels, where the carbon content of austenite exceeds 0.2% [47], it has been reported many times in low-carbon steels (even as low as 0.09%C) [11, 23, 48, 49]. For instance, Samuel [23] reported the presence of twinned martensite between grains of polygonal ferrite formed upon normalizing an HSLA steel with 0.1%C-1.5%Mn-1%Cr-0.003%B. For this reason, some have considered a lower threshold of carbon content for twinning, and found that replacement of slip by twinning (as modes of deformation) occurs over a range of 0.1–0.3 %C in plain carbon or C-Mn steels [31]. Any alloying that depresses the M_S temperature also promotes twinning. Increasing the cooling rate was also considered a factor that promotes twinning [31], likely due to the changes in the critical resolved shear stresses for slip and twinning that favour twinning [50]. Zhao [51] reported formation of twinned martensite in pure iron and dilute iron alloys at sufficiently high cooling rates. He showed that twinned martensite and lath martensite could be formed in one steel with separate M_S temperatures.

Twinning has been reported in ferrite too. Hutton *et al.* [40] examined the orientation relationship between a single ferrite grain and the transformation twin within the grain using a microbeam X-ray technique. They found transformation twins not only in iron-manganese alloys, but also in several high-purity irons. In fact, they found transformation twins "in all low-carbon steels examined when an attempt was made to locate them". Cooling from the austenitization treatment temperature was performed at various rates from furnace cooling to quenching in iced brine. The twins were also found in as-cast structures and hot-rolled sheets. The transformation twins in ferrite are not very noticeable. Fig. 6-18 shows the many shapes transformation twins can have in α-iron. Straight-sided twins stretching across the whole grain (type E in Fig. 6-18) are not observed very often. Non-coherent (irregular) interfaces are common (type A in Fig. 6-18).

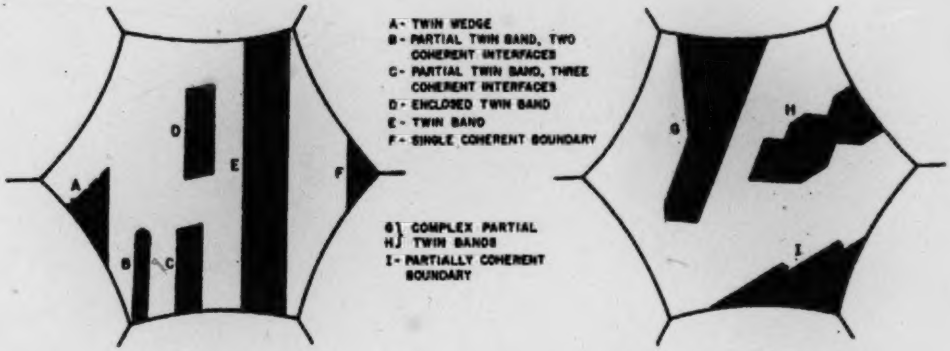
A
B
C
D
E
F
A - TWIN WEDGE
B - PARTIAL TWIN BAND, TWO COHERENT INTERFACES
C - PARTIAL TWIN BAND, THREE COHERENT INTERFACES
D - ENCLOSED TWIN BAND
E - TWIN BAND
F - SINGLE COHERENT BOUNDARY
G } COMPLEX PARTIAL
H } TWIN BANDS
I - PARTIALLY COHERENT BOUNDARY
G
H
I

FIG. 6-18. The different shapes of transformation twins in high-purity irons and low-carbon steels [40].

Heikkinen [39] also found many twins in the ferritic structures of V-bearing mild steels, cooled quite slowly from solution temperatures >1100°C. The transformation twins were crystallographically equivalent to mechanical twins, i.e., in terms of twinning planes and twinning directions (Table 6-1). However, they had a very different morphology. They were described as "thin prismatic crystals" with coherent twin boundaries, unlike mechanical twins that are in general narrow bands (also known as Neumann lamellae). Fig. 6-19 shows a dark-field TEM micrograph taken from a twin reflection, showing the difference between the two types of twinning, in a low-carbon V-bearing steel [52]. The two narrow lamellae are mechanical twins. The other bright structures are transformation twins. The steel had been austenitized at 1100°C for 30 min, cooled at a rate of 3.5°Cmin^{-1} (i.e., ~0.06°Cs^{-1}) and compressed slightly at -195°C.

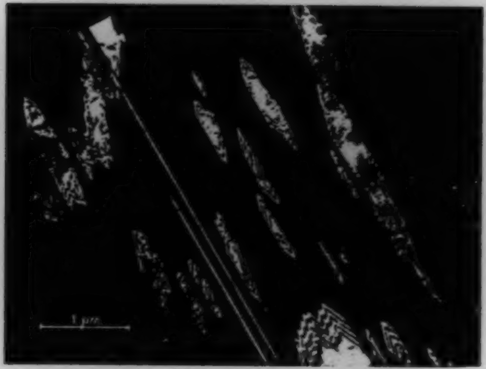

FIG. 6-19. Dark-field electron micrograph showing mechanical and transformation twins in a low-carbon steel microalloyed with vanadium [52].

4) Relaxation twinning

Relaxation twinning happens as a means of relaxation of high internal stresses that are accumulated in metals. Although the source of stress can be due to a phase transformation, this type of twinning does not occur directly as a result of a transformation and does not occur during or immediately after transformation. Danil'chenko [46] reported two modes of relaxation twinning in the martensite in a $\{011\}\langle 011\rangle$ system. One was observed in a number of quenched steels upon transition of as-formed martensite to stable martensite at cryogenic temperatures. This transition occurs upon a thermally-activated redistribution of carbon atoms in the lattice. The other mode was observed upon tempering quenched carbon steels (alloyed with either 9%Mn or 27% Ni) from cryogenic temperatures to 10–20°C.

6-2-3-3. Twinning in the HAZ

There are not many reports on observation of twinned martensite in the HAZ of low-carbon steels. It seems it is mostly accepted that twinned martensite may form in low-carbon-steel HAZ (Fig. 6-20), due to inhomogeneities in the austenite grains with respect to carbon concentration caused by the rapid thermal cycle of welding [1, 53]. Again, alloying with elements that increase hardenability, due to solid solubility, and increasing the cooling rate were found to lower the M_S temperature and, therefore, increase twinning in the HAZ [31, 50].

FIG. 6-20. Twinned martensite in the coarse-grained HAZ of a low-carbon HSLA steel weldment (left) and precipitated along ferrite boundaries (right) - dark field TEM images [1].

Deb *et al.* [53] found traces of transformation twinned martensite in the CGHAZ of an HY-80 (quenched and tempered) steel, with 0.18%C, welded by SMAW. They recognised this constituent as a phase most susceptible to HAC. The formation was attributed to the inhomogeneities within the austenite grains with respect to carbon concentration, presumably due to short times at temperatures that cause carbide dissolution. They found that preheat reduced the occurrence of transformation twinned martensite, presumably by reducing the amount of inhomogeneities (by slowing the thermal cycle the same way that an increase in the heat input would do). They concluded that since the volume fraction of the twinned martensite was low compared to other microstructural constituents, its effect on HAC susceptibility is limited compared to other parameters such as amount of hydrogen pick-up during or subsequent to welding.

6-2-3-4. Effect of twinning on mechanical properties

Twinning increases the strength and hardness by reducing the effective grain size [52]. However, the small volume fraction of twinned martensite observed in low-carbon steels is not expected to significantly affect the strength [11]. The effect of twinning on toughness and fracture properties is not conclusive. Many investigators have blamed twinning (e.g., mechanical twinning or transformation twinned martensite) for brittle fracture. For instance, Zener (as cited in [52]) postulated that the number of initiation sites for cleavage cracking increases in the presence of twins, due to the blockage of slip bands by twin boundaries. Akselsen *et al.* [54] considered formation of twinned martensite during the weld cooling cycle responsible for embrittlement in the intercritical HAZ of a low-carbon ferritic-pearlitic steel. Their conclusion was based on Charpy V-notch tests of many thermally cycled specimens and observation of twinned martensite in the samples. Twinned martensite has also been reported to be the most susceptible microstructure in the steel to hydrogen embrittlement. Even small amounts of twinning in slipped (lath) martensite have been reported in the literature [55] to increase the susceptibility of otherwise tough lath martensite to HAC.

Mahajan and Williams [35] considered deformation twins as a conceivable source of fracture. This was related to stress concentration and/or microcrack formation at the location of twin terminations within a grain or at the intersection of a twin with another twin or a grain boundary, as well as an elastic-plastic disturbance introduced during the high-speed propagation of the twins. It is conceivable that the reasons for a possible loss of ductility and toughness accompanied by twins in general (not restricted to mechanical twinning) are:

1- An increase in obstruction of dislocation movement and plastic deformation (at random orientations not those favourable to twinning).
2- Stress concentration or microcrack formation where twinning is arrested.
3- The elastic-plastic disturbances as a result of twin propagation.

Nevertheless, it is not conclusive whether twins are responsible for toughness deterioration or if they form in an alloy or under conditions that show poor mechanical properties. Heikkinen and Soininen [52] conclude that the transformation twins increase the strength more than they affect the ductility and, hence, must have a minor effect on the transition temperature. Twinning has been observed in the vicinity of the fracture, but as Mahajan and Williams [35] pointed out that does not necessarily mean it had an effect on fracture or even that twins were there before the fracture. Theoretical as well as experimental investigations of different metals including pure iron have shown that propagating cracks can create micro-twins.

6-2-4. Microstructural examination of the HAZ in low-C microalloyed steels

There is limited work on the microstructural examination of the HAZ in low-C microalloyed steels similar to Grade 100. Thaulow *et al.* [15] examined the phase structure and mechanical properties of a Nb microalloyed steel with 0.09%C, 1.56%Mn, 0.01%Mo, 0.01%N, 0.002%Ti, 0.01%V, 0.041%Nb and 0.036%Al. The BM consisted of ferrite and pearlite (due to low amounts of microalloying elements and likely low cooling rate during transformation) and a yield strength of only 379 MPa. The cooling times for simulated HAZ samples varied between 2.5 and 30s (similar to the range studied in present work). Fig. 6-21a shows the weld CCT diagram obtained for this material with a peak temperature of 1350°C. They found that the microstructure in the CGHAZ was mainly martensite for cooling times below 4–5s, mainly upper bainite (either side-plate or acicular ferrite) for cooling times above 10s, and a mixture of martensite and UB for cooling times between 4 and 10s (Fig. 6-21b). The only effect of cooling times above 10s on the CGHAZ microstructures was a slight increase in the amount of AF with some coarsening of the ferrite laths. They characterized FGHAZ as having fine grains of polygonal ferrite, regardless of the cooling time.

The notch toughness in the CGHAZ was found to drop drastically with an increase in cooling time (Fig. 6-21c). The toughness dropped to a very low shelf (~20 J) at a cooling time of 8–9s and remained at that level with a further increase in cooling time. This showed the inferior mechanical properties of UB compared with the low-C martensite. The hardness in the CGHAZ dropped gradually from a maximum of 360–370 HV5 at a cooling time of 2.5s to 230–240 HV5 at a cooling time of 30 s. The variation of microstructure and transformation temperature across the HAZ is shown for a cooling time of 8–9s in Fig. 6-21d. They concluded that a minimum heat input should be applied to avoid brittle zones, dominated by UB. A bainite content of 30–50% was enough to lower the notch toughness below 40 J.

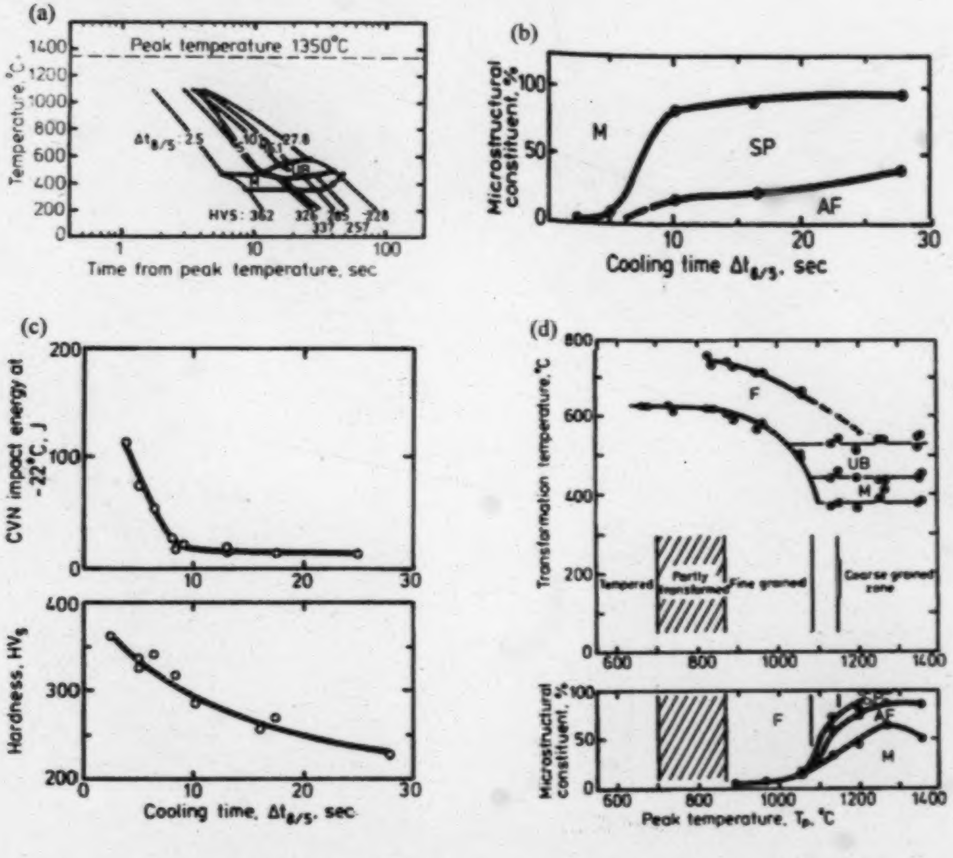

FIG. 6-21. HAZ properties of a low-carbon (0.09%) microalloyed steel, after Thaulow *et al.* [15]: a) The weld CCT diagram; b) simulated CGHAZ microstructure as function of cooling time; c) Variation of notch toughness and hardness in the CGHAZ (T_P= 1350°C) as a function of cooling time; d) variation of transformation temperature and microstructure across the HAZ for a cooling time of 8–9s.

Moon *et al.* [56] studied the microhardness and microstructure of the HAZ of some low carbon HSLA-100 steels with 0.035–0.055%C, 3.41%Ni and a maximum total of ~0.04% Ti+Nb+V. The weldments were produced by multi-pass gas metal arc welding. They found a mixture of "fine untempered lath martensite" and "coarse autotempered martensite" in the mid HAZ, where the hardness was highest (340–360 HV). The coarse martensite was an order of magnitude wider than the fine martensite. The presence of untempered lath martensite was deemed an undesired microstructure, susceptible to hydrogen cracking.

6-3. Grain growth

A fine-grained microstructure contains a large amount of grain boundary area, which represents an excess free energy in the system. Given the thermal activation energy, the system would like to release this energy through grain coarsening. Precipitates, on the other hand, exert a pinning force on the grain boundaries, the amount of which depends on their size and distribution.

Grain growth in the HAZ has several effects on the properties of the HAZ as well as the WM. The matrix grain size distribution originates from the primary austenite grains. Although the base metal grain-size distribution affects the HAZ grain sizes, the important factor to control is the austenite grain growth during the welding thermal cycle, or the "austenite grain size prior to transformation". The size of the transformed grains directly affects strength and toughness.

Austenite grain growth increases the hardenability and displaces the CCT diagrams to longer reaction times, hence causing the formation of Widmanstatten ferrite, bainite and martensite, upon cooling. The presence of these microstructures and coarse grains in the CGHAZ reduce the fracture toughness and increase the chance for cold cracking and reheat cracking. Also, the grain structure in the WM is dependent on the degree of grain growth in the CGHAZ, as solidification in the WM occurs on the coarsened grains in the HAZ.

6-3-1. Grain growth kinetics

If the mean radius of curvature of the grain boundaries is assumed to be proportional to the mean diameter of the grains, $\overline{D}$, the average driving force for grain growth is given by Equation 6-1 [3]. γ_{gb} is the grain boundary energy.

$$\Delta G \approx \frac{2\gamma_{gb}}{\overline{D}} \tag{6-1}$$

Equation 6-2 then gives the mean growth rate as being proportional to the mean driving force. M is the grain boundary mobility, which is highly dependent on temperature.

$$\frac{d\overline{D}}{dt} = M\frac{2\gamma_{gb}}{\overline{D}} \tag{6-2}$$

Integration on Equation 6-2 gives Equation 6-3, where $K = 4M\gamma_{gb}$, and D_0 is the original grain size.

$$\overline{D}^2 = D_0^2 + Kt \tag{6-3}$$

It should be added that the relation given by Equation 6-4 is experimentally found for isothermal grain growth of austenite in low alloy steels [57]. $\overline{D}$ is defined as the diameter of a regular tetrakaidecahedron so that $\overline{D} = 1.776\overline{L}$. $\overline{L}$ is the mean lineal intercept.

$$\overline{D}^n = D_0^n + Kt \tag{6-4}$$

For pure metals $n \approx 2$ (making Equations 6-3 and 6-4 equivalent), while for alloys $n>2$, due to impurity drag effects [3]. As grain growth is a thermally activated diffusional process, K follows the well-known Arrheinius relationship [5], i.e.:

$$K = K_0 \exp\left(\frac{-Q_G}{RT}\right) \tag{6-5}$$

where K_0 is a constant, R is the gas constant, T is the temperature in Kelvin and Q_G is the activation energy for grain growth. As the weld thermal cycle is not isothermal, it can be represented as a series of isothermal steps with small increments of holding time [57]. This translates to summing the area under the curve of $\exp\left(-Q_G / RT(t)\right)$ versus time, similar to the analysis for precipitate dissolution (Section 5-4-1-2). The value of this integration may be called the "kinetic strength" of the thermal cycle [58].

6-3-2. Grain growth inhibition

There are two mechanisms for grain growth/coarsening: 1) normal or primary grain growth/coarsening and 2) abnormal grain growth or secondary recrystallization [59]. In normal grain growth, many grains grow and collide and as the growth proceeds the driving force decreases and the growth is slowed. In abnormal grain growth, only a few grains grow and consume other fine grains, and maintain a rapid growth rate, at least until they impinge with other abnormal grains [5]. Fig 6-22 shows these two mechanisms for two types of steels, where grain sizes are shown after isothermal heating at different temperatures for 1 h. In a plain carbon steel, the grain size increases continuously with temperature, i.e., normal grain growth. In a grain-refined steel, microalloy precipitates inhibit grain-growth up to a temperature that depends on the chemistry and precipitate characteristics in the steel, as well as the holding time. At higher temperatures grain growth occurs under abnormal conditions, where the grain sizes developed will be larger than those in a steel without any grain refining additives. At considerably higher austenitizing temperatures, the grain-refined steel reverts to a normal grain growth process and the grain sizes developed will be similar to those in a plain carbon steel, due to substantive dissolution of the particles.

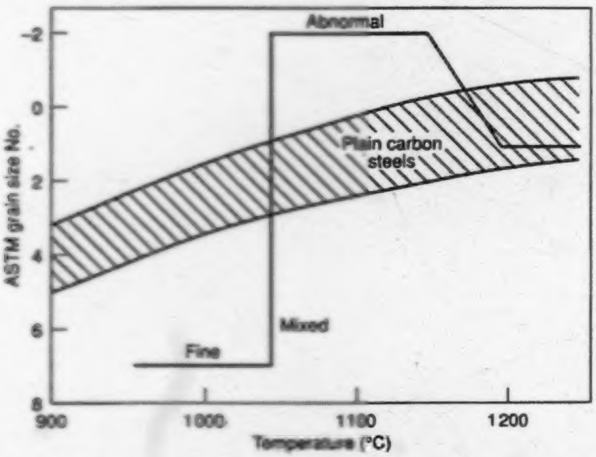

FIG. 6-22. Effect of austenitizing temperature and steel chemistry on austenite grain growth. Heat treatments last for 1 h [5].

Grain growth inhibition in microalloyed steels requires an adequate volume fraction of sub-critically sized particles. If the precipitates are smaller than a critical size they can inhibit the grain coarsening and, according to Palmiere [59], mechanism 1 (normal growth) prevails. If the precipitates are larger than the critical size they cannot effectively pin the grain boundaries and abnormal grain coarsening takes over. Gladman found this critical size, r_C, for precipitates, expressed by Equation 6-6, by equating the driving force for grain coarsening with the precipitate pinning force.

$$r_C = R_0 f_V \left(1 - \frac{4}{3Z}\right)^{-1} \qquad (6\text{-}6)$$

where f_V is the volume fraction of the precipitates, R_0 is the average grain size (in fact the edge length of a tetrahedron) and Z represents the ratio of the radii of the growing grains to the radii of the average grains ($Z = R / R_0 \approx 1.5$–2) [5]. As Easterling states [3], the problem in using these equations in practice lies in the difficulty in estimating f_V accurately.

Experimental work by Gladman and Pickering (as cited in [60]) showed that in steels containing Nb and Al, particle sizes up to 50nm could pin the austenite grains at temperatures as high as 1050°C. George and Irani [60] found finer critical sizes for Ti-bearing steels (~15 nm). The difference was attributed to the effect of volume fraction. The Ti-bearing steels had lower volume fractions of fine TiN. Both works showed good agreement with the prediction of Equation 6-6, when volume fractions were taken into account. However, some other experimental results suggested that these models underestimated the pinning force exerted by precipitates. Some experiments have shown that precipitation of NbCN can be localized. There may be segregation of solutes towards prior austenite grain boundaries, sub-grain boundaries and deformation bands. Therefore, upon precipitation, a higher volume fraction of NbCN is present at these locations, that will result in higher pinning forces than calculated based on a uniform particle distribution [59].

There is also another controlling factor, namely the effectiveness of precipitates in restricting austenite grain growth. Some precipitates, depending on their size and distribution, can suppress austenite grain growth until they coarsen or dissolve. V(C,N) are only effective up to 900°C, while Nb(C,N) can restrict grain growth up to around 1200–1250°C. Among all microalloy precipitates, TiN is the most stable at very high temperatures up to 1250–1300°C [1, 4].

The average grain size of the austenite can, therefore, be found from Equation 6-7, where in fact $\overline{D} = 2R_0$. This should determine the average austenite grain size where grain growth is inhibited (i.e., FGHAZ). Gladman's equation (Equation 6-7) is different from the well-known Zener equation (Equation 6-8), in that it takes into account a distribution of grain sizes. Also, note that in Zener's equation $\overline{D}$ is the diameter of a spherical grain.

$$\overline{D} = \frac{4r}{3f_V}\left(\frac{3}{2}-\frac{2}{Z}\right) \tag{6-7}$$

$$\overline{D} = \frac{2r}{3f_V} \tag{6-8}$$

Relationships of the general form of Equation 6-9 have been experimentally obtained for several microalloyed steels by Japanese investigators [3], where proportionality constants, K_{GG}, had values such as 0.24 in one case of Ti-bearing steel and 0.75 in another case of Ti-bearing steel. In fact, even for the theoretical equations of grain growth limit in the form of Equation 6-8, constants of proportionalities different from that given in [5] are found by other investigators [61], and this leaves some degree of uncertainty on the subject.

$$\overline{D} = K_{GG}\frac{r}{f} \tag{6-9}$$

6-3-3. Grain growth in the HAZ

It was found experimentally by Ikawa *et al.* (as cited in [3]) that the major increase in grain size occurs during the heating part of the thermal cycle in GTAW and SAW of some HSMA steels. Only 20% of the total grain growth occurred during the cooling part. The reason is that the driving force is high only during the initial stages of the welding.

Basically there are three factors that can hinder grain growth in the HAZ [3]:

a) Precipitates
b) Impurity drag
c) Temperature gradient

The effect of precipitates was discussed in the previous section. According to Equations 6-8 and 6-9, grain growth continues unrestricted after the precipitates are coarsened greatly or dissolved. However, segregation of certain solutes, especially Nb, P and S, to the grain boundaries exerts additional dragging forces and reduces the mobility of the grain boundaries. Temperature gradients exert another hindering force due to the gradient in the grain size profile. It has been suggested that the smaller grains at locations farther from the fusion line exert a "pinning" force on the larger neighboring grains closer to the fusion line [3]. This is referred to as "thermal pinning" in some of the literature [57]. Another hindering force is the "liquation pinning" that was deemed responsible for occurrence of a peak grain size at ~150-200 μm away from the fusion line and a decrease in grain size from that point towards the fusion line [62]. Grain boundary liquation, the formation of liquid films at the grain boundaries close to the fusion line, effectively pins the grain growth. This, however, is restricted to the regions very close to the fusion line only.

6-3-4. Grain-coarsening temperature

The temperature above which the undissolved precipitates can no longer retard grain growth is called the grain-coarsening temperature, T_{GC}. There have been different criteria adopted in defining the grain-coarsening temperature, T_{GC}. Gladman and Pickering (as cited in [60]) chose "the temperature at which the mean linear intercept corresponded to an ASTM grain size number of 5, which was approximately equivalent to the development of 20-30% of the coarse grains. George and Irani [60] used the first appearance of a large area of Widmanstatten ferrite across the HAZ for this purpose. In the HAZ of Grade 100 steel, the FGHAZ and CGHAZ show a distinct boundary, at which the grain sizes that showed a plateau in FGHAZ start to grow rapidly in the CGHAZ (as will be shown in Section 6-5-7). For this reason, the T_{GC} in this study was chosen to represent the boundary between CGHAZ and FGHAZ, as determined by optical microscopy.

The experimental work by Goerge and Irani [60] showed that the T_{GC} in grain-refined steels with Al, Nb and V is ~1100°C, while it has a value of ~1200°C in steels with titanium additions, when the ratio of Ti-to-N weight fraction is low (~2). They found that steels having higher Ti-to-N ratios (e.g., 6–7) give a low value of T_{GC}. In the presence of Nb, the ratio of Ti to N has to be even lower to have a high T_{GC}. Formation of TiC and subsequent coarsening of both TiC and TiN, due to dissolution of TiC at high temperatures, were found to be responsible for low T_{GC} in steels with high Ti-to-N ratios. TiC formed in these steels, due to availability of excess Ti in solution below the temperatures where all N is tied up with Ti.

It should be added that T_{GC} is time dependent and, therefore, a quoted T_{GC} should be accompanied by holding time [5]. The reason is due to coarsening of the particles (Ostwald ripening effect) and particle dissolution at high temperatures. Coarsening causes an increase in the particle size and dissolution causes a reduction in volume fraction, both of which will result in enhanced grain growth and lowering of T_{GC}. Welding heat input also has some effect on T_{GC}, which will be discussed in the next section.

6-3-5. Effect of heat input on grain growth

Heat input affects grain growth in two ways: heating rate and exposure time at high temperature (dwell time). The effect of dwell time on particle coarsening and dissolution is similar to the effect of holding time in isothermal heating, as discussed in the previous section. Fig. 6-23 shows the effect of heating rate on the T_{GC} for a V-Ti microalloyed steel, after Siwecki *et al.* (as cited in [61]). Encircled numbers refer to the size of austenite grains at the T_{GC}. It shows that the T_{GC} decreases with an increase of heating rate (equivalent to a decrease in heat input in weld thermal cycles). As the heating rate increases, and particularly in low-carbon steels (with little or no iron-carbides, whose interface with ferrite would be the primary nucleation site for austenite at low heating rates), nucleation of austenite occurs at more sites on the ferrite grain boundaries [5]. This increases the initial number of austenite grains, hence increasing the driving force for abnormal austenite grain coarsening [61]. Nevertheless, the short dwell periods at high temperatures during welding impose limitations in the extent of abnormal grain growth.

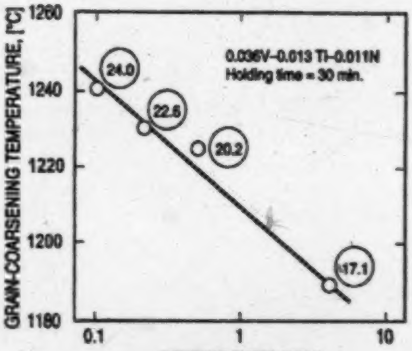

FIG. 6-23. Effect of heating rate on the grain-coarsening temperature (T_{GC}) for a V-Ti microalloyed steel [61]. The encircled numbers specify the austenite grain size in microns.

6-4. Experimental procedure

The basic metallographic samples for optical microscopy (OM) and transmission electron microscopy (TEM) were prepared as explained in Section 3-5. OM was performed using an Olympus light microscope at magnifications 150–1000x. Replicas were prepared as described in Section 5-6. For grain size measurement, samples were examined at low magnifications (1500–6000x) in the TEM. Thin-foil samples for TEM were prepared by a focused ion beam (FIB) technique at specific locations indicated on the pre-etched metallographic samples.

Fig. 6-24 shows how the FIB lift-out samples are prepared. First a layer of FIB-deposited tungsten is placed on the surface at the designated location. This is to protect the sample beneath from sputtering. Then two trenches are milled on either side of the tungsten, using a high current gallium (Ga^+) ion beam for fast ion milling. Further thinning of the central membrane to a thickness of ~1 μm is achieved by using a smaller beam current. The membrane is then framed by applying three cuts around it. The membrane inside these cuts will be ion polished until it is electron transparent. As the polishing proceeds the beam current is decreased. At the last step, the small attachments of the membrane to the bulk that were left for providing support during polishing are cut, which frees the membrane. The electrically charged membrane will stick to a glass needle, accurately moved by a micromanipulator, and is transferred to a TEM grid, typically made from copper mesh with a thin film of support material coating it [63]. The site specificity of FIB system makes it a very useful tool for making TEM samples from the exact region of interest in the HAZ. Compared to the conventional thin-foil samples prepared by electrojet polishing, FIB samples have larger areas of thinned sample for electron transparency purpose (~10x15 μm^2). This also reduces the amount of magnetic interference in the TEM column.

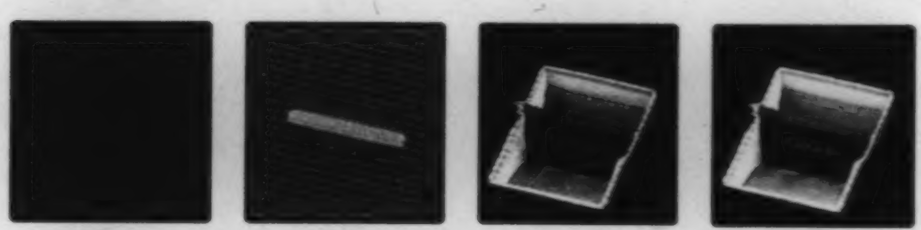

Step 1
Locate the Area of Interest

Step 2
FIB-deposit a Protective Tungsten Layer

Step 3
Mill Initial Trenches & Rough Polish

Step 4
Thin the Central Membrane

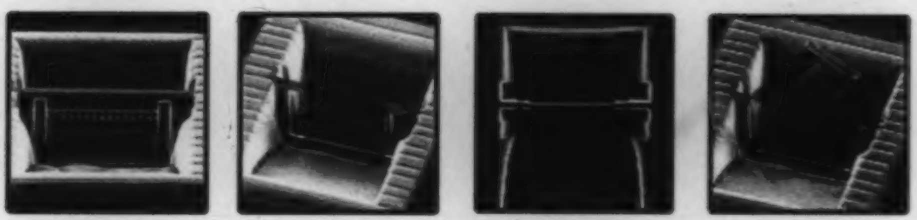

Step 5
Perform "Frame Cuts" on Central Membrane

Step 6
"Polish Mills" to Near Nominal Thickness

Step 7
Polish for Electron Transparency of Membrane

Step 8
FIB-mill to Free Membrane from Trenches

FIG. 6-24. The various steps in making TEM lift-out samples by FIB technique [63].

Simulated samples for examination of twinning in the CGHAZ were prepared by heat-treating small samples (approx. 7 mm x 15 mm) of Grade 100 steel of different thickness (0.50–2.00 mm). This consisted of solution annealing in a tube furnace at ~1200–1250 °C for various lengths of time (4–30 min), and then quenching in iced-brine (~ –10 °C). Fig. 6-25 shows the set-up for this experiment. A tube furnace and a type S thermocouple were used. A type K thermocouple and an argon gas tube were fed into a mullite tube from one end and the sample holder and another gas tube were attached to the tube from the other end. Argon flow protected the sample from oxidation and decarburization. The heating rate was 20 or 50 °C/min. The sample holder (a plug with a wire passed through it holding the sample at the end) was designed to be drawn out of the tube and inserted into a bucket of iced-brine rapidly. The quenched sample was then cut, mounted, ground and polished through conventional metallographic methods. Final polishing was achieved by diamond paste 1 µm. Samples were then etched with 2% Nital for about 10–20 seconds (medium etching). A Mitutoyo Vickers hardness testing machine was used to check the hardness at several locations. A suitable sample was chosen, and a location of interest, having the required hardness, was marked to make a thin-foil TEM sample by the FIB method (Fig. 6-26).

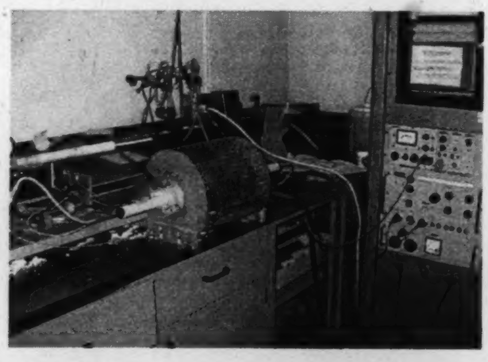

FIG. 6-25. The furnace setup for heat treatment and simulation of the CGHAZ.

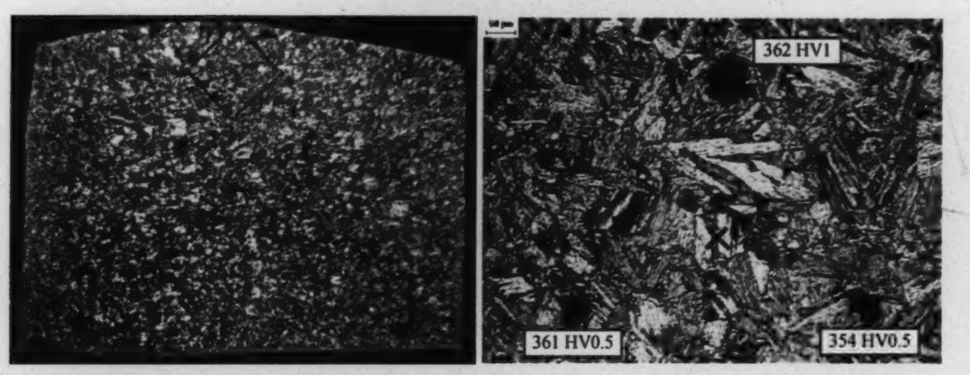

FIG. 6-26. The mill-out location on the sample chosen for preparation of the TEM-FIB sample: a) macrograph; b) micrograph - the location of the mill-out was exactly specified by the cross on the micrograph and by the hardness indentations in a triangular pattern.

6-5. Results and discussion

6-5-1. BM phase microstructure

Fig. 6-27 shows the microstructure of the BM obtained from a longitudinal section (w.r.t. RD). Initially, optical micrographs at magnifications 150–1000x were examined. The BM is made up of primarily oriented bainitic ferrite with smaller amounts of polygonal ferrite [64]. The banded structure is a result of segregation and TMCP. TEM replicas, however, resolve these microstructures much better at higher magnifications. Figure 6-28 shows a mosaic of TEM micrographs with original direct magnification of 3000x from the longitudinal and transverse sections of the BM. The boundaries of "pancaked" prior austenite grains, a result of controlled rolling below the no-recrystallization temperature during processing [24], can be discerned on the longitudinal section (Fig. 6-28a). These pancaked regions are less discernable on the transverse section (Fig. 6-28b).

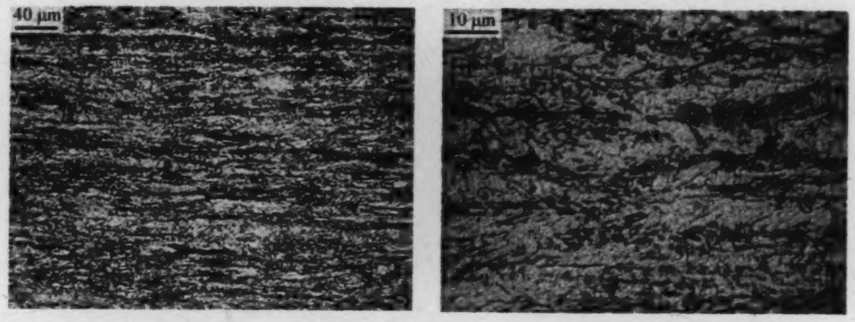

FIG. 6-27. OM from the BM (longitudinal section) at two magnifications.

Fig. 6-29 shows the grain structure of the BM at a higher magnification of 6000x. Packets of parallel ferrite laths are visible on the longitudinal section (Fig. 6-29a). The individual laths, having low-angle boundaries with the adjacent laths can be observed inside each packet. Two of these not-so-sharply etched grain boundaries are denoted with arrows. The transverse section shows elongated grains with irregular grain boundaries. TEM images of FIB samples, prepared from the BM, are shown in Fig. 6-30. It shows the jagged grain/sub-grain boundaries of the bainitic ferrite grains (Fig. 6-30a). A grain from another region is shown at higher magnification revealing a network of dislocations and fine precipitation on the dislocations. Such a network of dislocations was not observed in the other regions examined and, therefore, is not likely a representative sub-structural characteristic.

Another feature resolved better with the replicas is the patches of dark contrast (Fig. 6-29). These regions, when examined at high magnifications (50,000–100,000x) on the replicas do not show any diffraction contrast, which indicates that no particles (such as cementite) are present. The fine features can be either a result of structural banding (e.g., due to formation of M/A microconstituents rich in C) or chemical banding (i.e., etching differences due to segregation of alloying elements). Some elements such as Mn segregate drastically in steels [65]. Banding originates from the interdendritic segregation during solidification but evolves after reheating, rolling and austenite decomposition [66]. More investigation is required to see if these regions are richer in elements such as Mn, Si, P and C, using microanalysis in the SEM.

6-5-2. Phase microstructures across the HAZ

The iron matrix phase changes in different sub-zones of the HAZ are a result of re-austenitization during the heating leg of the weld thermal cycle and re-transformation from austenite to polygonal ferrite, bainitic ferrite or martensite during the cooling leg of the thermal cycle. The microstructures at each sub-zone will be examined for several heat inputs (0.5–2.5 kJ/mm).

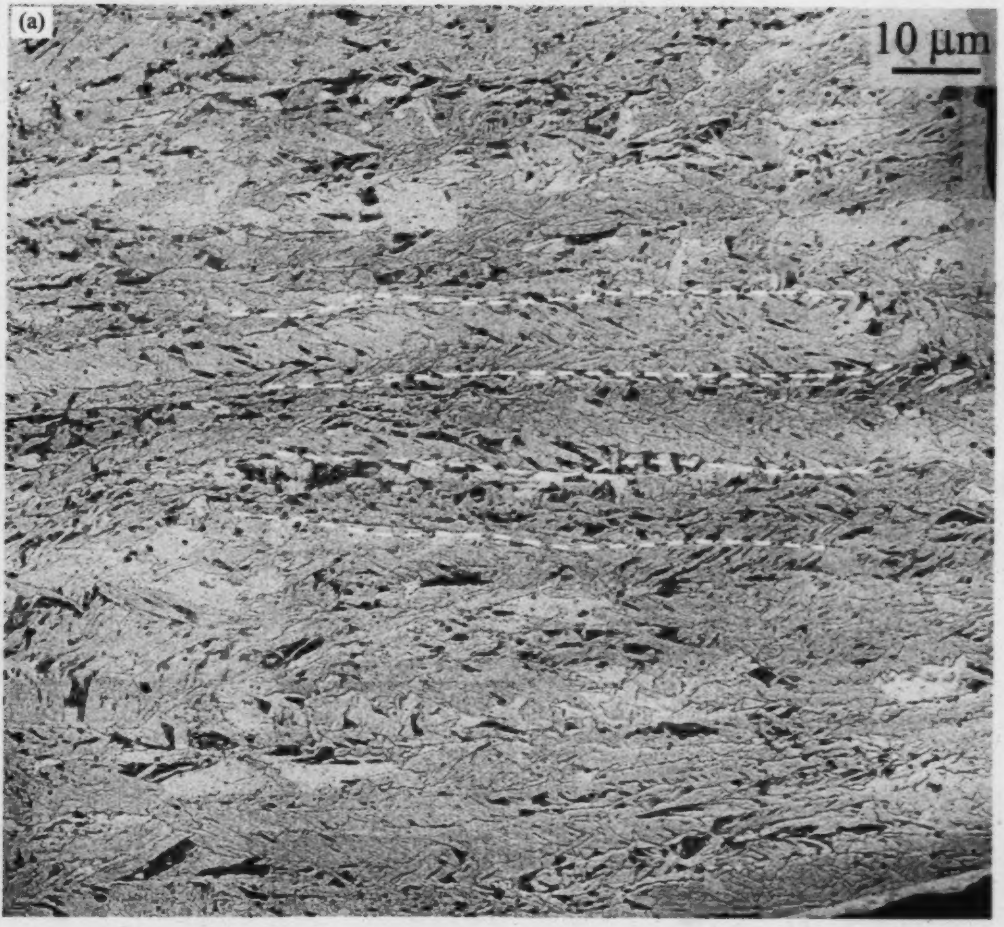
(a)
10 µm

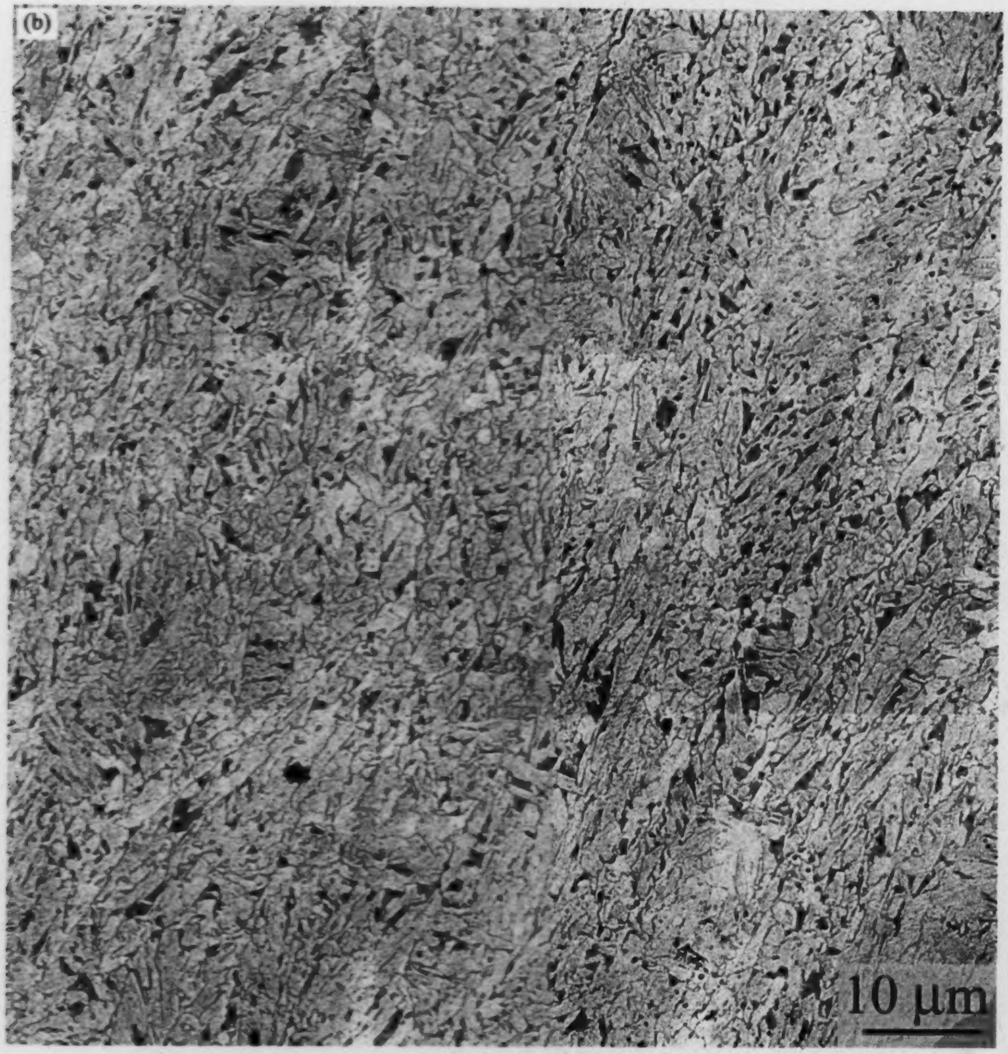

FIG. 6-28 – Mosaic of TEM replicas from the BM: a) longitudinal section; b) transverse section.

6-5-2-1. ICHAZ

Figure 6-31 compares the grain structure in the ICHAZ for several heat inputs (0.5–2.5 kJ/mm) with the BM. Transformation to austenite during the heating leg of the weld thermal cycle is not completed in this sub-zone and the amount of transformation depends on the distance from the fusion line (i.e., the peak temperature). Basically, the microstructure is mainly something between that of BM and FGHAZ. It is a mixture of untransformed bainitic ferrite and retransformed polygonal ferrite.

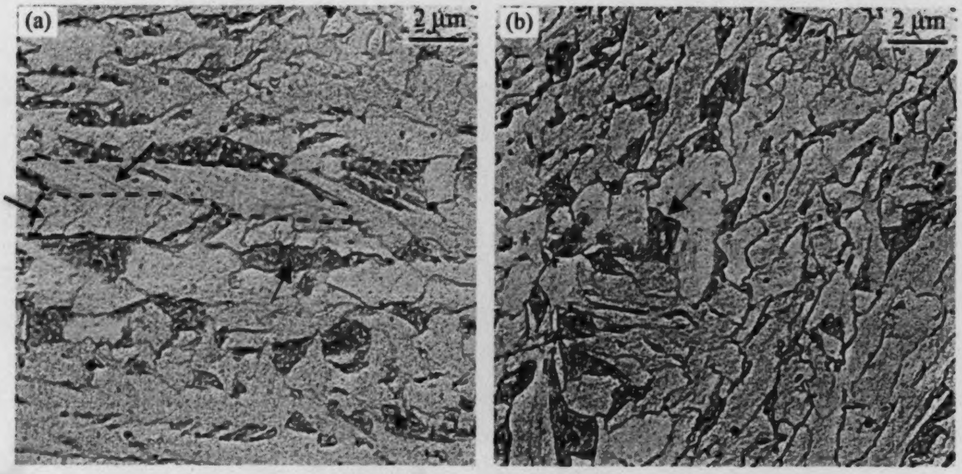

FIG. 6-29. Grain structure of the BM revealed by TEM–replicas: a) longitudinal section; b) transverse section.

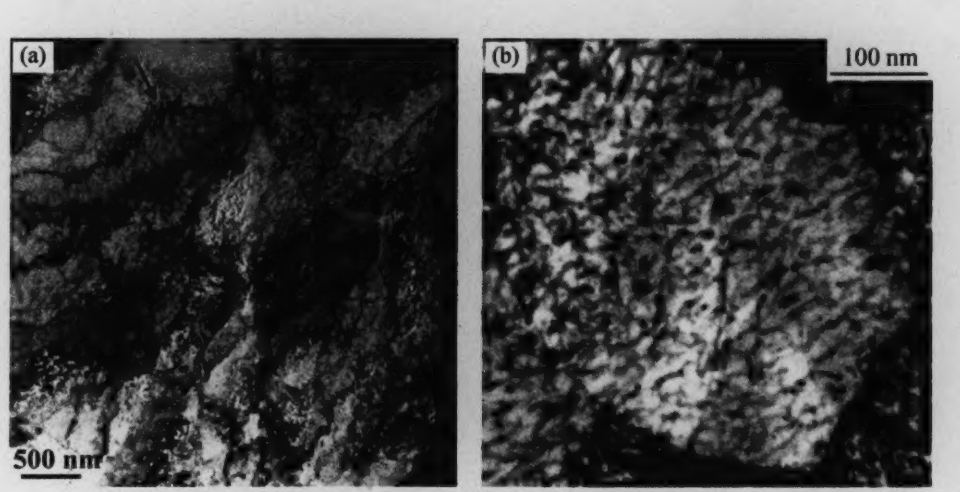

FIG. 6-30. TEM-BF images from FIB samples from the BM.

Figure 6-32 shows a mosaic of TEM micrographs with an original direct magnification of 3000x. The replicas were obtained from the transverse section (w.r.t. RD, which makes them parallel to the welding direction), as the longitudinal-to-welding sections provided large parallel-sided areas for each subzone. This increased the chance of making a good replica. The disadvantage was that the original oriented plate-shape grains (untransformed grains) are more discernable on longitudinal sections (w.r.t. RD). For a heat input of 2.5 kJ/mm, however, the replica was made from the longitudinal section, as the ICHAZ was not available on the transverse section. The replicas show a mixture of untransformed and retransformed microstructures. In some regions, groups of untransformed grains, denoted as region 1, and groups of retransformed grains, denoted as region 2, can be distinguished. An example of each is shown on the micrographs of Fig. 6-32.

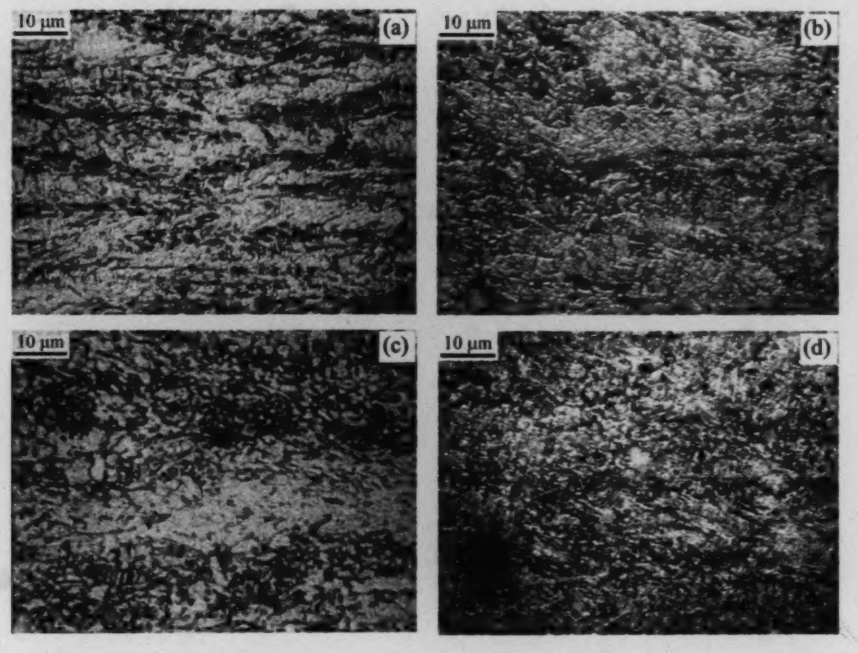

FIG. 6-31. Optical micrographs from ICHAZ as compared with BM: a) BM; b) ICHAZ–0.5kJ/mm; c) ICHAZ–1.5kJ/mm; d) ICHAZ–2.5kJ/mm.

Basically, the distinction between the untransformed bainitic and retransformed polygonal grains comes from their shape. Even on the transverse sections (Fig. 6-33a), the bainitic grains have larger aspect ratios and more irregular boundaries, while the polygonal grains have more straight boundaries with more equiaxed shapes. Also the new polygonal grains are mostly at the corners of the grain boundaries of the bainitic grains. Some of these grains are marked by arrows in Fig. 6-33. FIB samples also show the difference in the grain boundaries and grain structures in these two types of grains (Fig. 6-34).

6-5-2-2. FGHAZ

Figure 6-35 compares the grain structure in the FGHAZ for several heat inputs (0.5–2.5 kJ/mm) with the BM. Transformation to austenite during the heating leg of the weld thermal cycle is completed in this sub-zone. The FGHAZ microstructure revealed with OM seems somewhat similar for all three heat-inputs. In all cases, in particular the heat inputs of 1.5 and 2.5 kJ/mm, the matrix consists mainly of polygonal ferrite, <5 μm in size. The grain growth is suppressed for two reasons, both as a result of a not-so-high peak temperature: the grain boundary mobility is low and the precipitates pin the grain boundaries.

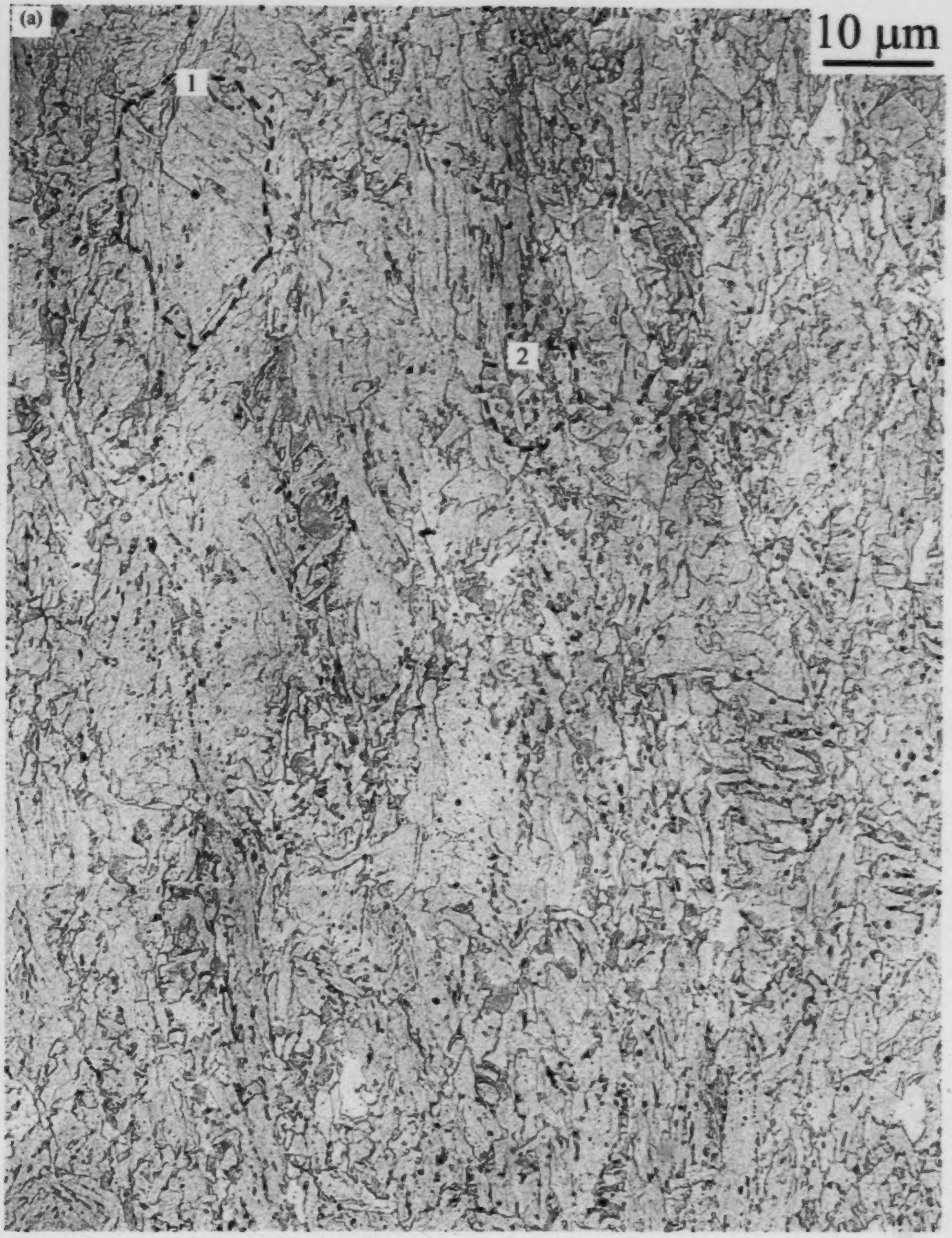
(a)
10 μm
1
2

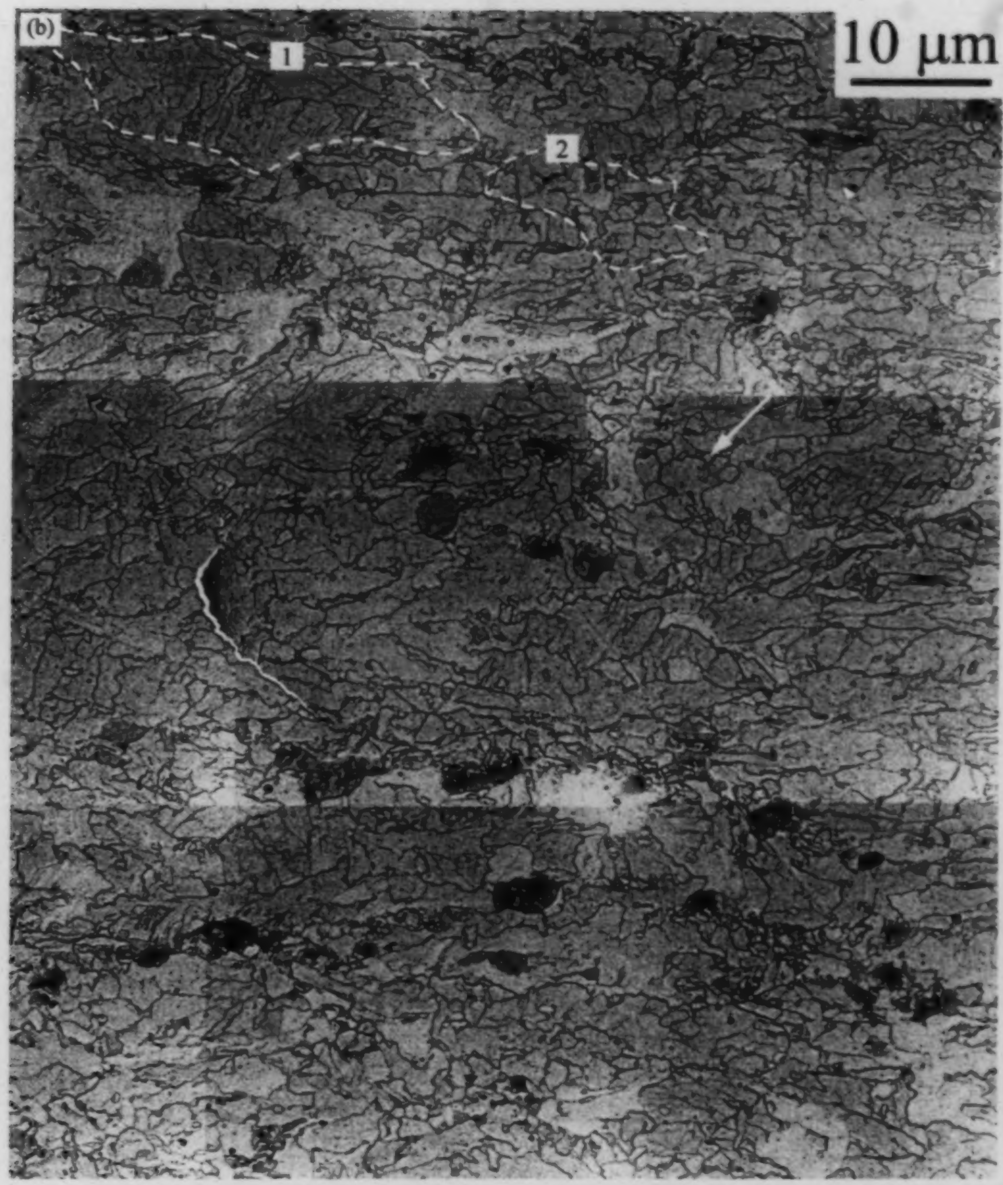
(b)
1
2
10 μm

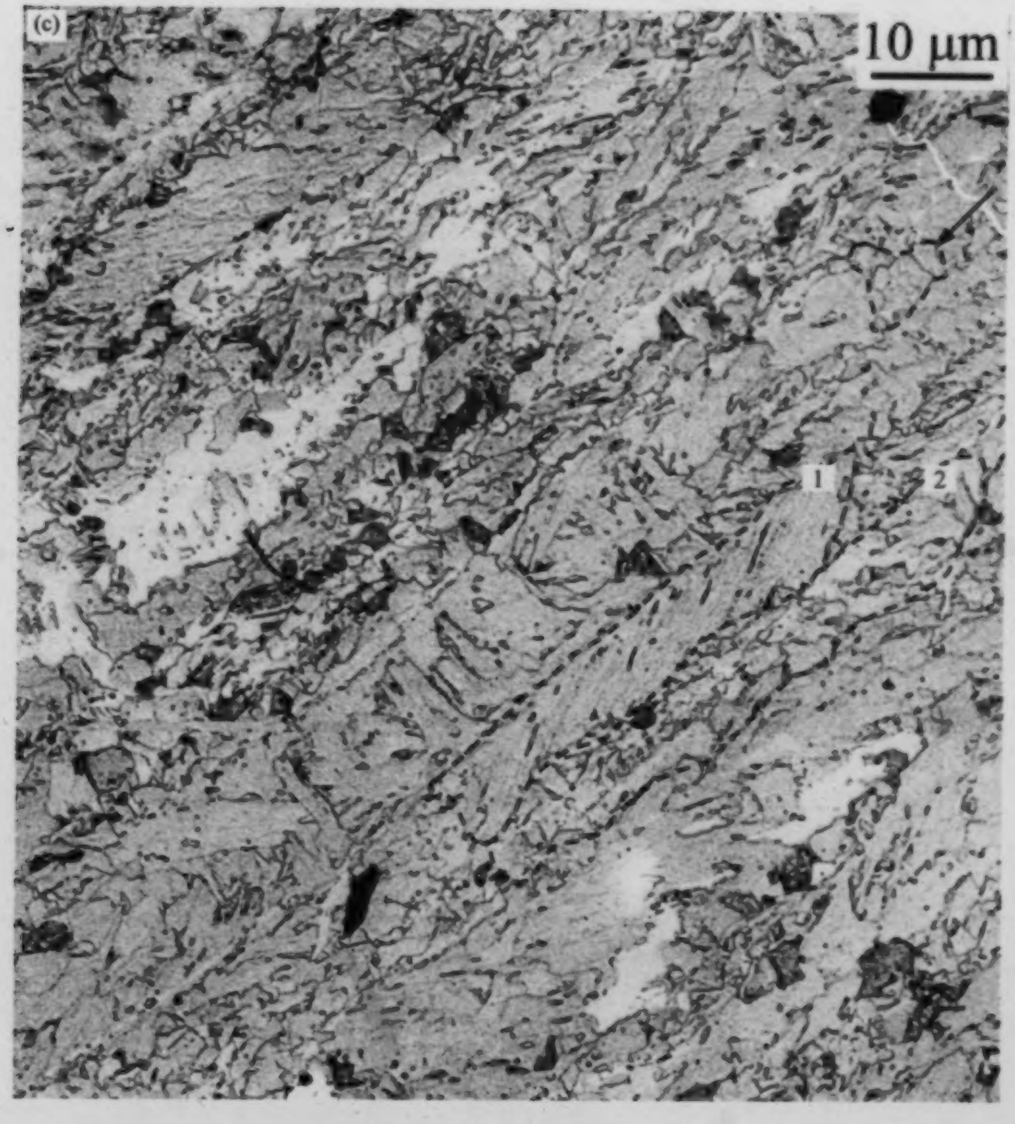

FIG. 6-32. Grain structure in the ICHAZ revealed using TEM–replicas: a) 0.5 kJ/mm; b) 1.5 kJ/mm; c) 2.5 kJ/mm. (a) and (b) transverse to rolling; (c) longitudinal to rolling.

Fig. 6-36 shows a mosaic of TEM micrographs with original direct magnification of 3000x. These replicas were also obtained from the longitudinal sections (w.r.t. welding direction). The replicas reveal the fine grain structure better than OM, especially for the low heat input of 0.5 kJ/mm. It can be observed that some grains have larger aspect ratios than those typical for polygonal ferrite. These are packets of bainitic ferrite with lamellar structures. This is better resolved in Fig. 6-37, where the grain structure for a heat input of 0.5 kJ/mm is compared with that of 1.5 kJ/mm. In FGHAZ–0.5 kJ/mm, two types of grains are recognizable: polygonal ferrite (marked as region 1) and bainitic ferrite (marked as region 2). Packets of bainitic ferrite are particularly visible in this micrograph. The rest of the grains have structures between polygonal ferrite and lamellar bainitic ferrite. The FGHAZ for heat inputs of 1.5 and 2.5 kJ/mm consisted mainly of polygonal ferrite. The higher cooling rate (10–20 times higher; Table 4-4) in the case of the heat input of 0.5 kJ/mm increased the chance of formation of bainitic structures, even though the prior austenite grain sizes are small. It is not easy to quantify the area fraction of bainitic structure. Moreover, it is quite possible that this fraction increases across the FGHAZ towards the fusion line. This phenomenon, which is due to an increase in carbon content due to dissolution of carbides (Fig. 5-16) and results in increase of hardness, will be discussed in Chapter 7.

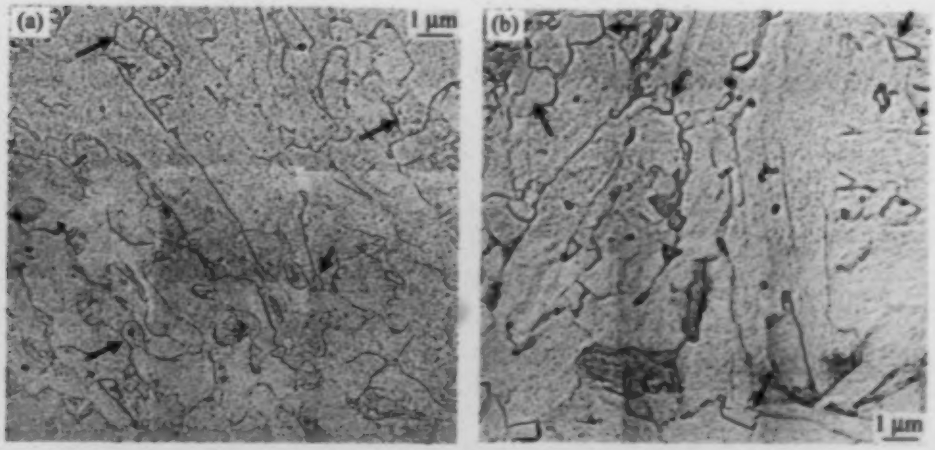

Fig. 6-33. Mosaics of TEM micrographs from the ICHAZ showing retransformed polygonal ferrite at grain boundaries of untransformed bainitic ferrite: a) 0.5 kJ/mm; b) 2.5 kJ/mm.

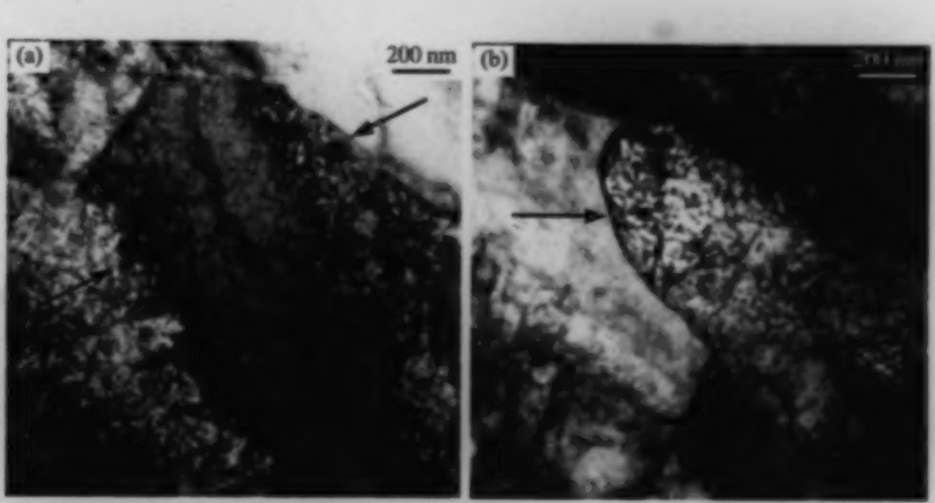

FIG. 6-34. TEM-BF images of FIB samples from ICHAZ-0.5 kJ/mm.

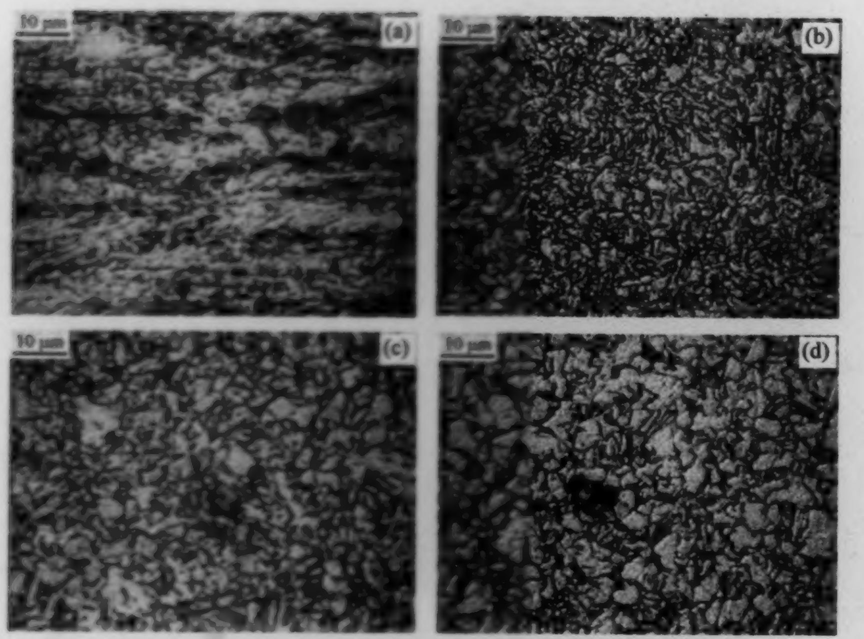
10 µm
(a)
10 µm
(b)
10 µm
(c)
10 µm
(d)

FIG. 6-35. Optical micrographs from the FGHAZ as compared with BM: a) BM; b) FGHAZ–0.5kJ/mm; c) FGHAZ–1.5kJ/mm; d) FGHAZ–2.5kJ/mm.

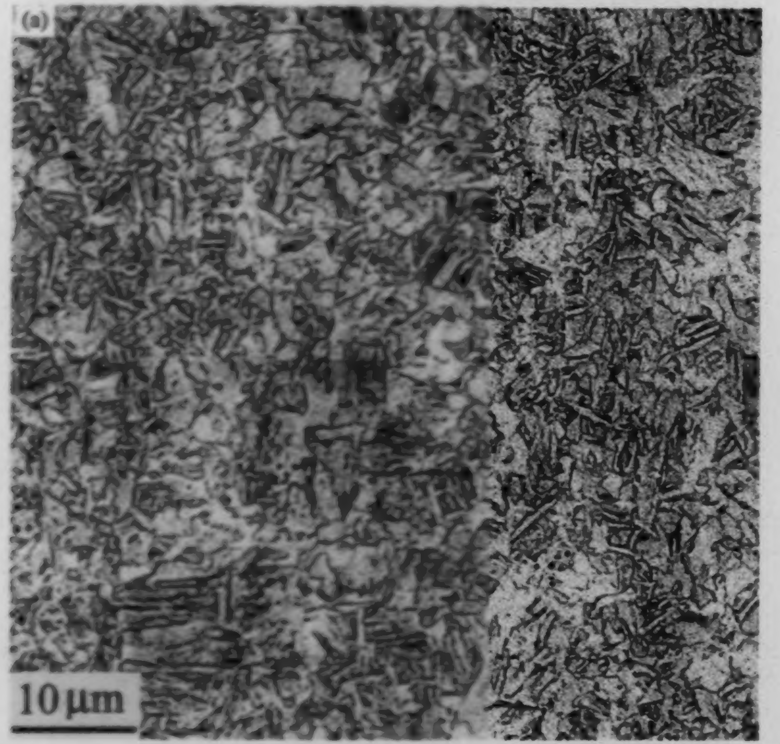

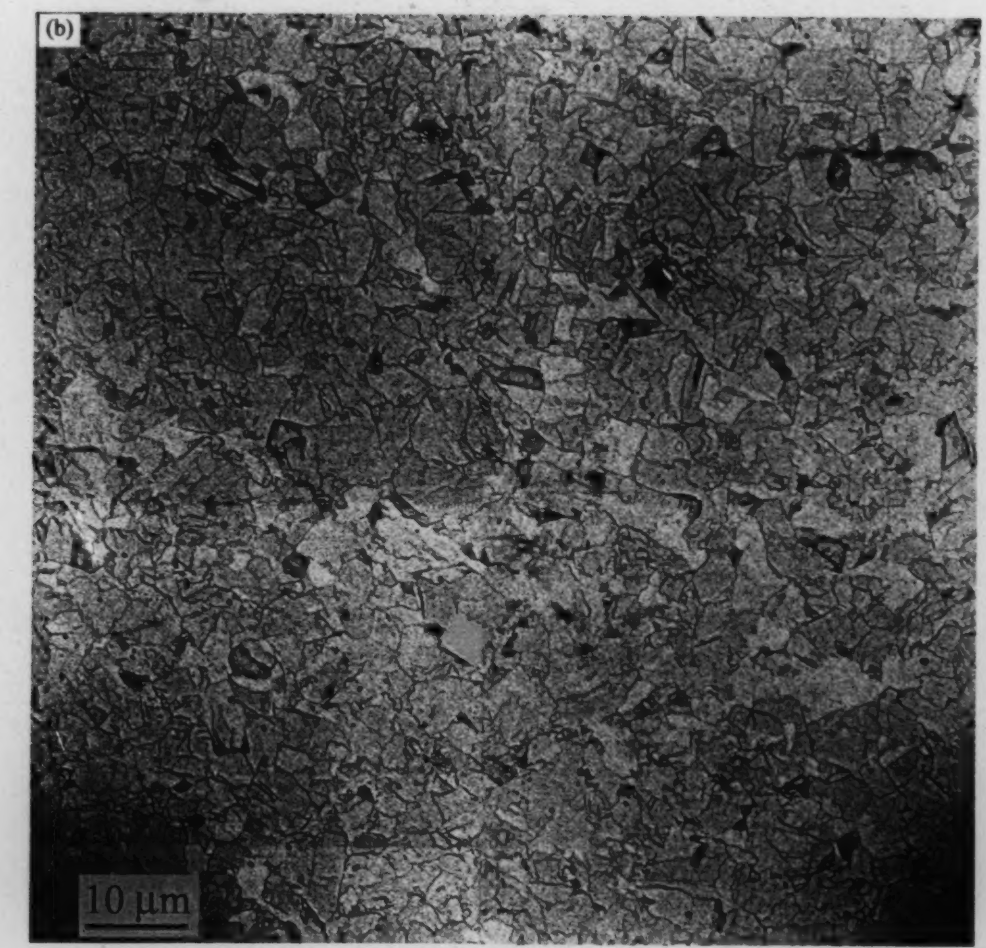
(b)
10 µm

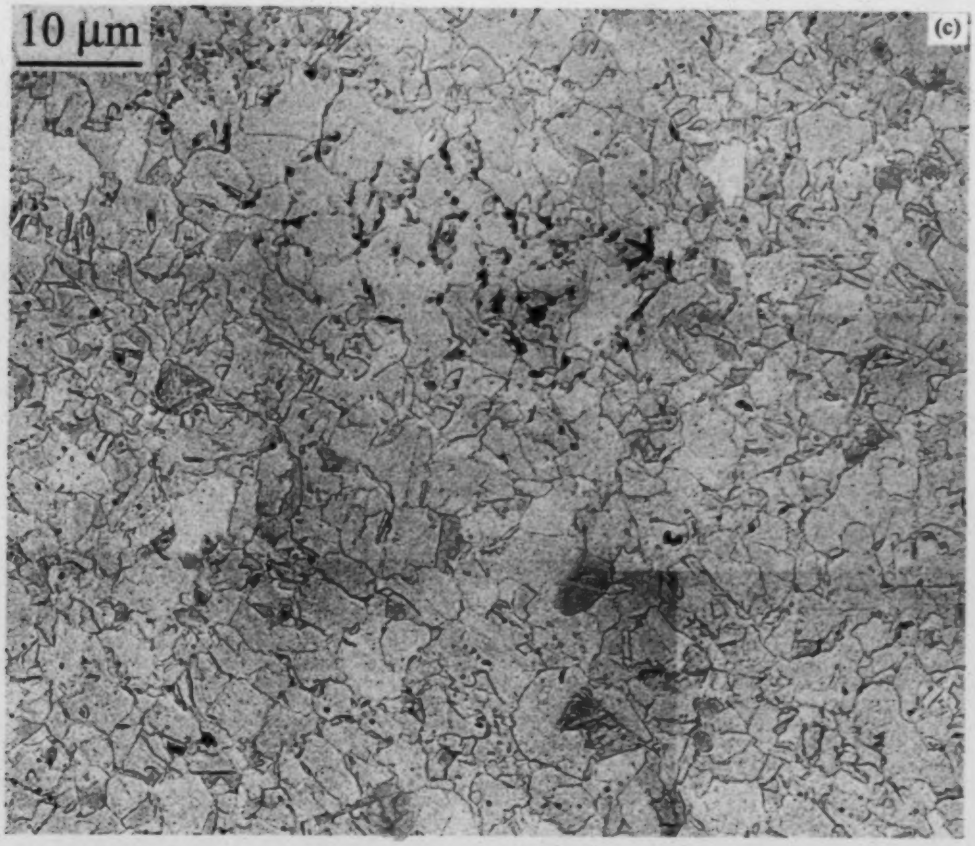

FIG. 6-36. Grain structure in the FGHAZ revealed using TEM–replicas: a) 0.5 kJ/mm; b) 1.5 kJ/mm; c) 2.5 kJ/mm.

TEM images of FIB samples, prepared from the FGHAZ for the different heat inputs, are shown in Figure 6-38 (a-e). The grain boundaries of the polygonal ferrite in the FGHAZ are straight and distinct (Fig. 6-38a, c and e), unlike the jagged grain boundaries in the BM (Fig. 6-30). The plate morphology in FGHAZ-0.5kJ/mm, shown in Fig. 6-38b, is again a result of the relatively high cooling rate (not the main morphology). Fig. 6-38d shows the region marked in (c) at higher magnification, revealing the fine distribution of carbides.

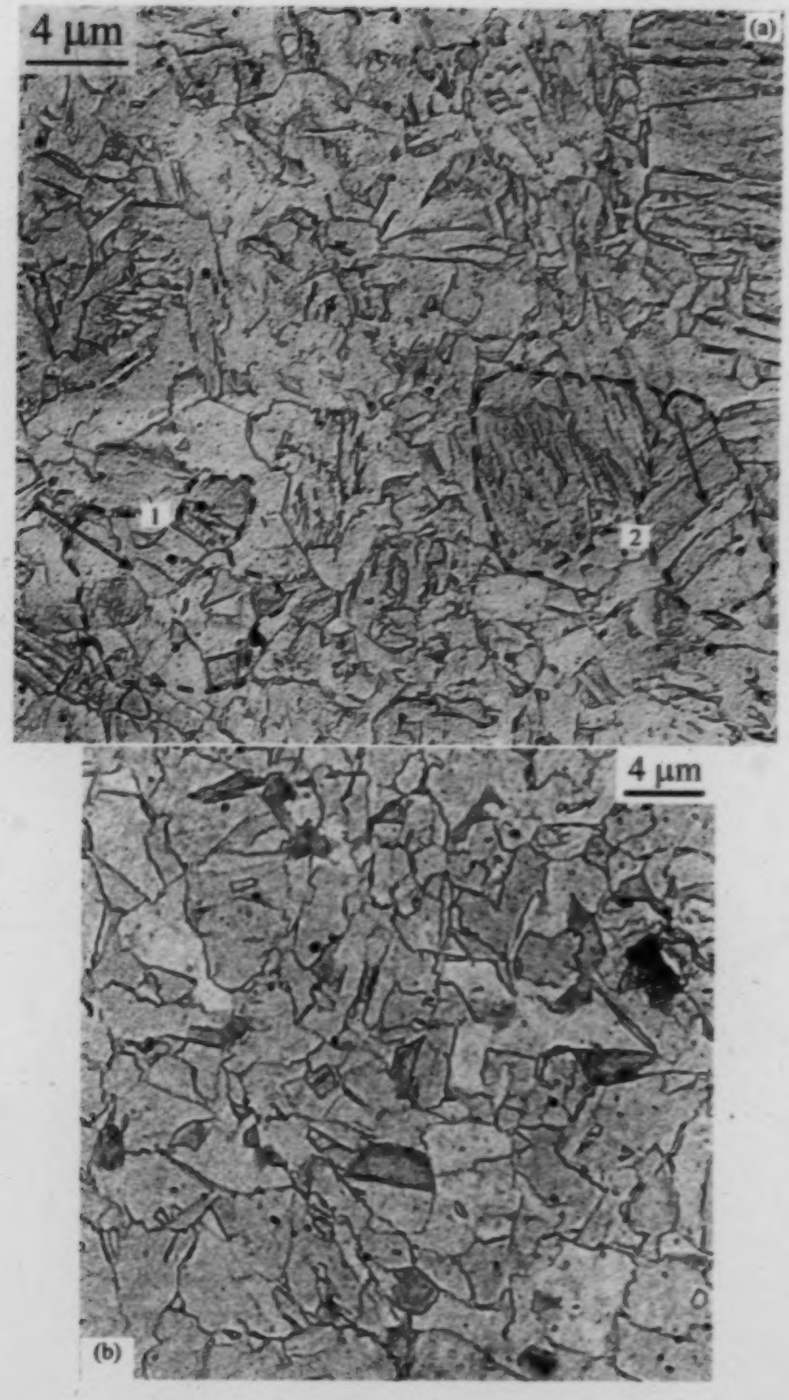
4 μm
(a)
1
2
4 μm
(b)

FIG. 6-37. TEM-replicas from the FGHAZ comparing the grain structure for two heat inputs: a) 0.5 kJ/mm; b) 1.5 kJ/mm.

6-5-2-3. CGHAZ

Figures 6-39 and 6-40 compare the grain structure in the CGHAZ for several heat inputs (0.5–2.5 kJ/mm) with the BM. The former shows a larger number of prior austenite grains in each micrograph from the CGHAZ, while the latter resolves the lamellar structures within the prior austenite grains better. Not only is the transformation to austenite during the heating leg of the weld thermal cycle completed in this sub-zone, but also austenite grain growth has occurred with little restriction. The amount of grain growth depends on the distance from the fusion line (i.e., the peak temperature). Basically, the CGHAZ is made up of large prior austenite grains (few tens of microns in size) with packets of lath martensite for the 0.5 kJ/mm weld sample, and mainly bainitic ferrite for the higher heat-input samples. As can be readily seen from the optical micrographs, the CGHAZ grain structure has more distinct grain boundaries for higher heat inputs of 1.5 and 2.5 kJ/mm than 0.5 kJ/mm, due to reprecipitation of carbides at these locations (Fig. 5-42e). Reprecipitation was mostly suppressed in the CGHAZ of the 0.5 kJ/mm weld sample (Section 5-6-4).

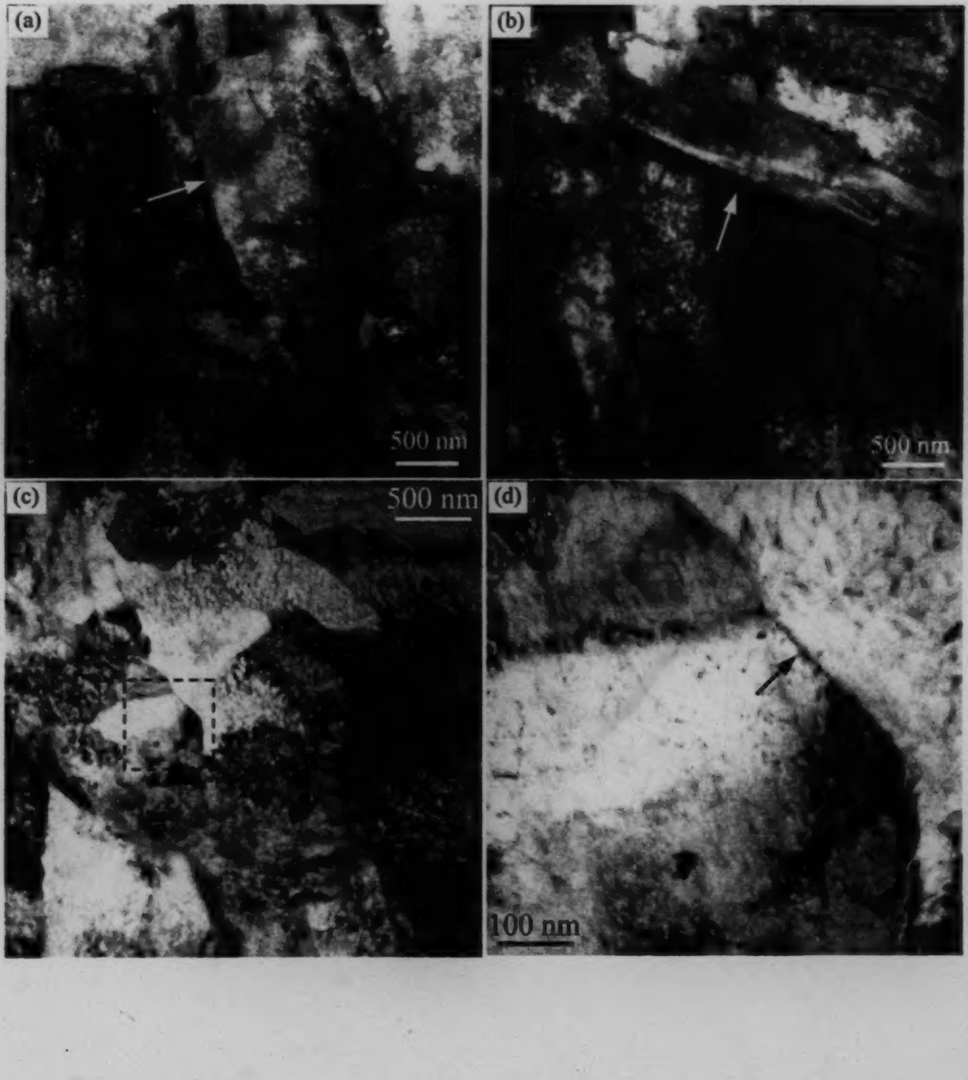

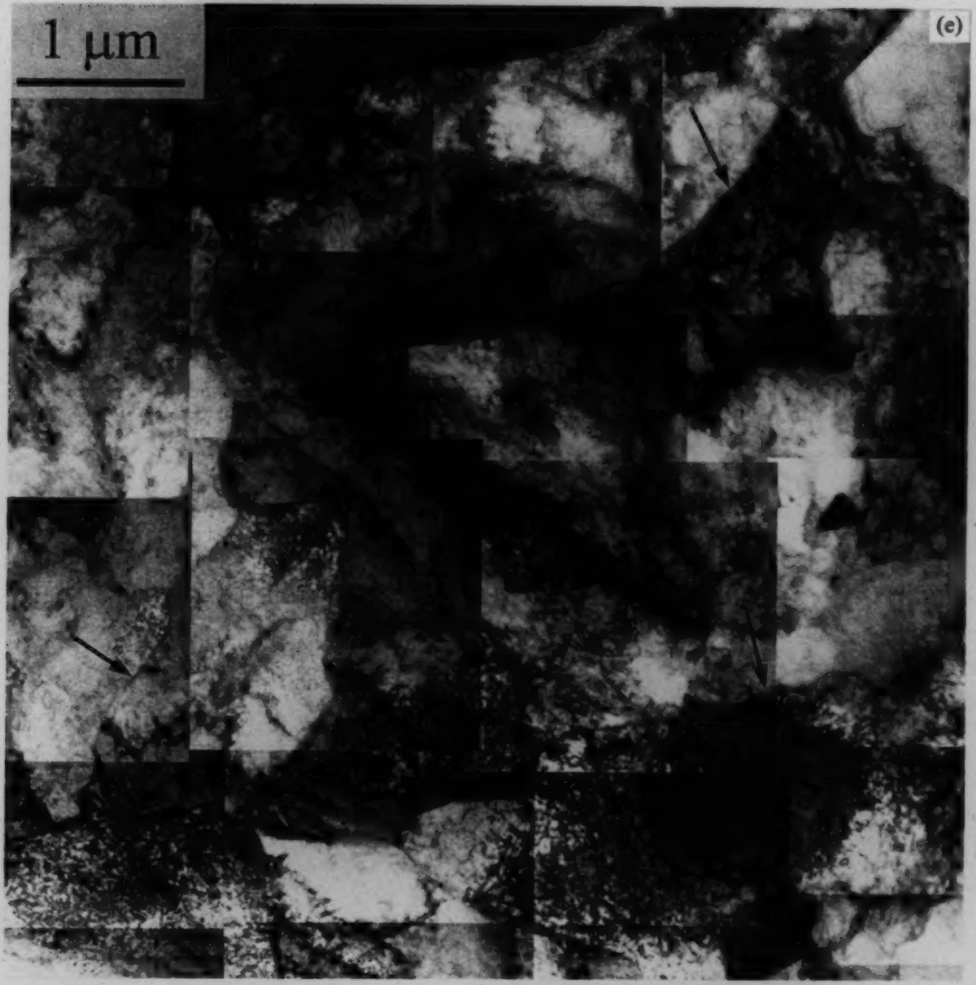

FIG. 6-38. TEM-BF images from FIB samples showing grain and sub-grain structures in the FGHAZ: a–b) 0.5 kJ/mm; c–d) 1.5 kJ/mm; e) 2.5 kJ/mm (a mosaic).

0.5 kJ/mm

The replicas for grain structure examination of the CGHAZ were also obtained from the longitudinal sections (w.r.t. welding direction). A main characteristic of the CGHAZ, unlike the FGHAZ, is the variation of prior austenite grain size across the sub-zone. This can induce microstructural and property variations across the CGHAZ. Figure 6-41a shows a replica spanning the whole width of the CGHAZ–0.5 kJ/mm. The mosaics from the three selected grids (R_1–R_3) are shown in Fig. 6-41 (b–d). The original direct magnification was 3000x. The variation in prior austenite grain size is noticeable. One prior austenite grain on each grid is indicated by an arrow for comparison. The diagonal lengths for these selected grains can be measured as around 15, 35 and 95 µm for grids R_1, R_2 and R_3, respectively.

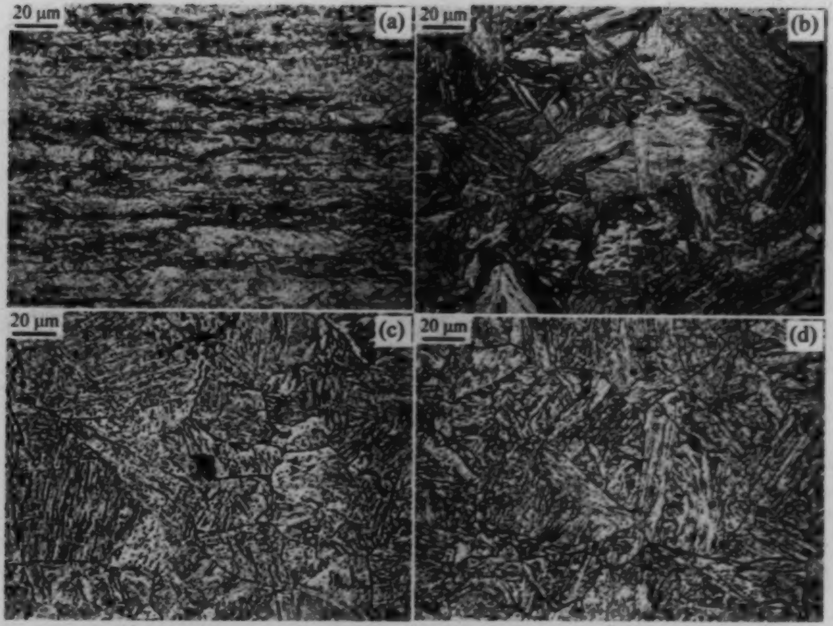
20 µm
(a)
20 µm
(b)
20 µm
(c)
20 µm
(d)

FIG. 6-39. Optical micrographs from the CGHAZ as compared with the BM: a) BM; b) CGHAZ–0.5kJ/mm; c) CGHAZ–1.5kJ/mm; d) CGHAZ–2.5kJ/mm. Prior austenite grains are visible in the CGHAZ.

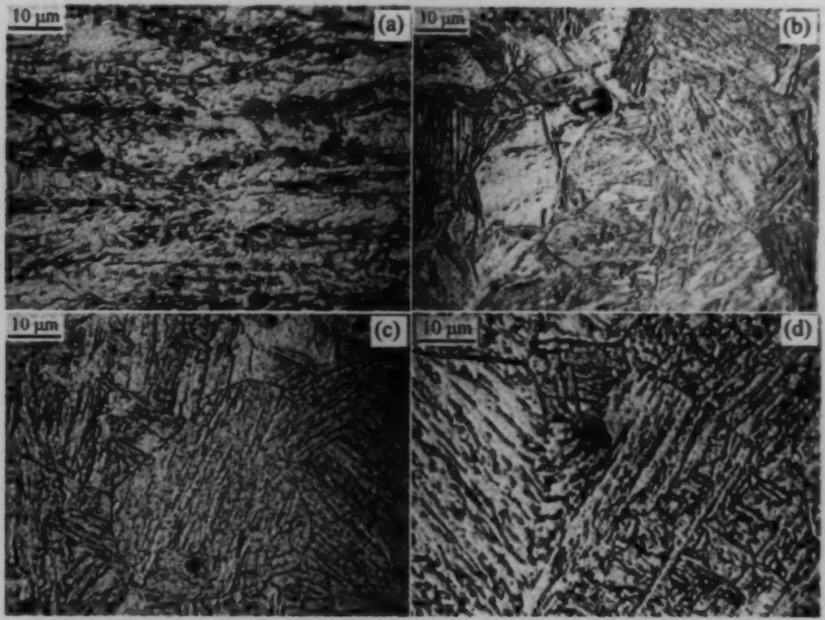
10 µm
(a)
10 µm
(b)
10 µm
(c)
10 µm
(d)

FIG. 6-40. Optical micrographs from the CGHAZ as compared with the BM: a) BM; b) CGHAZ–0.5kJ/mm; c) CGHAZ–1.5kJ/mm; d) CGHAZ–2.5kJ/mm. The lamellar structures within the prior austenite grains are better resolved here.

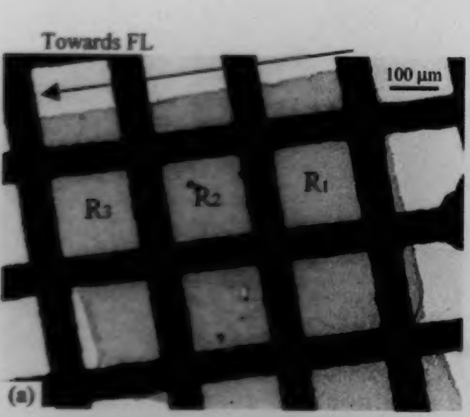
Towards FL
100 µm
R3
R2
R1
(a)

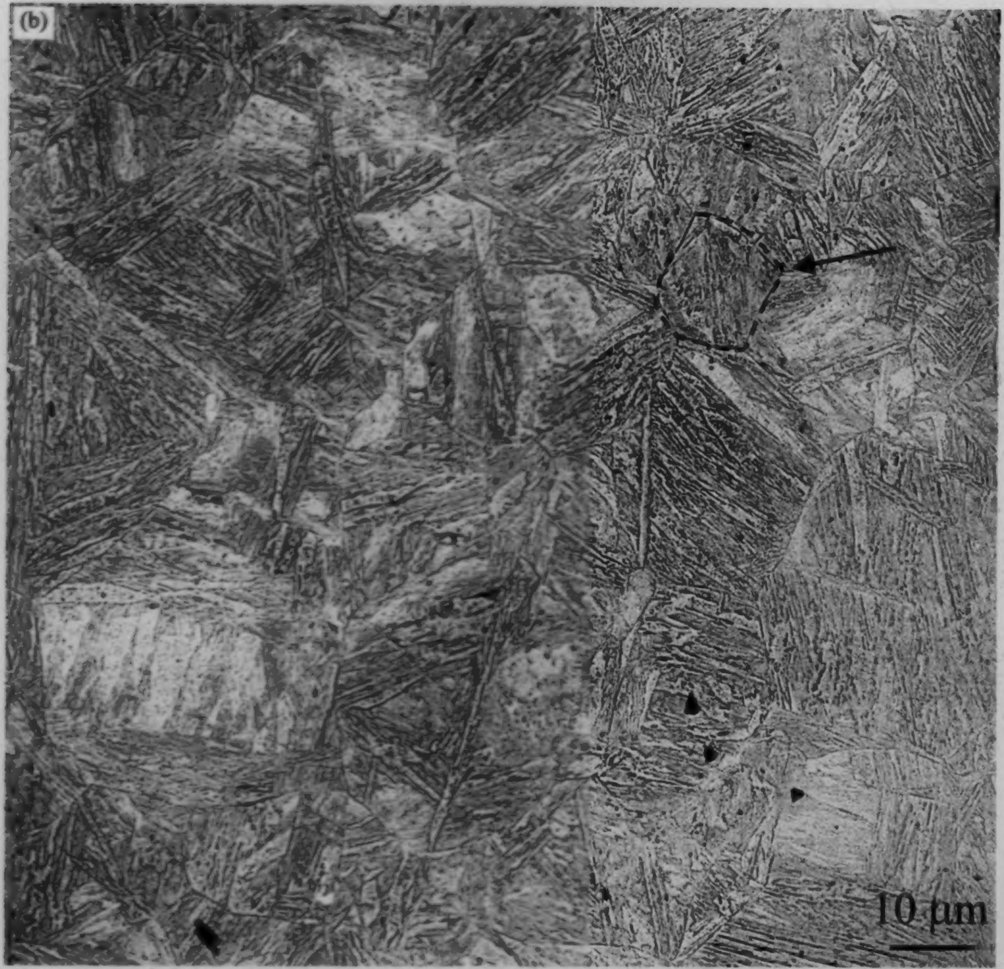
(b)
10 µm

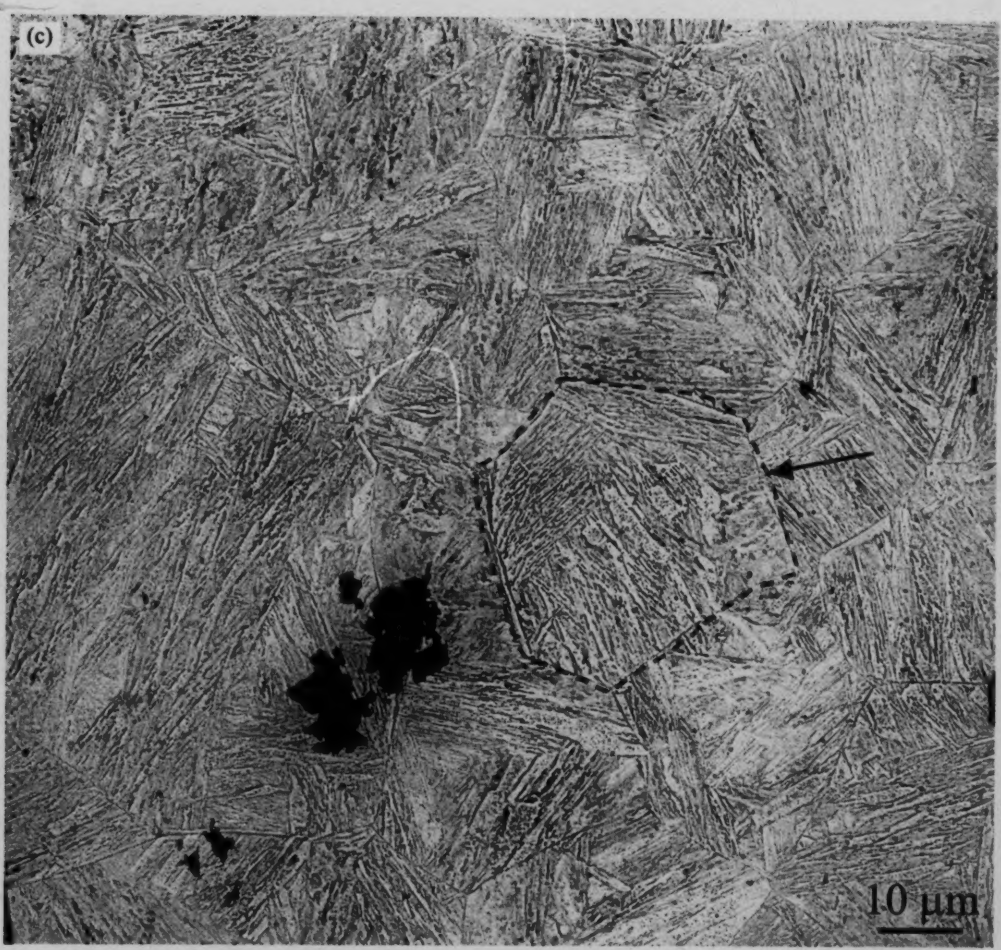
(c)
10 µm

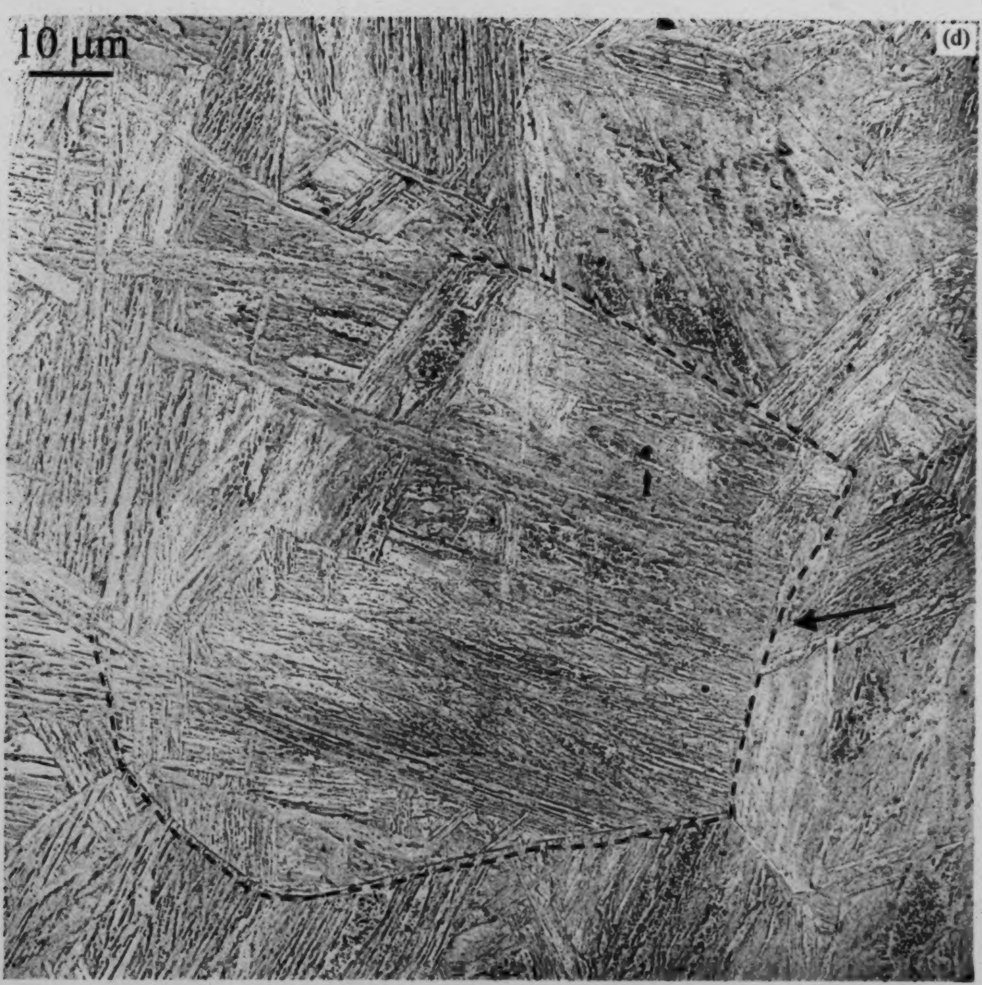

FIG. 6-41. Grain structure in the CGHAZ–0.5 kJ/mm revealed using TEM–replicas: a) the grid locations with respect to the fusion line (FL); b–d) Grids R_1–R_3.

A typical prior austenite grain chosen from grid R_2 is further magnified in Fig. 6-42a. A packet of fine lath martenitsite is indicated as region "1". Although this microstructure is a major morphology in CGHAZ–0.5 kJ/mm, other morphologies can be noticed. A very minor structure is grain-boundary ferrite that grows on the boundary of a prior austenite grain (indicated by arrow in Fig. 6-42a). Another major microstructure than can be noticed in many regions is wide plates of ferrite with intermediate-size particles inside. This is indicated in Fig. 6-42a as region "2". This microstructure, referred to as coarse autotempered (lath) martensite by some researchers [53, 56], is also indicated by arrows in Fig. 6-42b and c, which are selected from grid R_1. It has a width of 2–4 µm. The cementite particles that are few hundreds of nanometers in length (Fig. 6-49d) have certain angles within the plates (suggesting an orientation relationship with the matrix which is a charateristic of autotempered martensite). The cementite particles were observed more widely in CGHAZ–1.5 kJ/mm (examined in detail in Section 5-6-4). Another morphological feature is the formation of triangles of lath martensite. One of these is marked in Fig. 6-42c. The formation is due to certain variants of the orientation relationship between the laths and the prior austenite. Coarse martensite forms first from austenite (at relatively high temperatures) and as a result are autotempered, while fine LM forms at lower temperatures and are relatively heavily dislocated and untempered [53]. Another explanation can be that of Speich and Warlimont [11] who found massive ferrite along with lath martensite in the quenched low-carbon irons. Cementite precipitation in massive ferrite takes place after aging at room temperature for several days. Massive ferrite forms at higher temperatures through a massive transformation mechanism.

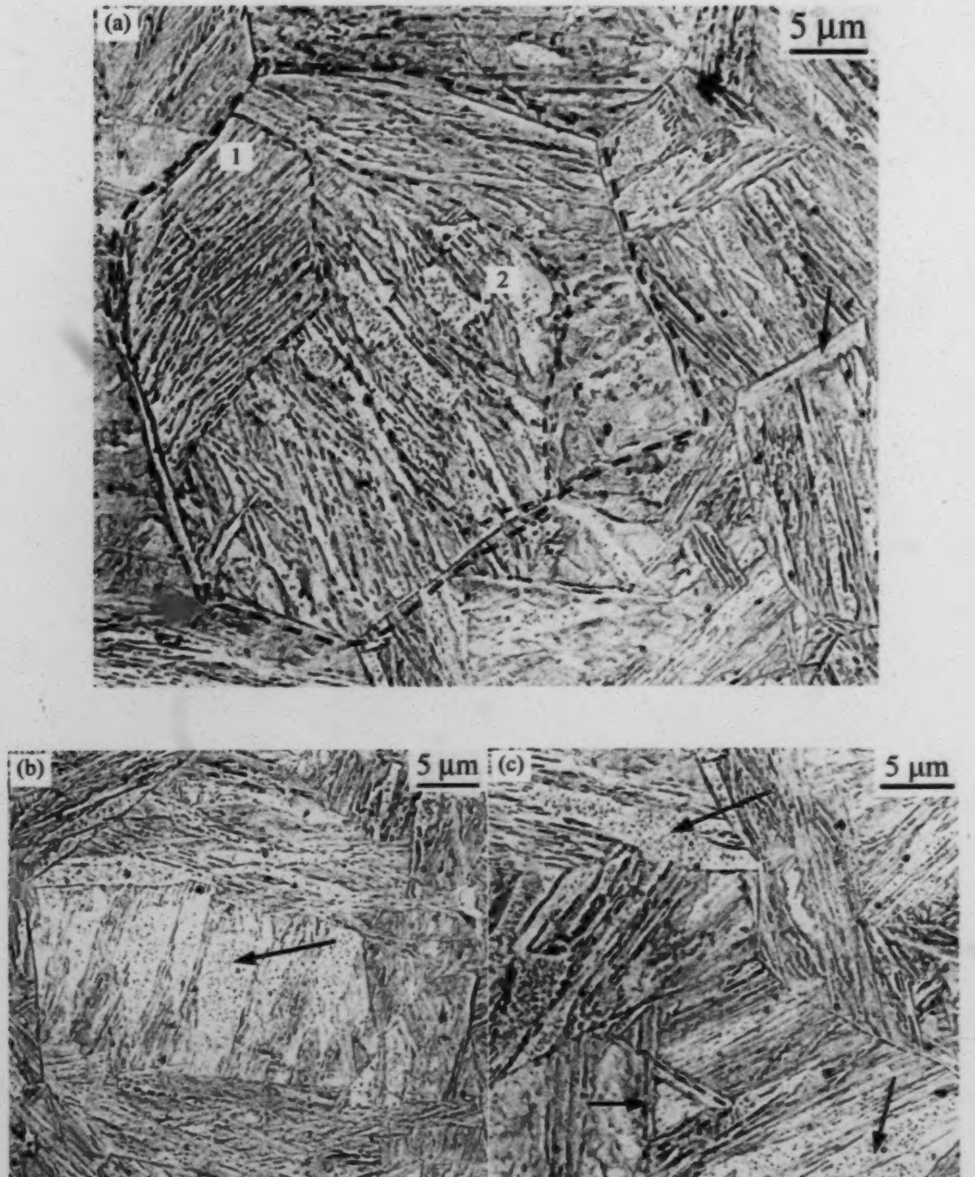

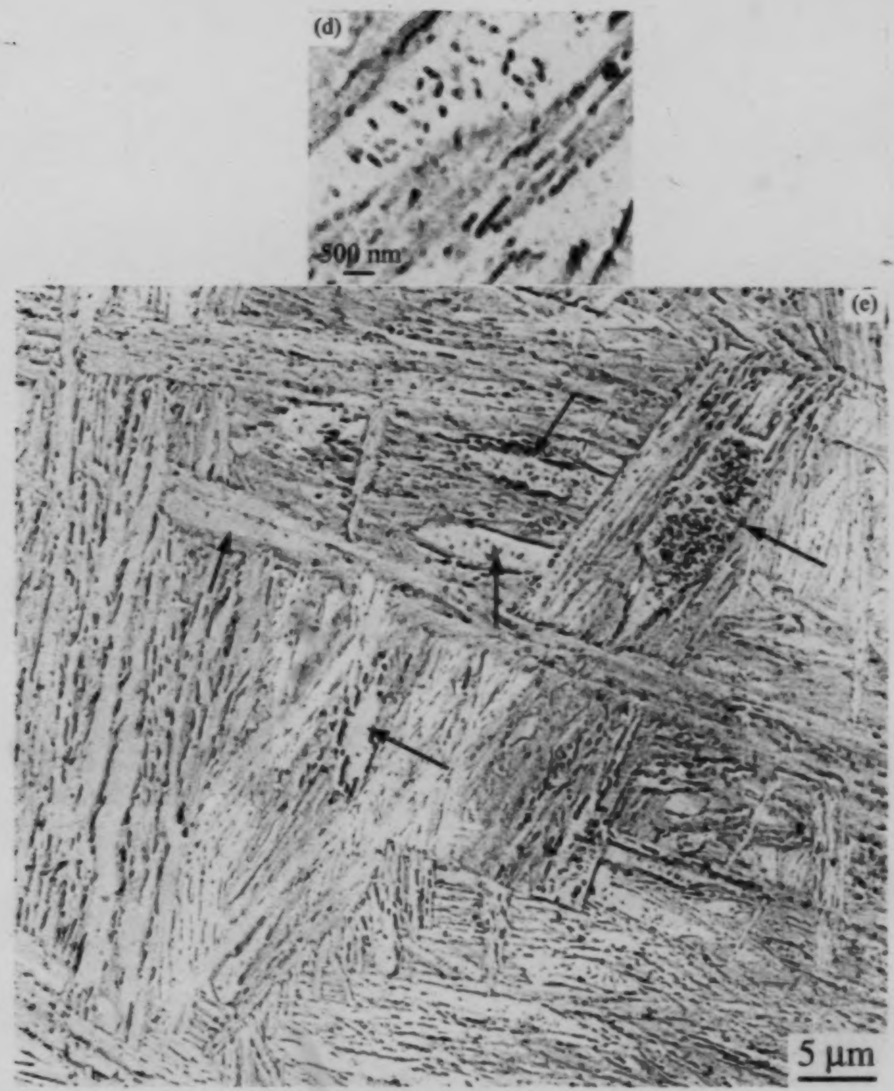

FIG. 6-42. Selected images from the CGHAZ–0.5 kJ/mm revealing different microstructures: a) selected from grid R_2; b) selected from grid R_1; d) selected from grid R_2; e) selected from grid R_3.

At regions closer to the fusion line, i.e., grid R_3, the prior austenite grains are very large, the packets are larger and the laths are longer. Nevertheless, individual plates of ferrite within the large grains can be observed (Fig. 6-42e). These might have nucleated on the inclusions and large TiN particles intragranularly (similar to acicular ferrite). They have various amounts of intermediate-size particles (likely cementite) inside them. They are indicated with arrows in Fig. 6-42e. These findings support the idea that the microstructure, although mainly martensitic, is not 100% martensite. As the carbon level decreases in steel, formation of martensite becomes more difficult [11]. The lath martensite structure in CGHAZ-0.5 kJ/mm, taken from the FIB samples, is shown in Fig. 6-43. The laths are 100–300 nm wide and 1–4 μm long. Their small width has a significant contribution to the strength and hardness.

1.5 kJ/mm

The grain structure variation for the CGHAZ–1.5 kJ/mm is shown in Fig. 6-44. Figure 6-44a shows schematically the replica, spanning across the whole width of the CGHAZ. The mosaics from the five selected grids (R_1–R_5) are also shown in Fig. 6-44 (b–f). The original direct magnification was 1000x. To get a sense of the variation in prior austenite grain size, one prior austenite grain on each grid is marked by an arrow. The diagonal lengths for these selected grains can be measured as ~7, 17, 31, 46 and 94 μm for grids R_1 to R_5, respectively. Note that they do not represent the average grain sizes at those locations; average grain size will be discussed in Section 6-5-7.

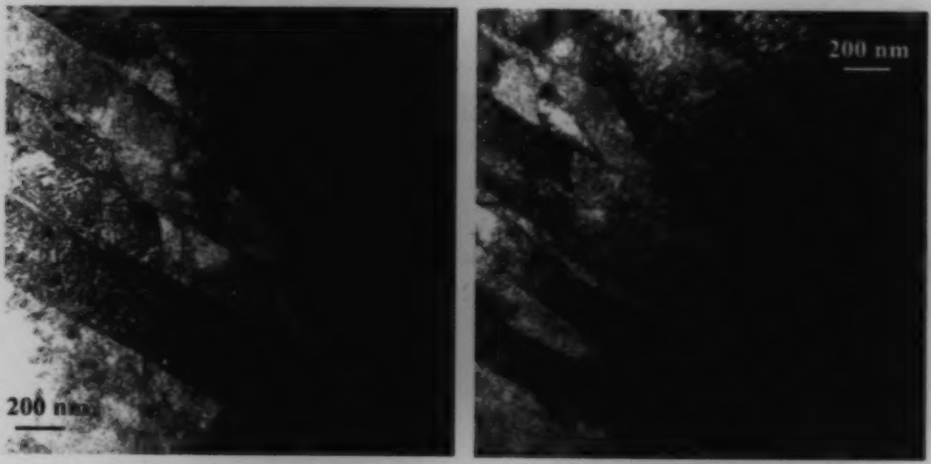

FIG. 6-43. Thin-foil TEM (FIB) showing fine lath martensite in CGHAZ-0.5 kJ/mm.

Part of grid R_4 is magnified in Fig. 6-45a. This is in fact a mosaic of TEM micrographs with an original direct magnification of 3000x. Some of the GF grains are indicated by arrows. Essentially, as the heat input increases (i.e., the cooling rate decreases), there will be an increase in the amount and frequency of higher-temperature transformation products, such as grain-boundary ferrite, acicular ferrite and upper bainite. The main constituent within the large prior austenite grains (such as region "1" in Fig. 6-45a) is the packets of dense bainitic ferrite laths that have replaced the lath martensite in the CGHAZ–0.5 kJ/mm. However, Fig. 6-45a also shows the morphological characteristics of other bainitic structures, which are better resolved in Fig. 6-45b and c. They show granular bainite comprising of massive ferrite (MF) and granules of M/A or bainitic laths. In many regions (e.g., Fig. 6-45c) cementite particles within the laths of ferrite are visible (lower bainite). Fig. 6-46 is a FIB-TEM image showing some of these particles. These were examined in detail in Section 5-6-4 (Fig. 5-41).

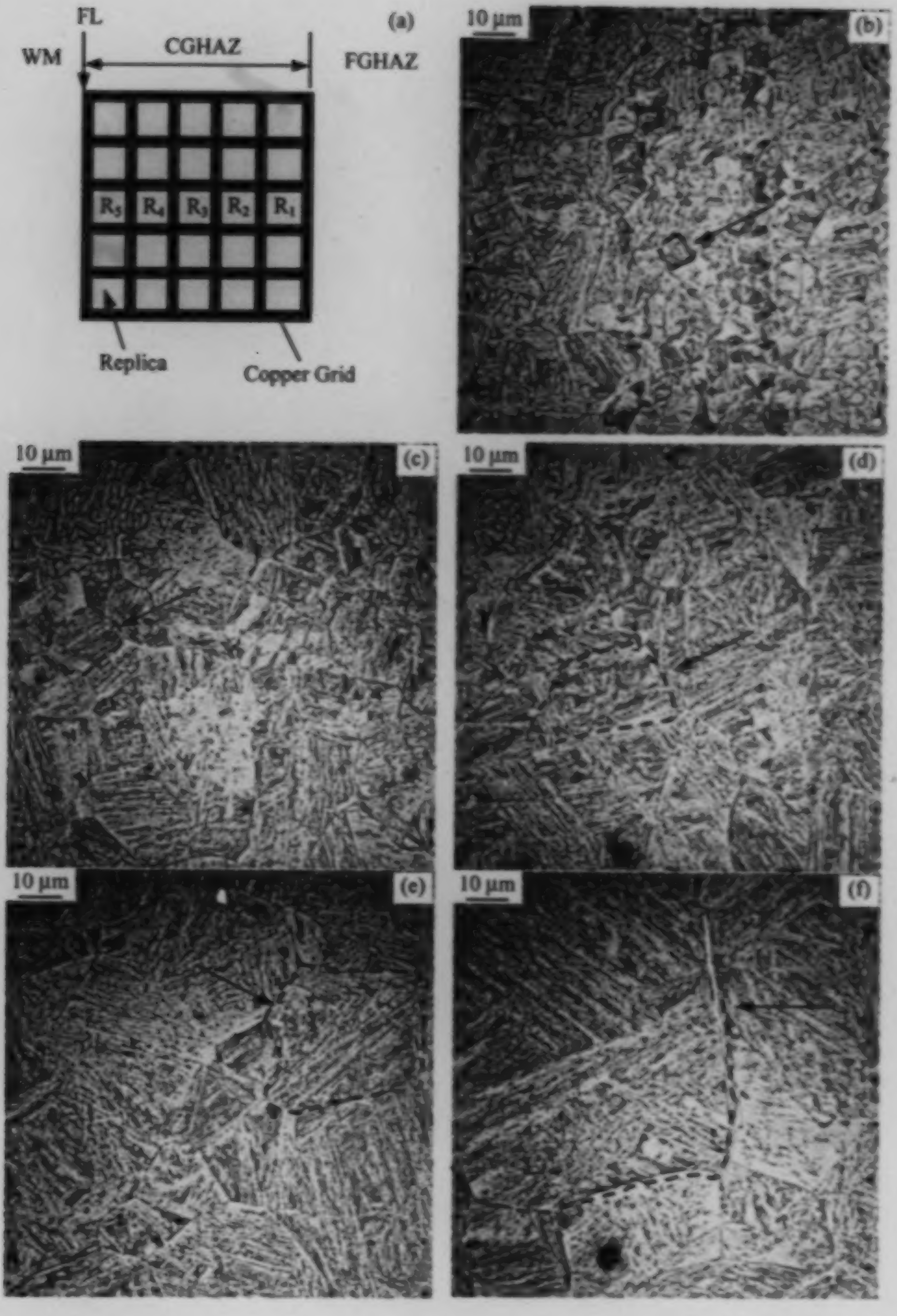
FL
(a)
WM
CGHAZ
FGHAZ
R_5
R_4
R_3
R_2
R_1
Replica
Copper Grid
10 µm
(b)
10 µm
(c)
10 µm
(d)
10 µm
(e)
10 µm
(f)

FIG. 6-44. Grain structure in the CGHAZ–1.5 kJ/mm revealed using TEM–replicas: a) the grid locations with respect to the fusion line (FL); b–f) Grids R_1–R_5.

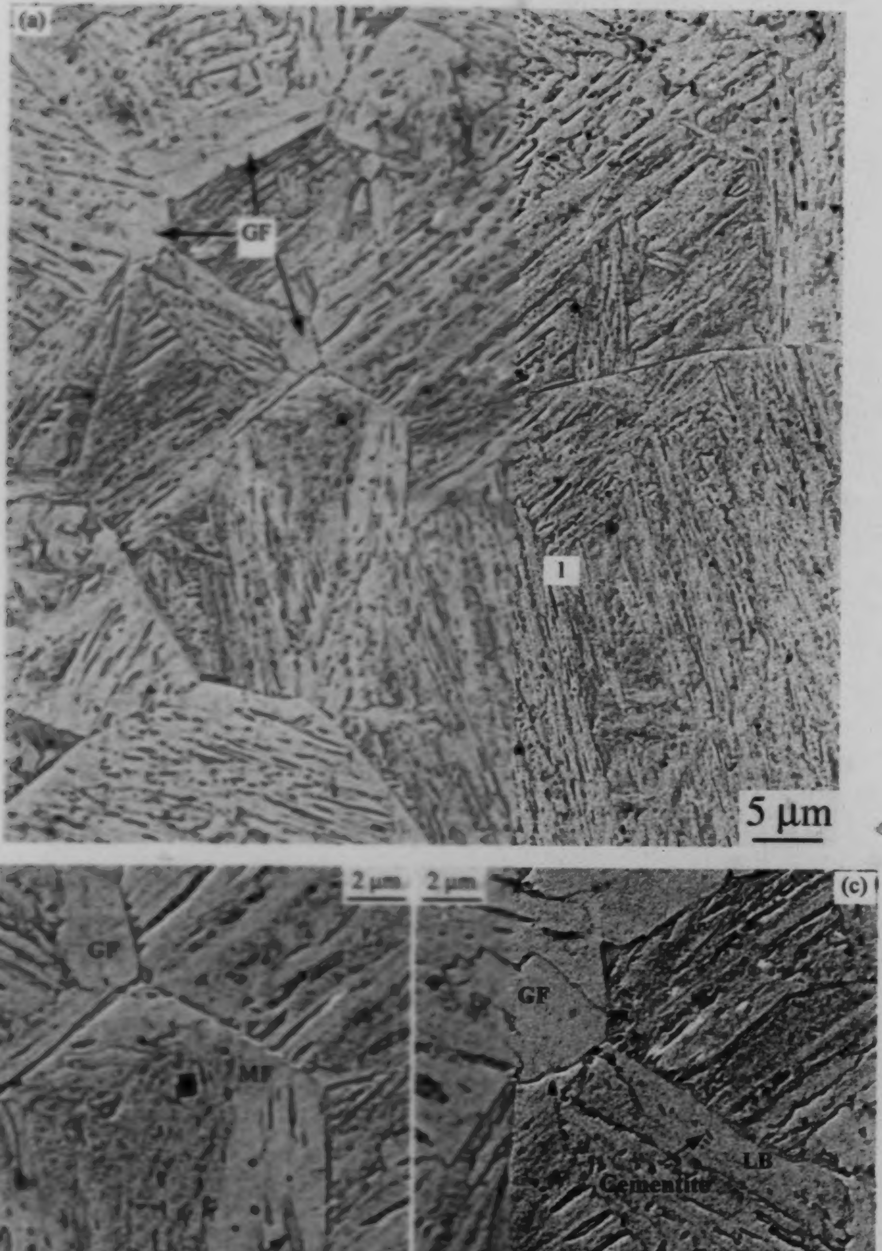
(a)
GF
1
5 µm
(b)
2 µm
GF
MF
Granules of
M/B/A
2 µm
(c)
GF
LB
Cementite

FIG. 6-45. Selected images from the CGHAZ–1.5 kJ/mm, grid R_4 in Fig. 6-40. GF: grain-boundary ferrite; MF: massive ferrite; M: martensite; (L)B: (Lower) bainite; A: retained austenite.

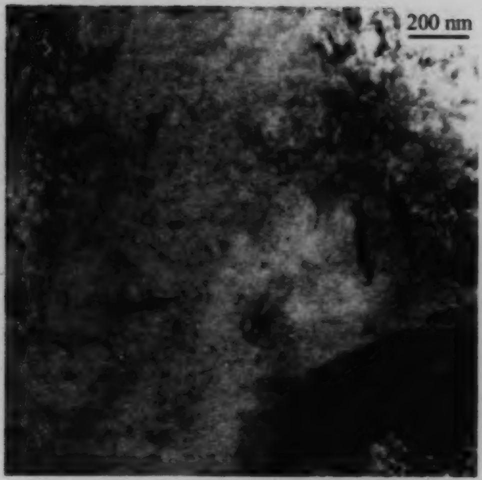

FIG. 6-46. A FIB-TEM image from the CGHAZ–1.5 kJ/mm showing some cementite particles.

2.5 kJ/mm

Fig. 6-47a shows a whole grid of a replica from near the middle of the CGHAZ–2.5 kJ/mm width. Three prior austenite grains are marked on the mosaic. The sizes vary between ~20 and 80 μm in diagonal length. The structure mainly consists of lamellar ferrite, particularly UB and GB with some AF.

Region 1, further magnified in Fig. 6-47b, shows a triangular arrangement of bainitic plates/laths due to growth in certain orientations in a prior austenite grain. Region 2 shows the same structure but sectioned transversely. It also shows a packet consisting of some AF, indicated by an arrow and further magnified in Fig. 6-47c. The AF plates, likely to have nucleated on nitrides or inclusions, show certain OR with prior austenite, indicated with the triangular arrangement. Region 3, further magnified in Fig. 6-47d, shows a smaller PAGS with a GB microstructure, consisting of MF and granules of M/A or bainitic laths. Very few GF regions were found in this sub-zone, which is somewhat surprising. This may be a sampling effect, i.e., only a small region is imaged. Otherwise, it is known that an increase in the heat input will result in an increase in the occurrence of GF and an increase of the width of GF along the prior austenite grain boundaries [67]. One region with GF is shown in Fig. 6-47e. Of course, it is known that the formation of GF in Nb-bearing low-carbon steels is generally suppressed at the heat inputs examined here [67], likely due to segregation of Nb at the prior austenite grain boundaries.

A large prior austenite grain (~60 μm in diagonal length) was found in another grid consisting mainly of AF (Fig. 6-47f). The star-shape of plates interwoven in the adjacent plates is noticeable. At this higher heat input, the reduced cooling rate provides the chance for nucleation of ferrite plates within the large prior austenite grains when there are sufficient nitrides or inclusions. The primary plates of AF grow on the nitrides and other inclusions, followed by growth of secondary plates on the primary plates. Note that the cooling rate is not too slow to allow formation of PF within the grains, as would be the case if much higher heat inputs than experienced here were applied [67]. The ferrite plates for this sample are characteristically wide. Fig. 6-48 shows some of the bainitic ferrite laths. Note that the plate width has increased to ~1–2 μm (also noticeable on replicas), to be compared with the width of martensite laths in the CGHAZ–0.5 kJ/mm, which were 100–300 nm. Heat inputs higher than 2.5 kJ/mm (not examined here) are expected to result in the formation of GF and WF at the prior austenite grain boundaries and AF and PF within the grains.

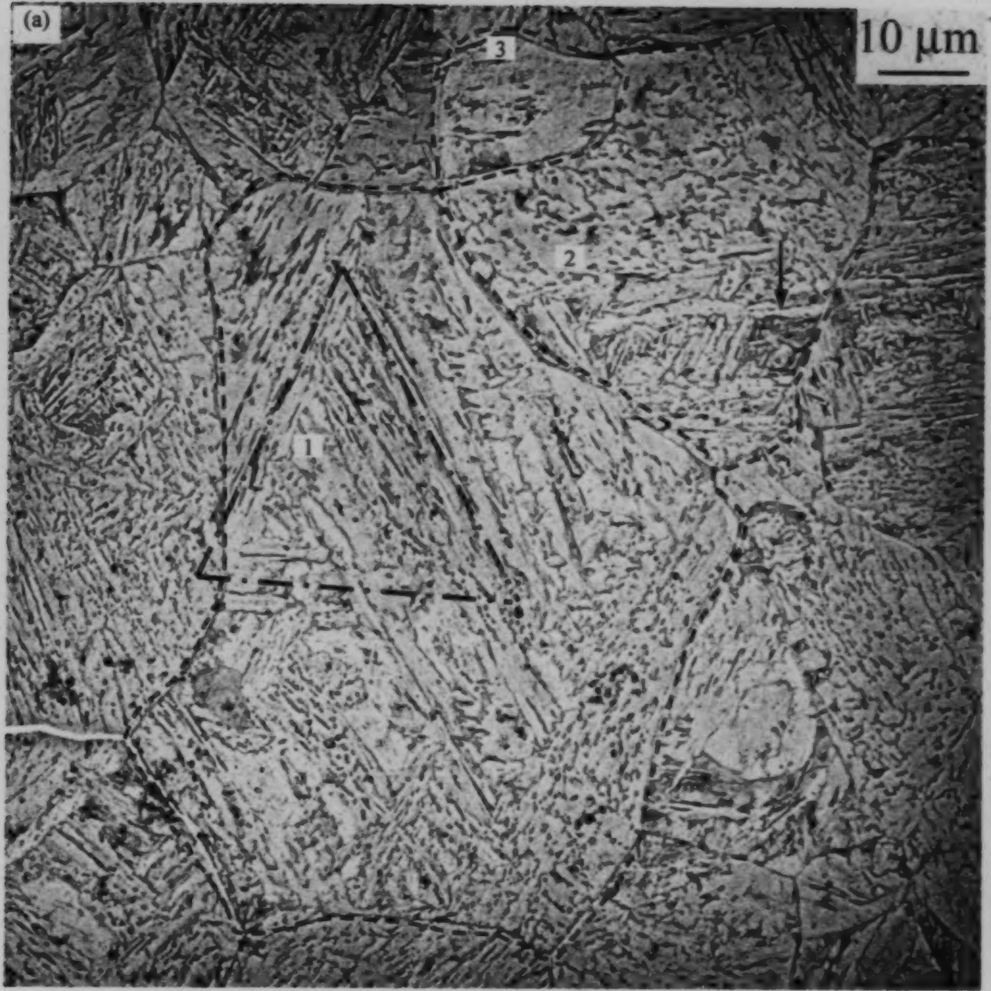
(a)
10 µm
1
2
3

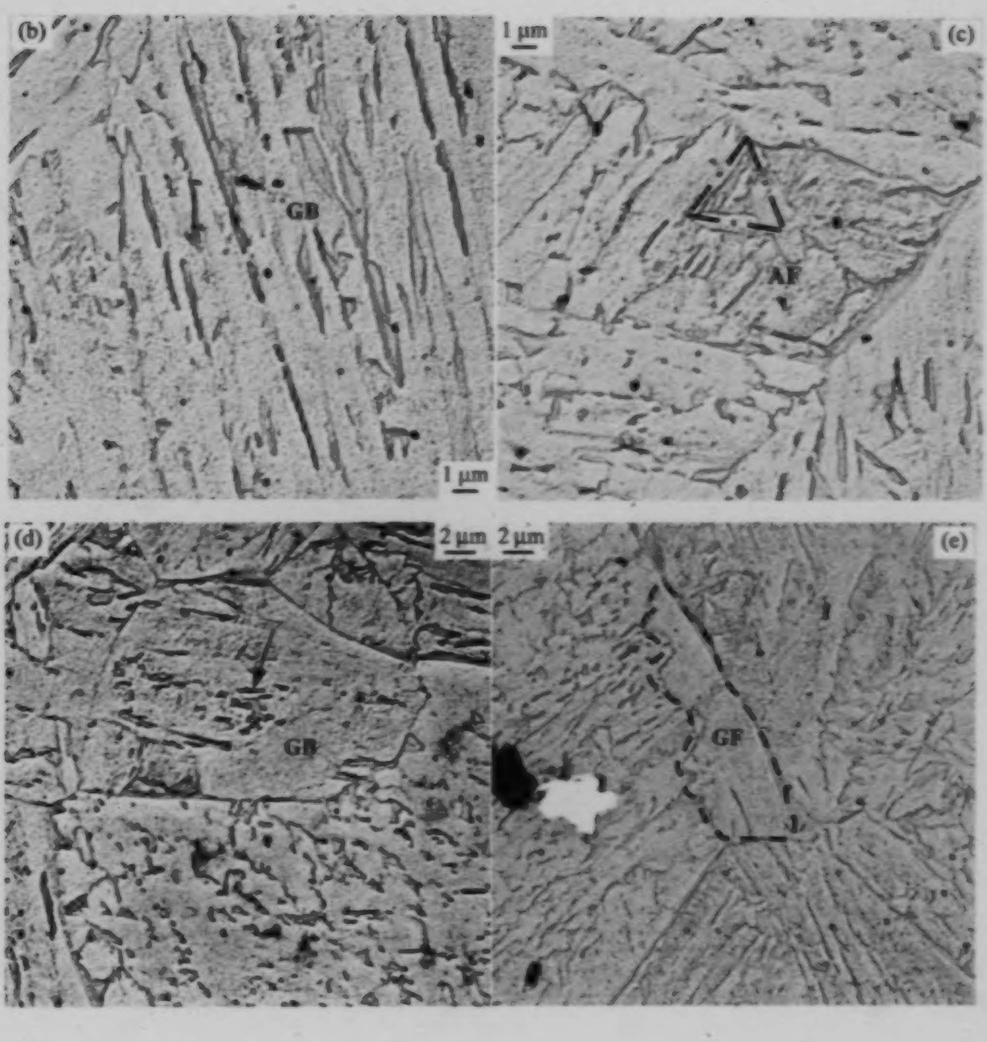
(b)
GB
1 µm
1 µm
(c)
AF
(d)
2 µm
GB
2 µm
(e)
GF

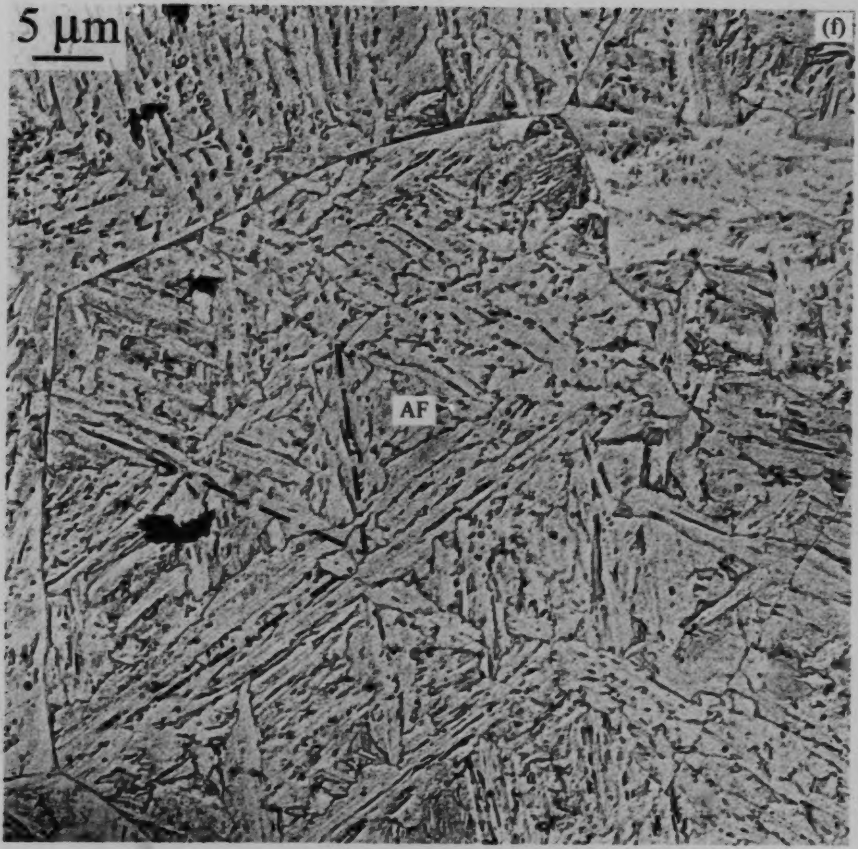

FIG. 6-47. Grain structure in the CGHAZ–2.5 kJ/mm revealed using TEM–replicas: a) a whole grid in the mid width; b–d) selected images from regions 1–3 in (a); e–f) selected images from other grids.

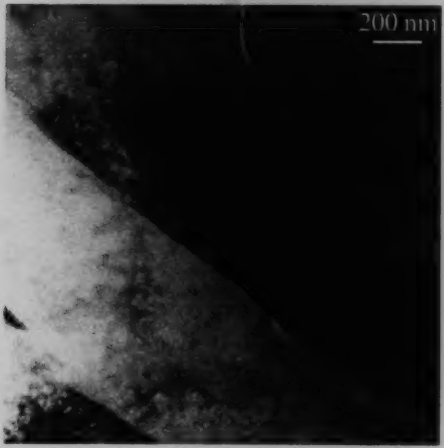

FIG. 6-48. A FIB-TEM images from CGHAZ–2.5 kJ/mm showing wide plates of bainitic ferrite.

6-5-3. Twinned regions

6-5-3-1. Across the HAZ [§]

While examining the FIB-TEM samples, regions exhibiting striations were observed in some subzones across the HAZ, particularly in CGHAZ-0.5 kJ/mm. Most of the areas were characterized as twinned structures through SAD. Fig. 6-49 shows a region in FGHAZ-1.5 kJ/mm where two groups of striated regions were observed. The SAD pattern, from region 2, was not taken at the proper orientation and, therefore, only shows the striated spots (Fig. 6-49b). Although it shows that the striated regions are bcc-iron, it does not prove they have twin relations with the matrix. The DF image shows the striations from region 2 (Fig. 6-49c). Figure 6-50a and b show another region in the same sample, before and after tilting to a proper orientation, where both the matrix and the striated laths were diffracting. The SAD pattern taken at this angle was indexed and showed the striated regions were twin-related with the matrix (Fig. 6-50c). The DF from a (200) twin plane shows the striations perpendicular to the <121> direction, i.e., normal to the twin plane in bcc crystals (Table 6-1). A twinned region was also found in the FGHAZ-2.5 kJ/mm too (Fig. 6-51), while no twinned regions were detected in FGHAZ-0.5 kJ/mm or ICHAZ (0.5–2.5 kJ/mm), even after repeated tilting at high magnifications.

In the CGHAZ, however, twinning was observed in the 0.5 kJ/mm weld sample but not in the 1.5 and 2.5 kJ/mm samples. Fig. 6-52a shows a mosaic of TEM images from a FIB sample prepared from the mid section of the CGHAZ-0.5 kJ/mm. Martensite laths as well as parallel striated features, resembling twins, are apparent. These striations are not as packed and as thin as those observed in FGHAZ (~10–20 nm in thickness) and normally are expected from twinned martensite in higher-carbon steels. The striations went in and out of contrast upon specimen tilting (Fig. 6-52b and c), indicating that the contrast arises from a change in diffraction conditions. To see if the striated features were indeed twins, the sample was tilted to a [012] zone axis (Fig. 6-53). BF and DF images from a region with striations, as well as the corresponding selected area diffraction (SAD) pattern, are shown in Fig. 6-53 (a-c). The SAD pattern contains the main matrix reflections (most intense spots), as well as additional reflections arising from the twins and double diffraction. The pattern has been fully indexed in the accompanying schematic (Fig. 6-53d). The twins appear bright in the DF image and are indicated by arrows. These twinned grains are elongated, 50–200 nm in thickness and 100–300 in length. They were sparsely distributed throughout the microstructure.

6-5-3-2. Simulated samples

Two conditions were simulated as explained in Section 6-4. The results are presented below.

Short term (4 min) heat treatment

Initially, samples were solution treated at ~1150°C for a short amount of time (~4 min), to simulate the CGHAZ. The real CGHAZ experiences *peak* temperatures from roughly 1100 to 1500°C, but for much shorter periods of time. A sample with an initial thickness of 1.5 mm was found to have a high hardness. Note that in the initial setup, the atmosphere was not controlled and a considerable amount of oxidation would happen. The microstructure of the selected sample is shown in Fig. 6-54a, which was very similar to that of CGHAZ–0.5 kJ/mm (Fig. 6-39b); the microstructure is mainly packets of lath martensite (width of ~100–300 nm and length of ~1–4 μm) in the relatively large (several tens of micron) prior austenite grains. The microhardness was also very similar: 364 ± 4 HV0.5 (also 365 HV1), indicating it was mainly martensitic. TEM examination of a FIB sample prepared from the sample is shown in Fig. 6-55. Although packets of fine lath martensite (LM) can be seen over large areas, regions of apparently massive ferrite (MF) can be observed as well. This is likely due to the low level of carbon in some regions, due to a very short delay in air during sample transfer from the furnace to the bucket of iced-brine, and the limited cooling rate (not exceeding 10^4 °Cs^{-1}). It is known that formation of LM becomes difficult under these conditions [11]. Nevertheless, the sample showed a considerable amount of twinning (Fig. 6-55b), but not as much as observed in CGHAZ-0.5 kJ/mm and only in some locations apparently void of densely packed fine LM. The diffraction pattern in the inset of Fig. 6-55c (with a zone axis [-113]), which shows the twinning relationship, was taken after tilting the sample to a suitable angle so that both the twins and the matrix were diffracting (not shown here).

[§] A version of this section has been published. K. Poorhaydari, B.M. Patchett and D.G. Ivey, 2004. Science and Technology of Welding and Joining. 9 (2), pp. 177-180.

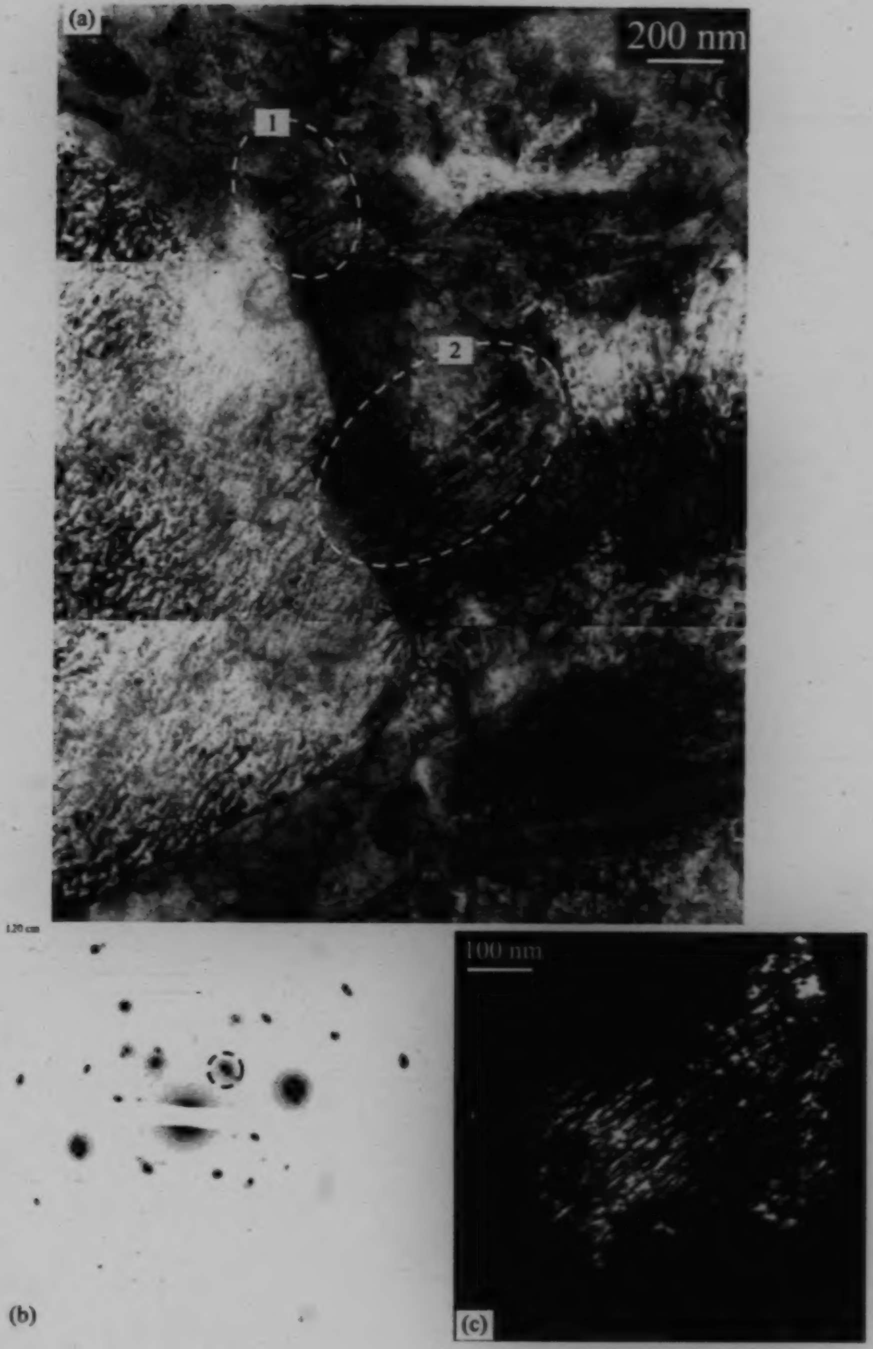
(a)
200 nm
1
2
100 nm
(b)
(c)

FIG. 6-49. FIB-TEM images from the FGHAZ-1.5 kJ/mm: a) two regions of striations; b) SAD from region 2; c) DF image from the spot circled in (b).

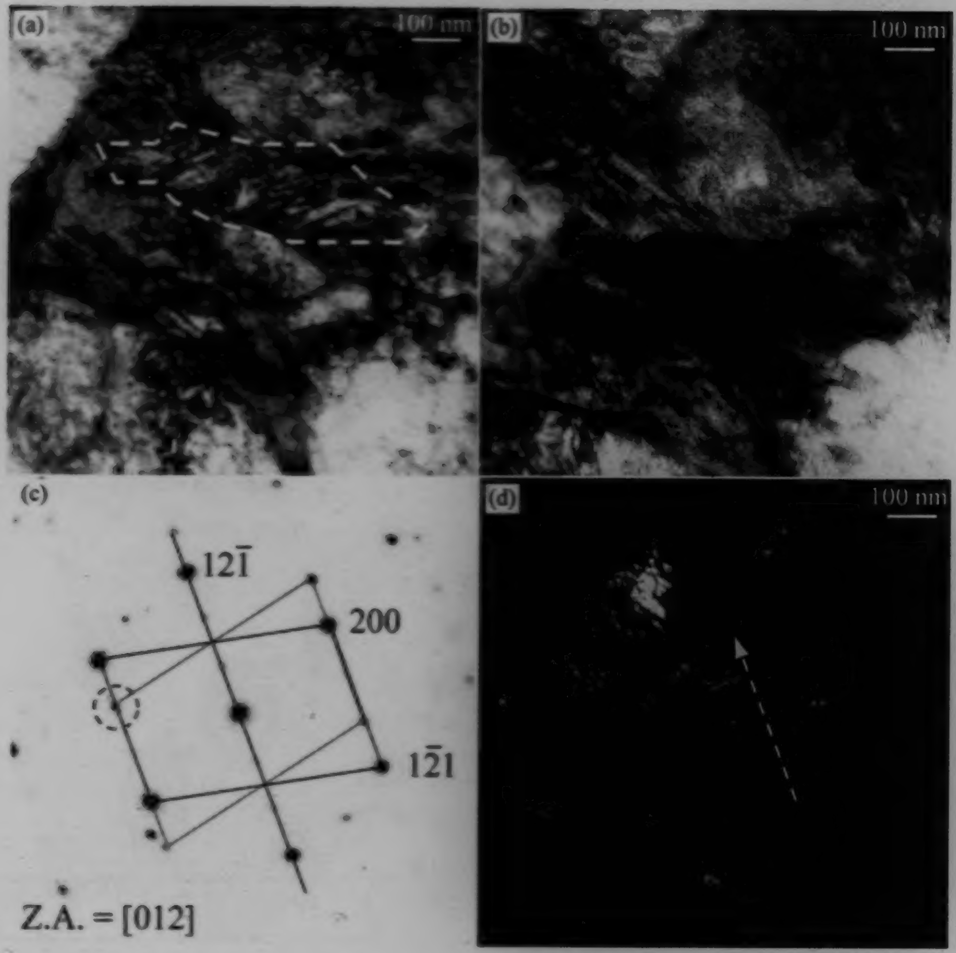
(a)
100 nm
(b)
100 nm
(c)
12$\bar{1}$
200
1$\bar{2}$1
Z.A. = [012]
(d)
100 nm

FIG. 6-50. FIB-TEM images from another region in FGHAZ-1.5 kJ/mm: a) before tilting to a [012] zone axis; b) after tilting to a [012] zone axis; c) SAD from the dark region in (b); d) DF image from the spot circled in (c). The arrow in (d) indicates the normal direction to the twin plane.

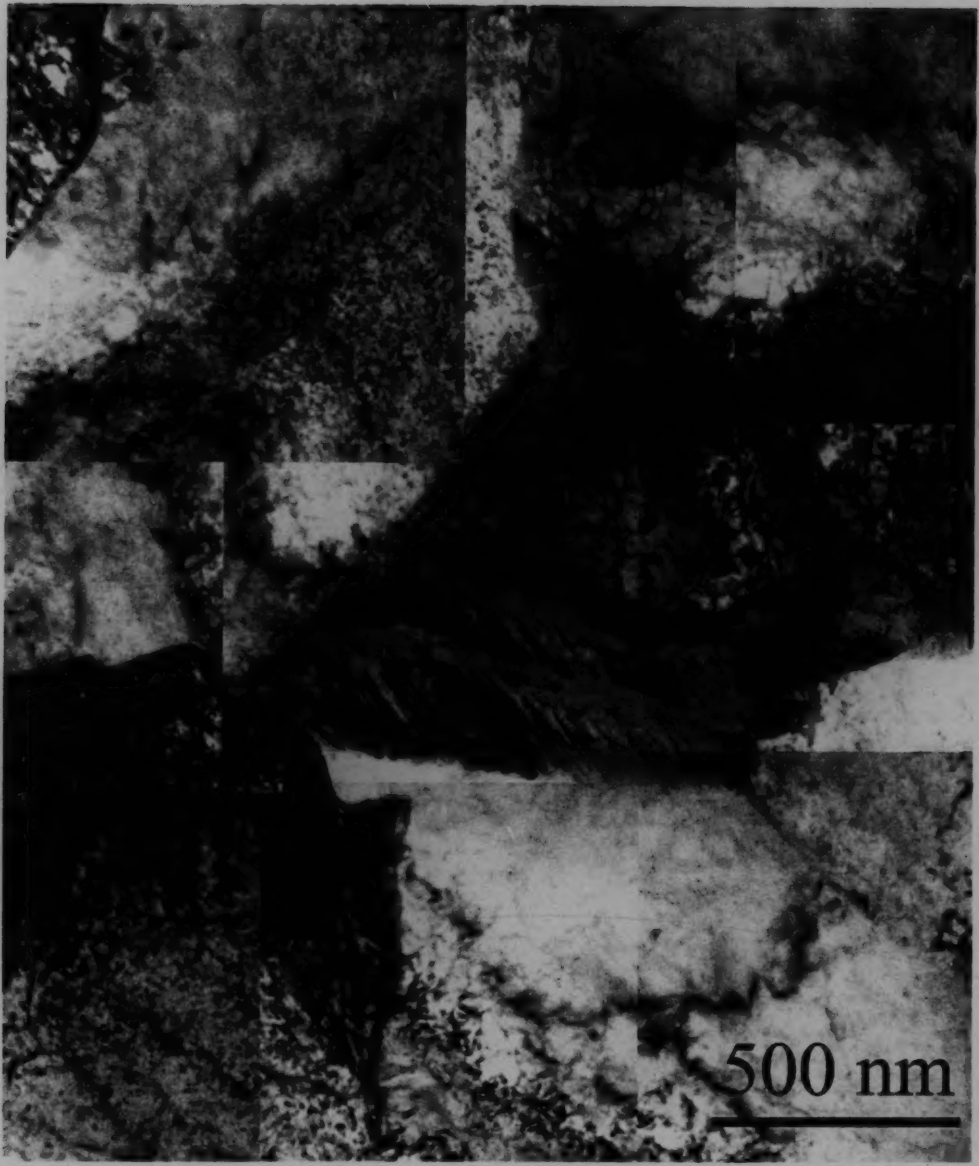

FIG. 6-51- A mosaic of FIB-TEM images from a region in FGHAZ-2.5 kJ/mm, which shows twinning.

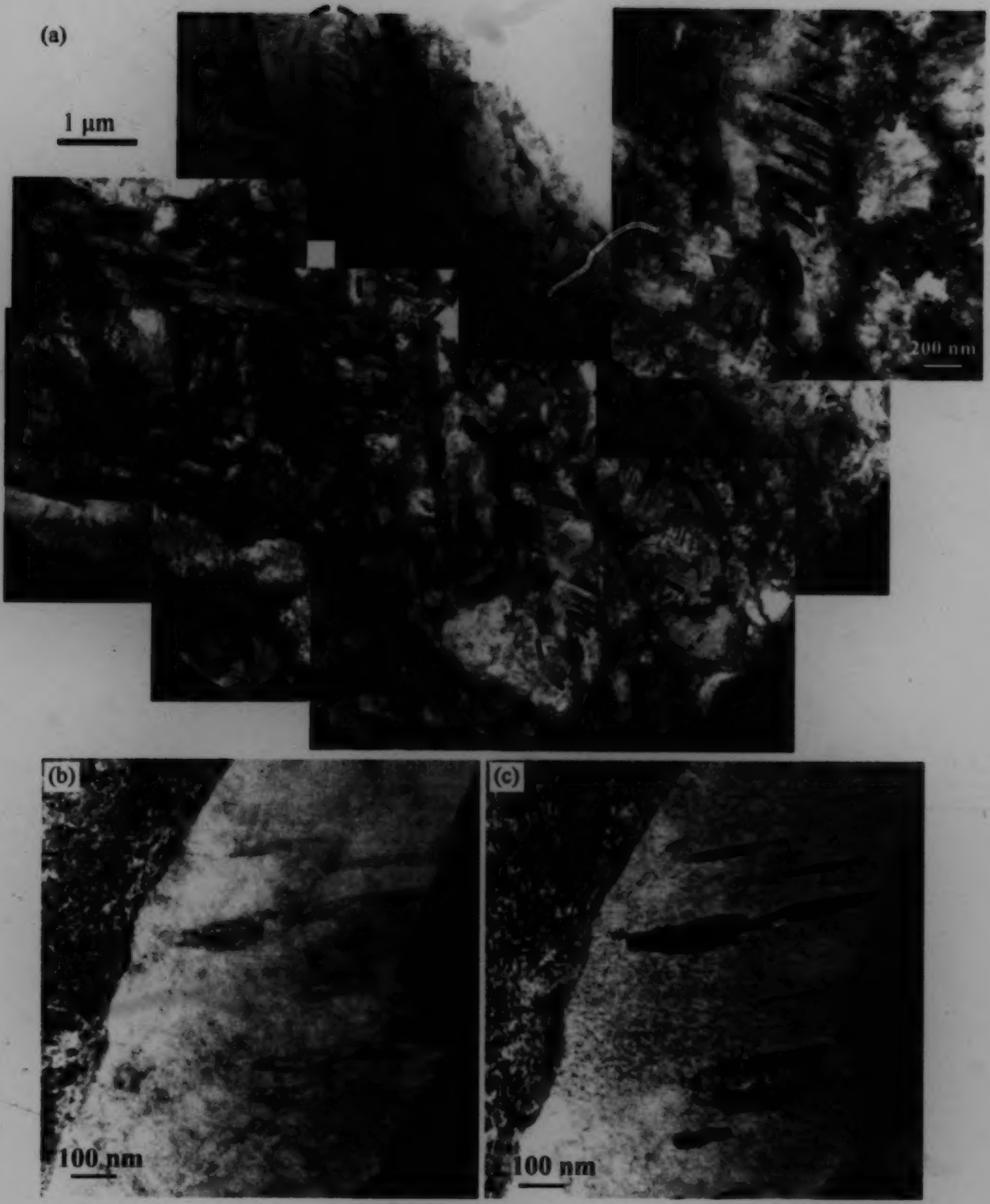

FIG. 6-52. FIB-TEM images from the middle of CGHAZ–0.5 kJ/mm: a) A mosaic of TEM-BF images showing several striated regions– The inset shows one of the regions at a higher magnification; b) TEM-BF image from showing striation in low contrast with the matrix; c) TEM BF image after tilting showing striations in high contrast with the matrix.

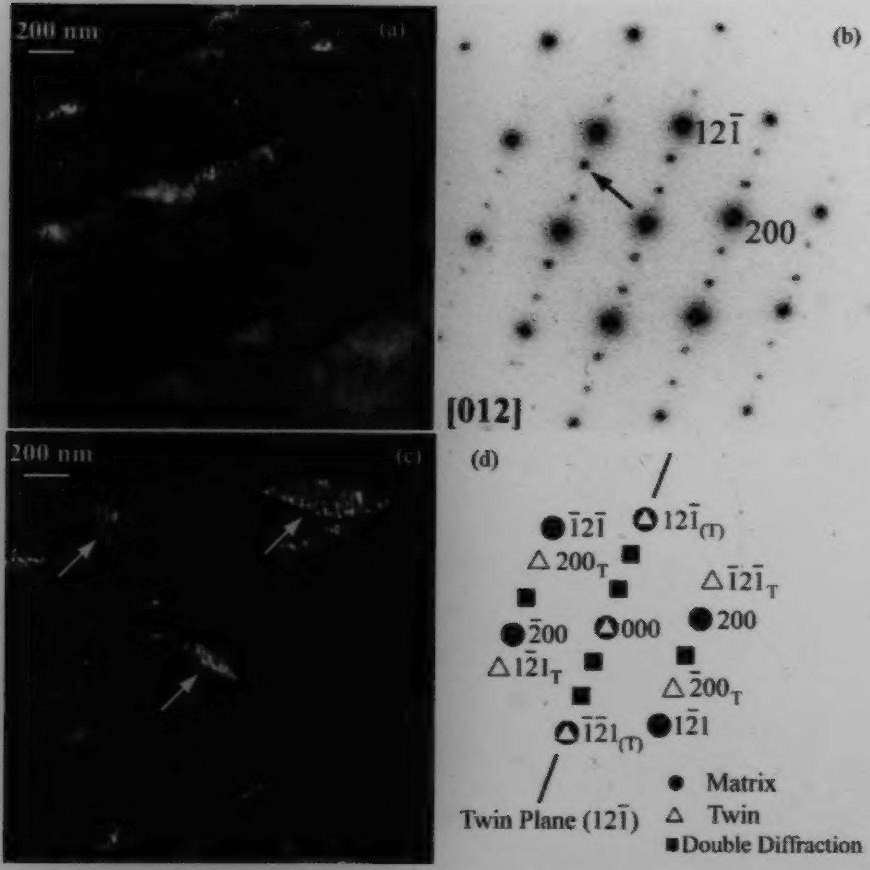
200 nm
(a)
(b)
121̄
200
[012]
200 nm
(c)
(d)
1̄21̄
121̄(T)
200T
1̄21̄T
2̄00
000
200
12̄1T
2̄00T
1̄2̄1(T)
12̄1
Twin Plane (121̄)
Matrix
Twin
Double Diffraction

FIG. 6-53- TEM images from another FIB sample from the middle of CGHAZ–0.5 kJ/mm: a) TEM-BF image tilted suitably for SAD; b) SAD pattern from (a); c) DF image from the 200 twin spot shown with an arrow in (b); d) Interpretation and indexing of the spots in (b) as matrix, twin and double-diffraction spots.

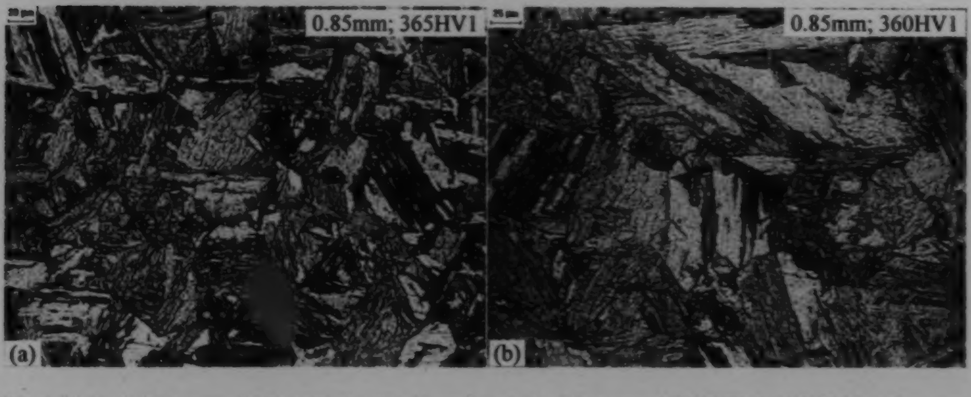
0.85mm; 365HV1
0.85mm; 360HV1
(a)
(b)

FIG. 6-54. Optical micrographs from the simulated samples: a) short-time anneal (1150 °C, 4 min); b) long-time anneal (~1225°C, 30 min).

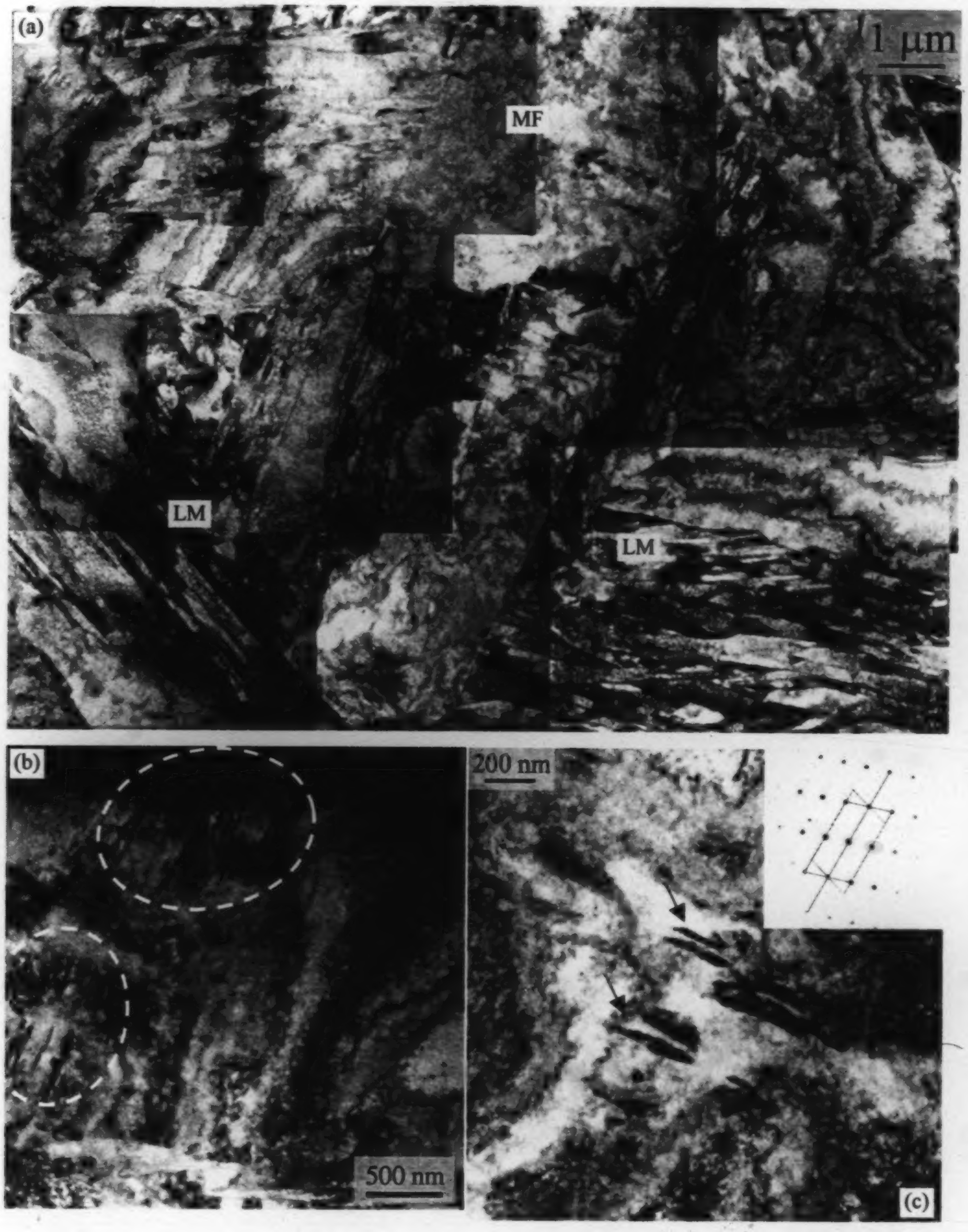
(a)
1 μm
MF
LM
LM
(b)
500 nm
200 nm
(c)

FIG. 6-55. BF-TEM micrographs from the first simulated sample (1150°C and 4 min): a) A mosaic showing the grain structure of lath martensite (LM) and massive ferrite (MF); b) several twinned regions; c) A twinned region with SAD pattern in the inset.

Long term (30 min) heat treatment

The next step was to see if twinned martensite would form in a quenched sample that had been solution treated at a high temperature (~1200–1250°C) for a sufficient period of time (~30 min), so that the austenite had been homogenized with respect to the solutes from the dissolved microalloy precipitates. NbC is supposed to completely dissolve at this temperature for Grade 100 steel. It was observed that there was an optimum sample thickness (~0.8–1.0 mm) where the hardness was maximum. As the thickness increases the quenching efficiency decreases. On the other hand, samples that are too thin get cooled too fast in air (temperature drops below $A_3 \approx 900°C$ before quenching in brine). Note that the atmosphere was neutral (argon) and scale formation did not happen. Some oxidation was inevitable. The sample with a thickness of 0.85 mm was the hardest sample and a location with a hardness of ~360 HV1 was chosen for preparation of a FIB-TEM sample (Figs. 6-26a and b). An optical image from that region, comparable to that annealed for a short time (Fig. 6-54a) and CGHAZ-0.5 kJ/mm (Fig. 6-39b), is shown in Fig. 6-54b.

Figure 6-56 shows a mosaic of TEM micrographs obtained from the sample. Two different structures, in some regions alternating, can be readily recognised. One is fully packed with fine LM, and the other has seemingly large and wide laths or is MF between packets of fine laths. The inset shows the outlines. Both of these structures show rather high dislocation densities. Figure 6-57a shows some of the locations where twinned regions were found. A twin region is further magnified in Fig. 6-57b and the corresponding SAD pattern (after proper tilting), DF image from a twin spot and BF image are also presented (Fig. 6-57 c-e). Note that the twinned regions were not readily noticed in this sample. Repeated tilting was necessary to find the twinned regions. At the correct orientation and particularly under the right DF conditions (from a twin spot), several twinned regions (not all shown here) were observed. This time they were in (or close to) both the LM and the massive regions.

6-5-3-3- Final comments regarding twinning

Twinning happens either to relieve local stress or to accommodate local strain [37]. There seems to be two explanations in the literature with regard to twin formation in low carbon steels. One is based on carbon concentration and heating/cooling rate, and the other is not based on these parameters and only relies on the fact that twinning can occur in ferrite to relieve local stress or accommodate strains. Seemingly, twinning has not been reported in the HAZ of a carbon steel with a carbon level as low as 0.08%C and microalloyed with Ti, Nb and V that consume considerable amount of the C and form stable carbides. The lowest carbon level found in the literature was 0.09% but a considerable amount of Ni that increased the hardenability was present too [49].

Two types of twinning were observed in the HAZ: 1) fine internal twins in the FGHAZ (10-20 nm thick platelets finely packed) and 2) coarse twins in the CGHAZ (50-200 nm thick platelets more widely spaced). It is not clear at this stage if they are really different in terms of the mechanism of formation and properties and more investigation is required. These twins were likely transformation twins that form in the transformed phases to relive the stresses accumulated as a result of solidification in the WM and phase transformation in the WM and HAZ. Volume fraction measurements of the twinned regions were not deemed meaningful for two reasons. Firstly, very small regions were examined by TEM (FIB samples) and twinned regions could be missed. Secondly, as Yu *et al.* [34] showed (and confirmed here), twinning appearance greatly depends on the sample tilt angle, so that a representative number of twinned regions cannot be counted at a given tilt angle. The comparisons here, therefore, are mainly qualitative after tilting over a wide angle range.

Basically, there are three questions to answer:

1) Are all the twins in the HAZ twinned martensite?
2) How much does localized accumulation of carbon and microalloying elements, as a result of dissolution of carbides during the heating portion of the weld thermal cycle, affect twinning? Any local enhancement of these elements would increase the hardenability locally.
3) How much does cooling rate affect twinning in the HAZ?

To answer these questions, first it would be helpful to recall the findings of previous investigators, such as Hutton *et al.* [40] and Heikkinen [39], who showed that twins could form:

1) In ferrite
2) In very low-carbon steels
3) At any cooling rate.

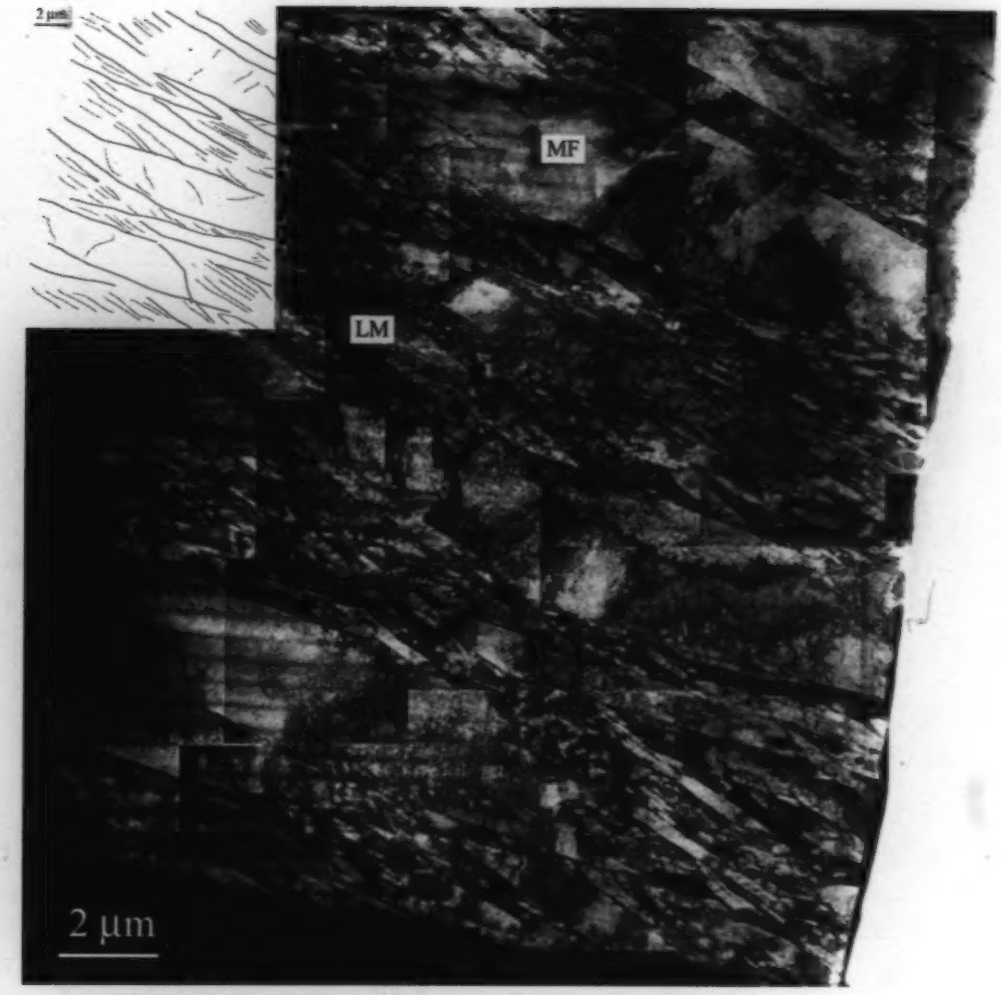

FIG. 6-56. A mosaic of TEM images showing the microstructure of the FIB sample prepared from the second simulated sample (~1225°C and 30 min). The alternating regions of massive ferrite (MF) and packets of fine lath martensite (LM) are outlined on the schematic inset.

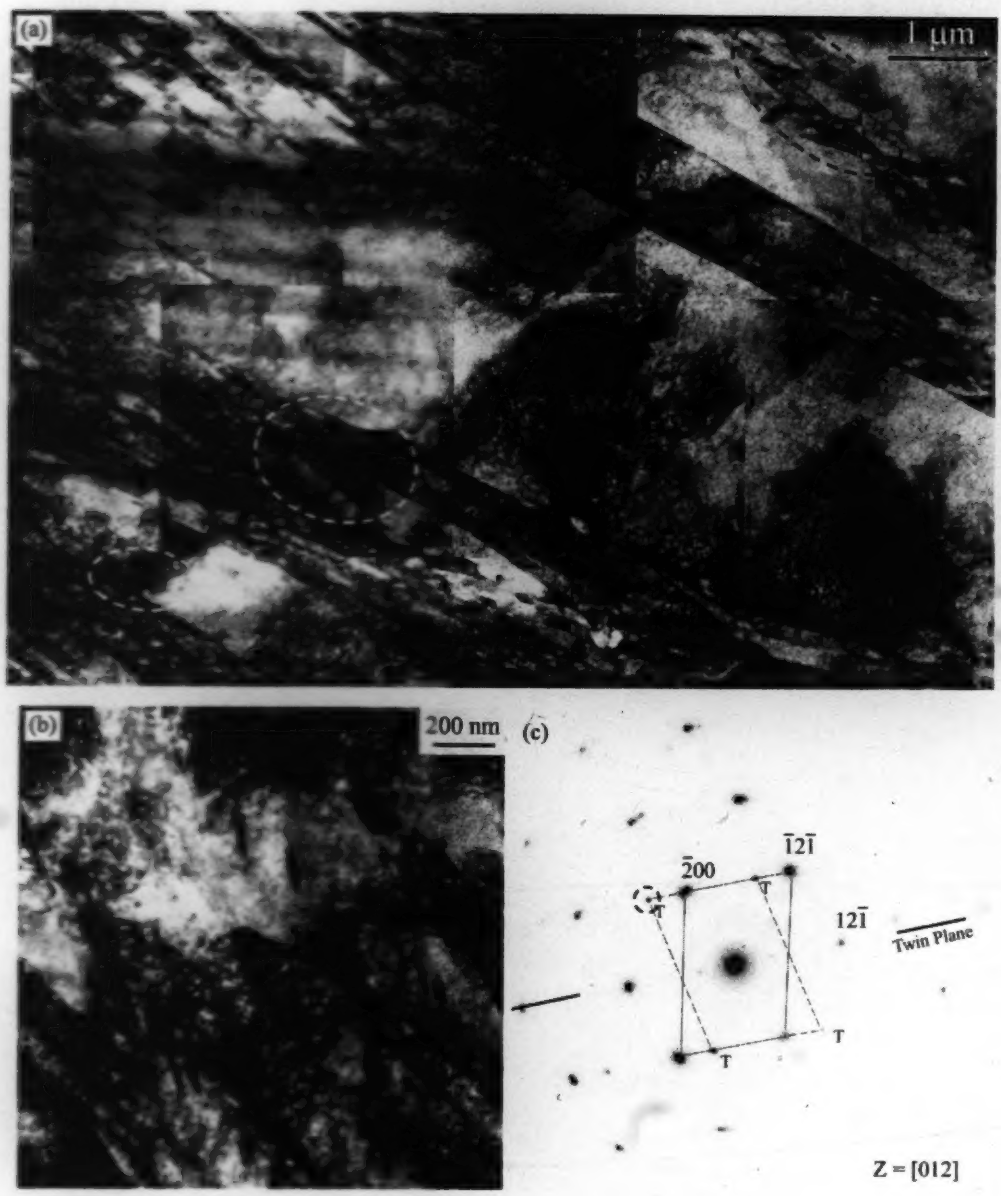
(a)
1 μm
(b)
200 nm
(c)
$\bar{2}00$
$\bar{1}2\bar{1}$
$12\bar{1}$
T
T
T
T
Twin Plane
Z = [012]

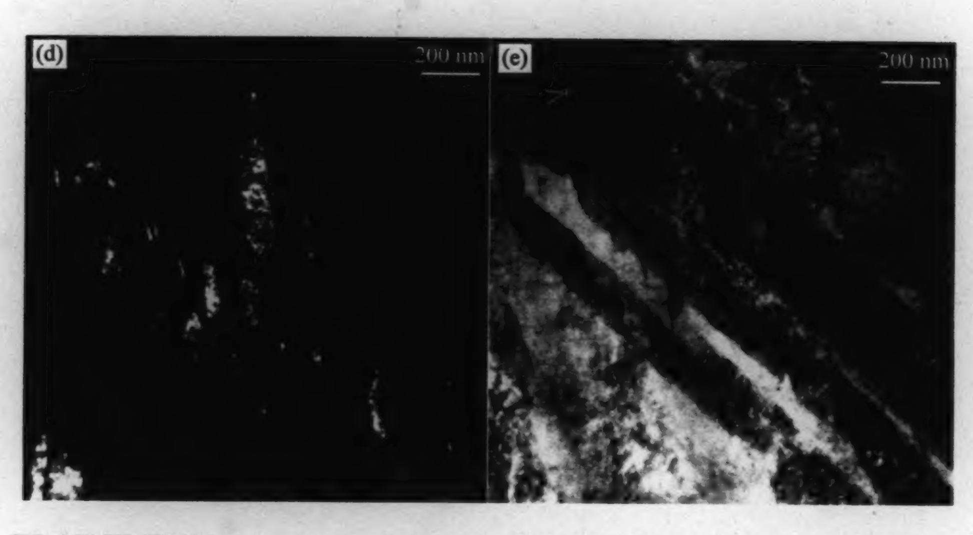

FIG. 6-57. FIB-TEM images from the second simulated sample (~1225°C; 30 min): a) A mosaic of TEM-BF images showing the locations where twins were found; b) a twin region selected for SAD analysis; c) SAD pattern from (b) after proper tilting; c) DF image from the 121 twin spot circled in (c); d) the corresponding BF image of (d).

With these in mind, observation of twins in the HAZ of Grade 100 microalloyed steel, regardless of heat input, should not be a surprise. Although twinning occurs as a result of cooperative displacement of atoms accompanied by a shear force (similar to the martensitic transformation), it differs from martensitic transformations in that twinning is a mechanism of deformation and not transformation. For a region to be called twinned martensite, the martensitic transformation (i.e., non-diffusional transformation by primary shear) should occur first, followed by twinning. There are no reasons to believe that a martensitic transformation can occur in the FGHAZ-1.5/2.5 kJ/mm of a low-carbon microalloyed steel, where the prior austenite grain size is small the cooling rate is less than 20°Cs^{-1} (Table 4-5).

TEM examination of all HAZ and the simulated samples showed:

1) Twinning occurred even when complete dissolution of carbides and homogenisation of austenite had happened (simulated sample with long annealing time). Lack of complete dissolution or austenite homogenisation may have had an effect on the twinning, but was not a major factor.
2) The amount of twinning in the CGHAZ-0.5 kJ/mm was much more than that of the simulated sample annealed for a short time. The cooling rate in the simulated sample was likely higher than that in the 0.5 kJ/mm weld sample (up to ~2000°Cs^{-1} as compared to ~200°Cs^{-1} – see Fig. 4-3 and Table 4-5). In both cases, carbides did not have enough time for complete dissolution and austenite homogenisation with respect to carbon and the alloying elements did not happen. The only explanation can be the much higher thermal, solidification-induced and transformation-induced stresses in the HAZ (which is constrained by the rest of the plate) than in the free-body small coupons used in the simulation.
3) The amount of twinning among the HAZ sub-zones and different heat inputs was a maximum in the CGHAZ-0.5 kJ/mm, where the peak temperatures as well as the heating/cooling rates were highest. In fact, the lower transformation temperature makes deformation by slipping more difficult, which translates to more twinning.
4) Twins were not observed in the ICHAZ. Twinned martensite had been reported to appear in this zone for higher carbon levels (for example in AISI 1045 steel with 0.45%C [68]) or for lower carbon contents when microalloy carbide formers were not used in the steel [54]. In these microstructures, pearlite appears in the BM, and twinning is a result of a very high local carbon concentration (~0.8%C) above a critical level (which depends on the subsequent cooling rate) in regions where the cementite part of the pearlitic structure is dissolved during the thermal cycle ($A_1 < T_P < A_3$) followed by rapid cooling [68].

5) The high stresses in the HAZ (Section 4-5-13) seems to be a major factor that can explain twin formation even where the peak temperature is not very high or the heating/cooling rates are low.

6-5-4. Bainitic transformation

Traditionally, attempts have been made to name each bainitic microstructure, which had a seemingly distinct morphology and/or carbide characteristic (location/size/morphology). For instance, Bhadeshia and Edmonds (as cited by Joarder and Sarma [19]) believed that upper and lower bainite form over two separate temperature ranges and have different mechanisms of transformation. However, the different bainitic microstructures seem to be the result of changes in a spectrum of variables, rather than being completely distinct. Pearlite is a lamellar aggregate of ferrite and cementite. The shape and width of cementite layers are comparable to that of ferrite. However, with increasing cooling rate, the formation of lamellar cementite becomes more difficult and the layer gets thinner and may become discontinuous, eventually becoming discrete and small (as in a typical upper bainite). Joarder and Sarma [19] have shown a transition microstructure between pearlite and upper bainite that forms upon cooling a 0.2%C-3.6%Ni steel from the austenitizing temperature to 500°C and isothermally holding for 100s (Fig. 6-58). This could not be considered a bainitic microstructure (according to classic definitions), as both the ferrite and cementite have lamellar arrangements. The authors also found that isothermal holding at 450°C for 10s could result in a mixed microstructure of upper and lower bainite (both in Ni steels and Mn steels), i.e., both the lath and plate ferrite morphologies, with cementite both along the lath boundaries as well as within the laths/plates. This shows again a transition between those states that had been classically considered as distinct. The trend towards the formation of cementite within the laths/plates can be attributed to diffusion limitations of carbon out of ferrite, as the isothermal holding temperature is decreased or the cooling rate in the continuously cooled steels is increased. Increasing the cooling rate eventually results in the formation of martensite, where complete suppression of cementite precipitation and the supersaturation of carbon occur. So the point is that all these changes are on a spectrum and not completely discrete and distinct. Classification of microstructures in iron and steel may need to be readdressed according to this kind of view.

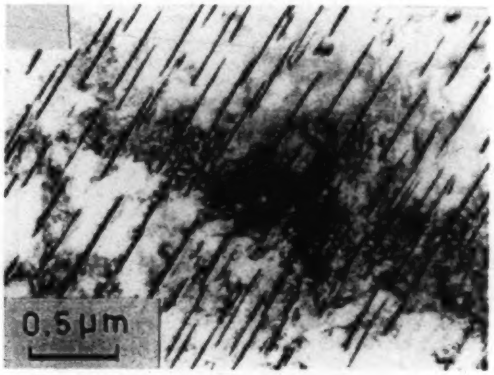

FIG. 6-58. A transition microstructure between pearlite and upper bainite [19].

6-5-5. Grain-size variations across the HAZ

The grain size variation profiles across the HAZ for two heat input extremes of 0.5 and 2.5 kJ/mm, obtained by optical microscopy (OM), are shown in Fig. 6-59. The boundaries of the various HAZ sub-regions are indicated on the graph in a relative manner, as the exact location of the sub-region boundaries depends on the heat input. It should be noted that the numbers reported here are the apparent grain sizes obtained by the intercept method, and not the actual grain size in three dimensions [5]. In fact, they should be referred to as mean linear intercepts. However, for the sake of simplicity, the term grain size is used in most cases. Also of note is that the grain sizes reported in Fig. 6-59 for the CGHAZ are actually the prior austenite grain sizes (PAGS); the actual grain size of bainitic ferrite and lath martensite is much smaller (as discussed in the previous sections). The average grain size variations show similar characteristics for both heat inputs. There is a plateau in the FGHAZ and an abrupt continuous grain size increase in the CGHAZ towards the fusion line. The average sizes are larger for the higher heat input. For instance, the ferrite grains in the FGHAZ have an average size of ~3.3 µm for the low heat input (0.5 kJ/mm) and ~4.7 µm for the higher heat input (2.5 kJ/mm). For the CGHAZ, however, another effect is observed in addition to an increase in the average grain size with increasing heat input. The variation from the average PAGS is larger for the higher heat input for the same distance from the fusion line. This is a consequence of grain coarsening due to longer exposure at high temperatures, that causes larger grains to grow at the expense of smaller ones [38].

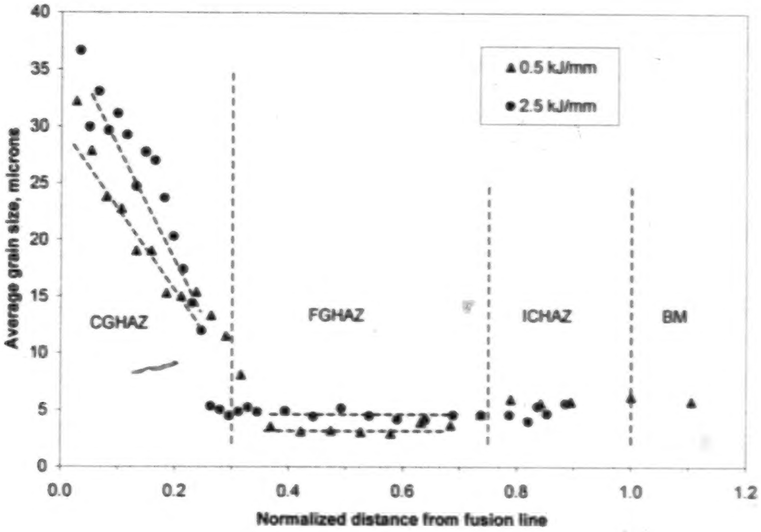

FIG. 6-59. Grain size variation across the HAZ for two heat inputs of 0.5 and 2.5 kJ/mm.

Many of the grains in the BM and FGHAZ were too small to be resolved by OM. Therefore, carbon extraction replicas, imaged at low magnification in the TEM (direct magnification of 3000x), were utilized for grain size measurement in these regions. Examples of these micrographs are shown in Fig. 6-60 for the BM and FGHAZ (several heat inputs). Grain boundary impressions were readily seen, facilitating measurement using the lineal intercept method. The pattern shown in Fig. 6-60f was superimposed on the images as a means of systematically covering all directions and preventing biased measurements along a specific direction. This was especially useful for measurements of the BM, where the grains have a relatively high aspect ratio due to pancaking of the austenite and the bainitic structure. The results of grain-size measurements for the OM and TEM micrographs are reported in Table 6-2. At least three and generally five micrographs were examined in each case and the numbers reported in Table 6-2 represent the "average ± the standard deviation".

The major difference in the microstructure of the FGHAZ for the different heat inputs was the grain size. The fact that the grain sizes were on average 50% larger for the higher heat inputs of 1.5 and 2.5 kJ/mm than for the low heat input of 0.5 kJ/mm (Table 6-2) can be attributed to the effect of cooling rate on nucleation and growth of ferrite grains from the relatively small PAGS in the FGHAZ. The faster cooling rate for a heat input of 0.5 kJ/mm will cause more supercooling from the equilibrium transformation temperature, which enhances nucleation. A faster cooling rate does not favour growth, which is a diffusion controlled process and dependent on temperature. The net result will be smaller grain sizes. This explanation is based on the assumption that the PAGS are the same (or differ slightly) for different heat inputs in the FGHAZ.

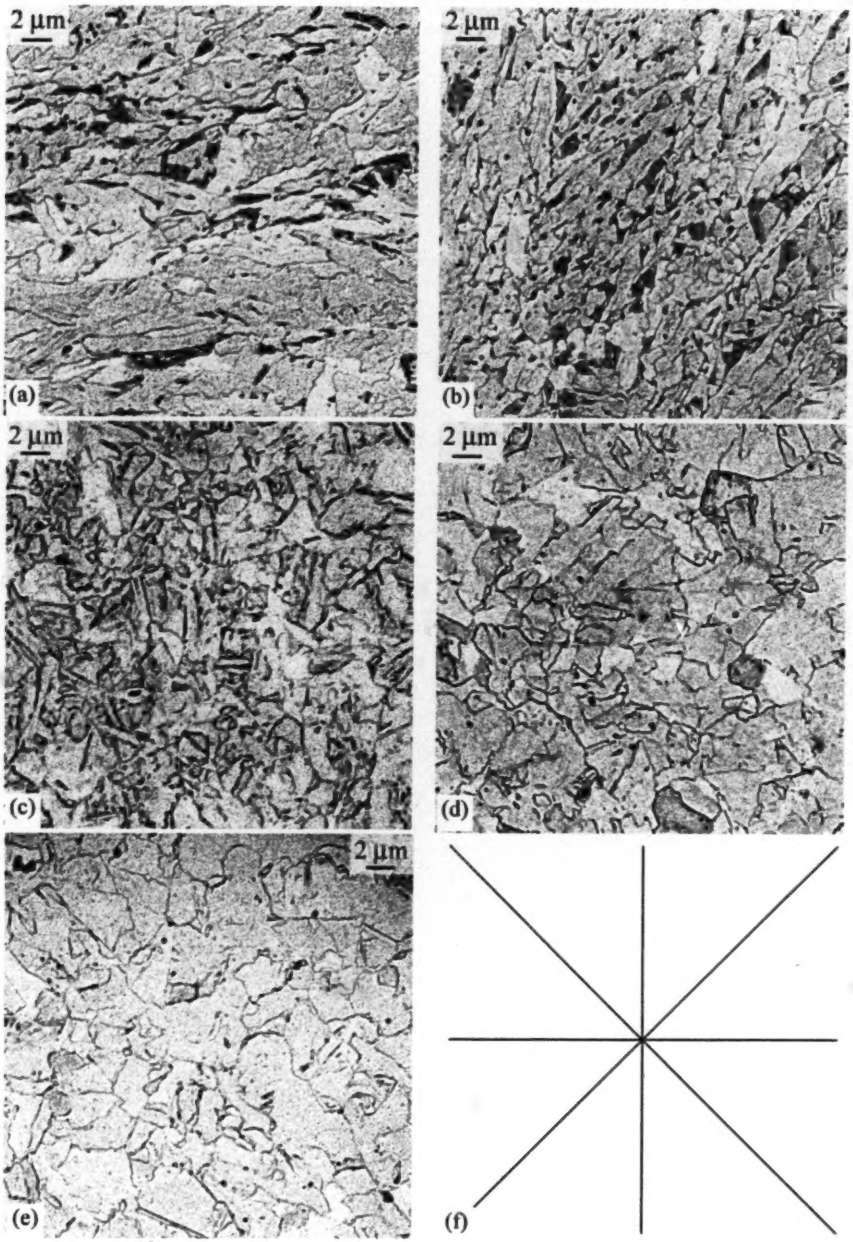

FIG. 6-60. TEM bright field (BF) low magnification images of replicas prepared from different regions: a) BM-transverse; b) BM-longitudinal; c) FGHAZ-0.5 kJ/mm; d) FGHAZ-1.5 kJ/mm; e) FGHAZ-2.5 kJ/mm; f) the pattern for lines superimposed on the micrographs for grain size measurements.

The PAGS in FGHAZ can be estimated based on Gladman's equation (Equation 6-7) to be $D \approx 1.7$ μm, when assuming $r = 2.5$ nm, $f = 10^{-3}$ and $Z = 2$. That translates to an average intercept length of ~1 μm.

Even assuming that the polygonal ferrite grains of almost the same size as the PAGS will form in FGHAZ at higher heat inputs, the estimated intercept length should have been at least 1.5 µm. The underestimation is not very large though, when considering the assumptions in the theory of grain growth inhibition and difficulties in estimation of precipitate volume fraction.

Table 6-2. Mean linear intercepts, *i*, measured at different magnifications for the BM and FGHAZ of Grade 100 steel

Region	Average *i* (µm)		
	400x ^{a}	1000x ^{a}	3000x ^{b}
BM	N.A. ^{c}	N.A. ^{c}	1.2±0.1 ^{d}
FGHAZ-0.5kJ/mm	3.3±0.2	1.8±0.1	1.0±0.1
FGHAZ-1.5kJ/mm	4.6±0.2	2.6±0.2	1.5±0.1
FGHAZ-2.5kJ/mm	4.7±0.2	2.6±0.2	1.5±0.1

a) OM; b) TEM–replicas; c) not resolved well enough for a meaningful measurement; d) the value of *i* for the BM is the average over transverse and longitudinal sections.

6-5-6. Effect of peak temperature on matrix phase structure

The microstructural evolution at different sub-zones across the HAZ for the same heat input is different. The $\Delta t_{8\rightarrow5}$, the time for cooling from 800 to 500°C, is essentially the same for all regions (with the exception of the ICHAZ where the cooling rate is slightly lower for T_P<840°C) and depends only on the heat input and plate thickness/geometry [3]. Moreover, austenitization will not result in a homogeneous microstructure, as the heating rate of the weld thermal cycle is very fast and the dwell time around the peak temperature (T_P) is only a few seconds. The difference in microstructural changes across the HAZ for different sub-zones is due mainly to the difference in T_P, which results in higher hardenability for the CGHAZ relative to the FGHAZ. The high T_P in the CGHAZ (~1200-1500°C) causes an abrupt increase in the PAGS (as shown in Fig. 6-60), as well as enrichment of the austenite in microalloying elements and carbon due to dissolution of the precipitates. Both of these effects increase the hardenability, i.e., the tendency to form lower temperature transformation products such as bainite and martensite. This explains the formation of lamellar structures of martensite and bainite in the CGHAZ of Grade 100 steel as opposed to polygonal ferrite (and some bainitic ferrite in the case of a low heat input of 0.5 kJ/mm) in the FGHAZ.

6-5-7. Effect of heat input on matrix phase structure

The main effect of heat input on phase transformations is through the cooling rate and PAGS. The PAGS in the CGHAZ did not differ greatly among the different weld samples (heat input from 0.5 to 2.5 kJ/mm). However, Otterberg *et al.* [67] found that the PAGS in simulated samples from low-carbon steels increased considerably with heat input over a wide range of heat inputs (causing cooling times of 50–750s). They found that increasing the heat input also resulted in an increase in the width of GF in the prior austenite grain boundaries and the lamellar ferrite width (in WF or B).

Decreasing the heat input results in an increase in cooling rate. A cooling rate of ~100–200°Cs^{-1} (Tables 4-4 and 4-5) resulted in a ferritic-bainitic structure in the FGHAZ and a martensitic structure in the CGHAZ for a heat input of 0.5 kJ/mm. This was accompanied by a transformation temperature ~400–430°C (Table 4-5) in the CGHAZ, which is consistent with the formation of martensite in low-carbon HSLA steels (M_S < 450°C) as reported by Shome *et al.* [69] through dilatation studies (also Fig. 6-11). Decreasing the cooling rate to ~10–20°Cs^{-1} in weld samples with a heat input of 1.5 and 2.5 kJ/mm resulted in the formation of mainly polygonal ferrite in the FGHAZ and mainly bainitic ferrite in the CGHAZ (various amounts of LB, UB, GB and AF). This was accompanied by transformation temperatures of 470–480°C for a heat input of 1.5 and 500–510°C for a heat input of 2.5 kJ/mm, in the CGHAZ. Again, this is consistent with the formation of bainitic structures in low-carbon HSLA steels (UB having a higher transformation temperature than LB).

The thermal analysis in Chapter 4 showed that the T_{GC} (grain coarsening temperature) decreased as the heat input decreased. This is equivalent to a wider CGHAZ relative to the HAZ total width at lower heat inputs. The reason for this phenomenon was attributed to the higher heating rate at lower heat inputs, as explained in Section 6-2-5. The final PAGS, however, decreased as the heat input decreased, due to much shorter exposure to high temperatures.

6-5-8. Advantages of low-mag TEM using replicas

The trend in microstructure development of steels is towards finer grains. Bainitic ferrite, with plates only a fraction of a micron in width, is common in HSMA steels. These plates have low-angle boundaries with adjacent plates and this makes the boundaries not very sharp or deep after etching and, therefore, difficult to resolve in low-resolution microscopes. Each of these plates, sometimes referred to as sub-grains, can be considered as a grain in the context of the Hall-Petch equation, since the lath/plate boundaries can act as obstacles to dislocation movement and hence contribute to the strength [5]. Examination of the grain structure in Grade 100 microalloyed steel shows that most fine grains cannot be resolved by OM, resulting in overestimation of the grain size. TEM at low magnification (1000–6000x) can resolve these boundaries very well, with the advantage of being able to increase the magnification on the same location/sample for further analysis of microstructure, particularly precipitates. The grain sizes obtained from replicas will be used for correlation studies with hardness (Chapter 8).

6-6. Summary

The iron matrix microstructure of the weld HAZ of Grade 100 microalloyed steel was examined in terms of different phase structures and grain size. Different sub-zones, i.e., ICHAZ, FGHAZ and CGHAZ, were examined for different weld samples with a heat input range of 0.5–2.5 kJ/mm. OM and TEM (both replicas and thin foils) were utilized. The results are summarized below:

1) The BM is made up of primarily oriented bainitic ferrite with smaller amounts of grain-boundary polygonal ferrite. Each packet of bainitic ferrite consists of parallel laths of ferrite separated from each other by low-angle boundaries. The ferrite laths and grains have jagged grain boundaries and are relatively highly dislocated.
2) The ICHAZ is a mixture of untransformed bainitic ferrite and retransformed polygonal ferrite, i.e., something between the microstructure of BM and FGHAZ. The new polygonal grains had smaller aspect ratios, straight or curved grain boundaries and were mostly located at the corners of the bainitic grains.
3) The FGHAZ consists mainly of polygonal ferrite. The FGHAZ of the 0.5 kJ/mm weld sample also consisted of packets of bainitic ferrite due to considerably higher cooling rates (10–20 times higher than that of the 1.5 and 2.5 kJ/mm weld samples) and had markedly smaller grains.
4) The CGHAZ is made up of large prior austenite grains, a few tens of microns in size. The CGHAZ grain structure has more distinct grain boundaries for higher heat inputs of 1.5 and 2.5 kJ/mm than 0.5 kJ/mm, due to reprecipitation of carbides at these locations.
5) The CGHAZ-0.5kJ/mm shows two structures of fine untempered lath martensite and either coarse autotempered martensite or aged massive ferrite. The untempered lath martensite had a very fine structure (100–300 nm in thickness) and was void of precipitates. The autotempered martensite or massive ferrite had a coarse structure (2–4 μm in thickness) with cementite particles.
6) The CGHAZ-1.5kJ/mm was made up of a mixture of lower bainite, granular bainite and a smaller amount of grain-boundary allotriomorphic ferrite. The CGHAZ-2.5kJ/mm consisted of a mixture of upper bainite, granular bainite and acicular ferrite. The plates/laths of ferrite in these higher heat inputs were 1–2 μm in thickness.
7) Two morphologies of transformation twins were observed in the HAZ: a) fine internal twins in FGHAZ-1.5/2.5 kJ/mm (10–20 nm thick platelets, finely packed) and b) coarse twins in CGHAZ-0.5 kJ/mm (50–200 nm thick platelets coarsely spaced). No regions of twins were observed in the BM, ICHAZ (all heat inputs), FGHAZ-0.5kJ/mm or CGHAZ-1.5/2.5kJ/mm.
8) Twinned regions were also observed in the simulated samples annealed at ~1200°C for short (4 min) and long times (30 min) and quenched in iced brine. The fact that twinning occurred even when austenite was homogenized suggests that dissolution of precipitates and local enrichment of the matrix cannot be the main reason for twinning.
9) Transformation twins formed in the HAZ to relieve high thermal, solidification-induced and transformation-induced stresses. The twinning amount was highest in the CGHAZ-0.5kJ/mm as the transformation temperature was the lowest (highest peak temperature and cooling rate) and slip could not happen easily.

10) Grain size variations across the HAZ showed a plateau in the FGHAZ and an abrupt continuous increase in the CGHAZ towards the fusion line. The grain sizes increased both in the FGHAZ and CGHAZ with increasing heat input from 0.5 to 1.5/2.5 kJ/mm. The grain sizes in the 1.5 and 2.5 kJ/mm weld samples were almost identical, especially in the FGHAZ.

11) The fine grains in the BM and FGHAZ could not be resolved well with OM. TEM examination of replicas at low magnification (3000x), which resolved the impression of the grain boundaries, resulted in a more accurate measurement of grain sizes. The mean intercept lengths of 1.2, 1.0 and 1.5 μm were obtained for the BM, FGHAZ-0.5kJ/mm and FGHAZ-1.5/2.5kJ/mm, respectively.

12) Replicas also revealed the prior austenite grain boundaries, packets and the fine laths within them in the CGHAZ very well. This proved that replicas are very good samples for grain size examination and measurement in the BM and HAZ of HSMA steels.

References

[1] Losz, J. M. B., and Challenger, K. D., 1990, "HAZ Microstructures in HSLA Steel Weldments," *Proc., First United States--Japan Symposium on Advances in Welding Metallurgy*, American Welding Society, Miami, pp. 323-357.

[2] Spanos, G., Fonda, R. W., Vandermeer, R. A., and Matuszeski, A., 1995, "Microstructural Changes in HSLA-100 Steel Thermally Cycled to Simulate the Heat-Affected Zone During Welding," Metall. Mater. Trans. A (USA), **26A** (12), pp. 3277-3293.

[3] Easterling, K. E., 1992, Introduction to the Physical Metallurgy of Welding, Butterworth-Heinemann Ltd, Oxford.

[4] Collins, L. E., Godden, M. J., and Boyd, J. D., 1983, "Microstructures of Linepipe Steels," Can. Metall. Q., **22** (2), pp. 169-179.

[5] Gladman, T., 1997, The Physical Metallurgy of Microalloyed Steels, The Institute of Materials, London.

[6] Rasanen, E., and Tenkula, J., 1972, "Phase Changes in the (Arc) Welded Joints of (Low Carbon) Constructional Steels," Scandinavian Journal of Metallurgy (Denmark), **1** (2), pp. 75-80.

[7] Handeland, T., Erkkila, E., and Gjonnes, J., 1986, "A Combined Electron Microscope and Optical Metallographic Study of Microstructures in High-Strength, Low-Alloy (HSLA) Steels after Welding," J. Microsc., **144** (3), pp. 251-259.

[8] Davenport, E. S., Bain, E. C., and Paxton, H. W., 1970, "Transformation of Austenite at Constant Subcritical Temperatures," Met Trans, **1** (12), pp. 3479-3530.

[9] Mitchell, P. S., Hart, P. H. M., and Morrison, W. B., 1995, "The Effect of Microalloying on HAZ Toughness," 1995, *Proc., Microalloying '95*, Iron and Steel Society Inc, Warrendale, pp. 149-162.

[10] Mangonon, P. L., 1976, "Effect of Alloying Ellements on the Microstructure and Properties of a Hot-Rolled Low-Carbon Low-Alloy Bainitic Steel," Metall. Trans. A, **7A**, pp. 1389-1400.

[11] Speich, G. R., and Warlimont, H., 1968, "Yield Strength and Transformation Substructure of Low-Carbon Martensite," J Iron Steel Inst, **206** (4), pp. 385-392.

[12] Okaguchi, S., Ohtani, H., and Ohmori, Y., 1991, "Morphology of Widmanstatten and Bainitic Ferrites," Materials Transactions, JIM (Japan), **32** (8), pp. 697-704.

[13] Ohmori, Y., Ohtsubo, H., Jung, Y. C., Okaguchi, S., and Ohtani, H., 1992, "Morphology of Bainite and Widmanstatten Ferrite," *Proc., Pacific Rim Symposium on the "Roles of Shear and Diffusion in the Formation of Plate-Shaped Transformation Products"*, Minerals, Metals & Materials Society, Warrendale, PA, pp. 1981-1989.

[14] Dolby, R. E., 1983, "Advances in Welding Metallurgy of Steel," Metals Technology, **10** (9), pp. 349-362.

[15] Thaulow, C., Gunleiksrud, A., Paauw, A. J., and Naess, O. J., 1985, "Heat Affected Zone Toughness of a Low Carbon Microalloyed Steel," Met. Constr., **17** (2), pp. 94-99.

[16] Godden, M. J., and Boyd, J. D., 1981, "Characterization of Microstructures in Weld Heat-Affected Zones by Electron Microscopy," *Proc., Microstructural Science, V. 9, 13th Annual Technical Meeting of the International Metallographic Society*, Elsevier North-Holland Inc., pp. 343-354.

[17] Davenport, E. S., Bain, E. C., and Kearny, N. J., 1930, "Transformation of Austenite at Constant Subcritical Temperatures," Trans. AIME, **90**), pp. 117-154.

[18] Bhadeshia, H. K. D. H., and Christian, J. W., 1990, "Bainite in Steels," Metall. Trans. A., **21A** (4), pp. 767-797.

[19] Joarder, A., and Sarma, D. S., 1991, "Bainite Structures in 0.2c--3.6ni Steel," Materials Transactions, JIM (Japan), **32 (8)**, pp. 705-714.

[20] Zhao, J., and Jin, Z., 1992, "Isothermal Decomposition of Supercooled Austenite in Steels," Materials Science and Technology, **8** (11), pp. 1004-1010.

[21] Samuel, F. H., 1984, "Some Aspects of Bainites in an HSLA Steel," Z. Metallkd., **75** (12), pp. 967-972.

[22] Hrivnak, I., 1995, "Granular Bainite in High Strength Steel Welds," Metallic Materials, **33** (1), pp. 24-30.

[23] Samuel, F. H., 1984, "Interrelations of Cooling Rate, Microstructure and Mechanical Properties in Four HSLA Steels," Metall. Trans. A, **15A** (10), pp. 1807-1817.

[24] Butron Guillen, M. P., and Jonas, J. J., 1993, "Effect of Austenite Recrystallization on Ferrite Transformation Textures," Materials Science Forum, **113-115**, pp. 691-696.

[25] Speich, G. R., and Breedis, J. F., 1985, *Martensitic Structures*, in ASM Handbook, Metallography and Microstructures, ASM International, Materials Park, pp. 668-674.

[26] Matsuda, F., Li, Z., Bernasovsky, P., Ishihara, K., and Okada, H., 1991, "An Investigation on the Behaviour of the M-a Constituent in Simulated HAZ of HSLA Steels," Welding in the World (UK), **29** (9-10), pp. 307-313.

[27] Padmanabhan, R., and Wood, W. E., 1984, "Microstructural Analysis of a Multistage Heat-Treated Ultra-High-Strength Low-Alloy Steel," Mater. Sci. Eng., **66** (2), pp. 125-143.

[28] Kelly, P. M., 1992, "Crystallography of Lath Martensite in Steels," Materials Transactions, JIM (Japan), **33** (3), pp. 235-242.

[29] Fairchild, D. P., Bangaru, N. V., Koo, J. Y., Harrison, P. L., and Ozekcin, A., 1991, "A Study Concerning Intercritical HAZ Microstructure and Toughness in HSLA Steels," Welding Journal, **70** (12), pp. 321-s to 329-s.

[30] Ferrante, M., De Souza, L. M., and Nadim, C. A., 1985, "The Influence of Step Quenching on the Strength and Microstructure of 300m Steel," *Proc., 8th Inter-American Conference on Materials Technology*, pp. 24.1-24.4.

[31] Boniszewski, T., and Watkinson, F., 1973, "Effect of Weld Microstructures on Hydrogen Induced Cracking in Transformable Steels: Part 1," Metals and Materials, 7 (2), pp. 90-96.

[32] Das, S. K., and Thomas, G., 1970, "Morphology and Substructure of Martensite," Met Trans, **1** (1), pp. 325-327.

[33] Zeng, D. C., Tan, Y. H., Qiao, G. W., and Chuang, Y.-C., 1994, "The Nature of Martensitic Morphologies in Medium and High Carbon Steels," Zeitschrift fur Metallkunde, **85** (3), pp. 203-206.

[34] Yu, H. T., Shu, Q. H., De, C. Z., Xi, C. D., and Yue, H. H., 1992, "New Observation of Martensitic Morphology and Substructure Using Transmission Electron Microscopy," Metallurgical Transactions A, **23A** (5), pp. 1413-1421.

[35] Mahajan, S., and Williams, D. F., 1973, "Deformation Twinning in Metals and Alloys," Int. Metall. Rev., **18**, pp. 43-61.

[36] Dieter, G. E., and Bacon, D., 1988, Mechanical Metallurgy, McGraw-Hill, Maidenhead, Berkshire.

[37] Paxton, H. W., 1953, "Experimental Verification of the Twin System in Alpha Iron," Acta metall., **1**, pp. 141-143.

[38] Porter, D. A., and Easterling, K. E., 1981, Phase Transformations in Metals and Alloys, Van Nostrand Reinhold, Wokingham, Berkshire.

[39] Heikkinen, V. K., 1974, "Transformation Twins in V-Bearing Mild Steels," Scand. J. Metallurgy, **3** (1), pp. 41-45.

[40] Hutton, D. S., Coleman, G. L., and Leslie, W. C., 1959, "Transfrormation Twins in Alpha Iron," Transactions of the metallurgica society of AIME, **215**, pp. 680-681.

[41] Igata, N., Kawata, K., Itabashi, M., Yumoto, H., Sawada, K., and Kitahara, H., 1991, "Plastic Deformation of Iron and Steel at High Strain Rate," *Proc., 2nd Japan International SAMPE Symposium -- Advanced Materials for Future Industries: Needs and Seeds*, pp. 1121-1129.

[42] Leslie, W. C., 1981, The Physical Metallurgy of Steels, Hemisphere Publishing Corp, McGraw-Hill.

[43] Avner, S. H., 1974, Introduction to Physical Metallurgy, McGraw-Hill Book Company.

[44] Inagaki, H., 1990, "Annealing Twins in Deformed Austenite of a Low-Carbon Steel," Zeitschrift fur Metallkunde, **81** (3), pp. 174-180.

[45] Roytburd, A. L., and Khachaturyan, A. G., 1970, "Interstitial Atoms and the Crystallographic Mechanism of Martensite Transformation in Steels," Phys Met Metallogr, **30** (6), pp. 68-77.

[46] Danil'chenko, V. E., 1994, "Mechanism of {011} Martensite Twinning in Quenched Steel," Scr. Metall. Mater., **30** (8), pp. 1061-1064.

[47] Speich, G. R., and Leslie, W. C., 1972, "Tempering of Steel," Metall Trans, **3** (5), pp. 1043-1054.

[48] Pirogov, V. A., Martsiniv, B. F., Sukhomlin, V. I., and Mikhaylichenko, E. N., 1987, "Effects of Austenite Transformation Temperature on Structure Morphology in Low Carbon Steels," Sov. Mater. Sci. Rev., **1** (1), pp. 15-20.

[49] Challenger, K. D., Brucker, R. B., Elger, W. M., and Sorek, M. J., 1984, "Microstructure--Thermal History Correlations for Hy-130 Thick Section Weldments," Welding Journal, **63** (8), pp. 254-s to 262-s.

[50] Mawella, K. J. A., and Honeycombe, R. W. K., 1984, "Electron-Beam Rapid Quenching of an Ultra High-Strength Alloy Steel," Journal of Materials Science, **19** (11), pp. 3760-3766.

[51] Zhao, J., 1992, "Continuous Cooling Transformations in Steels," Materials Science and Technology, **8** (11), pp. 997-1003.

[52] Heikkinen, V. K., and Soininen, R., 1974, "Effect of Transformation Twins on the Strength and Ductility of V-Bearing Mild Steels," Scand. J. Metallurgy, **3** (6), pp. 245-248.

[53] Deb, P., Challenger, K. D., and Clark, D. R., 1986, "Transmission Electron Microscopy Characterizations of Preheated and Non-Preheated Shielded Metal Arc Weldments of Hy-80 Steel," Materials Science and Engineering, **77**, pp. 155-167.

[54] Akselsen, O., Grong, O., and Solberg, J., 1987, "Structure--Property Relationships in Intercritical Heat Affected Zone of Low-Carbon Microalloyed Steels," Mater. Sci. Technol., **3** (8), pp. 649-655.

[55] Boniszewski, T., and Watkinson, F., 1973, "Effect of Weld Microstructures on Hydrogen Induced Cracking in Transformable Steels: Part 2," Metals and Materials, **7** (3), pp. 145-151.

[56] Moon, D. W., Fonda, R. W., and Spanos, G., 2000, "Microhardness Variations in HSLA-100 Welds Fabricated with New Ultra-Low-Carbon Weld Consumables," Welding Journal, **79** (10), pp. 278-s to 285-s.

[57] Alberry, P. J., Chew, B., and Jones, W. K. C., 1977, "Prior Austenite Grain Growth in Heat-Affected-Zone of a 0.5cr-Mo-V Steel," METALS TECHNOLOGY, **4** (6), pp. 317-325.

[58] Ion, J. C., Easterling, K. E., and Ashby, M. F., 1984, "A Second Report on Diagrams of Microstructure and Hardness for Heat-Affected Zones in Welds," Acta metall., **32** (11), pp. 1949-1962.

[59] Palmiere, E. J., 1995, "Precipitation Phenomena in Microalloyed Steels," *Proc., ISS, Proceedings of the International Conference "Microalloying '95"*, pp. 307-320.

[60] George, T., and Irani, J. J., 1968, "Control of Austenitic Grain Size by Additions of Titanium," J AUST INST METALS, **13** (2), pp. 94-106.

[61] Lagneborg, R., Siwecki, T., Zajac, S., and Hutchinson, B., 1999, "The Role of Vanadium in Microalloyed Steels," Scandinavian Journal of Metallurgy (Denmark), **28** (5), pp. 186-241.

[62] Wilson, A. L., Martukanitz, R. P., and Howell, P. R., 1998, "Experimental and Computer Simulation of Grain Growth in HSLA-100/80 Steels During Welding and Cladding," *Proc., 5th International Conference: Trends in Welding Research*, ASM International, Trends in Welding Research, pp. 161-166.

[63] *Lift-out TEM Specimen Preparation*. 2005, Fibics, Inc., www.fibics.com.

[64] Akhlaghi, S., Ivey, D. G., and Collins, L., 2000, "Microstructural Study of Grade 100 Steel," *Proc., 42nd Mechanical Working and Steel Processing Conference*, Iron and Steel Society/AIME, Warrendale, P.A., USA, **38**, pp. 419-428.

[65] Krauss, G., 2003, "Solidification, Segregation, and Banding in Carbon and Alloy Steels," Metallurgical and Materials Transactions B, **34B** (6), pp. 781-792B.

[66] Verhoeven, J. D., 2000, "A Review of Microsegregation Induced Banding Phenomena in Steels," Journal of Materials Engineering and Performance, **9** (3), pp. 286-296.

[67] Otterberg, R., Sandstrom, R., and Sandberg, A., 1980, "Influence of Widmanstatten Ferrite on Mechanical Properties of Microalloyed Steels," Met. Technol., **7** (10), pp. 397-408.

[68] Shiue, R. K., and Chen, C., 1991, "Microstructural Observations of the Laser-Hardened 1045 Steel," Scripta Metallurgica et Materialia, **25** (8), pp. 1889-1894.

[69] Shome, M., Gupta, O. P., and Mohanty, O. N., 2004, "Effect of Simulated Thermal Cycles on the Microstructure of the Heat-Affected Zone in HSLA-80 and HSLA-100 Steel Plates," Metallurgical and Materials Transactions A., **35A** (3), pp. 985-996.

Chapter 7

Mechanical Property Analysis in the HAZ

7-1. Introduction

The most important reason behind all microstructural studies of the HAZ is improvement of mechanical properties of this zone. A major advantage of microalloyed structural and linepipe steels is a reduction in carbon level that reduces both hardness and hardenability and therefore improves the weldability. Nevertheless, the HAZ in these steels still have characteristics and properties inferior to the engineered BM, which need investigation [1-3]. Interaction among many mechanical properties such as toughness, hardness and the level of strength mismatch (between different zones in the weld section) determine the overall property and efficiency of a weld joint [4]. The small size of the HAZ and variation of microstructure across it have an additional impact which complicates conventional mechanical tests and the interpretation of their results. Hardness can indirectly indicate variation of the mechanical properties to some degree, and hardness tests are easy to carry out even in very small regions.

In this chapter, after reviewing different aspects and tests for evaluation of the mechanical property variations in the HAZ, the results of the hardness measurements in and across the HAZ will be presented and discussed.

7-2. Mechanical properties

7-2-1. HAZ toughness

Toughness is perhaps the most important mechanical aspect. It is defined as the ability of a material to absorb energy in plastic deformation [5]. Static toughness of materials is represented by the total area under the stress-strain curve of that material, obtained in a simple tension test. However, the dynamic characteristic of toughness is better evaluated by impact toughness tests, like the Charpy test. These tests can lead to two important assessments: a) the ductile shelf energy and b) the impact transition temperature [6].

The formation of brittle constituents, together with the thermal stresses developed during welding, can cause cold cracking or re-heat cracking. In the absence of cracking, the mechanical properties of the HAZ are a function of the microstructure in this region [6]. The microstructural factors that control the HAZ toughness are (1) ferrite grain size (or lath/packet size), (2) carbon-rich constituents, and (3) the carbonitride precipitates [7]. Other factors are (4) the phases transformed from γ grains and (5) the amounts of impurities such as P, S and N [2]. In general, toughness decreases as the grain size and the volume fraction of carbon-rich constituents increase [7]. Precipitates have a more complex effect according to their size and volume fraction. They are essentially deleterious to toughness. Sometimes carbides crack or get separated from the matrix by interface decohesion. These mechanisms can contribute to void formation. Their high inherent strength and the strength of the bonds between them and the matrix lead to significant void nucleation strains [6]. More will be discussed in the next section.

7-2-2. HAZ toughness improvement

Improvement of HAZ toughness is mainly done by some metallurgical controls. Control of weld heat input is also important. These factors are described below.

7-2-2-1. Refinement of effective grain size

Refinement of grain size is done in two ways: (a) control of γ grain growth, and (b) promotion of ferrite nucleation inside the γ grain.

a) Austenite grain coarsening inhibition

Control of grain size, as explained earlier, is done by introducing proper precipitates, like TiN, and small particles like Ca(O,S) and REM(O,S) (rare earth metals), which act as grain coarsening inhibitors. The effective size of TiN, however, is believed to be below 50 nm [2]. It is likely that the TiN precipitates in the Grade 100 steel examined in this study (>100 nm and some in the size range of 2–8 μm) play little role in austenite grain growth control in the HAZ.

It has also been observed that TiN precipitates dissolve partially in the temperature range of 1300–1450°C, while Ca(O,S) and REM(O,S) are still stable and effective even at these high temperatures. In order to have a fine dispersion of these particles, the amounts of Ca and REM should normally be restricted to 50 ppm. In this case, Ca(O,S) and REM(O,S) particle size will be within 2–3 μm, which is sufficient to retard grain growth [2].

b) Nucleation of ferrite inside the austenite grain

There are many fine particles used as nucleation sites for ferrite or bainite inside the γ grain. Ti-oxides and nitrides, and complex precipitates of BN or $Fe_{23}(CB)_6$ have been used for this purpose [2]. The resulting microstructure will be acicular ferrite, which has a combination of high strength and good toughness.

7-2-2-2. Decrease of M-A constituents

Reduction of M-A constituents is done by reduction of the carbon equivalent (C.E.; Equations 2-1 and 2-2) in microalloyed steels, which is possible through the application of thermomechanical controlled processing (TMCP) [2]. Fig. 7-1 shows the relationship between C.E. and the HAZ toughness of HSLA steels. The toughness is given as a Charpy V-notch (CVN) absorbed energy in joules at -20°C. Basically, C.E. shows the effect of carbon and other elements on the *hardenability* of steel. There are several definitions for hardenability, but the most common and simple one is "the ability of steel to form martensite on quenching" [8].

Proper choice of alloying elements, to avoid the formation of M-A constituents, is also important. The following elements tend to increase M-A formation: B, N, C, Cr, Mo, Nb, V, Si, Cu, Ni and Mn [2]. These elements should be kept as low as possible in composition, as in general, an increase in chemical composition accelerates the formation of M-A.

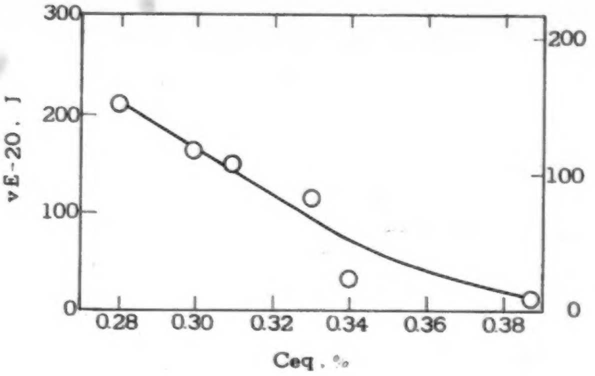

FIG. 7-1. Effect of carbon equivalent on HAZ Charpy toughness of HSLA steels [2].

7-2-2-3. Reduction of impurities

Reduction of impurity elements like P, S, O and N is necessary for the improvement of HAZ toughness [2, 9, 10]. Susceptibility to hot cracking and liquation cracking also decreases with reduction in the level of impurities too [11]. Impurity levels should be reduced at the steelmaking stage, or controlled by forming stable components later [12].

An increase in phosphorous levels above ~0.01% can reduce the toughness in the CGHAZ of low-carbon microalloyed steels drastically [13]. The mechanism of deterioration of the cleavage resistance of martensite as a result of an increase in phosphorous content is not well understood. Phosphorous does, however, prevent austenite grain growth at high heat inputs due to solute drag effects at the prior austenite grain boundaries.

7-2-2-4. Control of heat input

Bhole and Billingham [14] studied the effect of heat input on the toughness of various commercial HSLA steels microalloyed by Nb. The Charpy V-notch tip was located in the CGHAZ. The heat input in their study ranged from 1.5 to 9 kJ/mm for SAW. The CGHAZ microstructures of the control-rolled steels ranged from acicular ferrite (good toughness) to Widmanstatten ferrite and upper bainite (low toughness). The toughness decreased with heat input for the latter microstructure, but remained almost constant at an acceptable level with the former microstructure.

Smith *et al.* [15] also examined the effect of increasing the heat input in some HSLA steels. They compared the microstructure and Charpy toughness in simulated CGHAZ samples with heat inputs of 2 and 4 kJ/mm. The increase in heat input for low carbon low alloy steels resulted in the formation of large packets of bainite with low fracture toughness, while at the lower heat input small packets of low carbon lath martensite met the targeted toughness value at low temperatures. An increase in Ni in HSLA100, from 1.7 to 3.5%, retained the targeted toughness by increasing the hardenability and the formation of low-carbon martensite. The reason behind the improved fracture toughness energy in low-carbon martensite was the formation of relatively small (<5 μm) packets of lath martensite with high-angle interfaces between the packets. SEM fractography showed that the cleavage facet size was related to the packet size. Large packets of bainite that formed at higher heat input and leaner compositions provided a large length for easy propagation of cracks.

In general, an increase in the heat input may reduce the toughness due to the formation of grain-boundary/proeutectoid ferrite, Widmanstatten side-plates of ferrite and upper bainite, as well as precipitation of microalloy carbonitrides. These are the factors that result in the embrittlement in the CGHAZ of low-carbon microalloyed steels [16]. Fig. 7-2 shows the effect of cooling rate on the HAZ CVN toughness at –40°C for a series of low-carbon microalloyed steels, after Akselson *et al.* [13]. The chemical compositions of these steels were similar to that of Grade 100, but much leaner in microalloying elements. The main difference in the composition of these steels was the level of phosphorous, which was 180, 70 and 50 ppm for the steels A, B and C, respectively. Fast cooling rates ($\Delta t_{8/5} < 15$ s) accompanied with application of low heat input (<1.5 kJ/mm), are generally desirable in these steels. Low cleavage resistance in the steels was correlated with the high phosphorous content (>0.01%).

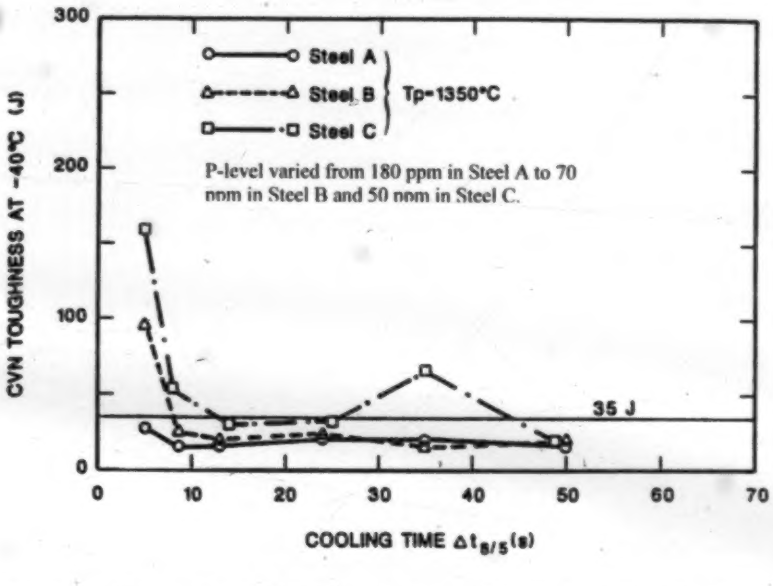

FIG. 7-2. Effect of cooling time on the CGHAZ Charpy toughness at –40°C for low-carbon microalloyed steels [13].

The hardness of the simulated CGHAZ of the low-carbon (0.04%) HSLA100-3.5Ni in the work of Smith *et al.* [15] was ~355–360 HV for both heat inputs. The microstructure and hardness of this sample is very similar to that of CGHAZ in the Grade 100 steel studied here with a heat input of 0.5 kJ/mm. Considering this and the results of others, in particular Akselson *et al.* (Fig. 7-2), it can be speculated that the CGHAZ–0.5 kJ/mm with low-carbon lath martensite has a higher toughness than the CGHAZ–2.5 kJ/mm with large packets of bainitic ferrite. This, however, does not necessarily indicate the fracture toughness or behaviour of the whole HAZ, as cracks may initiate in local brittle zones (LBZ; e.g., local regions of relatively high-carbon lath martensite or twinned martensite) but propagate in other regions.

7-3. Mechanical Tests

The most common mechanical tests used to assess metal toughness are the Charpy test, the drop weight tear test (DWTT), the crack tip opening displacement (CTOD) test, hardness measurements and the low-cycle fatigue test. In selection of the correct test and the correct fracture criteria for the assessment of HAZ fracture toughness, it should be realised that HAZ toughness should be related to crack initiation rather than to crack propagation [17]. This is because cracks that initiate in the HAZ seldom remain there during propagation. Therefore, for HAZ, only CTOD may be appropriate. Charpy tests (which assess the energy required for both initiation and propagation) may be useful for quality control tests and qualitative comparisons among different weld samples [18]. Even this can be questionable, as Charpy tests do not detect local brittle zones in the HAZ [19]. Tensile tests are used for the assessment of strength matching among the BM, HAZ, and WM. Other tests, such as hardness, can give an indirect assessment of mechanical properties.

7-3-1. Charpy test

The standard V-notch Charpy test has been used for evaluation of HAZ toughness with different levels of success [2, 14, 15, 17-22]. The advantages of a Charpy test are that it is simple, easy and cheap. The disadvantages are that the results are considerably scattered in nature, and the results are useful only for comparison. They cannot be used in design, as there is no correlation between Charpy data and the flaw size [5].

In some cases, standard Charpy specimens may be difficult to machine out of the actual HAZ samples due to plate thickness, and/or the shape of the HAZ. There may also be some concerns about the location of the root of the notch with respect to the HAZ or its sub-regions. Fairchild *et al.* [23] showed that Charpy tests may be insensitive and not show differences in local microstructures when the microstructure changes over small distances, as it does in the HAZ. Because of all these difficulties and concerns, some researchers have preferred to use simulated HAZ samples to assess the toughness of HAZ sub-regions of interest [24-26]. This is also questioned by some researchers as the accurate simulation of the exact thermal cycle may not be achievable [19]. Also, it has been found that the microstructural characteristics and properties of simulated samples can be different from the actual HAZ, due to the limited size of the HAZ and the presence of adjacent regions with different characteristics [27].

7-3-2. CTOD test

Compared to the Charpy test, the CTOD test is a more precise method. It gives data that can be used in fracture calculations and assessment of notch sensitivity. In this test, the amount of deformation at the tip of a crack, which is different in brittle and ductile fractures, can be quantified [28].

The CTOD test is a more sensitive test than Charpy testing to assess the toughness of LBZ in metals, and therefore is more suitable for toughness evaluation in weld metal and weld HAZ [23]. This test, however, is very time consuming. The position of the fatigue precrack at the notch tip in the weld section is the most important factor in CTOD testing of the weldments [29].

In spite of expected improvements in the HAZ toughness of modern low-carbon high-strength microalloyed (HSMA) steels, low CTOD values were recorded [1]. These values were related to the presence of LBZs. An LBZ is a region in the HAZ that produces a CTOD value lower than 0.10 mm [4]. It should be added that CTOA (crack tip displacement angle) testing has also been successfully used in the assessment of fracture behaviour of modern HSMA steels [30]. The constancy of the CTOA in the stable phase of crack propagation, regardless of the fracture length, suggests that a critical CTOA toughness value could be determined.

7-3-3. Tensile test

The importance of the tensile test is in the assessment of strength mismatch and degrees of softening/hardening in different regions of the weld joint. It is also used in the assessment of stress-corrosion cracking. There are three approaches used in this test, as explained below.

7-3-3-1. Sub-size tensile specimens

It is possible to make standard sub-size, round tensile specimens along the longitudinal direction of the weld run. The cross-section of such specimens will sample one or several sub-regions of the HAZ, depending on the width of the HAZ sub-regions (a function of heat input). The smallest diameter indicated in ASTM A 370 [31] is 2.50 mm. This is small enough to make a longitudinal specimen out of the FGHAZ–2.5 kJ/mm of Grade 100 (3.65 mm wide). For other sub-regions and heat inputs, a longitudinal specimen will sample more than one region in cross-section. Still, making longitudinal specimens at various distances from the fusion line can be used for estimation of the variation in mechanical properties across the HAZ and for different heat inputs.

It is also possible to make transverse tensile specimens normal to the fusion line [32]. Such a specimen will sample all the sub-regions along its length. The yielding and fracture should occur at the weakest sub-region. This method will assess the overall property of the weld HAZ, and is best to compare the overall effect of heat inputs, and the evaluation of hardening or softening [4].

7-3-3-2. Simulated HAZ samples

It seems that the first work on simulation of the various regions of weld HAZ is that of Nippes *et al.* in 1949 (as cited in [33]). The advantage of using a simulated sample is that such a sample can be large enough to make a standard specimen out of it. For this reason, simulated samples have been used extensively for assessment of strength in a specific sub-region of the HAZ (e.g., [34, 35]). It should be pointed out that the same general concerns mentioned in Section 7-3-1 on using simulated samples for performing Charpy tests apply to all mechanical tests, including tensile tests.

7-3-3-3. Miniature tensile samples

All the mechanical testing specimens, including tensile specimens, can be miniaturized, so that they sample only one sub-region in the HAZ [36]. Miniature tensile specimens can be designed by scaling down the dimensions of standard tensile specimens. The samples can be machined by electro-discharge machining (EDM) to leave the least amount of deformation in the reduced section of the specimen. The miniature tensile properties might be somewhat different from those of the standard-sized samples. Therefore, some correlation between these two properties should be established for a given alloy for different heat-treatment conditions.

7-3-4. Shear-punch test

Shear-punch tests have been used for determination of mechanical properties of the individual sub-regions in the HAZ [36]. These tests are carried out by devices similar to those used for preparation of conventional thin-foil TEM samples, i.e., punching 3-mm diameter disks out of the thinned sections of metals. The load-displacement curves obtained during a shear-punch test are analyzed to determine the shear properties. These properties are then converted to the tensile properties through linear relationships, which are empirical in nature, and need to be determined for a given alloy.

7-3-5. Hardness test

Hardness measurement can be used as an alternative, or as a complement, to impact toughness [11, 18, 37, 38]. Indentation hardness, which measures the resistance to plastic deformation (yield and flow), can replace a toughness test, and be used as a criterion to indicate mechanical property variation across the weldment, or to compare two weldments.

A Vickers hardness traverse is a well-accepted test for this purpose. In this test a very low weight, e.g., 1 kg, is applied and the test is carried out along a predetermined line, from the weld metal to the unaffected base metal, crossing the weld HAZ. A hardness traverse can be applied on several sections and several lines on each section. A hardness traverse can also be used to find roughly the width of the HAZ [39]. Another measure is to obtain a hardness map of the area of interest. This is more useful for the weld metal region [38], where the changes are in two dimensions, rather than one dimension in the HAZ.

7-3-6. Conversion of hardness to other mechanical properties

It had been shown that tensile properties, such as yield strength (σ_y), ultimate tensile strength (*UTS* or σ_u), and the work-hardening index (n), can be obtained from hardness measurements [40]. The theoretical-empirical equations are

$$\sigma_y = \frac{H}{3}(0.1)^n \tag{7-1}$$

$$\sigma_u = \frac{H}{3}(1-n)\left[\frac{12.5n}{1-n}\right]^n \tag{7-2}$$

$$n = m - 2 \tag{7-3}$$

$$K = \frac{H}{3(0.08)^n} \tag{7-4}$$

K is the strength coefficient in $\sigma = K.\varepsilon^n$ and m is the Meyer parameter determined from a *logP–logd* plot (Section 7-5-6). In cases where n could be determined relatively accurately, one could have an idea of the ductility and elongation, based on the fact that

$$\varepsilon_u = n \tag{7-5}$$

where ε_u is the true strain at the point of necking or maximum load [41]. It should be noted that there are also some empirical equations for calculation of the work-hardening index, e.g., the one given by Akselson *et al.* [35], in the general form:

$$n = a\left(\Delta t_{8/5}\right)^b$$

where a and b are constants that depend on the microstructure. For the CGHAZ of a range of low-carbon steels (C-Mn, microalloyed and quenched-and-tempered) the values of these constants were determined as 0.065 and 0.17, respectively.

Another result from Meyer tests is the conversion of a *logP-logd* plot to flow curves. In this method, stress and strain are calculated from the load, P_m, and the indentation diameter, d, by these equations, respectively [40]:

$$\sigma = P_m / 2.8 \tag{7-6}$$

$$\varepsilon = 0.2\ (d / D) \tag{7-7}$$

where D is the ball diameter.

The area under the stress–stain curve can be integrated to obtain the static toughness. Recently, Haggag and Phillips [42] used a modified version of this method, called an "automated ball indentation" (ABI) technique, to determine non-destructively the tensile properties as well as the fracture toughness of in-service steel pipelines at the BM, WM and HAZ. The key idea was generation of concentrated stress fields near and ahead of the indentation location, similar to the concentrated stress fields ahead of a crack. The initiation fracture toughness could be calculated from the integration of deformation energy up to a critical depth. The critical depth was determined from the critical fracture stress of the material or a critical strain of 0.12.

7-4. Experimental procedure

Transverse and longitudinal sections, made from the welded plates (Section 2-5), were used for hardness measurements. Vickers hardness tests, with loads of 5 kg and 500 g, were used to obtain the average hardness number in the middle of each sub-region as well as the hardness profiles across the HAZ, respectively, on both transverse and longitudinal sections. A Mittotoya hardness tester was used for macro- as well as microhardness measurements. Nanohardness measurements were carried out with a Hysitron® nano-mechanical probe with a load of 500 µN. Hardness numbers in GPa were calculated for each point [43].

7-5. Results and discussion

7-5-1. Macrohardness measurements: hardness averages

Table 7-1 shows the average macrohardness values for each HAZ sub-region, and for different heat inputs (0.5, 1.5 and 2.5 kJ/mm), obtained from the longitudinal sections. The width of the HAZ in each case, measured along the central vertical section, is also given. These values will be discussed later along with microstructural changes (Chapter 8).

Table 7-1. Average macrohardness numbers obtained at the mid-plane of each sub-region

Heat input, kJ/mm	Hardness, HV5				HAZ width, mm
	BM	ICHAZ	FGHAZ	CGHAZ	
0.5	285.8 ± 3.4	290.5 ± 1.0	304.3 ± 2.9	354.5 ± 3.3	1.9
1.5		280.9 ± 1.3	251.7 ± 2.4	291.4 ± 2.9	4.6
2.5		N.A.*	249.1 ± 1.9	270.4 ± 5.2	6.1

* The HAZ- 2.5 kJ/mm is so large that the ICHAZ is not available on vertical longitudinal sections

7-5-2. Microhardness measurements: hardness profiles across the HAZ

To have a better understanding of hardness variations across the HAZ, microhardness measurements were employed, by taking radial traverses on the transverse sections. Fig. 7-3 shows the microhardness profiles for five values of heat input, namely, 0.5, 0.7, 1.0, 1.5 and 2.5 kJ/mm. Note that the horizontal axis is normalized with respect to the HAZ width. For a heat input of 0.5 kJ/mm, the HAZ is too small to obtain a hardness traverse with good spatial resolution. There was a possibility that a hard region was missed on the profile. To resolve this, hardness mapping with a pattern shown in Fig. 7-4, was performed on the longitudinal section with a load of 0.5 kg. This not only increased the spatial resolution ~5 times compared to the radial traverses, it also increased the accuracy and reliability of the measurements as 3-4 measurements were obtained for a given distance from the fusion line (Fig. 7-5).

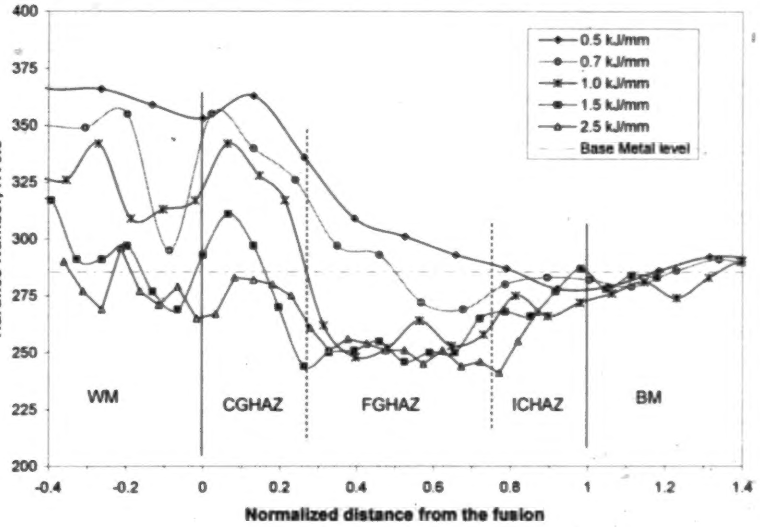

FIG. 7-3. Microhardness profiles across the HAZ for a range of heat inputs.

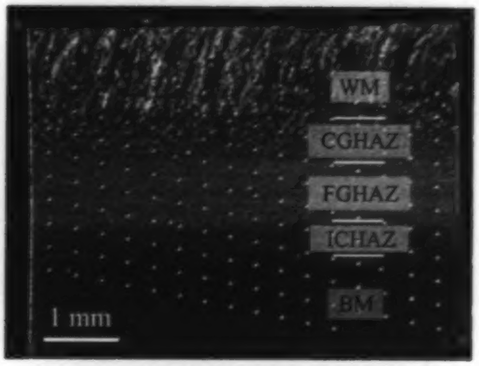

FIG. 7-4. Hardness mapping indentations– 0.5 kJ/mm.

7-5-3. Hardening and softening in the HAZ

Excessive hardening and softening in the WM/HAZ are both undesirable. Hardening in high-strength microalloyed or low alloy (HSMA/HSLA) steels make the welding potentially susceptible to cold cracking and stress corrosion cracking. Softening is also believed to be deleterious, due to the possible occurrence of "concentrated strain" that can lead to, for instance, SSCC (sulphide stress corrosion cracking) and ductile fracture [44].

For the heat input of 0.5 kJ/mm, there is considerable hardening from ~285 (BM) to a maximum of ~360 HV (CGHAZ). Initially, there is a moderate increase in the hardness across the FGHAZ (Fig. 7-5) reaching ~310 HV, while at the boundary between the FGHAZ and CGHAZ there is a very steep increase to ~360 HV. The hardness slightly decreases across the CGHAZ towards the fusion line (~340 HV). For the heat input of 0.7 kJ/mm, there is first some softening from ~285 to ~270 HV and then some hardening to ~300 in the FGHAZ (Fig. 7-3). This heat input seems to represent the transition between hardening and softening in the FGHAZ. For the higher heat inputs, however, softening occurs dominantly across the FGHAZ, i.e., the hardness decreases from ~285 to ~250 HV. Hardening occurs in the CGHAZ relative to the FGHAZ and BM for all samples, with a maximum depending on the heat input.

Hardening for the heat input of 0.5 kJ/mm is due to the fast thermal cycle induced by this heat input (Section 4-5). The fast cooling rate promotes formation of fine-grained ferrite in the FGHAZ and martensite in the CGHAZ with large prior austenite grains (Section 6-5-5). The moderate cooling rates induced by employing the higher heat inputs of 1.5 and 2.5 kJ/mm will result in larger ferrite grains in FGHAZ and bainitic ferrite in CGHAZ, as shown in Section 6-5-2. Note that the higher hardness in the CGHAZ relative to the FGHAZ, regardless of the heat input, is due to the microstructural changes in the CGHAZ, induced by large prior austenite grains that increase the hardenability. Correlation of hardness with microstructure will be discussed in more detail in Chapter 8.

7-5-4. Nanohardness measurements: hardness contours

As the microstructural constituents in the HAZ can form grains which are only a few microns, or even sub-micron, in size, nano-hardness mapping was employed to obtain the hardness contours in each sub-region. This was done for only one heat input, 0.5 kJ/mm, because this sample had the most critical changes in microstructure and hardness.

Fig. 7-6 shows hardness contours for the BM, FGHAZ and CGHAZ taken over areas about 3 μm x 4 μm. The CGHAZ appears to have a mixture of microstructural constituents with different hardness levels – some very hard and some only as hard as the BM. The correlation between the microstructure and nano-hardness will be addressed in Chapter 8.

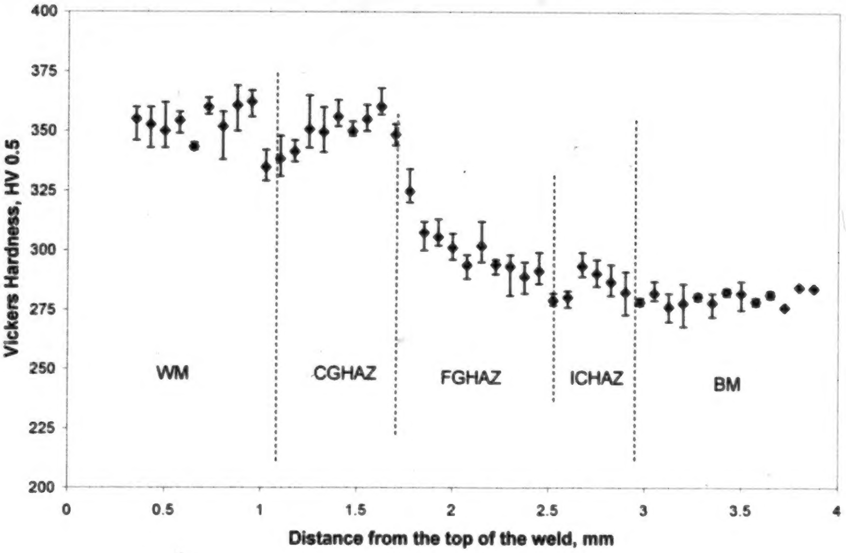

FIG. 7-5. Hardness mapping result for the sample with a heat input of 0.5 kJ/mm.

The FGHAZ, in general, is softer than the CGHAZ and harder than the BM, although one region with a hardness even higher than the hardest regions of the CGHAZ was detected (Fig. 7-6b). The high hardness value may be due to the indenter hitting a carbide particle. Table 7-2 shows the average hardness numbers for the three areas. The average hardness values correlated well with the Vickers values, exhibiting a linear relationship with the values reported in Table 7-1.

Table 7-2. Average nanohardness numbers obtained from the center of each sub-region for a weld section with a heat input of 0.5 kJ/mm

Region	Hardness, GPa
BM	1.2
FGHAZ	1.3
CGHAZ	3.0

7-5-5. Maximum hardness in the HAZ

A high hardness value of ~360 HV, indicative of a martensite structure for this level of carbon (Fig. 7-7), was obtained for a heat input of 0.5 kJ/mm in the CGHAZ. Hardness profiles for lower heat inputs than 0.5 were also obtained to see if a microhardness of ~360 HV is in fact the hardest value that could be obtained across the HAZ. The CGHAZ width for these samples were ~0.55, 0.58 and 0.60 mm, for heat input values of 0.3, 0.4 and 0.5 kJ/mm respectively. Fig. 7-8 shows vertical hardness traverses obtained on transverse sections for these samples. Table 7-3 compares the maximum and average microhardness numbers for these samples. The data show there is a real increase in microhardness (which is a local hardness) as the heat input decreases from 0.5 to 0.3 kJ/mm. Fig. 7-9 shows maximum microhardness in CGHAZ as a function of heat input for a larger range of heat inputs. The reason why the microhardness did not reach a plateau of maximum hardness of ~360 HV for this grade of steel might be the variation in local hardnesses as seen by nanohardness contours. The lower the heat input the faster the thermal cycle and the higher the chance for inhomogeneous microstructures. The high hardness numbers represent local regions with high solute contents. The macrohardness measurements, however, which are averages of large areas, show a maximum hardness of ~360 HV as the heat input is decreased (Fig. 7-10).

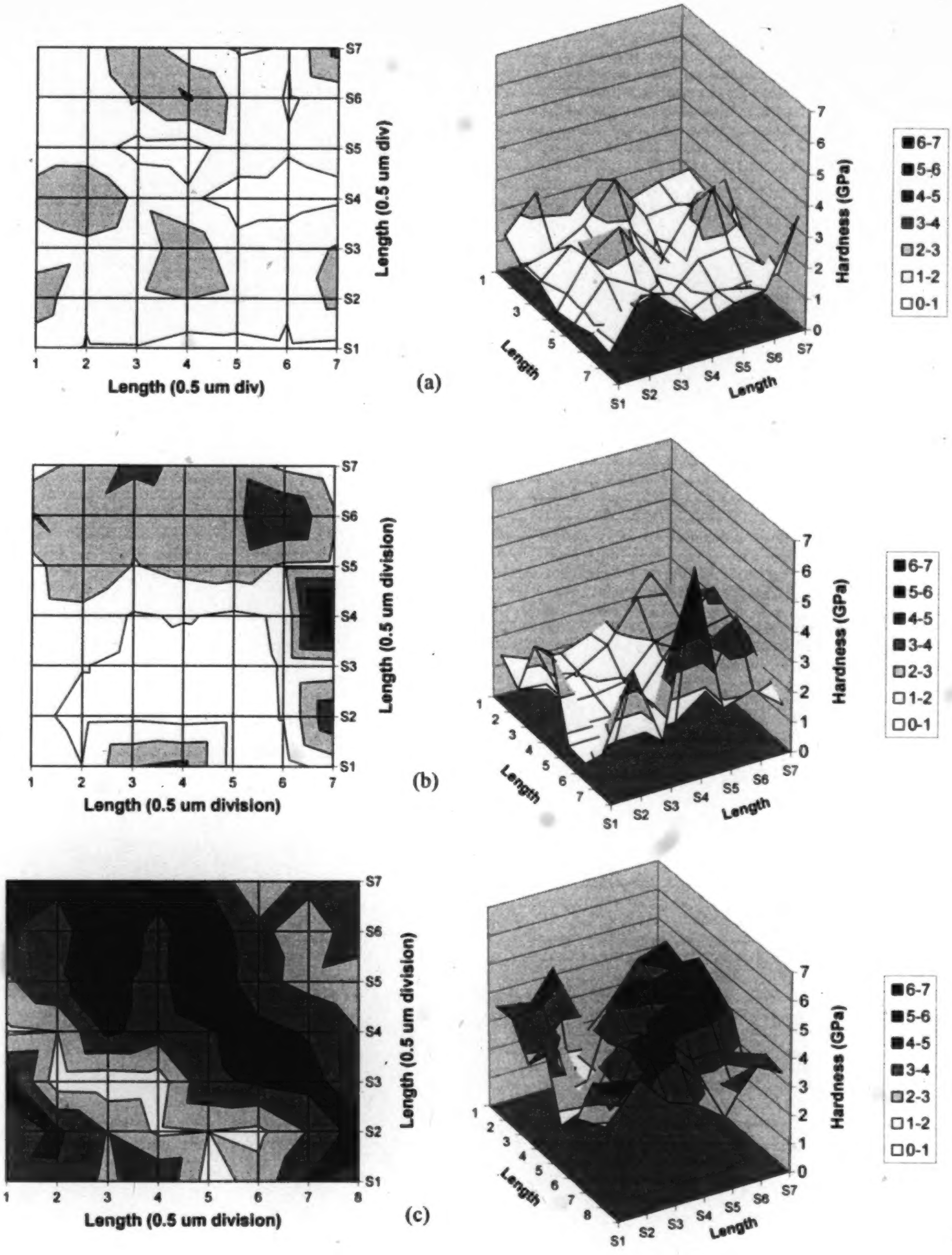

FIG. 7-6. Nanohardness contours for different sub-regions of the weld section with a heat input of 0.5 kJ/mm: a) BM; b) FGHAZ; c) CGHAZ.

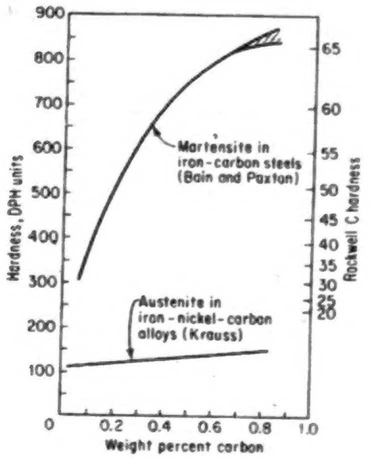

FIG. 7-7. Variation of martensite hardness with carbon content [48].

Table 7-3. Hardness variation in CGHAZ for low values of heat input

Heat input, kJ/mm	HV_{500}	
	Max hardness	Average hardness
0.3	375	364±7
0.4	360	350±8
0.5	358	350±7

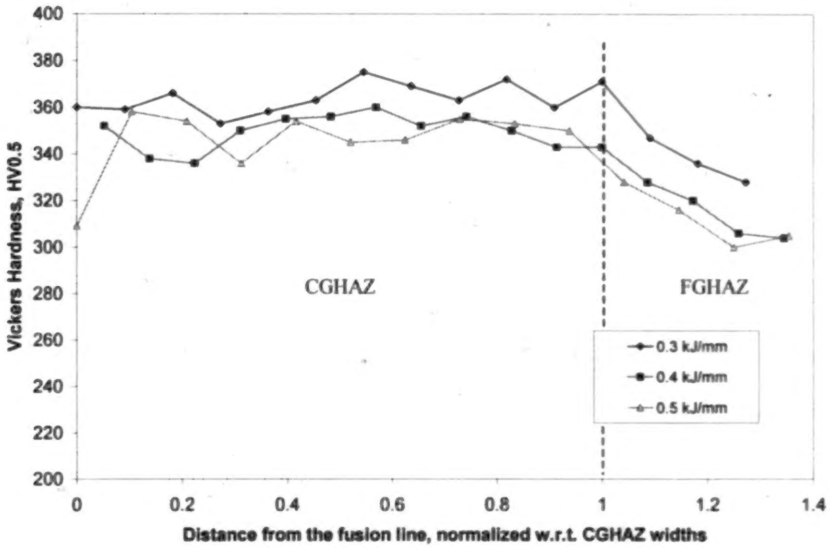

FIG. 7-8. Microhardness profiles across the CGHAZ on samples with very low heat input values.

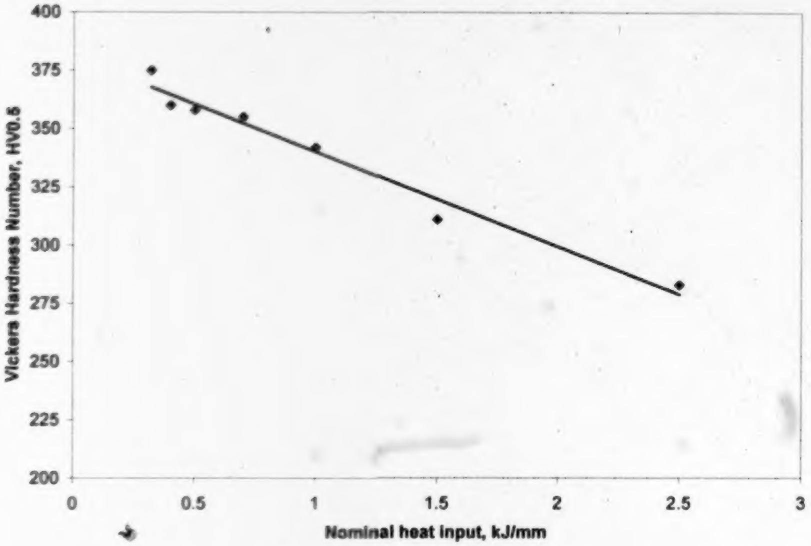

FIG. 7-9. Maximum microhardness in the CGHAZ as a function of heat input.

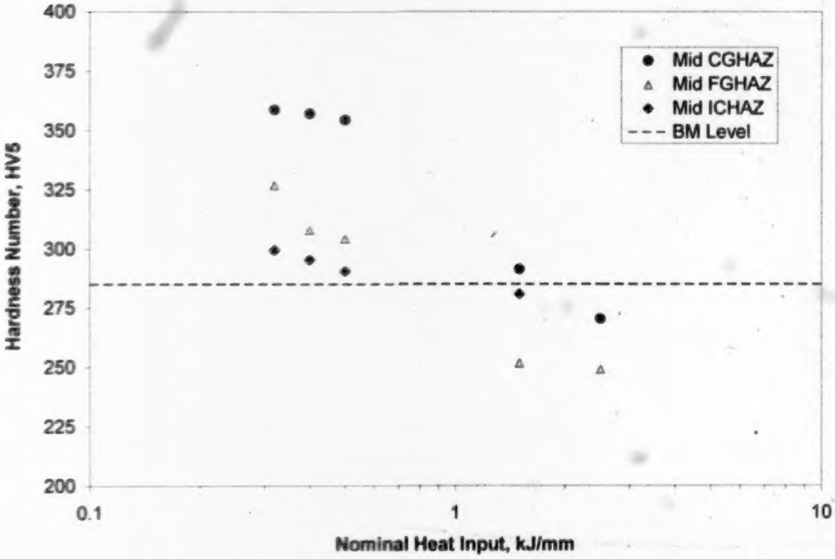

FIG. 7-10. Macrohardness variation across the HAZ sub-regions for a wide range of heat input.

7-5-6. Conversion of hardness to tensile parameters

A test was carried out to verify the precision of the method described in Section 7-3-5. For this reason, 4-mm round tensile specimens were prepared from Grade 100 steel in three conditions: as received, annealed and quenched. The required hardness (Brinell and Vickers) and tensile tests were performed on these samples with Wolpert and Instron machines, respectively. To find the Meyer parameter, *m*, a steel ball of diameter 1 mm, and loads between 1 and 30 kg were used on the hardness tester.

Fig. 7-11 shows the result of the Brinell tests for the Meyer parameter in a log-log plot for an as-received sample, which yields *m* = 2.19. The m-parameter for other samples, the hardness in Vickers and the tensile properties calculated according to equations 7-1 to 7-4 are reported in Table 7-4.

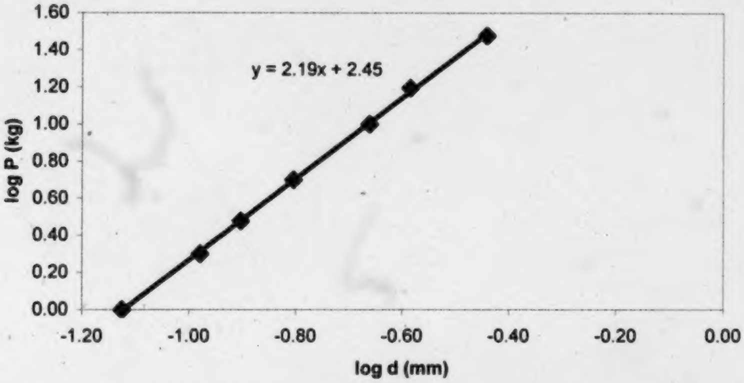

FIG. 7-11. The log P-log d curve, resulting in the Meyer parameter, m, from the Meyer equation $P=k.d^m$.

Table 7-4. Mechanical properties estimated based on hardness measurements and Equations 7-1 to 7-4.

Condition	VHN	m	σ_Y (MPa)	σ_u (MPa)	σ_u (kg/mm^2)	n	K (MPa)	VHN/3
As received-Long	286.3	2.19	604.5	930.4	94.8	0.19	154.2	95.4
As received-Trans	282.3	2.19	596.1	917.4	93.5	0.19	152.1	94.1
Annealed	208.3	2.16	471.3	657.5	67.0	0.16	104.0	69.4
Quenched	353.2	2.20	728.8	1160.6	118.3	0.20	195.1	117.7

The results of the tensile tests are shown in Fig. 7-12, which shows the flow curves (both engineering and true) for the samples in as-received, annealed (950°C; 8 min; furnace cooled) and quenched (1150°C; 8 min; quenched in brine) conditions. The important parameters obtained from these curves are summarized in Table 7-5. Assuming a power relationship between stress and strain, i.e., $\sigma = K.\varepsilon^n$, *K* and *n* were obtained by linear regression of the *log* σ against *log* ε plot with the data from the yield point to the *UTS*, i.e., the stable plastic deformation region. Toughness is the area under the flow curve.

Comparing the Tables 7-4 and 7-5, it can be seen that there is a very good estimation of *UTS* (within 1–5% error), an error of ~17–34 % for σ_y and an error of ~15–29 % for *K*. Interestingly enough, the simple equation *UTS=HV/3*, would predict as good a result for σ_u (last column in the Table 7-4). The estimation of *n* is very poor; there is a large error of ~24–150 %. However, Fig. 7-13 shows that there is a very good correlation between the uniform strain and work-hardening exponent under different heat treatment conditions ($\varepsilon_u = 0.70\ n - 0.02$). This correlation can be used to obtain ε_u from *n*. The only problem is that the relationship between *n* and *m* is not satisfactory. A better relationship should be sought. If a satisfactory relationship is found, this method, together with the correlation between n and ε_u, can yield an acceptable estimation of elongation. On the other hand, the estimation for strength is already satisfactory. Elongation and strength data can lead to toughness values that can be compared to different HAZ sub-regions.

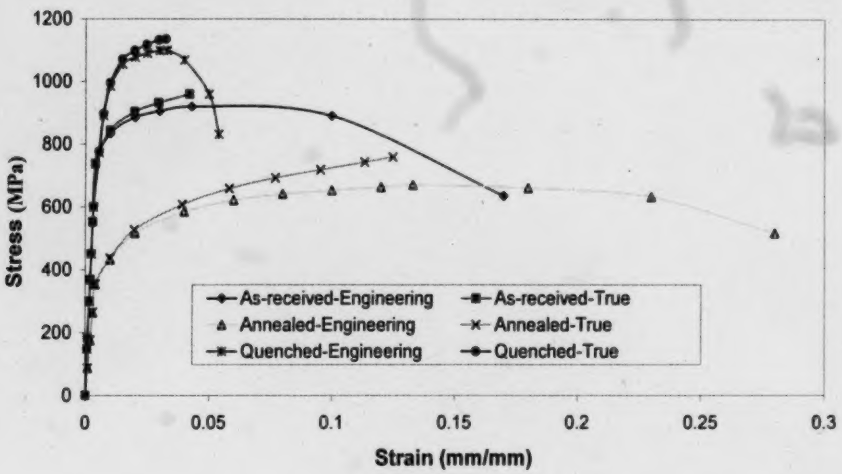

FIG. 7-12. The stress-strain curves.

Table 7-5. Mechanical properties obtained experimentally from tensile tests.

Condition	σ_Y (MPa)	σ_u (MPa)	e_f	ε_u	n	K (MPa)	Toughness (MPa)
As received-Long	788.0	920.8	0.18	0.06	0.09	1303.2	151.5
As received-Trans	789.5	937.2	0.18	0.04	0.09	1288.3	149.0
Annealed	350.6	671.2	0.28	0.13	0.21	1202.3	170.7
Quenched	878.0	1106.0	0.05	0.03	0.08	1479.1	53.2

Fig. 7-14 compares the stress-strain curves obtained from this conversion with the true stress-true strain curves obtained experimentally. As can be seen, though the flow curves are not precisely predicted, they are still close. Some of the discrepancies in the results might have come from a non-uniform heat treatment. The conditions on the surfaces of samples by hardness tests may be different from the conditions of the interiors used for tensile teats. Considering all these facts, this method seems to be promising for assessment of mechanical properties (including static toughness) at different regions of the HAZ. More investigation on the empirical equations and better heat treatments are recommended for future work.

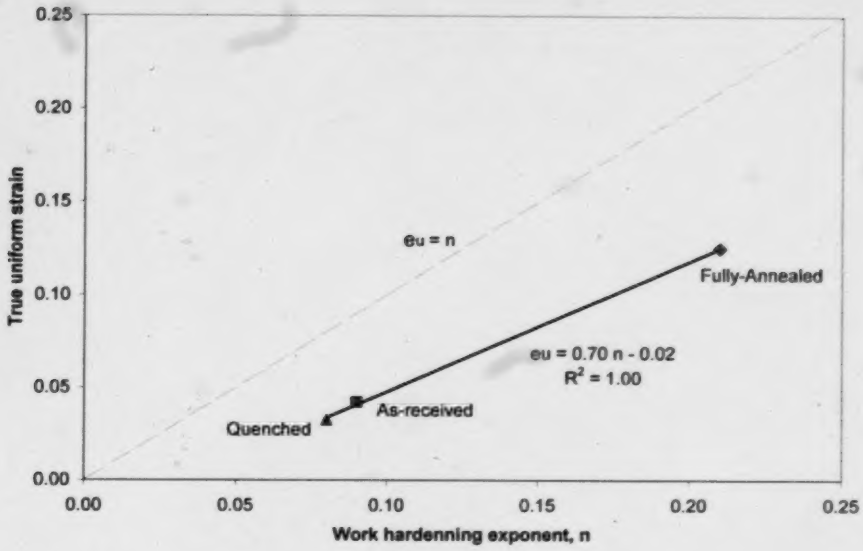

FIG. 7-13. Correlation between uniform strain and work-hardening exponent.

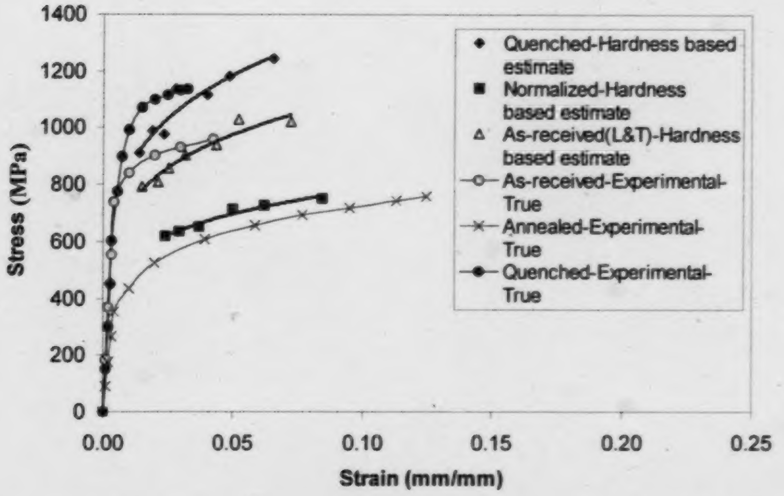

FIG. 7-14. Stress-strain curves obtained from hardness-based Meyer conversions along with corresponding experimental curves.

7-6. Summary

The degradation of fracture toughness and overall properties of the HAZ in low-carbon HSLA steels is attributed to the formation of LBZs. An LBZ is found most often in the CGHAZ of single-pass weld joints and the IRCGHAZ of multi-pass weldments. Due to the small size of the HAZ and its sub-regions, and the fact that crack initiation is the controlling criterion, only CTOD tests seem to be suitable for the assessment of the toughness in specific regions of the HAZ. Charpy tests can only assess the overall HAZ toughness qualitatively, and may be insensitive to LBZs. Moreover, the variation in microstructure and properties across the HAZ can impose large scatter in the results.

Miniature tensile samples may be a good replacement for standard tensile samples that are too big for HAZ sub-regions. Nevertheless, transverse sub-size standard tensile tests can assess the strength mismatch level and the degree of softening/hardening in the weld joint well. Hardness measurements, on the other hand, are suitable for the HAZ and are easy to carry out. There are also many investigations and reports based on hardness values, for instance, the susceptibility to HAC. One advantage of the hardness test is that it can be carried out at different levels (macro-, micro- and nano-scales) conveniently. There is also a promising method for converting the hardness results to other mechanical properties, even static toughness and some other fracture properties.

Hardness traverses across the HAZ showed considerable hardening from ~285 (BM) to a maximum of ~360 HV_{500} (CGHAZ) for a heat input of 0.5 kJ/mm. For the higher heat inputs (1.5 and 2.5 kJ/mm), however, softening occurs predominantly across the FGHAZ, i.e., the hardness decreases from ~285 to ~250 HV_{500}. Hardening occurs in the CGHAZ relative to FGHAZ for all samples, with a maximum of ~310 HV_{500} for a heat input of 1.5 kJ/mm and a maximum of ~280 HV for a heat input of 2.5 kJ/mm. A hardness of ~360 in the CGHAZ of a 0.5 kJ/mm weld sample is indicative of martensite. However, nano-hardness contours over this region showed that it had a mixture of microstructural constituents with different hardness levels – some very hard and some only as hard as the BM. This variation is believed to be due to the variation in phase microstructures in this region. Hardness measurements on weld samples with lower heat inputs than 0.5 kJ/mm show that hardness values can exceed 370 HV_{500}.

Whether or not the presence of martensite reduces the fracture toughness depends on the steel's carbon level, substructure, morphology and even the mechanical test method and procedure. However, the more important issue is the susceptibility of a microstructure to cracking for a given fabrication or service situation. Lath martensite might show higher toughness than bainite, but lower HAC resistance.

References

[1] Thaulow, C., 1989, "The Effect of HAZ Brittle Zones in Controlling the Fracture Toughness. (Retroactive Coverage)," *Proc., International Conference on Evaluation of Materials Performance in Severe Environments. Vol. 2*, The Iron and Steel Institute of Japan, pp. 643-656.

[2] Shiga, C., and Saito, Y., 1990, "Toughness Improvement in HAZ of HSLA Steels by TMCP in Japan," American Welding Society, pp. 177-205.

[3] Lambert-Perlade, A., Gourgues, A. F., Besson, J., Sturel, T., and Pineau, A., 2004, "Mechanisms and Modeling of Cleavage Fracture in Simulated Heat-Affected Zone Microstructures of a High-Strength Low Alloy Steel," Metallurgical and Materials Transactions A., **35A** (3A), pp. 1039-1053A.

[4] Denys, R., 1989, "The Effect of HAZ Softening on the Fracture Characteristics of Modern Steel Weldments and the Practical Integrity of Marine Structures Made by TMCP Steels. (Retroactive Coverage)," *Proc., International Conference on Evaluation of Materials Performance in Severe Environments. Vol. 2*, The Iron and Steel Institute of Japan, pp. 1013-1027.

[5] Dieter, G. E., and Bacon, D., 1988, Mechanical Metallurgy, McGraw-Hill, Maidenhead, Berkshire.

[6] Gladman, T., 1997, The Physical Metallurgy of Microalloyed Steels, The Institute of Materials, London.

[7] Godden, M. J., and Boyd, J. D., 1981, "Characterization of Microstructures in Weld Heat-Affected Zones by Electron Microscopy," *Proc., Microstructural Science, Vol. 9. 13th Annual Technical Meeting of the International Metallographic Society*, Elsevier North-Holland Inc., pp. 343-354.

[8] Isaac Garcia, C., 1995, "Transformation Strengthening of MA Steels," *Proc., ISS, Proceedings of the International Conference "Microalloying '95"*, pp. 365-375.

[9] Smith, N. J., Mcgrath, J. T., Gianetto, J. A., and Orr, R. F., 1989, "Microstructure/Mechanical Property Relationships of Submerged Arc Welds in HSLA 80 Steel," Welding Journal, **68** (3), pp. 112-s to 120-s.

[10] Morrison, W. B., 1995, "Microalloyed Steel for Offshore Application," *Proc., Microalloying '95*, Iron and Steel Society Inc, Warrendale, pp. 105-116.

[11] Easterling, K. E., 1992, Introduction to the Physical Metallurgy of Welding, Butterworth-Heinemann Ltd, Oxford.

[12] Hulka, K., 1992, "Modern Processing Facilities Favour the Application of Microalloyed Steels," *Proc., Clean Steel 4,* The Institute of Materials (UK), pp. 82-100.

[13] Akselsen, O. M., Grong, O., and Rorvik, G., 1990, "Embrittlement Phenomena in the Grain Coarsened Heat Affected Zone of Low Carbon Microalloyed Steels," Scandinavian Journal of Metallurgy (Denmark), **19** (6), pp. 258-264.

[14] Bhole, S. D., and Billingham, J., 1983, "Effect of Heat Input on HAZ Toughness in HSLA Steels," Met. Technol., **10** (9), pp. 363-367.

[15] Smith, N. J., Mcgrath, J. T., Bowker, J. T., and Gianetto, J. A., 1990, "Microstructure and Mechanical Property Relationships in HSLA 80 and HSLA 100 Weldments," *Proc., The Metallurgy, Welding, and Qualification of Microalloyed (HSLA) Steel Weldments*, American Welding Society (USA), pp. 306-324.

[16] Heisterkamp, F., Hulka, K., and Batte, A. D., 1990, "Heat Affected Zone Properties of Thick Section Microalloyed Steels--a Perspective," *Proc., The Metallurgy, Welding, and Qualification of Microalloyed (HSLA) Steel Weldments*, American Welding Society (USA), pp. 659-681.

[17] Mcgrath, J. T.: *Literature Review on Fracture Toughness Testing of the Heat-Affected Zone*. 1976, Energy, Mines and Resources Canada.

[18] Boyd, J. D., and Godden, M. J., 1978, "Evaluation of Heat-Affected Zone Toughness by the Cross-Weld Charpy Test," American Society for Metals, pp. 74-89.

[19] Pisarski, H. G., 1990, "HAZ Toughness Evaluation," *Proc., The Metallurgy, Welding, and Qualification of Microalloyed (HSLA) Steel Weldments*, American Welding Society, pp. 351-382.

[20] Gianetto, J. A., Tyson, W. R., and Bowker, J. T.: *Weld Metal and Heat-Affected Zone Toughness of HY 100 and HSLA 100 Weldments*. 1996, NTIS (USA): Springfield, VA. p. 46.

[21] Mitchell, P. S., Hart, P. H. M., and Morrison, W. B., 1995, "The Effect of Microalloying on HAZ Toughness," 1995, *Proc., Microalloying '95*, Iron and Steel Society Inc, Warrendale, pp. 149-162.

[22] Graville, B. A., 1980, "Heat-Affected-Zone Toughness of Microalloy Steels.--II," Can. Weld. Fabr., **71** (7), pp. 14-16.

[23] Fairchild, D. P., Bangaru, N. V., Koo, J. Y., Harrison, P. L., and Ozekcin, A., 1991, "A Study Concerning Intercritical HAZ Microstructure and Toughness in HSLA Steels," Welding Journal, **70** (12), pp. 321-s to 329-s.

[24] Krishnadev, M. R., Dionne, S., Bowker, J. T., Collins, L. E., Vasudevan, V. K., and Challenger, K. D., 1989, "Comparative Metallography of 690 MPa Grade High-Strength Steels," *Proc., Computer-Aided Microscopy and Metallography*, ASM International, pp. 281-293.

[25] Thaulow, C., Gunleiksrud, A., Paauw, A. J., and Naess, O. J., 1985, "Heat Affected Zone Toughness of a Low Carbon Microalloyed Steel," Met. Constr., **17** (2), pp. 94-99.

[26] Davis, C. L., and King, J. E., 1996, "Cleavage Initiation in the Intercritically Reheated Coarse-Grained Heat Affected Zone. Ii. Failure Criteria and Statistical Effects," Metallurgical and Materials Transactions A, **27A** (10), pp. 3019-3029.

[27] Geric, K., and Sedmak, S., 1998, "Crack Behaviour Analysis in the Heat Affected Zone of Microalloyed Steels," *Proc., ECF 12: Fracture from Defects. Volume 2*, Engineering Materials Advisory Services Ltd. (UK), pp. 865-870.

[28] Gourd, L. M., 1995, Principles of Welding Technology, Edward Arnold.

[29] Thaulow, C., Paauw, A. J., and Rorvik, G., 1987, "Fracture Mechanics Testing of Weld Metal for Low Carbon Microalloyed Steel," *Proc., Welding Metallurgy of Structural Steels*, The Metallurgical Society/AIME, pp. 277-301.

[30] Hashemi, S. H., Howard, I. C., Yates, J. R., Andrews, B., and Edwards, A. E., 2004, "Experimental Study of Thickness and Fatigue Precracking Influence on the CTOA Toughness Values of High Grade Gas Pipeline Steel," IPC04-0681, *Proc., 5th International Pipeline Conference*, ASME, Fairfield.

[31] 2003, *Standard Test Methods and Definitions for Mechanical Testing of Steel Products; A370-02*, in Annual Book of ASTM Standards, American Society for Testing and Materials, Philadelphia, pp. 142.

[32] Ranganath, V. R., Kumar, A. N., and Pandey, R. K., 1991, "Fracture Toughness Characterization of a Weldment in a Microalloyed Steel Using Resistance Curves," Materials Science and Engineering A (Switzerland), **A132**, pp. 153-160.

[33] Grosh, R. J., and Trabanat, E. A., 1956, "Arc-Welding Temperatures," Welding Journal, **35** (8), pp. 396-s to 400-s.

[34] Akselsen, O. M., Rorvik, G., and Kluken, A. O., 1994, "Prediction of Tensile Properties of Intercritical Heat Affected Zone," Mater. Sci. Technol., **10** (1), pp. 75-80.

[35] Akselsen, O. M., and Rorvik, G., 1990, "Tensile Properties of Heat Affected Zone of Medium Strength Low Carbon, C--Mn, and 2.25cr--1mo Steels," Mater. Sci. Technol., **6** (4), pp. 383-389.

[36] Karthik, V., Kasiviswanathan, K. V., Laha, K., and Raj, B., 2002, "Determination of Gradients in Mechanical Properties of 2.25cr-1 Mo Weldments Using Shear-Punch Tests," Welding Journal, **81** (12), pp. 265-s to 272-s.

[37] Bhole, S. D., and Fox, A. G., 1996, "Influence of GTA Welding Thermal Cycles on HSLA-100," Canadian Metallurgical Quarterly (Canada), **35** (2), pp. 151-158.

[38] Moon, D. W., Fonda, R. W., and Spanos, G., 2000, "Microhardness Variations in HSLA-100 Welds Fabricated with New Ultra-Low-Carbon Weld Consumables," Welding Journal, **79** (10), pp. 278-s to 285-s.

[39] Scoonover, T. M., Lukens, W. E., and Pande, C. S., 1984-1985, "Correlation of Heat Affected Zone Microstructure with Peak Heating Temperature in HSLA-80 Steel Weldments," 1986, *Proc., Unusual Techniques and New Applications of Metallography. Volume II*, American Society for Metals, pp. 91-104.

[40] Cahoon, J. B., Broughton, W. H., and Kutzak, A. R., 1971, "The Determination of Yield Strength from Hardness Measurements," Metall. Trans., **2**, pp. 1979-1983.

[41] Hosford, W. F., Caddell, R.M., 1983, Metal Forming: Mechanics and Metallurgy, Prentice-Hall, Inc.

[42] Haggag, F. M., and Phillips, L. D., 2004, "Innovative Nondestructive Method Determines Fracture Toughness of in-Service Pipelines," IPC04-0345, *Proc., 5th International Pipeline Conference*, ASME.

[43] Kuhn, L., 1998, *The Triboscope Nanomechanical Testing System*, in Hysitron Nanomechanical Test Instrument, User's Manual, Hysitron Inc, Edina, MN, pp. 1-11.

[44] Shiga, C., 1990, "Effects of Steelmaking, Alloying and Rolling Variables on the HAZ Structure and Properties in Microalloyed Plate and Linepipe," *Proc., The Metallurgy, Welding, and Qualification of Microalloyed (HSLA) Steel Weldments*, American Welding Society, pp. 327-350.

[45] Avner, S. H., 1974, Introduction to Physical Metallurgy, McGraw-Hill Book Company.

[46] Akselsen, O., Grong, O., and Solberg, J., 1987, "Structure--Property Relationships in Intercritical Heat Affected Zone of Low-Carbon Microalloyed Steels," Mater. Sci. Technol., **3** (8), pp. 649-655.

[47] Speich, G. R., and Warlimont, H., 1968, "Yield Strength and Transformation Substructure of Low-Carbon Martensite," J Iron Steel Inst, **206** (4), pp. 385-392.

[48] Krause, G. E., 1990, Properties and Selection: Irons, Steels and High Performance Alloys, ASM International, Metals Park, Ohio, pp. 127.

Chapter 8

Correlation between Mechanical Properties and Microstructure

8-1. Introduction

The main reason for performing microstructural examinations is to at least understand and ideally predict the mechanical properties of the material. This chapter tries to relate the separate studies in previous chapters, i.e., thermal analysis, microstructural analysis (precipitates, phase transformation and grain growth) and mechanical analysis, together for the BM and HAZ of Grade 100 steel. Before estimation/evaluation of mechanical properties in the BM or HAZ, the major strengthening mechanisms are reviewed. One should bear in mind that there are various models for estimation of strengthening components or their combined effects, and there is no universal agreement on them. Only those that have been elaborated in major books or papers (e.g., the works of Gladman [1] or Baker [2]) are used in this chapter. The strengthening components of the yield strength in the BM will be assessed quantitatively, and the microhardness variations across the HAZ for various weld samples will be explained mostly qualitatively.

8-2. Strengthening mechanisms

The yield strength and hardness of steel can be increased through several strengthening mechanisms. The main ones include grain refinement, solid solution strengthening, precipitation hardening and work (dislocation) hardening. All these mechanisms increase the stress required for plastic deformation (i.e., movement of dislocations) and hence increase the yield and flow strength of the material. The way these mechanisms act, the equations adopted and the assumptions made to estimate their contributions are briefly discussed in the following sections.

8-2-1. Grain refinement

Grain-size strengthening is based on the arrest of dislocation movement at the grain boundaries, followed by pile-up of dislocations at this region, which results in stress intensification at the head of the pile-up. When the stress at the head of the pile-up reaches a critical value, slip can be induced in the neighbouring grain. The stress intensification is a function of the number of dislocations at the pile-up, which in turn increases as the grain size increases. Therefore, as the grain size decreases dislocation re-activation becomes more difficult, and resistance to deformation (i.e., strength) increases [1]. The relationship between yield strength and grain size is known as the Hall-Petch relationship, due to experimental findings of Hall and Petch on steels in the early 1950's [3]:

$$\sigma_y = \sigma_0 + k_y d^{-1/2} \qquad (8\text{-}1)$$

where σ_y is the yield strength, σ_0 is the friction stress, k_y is the strengthening coefficient and d is the grain size. The friction stress is in fact the combined effects of other strengthening mechanisms and represents the "resistance to the motion of dislocations within the grain" [2]). It can be expanded in a linear manner as:

$$\sigma_0 = \sigma_i + \sigma_{ss} + \sigma_d + \sigma_p + \sigma_{sg} + \sigma_t \qquad (8\text{-}2)$$

where σ_i is the inherent friction stress (Peierls stress), σ_{ss} is the solid solution strengthening, σ_d is the dislocation strengthening (including work hardening), σ_p is the precipitation strengthening, σ_{sg} is the sub-grain strengthening and σ_t is the texture strengthening [2]. The grain size is actually the grain diameter, which cannot be directly measured. In practice, what can be measured on a planar metallographic section is the mean linear intercept (*m.l.i.*) measured by the Heyn intercept method [4]. This parameter can then be converted to grain diameter by making an assumption on the shape of the grains (e.g., spherical grains). The way *m.l.i.* is related to d is important, as it affects the magnitude of k_y, and therefore should be clearly indicated. Alternatively, to avoid confusion and for the sake of clarity, the parameter *m.l.i.* can be directly used in the context of Hall-Petch equation and the corresponding strengthening coefficient k'_y is reported:

$$\sigma_g = k_y d^{-1/2} = k'_y (m.l.i.)^{-1/2} \qquad (8\text{-}3)$$

The value of k_y was found to be 21.4 to 23.5 MPa mm$^{1/2}$ (equivalent to k'_y of 17.5 to 19.2 MPa mm$^{1/2}$). It should be noted that significantly lower k_y values are observed when fresh dislocations are introduced (e.g., by very light rolling deformations) [1]. The main question applicable here is validity of the Hall-Petch equation for very small grain sizes. This relationship, which was found at larger values of grain size, may not remain applicable to very fine grains.

8-2-2. Solid solution strengthening

The source of solid solution strengthening comes largely from elastic interaction between the strain fields of solutes with those of dislocations. Substitutional atoms, such as Mn and Si, give rise to a hydrostatic distortion in the lattice structure of iron, and therefore only interact with edge dislocations. Interstitial atoms, such as carbon and nitrogen in iron, give rise to asymmetrical distortions, which have both hydrostatic and shear components and therefore can interact with both edge and screw dislocations [1].

Experimental observations have shown that there is a linear dependency of strengthening magnitude with the composition of solutes (below their solubility limits), especially at room temperature and low solute levels. Both conditions apply to the case of microalloyed steels. This translates to

$$\Delta\sigma_{ss} = k_i.c_i \qquad (8\text{-}4)$$

where $\Delta\sigma_{ss}$ is the strength increase due to solute i, c_i is the concentration of solute i in wt% and k_i is the strengthening coefficient for solute i (Table 8-1). The total solid solution strengthening in the alloy can then be derived from:

$$\sigma_{ss} = \Sigma k_i.c_i \qquad (8\text{-}5)$$

Table 8-1. Solid solution strengthening coefficients in α-iron [1]

Solute	C (and N)*	P	Sn	Si	Cu	Mn*	Mo	Ni	Cr
k_i (MPa)	4620, 5544	678	123	83	39	31, 32	11	0	-31

* Two values found by two different investigators are reported.

8-2-3. Precipitation hardening

Precipitation can lead to a number of mechanisms that contribute to strengthening of the matrix, such as coherency strengthening, chemical hardening, precipitation (dispersion) hardening and interfacial area increase. The contribution of precipitation hardening has been estimated through two main methods in the literature [2]: a) The method of "difference" in which the combined contribution of other main mechanisms (such as grain size, solid solution and inherent friction stress) is compared with the measured yield strength and the difference is attributed to precipitation hardening. b) Evaluation of size and volume fraction of precipitates to be used in a model that directly estimates the amount of precipitation hardening. One of the models will be briefly described below.

In microalloyed steels, the main mechanism of strengthening from the precipitates is dispersion hardening that involves dislocation bowing/looping. The microalloy carbides/nitrides are so hard that particle cutting by dislocations cannot occur [1]. This, however, depends on their size too. If the precipitates are too small (i.e., smaller than ~5 nm), shearing might happen and then this model may not be valid [5]. The basic model of dislocation looping was developed by Orowan in the late 1950's, where he found an increase in the shear yield strength due to dispersion hardening:

$$\Delta\tau_y = Gb/L \qquad (8\text{-}6)$$

G is the elastic shear modulus, b is the Burgers vector of the matrix, and L is the inter-particle spacing. An important result from this equation is the understanding that the main factor in dispersion hardening is the inter-particle spacing, and the actual size of the particles would not directly matter [6]. The model was further developed by some other investigators, in particular Ashby, to include the effective inter-particle spacing of the random array of particles. The Ashby-Orowan equation gives

$$\Delta\tau_y = 0.84\,\left(\frac{1.2Gb}{2\pi L}\right)\ln\left(\frac{x}{2b}\right) \qquad (8\text{-}7)$$

where x is the average diameter of the particles in the plane of intersection. It can be shown that x relates to the actual particle diameter, X, according to

$$X = (\frac{3}{2})^{1/2} x \tag{8-8}$$

and x can be related to the precipitate volume fraction, f_V, and the number of particles per unit area, n_A (assuming area fraction is equal to volume fraction), according to

$$f_V = n_A \pi x^2 / 4 \tag{8-9}$$

Finally, n_A is related to L according to

$$L = (1/n_A)^{1/2} \tag{8-10}$$

Making the substitutions from Equations 8-8 to 8-10 into Equation 8-7 and assuming for iron [2] $G = 80{,}300$ MPa and $b = 2.5 \times 10^{-4}$ µm, the Ashby-Orowan equation for yield strength increase due to dispersion hardening (i.e., dislocation bowing around precipitates) becomes [1]:

$$\Delta\sigma_p \; (MPa) = (\frac{10.8 f_V^{1/2}}{X}) \ln(\frac{X}{6.125 \times 10^{-4}}) \tag{8-11}$$

Note that assuming lower values for G (e.g., 64 GPa [5]) will result in lower strengthening estimations. Also, remember that this model is based on interaction of dislocations with non-shearable precipitates.

8-2-4. Dislocation hardening

The increase in strength due to cold deformation is attributed to the dislocation density and dislocation arrangements (e.g., forest dislocations, cell structures or sub-grain boundaries) [1]. The forest dislocation contribution to strengthening is generally calculated from the Taylor expression as [2]:

$$\sigma_d = \alpha G b \rho^{-1/2} \tag{8-12}$$

ρ is the dislocation density and α is a proportionality constant (0.38 for polycrystalline iron when the stress is calculated in kg/mm²; other values such as 0.88, 1.06 and 1.4 have also been reported) [2]. Baker [2] calculated this component separate from the inherent friction stress and found that it made a considerable contribution (20-50% of the yield strength, depending on the dislocation density). He then found that the linear summation of all components overestimates the yield strength significantly, and the root mean square summation (Equation 8-13) would be in better agreement with the measured strength.

$$\sigma_y = \sqrt{\sigma_c^2 + \sigma_d^2} \tag{8-13}$$

σ_c is the linear summation of the other strengthening mechanisms. On the other hand, Gladman [1] does not include dislocation hardening in hot-rolled or normalized microalloyed steels. He only considers it for steels deformed below ~700°C. It seems he assumed that some dislocation strengthening is accounted for in the inherent friction stress. Extra cold deformation will increase the dislocation density, and that should be separately calculated. Cold deformation is not commonly used in Nb bearing microalloyed steels and, therefore, it is expected that this mechanism does not play a considerable role in Grade 100, considering that rolling is performed in austenite and not in the inter-critical region. Even if some rolling continues in the inter-critical region, the work hardening will cause further strengthening in the hot strip only [7]. The subsequent deformations such as coiling, uncoiling and levelling may remove most of the work hardening due to the Bauschinger effect. Therefore, the final product is expected to have little or no retained cold work. The other element that causes an increase in the dislocation density is the nature of the decomposition of austenite. The amount of dislocations in the final matrix increases as the shear component of transformation increases (i.e., as the transformation temperature drops). This is partly the reason for the higher matrix strength in bainite and especially martensite than in polygonal ferrite or pearlite.

8-2-5. Other mechanisms

Texture hardening is not a significant mechanism in microalloyed steels with dispersed second phases [1]. The effect of texture can be related to the difference in the tensile strength of the material obtained along the RD and transverse to the RD. Estimation of sub-grain hardening has been the subject of debate. According to Baker [2], when both grains and sub-grains are present in microstructure, σ_{sg} is expressed as:

$$\sigma_{sg} = C k_{sg} \, l^{-1/2} \tag{8-14}$$

C is the fraction of grains containing sub-grains, k_{sg} is the sub-grain strengthening coefficient and l is sub-grain size. As a simplifying assumption, this term can be neglected, if the cell or sub-grain boundaries (lath boundaries in the case of bainitic ferrite) are included during grain size measurements. However, note that some other researchers have considered an exponent of –1 instead of –1/2 for *l* in the above equation [2], in which case this simplification is not valid.

8-2-6. Combined strengthening effects

The expanded Hall-Petch relationship (assuming linear summation) for as-rolled microalloyed steels can be written as:

$$\sigma_y = \sigma_i + \sum k_i . c_i + k_y d^{-1/2} + (\frac{10.8 f^{1/2}}{X}) \ln(\frac{X}{6.125 \times 10^{-4}}) \qquad (8\text{-}15)$$

Note that other strengthening mechanisms, such as texture and excess dislocation hardening due to transformation, are considered to be small. There is a question if the assumption of linear additivity is valid for microalloyed steels. It was found that, in ultra-high strength steels, additivity of each mechanism in the way expressed in Equation 8-15 is not valid and it overestimates the strength [1].

8-3. Correlation between yield strength and microstructure of BM

The amount of each strengthening contribution in Grade 100 will be estimated in this section according to the equations reviewed in Section 8-2, and the combined effects will be compared with the measured yield strength.

8-3-1. Grain size strengthening

The value of k'_y used here was averaged between the reported values of 17.5 to 19.2 MPa mm$^{1/2}$, i.e., 18.1 MPa. A m.l.i of 1.2 µm (Table 6-2) will then result in a strengthening contribution of 523 MPa according to Equation 8-3. Alternatively, the lower value of 17.5 MPa could be used, as lower k_y (and k'_y) values are observed when fresh dislocations are introduced [1]. Grade 100 plates are lightly rolled or levelled at ~450°C. This would result in a strengthening contribution of 505 MPa. Nevertheless, the first approach was used here.

8-3-2. Solid solution strengthening

There were two groups of elements: a) those for which the amount of dissolution in the matrix was estimated (i.e., C, N and Mo), and b) those for which the amount of dissolution in matrix was unknown (i.e., the rest of the elements). For group b, half of the total amount of that element in the steel was assumed to be in solution with the matrix, as a very rough estimate. Table 8-2 shows the amount of solutes used in Equation 8-4 and the resultant strengthening contribution of each element. The total solid solution strengthening estimated for Grade 100 was ~91 MPa.

Table 8-2. Solid solution strengthening contribution of each element in Grade 100

Solute	C	N	P	Si	Cu	Mn	Mo	Ni	Cr
wt% in solution	0.008	0	0.0065	0.12	0.21	0.9	0.246	0.13	0.1
k_i, MPa	5082	5082	678	83	39	31.5	11	0	-31
$\Delta\sigma_i$, MPa	40.7	0.0	4.4	10.0	8.2	28.4	2.7	0.0	-3.1

8-3-3. Precipitation hardening

A microalloy carbide precipitate distribution with an average diameter of 5 nm (Table 4-9) and a volume fraction of 10^{-3} (Section 4-3-2) will result in a strengthening contribution of ~143 MPa in Grade 100 according to Equation 8-11. The precipitates were assumed to be hard so that shearing by dislocations does not happen.

8-3-4. Texture hardening

The difference in the tensile strength of Grade 100 obtained along the RD and transverse to the RD amounts to ~12.1 MPa (Table 2-2). This can be assumed to represent the value of texture hardening. The low value of plastic anisotropy may suggest the presence of excess interstitials. It was observed that if all interstitials are tied up with Nb and Ti in microalloyed steels, plastic anisotropy increases due to an increase in preferred (111) orientation in the rolled plate (Hudd, 1987, as cited by Gladman [1]).

8-3-5. Combined strengthening effects in Grade 100

Table 8-3 summarizes the estimation of the individual strengthening mechanisms. The table also shows the combined strengthening effects, estimated based on Equation 8-15. An average value of $\sigma_i = 60$ MPa was assumed here. The total strength is then ~817 MPa which is ~4% higher than the measured longitudinal yield strength of 788 ± 33 MPa (Table 2-2). The measured transverse yield strength was higher (~800 MPa), likely due to texture strengthening, which could not be analysed here. The 4% overestimation is really marginal, especially considering all the simplifying assumptions used in this analysis, such as those in the estimation of the parameters (e.g., precipitate size and volume fraction), theoretical equations (e.g., validity of Hall-Petch equation for low-angle grain boundaries and very small grain sizes) and the additivity rule in the estimation of the combined strengthening effects (linear summation).

Table 8-3. Estimated values for the strengthening contribution of different mechanisms

Strengthening mechanism	Values of the parameters used in calculations	Strengthening contribution (MPa)	Percentage of measured yield strength (%)
Constant	σ_i = 50–70 MPa	60	8
Solid solution	C=0.008, N=0, Mo=0.246, (Mn,Cu,Si,P,Ni,Cr)=half of total amount in steel	91	12
Grain size	*m.l.i*=1.2 μm; k'_y=18.1 MPa	523	66
Precipitates	X=5 nm; f=10^{-3}	143	18
Total	As compared to longitudinal yield stress (~788 MPa)	817	104

The highest contribution was found to be from grain refinement (~66%) due to the small lath/grain sizes in bainitic ferrite of the BM. Precipitate hardening only had a contribution of ~18%. Other mechanisms had even lower contributions. The estimated strengthening contribution of precipitates in HSMA steels has produced variable yield strength percentages in the literature, mainly because of all the difficulties in estimating the precipitate volume fraction and to a lesser degree the exact theoretical equation used to assess the strengthening contribution. Overall, it is agreed that the main role of precipitates in the strengthening of microalloyed steel is through their role in grain refinement and to a lesser degree through precipitation hardening [8]. For instance, the contribution of precipitation hardening from Nb carbonitrides in a Nb-bearing microalloyed steel was suggested to be only 6% compared with a 47% contribution from grain size (Morrison and Chapman, 1975, as cited in [8]). VC on the other hand is expected to have more precipitation hardening contribution in certain steels [8], likely due to the finer distribution that is a result of interphase and general precipitation in ferrite. Only half of the total V in Grade 100 was estimated to have precipitated (Table 5-3), likely due to a drop in the driving force for precipitation due to profuse precipitation of other microalloy elements.

8-4. Correlation between hardness and microstructure in the HAZ

Correlation between the microstructure and hardness has been the target of several papers on HSLA or HSMA steels, either qualitatively (e.g., [9, 10]) or quantitatively (e.g., [11-13]. Knowledge of hardness is essential for assessment of cold cracking and hydrogen embrittlement susceptibility. Since the quantitative analyses are complicated, require quantitative determination of many parameters (e.g., the amount of martensitic constituent in the microstructure in some cases), and have not been totally successful, correlation of hardness with microstructure has been carried out mostly qualitatively here.

Hardness measurements across the HAZ (Fig. 6-3) showed variations in each sub-zone for several values of heat input (0.5, 0.7, 1.0, 1.5 and 2.5 kJ/mm). This behaviour will be discussed for each sub-zone and explained in terms of microstructural changes. The microstructures examined for heat inputs of 0.5, 1.5

and 2.5 kJ/mm showed markedly different variations for a heat input of 0.5 kJ/mm from the other two heat inputs. For this reason, the microstructure-property correlation will be explained in more detail for the two extreme heat inputs (i.e., 0.5 and 2.5 kJ/mm). Figure 8-1 shows *HAZ profiles* for these two weld samples. The graphs combine hardness, peak temperature, grain size and precipitate dissolution variations across the HAZ.

8-4-1. ICHAZ

The ICHAZ (several heat inputs) essentially showed slight changes as compared with the BM and the hardness levels were between that of the BM and the FGHAZ, as expected for this sub-zone. Longitudinal mapping (as explained in Section 7-5-2) provided a very detailed and reliable account of hardness variation for the 0.5kJ/mm weld sample, as each point on the hardness profile (Fig. 7-5 with error bars and Fig. 8-1 without) represented an average over 3–4 measurements, and the points were very close (high spatial resolution). For this reason, the variations in the average hardness will be assumed to be a true representation of property changes across the HAZ for this sample. The average hardness increased linearly from ~278 to 293 HV0.5 from the side adjacent to the BM towards the FGHAZ (i.e., hardening similar to FGHAZ). This can be attributed to the linear increase in the fraction of retransformed grains in ICHAZ. The retransformed grains will have a characteristically higher hardness than the untransformed grains due to the increase in level of solutes (dissolution of Mo, V and Fe carbides upon austenitization) and the relatively high cooling rate (~100–200°Cs^{-1} as compared with the accelerated cooling rate of 15–20°Cs^{-1} during the TMCP of Grade 100 steel). These two factors result in finer ferrite grain sizes and slightly higher solute solution and dislocation strengthening. There is likely to be some bainitic transformation in this zone, but the chance for formation of martensite is slim, as the combination of PAGS, cooling rate and solute levels do not favour martensite formation.

The hardness profile showed a trough (sudden softening to ~280±3 HV0.5) over the boundary between ICHAZ and FGHAZ for the 0.5 kJ/mm weld sample. Considering the fact that there were two points at this hardness each averaged over four measurements and the standard deviation was considerably low, it is quite likely that this is a real phenomenon and not a result of scatter. However, the reason for such a drop in hardness is not known at this stage.

8-4-2. FGHAZ

In the FGHAZ, three types of behaviour were observed:

1) Hardening for a heat input of 0.5 kJ/mm (and conceivably below that).
2) A mix of softening and hardening for a heat input of 0.7 kJ/mm.
3) Softening for a heat input of 1.0 kJ/mm and higher.

In the 0.5 kJ/mm weld sample the average hardness increased almost linearly from ~291 to 307 HV0.5 towards the CGHAZ. As observed in the previous chapters, this was due to increased dissolution of carbides of V, Mo and Fe that enriched the austenite in solute levels, in particular carbon (Fig. 5-16). As the amount of C increases toward the CGHAZ, the hardenability increases. The relatively high cooling rate in this sample makes the transformation sensitive to the carbon level. The combined effect of increased hardenability and high cooling rate, promotes the formation of bainite (Fig. 5-37). Bainitic ferrite has a higher hardness than polygonal ferrite (the dominant microstructure in the FGHAZ) due to higher solute levels in solution, higher density of transformation dislocations and smaller grain sizes (low-angle grain boundaries). The amount of bainitic ferrite is almost linearly proportional to the peak temperature (~800°C<T_P<1130°C), which increases toward the CGHAZ. The formation of martensite in this zone is unlikely, as the combination of PAGS and cooling rate does favour martensite formation. The prior austenite grains were pinned with the fine and intermediate-size carbides and carbonitrides, which withstood the thermal cycle experienced in the FGHAZ.

The hardness variation in the 0.7 kJ/mm weld sample showed an initial softening to a hardness of ~270 HV0.5 from the boundary with the ICHAZ to the mid-FGHAZ and a hardening to ~300 HV0.5 from the mid-FGHAZ towards the CGHAZ. This suggests that the FGHAZ in this sample is actually comprised of two sub-zones, an inner FGHAZ and an outer FGHAZ. This sample was not selected for thermal/microstructural examination. Nevertheless, it can be speculated that softening is due to the combination of a not-so-high cooling rate (lower than that of 0.5 kJ/mm weld sample), small PAGS and the low solute level in the retransformed austenite. Although the accelerated cooling during the TMCP is not very high, the pancake shape of the large austenite grains and the higher level of solutes result in a lower overall transformation temperature and therefore a higher hardness than that of low FGHAZ. Further dissolution of carbides of V, Mo and Fe in the high FGHAZ will increase the number of solutes and hardenability beyond a critical point (for the cooling rate and PAGS in this sample), and results in a higher hardness level.

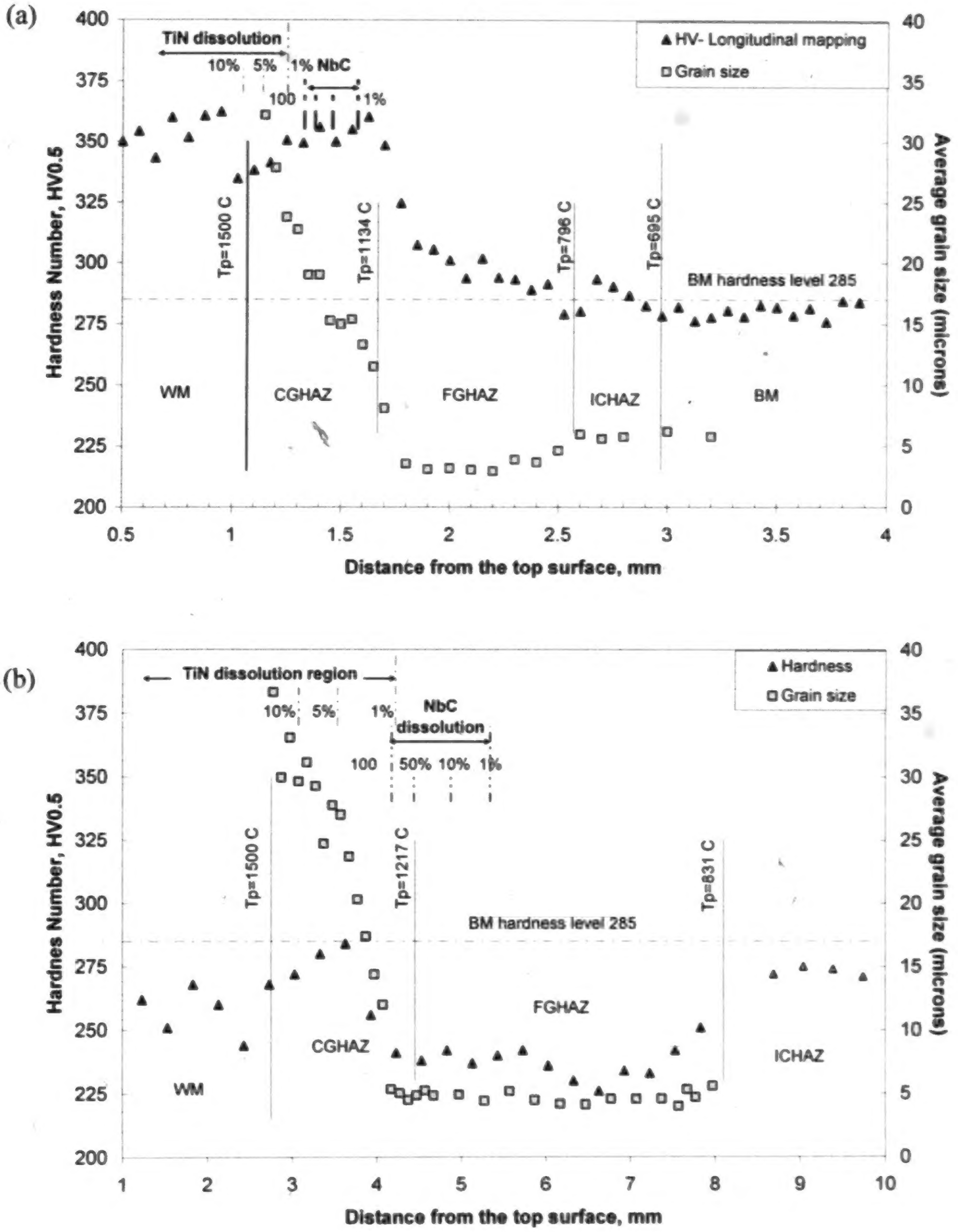

FIG. 8-1. HAZ profiles showing variations of grain size, hardness, peak temperature and precipitate dissolution (NbC and TiN) across the HAZ of Grade 100 for two heat inputs: a) 0.5 kJ/mm and b) 2.5 kJ/mm.

At higher heat inputs (1.0 kJ/mm and above), the transformation in FGHAZ is likely insensitive to the carbon level (in the range it was changed) due to the relatively low cooling rates. There was a hardness plateau in the FGHAZ for these samples. The microstructure was made up of polygonal ferrite with an average grain size of ~1.5 µm across the entire FGHAZ for the 1.5 and 2.5 kJ/mm weld samples (~800°C<T_P<1200°C).

The grain sizes obtained from replicas in FGHAZ and BM (Table 5-2) were used for correlation studies with hardness. Figure 8-2 shows the variation in hardness as a function of the inverse of the square root of the grain size (mean linear intercept length) for the FGHAZ of the Grade 100 subjected to several heat inputs as well as the BM of several grades of HSMA steels. The linear behaviour of the plot suggests a Hall-Petch type of relationship, which implies that any change in hardness in these materials, and for the FGHAZ, is mainly a grain size effect. In other words, other factors such as forest dislocation hardening, precipitation hardening and solute strengthening are more or less comparable for the different steel grades and heat inputs, or they cancel each other out. Note that others [14] have also found that hardness follows the same type of relation between microstructural parameters as strength does (i.e., a Hall-Petch type of relationship).

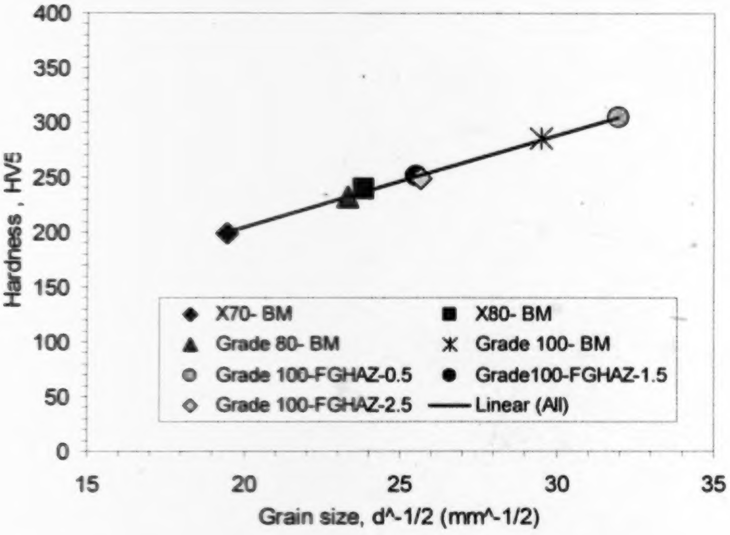

FIG. 8-2. Relationship between Vickers hardness and apparent grain size (mean linear intercept) for the BM of several grades of steel and for the FGHAZ of Grade 100 steel at several heat inputs.

The theoretical analysis of Section 5-4-1 showed that NbC precipitates do not get dissolved during the fast thermal cycles and not-so-high peak temperatures experienced in the FGHAZ. Replicas examinations in Section 5-6-5 also confirmed that the size-distribution of the fine precipitates does not change in the FGHAZ relative to the BM. It is also possible that the amount of the fine precipitates in the BM of the several grades of HSMA steels examined here are almost the same. The difference in the amount of carbon and microalloy elements in the steels cause a difference in the amount of large and intermediate-size precipitates that form prior and during solidification, reheating and rough rolling. The amount and size distribution of fine precipitates that form during finish rolling in austenite (strain-induced precipitation) or after transformation in ferrite (general precipitation) will not depend much on the initial levels of solutes in the steel, and is mainly a function of TMCP variables (time, temperature, deformation) at the last stages of processing. Moreover, the analysis in Section 8-3 showed that the dispersion strengthening contribution accounted for ~18% of the total strength, as compared with ~66% contribution from grain refinement. Other mechanisms had even less contribution. It is obvious that slight changes in the other mechanisms affect the strength much less than the changes in the grain size do. It is also conceivable that a small change in some of these mechanisms (e.g., precipitation and solid solution) cancel each other out.

8-4-3. CGHAZ

All the hardness traverses (Fig. 6-4) showed hardening in CGHAZ relative to the FGHAZ. They showed a sudden increase starting from the boundary between the FGHAZ and CGHAZ and reached a peak somewhere in the CGHAZ and then decreased slightly towards the fusion line. The onset of the increase in hardness coincided with the onset of an increase in grain size for all samples (optical observation and Fig. 8-1). These alterations can be better tracked and explained for the 0.5 kJ/mm weld sample, where longitudinal mapping provided a detailed account of hardness variation across the CGHAZ (Fig. 7.5). The hardenability increases with PAGS (Fig. 8-1a), resulting in a higher average microhardness. Microhardness reaches a maximum of ~360HV0.5 at a PAGS of ~13 μm and T_P of ~1170°C. At this point all carbides of Mo, V and Fe should be dissolved (NbC dissolution starts just above this temperature). This makes the matrix sufficiently rich in C (0.064%; Fig. 5-16) to promote the formation of martensite for such a cooling rate (100–200°Cs^{-1}). As the peak temperature increases beyond this point, the microhardness starts to decline gradually but steadily towards the fusion line, where it reaches an average microhardness of ~340HV0.5. This occurs while PAGS keeps rising towards the fusion line where it reaches a maximum of ~32 μm on average. The carbon level in austenite increases to a maximum level of 0.08% at a T_P = 1320°C, and remains constant afterwards. The increase in PAGS beyond a critical value (~13 μm here) results in a decrease of hardness, likely due to the hardness dependence of martensite on morphological parameters such as lath size, packet size and PAGS. In the context of the Hall-Petch equation, strength and hardness decrease as the grain size increases.

The same general scenario should apply to CGHAZ of other weld samples with different lamellar microstructures such as bainite (Fig. 8-1b). The maximum hardness, however, decreases as the heat input increases (Fig. 7-9), due to the increase in transformation temperature as a result of a decrease in heat input. Replacement of lath martensite with lower bainite, upper bainite and Widmanstatten ferrite is accompanied with a drop in hardness and strength as: a) the carbon saturation decreases, b) the dislocation density decreases and c) the lath/packet size increases. Nevertheless, the lath sizes in the bainitic ferrite of the 1.5 and 2.5 kJ/mm CGHAZ are small enough (~1 μm in width and several microns in length) to provide hardness levels almost comparable to the BM, even though the packet sizes and the PAGS in this region are very large (several tens of microns reaching a maximum mean intercept length of ~37 μm close to the fusion line for the 2.5 kJ/mm weld sample).

The nano-hardness contours in the CGHAZ-0.5 kJ/mm (Fig. 7-6) can now be understood better. Microstructural examination of this sub-zone (Section 6-5-2-3) showed two main constituents: a) fine untempered lath martensite, and b) coarse autotempered martensite or aged massive ferrite. The width and hardness of the band of hard region in Fig. 7-6c correlates well with the former constituent, while the relatively soft regions correlate well with the latter constituent (whether coarse martensite or massive ferrite). This is due to the low hardenability and high M_S temperature of Grade 100 microalloyed steel.

Microhardness measurements, which create much larger indentations, average the hardness over these regions and result in numbers expected for the carbon level in the steel. Still two questions remain: a) what the maximum hardness achievable in the CGHAZ of the Grade 100 steel is, and b) whether or not the maximum hardness is reached in CGHAZ-0.5 kJ/mm. Fig. 6-7 shows the martensite hardness dependence on carbon level in iron-carbon steels. It shows a hardness of ~340 HV for 0.08%C (assuming all C is dissolved but N is still tied up with Ti). If we assume only 0.064%C is in solution (i.e., where a maximum hardness was observed in CGHAZ-0.5 kJ/mm), the martensite hardness for an iron-carbon steel is expected to be ~325 HV. The martensitic structure in CGHAZ, however, showed higher hardness. The difference can be attributed to the difference in composition (effect of substitutional atoms on hardness, although this is considered to be minor [15], but a subject of debate [16]), the presence of inclusions and nitrides in austenite of the Grade 100 steel that may cause lath refinement (see below) and residual stresses in the HAZ.

The CGHAZ essentially showed (Fig. 6-9) a linearly inverse dependence of maximum microhardness on heat input (0.3–2.5 kJ/mm). This was attributed to the formation of very hard constituents in the microstructure as a result of an increase in cooling rate. The average microhardness along the traverses (load of 0.5 kg) was higher for a heat input of 0.3 kJ/mm than for a heat input of 0.4 or 0.5 kJ/mm (Table 7-3). The macro-hardness, however, approached asymptotically a maximum of ~360HV as the heat input decreased to 0.3 kJ/mm. Although at the first glance, it seems reasonable that the hardness reaches a maximum that depends on the interstitial level only and not on the cooling rate above a certain critical limit (classic view), the fact that the averages of the microhardness measurements were so different for the two samples (364±7 for 0.3 kJ/mm and 350±7 for 0.4 and 0.5 kJ/mm) does not support this view. It is possible that the width of the hard zone in CGHAZ becomes too small for a reliable macro-hardness measurement, so that the hardness measurements are lower than they should be as the hard zone is sandwiched between softer zones. Moreover, the cooling rate in the 0.5 kJ/mm sample is about 100–200°Cs^{-1}, while quenching in brine provides cooling rates of the magnitude 10^{4}°Cs^{-1}. Therefore, it can be concluded that not only higher hardness values than that predicted by carbon level can be reached, but also the hardness in the CGHAZ-0.5 kJ/mm is not the maximum that could be achieved for this steel.

8-5. Martensite strength

Classically, the hardness and strength of as-quenched martensite is assumed to be solely a function of the interstitial level (mainly carbon, but in fact carbon and nitrogen) and not the microstructure [15, 17]. There is a microstructure referred to as "fully martensitic" which is formed by an appropriate solution treatment (complete austenitization and carbide dissolution) followed by quenching in an appropriate medium (the critical cooling rate depending on the composition for a given sample with a given thickness). Nevertheless, some investigations suggest that the mechanical properties of martensite are affected by microstructural factors too [16, 18]. For this reason, it may be appropriate to consider all strengthening mechanisms as follows:

1) Solid solution hardening: this shows the effect of immobile carbon atoms [15]. Likely not a major mechanism in low-carbon steels.
2) Rearrangement of C atoms: This becomes a major factor in intermediate and high-carbon steels [15]. The distortion of the lattice in low-carbon steels is not large and therefore this is not a major strengthening factor for Grade 100 steel either.
3) Grain refinement: Any factor that affects the grain size, such as heat treatment and the presence of inclusions/nitrides/carbides, can affect the mechanical properties of martensite [18]. Grain size translates to lath width, packet size and PAGS, in the case of martensite. Padmanabhan and Wood [18] found that precipitates that can withstand the peak temperature of austenitization could provide additional sites for nucleation of martensite, which in turn results in smaller lath width.
4) Sub-structure hardening: According to Padmanabhan and Wood [18] dislocations or twins contribute to the strength equally. Since a decrease in one (e.g., twins) would result in an increase of the other (e.g., dislocations), their contribution could be assumed to be a constant. This also becomes a considerable strengthening factor in low-carbon martensite where the overall hardness and strength is not that high.
5) Dispersion hardening: Precipitation is normally suppressed in martensitic transformations. However, precipitates can be present in the final microstructure from two sources: a) those that survived the heating cycle and b) those that form as a result of subsequent heat treatment. The first group is usually not very fine, and therefore, may not have considerable contribution to the strength. The second group may have an overall positive or negative contribution, depending on their size distribution. This is because precipitation is accompanied by a decrease in solute content (which can be a major strengthening mechanism in martensite), and the direct contribution of dispersion is normally small (see the estimation of dispersion hardening in martensite by Padmanabhan and Wood [18]).
6) Work hardening: work hardening during the tensile, compression or hardness test also depends on the carbon level [15]. This is not expected to be a major strengthening effect in martensite.

Considering the above factors, it can be concluded that grain size (PAGS, packet size and especially lath width) is likely a major factor that can affect the strength and hardness in a martensitic structure, in particular when the carbon level is low (where substantial numbers of C atoms are accommodated by an abundance of dislocations). Whether the lath width follows a Hall-Petch relationship with strength or other relationships apply (e.g., the Langford-Cohen relationship $\sigma_y = \sigma_0 + Kd^{-1}$ [18]), and whether packet size and PAGS should be also accounted for, are not well established and need investigation. This, when understood, can quantitatively explain the variation of microhardness across the CGHAZ of a low-carbon steel (such as Grade 100 steel).

8-6. Summary

The following conclusions summarize the analyses of this chapter:

1) Rough estimation of the BM yield strength in Grade 100, based on linear summation of several strengthening mechanisms (i.e., grain refinement, solid solution hardening and dispersion hardening), was in good agreement with the tensile test results. The calculations overestimated the yield strength by ~4%.
2) Grain refinement (including the lath boundaries) had the highest contribution to the yield strength (~66%). That was followed by dispersion hardening from fine carbide precipitates (~18%) and solid solution hardening (~12%).
3) These results support the opinion that the main role of precipitates in the microalloyed steel is grain refinement and to a lesser degree precipitation hardening.
4) The hardness variation in the ICHAZ, with values between the BM hardness and the FGHAZ hardness, can be attributed mainly to partial re-transformation in this sub-zone, where the amount increases from the boundary with the BM towards the boundary with the FGHAZ. Generally, this region is not of concern in such a low-carbon microalloyed steel that is pearlite-free.
5) The hardness variation in the FGHAZ (softening, hardening or a mix of both) was mainly attributed to the change in the grain size of mainly polygonal ferrite. The correlation between the grain size and hardness suggested a Hall-Petch type of relationship. Ferrite grain size variation was mainly due to the differences in the cooling rate. An increase in the PAGS was suppressed by fine precipitates. The state of precipitates (in particular Nb and Ti carbides and nitrides) did not change considerably in this sub-zone and for the range of heat inputs examined here. Formation of bainitic ferrite in the FGHAZ-0.5 kJ/mm, due to a combination of Mo/V/Fe carbide dissolution and high cooling rate (100-200°Cs^{-1}), contributed to the hardening in the FGHAZ in this sample towards the boundary with the CGHAZ. At higher heat inputs (e.g., 1.5 and 2.5 kJ/mm), low values of cooling rate promoted formation of mainly polygonal ferrite with a plateau of grain size across the FGHAZ that was not sensitive to the slight differences in carbide dissolution amounts or cooling rates, and therefore resulted in low values of hardness that remained constant across the FGHAZ and among the different weld samples.
6) The hardening in the CGHAZ relative to the FGHAZ, regardless of heat input, is due to the formation of lamellar structures of martensite and bainite in the CGHAZ as opposed to polygonal ferrite (and some bainite) in the FGHAZ. The higher hardenability in this sub-zone was a result of the large PAGS and to a lesser degree dissolution of carbides, both due to higher peak temperatures. The hardness in CGHAZ can be related to a combination of small lath size, relatively high dislocation density and increased solid solution. Dispersion hardening plays only a minor role, as the reprecipitated fine carbides are either suppressed (0.5 kJ/mm) or coarsened and preferentially located at grain boundaries (1.5 and 2.5 kJ/mm).
7) The gradual decrease of hardness towards the fusion line beyond a hardness peak point in CGHAZ is likely due to an increase in lath size and packet size as the PAGS increases.
8) Comparison of average hardness over traverses across the CGHAZ in low heat-input weld samples with the classical martensite hardness shows that higher hardness than that predicted by the carbon level can be observed in the HAZ. Whether this suggests that martensite hardness depends on microstructure (e.g., lath size), which is in contrast to the classical view, or is because of compressive residual stresses in the CGHAZ is not clear at this stage. It is also possible that both reasons apply.
9) Both the nano-hardness contours and microstructural observations suggest that the microstructure in CGHAZ-0.5 kJ/mm was not 100% martensite. This could be due the fact that the cooling rate was only ~10^2°Cs^{-1} and the carbon level in Grade 100 steel is low.

References

[1] Gladman, T., 1997, The Physical Metallurgy of Microalloyed Steels, The Institute of Materials, London.

[2] Baker, T. N., 1982, "Determination of the Friction Stress from Microstructural Measurements," *Proc., Yield, Flow and Fracture of Polycrystals*, Applied Science Publishers, 1983, pp. 235-273.

[3] Petch, N. J., 1953, "The Cleavage Strength of Polycrystals," Journal of the Iron and Steel Institute, **174**, pp. 25-28.

[4] 2000, *Standard Test Methods for Determining Average Grain Size; E112*, in Annual Book of ASTM Standards, American Society for Testing and Materials, Philadelphia, pp. 245.

[5] Charleux, M., Poole, W. J., Militzer, M., and Deschamps, A., 2001, "Precipitation Behavior and Its Effect on Strengthening of an HSLA-Nb/Ti Steel," Metallurgical and Materials Transactions A, **32A** (7), pp. 1635-1647.

[6] Lagneborg, R., Siwecki, T., Zajac, S., and Hutchinson, B., 1999, "The Role of Vanadium in Microalloyed Steels," Scandinavian Journal of Metallurgy (Denmark), **28** (5), pp. 186-241.

[7] Dutta, B., and Sellars, C. M., 1987, "Effect of Composition and Process Variables on Nb(C,N) Precipitation in Niobium Microalloyed Austenite," Materials Science and Technology, **3** (3), pp. 197-206.

[8] Easterling, K. E., 1992, Introduction to the Physical Metallurgy of Welding, Butterworth-Heinemann Ltd, Oxford.

[9] Lin, X., and Dunne, D. P., 1990, "Microstructural and Hardness Changes in the Weld HAZ of a Copper Bearing HSLA Steel after Intercritical and Subcritical Postweld Heat Treatment," *Proc., Materials United in the Service of Man. Vol. 2*, Institute of Metals and Materials Australasia, Ltd., p. 10.

[10] Moon, D. W., Fonda, R. W., and Spanos, G., 2000, "Microhardness Variations in HSLA-100 Welds Fabricated with New Ultra-Low-Carbon Weld Consumables," Welding Journal, **79** (10), pp. 278-s to 285-s.

[11] Duren, C. F., 1990, "Prediction of the Hardness in the HAZ of HSLA Steels by Means of the Carbon-Equivalent," *Proc., Hardenability of Steels--Select Conference*, The Welding Institute, pp. 51-62.

[12] Kasuya, T., and Hashiba, Y., 1999, "Prediction of Hardness Distribution in Steel Heat Affected Zone," Science and Technology of Welding and Joining (UK), **4** (5), pp. 265-275.

[13] Bang, K.-S., and Kim, W.-Y., 2002, "Estimation and Prediction of HAZ Softening in Thermomechanically Controlled-Rolled and Accelerated-Cooled Steel," Welding Journal, **81** (8), pp. 174-s to 179-s.

[14] Otterberg, R., Sandstrom, R., and Sandberg, A., 1980, "Influence of Widmanstatten Ferrite on Mechanical Properties of Microalloyed Steels," Met. Technol., **7** (10), pp. 397-408.

[15] Leslie, W. C., 1981, The Physical Metallurgy of Steels, Hemisphere Publishing Corp , McGraw-Hill Book Co, New York.

[16] Speich, G. R., and Warlimont, H., 1968, "Yield Strength and Transformation Substructure of Low-Carbon Martensite," J Iron Steel Inst, **206** (4), pp. 385-392.

[17] Callister, W. D., Jr., 2000, Materials Science and Engineering: An Introduction, John Wiley & Sons, Inc.

[18] Padmanabhan, R., and Wood, W. E., 1984, "Microstructural Analysis of a Multistage Heat-Treated Ultra-High-Strength Low-Alloy Steel," Mater. Sci. Eng., **66** (2), pp. 125-143.

Chapter 9

Concluding Remarks

9-1. Introduction

The specific discussion and conclusions for each subject in this study were included in each chapter. This final chapter is devoted to the general discussion and conclusions that provide a general picture of the outcome of this research. Some specific achievements that were novel and/or outside the main focus of the study, as well as the suggestions for future work, will also be included.

9-2. General discussion and conclusions

9-2-1. Overview of the research

The main focus of this study was examination of microstructure and hardness variation in the HAZ of a Grade 100 microalloyed steel. The Grade 100 steel studied here has 0.08%C and a total of ~0.20% microalloy elements (Ti, Nb and V). The HAZ was produced by single-pass autogenous GTAW in the laboratory on a Grade 100 plate with a thickness of 8 mm. The welding parameter that changed was the travel speed that induced a variation in heat input (0.5–2.5 kJ/mm). The thermal cycles were recorded by thermocouples embedded in the plate and were analysed.

The fast and intense thermal cycles, experienced by the plate during welding, caused considerable changes in the HAZ microstructure and mechanical properties (indicated by hardness). OM and in particular TEM were engaged for examination of microstructure. The microstructural changes were analyzed theoretically and/or characterized experimentally in terms of precipitates (type, size distribution, volume fraction, dissolution, coarsening and reprecipitation) and iron-matrix grains (size, structure and substructure). The hardness variations (nano-, micro- and macro-hardness) were explained in terms of microstructural and composition changes in the HAZ.

9-2-2. General discussion

The experience from this research confirms that high-resolution microscopy, especially analytical TEM, is vital for examination of microalloy precipitates and the low temperature transformation products. TEM was also found to be useful for resolving the grain boundaries of fine grains in the BM and the HAZ.

Assessment of toughness is not easy in the HAZ due to its narrow width. However, traverse hardness measurements gave a hint of property variation across the HAZ. HAZ simulation to provide larger specimens for the thermal cycle of interest (distance from fusion line) for CTOD or even Charpy tests is also an alternative. However, simulations cannot exactly demonstrate the real weld situation. Miniature tests are also another alternative.

The ideal characteristics of the HAZ from hardness and microstructure points of view are:

1) The smallest amount of variation in hardness (or the smallest amount of strength mismatch) with respect to the BM and WM.
2) Not too high a hardness value (reduces susceptibility to HAC) and not too low a hardness value (reduces strain accumulation damage).
3) A gradual variation in hardness as opposed to a severe gradient.
4) Minimal amount of transformation twins.
5) Minimal amounts of coarse upper bainite, followed by granular bainite and lower bainite in the CGHAZ.
6) Smallest PAGS possible.
7) Minimal amount of large and intermediate size precipitates (i.e., TiN and Ti/Nb carbonitrides). Fine precipitates (<50 nm in size) are desirable.

In grain growth control, through precipitate pinning effects, it is not only the stability of the precipitates (dissolution temperature) that is important. An almost equally important characteristic is the distribution of the particles (volume fraction and particle size). The retardation of grain growth observed in the HAZ of the Grade 100 steel (the grain size plateau in the FGHAZ) is likely due to the presence of a relatively large volume fraction (~10^{-3}) of fine precipitates (<20 nm) of Nb-Mo carbides. The presence of intermediate size Ti-rich and Nb-rich carbonitrides has a limited effect on the degree of coarsening in the CGHAZ, along with the solute drag and grain-size gradient effects. In fact, it would be ideal to have TiN in a distribution similar to that of fine Nb-Mo carbides, in which case the FGHAZ would be virtually extended to the fusion line (elimination of CGHAZ). This, however, has not been practical to achieve yet.

9-2-3. Property assessment of the HAZ and the effect of heat input

Although the toughness or fracture properties of the HAZ or BM were not tested in this study, some general conclusions can be drawn based on the hardness/microstructure characteristics of different sub-zones and for different weld samples (heat input) and the published results in the literature. The ICHAZ in Grade 100 microalloyed steel should not be of a concern in general, as limited microstructural changes occur and the PAGS (of the transformed grains) is small in this region. This is true even for the lowest heat input examined here (0.5 kJ/mm), where the cooling rate is relatively high. Although the cooling rate remains almost constant (as expected from theoretical analysis) across the FGHAZ and CGHAZ for a given weld sample (constant heat input and plate thickness), the mean cooling rate between 800 (or the peak temperature, whichever is lower) and 500°C is lower in the ICHAZ. This is because the peak temperature in ICHAZ lies between, or close to, 800 and 500°C and the thermal behaviour around T_P, which is a transition from the heating cycle to the cooling cycle, will slow down the cooling. More importantly, as Grade 100 steel is virtually pearlite-free, no austenite with the eutectoid composition (~0.8%C) will form during the partial transformation of ferrite to austenite. All these factors reduce the possibility for formation of undesirable structures such as martensite (slipped or twinned) in ICHAZ.

The FGHAZ, consisting of fine grains of mainly polygonal ferrite, is expected to have good toughness and fracture properties. The microstructure was mainly a result of not-so-high peak temperatures and inhibition of grain growth by precipitates in this sub-zone. The main sub-zone of concern is the CGHAZ, where considerable grain growth occurs and the final microstructure consists of large PAGS of lamellar martensitic or bainitic structures. In general, the fracture properties are related to packet size or the PAGS (which is very large in the CGHAZ) in such microstructures. Many researchers have found that low-carbon martensite (found in low heat-input CGHAZ) has better toughness than upper bainite (found in high heat-input CGHAZ) [1-4]). Increasing the heat input generally increases the impact transition temperature and decreases the toughness, especially in the case of addition of Mn (more than a basic level of ~1.3wt%), V and Nb [1]. On the other hand, too high a hardness increases the chance for cold cracking and hydrogen-induced cracking.

Therefore, in Grade 100 microalloyed steel, the nominal heat inputs of 1.5 and 2.5 kJ/mm are likely prone to formation of low-toughness bainitic structures in the CGHAZ and low-strength polygonal structures (softening) in the FGHAZ. The sample with a nominal heat input of 0.5 kJ/mm, although expected to have a higher toughness value than the other two weld samples both in CGHAZ and in FGHAZ, has the disadvantage of exhibiting too high a hardness value and a considerable amount of transformation twins in the CGHAZ. It can be speculated from the hardness traverses (Fig. 7-3), and the microstructural trends in weld samples with heat input values of 0.5, 1.5 and 2.5 kJ/mm, that a weld sample with a nominal heat input of 0.8–0.9 kJ/mm exhibits the best combination of strength and hardness. The microstructure in CGHAZ will likely be martensitic/bainitic (definitely not upper bainite) and the amount of twinning will likely be low (if any). The FGHAZ will likely have very fine (~1.2 μm) grains of polygonal ferrite and probably some bainitic ferrite. The hardness traverses in FGHAZ suggest a good match with the BM and the hardness traverses in CGHAZ suggest a slight overmatch in the CGHAZ (which is desirable). The maximum microhardness in the CGHAZ will likely be below ~350 (good for cold cracking concerns). However, microstructural examinations and more mechanical tests are needed.

9-2-4. Composition effects

As discussed in Section 7-2, precipitates are deleterious to toughness. Grade 100 steel showed a range of undesirable precipitates. Large TiN particles (2–8 μm) were essentially useless. Although they are stable in the CGHAZ and dissolve a little (15% maximum dissolution, as estimated in Section 5-4-1), they are so sparsely distributed that cannot effectively pin prior austenite grains in the CGHAZ. Reduction of N and/or Ti will reduce the amount of TiN that forms at high temperatures (in liquid and during solidification) and can result in a finer distribution of nitrides and carbonitrides. Nb level also seems to be too high in this steel. Thermodynamic analysis of precipitates, along with replica examinations, showed that large amounts of intermediate-size Nb-rich carbides (50–300 nm) form during reheating or cooling from 1200 to 1000°C, where they do not seem to play any major role during TMCP. Their presence in the BM not only plays no role in the grain refinement in the HAZ and no role in dispersion hardening in the BM or HAZ, but also is harmful for toughness. Basically, the literature review showed that it is the fine carbides (<50 nm) that act as grain growth controllers and contribute to the strength, and the optimum Ti level is ~0.015% [5, 6]. Even if a higher level of Ti is required for removing the N in solution, precipitate analysis showed that the Ti level in Grade 100 is over-stoichiometric with respect to N. Reduction of Nb will reduce the amount of intermediate size Nb-rich precipitates, and may increase the driving force for precipitation of fine VC in ferrite, which is supposed to have a significant contribution to strengthening without negative effects on toughness.

The carbon level in Grade 100 steel also appears to be high. Precipitate analysis showed at least 0.014%C (assuming all the Mo, Nb and V precipitate; Section 5-3-1) and up to 0.050% (chemical dissolution results; Section 5-3-2) will not be tied up by microalloying elements. The remaining carbon can form carbon-rich constituents (such as M/A particles and iron carbides) that are not good for toughness (Section 6-2). Reduction of carbon (e.g., to ~0.06%), compensated by an increase in cooling rate during accelerated cooling (up to ~35°Cs^{-1}), will likely maintain a fine grained bainitic microstructure, while leaving less or no extra carbon in the matrix. Even a microstructure of bainite plus martensite, formed as a result of increasing the accelerated cooling rate from 20°Cs^{-1} to 50°Cs^{-1} while reducing the carbon level to 0.06% (C.E.= 0.43), has shown better weldability than a fully bainitic microstructure with a carbon level of 0.07% (C.E.= 0.48) [5]. This is due to the reduction of carbon while maintaining the strength above 100 ksi (equivalent to ~690 MPa). Reduction of carbon may also decrease the amount of transformation twins that may form in the CGHAZ when the cooling rate is high. Increasing the heat input from 0.5 to 0.9 kJ/mm will have an additional contribution to the reduction of twinning in the CGHAZ.

9-3. Novel methods and achievements

In addition to the detailed precipitate analysis (in particular extensive TEM-replica examination) in the HAZ of a high-strength microalloyed steel (i.e., Grade 100 steel), which has not been previously carried out, the following novel achievements were made:

1) A method of weighting for estimation of the cooling rate in plates of intermediate thickness. Instrumented welding (equipped with embedded thermocouples) was very helpful for obtaining thermal parameters and characteristics (peak temperature profiles, heating rate, cooling rate, dwell time above a certain temperature) across the weld HAZ. Nevertheless, the thermal experiments were difficult. Theoretical analysis, on the other hand, only provided upper-bound and lower-bound solutions. The novel method presented here that used the information obtained from the weld HAZ width on an etched section, proved to be very useful and capable of saving a great deal of experimental work. The method of weighting provided cooling rate estimations very close to those obtained experimentally.

2) Improvement of weld precipitate dissolution analysis. The conversion of a typical weld thermal cycle (composed of a heating leg, dwell time around a peak temperature and a cooling leg) to an equivalent isothermal cycle (composed of a pair of effective peak temperature and effective time) made application of non-equilibrium solubility curves (suggested by Ashby and Easterling) for quantitative analysis of precipitate dissolution during the weld HAZ easier. This method resulted in determination of critical points across the HAZ where dissolution of several fractions of a precipitate compound (e.g., NbC) was just completed upon application of a weld thermal cycle with a particular heat input. Eventually these findings resulted in construction of *precipitate dissolution maps and profiles* for Grade 100 steel for a nominal heat input range of 0.5–2.5 kJ/mm.

3) Correction of volume fraction estimation by replicas. The model presented for replica preparation of metals, with particles of several size ranges, provides a lower bound correction for the volume fraction estimations obtained from the replicas. The general idea behind this model was not new and was found in earlier work. The application to a matrix with several size-groups of precipitates and the explanations presented in Section 5-5-3 can be considered as supplementary. For instance, taking into account, as well as calculations, the largest particles that *could* be on a replica rather than those *found* on a replica can result in volume fraction estimations that are an order of magnitude further smaller in high-strength microalloyed steels.

4) Application of replicas for systematic measurement of grain size. Conventional optical microscopy was found incapable of resolving the grain and sub-grain boundaries in the BM and the HAZ of high-strength microalloyed steels well. This can lead to an overestimation of grain size, if optical micrographs are used for grain-size measurements. Extraction replicas made excellent samples for grain-size measurements in the BM and HAZ of high-strength microalloyed steels with very fine grain structures. Taking advantage of magnifications of 1000–6000x in the low magnification mode of the TEM, and the high-resolution capability inherent to TEM, made better estimation of grain size possible. The grain sizes

obtained from replicas correlated well with hardness variations in the FGHAZ and BM for selected high-strength microalloyed steels.

9-4. Future work

Several topics can be recommended for future work:

1) Application of the method of weighting to the thermal analysis of welding of plates with special geometries. The Rosenthal equations were derived for bead-on-plate welding. For instance, in actual welding, two pieces of metals (or two edges of a deformed plate) may be bevelled and when close together form a groove (e.g., V shape). The change in geometry (variation in thickness) requires some modifications in the original theoretical equations. Nevertheless, the general idea behind the method of weighting should still apply to the modified equations for the special geometries.

2) Investigation to better define heat input parameters to include plate thickness properly (see Sections 4-3-2 and 4-3-6). Application of heat density instead of heat input can be another topic for investigation. Heat input does not reflect the intensity of the heat source (see Section 4-3-1).

3) To reach a general form of cooling time formulation, as suggested in Section 3-5-2, investigation of the effect of plate thickness on the cooling time is needed. This can be achieved by instrumented welding with a heat input of 0.5 kJ/mm and a plate with initial thickness of ~12 mm (a 3D situation). The plate can be milled down to thickness values of 10, 8, 6, 5, 4, 3, 2 and possibly 1 mm (2D situation).

4) Analysis of thermal stresses during welding. Thermal stresses not only affect transformation kinetics and products (e.g., effect transformation temperature and possibly twinning before or after transformation) but also affect the measured mechanical properties due to residual stresses (e.g., hardness measurements). Residual stresses also affect the properties of the weld and HAZ (e.g., SCC or HIC).

5) Quantitative examination of precipitates with replicas. Intermediate-size microalloy precipitates were found to have various volume fractions from section to section. The variation in volume fraction appeared to be much higher than what can be attributed to replica efficiency. The reason was attributed to segregation during solidification. Systematic sectioning from different locations in the thickness of the plate and along the transverse/longitudinal directions of the plate is recommended for a reliable calculation. Increasing the number of replica samples (or even samples for chemical dissolution) prepared systematically from different locations will also result in a more confident assessment of size distribution and volume fraction of fine precipitates.

6) Examination of precipitate states at different stages of TMCP. This can be carried out by interruption of TMCP (quenching) on simulated samples (e.g., simulation by Gleeble). That will provide information on how much of the different types of precipitates (Section 5-2-4) will form at various stages.

7) Sub-critical annealing at temperatures from 100 to 700°C to reveal many microstructural and property characteristics (including the contribution of different strengthening components). Changes in the amount of cementite, due to tempering of the saturated bainitic structure, changes in microalloy precipitate size distribution, hardening/softening effects due to recovery, recrystallization, strain aging, etc. can be examined at different aging temperatures. Also, stain-aging tests can show if the interaction between the retained interstitials (mainly carbon in the case of Grade 100 steel) and dislocations can affect the mechanical properties of Grade 100 steel. It is also necessary to rule out the contribution of strain-aging during levelling, where the increased measured strength has been attributed to further precipitation hardening in ferrite [7].

8) Estimation of tensile properties through hardness measurements (Sections 7-3-6 and 7-5-6) is a promising approach applicable to the small regions in the HAZ. Refinement of the theoretical equations and/or careful and more extensive experiments are recommended for future work. Miniature mechanical tests on actual weld samples are likely another suitable alternative to conventional mechanical tests on simulated samples.

9) Nano-hardness contours should be established at different HAZ sub-regions and for different weld heat inputs. The nano-hardness contours along with SEM (scanning electron microscopy) images from the same region before and after the nano-hardness tests can provide more information about the distribution of microstructural phases and their properties.

10) HAZ microstructure/property examination for a range of heat inputs between 0.7 and 1.0 kJ/mm. Thermal cycle characteristics, microstructures and properties of the 1.5 and 2.5 kJ/mm weld samples were very close to each other, but very different from those of 0.5 kJ/mm weld sample. There seems to be a gap between the trend of changes as a function of heat input, which can be filled by examination of weld samples with heat inputs of 0.7–1.0 kJ/mm.

References

[1] Otterberg, R., Sandstrom, R., and Sandberg, A., 1980, "Influence of Widmanstatten Ferrite on Mechanical Properties of Microalloyed Steels," Met. Technol., **7** (10), pp. 397-408.

[2] Akselsen, O. M., Grong, O., and Rorvik, G., 1990, "Embrittlement Phenomena in the Grain Coarsened Heat Affected Zone of Low Carbon Microalloyed Steels," Scandinavian Journal of Metallurgy (Denmark), **19** (6), pp. 258-264.

[3] Bhole, S. D., and Billingham, J., 1983, "Effect of Heat Input on HAZ Toughness in HSLA Steels," Met. Technol., **10** (9), pp. 363-367.

[4] Smith, N. J., Mcgrath, J. T., Bowker, J. T., and Gianetto, J. A., 1990, "Microstructure and Mechanical Property Relationships in HSLA 80 and HSLA 100 Weldments," *Proc., The Metallurgy, Welding, and Qualification of Microalloyed (HSLA) Steel Weldments*, American Welding Society, pp. 306-324.

[5] Hulka, K., and Heisterkamp, F., 1998, "Development Trends in HSLA Steels for Welded Constructions," *Proc., Microalloying in Steels*, Materials Science Forum (Switzerland), **284-286**, pp. 343-350.

[6] Dolby, R. E., 1983, "Advances in Welding Metallurgy of Steel," Metals Technology, **10** (9), pp. 349-362.

[7] Bai, D. Q., and Asante, J., 2003, "Precipitation Strengthening in Low Carbon Microalloyed Steels," *Proc., Conference of Metallurgists 2003, The international symposium on transformation and deformation mechanisms in advanced high-strength steels*, M. Militzer, and W.J. Poole, eds., Metallurgical Society of the Canadian Institute of Mining, Metallurgy and Petroleum, pp. 235-244.